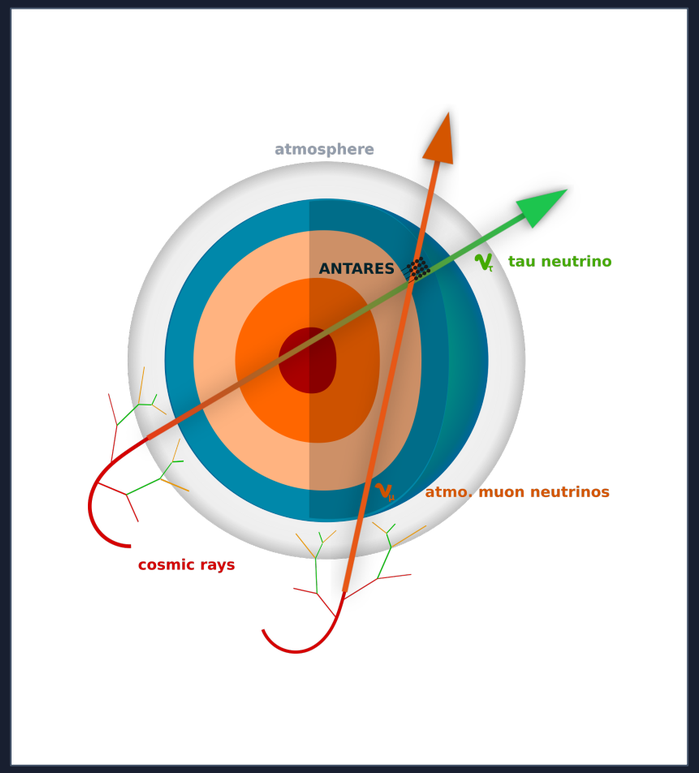

An illustration of the phenomenon of *Neutrino Oscillations*, described in this thesis. Cosmic rays impinge the upper atmosphere of the Earth leading to the creation of final state muon and electron neutrinos. The muon neutrino transmutes into a tau neutrino while traversing the Earth before being detected at ANTARES. The detector comprises an array of photomultiplier tubes to detect photons from the Cherenkov light emitted from the passage of charged particles created in neutrino interactions in sea water. Illustration by the author.

2021

Neutrinos beneath the waves

N. R. Khan Chowdhury

DEPARTAMENT DE FÍSICA ATÒMICA, MOLECULAR I NUCLEAR
INSTITUTO DE FÍSICA CORPUSCULAR

DOCTORAT EN FÍSICA

VNIVERSITAT DE VALÈNCIA

Search for Neutrino Non-Standard Interactions with ANTARES and KM3NeT-ORCA

Author:
Nafis Rezwan KHAN CHOWDHURY

Supervisors:
Dr. Juan de Dios ZORNOZA GÓMEZ
Dr. Sergio NAVAS CONCHA

Valencia, 2021

DOCTORAT EN FÍSICA

Search for Neutrino Non-Standard Interactions with ANTARES and KM3NeT-ORCA

Author:
Nafis Rezwan KHAN CHOWDHURY

Supervisors:
Dr. Juan de Dios ZORNOZA GÓMEZ
Dr. Sergio NAVAS CONCHA

A thesis submitted in partial fulfillment of the requirements for the degree of

Doctor of Philosophy

in the

Departamento de Física Atómica, Molecular y Nuclear
Instituto de Física Corpuscular (UV – CSIC)

València, April 2021

Title:
Search for Neutrino Non-Standard Interactions with ANTARES and KM3NeT-ORCA

Author:
Nafis Rezwan KHAN CHOWDHURY
Departamento de Física Atómica, Molecular y Nuclear
Instituto de Física Corpuscular (IFIC)
Universitat de València, Spain

Supervisors:
Dr. Juan de Dios ZORNOZA GÓMEZ
Departamento de Física Atómica, Molecular y Nuclear
Instituto de Física Corpuscular (IFIC)
Universitat de València, Spain
and
Dr. Sergio NAVAS CONCHA
Departamento de Física Teórica y del Cosmos
Facultad de Ciencias
Universidad de Granada, Spain

Cover image: An artist's impression of neutrino oscillations, by the author.

This research has been carried out at Instituto de Física Corpuscular, IFIC, Valencia, which is a joint centre of research between the Spanish Research Council (Consejo Superior de Investigaciones Científicas, CSIC) and the University of Valencia.

Typeset by the author using the Thesis-LaTeX class developed by Vel.
https://www.latextemplates.com/template/masters-doctoral-thesis

Nafis Rezwan KHAN CHOWDHURY has defended this dissertation on XX, May, 2021.
The dissertation was reviewed and approved* by the following committee:

Name: **Dr. João A. B. COELHO**
Designation: Associate Professor
Affiliation: Université Paris-Saclay, CNRS/IN2P3
Head of Committee

Name: **Dr. Mariam Amparo TORTOLA BAIXAULI**
Designation: Associate Professor,
Affiliation: Universitat de València, IFIC, CSIC
Secretary of Committee

Name: **Dr. Mathieu PERRIN TERRIN**
Designation: Associate Professor,
Affiliation: Aix Marseille University, CPPM, CNRS/IN2P3
Member of Committee

*The signatures are on the file in the Doctoral School.

Dr. Juan de Dios ZORNOZA GÓMEZ, profesor contratado doctor en el Departamento de Física Atómica, Molecular y Nuclear de la Facultad de Física de la Universidad de Valencia, y **Dr. Sergio NAVAS CONCHA**, catedrático de Universidad en el Departamento de Física Teórica y del Cosmos de la Universidad de Granada,

CERTIFICAN,

Que la presente memoria, "***Search for Neutrino Non-Standard Interactions with ANTARES and KM3NeT-ORCA***", ha sido realizada bajo su dirección en el Instituto de Física Corpuscular (Centro Mixto Universidad de Valencia - CSIC) por **Nafis Rezwan KHAN CHOWDHURY** constituye su Tesis Doctoral en el Departamento de Física Atómica Molecular y Nuclear de la Universidad de Valencia para optar al grado de Doctor en Física.

Y para que conste, en cumplimiento de la legislación vigente, firman el presente certificado en Paterna, el XY de octubre de 2020.

Dr. Juan de Dios ZORNOZA GÓMEZ

Dr. Sergio NAVAS CONCHA

*Las firmas están en el archivo de la Escuela de Doctorat.

To my mother and deceased father . . .

"Dear Radioactive Ladies and Gentlemen,

... I have hit upon a desperate remedy to save the "exchange theorem" of statistics and the law of conservation of energy. Namely, the possibility that in the nuclei there could exist electrically neutral particles, which I will call "neutrons", that have spin 1/2 and obey the exclusion principle and that further differ from light quanta in that they do not travel with the velocity of light.....

The continuous beta spectrum would then make sense with the assumption that in beta decay, in addition to the electron, a neutron is emitted such that the sum of the energies of neutron and electron is constant....

But so far I do not dare to publish anything about this idea, and trustfully turn first to you, dear radioactive ones, with the question of how likely it is to find experimental evidence for such a neutron...

I admit that my remedy may seem almost improbable because one probably would have seen those neutrons, if they exist, for a long time. But nothing ventured, nothing gained...

Thus, dear radioactive ones, scrutinize and judge."

Wolfgang Pauli [1],

December 4, 1930.

Abstract

Departamento de Física Atómica, Molecular y Nuclear

Instituto de Física Corpuscular (UV – CSIC)

UNIVERSITAT DE VALÈNCIA

Search for Neutrino Non-Standard Interactions with ANTARES and KM3NeT-ORCA

by Nafis Rezwan KHAN CHOWDHURY

The ANTARES neutrino telescope and its next-generation successor, KM3NeT, located in the abyss of the Mediterranean Sea, have been designed to study neutrinos from a variety of sources over a wide range of energies and baselines. One of the primary goals of the experiments is to measure the Earth-matter effects stemming from the energy and zenith angle dependence of the atmospheric neutrinos in the multi-GeV range. The study of atmospheric neutrinos is instrumental in addressing some of the outstanding issues in neutrino oscillation physics, especially the fundamental question of the neutrino mass ordering, as well as probing new physics scenarios beyond the Standard Model.

In this thesis, we exploit the data of ANTARES and explore the physics potential of KM3NeT-ORCA (ORCA being the low energy component of KM3NeT) to measure the sub-dominant effects in the atmospheric neutrino oscillations vis-à-vis non-standard neutrino interactions (NSIs). The Monte Carlo simulation framework, which comprises the simulation of neutrino interactions, particle generation and light propagation, event selection and reconstruction, as well as the statistical treatment of data and systematic uncertainties has been described in great detail. We present a likelihood search for NSIs with 10 years of atmospheric muon-neutrino data recorded with ANTARES and explore sensitivity projections for ORCA based on realistic detector simulations. Moreover, we outline the impact of NSIs on the discovery potential of ORCA towards the neutrino mass ordering. In addition, the sensitivity of ORCA towards the octant of θ_{23} has been reported. Remarkably, the bounds obtained with ANTARES excludes hitherto allowed regions from current experimental data, and represent the worldwide best limit in the $\mu - \tau$ sector up to date.

Contents

Introduction

> "Part of the blame, or the glory, they say, may belong to the flimsiest, quirkiest and most elusive elements of nature: neutrinos. These ghostly subatomic particles stream from the Big Bang, the Sun, exploding stars and other cosmic catastrophes, flooding the universe and slipping through walls and our bodies by the billions every second, like moonlight through a screen door."
>
> — DENNIS OVERBYE,
> *The New York Times, April 15, 2020.*

This thesis details a study of the statistical significance with which ANTARES is, and KM3NeT-ORCA (ORCA in what follows) will be, able to determine a signal from non-standard interactions of neutrinos and discusses its phenomenological consequences on the neutrino mass ordering measurement at ORCA. The document is organised as follows:

Chapter 1 introduces the theoretical background behind neutrino masses, mixing and oscillations with special emphasis on neutrino non-standard interactions (NSIs).

Chapter 2 discusses the production of atmospheric neutrinos, their relevant interactions in sea water, detection techniques and an overview of the current detectors. The study of time calibration of optical devices in KM3NeT is included.

Chapter 3 discusses the MC simulation chain and event reconstruction algorithms in ANTARES and ORCA. The overall scheme of computation of events is presented.

Chapter 4 presents the results of the search for NSIs with 10 years of ANTARES data as well as outlines the future sensitivities towards NSIs at ORCA. The impact of systematic uncertainties and errors on oscillations parameters are investigated.

Chapter 5 explores the phenomenological implications of NSIs on the neutrino mass ordering (NMO) resolution at ORCA. The effects of NSIs on the NMO sensitivity have been quantified.

In Chapter 6, we fall back to the scenario of standard three-flavour neutrino oscillations by switching off NSIs and estimate the sensitivity of ORCA towards the resolution of the θ_{23} octant.

Finally, an overview of the thesis is presented in the form of a Summary.

1 Neutrinos in the Standard Model and Beyond

"Your theory is crazy, but it's not crazy enough to be true."

— NIELS BOHR

Contents

This Chapter aims to give a basic overview on the phenomenon of neutrino oscillations, which can only be explained by adding mass to neutrinos. First, we introduce the framework of standard neutrino-matter interactions in Sec. 1.1. Then, the mathematical formulation behind the simple idea of oscillations is presented in Sec. 1.2, extrapolated to cases of neutrino propagation in vacuum and special cases of neutrinos passing through matter. Furthermore, one of the exotic physics scenarios, namely, non-standard neutrino-matter interactions (NSIs) during neutrino propagation through matter, which forms the heart of this thesis, is introduced briefly in Sec. 1.3. The impact of standard as well as non-standard neutrino-matter interactions on neutrino oscillation probabilities in vacuum are estimated. Finally existing bounds on non-standard interactions model parameters are reported.

1.1 Electroweak Interactions

The Standard Model (SM) is a Yang–Mills quantum field theory [2] based on the non-Abelian gauge symmetry group $SU(3)_C \otimes SU(2)_L \otimes U(1)_Y$. The group $SU(3)_C$

describes the strong interaction mediated by eight gluons ($g^i_\mu, i \in \{1,...,8\}$) and the corresponding quantum charges are called *colours*. The symmetry group $SU(2)_L \otimes U(1)_Y$ describes the electroweak interaction, mediated by four bosons ($W^i_\mu, i \in \{1,2,3\}$ and B_μ), whose corresponding quantum charges are called *weak isospins* ($\vec{I}$) and *weak hypercharge* (Y). The electroweak group is broken spontaneously [3, 4, 5] by the Brout-Englert-Higgs mechanism [6, 7]. The remaining symmetry, the Abelian $U(1)_{EM}$, describes the electromagnetic interaction, whose charge, Q, is given by the Gell–Mann–Nishijima relation [8, 9]:

$$Q = I_3 + \frac{Y}{2}, \tag{1.1}$$

where I_3 is the third component of the weak isospin and Y, the weak hypercharge.

After spontaneous symmetry breaking, four gauge bosons (three massive, W^+, W^- and Z^0, and one massless, γ) appear as a combination of the original W^i_μ and B_μ, which mediate the electroweak interactions:

$$W^\pm_\mu = \frac{1}{\sqrt{2}}(W^1_\mu \mp iW^2_\mu), \tag{1.2}$$

and,

$$\begin{bmatrix} W^3_\mu \\ B_\mu \end{bmatrix} = \begin{bmatrix} \cos\theta_W & \sin\theta_W \\ -\sin\theta_W & \cos\theta_W \end{bmatrix} \begin{bmatrix} Z_\mu \\ A_\mu \end{bmatrix}, \tag{1.3}$$

where $W^\pm_\mu$, Z_μ and A_μ represent the fields of the $W^\pm$, Z^0 and γ bosons, and θ_W ($= \arcsin(\frac{e}{g})$) is the weak or Weinberg angle with e being the electromagnetic charge and g being the weak coupling constant.

The lepton sector of the SM comprises three generations of left-handed doublets ($(l_{\alpha L}, \nu_{\alpha L})^\intercal$) and right-handed singlets[1] ($l_{\alpha R}$), with $\alpha = e, \mu$ or τ. The electroweak interactions among the particles of the leptonic sector is given by the following Lagrangian density $\mathcal{L}$:

$$\begin{aligned} \mathcal{L} &= eA_\mu \bar{l}_\alpha \gamma^\mu l_\alpha && \text{(EM interaction)} \\ &- \frac{g}{\sqrt{2}}[W^+_\mu \bar{\nu}_{\alpha L}\gamma^\mu l_{\alpha L} + W^-_\mu \bar{l}_{\alpha L}\gamma^\mu \nu_{\alpha L}] && \text{(CC weak interaction)} \\ &- \frac{g}{2\cos\theta_W}[Z_\mu(\bar{\nu}_{\alpha L}\gamma^\mu \nu_{\alpha L} - \bar{l}_{\alpha L}\gamma^\mu l_{\alpha L} - sin^2\theta_W \bar{l}_\alpha \gamma^\mu l_\alpha)], && \text{(NC weak interaction)} \end{aligned} \tag{1.4}$$

where $l_\alpha (= l_{\alpha L} + l_{\alpha R})$, ν_α are the charged lepton and neutrino fields for flavour α respectively and γ^i are the Dirac matrices. CC and NC stand for charged current (CC) and neutral current (NC) interactions, respectively (illustrated in Sec. 1.2.3).

1.2 Neutrino Mass, Mixing and Oscillations

The discovery of oscillations between neutrino families[2] has a long history full of experimental and theoretical insights. We give here a brief and necessarily limited account of how the story developed.

[1] The SM does not include right-handed neutrinos, $\nu_{\alpha R}$.

[2] The terms "flavours", "types", "generations" and "species" will be used interchangeably in this thesis.

The idea of neutrino oscillations was first proposed in 1957 by B. Pontecorvo [10]. He suggested that, in a way analogous to the $K^0 - \overline{K}^0$ oscillation phenomenon proposed by Gell-Mann and Pais [11], neutrinos and antineutrinos could oscillate. In 1962, Lederman, Schwartz and Steinberger showed experimentally that the neutrino associated with the muon was different than the one associated with the electron [12]. At around the same time, Maki, Nakagawa and Sakata discussed the possible "transmutation" between ν_e and ν_μ [13]. In 1967 Pontecorvo considered the possibility of oscillations between flavours [14] and discussed some astronomical implications, for instance that the flux at the Earth of electron neutrinos coming from the Sun could be smaller than the theoretical expectations.

In 1965, R. Davies started building the famous "Homestake experiment" to detect solar neutrinos. It began to take data in 1969 and already the first results indicated a deficit of neutrinos with respect to the theoretical calculations, deficit which was confirmed by subsequent results. It took some time to convince the scientific community that the experimental results and the theoretical calculations were correct within the known uncertainties [15, 16] and that there was a discrepancy, which was then referred to as the "solar neutrino problem". Other experiments such as GALEX/GNO [17], SAGE [18, 19], Kamiokande [20] and Superkamiokande [21] confirmed that the flux of neutrinos was lower than expected. All these experiments detected only electron neutrinos, which are the only type of neutrinos produced by the solar nuclear reactions.

The "solar neutrino problem" remained unsolved during a long time and although a variety of possible theoretical explanations were put forward (literally dozens of them). One of the most favoured ones was that electron neutrinos changed flavour during their flight to Earth, i.e. that oscillations among families were taking place.

During the 70s and 80s the theory underlying neutrino oscillations was further developed and a variety of theoretical predictions and experimental projects were proposed [22, 23]. In 1977, Wolfenstein pointed out that the oscillation pattern and parameters could change when neutrinos traversed matter [24]. Mikheyev and Smirnov then showed that under certain circumstances oscillations could be resonantly enhanced when neutrinos traversed matter [25, 26]. This so-called MSW effect or, in general, *matter effects*, have important consequences in the case of neutrinos from the Sun.

In 1984, H. H. Chen pointed out that using deuterium as a target, electron neutrinos could be detected in charge current interactions and the rest of families in neutral current interactions [27]. The possibility to measure electron neutrinos on the one hand, and all neutrino types on the other, could give invaluable information about the source of the solar neutrino deficit and prompted the proposal to build the SNO experiment. The results of SNO since 2001, indicated that the total flux of neutrinos of all families was in agreement with the theoretical expectations and that the oscillation hypothesis was the best explanation for the electron neutrino deficit [28, 29].

Before that, in 1998, the Super-Kamiokande experiment (Super-K in what follows) reported that the ratio between muon and electron neutrinos (N_{ν_μ}/N_{ν_e}) coming from atmospheric showers induced by cosmic rays was smaller than predicted [30]. This had already been observed by other experiments, such as Kamiokande [31] and IMB [32], but Super-K not only observed the effect with higher statistics, but also showed that the deficit depended on the neutrino's path length and energy in a way compatible with what was expected from neutrino oscillations.

The 2015 Nobel prize in Physics was awarded to A. McDonald (SNO) and T. Kajita (Super-K) "for the discovery of neutrino oscillations, which shows that neutrinos have mass".

The oscillation hypothesis was independently confirmed in experiments that used neutrinos produced in accelerators, such as K2K (KEK to Kamioka) [33], MINOS (Main Injector Neutrinos Oscillations) [34] and T2K (Tokai to Kamioka) [35]. In these experiments the disappearance of muon neutrinos in the beam produced in the laboratory was observed at long distances and provided better determinations of the parameters that determine the oscillations, the mixing angles and the squared mass differences (see next subsections).

Similarly, experiments using neutrinos from nuclear reactors served to pin down the oscillation parameters. The Kamioka Liquid-scintillator Antineutrino Detector experiment (KamLAND) using antineutinos from long distance reactors strongly favoured the large solar mixing angle solution [36] and provided an excellent determination of the solar squared mas difference [37].

In 2012, the Double Chooz nuclear reactor experiment disfavoured a null value for the θ_{13} mixing angle [38] and two other reactor experiments, Daya Bay [39] and RENO [40], reported measurements of θ_{13} different from zero with 5σ significance.

The oscillation parameters have been determined since then with higher precision in a variety of experiments (for reviews see for instance [41]) and new experiments are being proposed for further study of neutrinos properties.

Neutrino oscillations imply that at least two neutrino generations have mass, which in turn leads to a variety of issues that hint to physics beyond the SM. The absence of right handed neutrinos in the SM prevents to simply include Dirac mass terms in the SM Lagrangian[3]. If neutrinos are Majorana fermions, the generation of mass through the Higgs mechanism is only possible through terms that turn the model non-renormalizable. Moreover, the smallness of the neutrino masses compared to those of other SM fermions hints to high energy scales. All these questions exceed the scope of this introduction (for details look into [43, 44, 45, 46]) and we will limit ourselves in the following to discuss the phenomenology of neutrino mixing (of masses) and oscillations (of flavours) which are relevant to our work.

1.2.1 Neutrino Oscillations: n Flavours

Neutrinos $\{\nu_\alpha\}$ (α representing the flavour family) are produced in charged current (CC) and neutral current (NC) weak interaction processes. Each (neutrino) flavour eigenstate ν_α is a quantum superposition of multiple mass eigenstates $\{\nu_i\}$ with masses m_i. Oscillations are generated due to interference between different massive neutrinos

[3] Attempts to accommodate non-zero neutrino masses in an *extended* SM have been made by placing a Dirac mass term *"by hand"* with a right-handed neutrino field ($\nu_{\alpha R}$), which has no gauge interactions. However, this leads to the problem of large mass difference (eV – GeV) and huge disparities in the values of the Yukawa coupling ($10^{-12} - 10^{-2}$) for lepton masses within each generation (e, μ, τ). To get around this problem, one can introduce a Majorana mass term ($m_R[\frac{1}{2}\overline{\nu^C}_{\alpha R}\nu_{\alpha R} + \frac{1}{2}\overline{\nu}_{\alpha R}\nu^C_{\alpha R}]$ where $\nu^C_\alpha = \mathcal{C}\nu^\intercal_\alpha$), where $\nu_{\alpha R}$ is singlet under $SU(2)$ with weak hypercharge 0. Majorana mass term is invariant under SM gauge transformation. The introduction of a new Dirac-Majorana mass term gives the leverage to choose one heavy neutrino, predominantly $\nu_{\alpha R}$ with mass m_R at a scale $\mathcal{O}(10^{15}$ GeV) high above the electroweak scale $\mathcal{O}(10^2$ GeV), thereby producing a light neutrino, predominantly $\nu_{\alpha L}$ with mass $\frac{m_D^2}{m_R}$. This scheme of suppression of mass scale (thus providing a natural description for the lightness of the left-handed neutrinos) is known as type I Seesaw mechanism [42].

$\{\nu_i\}$, which are produced and detected coherently as $\{\nu_\alpha\}$ with small mass differences. This implies that when a neutrino of a certain flavour (say ν_α) is produced in a weak interaction process and propagates through space (or medium), each of the mass eigenstates $\{\nu_i\}$ travel with different speed leading to a phase lag between them. After a certain distance, the composition of the mass eigenstates is different from the initial state. The final composition of mass eigenstates might constitute a neutrino of completely different flavour $\{\nu_\beta : \beta \neq \alpha\}$. This process of transmutation of flavour from a ν_α into a ν_β is called *neutrino oscillation*. It is basically analogous to the quantum mechanics of mixed states, which itself is equivalent to the classical theory of coupled oscillators. Let us discuss the theory of neutrino oscillations in a quantitative way in the following.

In the standard theory of neutrino oscillations[4] with n[5] number of light neutrino generations, a neutrino flavour eigenstate can be expressed as a linear superposition of n mass eigenstates (or the other way round):

$$|\nu_\alpha\rangle = \sum_{i=1}^{n} U^*_{\alpha i}|\nu_i\rangle, \quad (or\, |\nu_i\rangle = \sum_{\alpha} U_{\alpha i}|\nu_\alpha\rangle,) \tag{1.5}$$

where $U_{\alpha i}$ is the mixing matrix, which relates the mass basis $\{\nu_i\}$ (eigenstates of the Hamiltonian) to the flavour basis $\{\nu_\alpha\}$ (eigenstates of the gauge group). $U_{\alpha i}$ satisfies the following conditions:

$$U^\dagger U = \mathbb{I}_{n\times n}, \quad \sum_i U_{\alpha i}U^*_{\beta i} = \delta_{\alpha\beta}, \quad \sum_\alpha U_{\alpha i}U^*_{\alpha j} = \delta_{ij}. \tag{1.6}$$

The Latin indices $i, j = 1, 2, 3...$ correspond to the mass eigenstates, while the Greek indices $\alpha, \beta = e, \mu, \tau....$ correspond to the flavour eigenstates.

The amplitude of $|\nu_\alpha\rangle \to |\nu_\beta\rangle$ transition as a function of time is given by

$$A_{\nu_\alpha\to\nu_\beta}(t) = \langle\nu_\alpha|\nu_\beta\rangle_t = \sum_i U^*_{\alpha i}U_{\beta i}e^{-iE_i t}. \tag{1.7}$$

The transition probability then reads

$$P_{\nu_\alpha\to\nu_\beta}(t) = |A_{|\nu_\alpha\rangle\to|\nu_\beta\rangle}(t)|^2 = \sum_{i,j} U^*_{\alpha i}U_{\beta i}U_{\alpha j}U^*_{\beta j}e^{-(E_i-E_j)t}. \tag{1.8}$$

For ultra relativistic neutrinos ($E_i \simeq P_i + \frac{m_i^2}{2E}$ in the limit $m_i^2 \ll P_i$), assuming same momentum for all massive neutrino components ($P_i = P \;\forall i$) and using light-ray approximation ($t \simeq L\,(c = 1)$), the transition probability can be approximated by [47, 49]

$$\begin{aligned} P_{\nu_\alpha\to\nu_\beta}(L) = \delta_{\alpha\beta} &- 4\sum_{i>j}\mathbb{R}e[U^*_{\alpha i}U_{\beta i}U_{\alpha j}U^*_{\beta j}]\sin^2\phi_{ij} \\ &\pm 2\sum_{i>j}\mathbb{I}m[U^*_{\alpha i}U_{\beta i}U_{\alpha j}U^*_{\beta j}]\sin 2\phi_{ij}, \end{aligned} \tag{1.9}$$

[4] For a concrete derivation, see [47].

[5] Precision measurement of the decay width of Z at LEP [48] indicate that there are three generation of neutrinos, (accompanying their charged lepton partners) which take part in weak interactions.

where

$$\phi_{ij} = \Delta m^2_{ij} \frac{L}{4E_\nu} \simeq 1.267 \Delta m^2_{ij} \frac{L}{E_\nu} \frac{[\text{eV}^2][\text{km}]}{[\text{GeV}]}. \tag{1.10}$$

The coefficients of the massive neutrino components of flavour antineutrinos are simply related to the corresponding coefficients of massive neutrino components of flavour neutrinos by complex conjugation $U_{\alpha i} \rightarrow U^*_{\alpha i}$. Hence, the antineutrino oscillation probabilities differ from the corresponding neutrino oscillation probabilities only in the sign of the terms depending on the imaginary parts of the quartic products of the mixing matrix elements. The imaginary part in Eq. 27 depends on whether neutrinos $(+)$ or antineutrinos $(-)$ are considered.

Salient features regarding the expression of oscillation probabilities (Eq. 27) are summed below.

- Non-zero oscillation probabilities not only necessitate unequal neutrino masses ($m_i \neq m_j \, \forall \, i \neq j$), but also non-trivial mixing (i.e. non-zero off-diagonal mixing elements).
- The oscillation probabilities depend on the quartic product of mixing matrix elements $U_{\alpha i}$, which determines the amplitude of oscillations and mass-squared differences Δm^2_{ij}, which decides the phase (both set by Nature). The oscillation probabilities also depend on the distance between source and detector L and on the neutrino energy E (both set by experiments).
- At $L \gg \frac{2E}{\Delta m^2_{ij}}$, the oscillatory term is averaged out leading to a constant conversion.
- The mass-squared difference sits inside an even function $\sin^2(\phi_{ij})$ in the real term, thereby making it insensitive to its sign, whereas the imaginary part contains a component $\sin(2\phi_{ij})$ which is sensitive to the sign of the mass-squared difference.
- Eq. 24 translates to conservation of total probability:
  a) The sum of the transition probability from a flavour ν_α to all other flavours ν_β (including $\beta = \alpha$) is equal to unity:

$$\sum_\beta P_{\nu_\alpha \rightarrow \nu_\beta} = 1. \tag{1.11}$$

  b) The sum of the transition probability from any flavour ν_α (including $\alpha = \beta$) to a flavour ν_β is equal to unity:

$$\sum_\alpha P_{\nu_\alpha \rightarrow \nu_\beta} = 1. \tag{1.12}$$

In an n-flavour neutrino scenario, there are $n(n-1)/2$ mixing angles, $(n-1)(n-2)/2$ Dirac phases, additional $n-1$ Majorana phases (if neutrinos are Majorana-type particles) and $n-1$ mass squared differences. However, oscillation probabilities are invariant regardless of whether neutrinos are Dirac- or Majorana-type particles.

The oscillation probabilities with $\alpha \neq \beta$ are called *transition probabilities* (referring to appearance channels) and the oscillation probabilities with $\alpha = \beta$ are called *survival probabilities* (referring to disappearance channels).

1.2.2 Neutrino Oscillations in Vacuum

In the standard oscillation framework involving three active light neutrino species $\{\nu_\alpha\}$ with $\alpha = e, \mu, \tau$, the 3×3 unitary matrix takes the form:

$$\begin{bmatrix} \nu_e \\ \nu_\mu \\ \nu_\tau \end{bmatrix} = \begin{bmatrix} U_{e1} & U_{e2} & U_{e3} \\ U_{\mu 1} & U_{\mu 2} & U_{\mu 3} \\ U_{\tau 1} & U_{\tau 2} & U_{\tau 3} \end{bmatrix} \begin{bmatrix} \nu_1 \\ \nu_2 \\ \nu_3 \end{bmatrix} \tag{1.13}$$

The unitary conditions in Eq. 24 translate into normalisations of three row and three column elements:

$$|U_{\alpha 1}|^2 + |U_{\alpha 2}|^2 + |U_{\alpha 3}|^2 = 1; \quad (\alpha = e, \mu, \tau), \tag{1.14}$$

$$|U_{ei}|^2 + |U_{\mu i}|^2 + |U_{\tau i}|^2 = 1; \quad (i = 1, 2, 3), \tag{1.15}$$

and six angle closures:

$$|U_{\alpha 1} U^*_{\beta 1} + U_{\alpha 2} U^*_{\beta 2} + U_{\alpha 3} U^*_{\beta 3}|^2 = 0; \quad (\alpha, \beta) = ((e, \mu), (e, \tau), (\mu, \tau), \tag{1.16}$$

$$|U_{ei} U^*_{ej} + U_{\mu i} U^*_{\mu j} + U_{\tau i} U^*_{\tau j}|^2 = 0; \quad (i, j) = (1, 2), (1, 3), (2, 3). \tag{1.17}$$

For three generations, the PMNS mixing matrix can be conveniently parameterised by 3 mixing angles $(\theta_{12}, \theta_{13}, \theta_{23})$, one Dirac CP phase (δ_{CP}) and 2 Majorana phases (γ_1, γ_2) as

$$\begin{aligned} U_{PMNS} &= O(\theta_{23}) O(\theta_{23}, \delta_{13}) O(\theta_{12}) O_M(\gamma_1, \gamma_2) \\ &= \begin{bmatrix} 1 & 0 & 0 \\ 0 & c_{23} & s_{23} \\ 0 & -s_{23} & c_{23} \end{bmatrix} \begin{bmatrix} c_{13} & o & s_{13} e^{-i\delta_{CP}} \\ 0 & 1 & 0 \\ -s_{13} e^{-i\delta_{CP}} & 0 & c_{13} \end{bmatrix} \begin{bmatrix} c_{12} & s_{12} & 0 \\ -s_{12} & c_{12} & 0 \\ 0 & 0 & 1 \end{bmatrix} \begin{bmatrix} e^{i\gamma_1} & 0 & 0 \\ 0 & e^{i\gamma_2} & 0 \\ 0 & 0 & 1 \end{bmatrix} \\ &= \begin{bmatrix} c_{12} c_{13} & s_{12} c_{13} & s_{13} e^{-\imath \delta_{CP}} \\ -s_{12} c_{23} - c_{12} s_{23} s_{13} e^{\imath \delta_{CP}} & c_{12} c_{23} - s_{12} s_{23} s_{13} e^{\imath \delta_{CP}} & s_{23} c_{13} \\ s_{12} s_{23} - c_{12} c_{23} s_{13} e^{\imath \delta_{CP}} & -c_{12} s_{23} - s_{12} c_{23} s_{13} e^{\imath \delta_{CP}} & c_{23} c_{13} \end{bmatrix} diag(e^{i\gamma_1}, e^{i\gamma_2}, 1), \end{aligned} \tag{1.18}$$

where $s_{ij} \equiv \sin\theta_{ij}$, $c_{ij} \equiv \cos\theta_{ij}$. Majorana phases are inaccessible to oscillations, so we drop them.

The oscillation probabilities for three generations can be obtained from Eq. 27, taking into account that the Latin indices run from 1 to 3:

$$\begin{aligned} P_{\nu_\alpha \to \nu_\beta}(L) = \delta_{\alpha\beta} &- 4 \sum_{i>j=1}^{3} \mathbb{R}e[U^*_{\alpha i} U_{\beta i} U_{\alpha j} U^*_{\beta j}] \sin^2(\Delta m^2_{ij} \frac{L}{4E}) \\ &\pm 2 \sum_{i>j=1}^{3} \mathbb{I}m[U^*_{\alpha i} U_{\beta i} U_{\alpha j} U^*_{\beta j}] \sin(\Delta m^2_{ij} \frac{L}{2E}). \end{aligned} \tag{1.19}$$

For three neutrino states, ν_1, ν_2, ν_3 with masses m_1, m_2, m_3, there are two unique mass-squared differences Δm^2_{21} and Δm^2_{31} $(\Delta m^2_{21} + \Delta m^2_{32} + \Delta m^2_{13} = 0)$. The sign of Δm^2_{21} is known to be positive from solar neutrino experiments [29]. Depending on the sign of the mass-squared splitting Δm^2_{31}, the relative mass spectrum of neutrinos can have two possible scenarios: Normal Ordering (NO) with $(m_3 > m_2 > m_1)$ or Inverted Ordering (IO) with $(m_2 > m_1 > m_3)$. The two scenarios are nicely represented in Fig. 1.1.

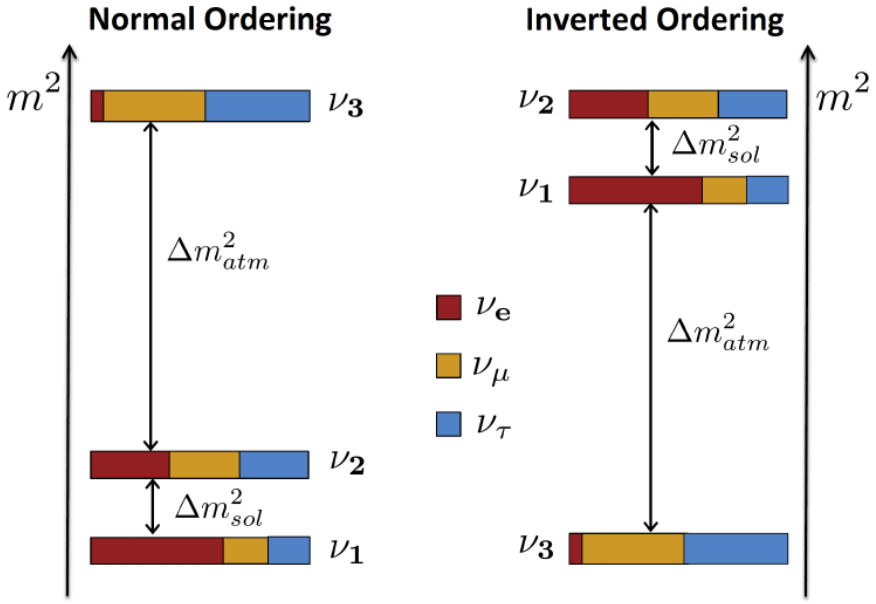

Figure 1.1: The two possible orderings of neutrino masses: Normal (left) and Inverted (right). The color codes illustrate the mixing between flavour eigenstates ν_α and neutrino mass eigenstate ν_i, quantified by the norm $|U_{\alpha i}|^2$ with $\alpha = e, \mu, \tau$.

The expression for the oscillation probability in the electron appearance channel can be written in the approximation of the mass splitting Δm^2_{21} and the angle θ_{13} being small and negligible beyond two orders of magnitude:

$$\begin{aligned} P_{\nu_\mu \to \nu_e} = \alpha^2 \sin^2 2\theta_{12} c_{23}^2 (\frac{\lambda L}{2})^2 + 4 s_{13}^2 s_{23}^2 sin^2(\frac{\lambda L}{2}) \\ + 2\alpha s_{13} \sin 2\theta_{12} \sin 2\theta_{23} (\frac{\lambda L}{2}) \sin(\frac{\lambda L}{2}) \cos(\delta_{CP} + \frac{\lambda L}{2}), \end{aligned} \tag{1.20}$$

where $\alpha = \frac{\Delta m^2_{21}}{\Delta m^2_{31}}$ and $\lambda = \frac{\Delta m^2_{31}}{2E_\nu}$. The probability expressions for other channels can be found in [50].

The oscillation probability for two flavour neutrino scheme in much simpler since there is only one mixing angle θ and one mass-squared difference Δm^2. The oscillation probability in the appearance channel is given by

$$\begin{aligned} P_{\nu_\mu \to \nu_e} \overset{\text{T}}{=} P_{\nu_e \to \nu_\mu} \overset{\text{CP}}{=} P_{\overline{\nu}_e \to \overline{\nu}_\mu} \overset{\text{T}}{=} P_{\overline{\nu}_\mu \to \overline{\nu}_e} \\ = \sin^2 2\theta \times \sin^2 (1.27 \times \Delta m^2 \frac{L}{4E_\nu} \frac{[\text{eV}^2][\text{km}]}{[\text{GeV}]}). \end{aligned} \tag{1.21}$$

Charge and Parity (CP) transformation ($P_{\nu_e \to \nu_\mu} \iff P_{\overline{\nu}_e \to \overline{\nu}_\mu}$) changes ν_α to $\overline{\nu}_\alpha$, and Time (T) transformation ($P_{\nu_\mu \to \nu_e} \iff P_{\nu_e \to \nu_\mu}$) changes $\alpha \rightleftharpoons \beta$. CPT transformation being the symmetry of any local quantum field theory.

1.2.3 Neutrino Oscillations in Matter

Neutrinos (and antineutrinos) of all flavours, ν_e, ν_μ, ν_τ, propagating through matter are subjected to coherent forward scattering (Fig. 1.2) with fermions (electrons, protons and

neutrons) in the medium via neutral current (NC) weak interactions mediated by Z^0 bosons, while electron neutrinos and antineutrinos interact with electrons via charged current (CC) weak interactions mediated by $W^{\pm}$ exchange. These SM CC and NC interactions are encoded in the Lagrangian in the form:

$$\mathcal{L}^{CC}_{mat} = -2\sqrt{2}G_F[\overline{\nu}_e\gamma_\rho Le][\overline{e}\gamma^\rho L\nu_e] + h.c. = -2\sqrt{2}G_F[\overline{\nu}_e\gamma_\rho L\nu_e][\overline{e}\gamma^\rho Le] + h.c. \tag{1.22}$$

$$\mathcal{L}^{NC}_{mat} = -2\sqrt{2}G_F\sum_{\alpha,f}[\overline{\nu}_\alpha\gamma_\rho L\nu_\alpha][\overline{f}\gamma^\rho(g^f_V - g^f_A)\gamma^5 f], \tag{1.23}$$

where G_F is the Fermi constant, $L = (1-\gamma^5/2)$ denotes the left chiral operator and g^f_V and g^f_A are the vector and axial coupling constants of the Standard Model respectively.

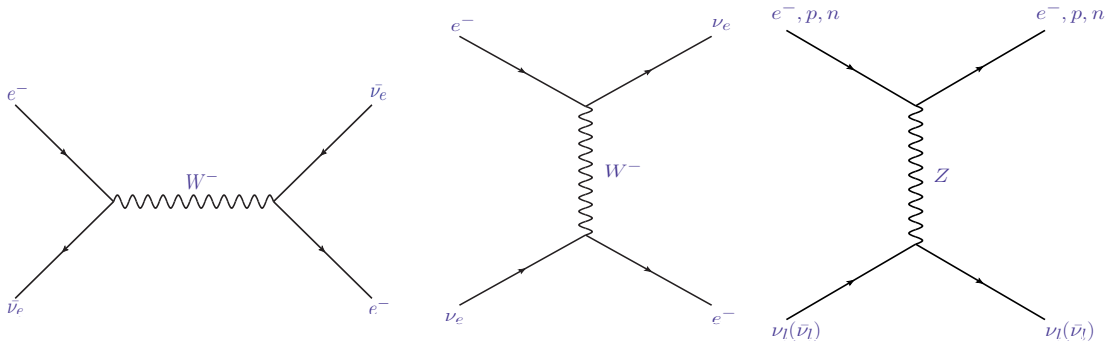

Figure 1.2: Feynman diagrams representing CC and NC (most right) neutrino interaction processes through $W^{\pm}$ and Z^0 exchange.

The effective Hamiltonian governing the evolution of neutrino flavour states in matter takes the form:

$$H^m = \frac{1}{2E_\nu}U_{ik}\begin{bmatrix} m_1^2 & 0 & 0 \\ 0 & m_2^2 & 0 \\ 0 & 0 & m_3^2 \end{bmatrix}U^\dagger_{kj} + \begin{bmatrix} V_{CC}+V_{NC} & 0 & 0 \\ 0 & V_{NC} & 0 \\ 0 & 0 & V_{NC} \end{bmatrix} \tag{1.24}$$

where,

$$V_{CC} = \sqrt{2}G_F N_e(x), \quad \text{and} \quad \mathrm{V_{NC}} = -\sqrt{2}\mathrm{G_F N_n(x)}/2, \tag{1.25}$$

with $N_e(x)$ and $N_n(x)$ being the electron and neutron densities in matter. V_{NC} is common to all flavours and hence does not modify the evolution equations. We can always subtract a phase from each diagonal term of H^m, such that $H^m = H^m - V_{NC}$.

After diagonalising the Hamiltonian by orthogonal transformations, we obtain the new effective mixing angle and mass-squared differences in matter (in terms of their vacuum counterparts) as:

$$\sin^2(2\theta^m_{13}) = \frac{\sin^2(2\theta_{13})}{(\cos 2\theta_{13} - A_{CC}/\Delta m^2_{31})^2 + \sin^2(2\theta_{13})} \tag{1.26}$$

$$\Delta m^2_{31m} = \Delta m^2_{31}[(\cos 2\theta_{13} - A_{CC}/\Delta m^2_{31})^2 + \sin^2(2\theta_{13})], \tag{1.27}$$

where, $A_{CC} = 2E_\nu V_{CC}$. For antineutrinos the particle number is negative and hence the effective potential A_{CC} flips its sign. A close inspection of the above expressions

will reveal that if the mass-squared difference Δm^2_{31} is positive, a resonance condition is satisfied and the transition probability hits a maximum for a definite incident neutrino energy E_ν and specific potential V_{CC}. This is called *Mikheyev-Smirnov-Wolfenstein* (MSW) effect [51, 26]. The effective mixing angle θ^m_{13} takes the value $\frac{\pi}{4}$ (irrespective of θ_{13} in vacuum) at the resonance point defined by:

$$A_{CC} = \Delta m^2_{31} \cos 2\theta_{13}. \tag{1.28}$$

Moreover, there is no resonance for antineutrinos ($A_{CC} \to -A_{CC}$). On the other hand for negative Δm^2_{31}, the situation is exactly reversed. The expression of electron appearance probability in the *One Mass Scale Dominance (OMSD)* approximation is given by:

$$P^m_{\nu_\mu \to \nu_e} = \sin^2\theta_{23} \sin^2 2\theta^m_{13} \sin^2(\Delta m^2_{31m} \frac{L}{4E_\nu}). \tag{1.29}$$

Further expressions for other oscillation channels and discussions on matter effects can be found in [50].

1.2.4 Oscillograms: Vacuum vs Matter

Atmospheric neutrino experiments consist of a copious source of electron and muon neutrinos (and antineutrinos) produced in the upper atmosphere. Their energies span across a few GeV to hundreds of GeV, down-pouring almost iso-tropically on the detector. For a given set of oscillation parameter values and assumed mass ordering (normal or inverted), the oscillation probabilities depend on two physical variables (*observables*) that we measure at experiments: the neutrino energy E_ν, and the cosine of the zenith angle of the incident neutrino $\cos\theta_z$. A value $\cos\theta_z = -1$ corresponds to vertically up-going neutrinos traversing across the Earth core passing through all the density layers of the Earth matter, whereas $\cos\theta_z = 0$ corresponds to horizontally moving neutrinos passing through the Earth atmosphere.

The term *oscillogram* refers to a 2D heat map of oscillation probabilities in the (E_ν, $\cos\theta_z$) plane. Oscillograms are very helpful to gauge the physics potential of atmospheric neutrino experiments benefiting from its access to a wide range of neutrino energies and baselines. Typically, they help us to fine tune our detector or analysis in regions of the (E_ν, $\cos\theta_z$) plane, where larger effects are expected. In this section, we will use oscillograms of neutrinos propagating through Earth to observe the effects of standard neutrino-matter interactions on various oscillation channels at atmospheric neutrino experiments.

For the calculation of oscillation probabilities, the neutrino evolution equation in the full three-flavour neutrino scheme (Eq. 1.24) is solved numerically (without ignoring Δm^2_{21}, θ_{12}, θ_{13}) with the OscProb [52] package taking into account the Earth matter density profile, consisting of 44 layers, as it is assumed in the Preliminary Reference Earth Model (PREM) [53]. This model parameterises the Earth's density into concentric spheres of uniform density as shown in Fig. 1.3.

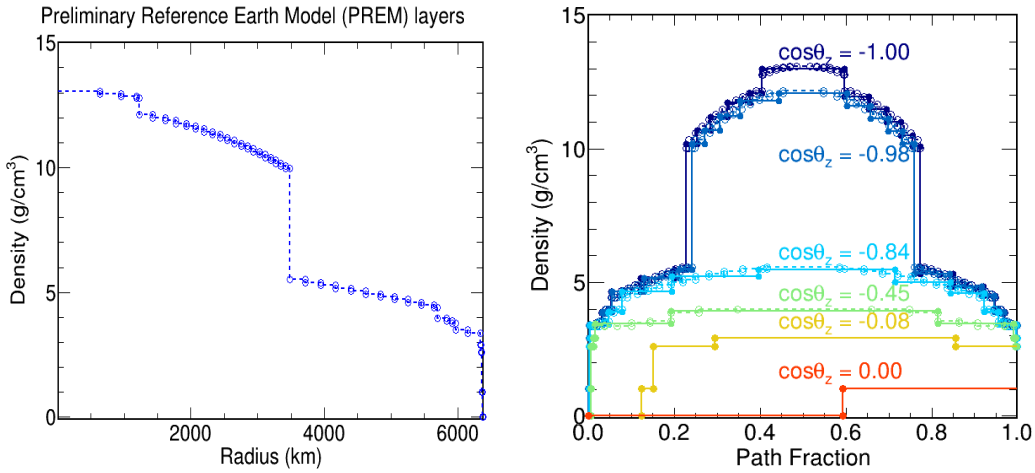

Figure 1.3: Left: Density profile of the PREM model [53] consisting of 44 radial layers; right: Visualisation of the neutrino path (as a function of path fraction = $\frac{x}{D}$ with x, D being the path length and the diameter of Earth respectively) corresponding to different zenith angles of an incoming neutrino. $\cos\theta_z = 0\,(-1)$ corresponds to horizontal (vertically up-going) neutrinos.

$\nu_e \to \nu_x$ oscillation channels

Fig. 1.4 depicts oscillograms for electron neutrinos for the vacuum case (left) and in presence of standard neutrino-matter interactions (right). The upper, middle and bottom panels correspond to electron disappearance, muon appearance and tau appearance channels respectively. The sum of the three channels in each column add up to unity. Hence, a ν_e deficit is accompanied by ν_μ and ν_τ excesses with respect to the unitarity condition in Eq. 24. MSW effects [24] are more prominent for mantle-core crossing ($\cos\theta_z \leq -0.8$) neutrinos, since they experience large matter effects while traversing across the Earth before reaching the detector. In these examples MSW resonance happens for neutrinos since normal ordering (NO) is assumed.

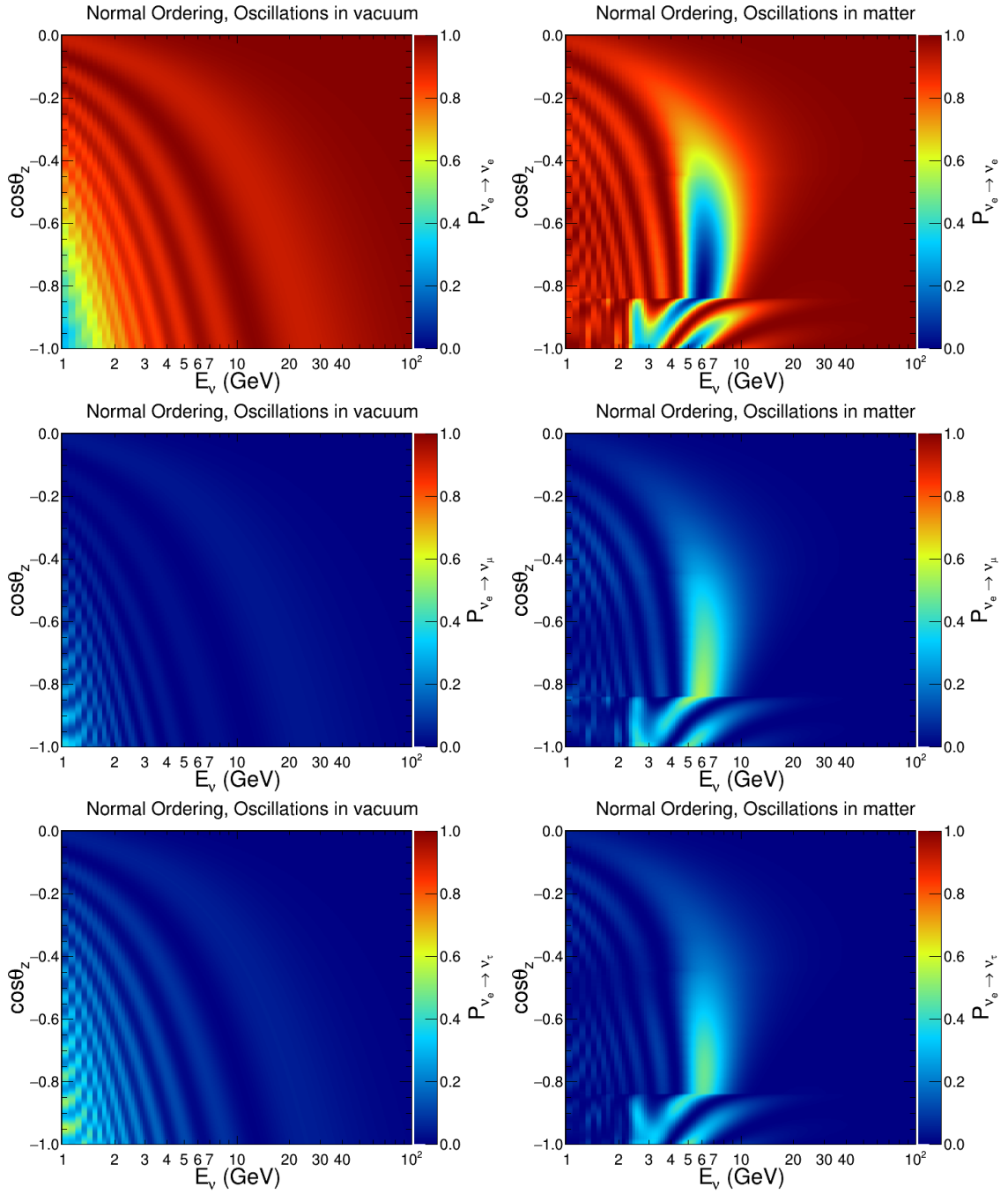

Figure 1.4: $P_{\nu_e \to \nu_x}(x = e, \mu, \tau)$ for vacuum assumption (left) and in presence of matter (right) as a function of neutrino energy E_ν and cosine of the zenith angle $\cos\theta_z$. The top, middle and bottom panels correspond to electron disappearance, muon appearance and tau appearance channels, respectively. Normal Ordering is assumed.

$\overline{\nu}_e \to \overline{\nu}_x$ oscillation channels

Fig. 1.5 depicts oscillograms for electron antineutrinos for the vacuum case (left) and in presence of standard neutrino-matter interactions (right). In NO, even in the presence of matter, electron antineutrinos follow almost vacuum oscillations, in which they hardly mix with other flavours. The situation is exactly reversed for neutrinos and antineutrinos in IO assumption for $\delta_{CP} = 0$.

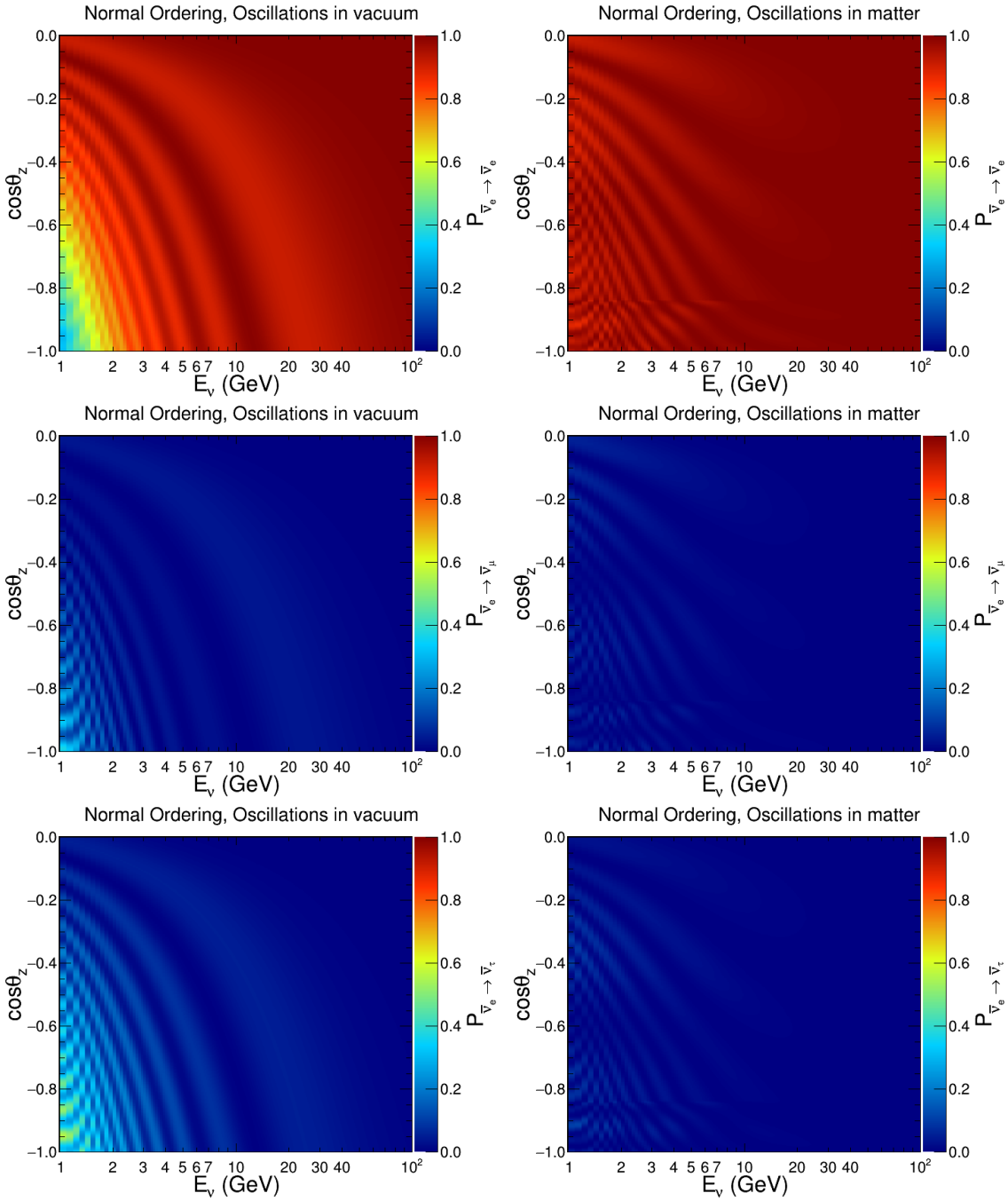

Figure 1.5: $P_{\overline{\nu}_e \to \overline{\nu}_x}(x = e, \mu, \tau)$ for vacuum assumption (left) and in presence of matter (right) as a function of neutrino energy E_ν and cosine of the zenith angle $\cos\theta_z$. The top, middle and bottom panels correspond to electron disappearance, muon appearance and tau appearance channels, respectively. Normal Ordering is assumed.

$\nu_\mu \to \nu_x$ oscillation channels

Fig. 1.6 depicts oscillograms for muon neutrinos for the vacuum case (left) and in presence of standard neutrino-matter interactions (right). The upper, middle and bottom panels correspond to electron appearance, muon disappearance and tau appearance channels.

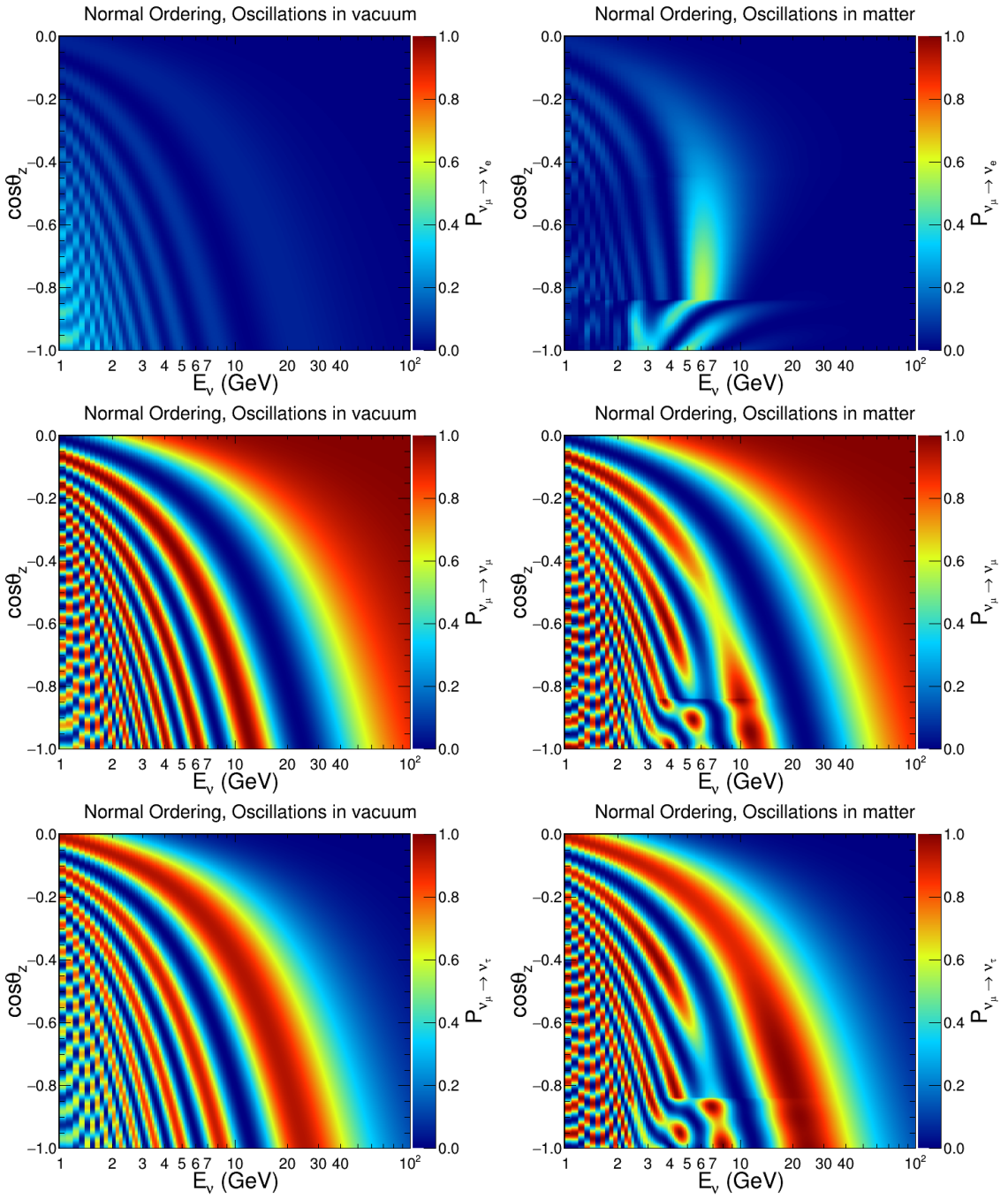

Figure 1.6: $P_{\nu_\mu \to \nu_x}(x = e, \mu, \tau)$ for vacuum assumption (left) and in presence of matter (right) as a function of neutrino energy E_ν and cosine of the zenith angle $\cos\theta_z$. The top, middle and bottom panels correspond to electron appearance, muon disappearance and tau appearance channels, respectively. Normal Ordering is assumed.

$\overline{\nu}_\mu \to \overline{\nu}_x$ oscillation channels

Fig. 1.7 depicts oscillograms for muon antineutrinos for the vacuum case (left) and in presence of standard neutrino-matter interactions (right). In NO, even in the presence of matter, muon antineutrinos follow almost vacuum oscillations, in which they hardly mix with other flavours. The situation is exactly reversed for neutrinos and antineutrinos in IO assumption for $\delta_{CP} = 0$.

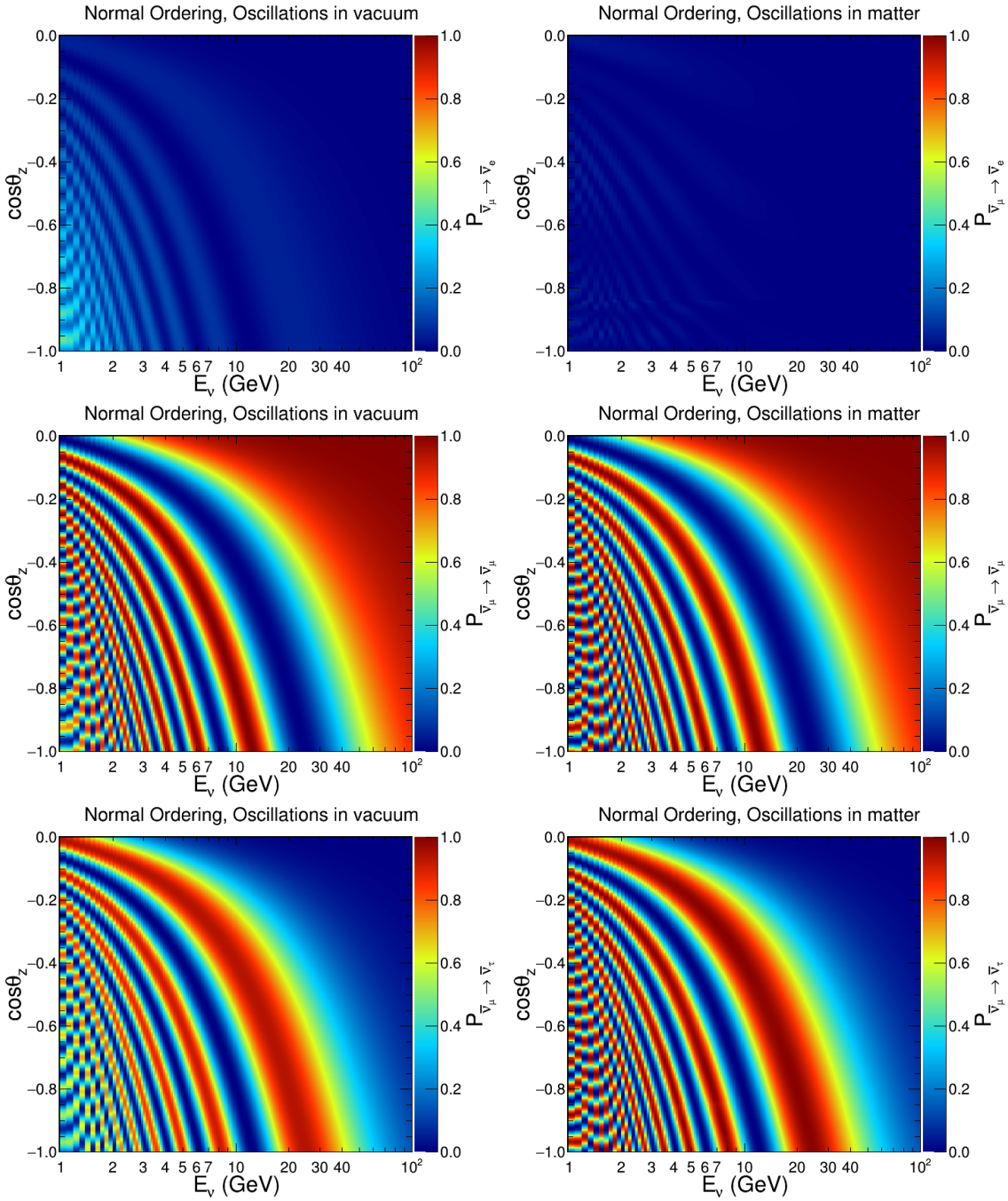

Figure 1.7: $P_{\overline{\nu}_\mu \to \overline{\nu}_x}(x = e, \mu, \tau)$ for vacuum assumption (left) and in presence of matter (right) as a function of neutrino energy E_ν and cosine of the zenith angle $\cos\theta_z$. The top, middle and bottom panels correspond to electron appearance, muon disappearance and tau appearance channels, respectively. Normal Ordering is assumed.

1.2.5 Current status

As mentioned in Sec. 1.2.2, the standard framework of neutrino oscillations with three generations is governed by three mixing angles, θ_{12}, θ_{13}, θ_{23}, one Dirac CP phase, δ_{CP}, and two mass-squared differences, Δm^2_{21}, Δm^2_{31}. The current experimental knowledge of these parameters is summarised below.

- The analysis of solar data collected by KamLAND [54, 36], Super-K [55] as well as global analyses of oscillation data [56] have determined the solar mixing parameters θ_{12} and Δm^2_{21} with great precision.
- The short baseline reactor experiments, namely, Daya Bay [57], RENO [58], Double Chooz [59] have recently measured the non zero value of θ_{13}.
- The atmospheric neutrino experiments, namely, ANTARES [60], Super-K [61], IceCube-DeepCore [62] as well as long baseline experiments, namely, MINOS [63], T2K [64], NOνA [65] have measured the atmospheric mixing parameters θ_{23} and $|\Delta m^2_{31}|$. However the precise values of θ_{23} and Δm^2_{31} (along with its sign) are expected to be probed by ongoing and upcoming experiments, namely, KM3NeT-ORCA [66], IceCube-PINGU [67], Hyper-Kamiokande [68].
- A recent analysis by T2K [69] excluded large phase space area of possible δ_{CP} values. Upcoming experiments like P2O [70], DUNE [71], T2HK [72] will have unprecedented sensitivity to δ_{CP}, which causes CP violation in the lepton sector.

The current global best fit values of oscillation parameters are listed in Tab. 1.1 and the 3σ ranges of the matrix elements are listed in Eq. 1.30.

NuFIT 5.0 (2020)

		Normal Ordering (best fit)		Inverted Ordering ($\Delta\chi^2 = 2.7$)	
		bfp $\pm 1\sigma$	3σ range	bfp $\pm 1\sigma$	3σ range
without SK atmospheric data	$\sin^2\theta_{12}$	$0.304^{+0.013}_{-0.012}$	$0.269 \to 0.343$	$0.304^{+0.013}_{-0.012}$	$0.269 \to 0.343$
	$\theta_{12}/^\circ$	$33.44^{+0.78}_{-0.75}$	$31.27 \to 35.86$	$33.45^{+0.78}_{-0.75}$	$31.27 \to 35.87$
	$\sin^2\theta_{23}$	$0.570^{+0.018}_{-0.024}$	$0.407 \to 0.618$	$0.575^{+0.017}_{-0.021}$	$0.411 \to 0.621$
	$\theta_{23}/^\circ$	$49.0^{+1.1}_{-1.4}$	$39.6 \to 51.8$	$49.3^{+1.0}_{-1.2}$	$39.9 \to 52.0$
	$\sin^2\theta_{13}$	$0.02221^{+0.00068}_{-0.00062}$	$0.02034 \to 0.02430$	$0.02240^{+0.00062}_{-0.00062}$	$0.02053 \to 0.02436$
	$\theta_{13}/^\circ$	$8.57^{+0.13}_{-0.12}$	$8.20 \to 8.97$	$8.61^{+0.12}_{-0.12}$	$8.24 \to 8.98$
	$\delta_{\rm CP}/^\circ$	195^{+51}_{-25}	$107 \to 403$	286^{+27}_{-32}	$192 \to 360$
	$\frac{\Delta m^2_{21}}{10^{-5}\ \text{eV}^2}$	$7.42^{+0.21}_{-0.20}$	$6.82 \to 8.04$	$7.42^{+0.21}_{-0.20}$	$6.82 \to 8.04$
	$\frac{\Delta m^2_{3\ell}}{10^{-3}\ \text{eV}^2}$	$+2.514^{+0.028}_{-0.027}$	$+2.431 \to +2.598$	$-2.497^{+0.028}_{-0.028}$	$-2.583 \to -2.412$
		Normal Ordering (best fit)		Inverted Ordering ($\Delta\chi^2 = 7.1$)	
		bfp $\pm 1\sigma$	3σ range	bfp $\pm 1\sigma$	3σ range
with SK atmospheric data	$\sin^2\theta_{12}$	$0.304^{+0.012}_{-0.012}$	$0.269 \to 0.343$	$0.304^{+0.013}_{-0.012}$	$0.269 \to 0.343$
	$\theta_{12}/^\circ$	$33.44^{+0.77}_{-0.74}$	$31.27 \to 35.86$	$33.45^{+0.78}_{-0.75}$	$31.27 \to 35.87$
	$\sin^2\theta_{23}$	$0.573^{+0.016}_{-0.020}$	$0.415 \to 0.616$	$0.575^{+0.016}_{-0.019}$	$0.419 \to 0.617$
	$\theta_{23}/^\circ$	$49.2^{+0.9}_{-1.2}$	$40.1 \to 51.7$	$49.3^{+0.9}_{-1.1}$	$40.3 \to 51.8$
	$\sin^2\theta_{13}$	$0.02219^{+0.00062}_{-0.00063}$	$0.02032 \to 0.02410$	$0.02238^{+0.00063}_{-0.00062}$	$0.02052 \to 0.02428$
	$\theta_{13}/^\circ$	$8.57^{+0.12}_{-0.12}$	$8.20 \to 8.93$	$8.60^{+0.12}_{-0.12}$	$8.24 \to 8.96$
	$\delta_{\rm CP}/^\circ$	197^{+27}_{-24}	$120 \to 369$	282^{+26}_{-30}	$193 \to 352$
	$\frac{\Delta m^2_{21}}{10^{-5}\ \text{eV}^2}$	$7.42^{+0.21}_{-0.20}$	$6.82 \to 8.04$	$7.42^{+0.21}_{-0.20}$	$6.82 \to 8.04$
	$\frac{\Delta m^2_{3\ell}}{10^{-3}\ \text{eV}^2}$	$+2.517^{+0.026}_{-0.028}$	$+2.435 \to +2.598$	$-2.498^{+0.028}_{-0.028}$	$-2.581 \to -2.414$

Table 1.1: Global *best fit points* (bfp) of oscillation parameters and their allowed ranges. The left column refers to $\Delta m^2_{31} > 0$ for NO and the right column refers to $\Delta m^2_{31} < 0$ for IO. Adapted from [73].

NuFIT 5.0 (2020)

$$|U|^{\text{w/o SK-atm}}_{3\sigma} = \begin{pmatrix} 0.801 \to 0.845 & 0.513 \to 0.579 & 0.143 \to 0.156 \\ 0.233 \to 0.507 & 0.461 \to 0.694 & 0.631 \to 0.778 \\ 0.261 \to 0.526 & 0.471 \to 0.701 & 0.611 \to 0.761 \end{pmatrix}$$

$$|U|^{\text{with SK-atm}}_{3\sigma} = \begin{pmatrix} 0.801 \to 0.845 & 0.513 \to 0.579 & 0.143 \to 0.155 \\ 0.234 \to 0.500 & 0.471 \to 0.689 & 0.637 \to 0.776 \\ 0.271 \to 0.525 & 0.477 \to 0.694 & 0.613 \to 0.756 \end{pmatrix} \quad (1.30)$$

1.3 Beyond Standard Oscillations

The study of new physics at a higher energy scale can be approached in a model independent way through effective field theories (EFTs). The new physics at some high scale Λ can be described in a given EFT as

$$\mathcal{L}_{eff} = \mathcal{L}_{SM} + \sum_{n\geq 5} \frac{\mathcal{L}^{(n)}}{\Lambda^{n-4}} = \mathcal{L}_{SM} + \sum_{n\geq 5} \sum_{i} \frac{1}{\Lambda^{n-4}} C_i \mathcal{O}_i^{(n)}, \tag{1.31}$$

where $\mathcal{L}_{SM}$ is the Lagrangian density of the Standard Model, $\mathcal{O}_i$ are operators of higher mass dimension involving the fields that are relevant at the low energy scale and C_i are the so-called Wilson coefficients. The operators for $n \geq 5$ are non-renormalizable and the corresponding terms are suppressed by factors of Λ^{-n}. The operators can be constructed so as to respect the corresponding symmetries, gauge and Lorentz invariance.

In the case of neutrinos, the interactions to which the new terms give rise have been dubbed "Generalised Neutrino Interactions" (GNIs) [74]. Historically the first type of interactions beyond the SM studied were the so-called "Neutrino Non-Standard Interactions" (NSIs) [75, 76]. NSIs are a subset of GNIs that include only dimension-six, vector operators which respect the residual $SU(3)_C$ x $U(1)_{em}$ symmetry. The relationship between NSIs and GNIs is studied in [74]. In this work, we limit ourselves to NSIs.

1.3.1 Non-Standard Interactions

Most models explaining mechanisms of neutrino mass generations [43] imply extra interactions apart from the standard electroweak interactions (Sec. 1.1). Once we invoke new physics to explain the mass of the neutrinos, it becomes very unnatural to avoid the extra interactions rooting from neutrino mass as, for instance, in seesaw models [77]. Most Physics models that predict such non-standard neutrino-matter interactions include radiative neutrino mass models [78], R-parity violating supersymmetric models [79] and extensions of SM gauge group [74].

Non-Standard Interactions are interactions between neutrinos of all flavours with matter fermions (e, u and d) that will affect the neutrino oscillation as a sub-leading mechanism in neutrino flavour transitions. In general, NSIs can alter the oscillation signals via charged current (CC) interactions and neutral current (NC) interactions. The CC NSIs would affect the production and detection processes of neutrino states at a neutrino oscillation experiment. On the other hand, the NC NSIs would affect the neutrino propagation by coherent forward scattering of neutrinos in Earth matter.

In the low energy regime, the common ansatz to parameterise these additional interactions of neutrinos is in terms of 6-dimensional operators appearing in an effective four-fermion Langrangian (Eq. 1.31). The new operators are of the form [75, 76]:

$$\mathcal{L}_{NSI}^{CC} = -2\sqrt{2}G_F \sum_{P,f,f'} \epsilon_{\alpha\beta}^{CC,P,f,f'} [\overline{\nu}_\alpha \gamma_\rho L l_\beta][\overline{f}\gamma^\rho P f'] + h.c., \tag{1.32}$$

$$\mathcal{L}_{NSI}^{NC} = -2\sqrt{2}G_F \sum_{P,f} \epsilon_{\alpha\beta}^{NC,P,f} [\overline{\nu}_\alpha \gamma_\rho L \nu_\beta][\overline{f}\gamma^\rho P f], \tag{1.33}$$

where G_F is the Fermi constant, P = L, R denotes the chiral operators $(1 \pm \gamma^5/2)$ respectively, f is first generation SM fermion (e, u or d-quarks), f' belongs to the same

weak doublet of f, and α and β denote the neutrino flavours: e, μ or τ. The dimensionless coefficients $\epsilon_{\alpha\beta}^{CC,P,f,f'}$ and $\epsilon_{\alpha\beta}^{NC,P,f}$ quantify the strength of NSIs between the neutrinos of flavour α and β and the matter fermion $f \in \{e, u \text{ or } d\}$ (for NC NSIs) and $f \neq f' \in \{u,d\}$ (for CC NSIs). The Standard Model scenario is recovered in the limit $\epsilon \to 0$.

While the former are tightly constrained and totally discernible at near detectors, we are interested in NC NSIs that alters the propagation of neutrinos while traversing across large path lengths before being detected. Solar, atmospheric and long baseline experiments are expected to give better constraints on NSIs in propagation owing to large matter effects, while non-oscillation experiments are more sensitive to NSIs in production and/or detection.

The effect of NC interactions with fermions (f) affecting neutrino propagation in matter (m) is usually referred as $\epsilon_{\alpha\beta}^{mf}$. Since the potential is sensitive to the vector part of the interaction ($\epsilon^{fV} = \epsilon^{fL} + \epsilon^{fR}$), neutrino propagation in a medium is sensitive to the combination:

$$\epsilon_{\alpha\beta}^{fV} = \epsilon_{\alpha\beta}^{eV} + \frac{N_u}{N_e}\epsilon_{\alpha\beta}^{uV} + \frac{N_d}{N_e}\epsilon_{\alpha\beta}^{dV}. \tag{1.34}$$

Most bounds from oscillation experiments are presented in terms of effective Lagrangian coefficients $\epsilon_{\alpha\beta}^{fV}$ for interactions with d-quarks only. For neutral un-polarised Earth matter, $N_u \simeq N_d \simeq 3N_e$. This makes the relation between components of NSI couplings very straightforward and one can extrapolate bounds on different components of NSI couplings by a simple normalisation factor calculated from the ratio of their relative abundance in matter. The non-diagonal terms $\epsilon_{\alpha\beta}$ with $\alpha \neq \beta$ allow for new sources of flavour violation and represent *flavour-changing-neutral-current* (FCNC) interactions, while the diagonal terms $\epsilon_{\alpha\alpha}$ allow for different neutral current (NC) interaction-amplitudes for different neutrino flavours which imply lepton non-universality (NU). They are schematically in shown in Fig. 1.8.

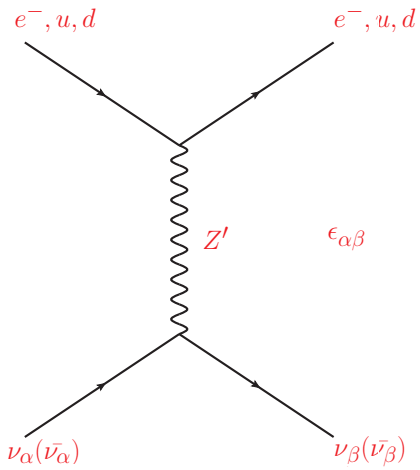

Figure 1.8: Feynman diagram representing a neutral current non-standard interaction process. A neutrino (or antineutrino) of flavour α interacts with a matter fermion (e, u or d) mediated by a heavy (non-standard) boson Z′. The strength of the interaction is parameterised by the NSI coupling parameter $\epsilon_{\alpha\beta}$.

We are going to consider NC NSI with interactions between neutrinos and d-quarks (e and u-quark couplings set to 0) parameterised simply as $\epsilon_{\alpha\beta}$ ($\epsilon_{\alpha\beta} = \epsilon^{eff}_{\alpha\beta} = \frac{N_d}{N_e}\epsilon^{dV}_{\alpha\beta}$) for brevity.

1.3.2 Neutrino Flavour Transitions with NSIs

NC NSIs of neutrinos are usually modelled as perturbations in the standard MSW potential V_{CC} [24]. The effective Hamiltonian [75, 80] governing the evolution of neutrino flavour states in matter in the presence of NSI takes the form:

$$H^{3flv}_{NSI} = \frac{1}{2E_\nu} U_{ik} \begin{bmatrix} m_1^2 & 0 & 0 \\ 0 & m_2^2 & 0 \\ 0 & 0 & m_3^2 \end{bmatrix} U^\dagger_{kj} + V_{CC} \frac{N_f(x)}{N_e(x)} \begin{bmatrix} \delta_{ef} + \epsilon_{ee} & \epsilon_{e\mu} & \epsilon_{e\tau} \\ \epsilon^*_{e\mu} & \epsilon_{\mu\mu} & \epsilon_{\mu\tau} \\ \epsilon^*_{e\tau} & \epsilon^*_{\mu\tau} & \epsilon_{\tau\tau} \end{bmatrix}, \tag{1.35}$$

where, E_ν is the neutrino energy; U_{ik} is the PMNS matrix [81], which describes the standard neutrino mixing as rotations between the flavour and mass eigenstates parameterised by unique mixing angles θ_{ik}; and m^2_{ij} is the mass-squared value of the mass eigenstate i. $N_f(x)$ and $N_e(x)$ are the fermion and electron number density along the neutrino path, respectively, and the $\epsilon_{\alpha\beta}$ ($= |\epsilon_{\alpha\beta}|e^{i\phi_{\alpha\beta}}$) represent the strength of NSI coupling. In case of antineutrinos, we should flip the sign of $N_e(x)$ and $N_f(x)$ for the charge current matter and neutral current NSI potential respectively. Setting all $\epsilon_{\alpha\beta}$ to zero, we will fall back to the SM neutrino oscillations with MSW effects.

From the form of the Hamiltonian in Eq. 1.35, one can find some interesting features concerning the impact of NSI couplings in neutrino propagation:

a) The diagonal elements in the NSI matrix, $\epsilon_{\alpha\alpha}$, could be interpreted as NSI induced mass-squared differences (mimicking the standard Δm^2_{ij}), which could induce extra resonances even in the absence of neutrino mass [82, 83].

b) The off-diagonal elements, $\epsilon_{\alpha\beta}$, could induce flavour transitions and could be interpreted as mixing angles. Even in the absence of neutrino mixing, the off-diagonal terms can mimic oscillations [82, 83].

c) The complex phases $e^{i\phi_{\alpha\beta}}$ on the off-diagonal elements $\epsilon_{\alpha\beta}$ could be new sources of CP violation [84].

Inclusion of real NSIs ($\phi_{\alpha\beta} = 0$) implies the introduction of six additional parameters ϵ_{ee}, $\epsilon_{\mu\mu}$, $\epsilon_{\tau\tau}$, $\epsilon_{e\mu}$, $\epsilon_{e\tau}$ and $\epsilon_{\mu\tau}$ (if we account for hermicity and unitary constraints [85]), which will have further degeneracies with oscillation parameters and systematic uncertainties [86]. In what follows in the thesis, we neglect possible sources of CP violation from these new interactions and assume all NSI parameters to be real.

In a similar strategy to the SM matter case (Sec. 1.2.3), one can diagonalise the Hamiltonian H_{NSI} using a modified unitary matrix $\tilde{U}_{ik}$:

$$H^{3flv}_{NSI} = \frac{1}{2E_\nu} \tilde{U}_{ik} \begin{bmatrix} \tilde{m}_1^2 & 0 & 0 \\ 0 & \tilde{m}_2^2 & 0 \\ 0 & 0 & \tilde{m}_3^2 \end{bmatrix} \tilde{U}^\dagger_{kj}, \tag{1.36}$$

where $\tilde{m}^2_i$s are the effective neutrino mass-squared eigenvalues and $\tilde{U}$ is the effective mixing matrix when MSW and NSIs are taken into consideration.

After similar algebra, the transition probability can be read off as

$$P_{\nu_a\to\nu_b}(L,E) = \delta_{ab} - 4\sum_{j>i} Re[\tilde{U}_{ai}\tilde{U}^*_{bi}\tilde{U}^*_{aj}\tilde{U}_{bj}]\sin^2(\frac{1.27\times\Delta\tilde{m}^2_{ij}L}{4E}) \\ +2\sum_{j>i} Im[\tilde{U}_{ai}\tilde{U}^*_{bi}\tilde{U}^*_{aj}\tilde{U}_{bj}]\sin^2(\frac{1.27\times\Delta\tilde{m}^2_{ij}L}{2E}). \tag{1.37}$$

This expression looks very similar to the vacuum counterpart (Eq. 1.19), while replacing the vacuum masses m^2_i and the leptonic mixing matrix U with effective ones. The effective masses $\tilde{m}^2_i$ with NSIs include the interaction terms corresponding to standard matter effects plus NSIs, and have the following expressions [87]:

$$\tilde{m}^2_1 \simeq \Delta m^2_{31}[\tilde{V} + \alpha s^2_{12} + \tilde{V}\epsilon_{ee}] \tag{1.38}$$
$$\tilde{m}^2_2 \simeq \Delta m^2_{31}[\alpha c^2_{12} - \tilde{V}s^2_{23}(\epsilon_{\mu\mu} - \epsilon_{\tau\tau}) - \tilde{V}s_{23}c_{23}(\epsilon_{\mu\tau} + \epsilon^*_{\mu\tau}) + \tilde{V}\epsilon_{\mu\mu}], \tag{1.39}$$
$$\tilde{m}^2_3 \simeq \Delta m^2_{31}[1 + \tilde{V}\epsilon_{\tau\tau} + \tilde{V}s^2_{23}(\epsilon_{\mu\mu} - \epsilon_{\tau\tau}) + \tilde{V}s_{23}c_{23}(\epsilon_{\mu\tau} + \epsilon^*_{\mu\tau})]. \tag{1.40}$$

The elements of the effective mixing matrix are given by:

$$\tilde{U}_{e2} \simeq \frac{\alpha s_{12}c_{12}}{\tilde{V}} + c_{23}\epsilon_{e\mu} - s_{23}\epsilon_{e\tau}, \tag{1.41}$$
$$\tilde{U}_{e3} \simeq \frac{s_{13}e^{-i\delta} + \tilde{V}(s_{23}\epsilon_{e\mu} + c_{23}\epsilon_{e\tau})}{1-\tilde{V}}, \tag{1.42}$$
$$\tilde{U}_{\mu 2} \simeq c_{23} + s^2_{23}c_{23}\tilde{V}(\epsilon_{\tau\tau} - \epsilon_{\mu\mu}) + s_{23}\tilde{V}(s_{23}\epsilon_{\mu\tau} - c^2_{23}\epsilon^*_{\mu\tau}), \tag{1.43}$$
$$\tilde{U}_{\mu 3} = s_{23} + \tilde{V}[c_{23}\epsilon_{\mu\tau} + s_{23}c^2_{23}(\epsilon_{\mu\mu} - \epsilon_{\tau\tau}) - s^2_{23}c_{23}(\epsilon_{\mu\tau} + \epsilon^*_{\mu\tau})]. \tag{1.44}$$

Here, $s_{ij} = \sin\theta_{ij}$, $c_{ij} = \cos\theta_{ij}$, $\alpha \equiv \Delta m_{21}/\Delta m_{31}$, $\tilde{V} \equiv V_{CC}/\Delta m^2_{31}$ and δ corresponds to the CP violating phase. The expressions for three-flavours neutrino propagation in matter including NSIs can be quite complicated. To illustrate the effect of NSIs on the mixing parameters and mass eigenvalues, it is easier to work in a two flavour neutrino scheme to avoid complex calculations. An accurate discussion regarding the two flavour neutrino scheme in presence of NSIs can be found in [88].

In a hand waving way, for a given neutrino energy E_ν, and the matter density ρ, the impact of propagation NSIs in neutrino oscillation is determined by the magnitude of the dimensionless quantity:

$$\eta_{\alpha\beta} = \epsilon_{\alpha\beta}\tilde{V} \approx 0.1\times\epsilon_{\alpha\beta}\left[\frac{E_\nu}{\text{GeV}}\right]\left[\frac{2.4\times10^{-3}eV^2}{\Delta m^2_{ij}}\right]\left[\frac{\rho}{\text{g cm}^{-3}}\right]. \tag{1.45}$$

The larger the value of $\eta_{\alpha\beta}$, the larger the impact of NSI in propagation. Usually, NSI effects are more pronounced at high energies, at which the oscillation signal is mostly phased out. The presence of NSI will manifest at detectors as a distortion in the oscillation signal expected with respect to SM 3-flavour oscillation predictions. The observation of such phenomenon would be considered as an evidence for NSI and a signal of new physics. In the next section, we will quantify the distortions in the oscillation signal predicted in presence of NSIs.

1.3.3 NSIs at Atmospheric Neutrino Experiments

For atmospheric neutrinos, the effect of NSIs can be estimated by studying the muon neutrino and antineutrino survival probabilities for different zenith angles, $\cos\theta_z$. In atmospheric neutrino experiments, where the atmospheric neutrino flux is dominated by ν_μ in the GeV energy range, NSI in the $\mu-\tau$ sector can be discerned by probing the deficit of ν_μ events, which primarily transform into ν_τ governed by a large mixing angle θ_{23} and by the NSI coupling parameter $\epsilon_{\mu\tau}$.

The analysis of atmospheric neutrinos is usually done in a two-flavour neutrino scheme, considering lepton non-universal $\nu_\mu + f \rightarrow \nu_\mu + f$ and $\nu_\tau + f \rightarrow \nu_\tau + f$ and flavour changing $\nu_\mu + f \rightarrow \nu_\tau + f$ processes, such that all the NSI electron couplings $\epsilon_{e\alpha}$ terms are set to zero. In such an approximation ($\Delta m^2_{31} \equiv \Delta m^2$ and $\theta_{23} \equiv \theta$, $\Delta m^2_{21} = \theta_{23} = \theta_{23} = 0$), the 2×2 Hamiltonian matrix

$$H^{2flv}_{NSI} = \frac{1}{2E_\nu}\tilde{U}\begin{bmatrix}0 & 0\\ 0 & \Delta m^2\end{bmatrix}\tilde{U}^\dagger + V_{CC}\frac{N_d}{N_e}\begin{bmatrix}\delta_{ed} & \epsilon_{\mu\tau}\\ \epsilon_{\mu\tau} & (\epsilon_{\tau\tau}-\epsilon_{\mu\mu})\end{bmatrix}, \tag{1.46}$$

can be diagonalised with an effective mixing angle given by [75, 76, 89]

$$sin^2 2\tilde{\theta} = \frac{1}{R^2}[sin^2\theta + 2R_0 sin2\theta sin2\zeta + R_0^2 sin^2 2\zeta], \tag{1.47}$$

where

$$R = \sqrt{[1 + R_0^2 + 2R_0(cos2\theta cos2\zeta + sin2\theta sin2\zeta)]}. \tag{1.48}$$

The NSI couplings are contained in the auxiliary parameters:

$$R_0 = \sqrt{2}G_F N_f \frac{4E}{\Delta m^2}\sqrt{|\epsilon|^2 + \frac{\epsilon'^2}{4}} \tag{1.49}$$

$$\zeta = \frac{1}{2}\arctan\frac{\epsilon}{\epsilon'}. \tag{1.50}$$

The muon survival probability, assuming constant matter density and that neutrinos only interact with d-quarks, reads

$$P_{\nu_\mu\rightarrow\nu_\mu} = 1 - sin^2 2\tilde{\theta} sin^2\left[\frac{\Delta m^2 L}{4E}\zeta\right]. \tag{1.51}$$

The oscillation signature in the muon disappearance channel, predicted in presence of $\nu_\mu \rightarrow \nu_\tau$ NSIs, parameterised by non-zero $\epsilon_{\mu\tau}$ ($\epsilon_{\mu\mu} = \epsilon_{\tau\tau} = 0$), at a fixed zenith angle corresponding to up-going neutrinos (i.e., $\cos\theta_z = -1.0$) is shown in Fig. 1.9.

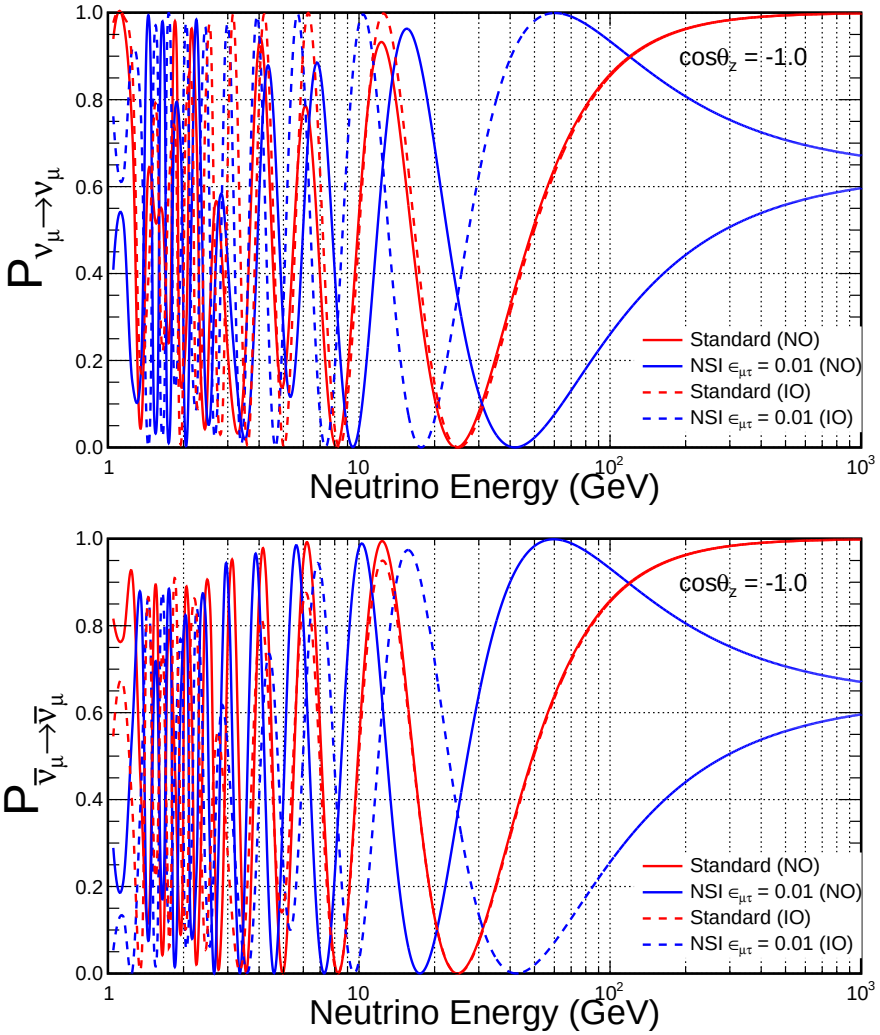

Figure 1.9: $\nu_\mu \rightarrow \nu_\mu$ (top) and $\overline{\nu}_\mu \rightarrow \overline{\nu}_\mu$ (bottom) survival probabilities for fixed baseline $\cos\theta_z = -1$, corresponding to vertically up-going neutrinos. The red line shows the global best-fit oscillations [90], while the blue line corresponds to $\epsilon_{\mu\tau} = 0.01$ NSI, both assuming NO (solid) and IO (dashed) hypothesis.

Besides the dominant $\nu_\mu \rightarrow \nu_\mu$ oscillation channel, one can also consider the $\nu_e \rightarrow \nu_\mu$ case in the presence of NSIs in the $e \rightarrow \tau$ sector, meaning non-zero $\epsilon_{ee}, \epsilon_{e\tau}$ and $\epsilon_{\tau\tau}$. Similarly, the oscillation signature in the muon appearance channel, predicted in presence of $e \rightarrow \tau$ NSIs, parameterised by non-zero $\epsilon_{e\tau}$ ($\epsilon_{ee} = \epsilon_{\tau\tau} = 0$), at a fixed zenith angle corresponding to up-going neutrinos (i.e., $\cos\theta_z = -1.0$) is shown in Fig. 1.10.

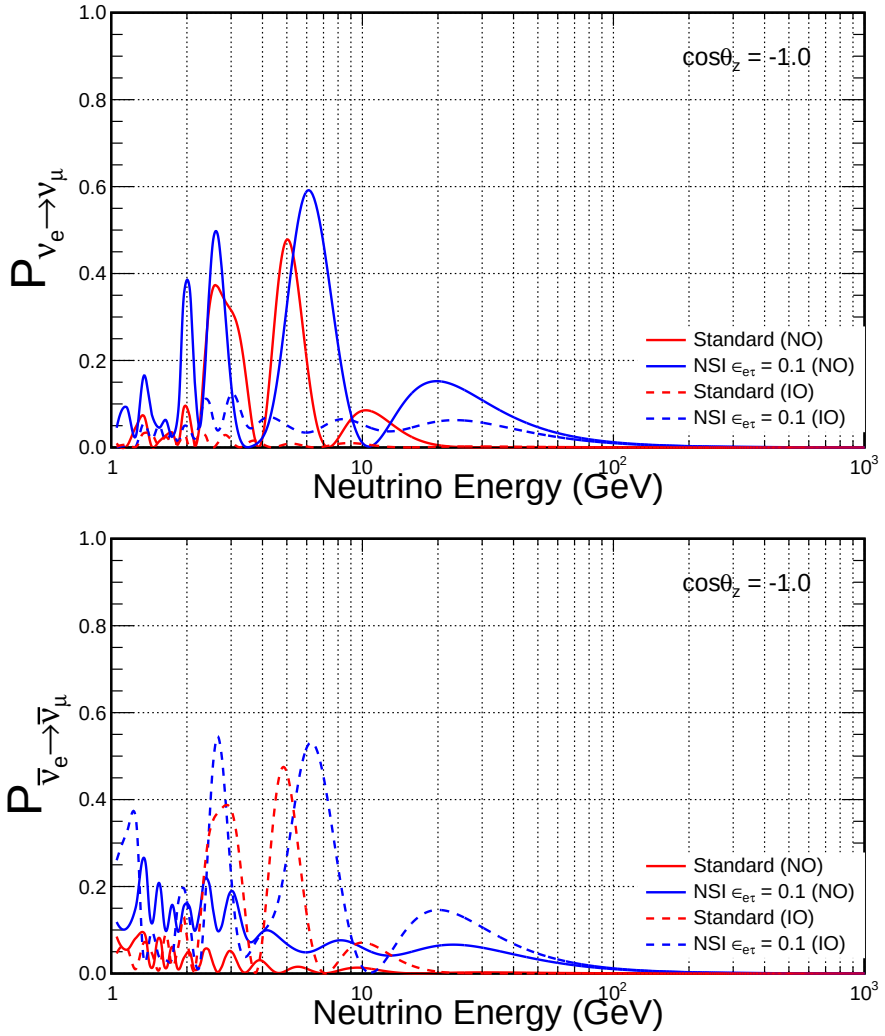

Figure 1.10: $\nu_e \rightarrow \nu_\mu$ (top) and $\overline{\nu}_e \rightarrow \overline{\nu}_\mu$ (bottom) transition probabilities for fixed baseline $\cos\theta_z = -1$, corresponding to vertically up-going neutrinos. The red line shows the global best-fit oscillations [90], while the blue line corresponds to $\epsilon_{e\tau} = 0.1$ NSI, both assuming NO (solid) and IO (dashed) hypothesis.

In both muon appearance and disappearance channels, the impact of NSIs can be clearly seen from the difference between the red and the blue curves for a definite mass ordering assumption. For $\delta_{CP} = 0$, the behavior of neutrinos in NO (IO) is exactly degenerate with antineutrinos in IO (NO). For an assumed mass ordering hypothesis, although the NSI effects are anti-symmetric for neutrinos and antineutrinos, they are not exactly opposite, thereby leading to albeit small yet appreciable signal at charge blind iso-scalar detectors like ANTARES and KM3NeT.

1.3.4 Oscillograms in presence of NSIs

In this section, we will use oscillograms of neutrino propagating through Earth to study the effects of presence of non-standard neutrino-matter interactions on oscillation channels at atmospheric neutrino experiments.

$\nu_e \to \nu_x$ oscillation channels

Fig. 1.11 depicts oscillograms for electron neutrinos for the SM case (left) and for NSI (right), parameterised by $\epsilon_{e\tau} = 0.5$, an arbitrary value chosen within current experimental limits (Sec. 1.3.5). Non-zero $\epsilon_{e\tau}$ induces $\nu_e \to \nu_\tau$ flavour transitions apart from the standard $\nu_e \to \nu_\tau$ oscillations (bottom left), thereby, leading to a deficit of events in the electron disappearance channel (top right) from SM predictions. These missing events in the electron disappearance channel shows up as flavour transmuted events in tau appearance channel (bottom right), which will further decay to ν_μ (BR $\simeq$ 17%) leading to an excess of events in the muon appearance channel (middle right) from SM estimations. The sum of the three panels in each column adds up to unity.

NSI parameters $\epsilon_{e\tau}$ and $\epsilon_{e\mu}$ appear in leading order in the probability expression of the ν_e oscillation channels. Hence the impact of $\epsilon_{e\tau}$ and $\epsilon_{e\mu}$ would be more prominent compared to $\epsilon_{\mu\tau}$ appearing in sub-leading terms. The effect of NSIs is more prominent at higher energies, since oscillation effects are phased out at those energies.

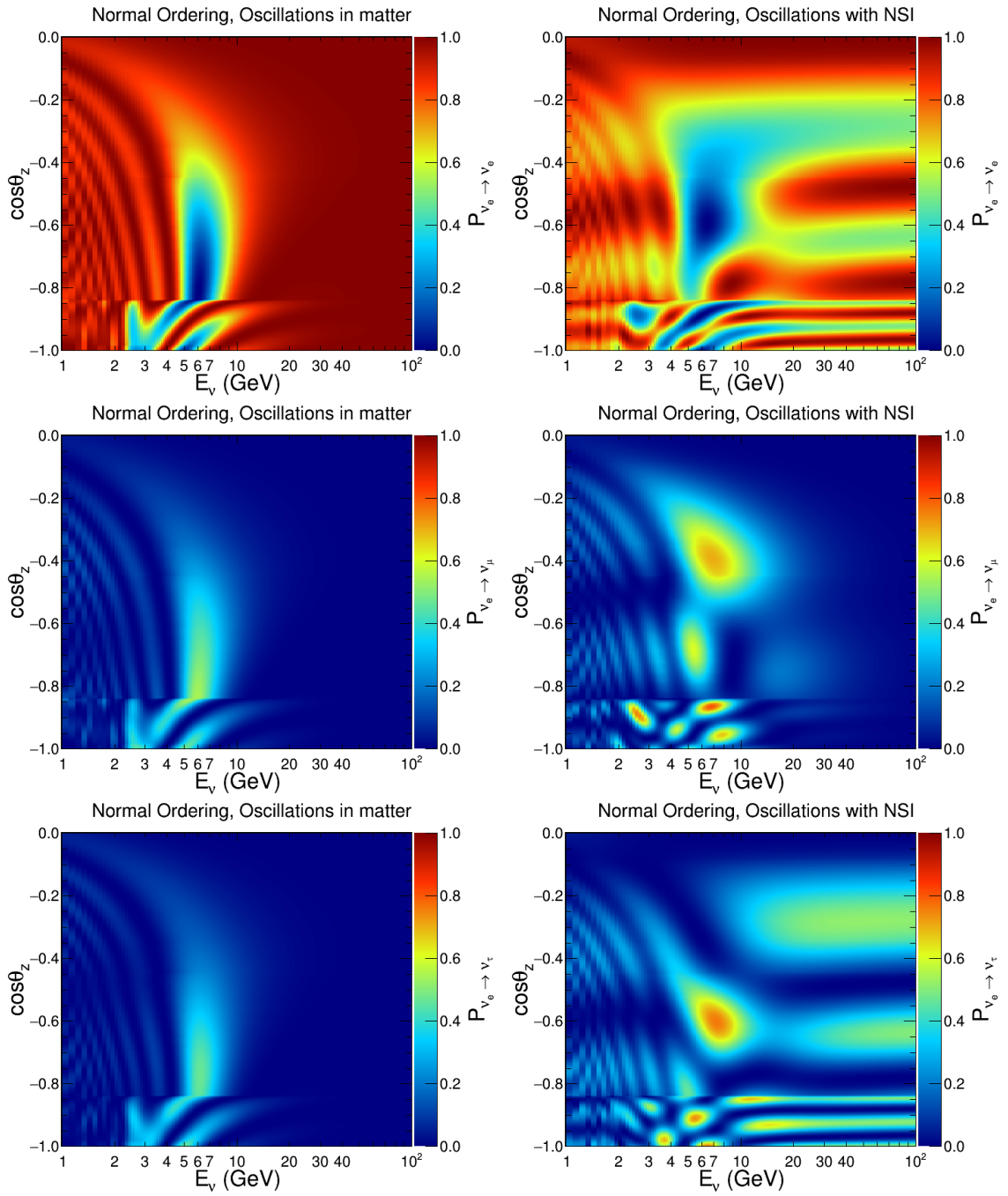

Figure 1.11: $P_{\nu_e \to \nu_x}(x = e, \mu, \tau)$ for SM case (left) and when NSI is considered (right), assuming $\epsilon_{e\tau} = 0.5$, as a function of neutrino energy E_ν and cosine of the zenith angle $\cos\theta_z$. NO is assumed.

$\overline{\nu}_e \to \overline{\nu}_x$ oscillation channels

Fig. 1.12 depicts oscillograms for electron antineutrinos for the SM case (left) and for NSI (right), parameterised by $\epsilon_{e\tau} = 0.5$. Since we are assuming NO, MSW resonance happens for neutrinos. However, non-zero $\epsilon_{e\tau}$ induces $\overline{\nu}_e \to \overline{\nu}_\tau$ flavour transitions, thereby, leading to a deficit of events in the electron disappearance channel (top right) from SM predictions. These missing events in the electron disappearance channel shows up as flavour transmuted events in tau appearance (bottom right) and muon appearance (middle right) channels.

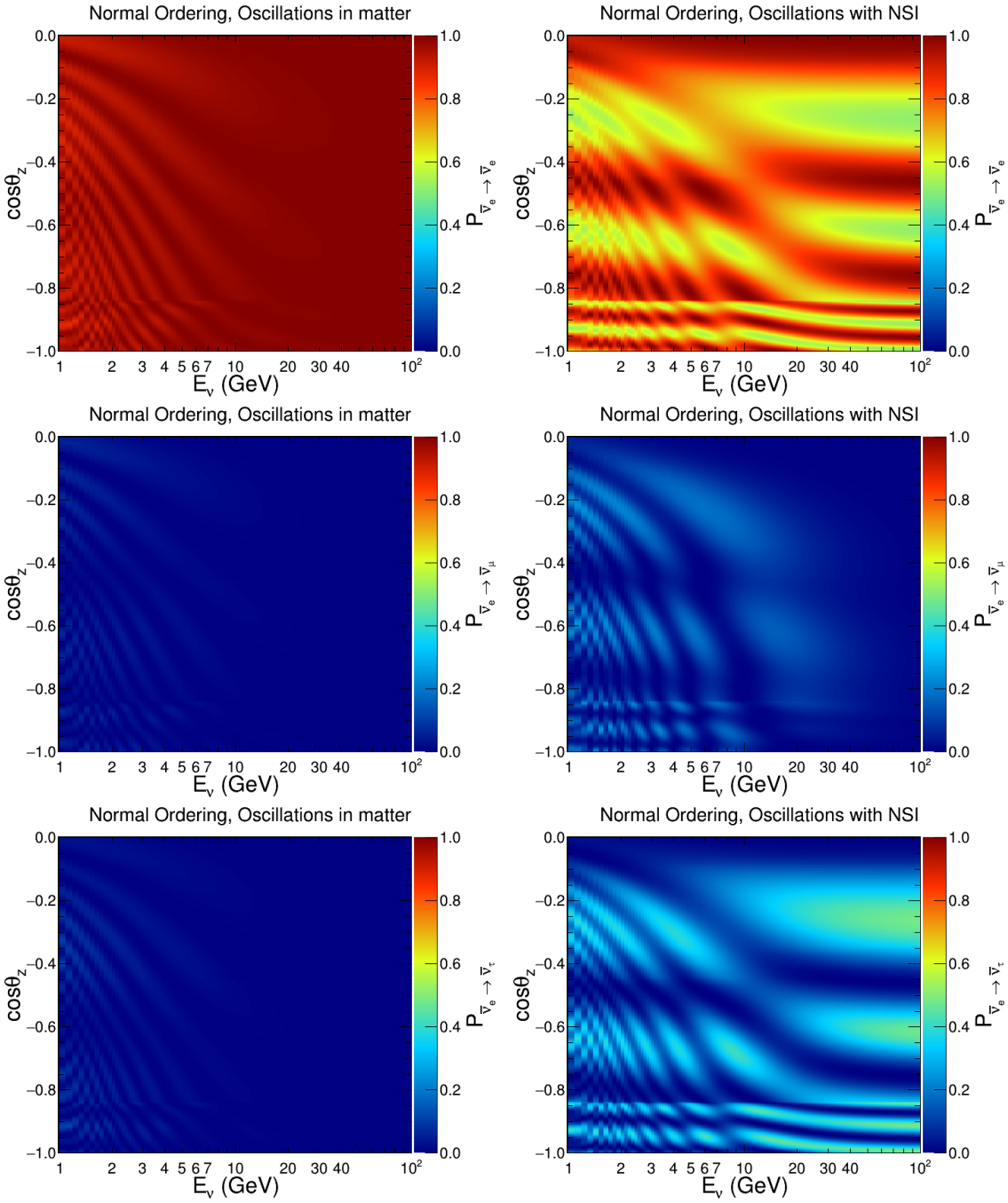

Figure 1.12: $P_{\overline{\nu}_e \to \overline{\nu}_x}(x = e, \mu, \tau)$ for SM case (left) and when NSI is considered (right), assuming $\epsilon_{e\tau} = 0.5$, as a function of neutrino energy E_ν and cosine of the zenith angle $\cos\theta_z$. NO is assumed.

$\nu_\mu \to \nu_x$ oscillation channels

Fig. 1.13 depicts oscillograms for muon neutrinos for the SM case (left) and for NSI (right), parameterised by $\epsilon_{\mu\tau} = 0.05$. Non-zero $\epsilon_{\mu\tau}$ induces $\nu_\mu \to \nu_\tau$ flavour transitions apart from the standard $\nu_\mu \to \nu_\tau$ oscillations (bottom left), thereby, leading to a deficit of events in the muon disappearance channel (middle right) from SM predictions. These missing events in the muon disappearance channel shows up as flavour transmuted events in tau appearance channel (bottom right). The electron appearance channel (top right) follows almost like the standard matter oscillations.

Three NSI parameters: $\epsilon_{\mu\tau}$, $\epsilon_{\mu\mu}$ and $\epsilon_{\tau\tau}$, appear in leading order in the probability expression of the $\nu_\mu \to \nu_\mu$ disappearance and $\nu_\mu \to \nu_\tau$ appearance channels. However, $\epsilon_{e\tau}$ and $\epsilon_{e\mu}$ play a sub-dominant role in this channel.

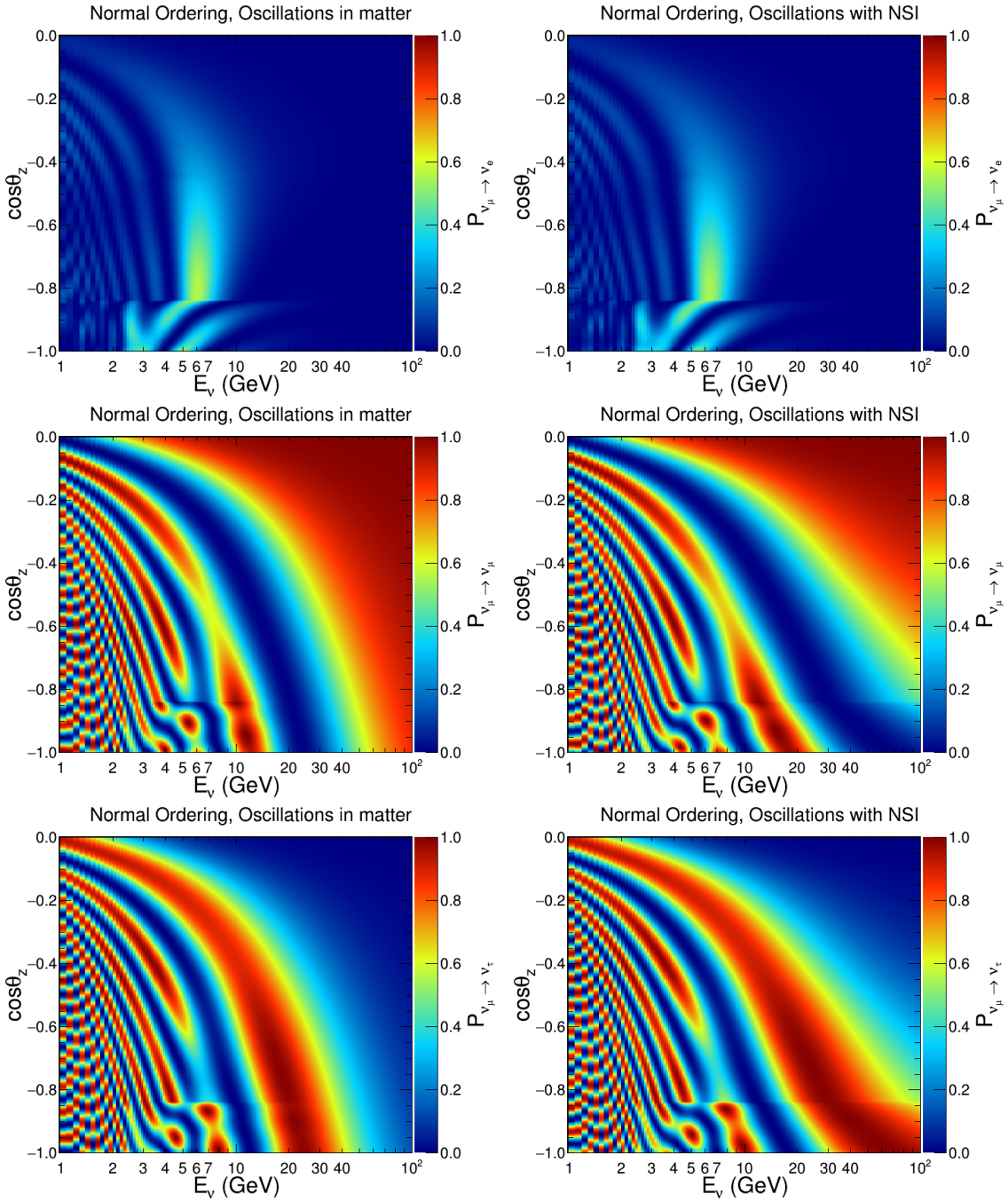

Figure 1.13: $P_{\nu_\mu \to \nu_x}(x = e,\ \mu,\ \tau)$ for SM case (left) and when NSIs are considered (right), assuming $\epsilon_{\mu\tau} = 0.05$, as a function of neutrino energy E_ν and cosine of the zenith angle $\cos\theta_z$. NO is assumed.

$\overline{\nu}_\mu \to \overline{\nu}_x$ oscillation channels

Fig. 1.14 depicts oscillograms for muon antineutrinos for the SM case (left) and for NSI (right), parameterised by $\epsilon_{\mu\tau} = 0.05$. MSW resonance does not happen since NO is assumed. However, non-zero $\epsilon_{\mu\tau}$ induces flavour transitions in $\overline{\nu}_\mu \to \overline{\nu}_\tau$ channel, thereby affecting the $\overline{\nu}_\mu \to \overline{\nu}_\mu$ channel. The effect is opposite for neutrinos and antineutrinos. This is because there is a degeneracy between the sign of $\epsilon_{\mu\tau}$ and the ordering, which in turn is equivalent to switching between neutrinos and antineutrinos assuming $\delta_{CP} = 0$.

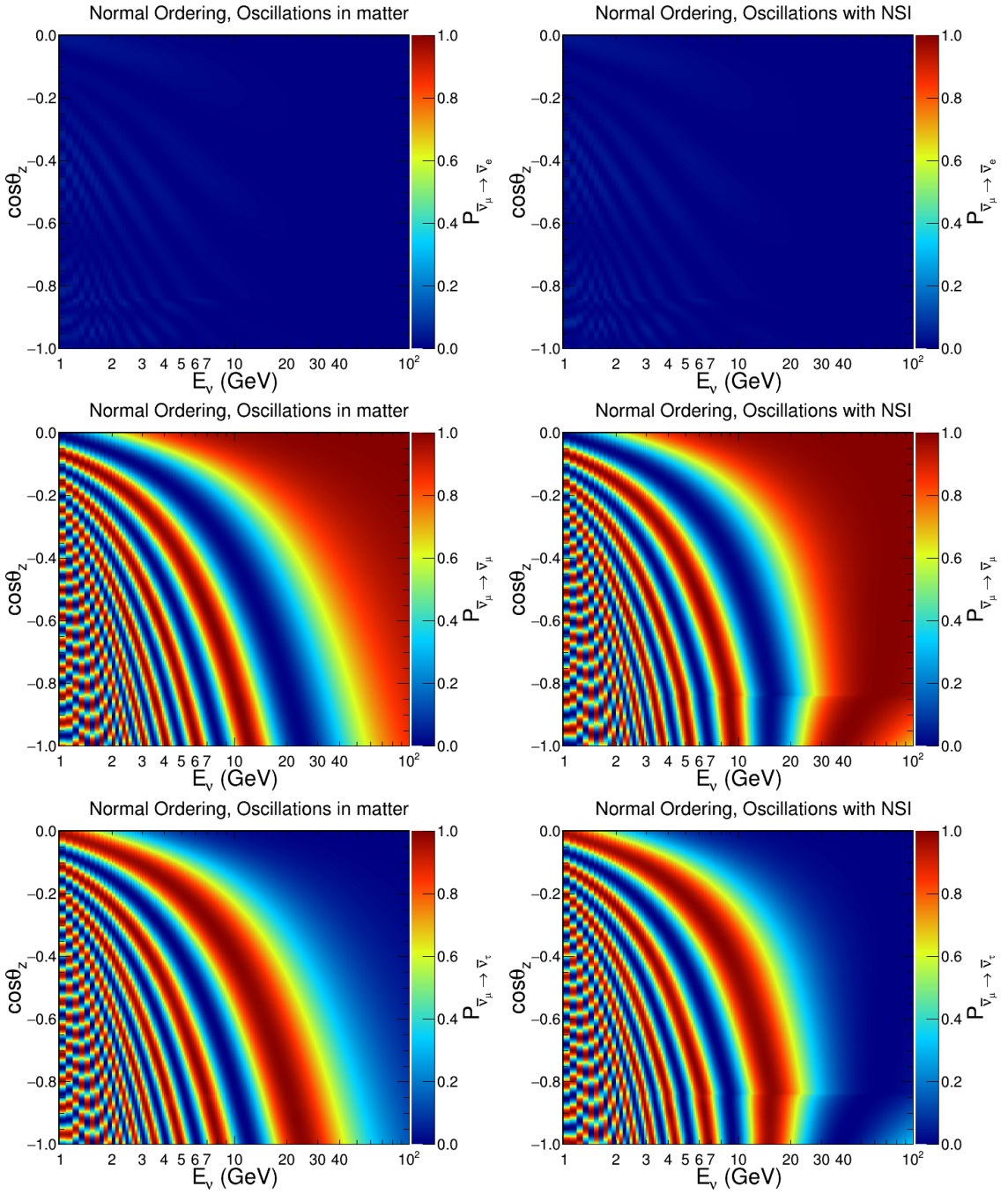

Figure 1.14: $P_{\nu_\mu \to \nu_x}(x = e,\ \mu,\ \tau)$ for SM case (left) and when NSIs are considered (right), assuming $\epsilon_{\mu\tau} = 0.05$, as a function of neutrino energy E_ν and cosine of the zenith angle $\cos\theta_z$. NO is assumed.

1.3.5 Current limits on NSIs

Currently, almost all the neutrino oscillation data are consistent with the standard three-flavour scheme of massive and mixed neutrinos. Thus, if NSIs exist, they will manifest as a subdominant effect in oscillation data. NSIs in propagation has been constrained by the oscillation data collected by solar [91], atmospheric [92, 93] and accelerator neutrino experiments [94] or by a combination of all [95, 96, 97]. Reactor or short baseline experiments are not relevant in constraining NSIs in propagation due to negligible matter effects, but they can constrain detection NSIs. Here we review the current bounds on NSIs in propagation for interaction of neutrinos with d-quarks (notation used in this thesis) from different experiments.

The Super-K collaboration analysed their atmospheric neutrino data collected during its first and second phase and obtained constraints on NSIs in the $\mu - \tau$ sector assuming NSIs with d-quarks. The bounds are [92]

$$|\epsilon_{\mu\tau}| < 0.011 \quad \text{and} \quad |\epsilon_{\mu\mu} - \epsilon_{\tau\tau}| < 0.049 \quad (\text{at } 90\% \text{ C.L}). \tag{1.52}$$

The IceCube collaboration also analysed three years of atmospheric muon neutrino disappearance data collected with DeepCore and placed the following limits [93]:

$$-6.7 \times 10^{-3} < \epsilon_{\mu\tau} < 8.1 \times 10^{-3} \quad (\text{at } 90\% \text{ C.L}). \tag{1.53}$$

The bounds obtained by the MINOS collaboration, translated to NSIs d-quark couplings are [94]

$$-0.067 < \epsilon_{\mu\tau} < 0.023 \quad (\text{at } 90\% \text{ C.L}). \tag{1.54}$$

Bounds on NSIs obtained from the analysis of global oscillation data can be found in [97]. In Tab. 1.2, the bounds on NSIs in propagation are collected.

NSI Couplings	Bounds	Reference	Experiment
Flavour diagonal (FD)			
$\epsilon_{ee} - \epsilon_{\mu\mu}$	$(-0.027, 0.474)$	[98]	-
$\epsilon_{\tau\tau} - \epsilon_{\mu\mu}$	$(-0.005, 0.095)$	[98]	-
$\epsilon_{\tau\tau} - \epsilon_{\mu\mu}$	$(-0.036, 0.031)$	[99]	-
$\epsilon_{\tau\tau} - \epsilon_{\mu\mu}$	$(-0.049, 0.049)$	[92]	Super-K
Flavour changing (FC)			
$\epsilon_{e\mu}$	$(-0.061, 0.049)$	[98]	-
$\epsilon_{e\tau}$	$(-0.247, 0.119)$	[98]	-
$\epsilon_{e\tau}$ (for $\epsilon_{ee} = -0.5$)	$(-0.05, 0.05)$	[92]	Super-K
$\epsilon_{e\tau}$ (for $\epsilon_{ee} = 0.5$)	$(-0.019, 0.013)$	[92]	Super-K
$\epsilon_{\mu\tau}$	$(-0.01, 0.01)$	[98]	-
$\epsilon_{\mu\tau}$	$(-0.0061, 0.0056)$	[99]	-
$\epsilon_{\mu\tau}$	$(-0.006, 0.0054)$	[100]	-
$\epsilon_{\mu\tau}$	$(-0.011, 0.011)$	[92]	Super-K
$\epsilon_{\mu\tau}$	$(-0.0067, 0.0081)$	[93]	IceCube
$\epsilon_{\mu\tau}$	$(-0.067, 0.023)$	[94]	MINOS

Table 1.2: Constraints on the propagation NSIs at 90% C.L. for the interaction of neutrinos with d-quarks. Only one NSI parameter is considered at a time.

In the study presented in subsequent chapters of this thesis, we calculate new constraints on the NSI model parameters with atmospheric muon neutrino data collected by the ANTARES undersea neutrino telescope and estimate the sensitivity of its successor experiment, KM3NeT-ORCA.

2 Neutrino Telescopes

"If your experiment needs statistics, you ought to have done a better experiment."

— ERNEST RUTHERFORD

Contents

This chapter discusses how neutrinos are produced in the atmosphere, their interactions in sea water and finally their detection at Cherenkov neutrino telescopes. It also provides an overview of the two operational neutrino observatories in the Northern Hemisphere, namely, ANTARES and its sibling KM3NeT. The origin of atmospheric neutrinos is briefed in Sec. 2.1, their interaction with matter is explained in Sec. 2.2, the basics of their detection principle at neutrino telescopes is discussed in Sec. 2.3, followed by a description of the detectors in Sec. 2.4.

This Chapter is completed with the description of a method to obtain time calibration constants with atmospheric muons in KM3NeT, reported in Sec. 2.5.

2.1 Atmospheric Neutrinos

The upper atmosphere of the Earth is being ubiquitously impinged by cosmic rays almost isotropically. Primary cosmic ray particles (mostly protons, p,) collide with the nuclei (N) in the atmosphere, the interactions of which produce charged mesons:

$$p + N \rightarrow X + \pi^{\pm}, K^{\pm}. \tag{2.1}$$

The decay of these secondary particles to muon and muon neutrinos form a copious source of the conventional atmospheric neutrino flux [101]:

$$\begin{aligned}
\pi^- &\rightarrow \mu^- + \overline{\nu}_\mu \rightarrow e^- + \overline{\nu}_e + \nu_\mu + \overline{\nu}_\mu && \text{(BR: 99.9\%)} \\
K^- &\rightarrow \mu^- + \overline{\nu}_\mu \rightarrow e^- + \overline{\nu}_e + \nu_\mu + \overline{\nu}_\mu && \text{(BR: 63.6\%)} \\
&\rightarrow \pi^- + \pi^0 && \text{(BR: 20.7\%)} \\
&\rightarrow \pi^- + \pi^- + \pi^+ && \text{(BR: 5.6\%)} \\
&\rightarrow \pi^0 + e^- + \overline{\nu}_e && \text{(BR: 5.1\%)} \\
&\rightarrow \pi^0 + \mu^- + \overline{\nu}_\mu && \text{(BR: 3.4\%)} \\
&\rightarrow \pi^- + \pi^0 + \pi^0 && \text{(BR: 1.8\%)}
\end{aligned} \tag{2.2}$$

The muon decays are the main sources for $\nu_e(\overline{\nu}_e)$ production below 1 GeV. However, with increasing energy, the ratio of $(\nu_e + \overline{\nu}_e)$ to $(\nu_\mu + \overline{\nu}_\mu)$ decreases due to time dilation of high energetic muons.

From (2.2), it can be seen that the $\nu_e : \nu_\mu$ fraction is roughly $1 : 2$, the $\nu_\mu : \overline{\nu}_\mu$ ratio is proportional to the $\mu^- : \mu^+$ ratio and the ratio of ν_e to $\overline{\nu}_e$ is proportional to $\mu^+ : \mu^-$. The atmospheric neutrino flux follows a power-law energy spectrum $E^{-\gamma}$ with a spectral index (γ) close to 3 in the few GeV range. Fig. 2.1 (left) shows the direction averaged energy spectra of atmospheric neutrino fluxes for each flavour. As expected, $\nu_\mu(\overline{\nu}_\mu)$ have a harder energy spectra compared to $\nu_e(\overline{\nu}_e)$. The flux of antineutrinos is lower than neutrinos, especially for muon antineutrinos. The atmospheric flux that reaches the detectors are different due to oscillation effects. This makes the neutrino flux at the detectors highly zenith dependent. Fig. 2.1 (right) shows the total ν_μ (and $\overline{\nu}_\mu$) to ν_e (and $\overline{\nu}_e$) ratio based on different neutrino energies and zenith angles. The ratios change drastically with neutrino energy and zenith angle due to neutrino oscillations.

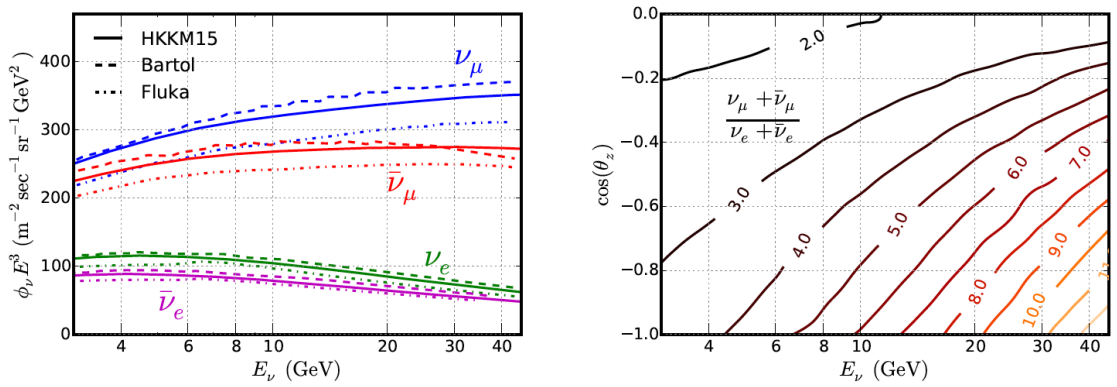

Figure 2.1: Left: direction-averaged energy spectra of atmospheric neutrino flux for $\{\nu_e, \overline{\nu}_e, \nu_\mu, \overline{\nu}_\mu\}$ for different models. Right: isocontour curves of flux ratio $(\nu_\mu + \overline{\nu}_\mu)/(\nu_e + \overline{\nu}_e)$. From [102].

Note that no $\nu_\tau(\overline{\nu}_\tau)$ are produced in cosmic ray interactions. However, they are produced from transitions of muon and electron flavours driven by $P_{\nu_\mu \to \nu_\tau}$ and $P_{\nu_e \to \nu_\tau}$, respectively.

For the work in this thesis, the atmospheric neutrino flux model developed by the HKKM group [103] has been used. It is further illustrated in Sec. 3.3.1. The uncertainty on the ratio of ν_μ to ν_e, the modification of the ratio $\nu/\overline{\nu}$ (applied on both ν_e and ν_μ), the uncertainty on the ratio of up-going to horizontal neutrinos, and the error on the spectral index ($\Delta\gamma$) are adopted from [104] and treated as systematic uncertainties in our study (Sec. 4.3.3).

2.2 Neutrino Interactions

Neutrinos interact weakly via charged-current (CC, exchange of $W^\pm$) or neutral-current (NC, exchange of Z^0) processes. While CC interactions produce a hadronic shower and a lepton, NC interactions of all flavours induce a hadronic shower and a scattered neutrino. Fig. 2.2 depicts the four distinct neutrino interaction channels.

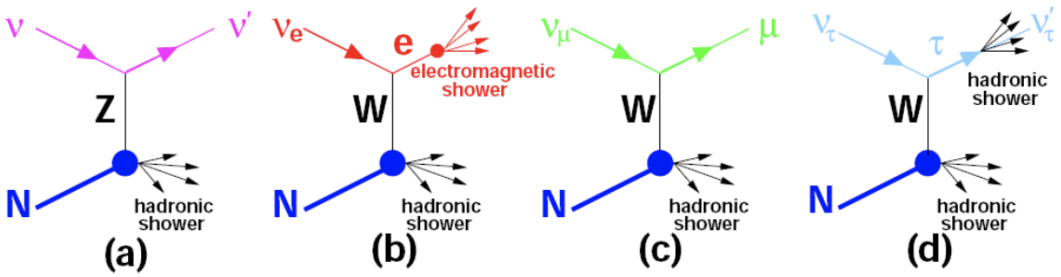

Figure 2.2: Neutrino interaction channels, mediated by Z^0 and $W^\pm$, relevant for neutrino telescopes. (a) NC interaction of all neutrino flavours resulting in a hadronic shower and a scattered neutrino. (b) CC interaction of ν_e, which produces an electromagnetic shower and a hadronic shower. (c) CC interaction of ν_μ producing a μ^- and a hadronic shower. (d) CC interaction of ν_τ resulting in two hadronic showers (see text). The N particle represents any nucleon present in the detector medium. From [105].

NC interactions (Fig. 2.2 (a)) result in the neutrino scattering from a nucleon without a flavor change. The outgoing neutrino, which is accompanied by a visible hadronic cascade, remains unobserved in the detector. The NC interactions can be expressed as

$$\nu_l(\overline{\nu}_l) + N \to \nu_l(\overline{\nu}_l) + X \quad (l = e, \mu, \tau). \tag{2.3}$$

In CC interactions (Fig. 2.2 (b – d)), the outgoing charged leptons will have the flavour matching of the flavour of parent neutrinos, due to flavor conservation. Thus, a ν_μ $(\overline{\nu}_\mu)$ yields a μ^- (μ^+), a ν_e $(\overline{\nu}_e)$ yields a e^- (e^+) and a ν_τ $(\overline{\nu}_\tau)$ yields a τ^- (τ^+). The CC interactions can be expressed as

$$\nu_l(\overline{\nu}_l) + N \to l^\pm + X \quad (l = e, \mu, \tau), \tag{2.4}$$

where l denotes the initial neutrino flavor and N represents any arbitrary nucleon. This produces a charged lepton of the associated neutrino flavor and a hadronic cascade (X) localized at the interaction vertex.

2.2.1 Neutrino – fermion scattering

We first discuss the scattering of neutrinos off fermions, i.e. leptons or quarks [106, 107], which depend on the spin configurations of the initial states. While the CC interaction is maximally parity-violating choosing only left-handed[1] neutrinos and right-handed antineutinos, in case of NC interactions, a left-handed neutrino can scatter off a right-handed fermion.

In the following, it is assumed that the four momentum transfer Q^2 is small compared to the mediating boson mass, i.e. $Q^2 \ll M^2_{Z^0,W^\pm}$, and that the centre-of-mass energy $\sqrt{s}$ is larger compared to the lepton mass, i.e. $s \gg m_f^2$.

Neutrino – fermion CC interaction

The process in which a neutrino ν_l scatters off a free fermion f to produce a lepton l and a different fermion f' is

$$\nu_l + f \to l + f' \quad (l \neq f). \tag{2.5}$$

The differential and total cross-section for such a process is given by [108]:

$$\frac{d\sigma_{CC}(\nu f)}{d\Omega} = \frac{G_F^2 s}{4\pi^2}, \quad \sigma_{CC}(\nu f) = \frac{G_F^2 s}{\pi}, \tag{2.6}$$

where the G_F ($\approx 1.13 \times 10^{-5}\,\mathrm{GeV}^{-2}$) is the Fermi constant. The cross-section linearly increases with $s = 2m_f(m_f + E_\nu)$.

Antineutrino – fermion CC interaction

A similar process but with antineutrino in the initial state is

$$\overline{\nu}_l + f \to l + f' \quad (l \neq f). \tag{2.7}$$

The differential and total cross-section for such a process is given by [106]

$$\frac{d\sigma_{CC}(\overline{\nu} f)}{d\Omega} = \frac{G_F^2 s}{16\pi^2}(1 - \cos\theta)^2, \quad \frac{d\sigma_{CC}(\overline{\nu} f)}{dy} = \frac{G_F^2 s}{\pi}(1 - y)^2, \quad \sigma_{CC}(\overline{\nu} f) = \frac{G_F^2 s}{3\pi}, \tag{2.8}$$

where θ is the neutrino-lepton scattering angle in the centre-of-mass frame, y is the fraction of the neutrino energy transferred to the target system, referred as *inelasticity* or *Bjorken-y*:

$$y = \frac{E_\nu - E_f}{E_\nu}. \tag{2.9}$$

The cross-section for antineutrinos turns out to be three times lower than for neutrinos, i.e. $\sigma_{CC}(\nu f)/\sigma_{CC}(\overline{\nu} f) \approx 3$. This suppression stems from helicity constraints [109].

[1] For (Dirac) neutrinos the intrinsic spin is always opposite to the linear momentum which is referred to as "left-handed", whereas the antineutrinos are always "right-handed". "Right-handed" neutrinos and "left-handed" antineutrinos do not exist within the Standard Model.

(Anti)neutrino – fermion NC interaction

The NC interaction can couple to both, left-handed and right-handed components of the fermion f:

$$\nu_l(\overline{\nu}_l) + f \rightarrow \nu_l(\overline{\nu}_l) + f' \quad (l \neq f). \tag{2.10}$$

The differential and total cross-section for such a process is given by [107]

$$\frac{d\sigma_{NC}(\nu f)}{dy} = \frac{G_F^2 s}{\pi}[g_L^2 + (1-y)^2 g_R^2], \quad \frac{d\sigma_{NC}(\overline{\nu} f)}{dy} = \frac{G_F^2 s}{\pi}[g_L^2 (1-y)^2 + g_R^2], \tag{2.11}$$

where g_L and g_R are the left-handed and right-handed couplings of the fermion, whose values are listed in Tab. 2.1.

Z^0 coupling	g_L	g_R
ν_e, ν_μ, ν_τ	$\frac{1}{2}$	0
e, μ, τ	$-\frac{1}{2} + \sin^2\theta_W$	$\sin^2\theta_W$
u, c, t	$\frac{1}{2} - \frac{2}{3}\sin^2\theta_W$	$-\frac{2}{3}\sin^2\theta_W$

Table 2.1: Weak neutral current couplings g_L and g_R. The value of the weak mixing angle θ_W is $\approx 29°$ [106].

The total cross-section for scattering of a muon neutrino off an electron is:

$$\sigma_{tot}(\nu_\mu + e^- \rightarrow \nu_\mu + e^-) = \sigma_{NC} = \frac{G_F^2 s}{\pi}\left(\frac{1}{4} - \sin^2\theta_W + \frac{4}{3}\sin^4\theta_W\right), \tag{2.12}$$

while for scattering of an electron neutrino off an electron, the total cross-section is composed of CC as well as NC contributions:

$$\sigma_{tot}(\nu_e + e^- \rightarrow \nu_e + e^-) = \sigma_{CC} + \sigma_{NC} = \frac{G_F^2 s}{\pi}\left(1 - 2\sin^2\theta_W + \frac{4}{3}\sin^4\theta_W\right). \tag{2.13}$$

2.2.2 Neutrino – nucleon scattering

In the relevant energy range for ORCA, the neutrino cross-section is dominated by the scattering of neutrinos off nucleons. For neutrino energies of $\mathcal{O}$(GeV), there are three main processes that contribute to the total cross section. The four-momentum transfer Q^2 decides the type of interaction. For higher Q^2, the interaction becomes more and more inelastic.

- **Elastic and quasi-elastic scattering (QE):** At low Q^2, the neutrino scatters off an entire nucleon. In the case of a charged (neutral) current interaction this is called quasi-elastic (elastic) scattering. QE scattering dominates at energies ≤ 1 GeV.
- **Resonance Production (RES):** For higher energies, the neutrino can also excite the nucleon, which then decays, in a resonance production process. The resonance productions then decay to nucleons along with single or multiple pions, kaons and/or radiative photons. The RES production plays a dominant role in the energy range $[1-4]$ GeV.
- **Deep inelastic scattering (DIS):** With even higher Q^2, the neutrino can resolve the internal structure of the nucleon and scatter directly off the quark constituents. This splits up the nucleon leading to a jet of hadrons. This is the main component in the ν_τ-nucleon scattering and dominant for energies $>\sim 4$ GeV. For details, see [107].

Existing measurements of total neutrino and antineutino cross-sections are shown in Fig. 2.3.

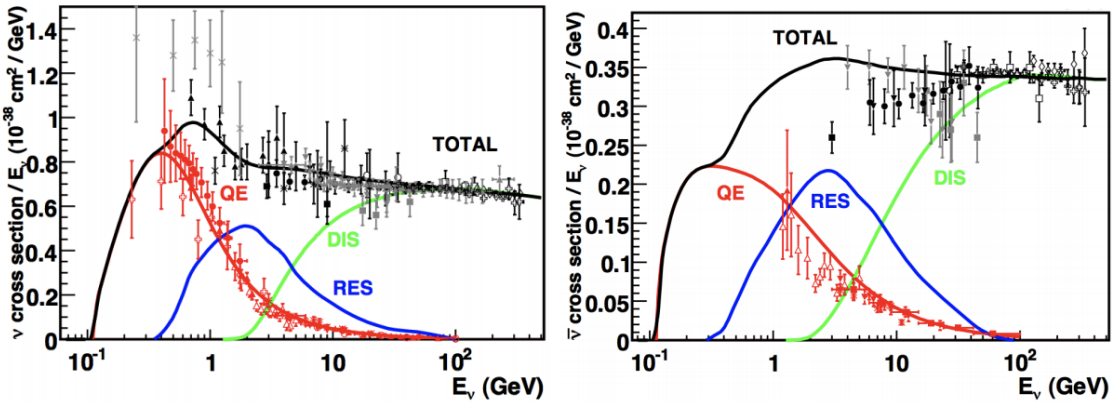

Figure 2.3: Muon neutrino (left) and antineutrino (right) CC cross section measurements and predictions from the NUANCE generator [110] as a function of neutrino energy. The contributing processes in this energy region include quasi-elastic (QE) scattering, resonance production (RES) and deep inelastic scattering (DIS). The error bars (typically 10 – 40%, depending on the channel) reflect the uncertainties on these cross sections. Mind the scale on $Y-$axis. From [111].

Note that each of the above mentioned processes have both CC and NC counterparts, the NC interaction cross-section being ~ 3 times smaller than the associated CC interaction cross-sections. Additionally, the cross-section for neutrinos is about a factor of 2 higher than those for antineutinos.

The resulting cross-sections for all flavours used in the simulation (Sec. 3.3.3) are shown in Fig. 2.4. The ν_τ interaction cross-section is reduced with a threshold of ~ 3.5 GeV, due to the large τ mass. The severely suppressed ν_τ CC cross-section is discussed in [112].

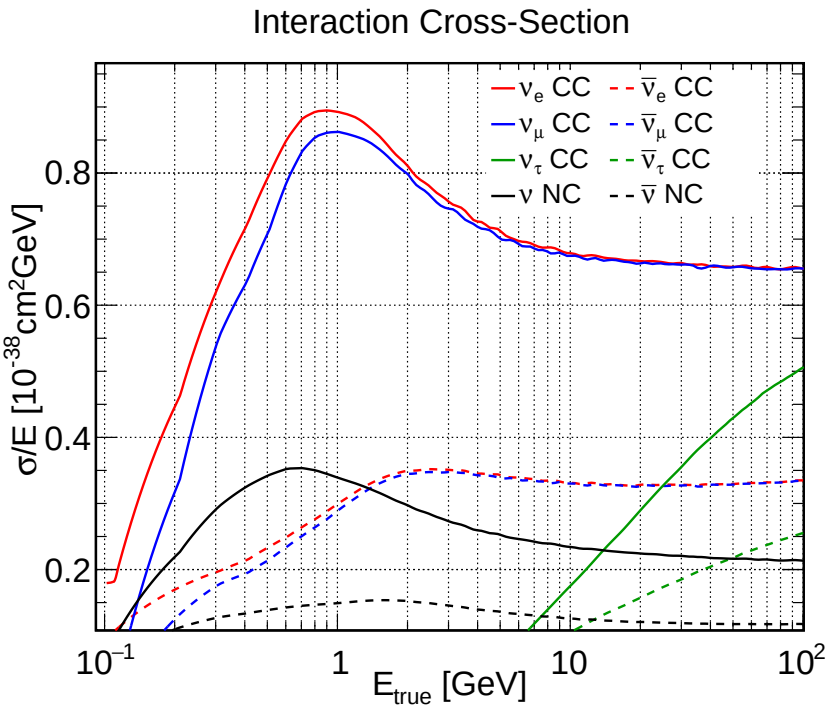

Figure 2.4: Total neutrino-nucleon interaction cross-section divided by energy for several interaction channels, as indicated in the labels. Adapted from [111].

2.3 Neutrino Detection

Even though neutrinos cannot be directly detected, the secondary charged particles produced in neutrino–nucleon interactions in sea water can be observed. The light from Cherenov radiation produced along the trajectory of the relativisitic charged particles can be detected by photo-multiplier tubes (PMTs) instrumented within the detector volume. The charge, time and space information of the digitised signals recorded in the PMTs (hits), can be used to infer the direction and energy of the parent neutrino.

2.3.1 Cherenkov Radiation

Charged particles travelling in a dielectric medium at a velocity greater than the phase velocity of light in that medium emit radiation akin to the sonic blast of an aircraft travelling at supersonic speeds. This phenomenon is called the Cherenkov effect and the radiation thus emitted is called Cherenkov light [113].

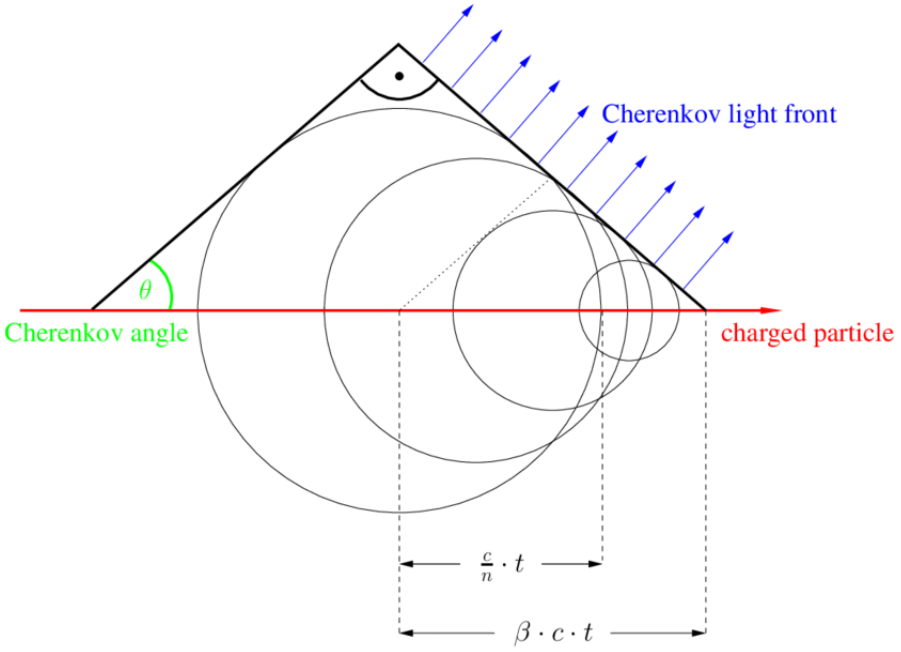

Figure 2.5: A schematic of the Cherenkov effect showing a traversing particle with velocity greater than the phase velocity of light in the medium, emitting radiations in concentric circles which overlap and interfere constructively to produce coherent radiation in a cone. The distance travelled by light is $\frac{c}{n}t$ while the particle travels a distance of βct in the same time t. From [114].

Cherenkov light is emitted in a cone around the direction of the particle with a characteristic opening angle θ_c. The emitting particle lies at the vertex of the cone. The emitted radiation at each point overlaps and interferes constructively at the edges of the cone (Fig. 2.5). θ_c is related to the speed of the particle ($\beta = \frac{v}{c}$) and the refractive index n of the medium by the following formula:

$$\cos\theta_c = \frac{1}{\beta n}. \tag{2.14}$$

Assuming $\beta \approx 1$ for a highly relativistic particle, the Cherenkov angle becomes independent of the particle's energy. For sea water, $n \approx 1.35$, and hence, $\theta_c \approx 42^\circ$.

Most of the observed Cherenkov radiation falls in the ultraviolet region and the blue band of the visible spectrum due to the dispersion properties of water. The number of photons N emitted within a wavelength interval $d\lambda$ by a charged particle with charge ze per path length dx is given by

$$\frac{d^2N}{dxd\lambda} = \frac{2\pi\alpha}{\lambda^2}\left(1 - \frac{1}{\beta^2 n^2}\right), \tag{2.15}$$

where λ is the Cherenkov photon's wavelength and $\alpha(\approx \frac{1}{137})$ is the fine-structure constant. For the wavelength range of 300 – 600 nm, which is the relevant one to water-based neutrino telescopes, the above equation provides an estimate of the number of Cherenkov photons to be expected per track length:

$$\frac{dN}{dx} = 340 \text{ cm}^{-1}. \tag{2.16}$$

The Cherenkov threshold for a particle with rest mass m_0 is given by:

$$E_c = \frac{m_0}{\sqrt{1 - 1/n^2}}. \tag{2.17}$$

This translates into a kinetic energy ($T_c = E_c - m_0c^2$) of $T_c(e) \approx 0.25$ MeV for electrons and $T_c(\mu) \approx 53$ MeV for muons in sea water.

2.3.2 Particle Propagation

While the Cherenkov effect is the main physical process exploited by neutrino telescopes for detection of muons, it is not the major source of energy loss for muons travelling in an optical medium. Energy loss for muons in water mainly happens via ionization (dominant at $E_\mu < 1$ TeV), e^+e^- pair production (dominant at $E_\mu > 1$ TeV), bremsstrahlung and nuclear interactions. The total contribution can be parameterised as

$$-\frac{dE_\mu}{dx} = a + b \cdot E_\mu, \tag{2.18}$$

where the ionization and stochastic loss terms (a and b, respectively) are assumed independent of the muon energy. The typical values in water are: $a = 0.274$ GeV m^{-1} and $b = 3.492 \times 10^{-2}$ m^{-1} [115, 116].

The signature of few-GeV muons in sea water is a single uniform track, the range, R, of which can be derived from

$$R = \frac{1}{b} \cdot \ln\left(1 + \frac{b \cdot E_0}{a}\right). \tag{2.19}$$

The length of the track is $\sim$ 4 m per GeV. Eventually, the muon decays ($T_\mu^{\text{rest}} \sim 2.2\ \mu s$) into two neutrinos and an electron, which initiates an electromagnetic shower.

Electrons lose energy mainly via bremsstrahlung and ionisation. The radiated photon in turn undergoes pair production or Compton scattering off electrons. This results in a cascading of electrons and positrons producing photons and vice versa, called *electromagnetic shower* (EM). Compared to clean muon tracks, showers appear as point-like burst of light sources in the detector localised within a distance below the Molière radius [117], which is less than 10 cm in sea water. The mean length and the total Cherenkov light yield are proportional to the initial shower energy, allowing for a calorimetric energy measurement. The signature of a *hadronic shower* is similar to that of EM showers in the detector to a first approximation, apart from the fact that they are induced by hadronic interactions rather than EM interactions. The characteristic evolution of hadronic showers and the corresponding Cherenkov light emission in water and ice is discussed in [118, 119, 120].

2.3.3 Light Detection

The number, arrival time and arrival direction of the Cherenkov photons are largely affected by the light attenuation processes, namely, absorption and scattering. While absorption reduces the photon content, scattering reduces the information content about

the arrival times and directions. In particular, scattering limits the angular resolution, since the scattered particles do not point back to their parent particle. The limitations set by this attenuation on the effective path length of Cherenkov photons determine the layout of detector elements in a typical under water/ice neutrino telescope.

The parameter governing absorption is the absorption length λ_a, which is wavelength-dependent. The corresponding parameter for scattering is the mean scattering length λ_s. These parameters correspond to the path length x travelled by light of wavelength λ, at which its photon survival probability (intensity) I_0 is reduced by a factor of $1/e$:

$$I(x) = I_0 \cdot e^{\frac{-x}{\lambda_{a,s}}}. \tag{2.20}$$

In addition to the scattering length, scattering processes are characterised by the distribution of the scattering angle $\beta(\theta_s)$, also called the phase function which determines the effective scattering length:

$$\lambda_s^{eff} = \lambda_s / [1 - \langle \cos\theta_s \rangle], \tag{2.21}$$

where $\langle \cos\theta_s \rangle$ is the average cosine of the scattering angle. For seawater and a wavelength of ~ 470 nm, the measured values of these parameters are : $\lambda_a \approx 60$ m [121, 122] and $\lambda_s^{eff} = 265$ m [122].

The arrival time of Cherenkov photons depends on the group velocity v_g of the medium:

$$v_g = c/n_g, \quad \text{with} \quad n_g = \frac{n}{1 + \frac{\lambda}{n}\frac{dn}{d\lambda}}, \tag{2.22}$$

where n_g is the group refractive index of the medium. For a photon wavelength of ~ 470 nm, the refractive indices for sea water are $n \approx 3.5$ and $n_g \approx 1.4$ [123].

The Cherenkov photons reaching the detector are detected using photo-multiplier tubes (PMTs), which are housed along with associated readout electronics within a spherical glass called *Digital Optical Modules* (DOMs). The glass sphere shields the PMTs from environmental nuances while being totally transparent to Cherenkov photons in the relevant energy range. Photons incident on the PMT photocathode area are converted into electrons (via photoelectric effect) with some efficiency (quantum efficiency, QE) and amplified. The information of the electrical charge and the timestamp of the photon striking on a PMT with a particular position and orientation is called a *hit*.

2.3.4 Background

Neutrino physics is a study of low statistics with abundant background. Neutrino telescopes have mainly two categories of background: optical noise encountered in the deep-sea environment, and a physical background of cosmic ray induced particles.

Optical noise

Sea water contains a trace amount of some radioactive isotopes, including ^{40}K which corresponds to 0.012% of potassium in Nature. The dominant decay channels of ^{40}K

nuclei are:

$$\beta^- \text{decay} : {}^{40}K \rightarrow {}^{40}Ca + e^- + \overline{\nu}_e \quad \text{(BR: 89.3\%)}$$
$$\text{Electron Capture} : {}^{40}K + e^- \rightarrow {}^{40}Ar + \gamma + \nu_e \quad \text{(BR: 10.7\%)} \tag{2.23}$$

The resulting electron, emitted in a β^- decay, has a maximal energy of 1.3 MeV, which is sufficient to generate Cherenkov light. The emitted photon from the excited state of ${}^{40}Ar$ produced via electron capture of ${}^{40}K$ has an energy of 1.46 MeV, which can generate Compton electrons capable of emitting Cherenkov light.

On the other hand, bacteria and other sea microorganisms can create bioluminescence. Bioluminescent light is spread out over a large band of wavelengths. One is a baseline noise resulting from a continuum of hits (60 – 120 kHz) throughout the detector; the other is manifested as short bursts of a few seconds on top of the baseline noise taking the hit count to over a MHz for those time periods. Seasonal variation of the bioluminescence baseline rate, due to changing sea currents and vertical convection of heat at the detector depths. Random optical noise accounts for single noise per PMT (about 10 kHz in ANTARES [124]), which is vetoed with proper trigger algorithms.

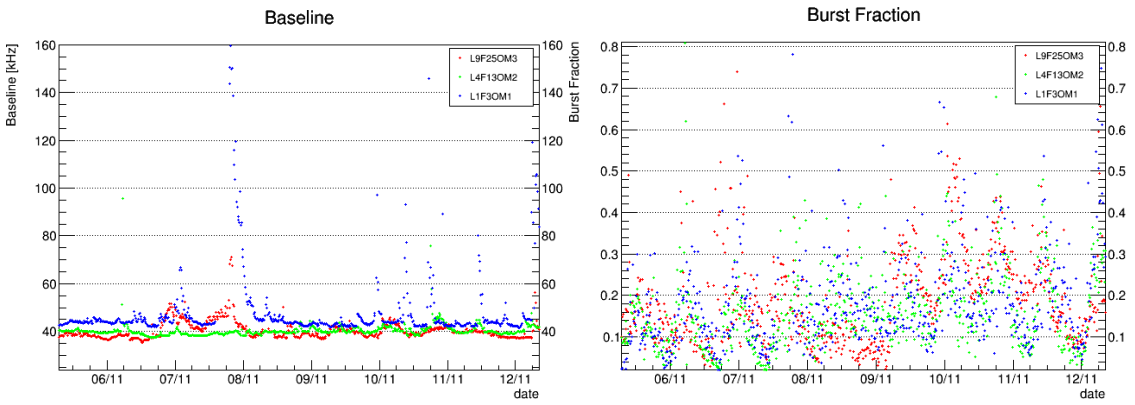

Figure 2.6: Left: live monitoring of the baseline rate of bioluminescence at the ANTARES site. Right: fraction of bursts at the ANTARES site. Snapshot from the live monitoring channel.

Physical background

Cosmic ray protons impinging on the upper Earth's atmosphere with sufficient energies produce extensive air showers in the atmosphere, consisting of charged pions and kaons among other particles, both of which decay to contribute to the muon and neutrino flux on the Earth's surface (Sec. 2.1). Neutrino detectors are usually placed at great depths, shielded by water, rock or ice, to reduce this background of atmospheric muon bundles arriving at the detector from above.

The muon flux is several orders of magnitude higher than the flux of muon neutrino induced muons (Fig. 2.7). To chop off atmospheric muons from above, analyses usually select a rejection criterion based on the zenith angle. However, there can be atmospheric events near the horizon, which are truly downgoing but reconstructed as up-going and hence can mimic neutrino-induced signal events. Precise track reconstruction algorithms, event containment conditions and multivariate classifiers are used to curtail the atmospheric muon background from signal neutrino events.

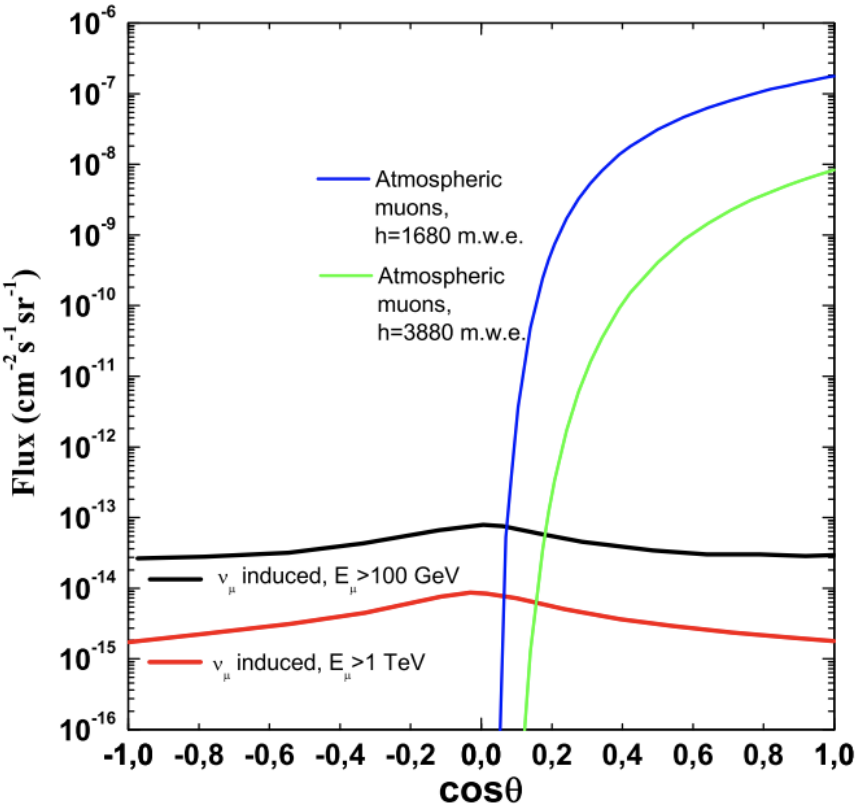

Figure 2.7: Flux of atmospheric muons and atmospheric neutrinos at two depths (1680 and 3880 m water equivalent) for two different muon energy thresholds (100 GeV and 1 TeV) as a function of the cosine of the zenith angle. From [125].

2.4 Neutrino Telescopes

The term neutrino telescope refers to an array of optical devices arranged in a definite geometry within a large volume of natural (and transparent) medium with the objective of detecting Cherenkov radiation from neutrino interactions [126]. The directional sensitivity is the reason to call them telescopes.

The first attempt to realise this idea was achieved in the DUMAND project [127] set up in Hawaii, which unfortunately failed due to technological problems. However, it was followed by the Baikal detector [128] in the water of Lake Baikal, the AMANDA detector [129] in the glacial ice at the South Pole and the ANTARES detector [130] in the abyss of the Mediterranean Sea. Based on the success of some prototype projects, the larger IceCube detector [131] was built at the South Pole. KM3NeT [66] is being built in the Mediterranean Sea and Baikal GVD [132] is under construction in Lake Baikal. In the following, the undersea running telescope in the Northern hemisphere, i.e. the ANTARES detector, and its successor next generation flagship experiment, i.e. the KM3NeT detector, will be described in more detail.

2.4.1 ANTARES

ANTARES (acronym for Astronomy with a Neutrino Telescope and Abyss environmental RESearch) [130] is an under-water neutrino telescope located 40 km offshore from Toulon, France at (42° 48′ N, 6° 10′ E), anchored about 2475 m below the surface of the

Mediterranean Sea. The first line was deployed in March 2006 and the detector was completed in May 2008.

Detector layout

Fig. 2.9 shows a schematic view of the ANTARES detector. ANTARES consists of 12 vertical detection lines, instrumented in an octagonal configuration with a (horizontal) separation of 60–75 m. The lines are anchored to the sea floor by means of a titanium structure (Bottom String Socket) acting as a dead weight and buoy on its top to stay vertical (optical modules have also their own buyoncy). Each line holds 25 storeys (apart from line 12 with 20 storeys) starting 100 m above the sea floor with a (vertical) separation of 14.5 m amounting to a total height of 450 m. The instrumented volume of ANTARES is ~ 0.01 km^3.

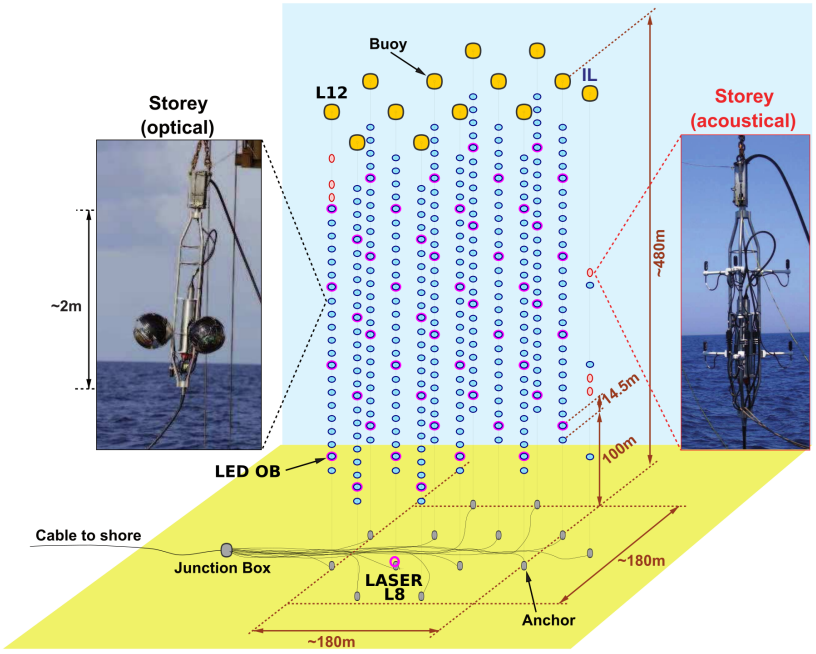

Figure 2.8: Schematic diagram of the ANTARES detector. Photos of two storeys holding optical and acoustic equipment are shown. From [130].

Optical Module

A storey is a titanium structure that hosts the Local Control Module (LCM), i.e. a titanium cylinder containing three optical modules (OMs), associated electronics and an ethernet switch. The OMs are 17-inch diameter (pressure resistant) glass spheres housing 10-inch Hamamatsu PMTs [133]. A total number of 885 OMs are placed in triplets around the LCMs with an equal spacing of 120° and facing downwards at an angle of 45° from the vertical.

The glass sphere is optically coupled to the PMT by means of an optical gel of refractive index 1.4. A hemispherical μ–metal magnetic cage surrounds the bulb of the PMT in order to shield it from the effects of the Earth's magnetic field. The PMTs are sensitive to photons with wavelengths between 300–600 nm, with a transit time spread (TTS) $\sim$ 3 ns (FWHM) and a quantum efficiency of $\sim$ 25% for a wavelength of 400 nm.

A String Control Module (SCM) placed at the bottom of each line contains the electronics for the data transfer between the string and the Junction Box (JB). The JB is linked to the

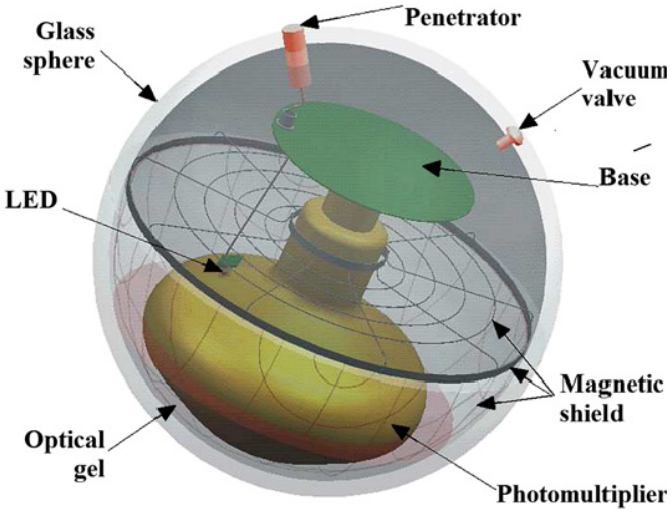

Figure 2.9: Schematic view of an ANTARES optical module. From [130].

shore station via a 42 km long and 58 mm diameter Main ElectroOptical Cable (MEOC), which is responsible for powering the detector, transfer of data, synchronisation of the clock signals and commands between shore station and the detector.

Data acquisition and trigger

The analogue signals registered by the PMTs is transformed into a readable format for the purpose of physics analyses. This is achieved through a chain of steps handled by the Data AcQuisition system (DAQ) [134]. The DAQ framework follows an "all-data-to-shore" strategy, which entail all the information recorded by the PMTs being transported to shore where it is digitised, filtered and stored. The DAQ begins with the digitalisation of the hits by means of two Analogue Ring Sampler (ARS) chips located in the LCM of each OM. A threshold of 0.3 p.e. (L0 threshold) is applied on the integrated charge in order to reduce the dark current noise of the PMTs. A local clock and two time-to-voltage converters (TVCs) in each LCM are used to timestamp every hit above threshold. The ARS chips work in a token-ring configuration in order to reduce the impact of the dead time of 200 ns which follows the integration time. The signal collected by the LCMs is transferred to the JB and then sent to the shore station using a Dense Wavelength Division Multiplexing (DWDM). The optical background determines a data output rate of the detector around 1 GB/s. A data filtering process is performed by the Data Filter programs which applies various algorithms (triggers) [135] based on different physics interests. A list of the most relevant triggers is tabulated in Tab. 2.2.

Trigger	Description
L0	The level-zero filter (L0) referring to the threshold for the analogue pulses (0.3 p.e.) which is applied off shore.
L1	The level-one filter (L1) refers to a coincidence of two (or more) L0 hits in the same storey within a 20 ns time window.
3N	5 L1 hits within 20 ns.
T3	2 L1 hits within 100 ns in adjacent storeys or within 200 ns in next-to-adjacent storeys.
TQ	2L1 + 4 L0 hits within 20 ns.

Table 2.2: Summary of the "most relevant triggers" used in ANTARES [135].

During its decadal years of operation, the ANTARES Collaboration has produced scientific results in a variety of analyses, ranging from point source [136], transient sources [137], diffuse fluxes [138], GRBs [139], dark matter [140] searches to measurement of neutrino oscillations [60]. The decommissioning of the detector is planned for 2021.

2.4.2 KM3NeT

KM3NeT (acronym for KiloMetre cube Neutrino Telescope) [66] is a next generation deep-sea Cherenkov neutrino observatory, currently under construction in the Mediterranean Sea. Based on the granularity of the optical modules (to target different neutrino energy regimes), KM3NeT will house two detector sub-arrays:

- **ORCA** (Oscillation Research with Cosmics in the Abyss): densely instrumented sub-array of $\sim 5 \times 10^{-3}$ km^3 volume, located offshore of Toulon, France at (42°41′ N, 6°02′ E), designed primarily for studying neutrino properties and low-energy astrophysics;
- **ARCA** (Astroparticle Research with Cosmics in the Abyss): sparsely instrumented sub-array of ~ 1 km^3 volume, located offshore of Sicily, Italy at (36°16′ N, 16°06′ E), designed primarily for detection of high-energy cosmic neutrinos and neutrino astronomy.

The term "ORCA" ("ARCA") will be used henceforth to designate the KM3NeT-ORCA (-ARCA) detector.

Detector layout

The three-dimensional array built in a particular layout is called a “building block” (BB). KM3NeT will consist of two BBs for ARCA and one BB for ORCA to reach the desired instrumented volumes. Fig. 2.10 shows a schematic view of one BB of the KM3NeT detector. Each building block will consist of a three-dimensional array of $\sim$ 64,000 PMTs distributed among 115 detection strings (also known as "DUs"[2]) with 18 spherical Digital Optical Modules (DOMs) per line. Starting about 40 m (80 m) from the sea floor, the DUs of ORCA (ARCA) are 200 m (700 m) high, horizontally separated by about 20 m (95 m), with 18 DOMs spaced 9 m (36 m) apart in the vertical direction.

[2]The terms "DU", "string" and "line" have been used interchangeably in this thesis.

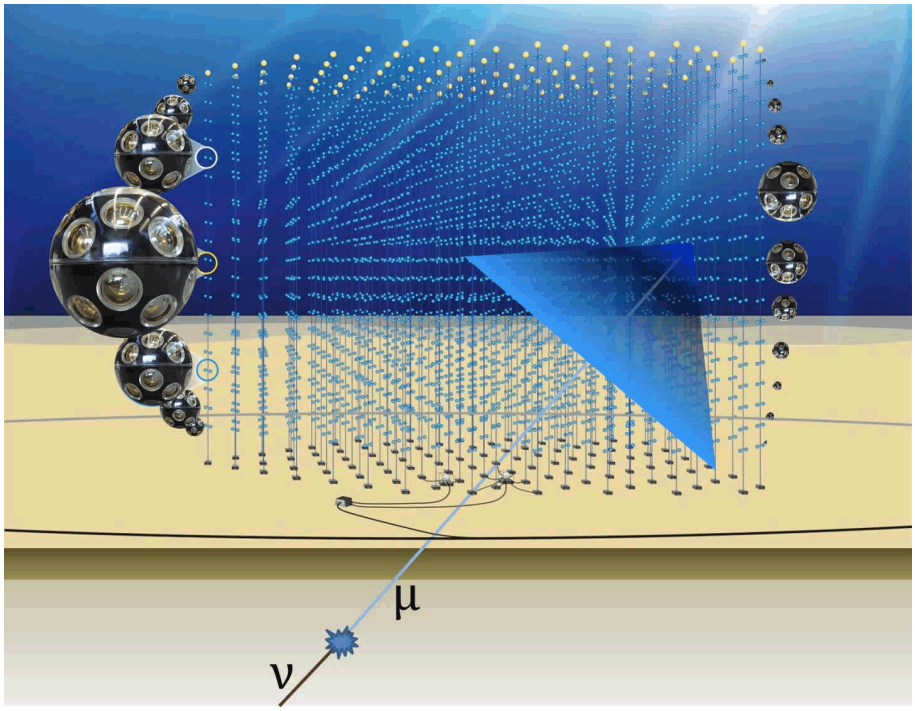

Figure 2.10: Conceptual view of the KM3NeT detector. The blue line represents an up-going neutrino undergoing ν_μ–CC interaction close to the fiducial volume leading to track-like event and creating a Cherenkov cone along its path. From KM3NeT internal documentation.

Digital Optical Module

Each 17-inch diameter DOM houses 31 PMTs of 3-inch each, looking towards different directions, along with their readout electronics and other sensors. Within each DOM, the PMTs are arranged in 5 rings of 6 PMTs each, plus the bottom-most PMT pointing vertically downwards. The upper hemisphere of the DOM contains 12 PMTs arranged in 2 rings, while the lower hemisphere houses the remaining 19 PMTs arranged in 3 rings. The consecutive rings are staggered by 30° in zenith and the PMTs within a ring are separated by 60° in azimuth.

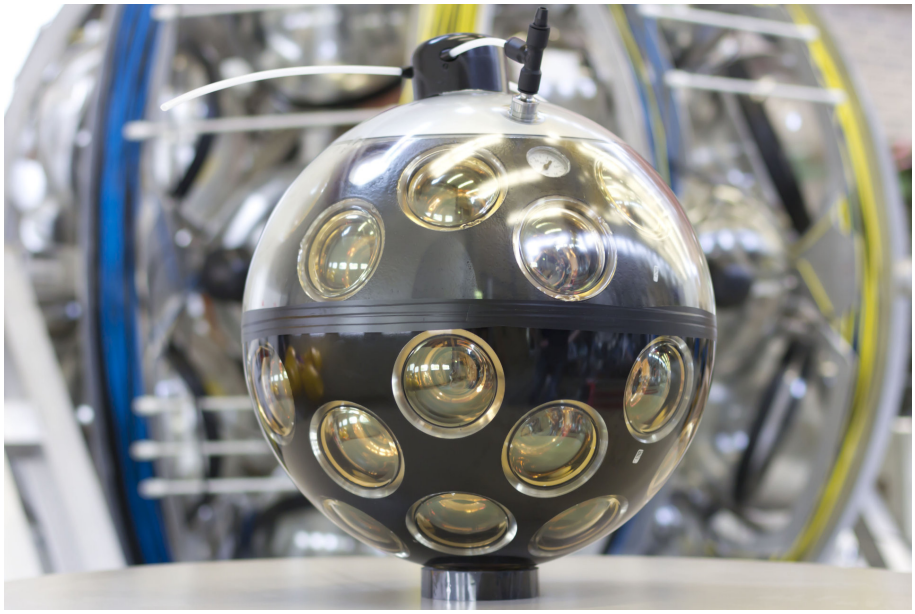

Figure 2.11: A KM3NeT Digital Optical Module.

KM3NeT uses Hamamatsu R12199-02 PMTs with a maximum quantum efficiency of $\sim$ 30% [141]. The high-voltage bias is set to provide a gain of 3×10^6. Each PMT can be individually tuned in voltage. The FWHM of transition time spread is less than 5 ns, allowing for a good accuracy in photon arrival timing.

The instrumentation mounted in each DOM comprises a piezo-sensor for acoustic positioning purposes, a tiltmeter and a compass, as well as sensors of the temperature and humidity inside the DOM for monitoring purposes. A breakdown of the DOM structure is shown in Fig. 2.12.

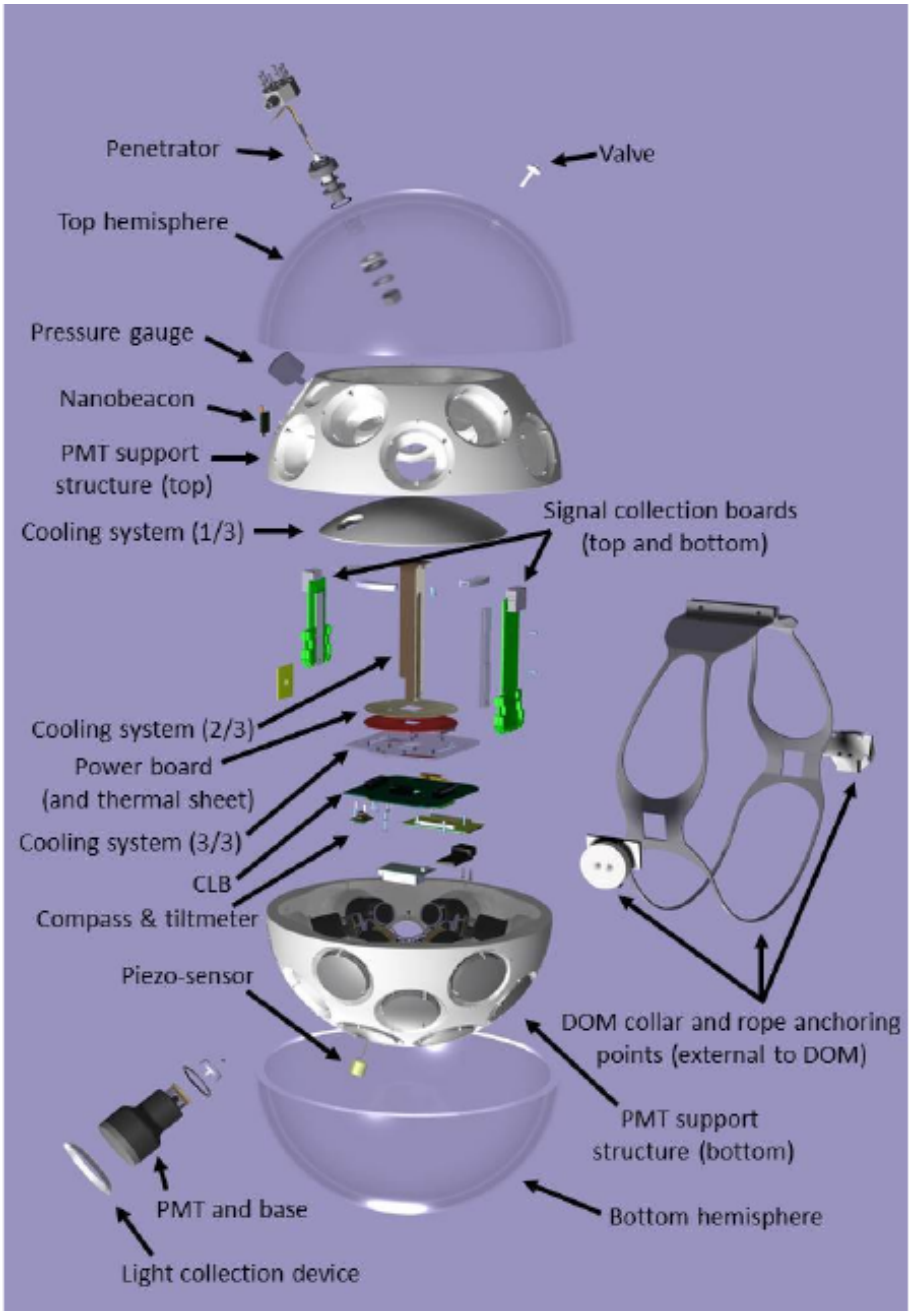

Figure 2.12: Exploded view of a KM3NeT Digital Optical Module (DOM). From [142].

Similar to ANTARES, DOMs are immersed in the sea in ensembles of 18, laid out vertically, anchored to the seafloor and kept taught by a buoy on the top. Each DOM is attached to the string via a titanium collar. An electro-optical cable that provides high-voltage connections to each DOM for power and two optical fibres for communication and data transfer to the shore is attached to each DU.

Installation sites

The construction of the detector has been distributed into phases. Phase 1 foresees the deployment of 6 DUs for the ORCA detector (achieved) and at least 24 DUs for the ARCA detector to be completed by Fall of 2021. Phase 2 includes the construction of the entire ORCA detector (single building block) and 2 building blocks of the ARCA detector.

Beyond Phase 2, further detector expansion, with possibly a separate building block at the Greek site, is planned. Fig. 2.13 shows the three proposed sites for the realization of KM3NeT. The Toulon site located in the Ligurian Sea at a depth of 2475 m, the Capo Passero site in the West Ionian Sea at a depth of 3500 m, the Pylos site in the East Ionian Sea in three possible location at depths of 5200 m, 4500 m and 3750 m from the surface of the Mediterranean sea. To date, 6 ORCA and 1 ARCA DUs are operational.

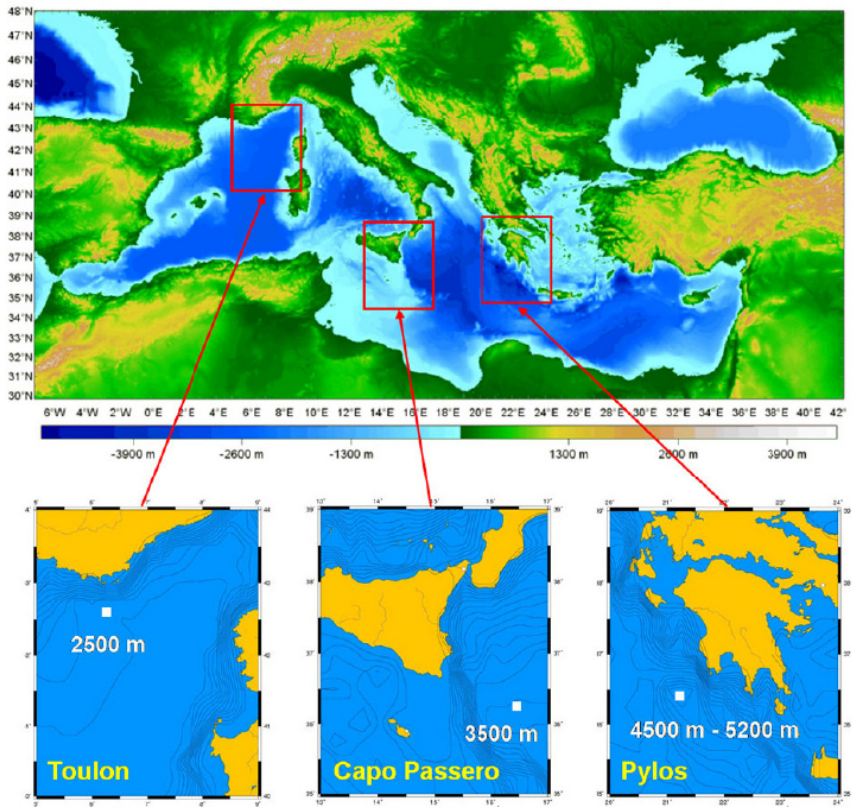

Figure 2.13: The installation sites of KM3NeT in the Mediterranean Sea. From [142].

Data acquisition and trigger

Similar to ANTARES, the KM3NeT the Data AcQuisition (DAQ) framework follows an "all-data-to-shore" strategy [66, 143]. The filtering of interesting events is performed via trigger algorithms (see Tab. 2.2) based on local coincidences within a particular time window respecting causality conditions [66, 144].

2.5 Detector Calibration

In order to achieve a good quality in the reconstruction of the events, a precise calibration of charge, position and arrival time of the Cherenkov photons reaching the PMTs is imperative. A good charge calibration ensures good energy resolution, while a good position and time calibration ensure good angular resolution on the reconstruction of the event direction.

2.5.1 Position calibration

Since the detection lines are flexible, the upper-most storeys can be dragged by deep-sea currents up to $\sim$ 10 m. To account for this variation of relative positions of DOMs, the Acoustic Positioning System (APS) based on acoustic devices, a tiltmeter and a compass has been developed [145, 146]. The acoustic devices consist of a set of acoustic transceivers and hydrophones. Using the time of flight of acoustic signals, the calibration system provides the position of the telescope's mechanical structures in a geo-referenced coordinate system. A Tiltmeter-Compass System (TCS) attached to the LCM determines the orientation of the DOMs by measuring its pitch, yaw and roll.

2.5.2 Charge calibration

When a photon impinges on the photocathode area at the entrance window of a PMT, it produces electrons, which are then accelerated by a high-voltage field and multiplied in number within a chain of dynodes by the process of secondary emission. This is the working principle of a PMT, which is based on the amplification of secondary emission of electrons off dynodes via photoelectric effect. The charge of the signal generated by the photoelectrons is digitised by an Analog-to-Voltage Converter into a value, AVC, which is related to the number of photoelectrons produced in the PMT, $N_{p.e.}$, by

$$N_{p.e.} = \frac{\mathrm{AVC} - \mathrm{AVC}_{0p.e.}}{\mathrm{AVC}_{1p.e.} - \mathrm{AVC}_{0p.e.}}. \tag{2.24}$$

$\mathrm{AVC}_{0p.e.}$ refers to the value of AVC corresponding to zero photoelectrons, while $\mathrm{AVC}_{1p.e.}$ corresponds to the single photoelectron peak. Regular charge calibration runs are performed to determine these two characteristic parameters. Over time, the measured values degrade, so regular high voltages tunings of the PMTs are performed to maintain a 0.3 *p.e.* threshold.

2.5.3 Time calibration

The aim of time calibration at neutrino telescopes is two folds:

- absolute time calibration: monitor the absolute timing of an event with respect to the Coordinated Universal Time (UTC) to correlate events related to any celestial phenomenon observed by other experiments;
- relative time calibration: estimate the relative calibration constants between PMTs to obtain a good angular resolution of reconstructed events.

We limit our discussion to the relative time calibration pursued in the context of KM3NeT. Relative time calibration [147, 148] has some intrinsic, unavoidable limitations, which add up to the total uncertainty, σ_{tot}:

$$\sigma_{tot}^2 = \frac{\sigma_{TTS}^2}{N_{p.e}} + \frac{\sigma_w^2}{N_\gamma} + \sigma_e^2\,, \tag{2.25}$$

where σ_{TTS} ($\approx$ 5 ns) is the uncertainty on the transit time of electrons between dynodes in the PMTs (Transit Time Spread); σ_w ($\approx$ 2 ns for a traveling distance of 50 m) is the uncertainty on the light propagation time in sea water due to scattering and dispersion; N_γ is the number of Cherenkov photons emitted; σ_e ($\approx$ 0.5 ns) is the intrinsic uncertainty due to electronics. Taking into account these intrinsic uncertainties, the required precision of the time calibration system for neutrino event reconstruction with

an angular precision better than 1° should be < 1 ns and their position determined with better than a meter precision.

Several strategies have been developed to account for these uncertainties within the KM3NeT collaboration [147, 148].

- **Intra-DOM calibration**: Simultaneous coincident hits from radioactive ^{40}K decays in sea water is used for time calibration between PMTs within the same DOM.
- **Inter-DOM calibration**: Each DOM is equipped with nanobeacons to provide light detection from one DOM to the neighboring DOMs for inter-DOM time calibration. Vertically downgoing atmospheric muons also provide inter-DOM calibration, which is our focus of work (reported in next section). Both methods serve as a cross-check to each other.
- **Inter-DU calibration**: Laser beacons installed on the DU base provide light detection by DOMs on different lines for the measurement of the Round-Trip-Time (RTT) delay of the laser signal due to the length of the optical fiber.

We limit ourselves to inter-DOM calibration using atmospheric muons.

Inter-DOM calibration with atmospheric muons

Inter-DOM time calibration using atmospheric muons has been previously developed within the ANTARES Collaboration [149, 150, 151, 152, 153]. A similar technique has been implemented in KM3NeT [154]. However, the strategy for calculation of time offsets used in [155] is slightly different and is based on the comparison of hit-time residual distributions of data with the *run-by-run* Monte-Carlo (MC). Our work [156] focuses on implementing the old strategy implemented in ANTARES, which is independent of MC and converges faster.

Time calibration with atmospheric muons is an off-shore calibration strategy applicable for inter-DOM calibration. The method is based on the estimation of hit time residuals (HTR). For each event, the hits recorded by a random DOM ("probe-DOM") are excluded, and the event is reconstructed using the hits detected by the other DOMs, providing the values of the expected hit times on the probe-DOM i. The difference between the expected arrival time (t_{fit}) and the measured arrival time (t_{stamp}) is a time residual ($t_{res} = t_{fit} - t_{stamp}$). Asynchronous clocks and different cable lengths can lead to relative offsets for each DOM. Moreover, the PMTs can have their own offsets, which are estimated in intra-DOM calibration with ^{40}K. If a DOM is correctly calibrated, the distribution of these hit time residuals should peak at zero; otherwise, we must adjust a DOM-specific time offset (by adding/subtracting a fixed number to all PMTs on this DOM in the detector file). Our goal is to estimate these time offsets for DOMs corresponding to specific period of time. Note that these time offsets evolve with time subjected to environmental changes.

Methodology

This method involves the following iterative steps:

- A “probe-DOM” is randomly selected among all DOMs in a line (DU).
- The muon track is reconstructed with a minimum of 7 hits on each DOM (within a 25 ns window) excluding the "probe-DOM".
- Time residuals for the "probe-DOM" are calculated with respect to the fitted tracks.

- Distribution of these residuals are histogramed and the value of the median of the distribution is stored.
- The median (t_i) is introduced as a correction to the hit times in the detector file.
- The muon track reconstruction is redone with the updated detector file.
- The HTR distribution peaks with a new median (t_{i+1}), which is introduced again in the detector file as a further correction.
- The process of introducing the median and reconstructing the muon track is repeated until the recomputed median is < 0.5 ns.

The measured time offset T_0^n at n^{th} iteration is the cumulative summation of these medians t_is till the n^{th} iteration. To account for the asymptotic behavior of the evolution of the time offsets with the number of iterations and due to the uncertainty on the total number of iterations, the final average time offset $\langle T_0 \rangle$ is read after by performing a fit to the measured time offsets per iteration. The fit function follows a simple exponential fit:

$$T_0^n = \langle T_0 \rangle + [\alpha \cdot e^{-\lambda_\alpha i} + \beta \cdot e^{-\lambda_\beta i}], \tag{2.26}$$

where α, β, λ_α, and λ_β are arbitrary constants which are fitted. The quality of reconstruction improves with the number of iterations i and therefore the number of reconstructed events with good quality factor also increases.

Proof of principle

In order to cross-check the robustness of the method, we compared the values of time offests $\langle T_0 \rangle$ obtained from our approach to the method implemented in [154]. The comparison of time offsets of various DOMs (18 DOMs per DU) of ARCA DU1 is shown in Fig. 2.14. The MC-independent approach was seen to converge faster and is in good agreement with the MC-dependent approach within ~ 2.0 ns.

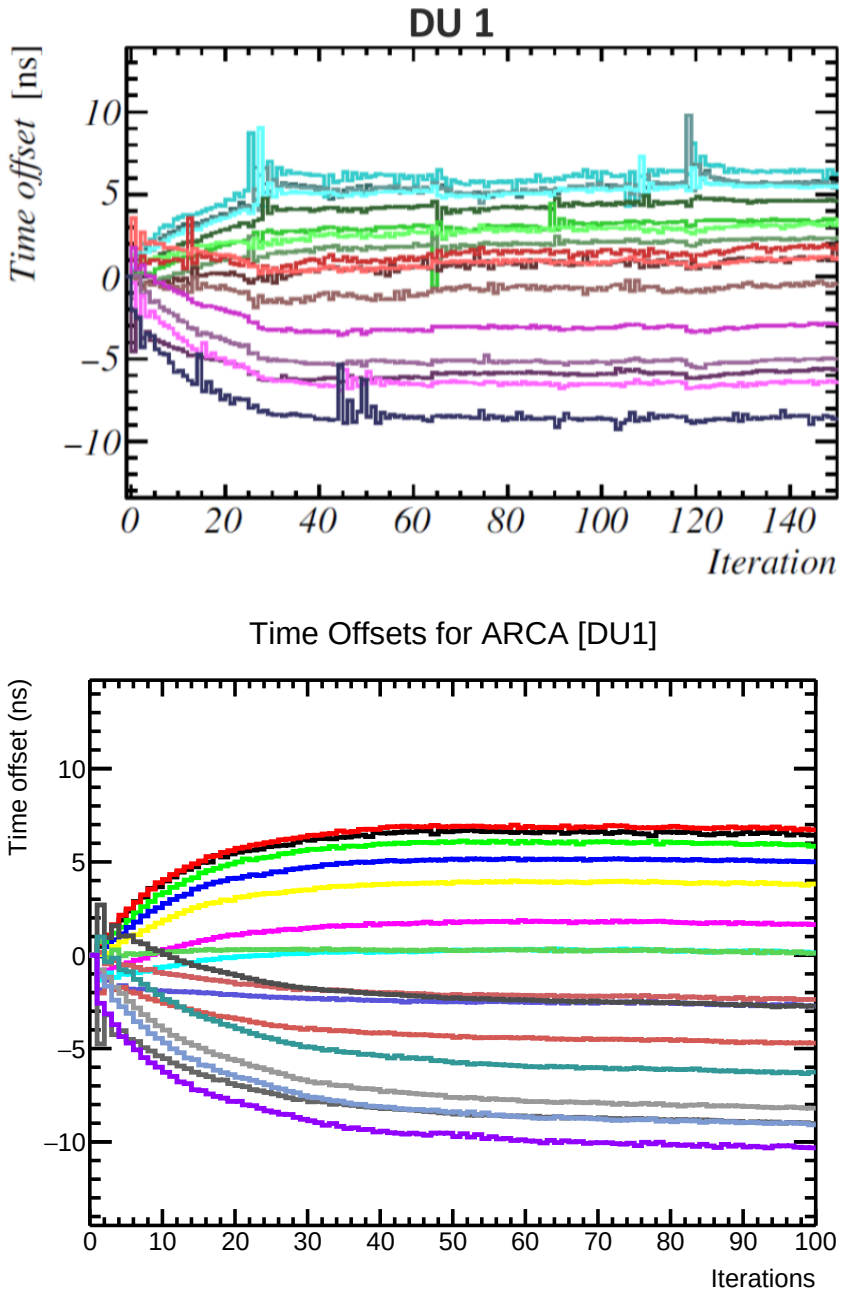

Figure 2.14: Evolution of cumulative time offsets, T_0^n, for ARCA DU1 with the *old* MC-dependent strategy [154] (top) and the *new* MC-independent strategy (bottom) developed for this work. Each of the 18 coloured curves denotes the evolution of time offsets with the number of iterations.

Additionally, the calibration procedure has been first employed for ARCA MC runs assuming a perfect detector (before applying to data runs with a realistic detector). The ARCA MC files refer to run numbers from 5009 to 5046, which correspond to a run period between 13/12/2016 and 01/01/2017. The evolution of time offsets is shown in Fig. 2.15 and the final offsets for different DOMs are shown in Fig. 2.16.

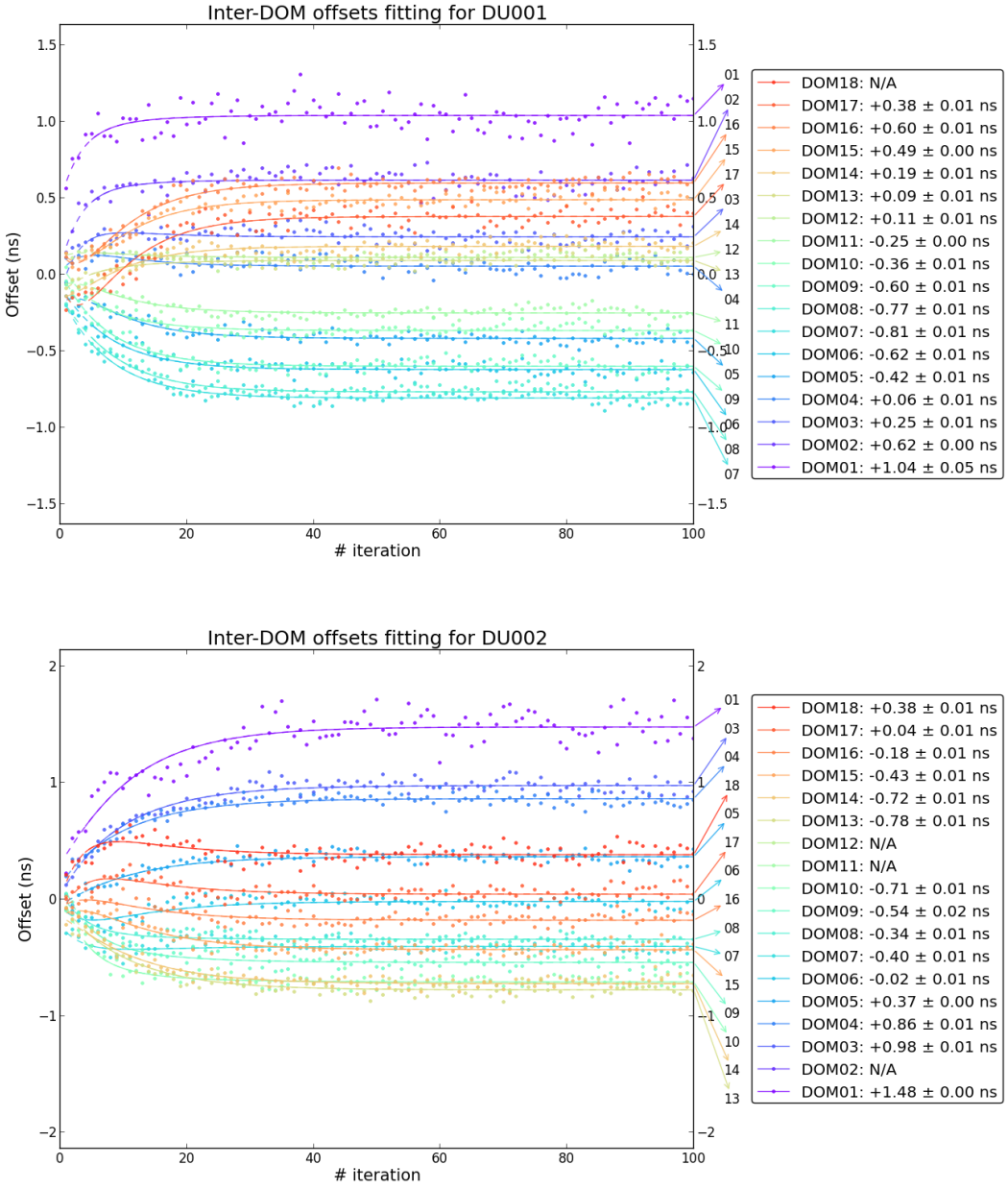

Figure 2.15: Evolution of cumulative time offsets, T_0^n, for ARCA DU1 & DU2 for MC runs assuming a perfect detector. The final offsets are also listed.

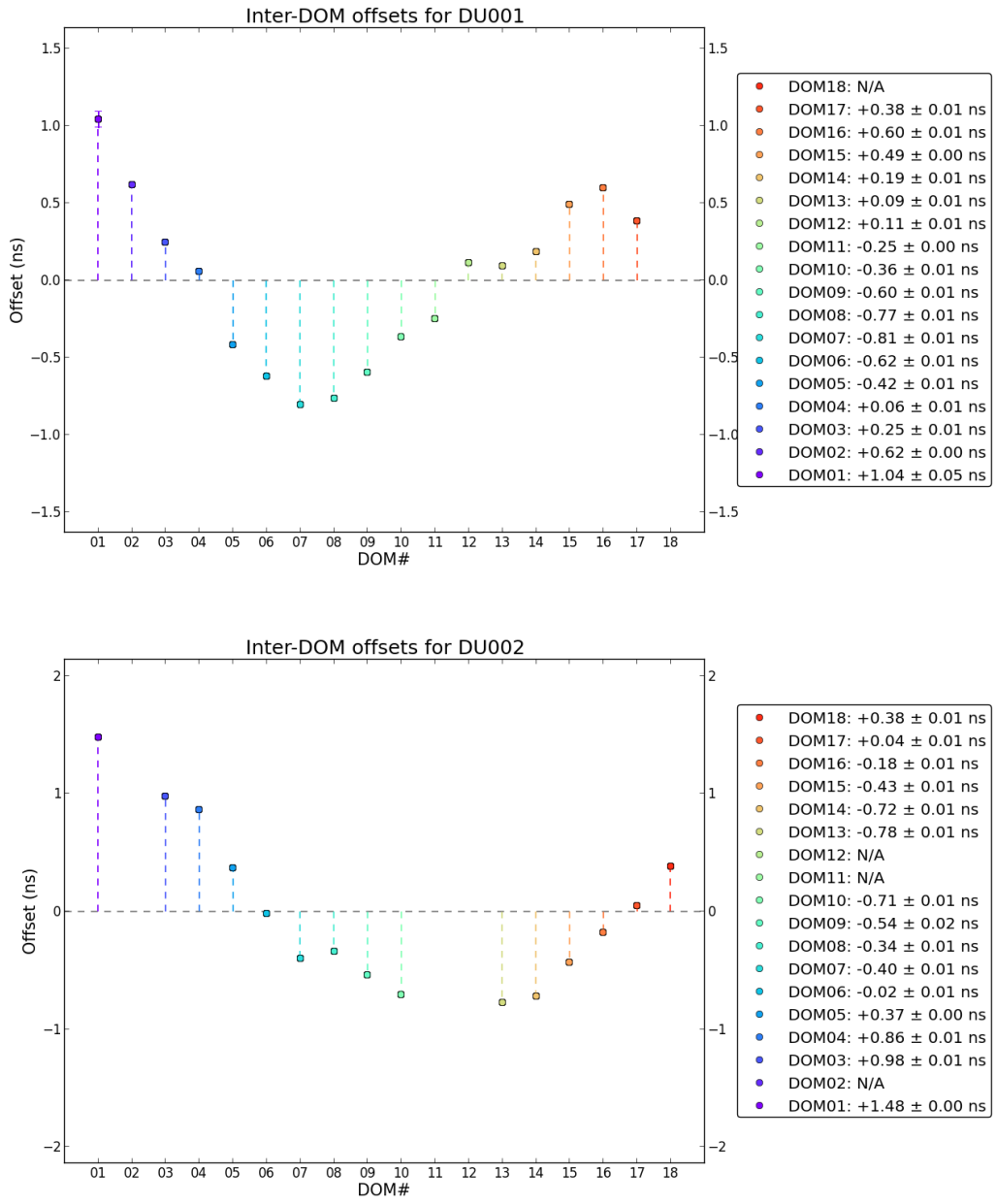

Figure 2.16: Final time offsets, $\langle T_0 \rangle$, for ARCA DU1 & DU2 for MC runs assuming a perfect detector.

Results

Finally, the procedure was employed on ARCA and ORCA data runs to calculate the real time offsets of the DOMs within DUs. A run period for ARCA data similar to the ARCA MC runs was chosen. The ORCA data files refer to run numbers from 3165 to 3192, which correspond to a run period between 04-12-2017 and 08-12-2017. The evolution of time offsets for ARCA DU1 and DU2 are shown in Fig. 2.17 and their final time offsets of different DOMs are shown in Fig. 2.18.

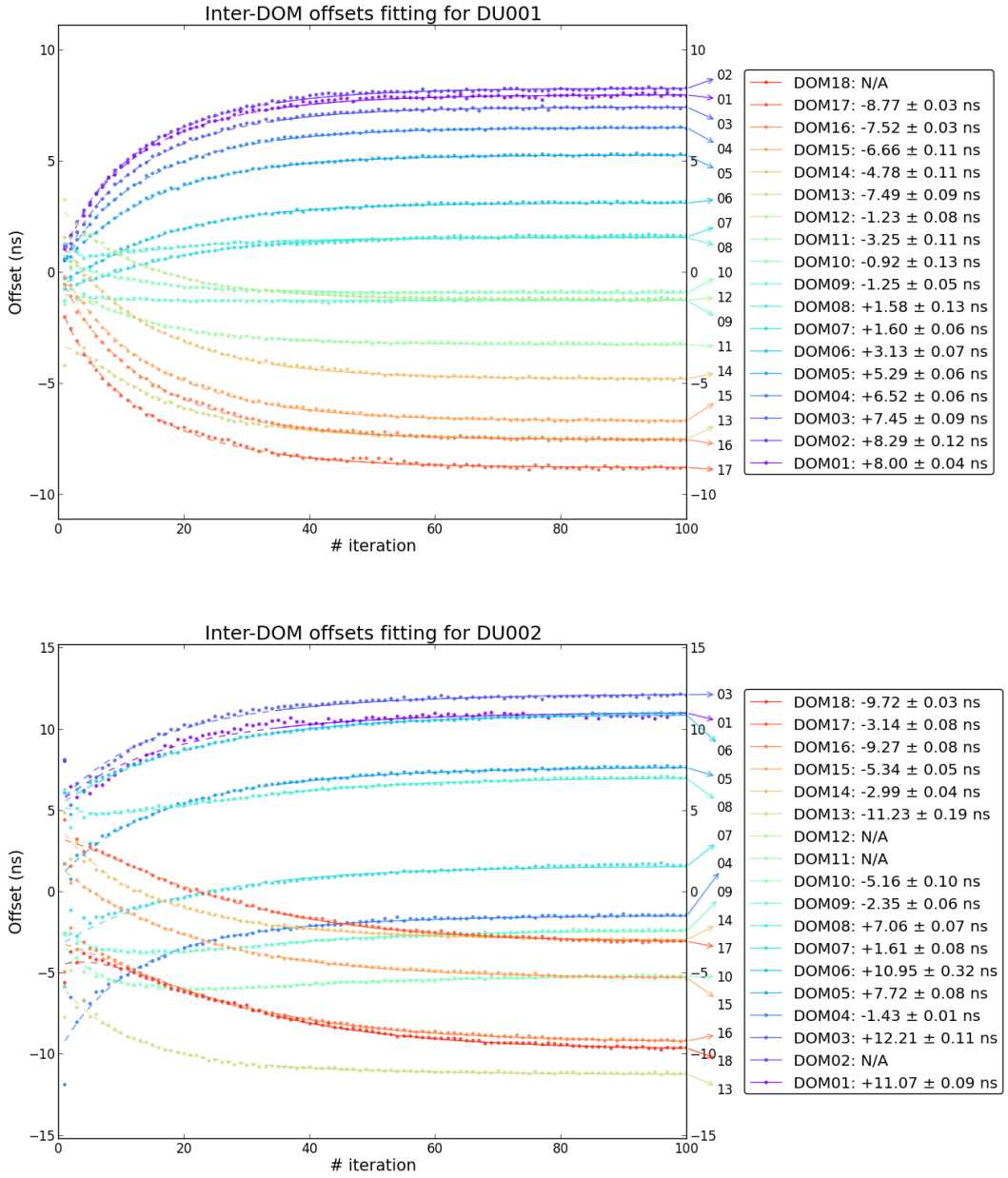

Figure 2.17: Evolution of cumulative time offsets, T_0^n, for ARCA DU1 & DU2. This corresponds to a run period between 13/12/2016 and 01/01/2017. The final offsets are also listed.

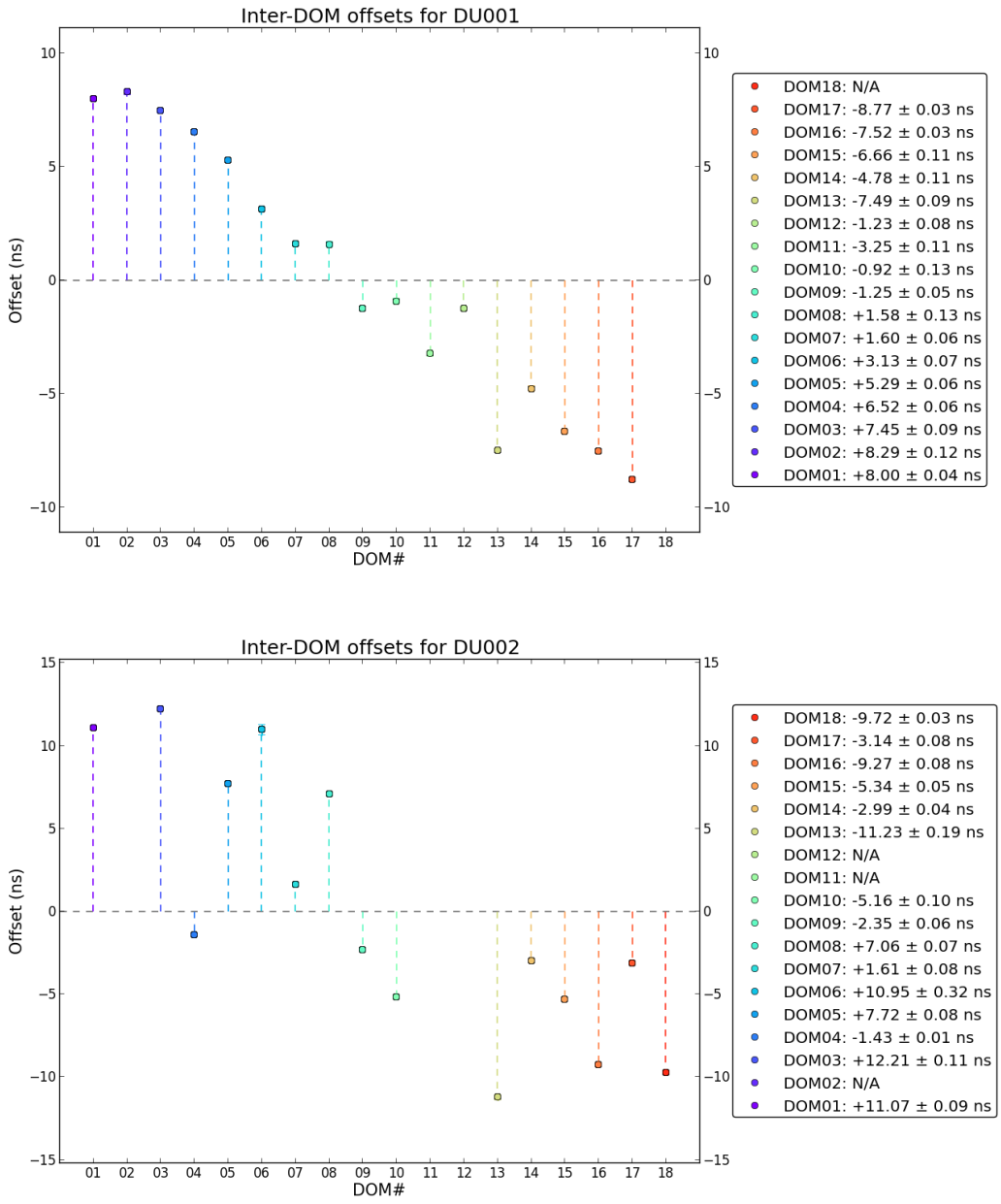

Figure 2.18: Final time offsets, $\langle T_0 \rangle$, for ARCA DU1 & DU2. This corresponds to a run period between 13/12/2016 and 01/01/2017.

The corresponding evolution of time offsets for ORCA DU2 and their final time offsets for different DOMs are shown in Fig. 2.19.

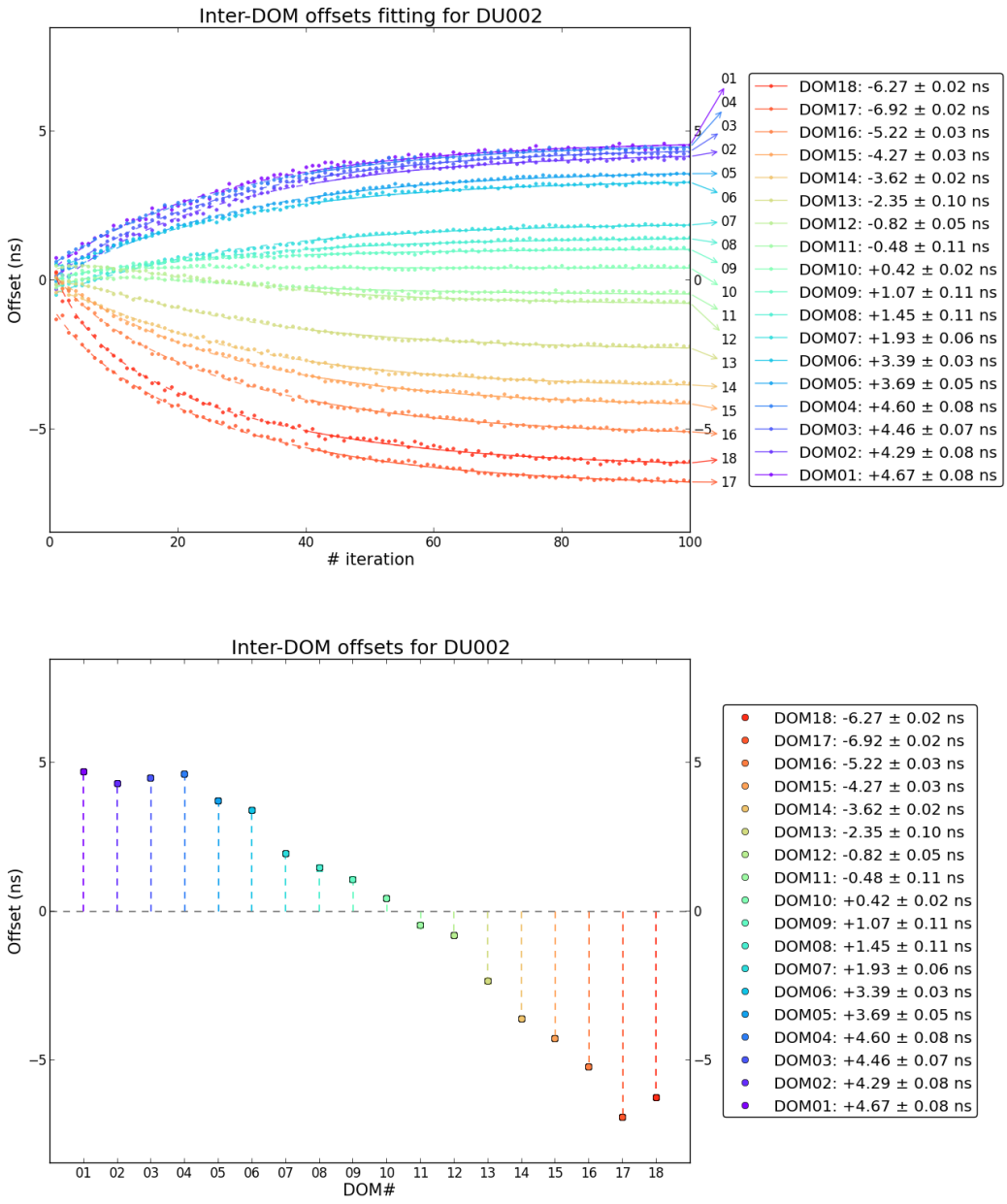

Figure 2.19: Evolution of cumulative time offsets, T_0^n (top), and final time offsets, $\langle T_0 \rangle$ (bottom), for ORCA DU2. This corresponds to a run period between 04-12-2017 and 08-12-2017.

The resulting time offsets were also compared with the ones obtained from inter-DOM calibration with nano-beacons and was found in comfortable agreement (Fig. 2.20). One of the limitations of this method was that it does not take into account possible errors due to DU elongation, i.e. the accurate positioning and orientation of the DOMs. Hence, further steps involves developing novel techniques in the light of real-time positioning of DOMs in sea water.

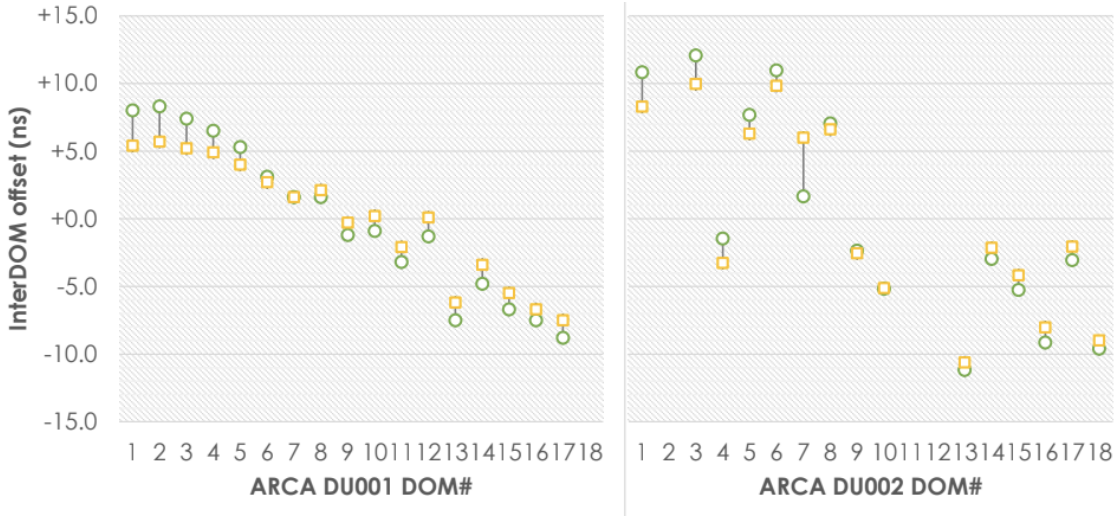

Figure 2.20: Comparison of final time offsets, $\langle T_0 \rangle$, for ARCA DU1 (left) & DU2 (right) obtained from calibration with nanobeacons (yellow squares) and with atmospheric muons (green circles). They correspond to a run period between 13/12/2016 and 01/01/2017. From [156].

3 Monte Carlo Simulations and Event Reconstruction

"You see my physics students don't understand it... That is because I don't understand it. Nobody does."

— RICHARD P. FEYNMAN

Contents

The aim of Monte Carlo (MC) simulations is to reproduce the event distributions expected at the detector in the most realistic way by folding the apparatus response to the recorded events. The motivation behind MC productions does not lie only in the understanding of the detector performance, but also in optimising selection cuts to enhance the sensitivity to signal events. The output of the MC simulation is fed to the event reconstruction algorithms, which in turn give out the reconstructed neutrino energy and the direction of the incoming neutrino (among other event properties) based on the information of the Cherenkov light induced by the propagation of the secondary particles within the medium. The precision achieved in the reconstruction of the energy and direction determines the accuracy with which we can probe the neutrino properties and their sources. In this Chapter, the MC simulation chain

and the corresponding reconstruction algorithms used in the ANTARES and KM3NeT experiments are described.

3.1 MC Simulations in ANTARES

A *run-by-run* MC approach [157] is followed in order to simulate the response of the detector, which is subjected to seasonal evolution of environmental phenomena and operational situations leading to changes in the rates registered at the neutrino telescope. The varying optical background conditions, measured every 0.1 seconds, the acoustic positioning, performed every few minutes, and PMT efficiencies of individual OMs, calculated at weekly intervals, are accounted to fold in the temporal evolution of the detector response in the most realistic way to represent the data taken by the detector as closely as possible.

The simulation chain in ANTARES involves three steps:

1. **particle generation**: particles capable of inducing observable signatures at the detector are generated with a given energy and spatial distribution;
2. **particle propagation and light emission**: particles interacting with the medium leading to energy losses and production of secondary particles are simulated. The Cherenkov light generated by charged particles is tracked;
3. **light detection**: the response of the apparatus is folded in the form of the photon arrival information at the OMs.

3.1.1 Particle generation

The instrumented volume of the detector is assumed to be a wide cylinder comprising all the OMs. A larger cylindrical (generation) volume typically referred as the *can*, within which the Cherenkov light is generated, engulfs the instrumented volume. The dimension of the can has to be large enough to sustain the volume within which most of the Cherenkov light detected by the experiment is generated. Typically it extends beyond three absorption lengths of light in water. The geometry of the can used in the event generation is shown in Figure 3.1. Cherenkov light is generated only for particles within the can, whereas outside the can, charged particles are only propagated till the surface of the can.

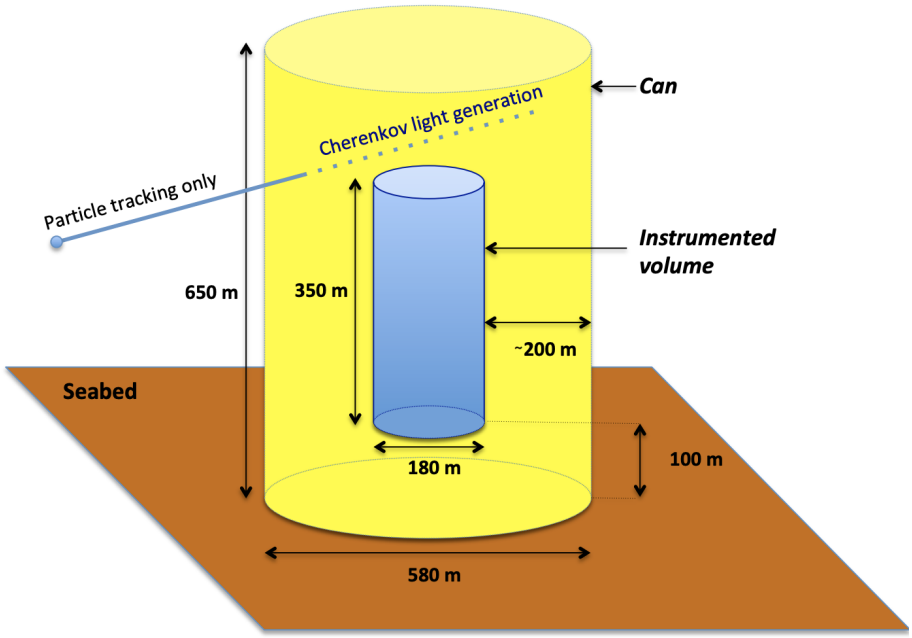

Figure 3.1: Layout of detector geometry used for event generation in ANTARES [158].

Atmospheric neutrino generation

Neutrino interactions in ANTARES are simulated following the flux calculation of Honda *et al.* [103] and using the interaction physics in the GENHEN [158] package. The latter allows to simulate neutrino events of all flavours and for both CC and NC interactions with an energy spectrum ranging from few-GeV to multi-PeV. Neutrinos are generated following a $E^{-1.4}$ power-law energy spectrum (which will be later reweighted according to the flux we want to reproduce), while the neutrino directions are generated isotropically. Neutrino interactions $\mathcal{O}(10^{10})$ are simulated within the generation volume which is determined by the maximal muon range associated with the highest neutrino energy ($E_\nu^{max} = 10^8$ GeV).

The LEPTO [159] software is used for the calculation of differential neutrino-nucleon interactions within the generation volume, by using the CTEQ6-D parton distribution functions.

The probability for a neutrino to traverse the Earth (see Fig. 3.2) depends on the interaction cross-section ($\sigma(E_\nu)$) and the density of the Earth matter ($\rho(\theta)$) and is

$$P_{\text{Earth}}(E_\nu, \theta) = e^{-N_A \sigma(E_\nu) \rho(\theta)}, \tag{3.1}$$

where N_A is the Avogadro's number and θ is the zenith angle of the incident neutrino. (A value $\cos\theta_z = 0\,(-1)$ corresponds to horizontal (vertically up-going) neutrinos traversing across the Earth. High energy vertically up-going neutrinos are more likely to interact with Earth matter, thereby having a smaller chance to reach the detector without interacting.

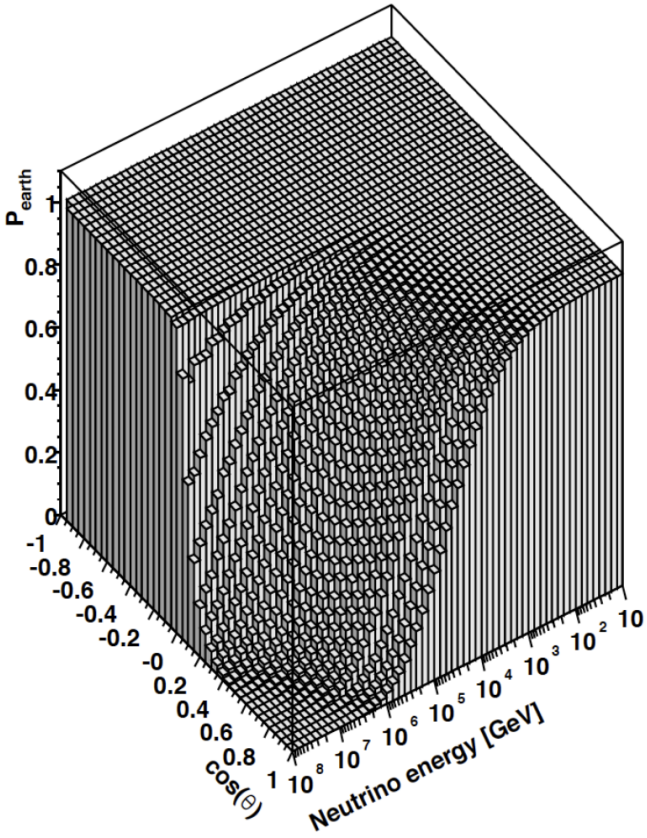

Figure 3.2: Probability of a neutrino to traverse the Earth without undergoing an interaction as a function of the neutrino energy and direction [158].

Since neutrinos are generated with a power law $E^{-\gamma}$ spectrum, the generated neutrino can be normalised with a generation weight accordingly to represent atmospheric or cosmic neutrino fluxes. A generation weight W_{gen} is defined to calculate neutrino fluxes in accordance to relevant models:

$$W_{gen} = V_{gen} \cdot t_{gen} \cdot I_\theta \cdot I_E \cdot E^\gamma \cdot \sigma_{E_\nu} \cdot \rho \cdot N_A \cdot P_{Earth}, \tag{3.2}$$

where

- V_{gen} is the generation volume [m^3];
- t_{gen} is the time represented in simulations;
- $I_\theta = 2\pi\ (\cos\theta_{max} - \cos\theta_{min})$, is the angular factor taking into account the range of sky with neutrino zenith angle $\cos\theta_z$;
- $I_E = \int_{E_{min}}^{E_{max}} E^{-\gamma} dE$ is the energy factor taking into account the range of neutrino energies for which the simulation is performed;
- γ is the spectral index of the generated neutrinos;
- σ_{E_ν} is the total neutrino-nucleon interaction cross-section;
- $\rho \cdot N_A$ is the total number of target nucleons per unit volume, where ρ is the target density;

- P_{Earth} is the neutrino transmission probability through the Earth.

The atmospheric flux $\phi(E_\nu, \theta_\nu)$ is then re-weighted to get the number of neutrino events $N(E_\nu, \theta_\nu)$ per year in each energy and zenith angle bin [160]:

$$N(E_\nu, \theta_\nu) = \frac{W_{gen}}{[\mathrm{GeV}^{-1}\mathrm{m}^{-2}\mathrm{s}^{-1}\mathrm{sr}^{-1}]} \times \frac{\phi(E_\nu, \theta_\nu)}{[\mathrm{GeV} \cdot \mathrm{m}^2 \cdot \mathrm{s} \cdot \mathrm{sr} \cdot \mathrm{yr}]} \,. \tag{3.3}$$

In ANTARES, to ensure larger statistics at high energies, the neutrinos (and antineutrinos) are simulated with a spectral index $\gamma = 1.4$, within an energy range of $10 - 10^8$ GeV.

Atmospheric muon generation

Atmospheric muons are generated as the consequence of hadronic showers produced in the interaction of cosmic rays in the upper atmosphere. They are the most abundant events, constituting the main source of background. However, a major fraction of these events are rejected by appropriate selection criteria.

A full simulation of atmospheric muons is done with CORSIKA [161] package, which allows for the generation of atmospheric showers, the production of muons from hadronic interactions and their propagation down to the sea surface. However, this accurate reproduction requires a large CPU usage, for which parameterisations are used. CORSIKA describes the muon energy spectrum, the angular distribution, the multiplicity of the muon bundles and all other kinematics of the muon on the surface. The simulation range extends from 1.5 km to 5 km water equivalent (w.e.) vertical depths and from 0° up to 85° zenith angles.

3.1.2 Particle propagation and light emission

A GEANT-based [162] package, named, KM3 [163] is used to propagate neutrino events and their decay products, including muons, hadrons and electromagnetic showers. Relevant physics processes like multiple scattering, energy losses, radiative processes and hadronic interactions are taken into account. The Cherenkov photons produced by the final state particles are propagated through seawater taking into account the influence of absorption and scattering of light [122] in seawater, before they reach the OM surface, producing a *hit* (defined in Sec. 2.3.3.

Cherenkov photons are not tracked from generation to detection at PMTs, being computationally unaffordable because of their extremely higher number. Rather, KM3 uses the so-called "photon tables", obtained in advance from a full simulation of photons with GEANT [162], which stores the distributions of the number and arrival time of PMT hits at different distances, positions and orientations of the PMTs depending on the event topology (tracks or showers).

The propagation of background muons generated with MUPAGE [164] is similar to that of the secondary muons from neutrino interactions. KM3 includes a modified version of MUSIC [165] to propagate muons within the can volume.

3.1.3 Light detection

The TriggerEfficiency program [144] simulates the detector response by taking into account the electronics and trigger algorithms [166]. Optical noise, from ^{40}K decays and

bioluminescence in water, observed from counting rates in data is added to each run to reproduce the actual data taking situations.

The analogue signal of the PMTs is summed up for a time window of 25 ns taking into account the angular acceptance and quantum efficiency of the PMTs [167]. The hit times of the single photoelectron (p.e) signals are smeared by a Gaussian function with width, $\sigma = \frac{1.3}{\sqrt{N_\gamma}}$ ns, with N_γ being the number of photons detected simultaneously, to account for the Transit Time Spread (TTS) of the PMTs. The amplitude of collected charge is measured by smearing the integrated number of detected photons with a Gaussian of width 0.3 p.e.

At this point, the output looks like hits from the DAQ [134]. The position, time and collected charge of the hits are used to infer the direction and energy of the incident neutrino.

3.2 Event Reconstruction for ANTARES

Event reconstruction algorithms use the timing and position information of the hits at the PMTs to estimate the location of the outgoing lepton emanating from neutrino-nucleon interaction vertices as the well as the energy of the lepton. Two different track reconstruction algorithms are used in ANTARES. We would call them method $\mathcal{A}$ and method $\mathcal{B}$.

3.2.1 Direction estimation

The trajectory of the particle is parameterised by the direction and position of the lepton at some arbitrary time t as $(\vec{r}_t, \vec{p}_t)$.

Method $\mathcal{A}$

This is an online fast reconstruction algorithm [168] for quick fit of tracks. It is particularly suited for real-time applications like online visualisation of event display and triggering of follow-up events for multi-messenger studies.

This method [168] assumes a simplified detector geometry consisting of straight vertical detection lines. The geometry of the OMs is neglected and possible distortions due to sea currents are ignored.

In order to select direct Cherenkov photons coming from a muon track, a hit selection based on causality conditions is made. All hits detected within a time window of 20 ns are merged and events with a multiplicity of 5 hits are accepted.

The photons are then projected along the muon track to find the first and last emission point within the detector geometry. If the selected points occur on several detector lines, a multi-line (ML) fit is performed; otherwise a single-line (SL) fit is performed for points lying on one detector line. The fit function follows the strategy of a χ^2 minimisation defined as a function of the time difference between the observed hit time t_i and the expected arrival time of the photon t_γ. A quality parameter used to discriminate good and badly reconstructed events is defined as

$$\lambda_{\mathcal{A}} = \frac{\chi^2}{N_{d.o.f.}}, \tag{3.4}$$

where $N_{d.o.f.}$ is the number of degrees of freedom in the fit, defined as the number of hits minus the number of fitted parameters. The median of the angular error is defined as the difference between the true muon direction and the reconstructed muon direction. In the 20 GeV energy regime, the median angular resolution is 3° for SL and 0.8° for ML events [169]. The distributions of $\lambda_{\mathcal{A}}$ for atmospheric neutrinos and atmospheric muons are shown in Fig 3.3. More details can be found in [168].

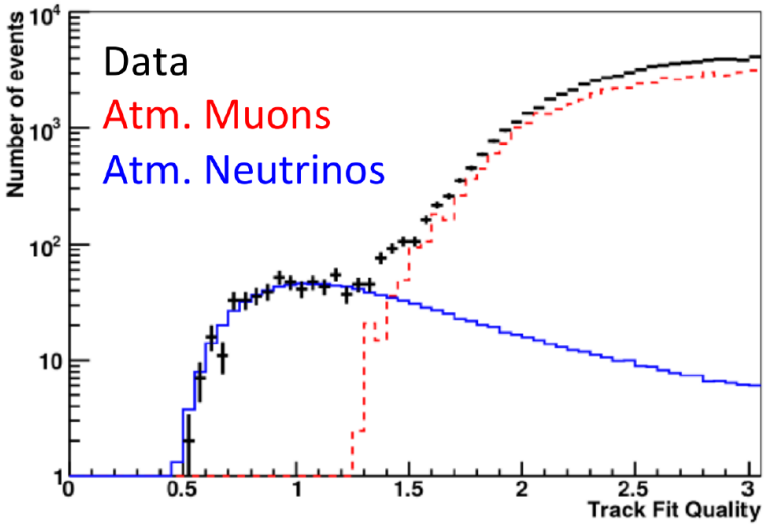

Figure 3.3: Distribution of $\lambda_{\mathcal{A}}$ variable of method $\mathcal{A}$ for events reconstructed as up-going, for ML tracks recorded data (black) compared to MC sample of up-going atmospheric neutrinos (blue) and downgoing muons (red). From [170].

Method $\mathcal{B}$

This method [171] involves a direction prefit based on a directional scan of isotropically distributed directions, followed by a maximum log-likelihood fit to get the track estimation. This method is more robust and is used in the majority of the offline ANTARES physics analyses.

It consists of a chain of subsequent fits:

- **linear prefit:** the reconstruction chain starts with a random hit selection based on local clusters, patterns, coincidence and hits of events in neighbouring floors. It assumes that the muon track passes through the positions of the selected hits. This provides a rough estimation of the muon track to be used as a starting point for the next steps.
- **M-estimator fit:** hits closer than 100 m of linear prefit and whose time residuals fall within a time window of ±150 ns with respect to the expected hit time are selected. The expected arrival time t_{th} of a Cherenkov photon for a given muon position and direction at an arbitrary time t_0 is given by:

$$t_{th} = t_0 + \frac{1}{c}(l - \frac{k}{\tan\theta_c} + \frac{1}{v_g}\frac{k}{\sin\theta_c}), \tag{3.5}$$

  where v_g is the group velocity of light, θ_c is the Cherenkov angle, and k is the shortest distance between the track and the OM. The difference between t_{th} and

the measured arrival time of the photon is called *time residual*. A schematic representation of the muon track is shown in Fig. 3.4.

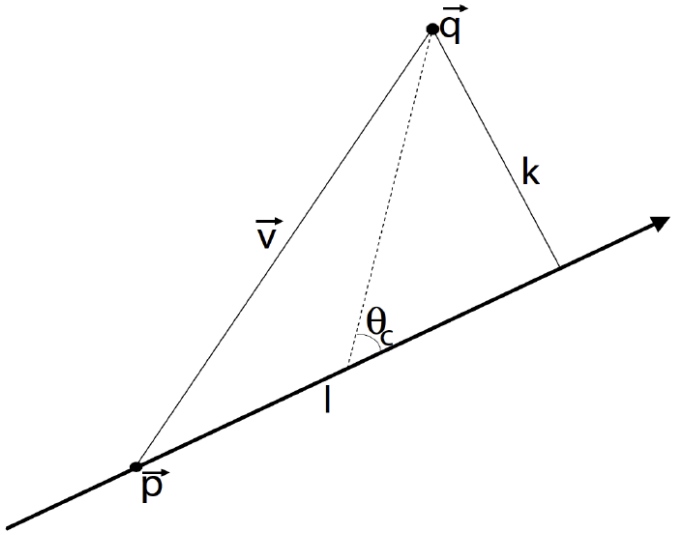

Figure 3.4: Geometrical representation of a muon track. The muon passing through the detector induces a Cherenkov light emission at an angle θ_c w.r.t. its trajectory. A photon travelling at speed v is detected by an OM at a position $\vec{q}$, with k being the distance of closest approach to the muon track. From [170].

- **maximum likelihood fit:** a probability density function is defined as a function of track parameters to maximise the likelihood of obtaining a certain event

$$\mathcal{L}(\vec{r},\vec{p}) = \prod P(t|t_{th},\vec{r},\vec{p}), \tag{3.6}$$

where the sum runs over the number of hits. The probability of a hit being due to background is also accounted for. The goodness of the reconstruction is quantified by the parameter:

$$\lambda_{\mathcal{B}} = \frac{\log \mathcal{L}^{max}}{N_{d.o.f.}} + 0.1 \times (N_{comp} - 1), \tag{3.7}$$

where $\mathcal{L}^{max}$ is the maximum value of the likelihood, $N_{d.o.f}$ is the number of degrees of freedom of the fit given by $N_{d.o.f.} = N_{hits} - 5$, with N_{hits} being the number oh hits used in the reconstruction, and N_{comp} is the number of repetitions of the M-estimator and the maximum-likelihood prefits which gives a track direction within 1° from the selected one.

The track angular error estimate can be obtained from the errors on the zenith angle σ_θ and azimuthal angle σ_ϕ:

$$\beta_{\mathcal{B}} = \sqrt{\sin^2(\theta_{rec})\sigma_\phi^2 + \sigma_\theta^2} \tag{3.8}$$

A median angular resolution better than 0.4° is achieved for energies above 10 TeV. The distributions of λ_B for atmospheric neutrinos and atmospheric muons is shown in Fig 3.5. More details can be found in [170].

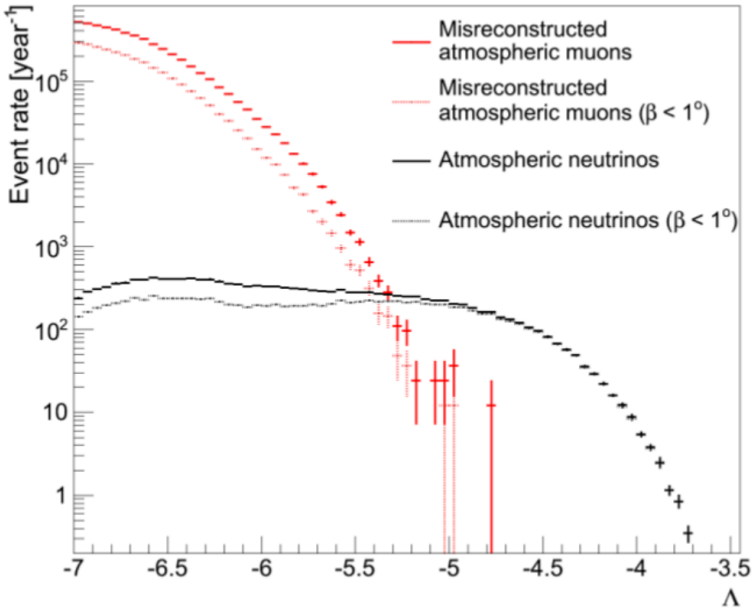

Figure 3.5: Distribution of $\lambda_{\mathcal{B}}$ variable of method $\mathcal{B}$ for events reconstructed as up-going, for atmospheric neutrinos (black) and atmospheric muons (red). From [170].

3.2.2 Energy estimation

Method $\mathcal{A}$

The muon track length in the detector is used as a proxy for the neutrino energy estimation. The total length of the track L_μ is directly related to the energy of the track as

$$E_{tracks} = L_\mu \frac{dE_\mu}{dx}, \tag{3.9}$$

where the differential energy energy loss of a minimum ionising muon in water in the energy range $10 - 100$ GeV, $\frac{dE_\mu}{dx}$, is fixed to 0.24 GeV/m [117].

For SL events, the z coordinates of the initial hit and final hit, z_i and z_f, are chosen to estimate the muon track length:

$$L_\mu = (z_f - z_i)/\cos\theta_z, \tag{3.10}$$

where θ_z is the reconstructed zenith angle. For ML events, the muon track length can be computed from the difference between the spatial coordinates of the initial and final track points:

$$L_\mu = \sqrt{(x_f - x_i)^2 + (y_f - y_i)^2 + (z_f - z_i)^2}, \tag{3.11}$$

Whereas for ML events the threshold energy of the final neutrino sample is about 50 GeV, for SL nearly vertical events set the threshold of the energy estimation in ANTARES as low as 20 GeV, thereby reaching close to the first oscillation minimum. The presence of a hadronic shower at the interacting vertex is ignored, as well as the fact that the muon track might be partially contained. The secondary muon from a primary neutrino interaction might have entered the detector after traversing a subsequent part of its track length outside the instrumented volume, thereby making only a fraction of its actual range accessible to measurement. For muons leaving the detector, only a lower threshold of their energy can be derived. The energy resolution of the muonic events is found to be around 50% ± 22% [147].

Method $\mathcal{B}$

The neutrino energy estimation in this method is based on the total deposited muon energy, $\frac{dE_\mu}{dx}$, on an event-by-event basis [172]:

$$\frac{dE_\mu}{dx} \sim \rho = \frac{\sum_i^{N_{hits}} Q_i}{\epsilon(\vec{r})} \frac{1}{L_\mu(\vec{r})}, \tag{3.12}$$

where Q_i is the charge registered by the OM i, $\epsilon(\vec{r})$ is the light detection efficiency, L_μ is the muon track length and $\vec{r}$ is the muon track direction. The light detection efficiency depends on the position and direction of the muon track:

$$\epsilon(\vec{r}) = \sum_i^{N_{OMs}} \exp(-\frac{r_i}{\lambda_{abs}}) \cdot (\frac{\alpha_i(\theta_i)}{r_i}) \tag{3.13}$$

where the sum runs over all active OMs, r_i is the distance between the OM i and the muon track, λ_{abs} is the absorption length and $\alpha_i(\theta_i)$ parameterises the angular acceptance of the OM i with θ_i being the impact point of the photon on the OM i.

3.3 MC Simulation for ORCA

In this section, the scheme for computation of expected event signals in ORCA is described. The simulation chain involves series of subsequent steps, in which the process from the atmospheric neutrino flux to the observed event spectra is modelled. Each subsequent stage, except the (initial) flux stage takes the output of the previous stage as input and makes a functional transformation. Since the individual stages are independent of each other, a parameter change affecting one stage does not affect the transformation induced by other stages. A schematic view of the simulation chain is shown in Fig. 3.6.

3.3.1 Atmospheric neutrino flux

The first data of interest are the tabulated atmospheric neutrino flux predictions provided in bins of true neutrino energy E_{true} and cosine of the true zenith angle $\cos\theta_{true}$:

$$\phi^{\nu_\alpha}_{E_{true},\cos\theta_{true}} \text{ and } \phi^{\overline{\nu}_\alpha}_{E_{true},\cos\theta_{true}}. \tag{3.14}$$

They represent the number of atmospheric (anti)neutrino of flavour ($\overline{\nu}_\alpha$) ν_α with energy and zenith angle within the range of $[E_{true}, \cos\theta_{true}]$ bin passing through unit area of the detector per unit time, oscillations neglected.

The table entries are collected from Honda *et al.* [103] (discussed in 2.1). Due to the proximity of the Fréjus site[1] to the ORCA site, the year-averaged tables at solar minimum without effects of the mountain top at the Fréjus site is expected to resemble the flux at the ORCA site. The Honda flux tables are provided in 101 equidistant bins of $\log(E)$ from 0.1 to 10,000 GeV and 20 equidistant bins of $\cos\theta_z$ ranging from -1 (up-going) to $+1$ (downgoing).

In ORCA simulations, the energy range is divided into 40 bins with bin centers equidistant in $\log(E)$, with $E \in [1, 100]$ GeV. The zenith angle is binned 40 bins equidistant in $\cos\theta_z$ from -1 to 1. The choice of the binning is made to retain the numerical accuracy and to reduce the computational load while avoiding smearing out the physical effects under study.

The Honda flux tables are rebinned using a bilinear spline interpolation for each target $[E_{true}, \cos\theta_{true}]$ bin, shown in Fig. 3.7 and Fig.3.8. The unoscillated atmospheric tau (anti)neutrino fluxes are assumed to be negligible. The same binning in true variables is retained till the detection stage, after which, a coarser binning is used for reconstruction due to limited resolutions. A 20×20 binning in reconstructed space, $[E_{reco}, \cos\theta_{reco}]$, is chosen in order to complement the detector resolutions, while ensuring enough statistics in each bin.

[1] This refers to the Fréjus Underground Laboratory located near Modane, France.

Figure 3.6: Flowchart of the simulation chain. The horizontal blocks represent the intermediate results in bins of either true or reconstructed energy and zenith angle. The vertical blocks refer to the transformation being carried out at respective stages of the simulation chain. The first three stages are detector independent, while the latest ones are detector specific. The final event templates observed at the detector are marked in blue (tracks) and red (showers) boxes.

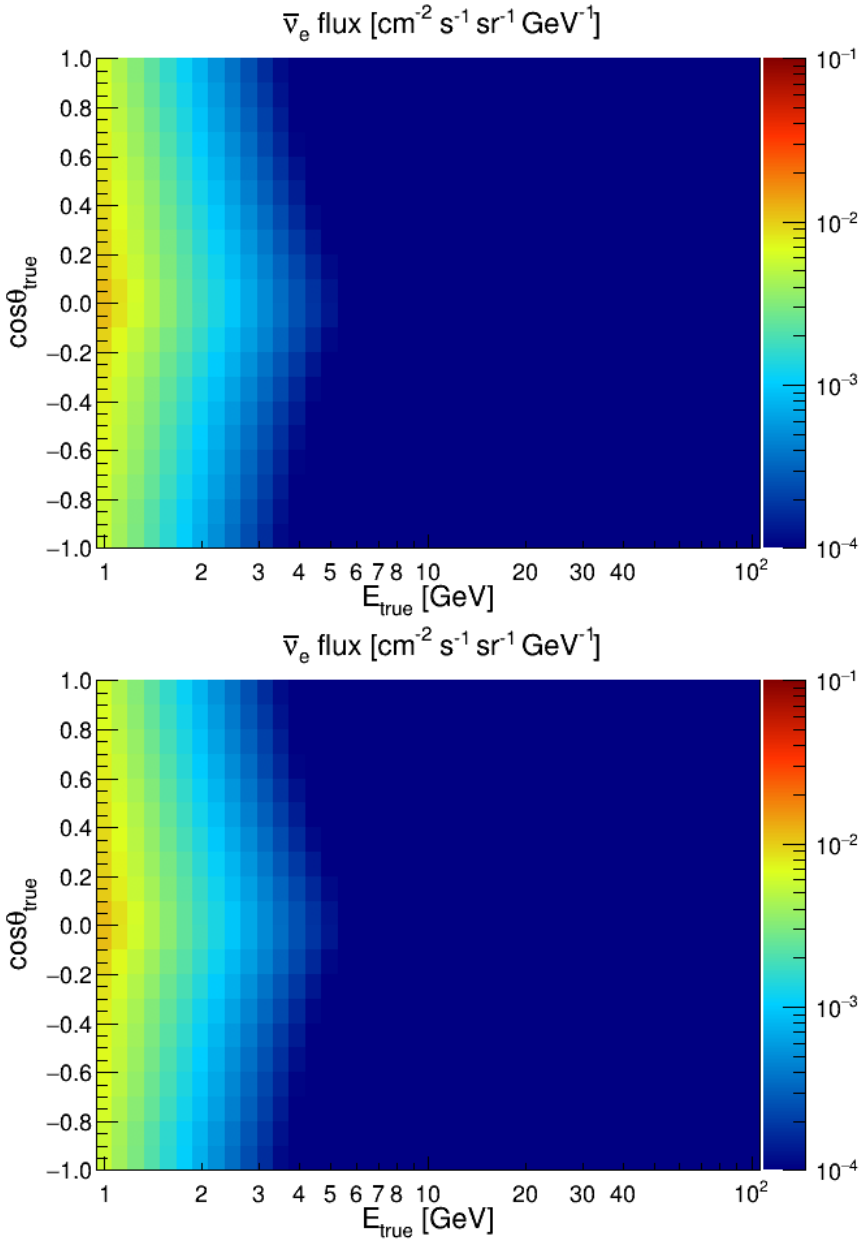

Figure 3.7: Distribution of atmospheric electron neutrino (top) and anti-electron neutrino flux (bottom) based on the year-averaged flux at the Fréjus site without mountain at solar minimum [103]. The colour code gives the integrated flux over the energy-zenith bin.

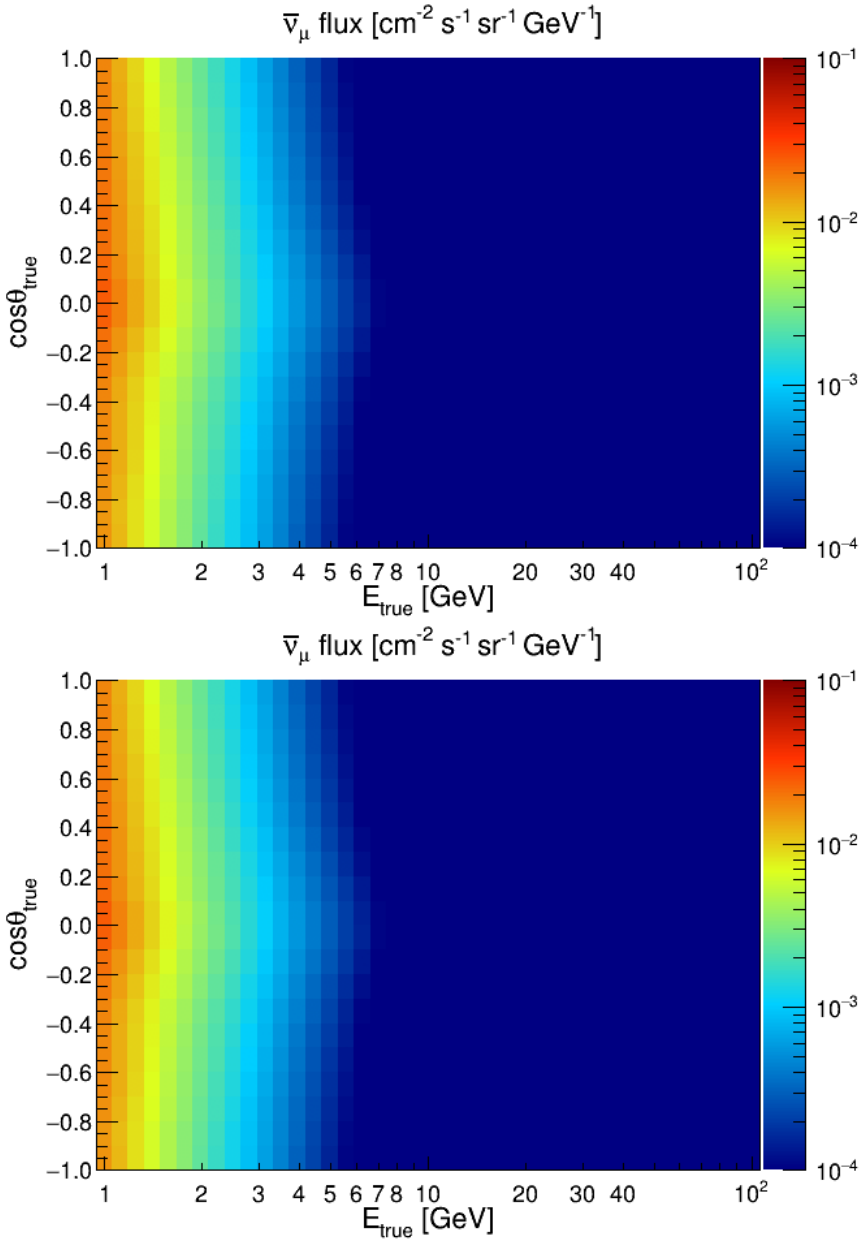

Figure 3.8: Distribution of atmospheric muon neutrino (top) and anti-muon neutrino flux (bottom) based on the year-averaged flux at the Fréjus site without mountain at solar minimum [103]. The colour code gives the integrated flux over the energy-zenith bin.

3.3.2 Neutrino propagation through Earth

The Earth is modelled as a series of concentric spherical layers of constant matter density called shells (Fig. 1.3), and adopted from PREM [53]. The OscProb [52] neutrino oscillation calculator allows the definition of a radial planetary model and position of the detector within this model to calculate oscillation probabilities.

The oscillation probabilities as a function of true variables for the adopted binning are shown in Fig. 3.9 and Fig. 3.10. The oscillation probabilities are multiplied by the

unoscillated fluxes from the previous step to yield the oscillated neutrino fluxes:

$$\phi^{\nu_\beta,\,\mathrm{osc}}_{E_\nu,\cos\theta_z} = \sum_\alpha P_{\nu_\alpha\to\nu_\beta}(E_\nu,\cos\theta_z)\cdot\phi^{\nu_\alpha}_{E_\nu,\cos\theta_z},$$
$$\phi^{\overline{\nu}_\beta,\,\mathrm{osc}}_{E_\nu,\cos\theta_z} = \sum_\alpha P_{\overline{\nu}_\alpha\to\overline{\nu}_\beta}(E_\nu,\cos\theta_z)\cdot\phi^{\overline{\nu}_\alpha}_{E_\nu,\cos\theta_z}. \tag{3.15}$$

Oscillations effects are negligible for downgoing neutrino events ($\cos\theta_z > 0$).

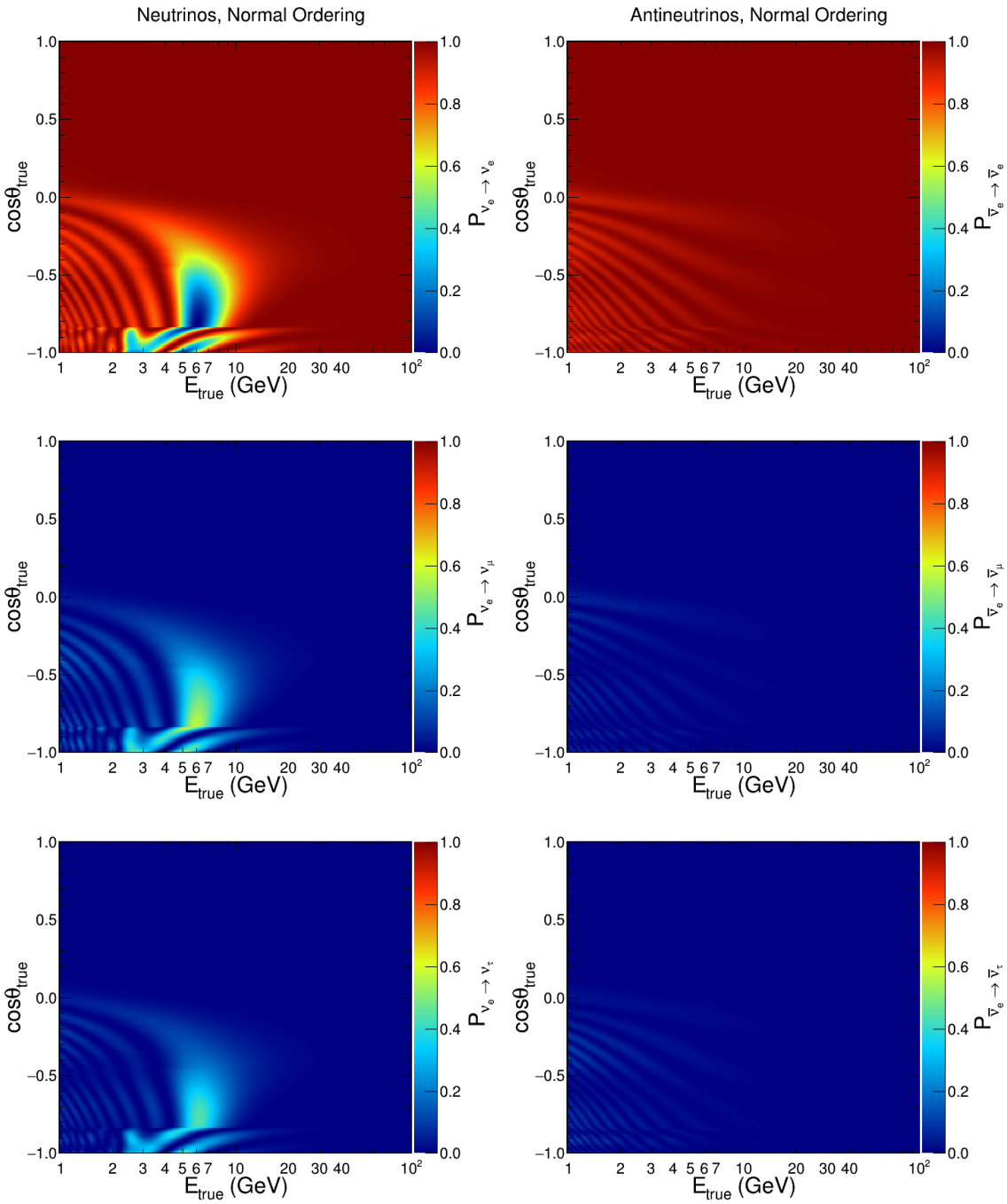

Figure 3.9: $P_{\nu_e\to\nu_x}(x = e,\,\mu,\,\tau)$ for neutrinos (left) and antineutrinos (right) as a function of true neutrino energy E_{true} and cosine of the true zenith angle $\cos\theta_{true}$. The top, middle and bottom panels correspond to electron disappearance, muon appearance and tau appearance channels, respectively. Normal Ordering is assumed.

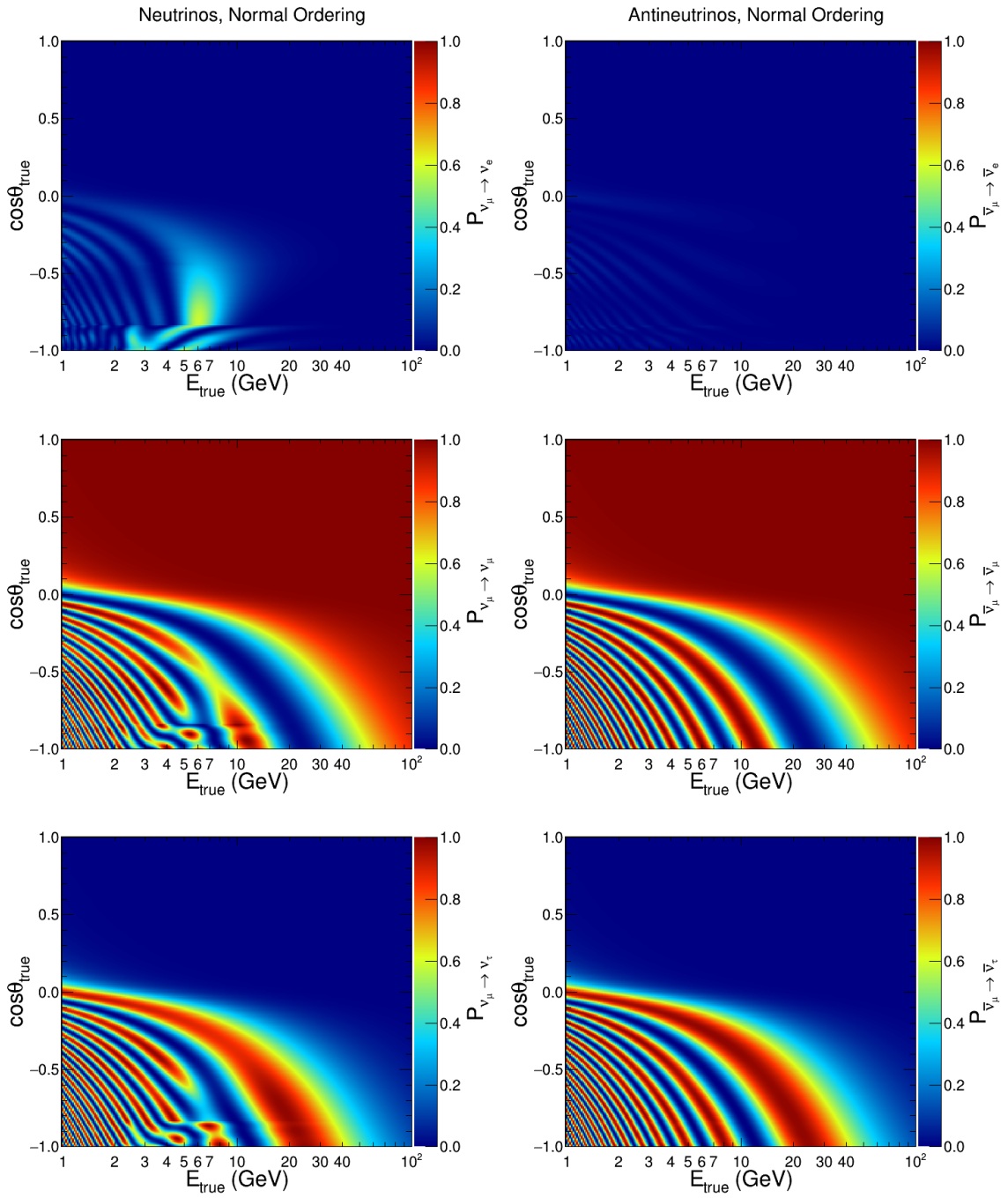

Figure 3.10: $P_{\nu_\mu \to \nu_x}(x = e, \mu, \tau)$ for neutrinos (left) and antineutrinos (right) as a function of neutrino energy E_ν and cosine of the zenith angle $\cos\theta_z$. The top, middle and bottom panels correspond to electron disappearance, muon appearance and tau appearance channels, respectively. Normal Ordering is assumed.

3.3.3 Interaction Cross-sections

Neutrino-nucleon interactions are described in Sec. 2.2. Based on the different interaction types, eight distinguishable interactions indexed by $\mathcal{X}$ are considered in the simulated chain:

- CC interactions for each of the six neutrino flavours $\nu_e, \nu_\mu, \nu_\tau, \overline{\nu}_e, \overline{\nu}_\mu$, and $\overline{\nu}_\tau$;
- NC interactions of all flavours ν_y and $\overline{\nu}_y$.

Flavour distributed NC interactions are not considered since their cross-sections are identical and they leave identical signature at the detector. A total combined CC interaction cross-section is used irrespective of the type of underlying CC interactions (DIS, QE, RES) since their experimental signature cannot be probed at ORCA.

Neutrino interactions are simulated with the gSeagen code [173], developed within the KM3NeT collaboration. It is based on the widely used GENIE neutrino Monte Carlo generator package [174], that incorporates theoretical models and constraints from experimental data to model neutrino interactions over a wide range of energies for different neutrino flavours and target material types. Electron and muon neutrinos (and antineutrinos) in the energy range from 1 GeV to 100 GeV are simulated and weighted accordingly to reproduce the atmospheric neutrino flux following the Honda model [103]. The scheme for neutrino event generation in ORCA follows the strategy adopted for ANTARES, as discussed in Sec. 3.1.1. The cross-section per nucleon is calculated by taking a weighted mean of the cross-sections on free target protons and on oxygen nuclei:

$$\sigma_{nucleon} = \frac{2 \times \sigma(^{1}_{1}\mathrm{H}) + \sigma(^{16}_{8}\mathrm{O})}{2+16}. \tag{3.16}$$

The resulting cross-sections are shown in Fig. 2.4. In simulations, $\sigma(E)$ is interpolated from these curves for each interaction channel. The ν_e and ν_μ interaction cross-sections are almost identical. The neutrino cross-sections are twice or more as high as their antineutrino cross-sections. The ν_τ interaction cross-section is suppressed with a threshold ~ 3.5 GeV, due to the large τ mass.

The interaction rates are estimated from the oscillated neutrino fluxes Eq. 3.15 by:

$$\begin{aligned}
R^{CC,\nu_\alpha}_{E_\nu,\cos\theta_z} &= \sigma^{CC,\nu_\alpha}(E_\nu) \times \phi^{\nu_\alpha,\,\mathrm{osc}}_{E_\nu,\cos\theta_z}, \\
R^{CC,\overline{\nu}_\alpha}_{E_\nu,\cos\theta_z} &= \sigma^{CC,\overline{\nu}_\alpha}(E_\nu) \times \phi^{\overline{\nu}_\alpha,\,\mathrm{osc}}_{E_\nu,\cos\theta_z}, \\
R^{NC,\nu}_{E_\nu,\cos\theta_z} &= \sigma^{NC,\nu}(E_\nu) \times \sum_\alpha \phi^{\nu_\alpha,\,\mathrm{osc}}_{E_\nu,\cos\theta_z}, \\
R^{NC,\overline{\nu}}_{E_\nu,\cos\theta_z} &= \sigma^{NC,\overline{\nu}}(E_\nu) \times \sum_\alpha \phi^{\overline{\nu}_\alpha,\,\mathrm{osc}}_{E_\nu,\cos\theta_z},
\end{aligned} \tag{3.17}$$

where $\sigma^{\mathcal{X}}$ represents the interaction cross-section per target nucleon for interactions of type $\mathcal{X}$ at a particular neutrino energy E_ν.

Since the interaction cross-sections are very low, the neutrino interaction rates in Eq. 3.17, which give the number of interactions per unit time per target nucleon, are also very small. It is rather convenient to work with interaction rates per unit target mass:

$$R^{\mathcal{X}}/m_N, \tag{3.18}$$

where m_N is the average between the proton and the neutron masses[2].

Fig. 3.11 to 3.14 show the results of the calculations of the expected rates of neutrino events per megatonne[3] per year. The oscillation effects for electron neutrinos in Fig. 3.11

[2]This approximation does not take into account the difference between the atomic mass and the sum of the mass of the individual nucleons. However, this only incorporates a sub-percent error in the estimation of the overall expected events, which is rather small compared to the systematic uncertainty on the atmospheric neutrino flux.

[3]The mass of large volume neutrino telescopes are usually expressed in megatonne (Mton).

are hardly discernible due to steep energy dependence of the flux. The disappearance of muon neutrinos in Fig. 3.12 and the corresponding appearance of tau neutrinos in Fig. 3.13 are clearly visible. The τ threshold suppressing ν_τ interactions at low energies can be seen. The antineutrino rates look very similar to neutrino rates in shape. However they differ in magnitude, shown by the colour scale.

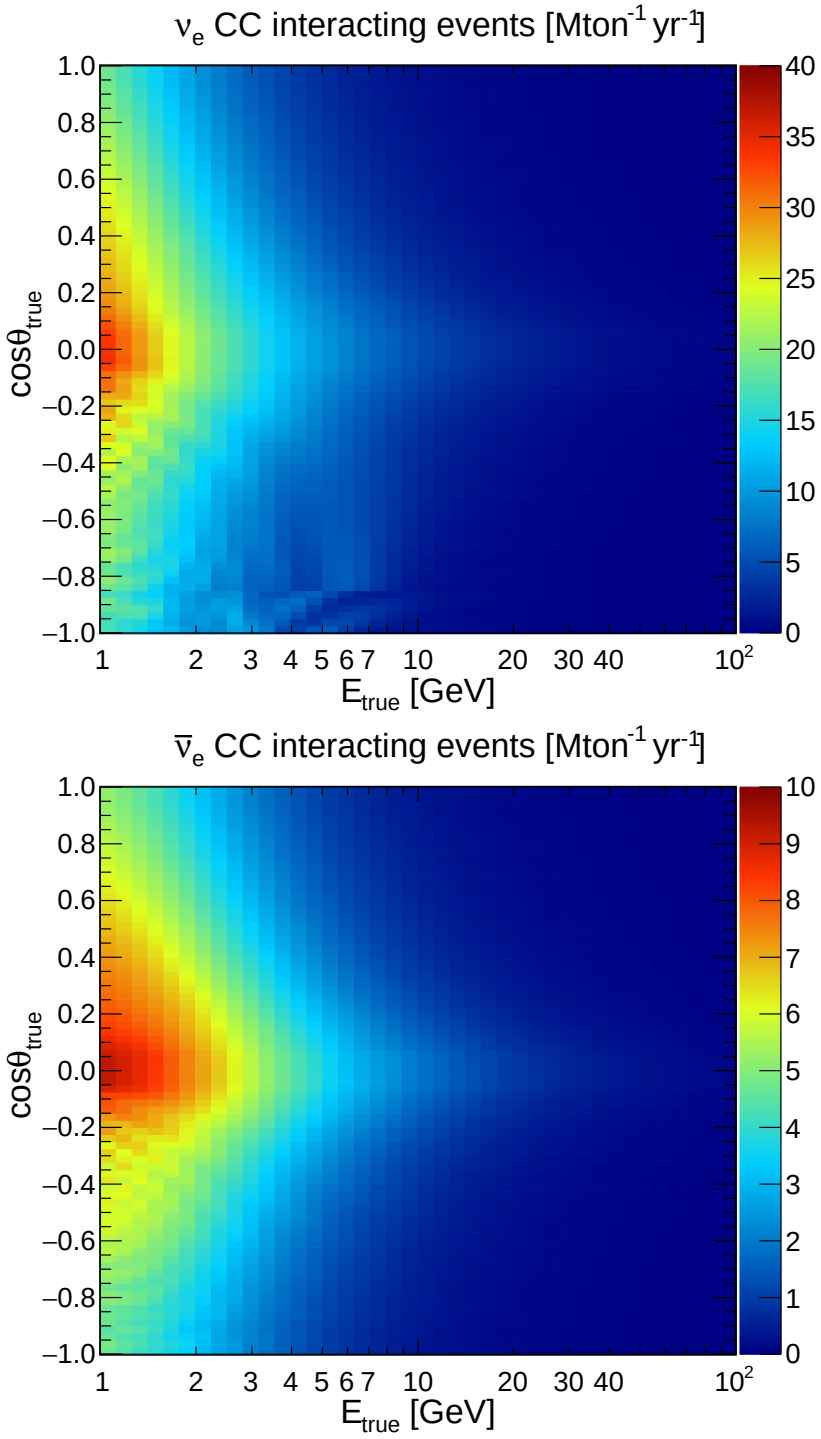

Figure 3.11: ν_e (top) and $\bar{\nu}_e$ (bottom) CC interaction rates at the detector. The colour code gives the number of neutrino interactions (per Megaton per year). Mind the difference in the colour scales on individual plots.

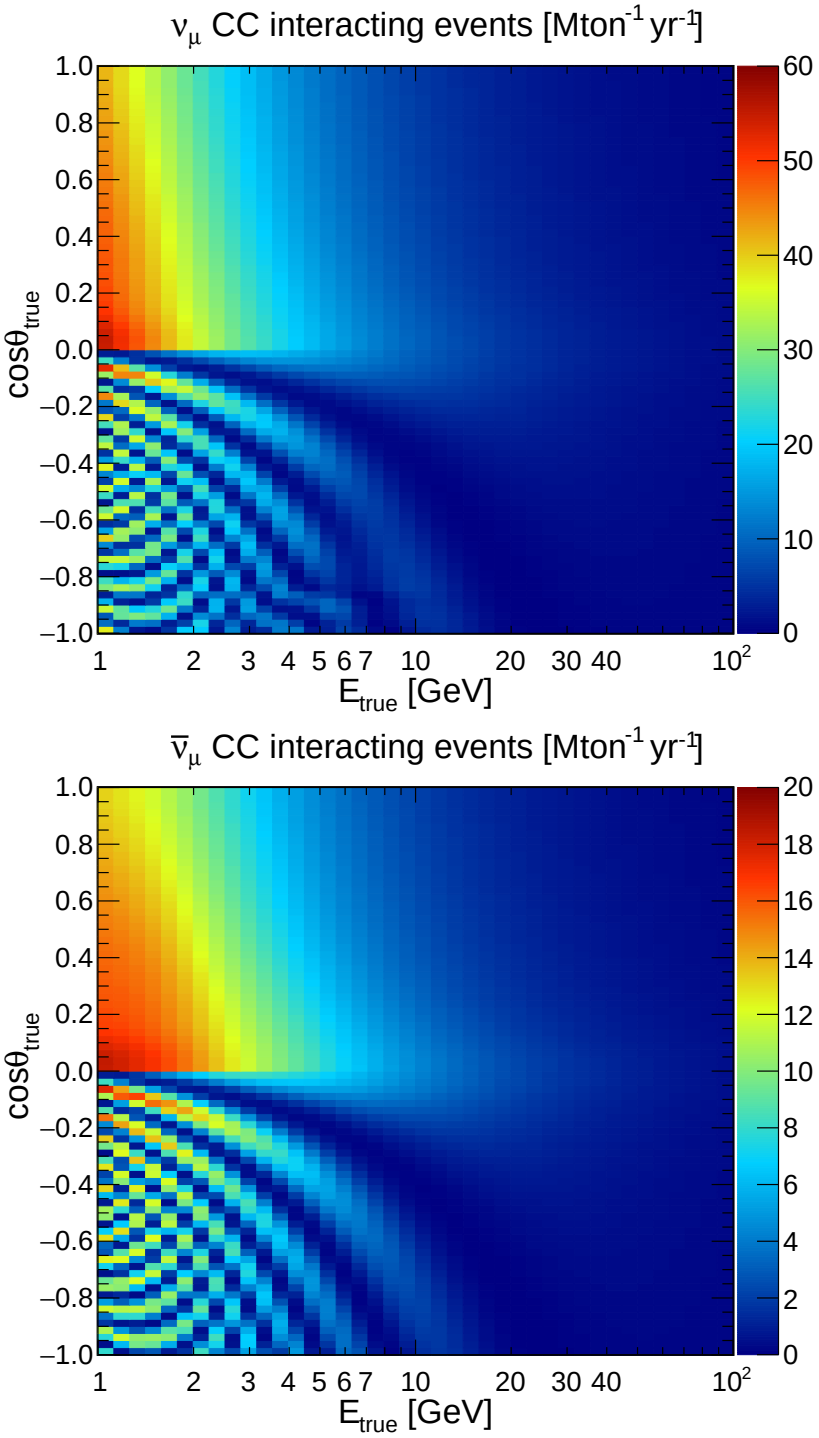

Figure 3.12: ν_μ (top) and $\bar{\nu}_\mu$ (bottom) CC interaction rates at the detector. See also the caption of Fig. 3.11.

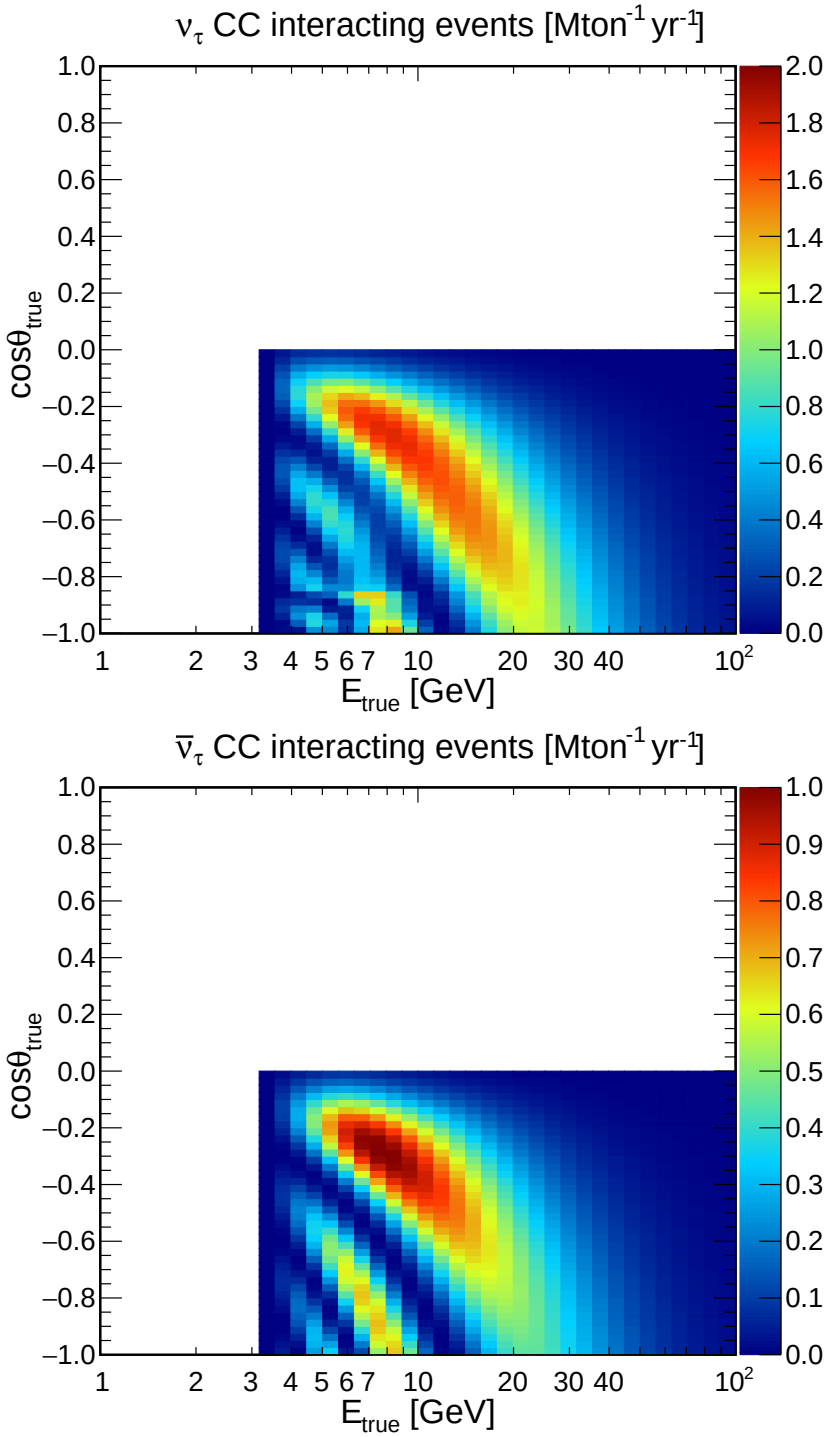

Figure 3.13: ν_τ (top) and $\bar{\nu}_\tau$ (bottom) CC interaction rates at the detector. See also the caption of Fig. 3.11.

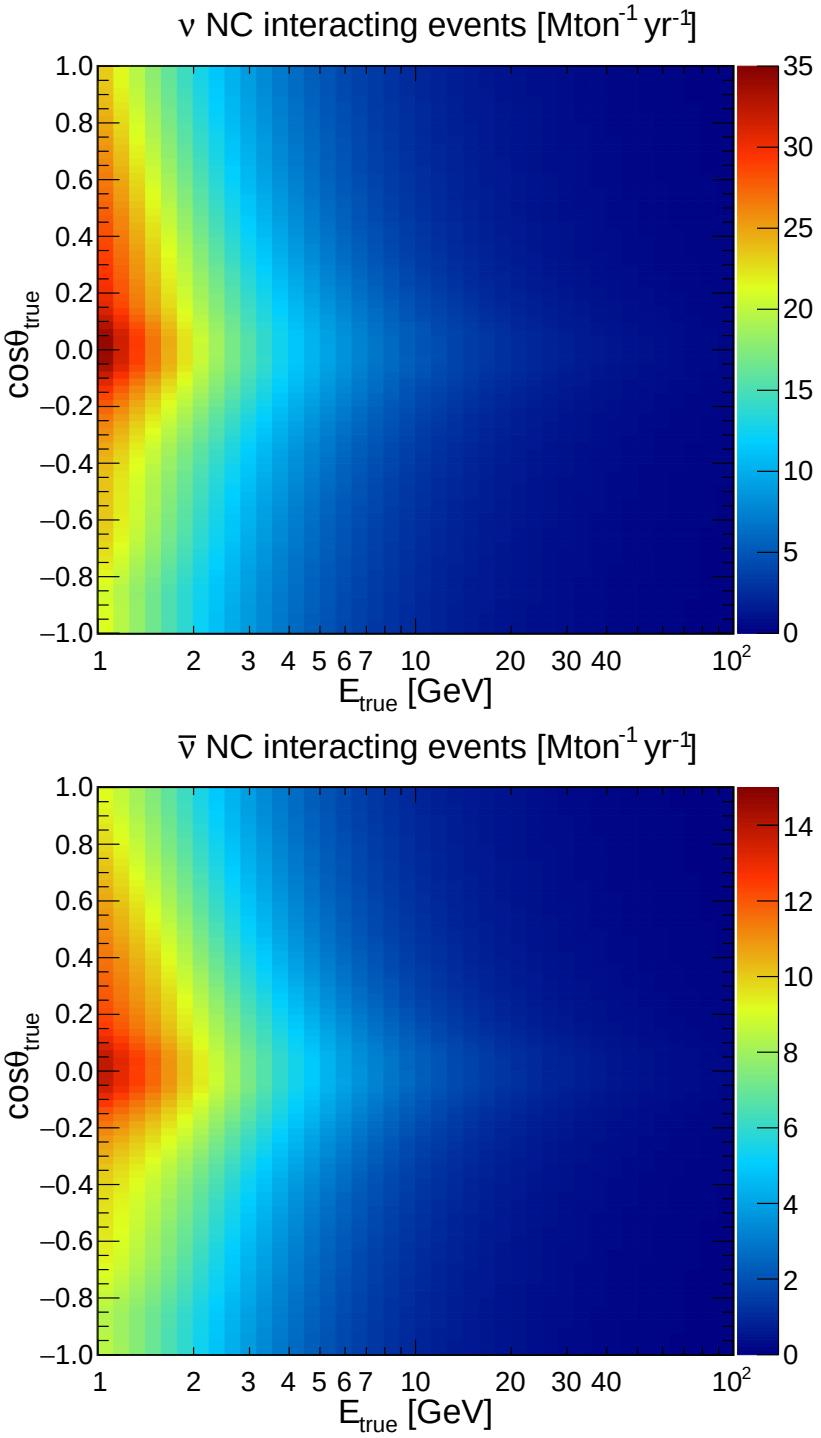

Figure 3.14: ν (top) and $\bar{\nu}$ (bottom) NC interaction rates at the detector. See also the caption of Fig. 3.11.

3.4 Detector Response for ORCA

The second part of the simulation chain models the detector response to neutrino interactions. Similar to ANTARES, the Monte Carlo chain for ORCA is based on a multi-stage process consisting of an event generator, a simulator for Cherenkov light generation and tracking of particles in seawater and simulation of the detector response

and triggering.

Neutrino induced interactions in seawater are simulated with gSeaGen [173]. All particles emerging from neutrino interactions are propagated with the GEANT4-based software package KM3Sim [163] developed within the KM3NeT Collaboration. Atmospheric muon events are generated using the MUPAGE package [164], and the KM3Sim package is used for tracking the muons in seawater and subsequent Cherenkov light production and propagation.

Randomly distributed hits due to Cherenkov light emission from β-decays of ^{40}K are also added. An uncorrelated hit rate of 10 kHz per PMT as well as time-correlated noise per DOM (600 Hz twofold, 60 Hz threefold, 7 Hz fourfold, 0.8 Hz fivefold and 0.08 Hz sixfold) is added. This optical background rates are estimated from the data of the first deployed DUs [175].

Trigger algorithms [143] based on only one local coincidence and a tunable number of causally connected single hits on DOMs in vicinity have been developed to account for the multi-PMT peculiarities of ORCA. The trigger rate for atmospheric muons is $\sim$ 50 Hz and pure-noise events $\sim$ 4 Hz, while atmospheric neutrinos are triggered with a rate $\sim$ 7.6 mHz[4]. To reduce the computational load of simulating a "full statistics" corresponding to several years of equivalent livetime for atmospheric muons and pure noise, only 14 days of atmospheric muons and 1.4 days of pure noise are simulated. For atmospheric neutrinos, events with an equivalent livetime of $\sim$ 15 years are simulated.

3.4.1 Effective mass

The next intermediate stage in the simulation chain is the computation of detected events. The detected events correspond to those neutrino interactions that meet the following criteria:

- the event passes the L1 trigger[5] (Sec. 2.4.1);
- the event is successfully reconstructed by any of the reconstruction algorithms (Sec. 3.4.2);
- the event passes the atmospheric muon and pure noise rejection criteria (Sec. 3.4.3);
- the event is classified as a *track* or a *shower* (Sec. 3.4.3).

The expected number of detected events for each interaction type $\mathcal{X}$, $N^{\mathcal{X}}$, is calculated in the following way:

$$N^{\mathcal{X}}(E_\nu, \cos\theta_z) = \frac{R^{\mathcal{X}}}{m_N} \times M^{\mathcal{X}}_{eff}(E_\nu, \cos\theta_z) \times T, \tag{3.19}$$

where, $R^{\mathcal{X}}/m_N$ is the interaction rate per unit target mass of interaction type $\mathcal{X} \in \{(\nu_e, \overline{\nu}_e, \nu_\mu, \overline{\nu}_\mu, \nu_\tau, \overline{\nu}_\tau$ - CC) and $(\nu, \overline{\nu}$ - NC)$\}$, T is the time duration of data taking, $M^{\mathcal{X}}_{eff}$ is the energy- and zenith angle-dependent effective mass corresponding to the interaction type $\mathcal{X}$.

[4]It should be kept in mind that these quoted rates are not comparable among them, since some refer to event rates and other to hit events.

[5]The level-one filter (L1) refers to a coincidence of two (or more) L0 hits from different PMTs in the same optical module within a 10 ns time window.

The effective mass M^{χ}_{eff} incorporates the totality of the effects related to the detector instrumented volume as well as the detector's ability to identify a neutrino interaction. It is defined as

$$M^{\chi}_{eff} = \frac{N_{det}}{N_{sel}} \times V_{gen} \times \rho_w, \tag{3.20}$$

where, N_{det} is the number of interactions events that meet the requirements to be counted as a detected event, N_{sel} is the total number of interactions generated within the instrumented volume V_{gen} and ρ_w is the density of seawater $(= 1.025\,\mathrm{g\,cm^{-3}})$.

The ORCA detector (Sec. 2.10), upon completion, will consist of 115 DUs arranged in circular geometry with a radius of $\sim$ 115 m. Along a DU, the average vertical spacing between DOMs is $\sim$ 9 m. The horizontal spacing between DUs is an optimisation between the technical constraints of the deployment procedure from the engineering perspective and the instrumentation density required for the measurement of the the neutrino mass ordering from the physics point of view. For the NSI study, we are going to use the two average horizontal distance that have been considered by the collaboration:

- **ORCA115 – 23 m**: 115 DUs are spaced apart by 23 m, amounting to an instrumented volume of $\sim$ 8 Mton.
- **ORCA115 – 20 m**: 115 DUs are spaced apart by 20 m, amounting to an instrumented volume of $\sim$ 6 Mton.

The effective masses are estimated for both detector geometries. They are represented by eight two-dimensional tables in true energy and zenith angle, as shown in Fig. 3.15 to Fig. 3.18.

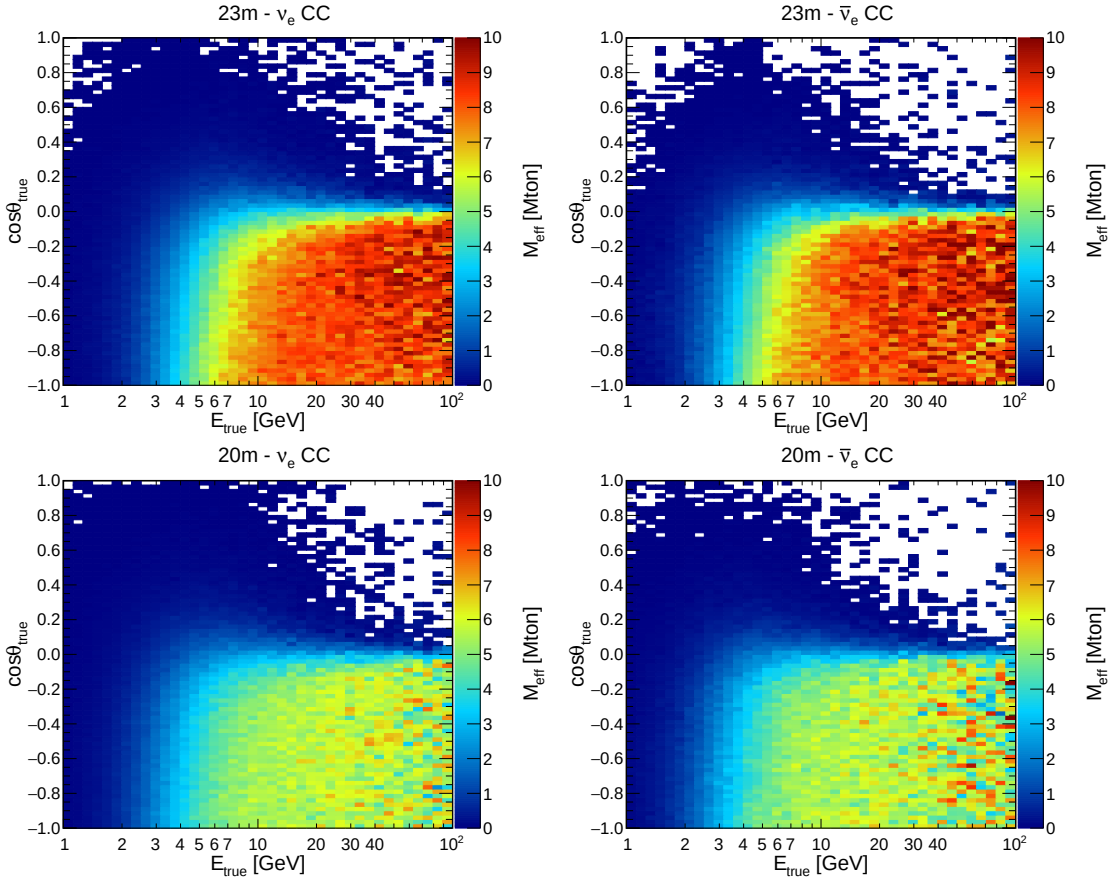

Figure 3.15: ν_e (left) and $\overline{\nu}_e$ (right) CC effective masses as a function of true neutrino energy and zenith angle for two horizontal spacing of ORCA DUs: 23 m (top panels) and 20 m (bottom panels). The colour code gives the effective masses in Mton.

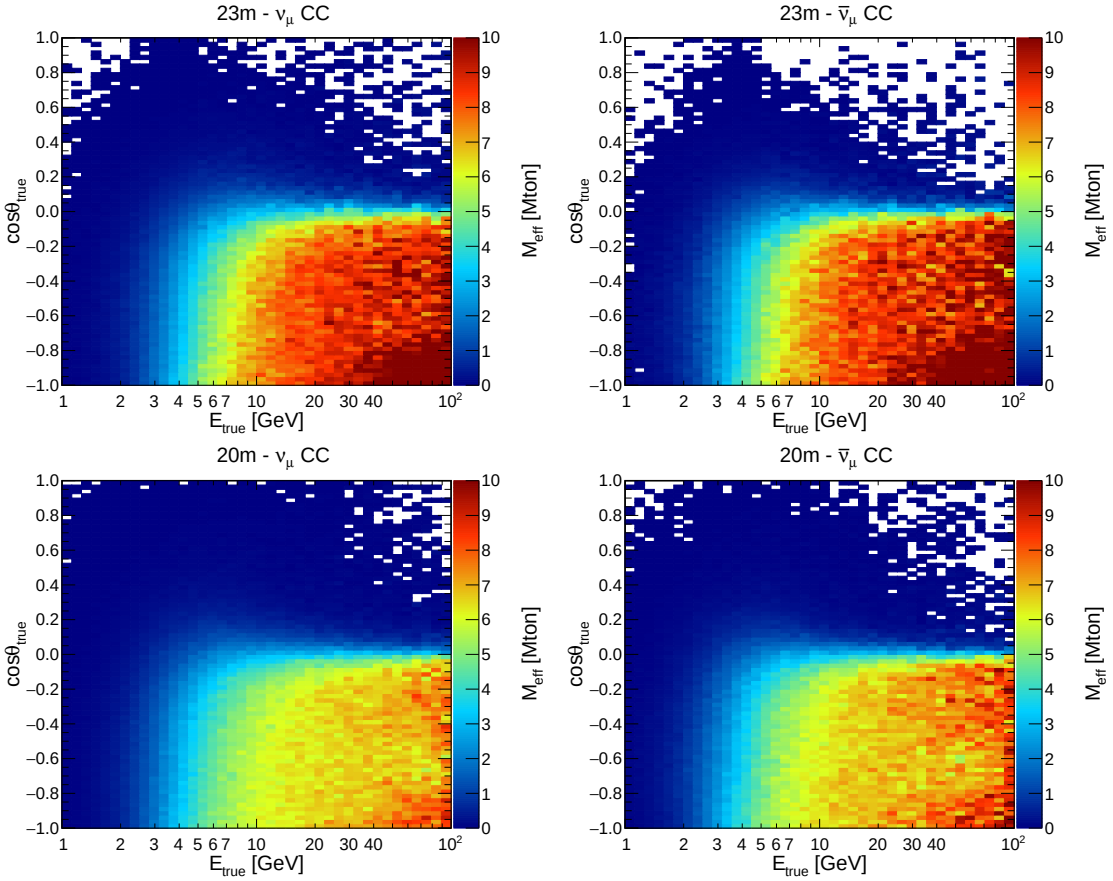

Figure 3.16: ν_μ (left) and $\overline{\nu}_\mu$ (right) CC effective masses as a function of true neutrino energy and zenith angle for two horizontal spacing of ORCA DUs: 23 m (top panels) and 20 m (bottom panels). The colour code gives the effective masses in Mton.

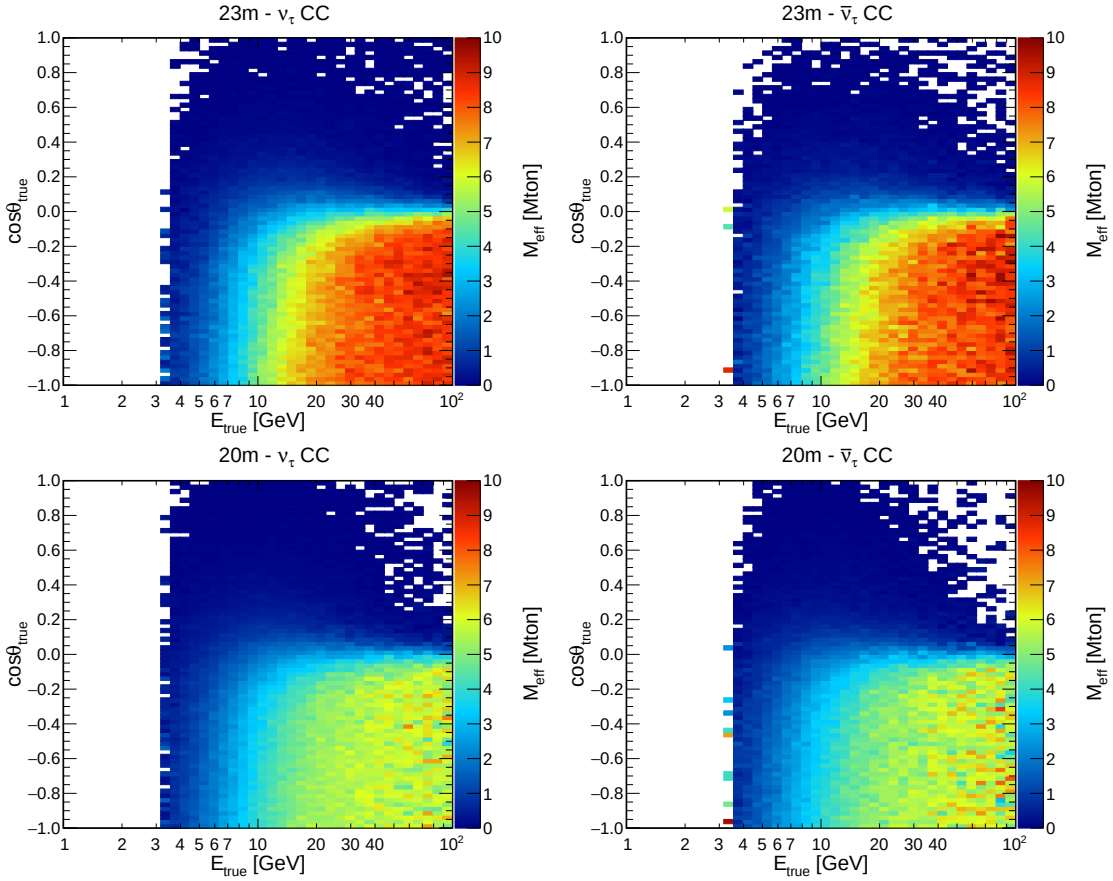

Figure 3.17: ν_τ (left) and $\overline{\nu}_\tau$ (right) CC effective masses as a function of true neutrino energy and zenith angle for two horizontal spacing of ORCA DUs: 23 m (top panels) and 20 m (bottom panels). The colour code gives the effective masses in Mton.

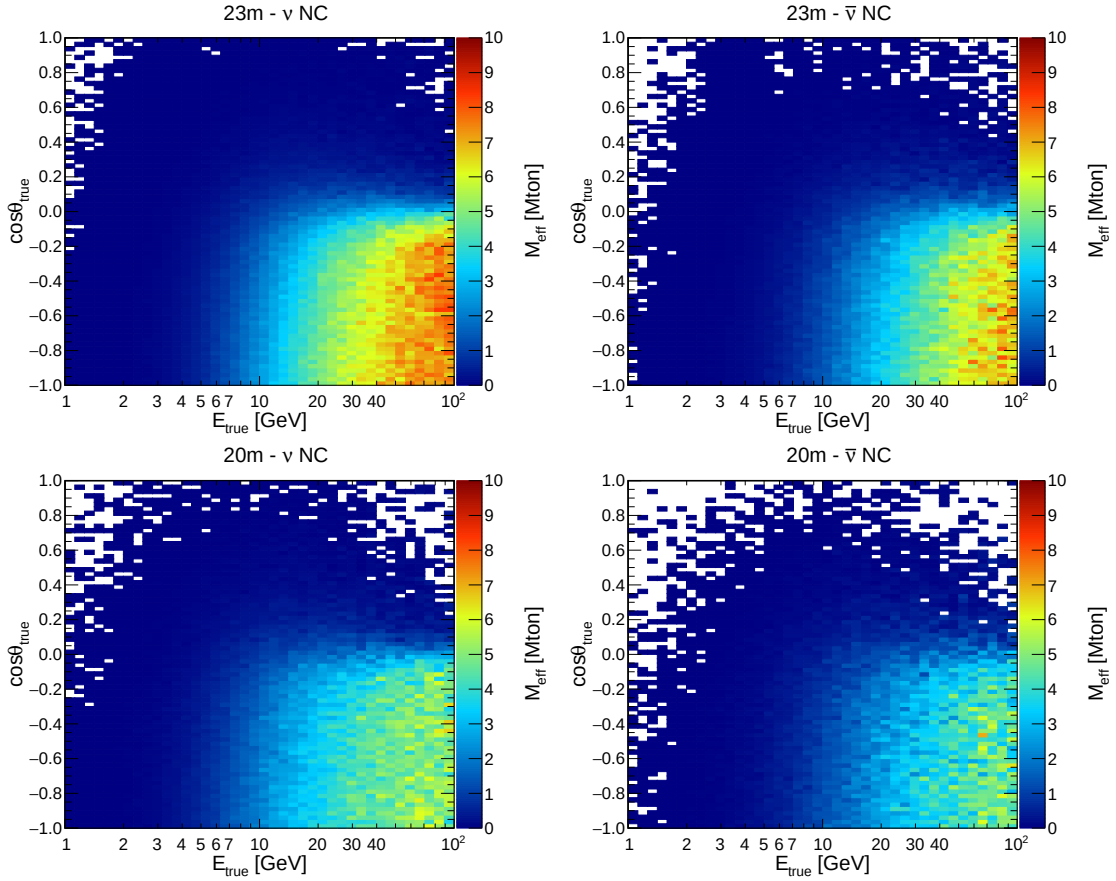

Figure 3.18: ν (left) and $\overline{\nu}$ (right) CC effective masses as a function of true neutrino energy and zenith angle for two horizontal spacing of ORCA DUs: 23 m (top panels) and 20 m (bottom panels). The colour code gives the effective masses in Mton.

The sharp zenith-dependence of effective mass roots from two effects:

- the atmospheric muon rejection criteria disfavours downgoing events;
- the asymmetry in the number of PMTs within the DOMs in either hemisphere. More downward-looking PMTs (19, housed in the lower hemisphere) and the fact that Cherenkov light is emitted in the forward direction results in a higher photon detection efficiency and consequently higher effective masses for up-going neutrinos.

Integrating over the zenith angles for up-going events, the effective masses for different neutrino event types are shown in Fig. 3.19. The effective masses increases with energy since high energy neutrino events produce more light and are more probable to be detected. At $E \sim$20 GeV, a plateau of the order of the instrumented mass ($V_{inst} \cdot \rho_w$) is reached for ν_e and ν_μ CC events.

In case of CC events, the effective masses for antineutrinos are higher than for neutrinos, since the outgoing lepton on average receives a larger fraction of the initial neutrino energy in antineutrino interactions. In case of NC events, the effect is reverse. In antineutrino NC interactions the outgoing lepton on average carries more energy, which is not visible in the detector. A higher average horizontal spacing of 23 m (compared to 20 m) results in higher effective mass and consequently higher number of events. A

turn-on is observed at 20% shifted lower energies due to improved trigger [143] and effective reconstruction [155] compared to earlier studies in [66].

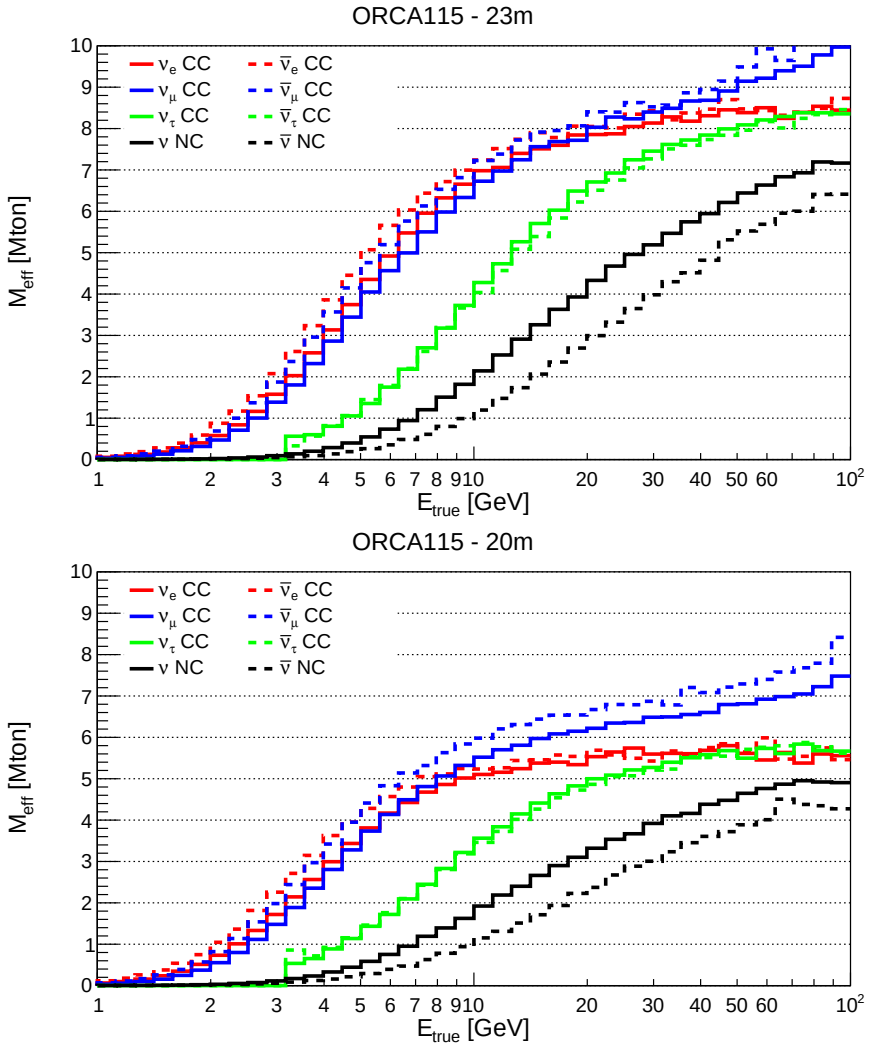

Figure 3.19: Effective mass of the detector as a function of neutrino energy E for different neutrino interaction channels $\mathcal{X}$ separated by flavour for the two spacing. Only up-going events are considered.

The expected number of detected events at ORCA with 20 m horizontal spacing between DUs are shown in Fig. 3.20 to Fig. 3.23. Most of the detected CC events fall in the energy range of 3 to 30 GeV. The effect of oscillations is still visible.

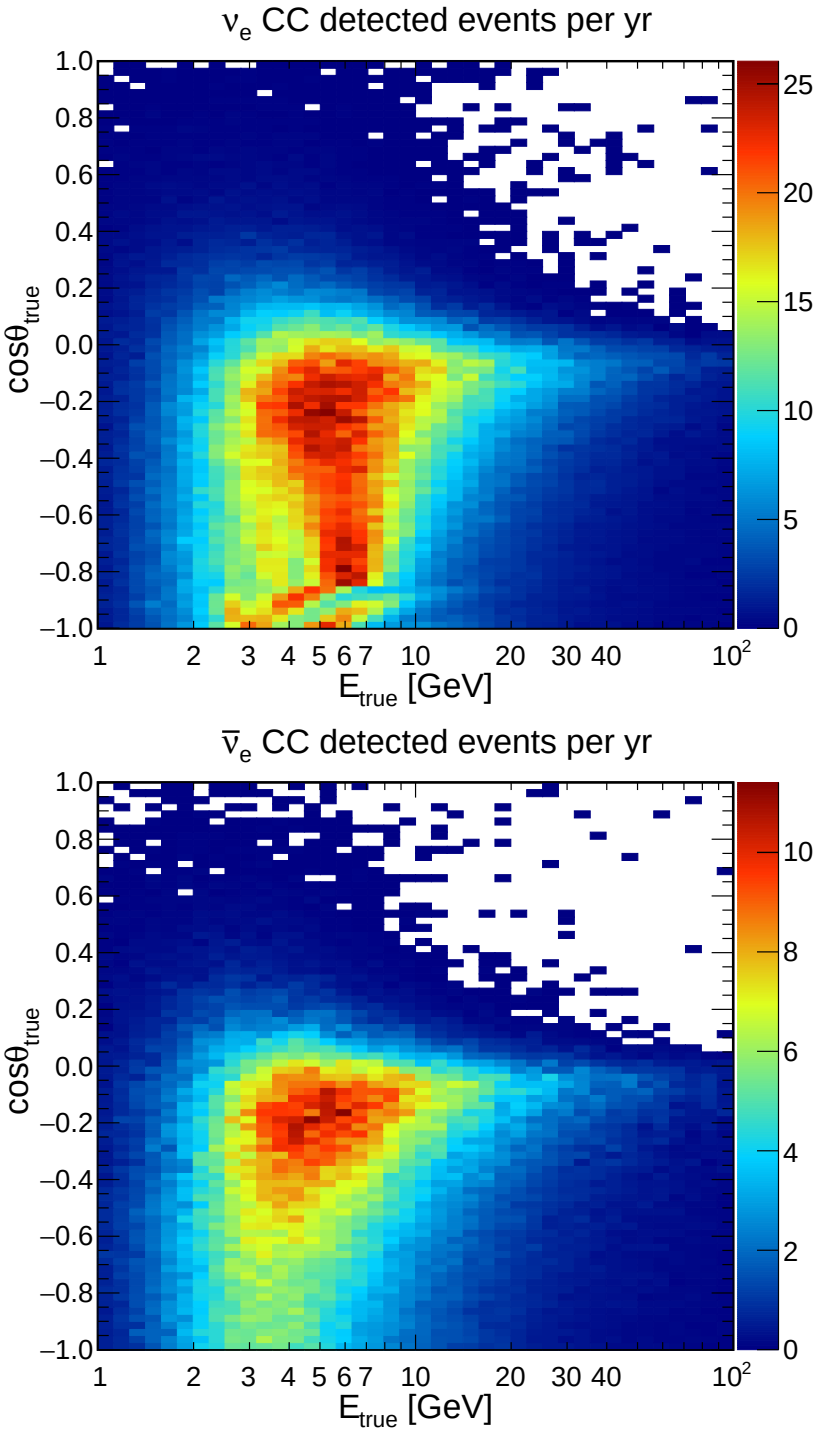

Figure 3.20: Rates of ν_e (top) and $\bar{\nu}_e$ (bottom) CC detected events in ORCA as a function of true neutrino energy and zenith angle for 20 m spacing. The colour code gives the number of detected neutrino events. Mind the difference in the colour scales on individual plots.

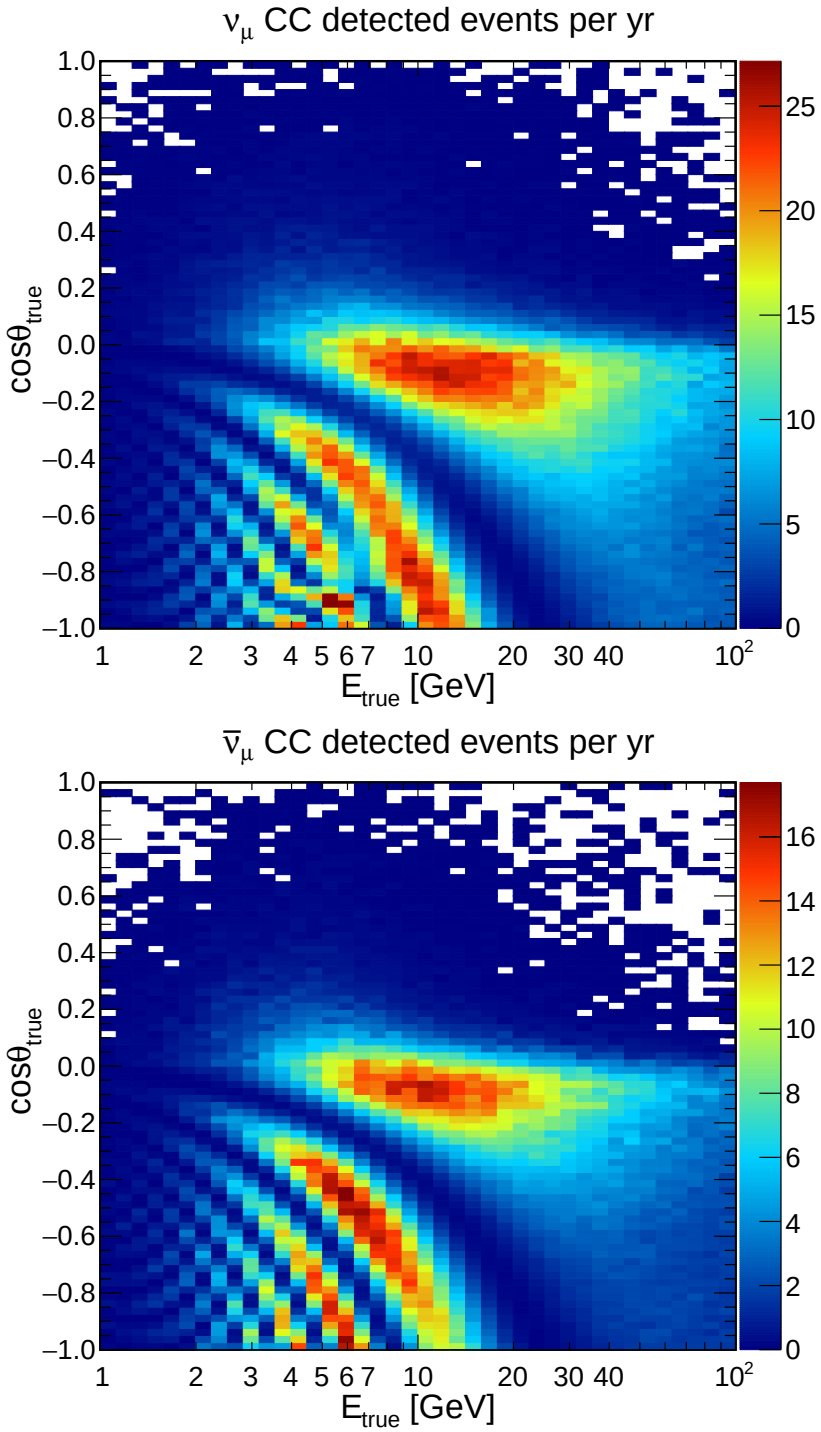

Figure 3.21: Rates of ν_μ (top) and $\bar{\nu}_\mu$ (bottom) CC detected events in ORCA as a function of true neutrino energy and zenith angle for 20 m spacing. See also the caption of Fig. 3.11.

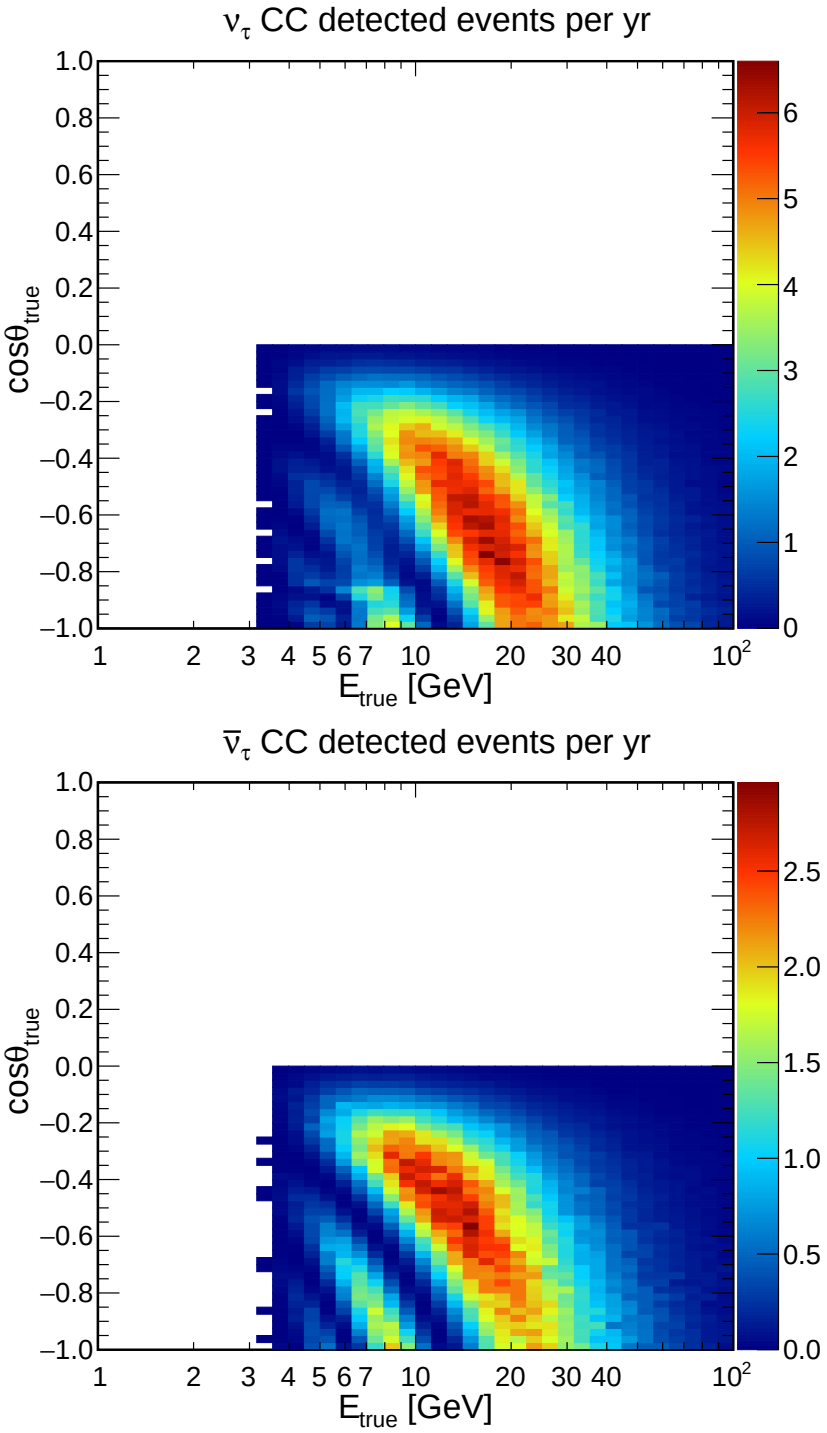

Figure 3.22: Rates of ν_τ (top) and $\bar{\nu}_\tau$ (bottom) CC detected events in ORCA as a function of true neutrino energy and zenith angle for 20 m spacing. See also the caption of Fig. 3.11.

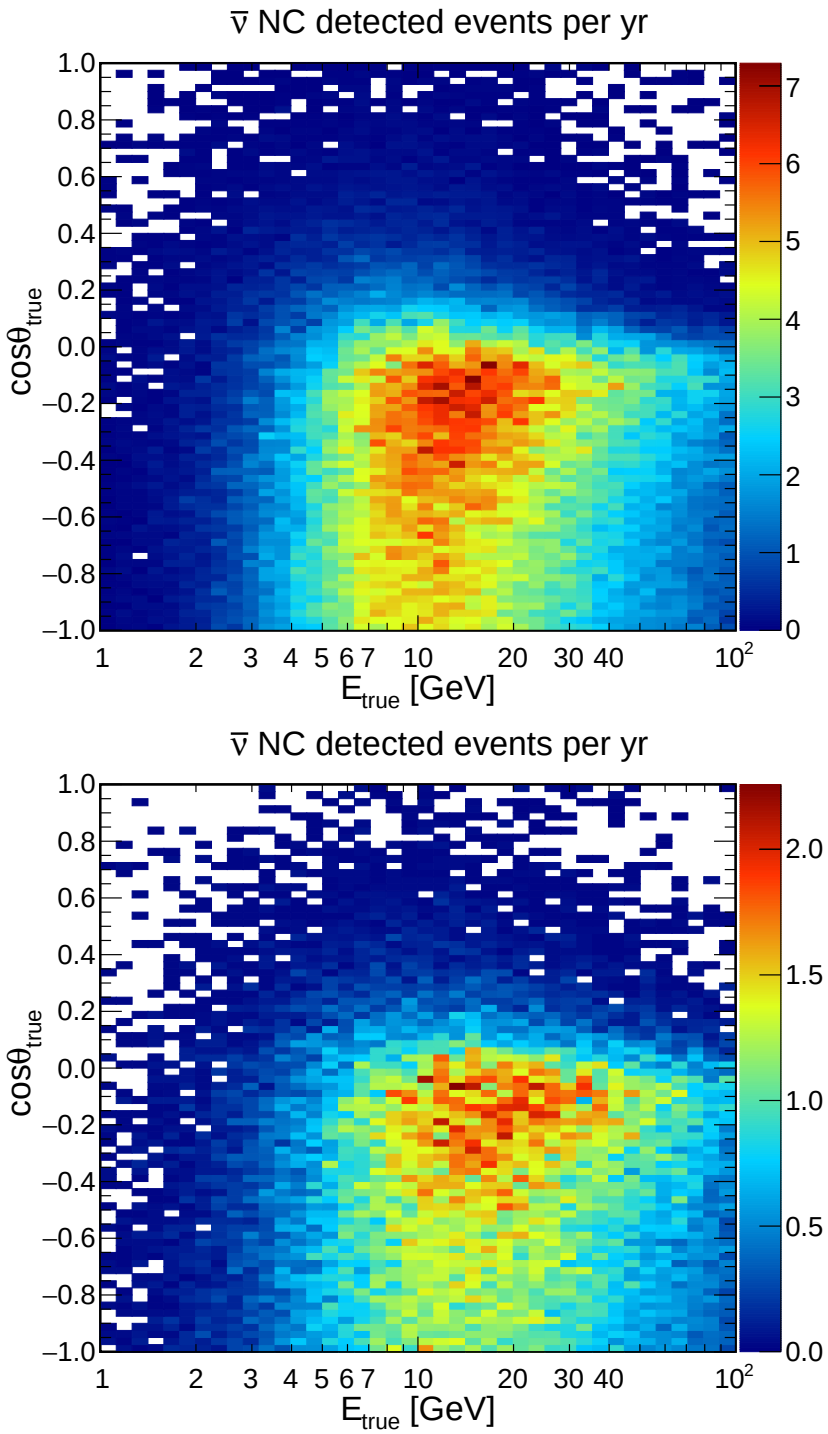

Figure 3.23: Rates of ν (top) and $\bar{\nu}$ (bottom) NC detected events in ORCA as a function of true neutrino energy and zenith angle for 20 m spacing. See also the caption of Fig. 3.11.

3.4.2 Reconstruction

The next ingredient in the simulation chain for predicting the observed event distributions is to model the performance of the reconstruction algorithms. So far, the tables are presented as a function of true neutrino energy and zenith angle. This stage comprises mapping from true to reconstructed variables, the ones actually observed in

the detector. The KM3NeT track and shower reconstruction algorithms [170, 155] which are used for the ORCA analyses, are discussed briefly in this section.

The energy and direction of the incoming neutrino as well as the event topology can be reconstructed from the arrival time of the Cherenkov photons at the PMTs and the position of the PMTs. The distribution of reconstructed energy and zenith angles for a given true energy and zenith angle for MC events gives the resolution of the experiment at that given true values.

Direction estimation

Similar to track reconstruction in ANTARES (Sec. 3.2.1), the first step is the hit selection based on local coincidence of causally connected hits and hits which are closer than 50 m to at least 40% of all the hits. This is followed by a "prefit": a linear fit through the positions of the hits called prefit. The prefit procedure is repeated for different directions in steps of 5° over the whole sky. This is followed by the likelihood maximisation based M-estimator fit, that depends on the time residuals, i.e. the difference between the exact time of the hits and the expected times according to the track hypothesis. After this, a probability density function (PDF) is created based on the light emission profiles of muons obtained from simulations [170]. The PDF, P, is a function of the minimum distance of the muon to the PMT i, ρ_i, the orientation of the PMT, ϕ_i, and θ_i and the time residual of the hit, t_{res}. P is used to calculate the likelihood:

$$\mathcal{L} = \prod_{hits} \left[\frac{\delta P(\rho_i, \phi_i, \theta_i, t_{res})}{\delta t} \right]. \tag{3.21}$$

Maximising $\mathcal{L}$ gives the reconstructed vertex and the direction of the muon trajectory. The distribution of reconstructed zenith angles for ν_e CC and ν_μ CC events in the detector are shown in Fig. 3.24 and Fig. 3.25. Events with reconstructed vertices within the detector volume are considered.

The shower reconstruction [176, 177, 178] is performed in two steps. In the first step the vertex is reconstructed based on the recorded time of the PMT signals and in the second step the direction, energy and inelasticity are reconstructed based on the number of hits and their distribution in the detector. In both steps a maximum likelihood fit is performed for many different starting shower hypotheses and the solution with the best likelihood is chosen. The neutrino direction resolution is dominated by the intrinsic lepton scattering kinematics [179]. See [179, 120] for further details on shower reconstruction.

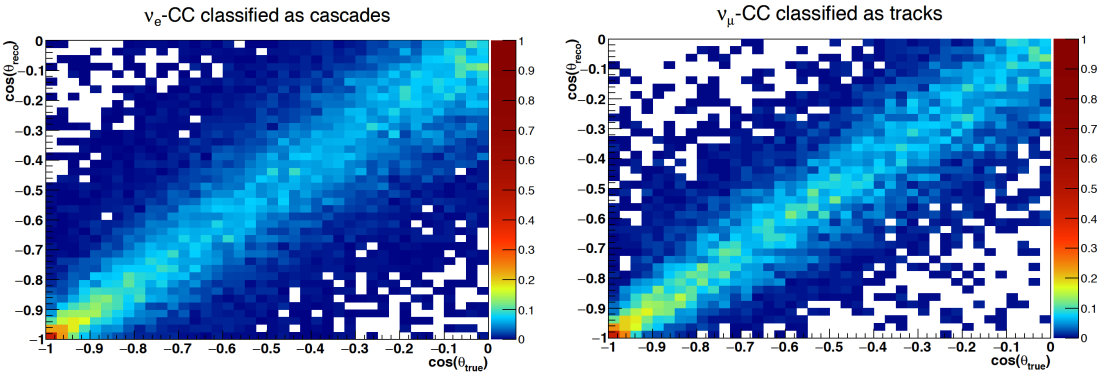

Figure 3.24: Cosine of the true zenith vs cosine of the reconstructed zenith angle for up-going ν_e CC classified as shower-like events (left) and ν_μ CC classified as track-like events (right). From [180].

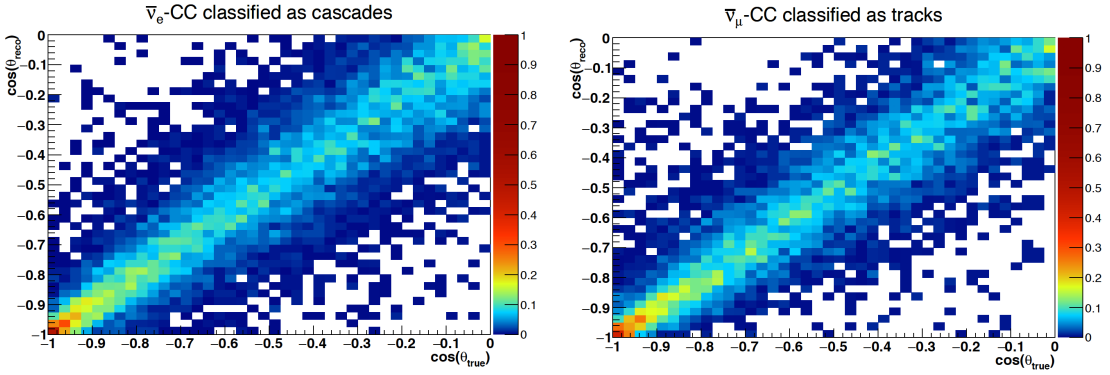

Figure 3.25: Cosine of the true zenith vs cosine of the reconstructed zenith angle for up-going $\overline{\nu}_e$ CC classified as shower-like events (left) and $\overline{\nu}_\mu$ CC classified as track-like events (right) . From [180].

The spread of the distribution for a specific θ_{true} gives a measure of the angular resolution of the detector. The median relative error, $(med|\theta_{true} - \theta_{reco}|)$, on the measured direction is defined as the resolution. The median resolution on the neutrino direction for $\nu_e/\overline{\nu}_e/\nu_\mu/\overline{\nu}_\mu$ CC events is $9.3°/7.0°/8.3°/6.5°$ at $E_\nu = 10$ GeV.

Energy estimation

The neutrino energy estimation for muons is performed in two steps: first the muon energy is estimated by reconstructing the muon track length and the interaction vertex. The neutrino energy is estimated depending on the reconstructed muon length and the number of hits used by the track reconstruction algorithm. The number of hits N_{hits} is defined by integrating the PDF, P, over a time window Δt. The length of the muon track is obtained by calculating the distance between the first and last DOM along the track. The relation between number of hits and the energy of the interacting neutrino, for a certain interval of reconstructed muon track length, is obtained by fitting the median distribution of E_ν as a function of N_{hits}. A short track with large number of hits is an indication of an energetic hadronic shower and the neutrino energy is scaled up accordingly. In case of showers, the light yield is in first order proportional to the shower energy [120, 179].

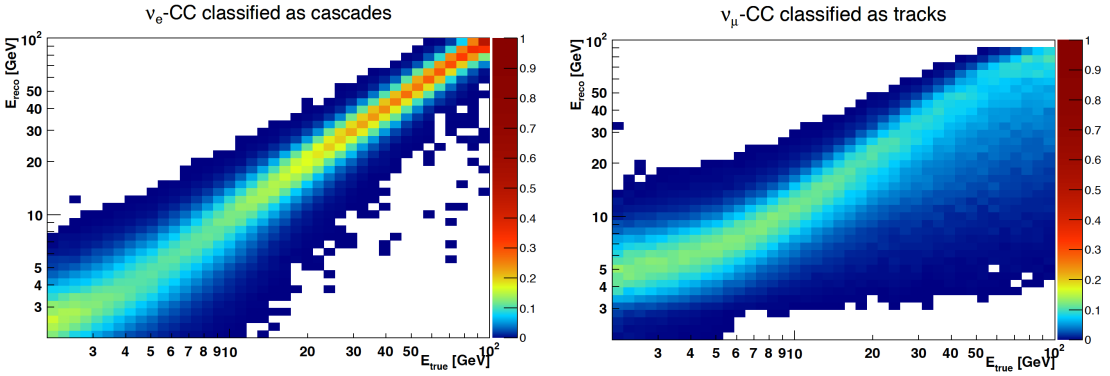

Figure 3.26: True neutrino energy vs reconstructed neutrino energy for up-going ν_e CC classified as shower-like events (left) and ν_μ CC classified as track-like events (right). From [180].

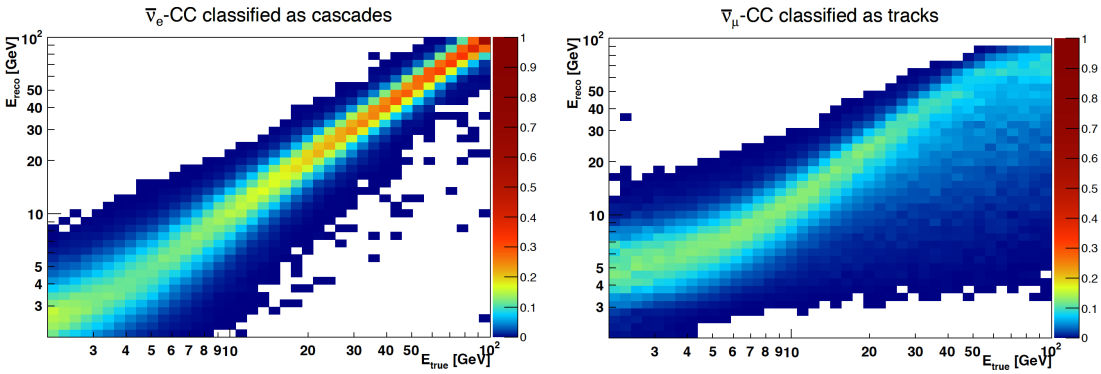

Figure 3.27: True neutrino energy vs reconstructed neutrino energy for up-going $\bar{\nu}_e$ CC classified as shower-like events (left) and $\bar{\nu}_\mu$ CC classified as track-like events (right). From [180].

The median energy resolution for ν_e CC events is 25% at E_ν = 10 GeV, while for ν_μ CC events, it is $\sim$ 30% since the outgoing muon tends to leave the detector depositing only a fraction of its total energy (Fig. 3.28).

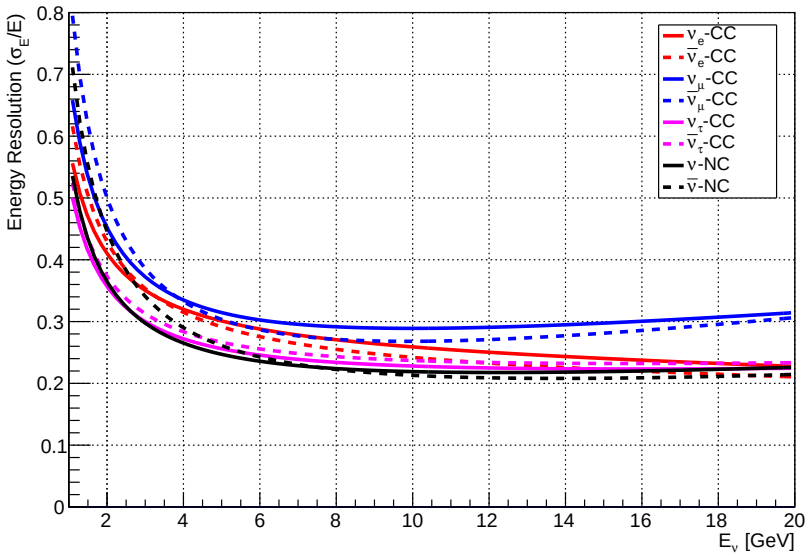

Figure 3.28: Energy resolution of ORCA as a function of neutrino energy E for different neutrino interaction channels $\mathcal{X}$ separated by flavour.

The reconstruction performance is encoded within response functions $\mathcal{R}^{\mathcal{X}}(E_{true}, \theta_{true}, E_{reco}, \theta_{reco})$, which is used to calculate the number of detected events in the reconstructed phase space variables:

$$\widetilde{N}^{\mathcal{X}}_{E_{reco},\theta_{reco}} = \mathcal{R}^{\mathcal{X}}(E_{true}, \theta_{true}, E_{reco}, \theta_{reco}) \times N^{\mathcal{X}}_{E_{true},\theta_{true}}, \tag{3.22}$$

where, $\mathcal{R}^{\mathcal{X}}(E_{true}, \theta_{true}, E_{reco}, \theta_{reco})$ represents the conditional probability for an event occurring in true $(E_{true}, \theta_{true})$ bin to be detected, successfully reconstructed and selected in the bin of observed characteristics $(E_{reco}, \theta_{reco})$. This is implemented within the KM3NeT custom oscillation framework SWIM [181, 182].

The modelling of the detector response is based on full MC simulations rather than parameterised detector response functions. Each entry in multi-dimensional response matrices $\mathcal{R}^{\mathcal{X}}(E_{true}, \theta_{true}, E_{reco}, \theta_{reco})$ for different $\mathcal{X}$ is represented by a single dimensionless coefficient (or weight), that gives the efficiency of detection, reconstruction and selection for a true bin $(E_{true}, \theta_{true}$ and is computed as:

$$\mathcal{R}^{\mathcal{X}}(E_{true}, \theta_{true}, E_{reco}, \theta_{reco}|\mathcal{X}) = \frac{N_{sel}^{MC}(E_{true}, \theta_{true}, E_{reco}, \theta_{reco})}{N_{gen}^{MC}(E_{true}, \theta_{true})}, \tag{3.23}$$

where $N_{sel}^{MC}(E_{true}, \theta_{true}, E_{reco}, \theta_{reco})$ is the number of "selected" (triggered, reconstructed and classified) MC events in the reconstructed bin $(E_{reco}, \theta_{reco})$ for a given interaction channel $\mathcal{X}$, and $N_{gen}^{MC}(E_{true}, \theta_{true})$ is the number of "generated" MC events in the true $(E_{true}, \theta_{true})$. Building response matrices would require filling 5-dimensional[6] tables in $(E_{true}, \theta_{true}, E_{reco}, \theta_{reco})$ phase space for each interaction channel $\mathcal{X} \in \{(\nu_e, \overline{\nu}_e, \nu_\mu, \overline{\nu}_\mu, \nu_\tau, \overline{\nu}_\tau$ - CC) and $(\nu, \overline{\nu}$ - NC)$\}$. Building response matrices involves looping over selected and generated events and is computationally costly. However, once it is built, mapping of all the events from true to reconstructed variables spaces is very fast. The binning scheme adopted for this analysis is listed in Tab. 3.1.

	$\log(E_{true})$	$\cos\theta_{true}$	$\log(E_{reco})$	$\cos\theta_{reco}$
Bins	40	40	20	20
Units	[1, 100]	[-1, 0]	[3, 100]	[-1, 0]

Table 3.1: Binning scheme adopted for this analysis.

A coarse 20×20 binning in reconstructed space is chosen in order to complement the detector resolutions, while ensuring enough statistics in each bin. Equidistant logarithmic bins are used in harmony with power-law spectra of atmospheric neutrino fluxes, to ensure enough statistics in high energy bins. Constant binning in $\cos\theta$ is also a choice to equally populate bins due to the (first order) isotropic nature of atmospheric fluxes.

3.4.3 Event classification

As discussed earlier, depending on the Cherenkov signatures of the outgoing lepton from the ν_e and ν_μ CC and NC interactions, two distinct event topologies are observed at the detector: track-like and shower-like events. ν_μ CC and those ν_τ CC interactions with muonic τ decays mostly account for track-like topology, since the outgoing muon appears as a track within the detector. The shower-like topology has events from ν_e CC, ν_τ CC interactions with non-muonic τ decays and NC interactions of all flavours. Showers appear as blob-like light sources within the detector.

The reconstruction information is fed to a Particle IDentification (PID) chain, which is based on a multivariate analysis (MVA) technique. MVA techniques can be divided into:

- **classification**: qualitative output predicting a category or class;
- **regression**: quantitative output predicting the value of a variable.

[6] Additional dimension to store a discrete integer flag indexing the type of interaction.

The Random Decision Forest (RDF) [183] classifier, which is a machine learning (ML)[7] algorithm, is used in our case. This is built within the collaboration [184]. RDF consists of an ensemble of consecutive binary decision trees. Each individual tree in the random forest of reconstructed heuristics outputs a class prediction and the class with the majority of votes becomes our prediction. The output score reflects the fraction of trees that voted for a predicted class. In this way, a tunable output parameter f is obtained, which can be used to cut on in the analysis. ν_μ CC events have been used to represent the track-like event topologies, while ν_e CC and NC events have been used to represent the shower-like event topologies while training the classifier.

The output ntuples[8] contain 3 different types of classifiers (f), two to filter out background and one for physics:

- `atmospheric_muon_score`: atmospheric muon vs neutrino decision to reject atmospheric muons;
- `pure_noise_score`: pure noise vs neutrino event decision to reject events that appear very noise-like in the detector;
- `track_score`: to distinguish between track-like and shower-like events.

The event type classifier for neutrinos, f, can be defined as:

$$\widetilde{N}^{\mathcal{X},C}_{E_{reco},\theta_{reco}} = f^{\mathcal{X}}_{C}(E_{true}) \times \widetilde{N}^{\mathcal{X}}_{E_{reco},\theta_{reco}}, \tag{3.24}$$

where, $\widetilde{N}^{\mathcal{X}}_{E_{reco},\theta_{reco}}$ is the number of detected events of interaction type $\mathcal{X}$, C indicates the PID class (track or shower), $\widetilde{N}^{\mathcal{X},C}_{E_{reco},\theta_{reco}}$ is the number of detected events of interaction type $\mathcal{X}$ and classified as C, $f^{\mathcal{X}}_{C}$ is the energy-dependent event classification probability for interaction types $\mathcal{X}$ satisfying the condition:

$$\sum_{C} f^{\mathcal{X}}_{C} = f^{\mathcal{X}}_{tracks} + f^{\mathcal{X}}_{shower} = 1. \tag{3.25}$$

The classifier performance of the event type classifier for neutrinos ($f^{\mathcal{X}}_{tracks}, f^{\mathcal{X}}_{shower}$) is shown in Fig. 3.29 and Fig. 3.30.

[7] Machine learning (ML) refer to computer algorithms that involve automatic improvement of predictions through experience/learning. It can be *supervised learning* or *unsupervised learning* based on the training with a sample in which the real output is known or unknown respectively.

[8] An ntuple is a tabular representation of events where each event consists of a fixed length row of data. It uses the same basic format as ROOT [185] trees.

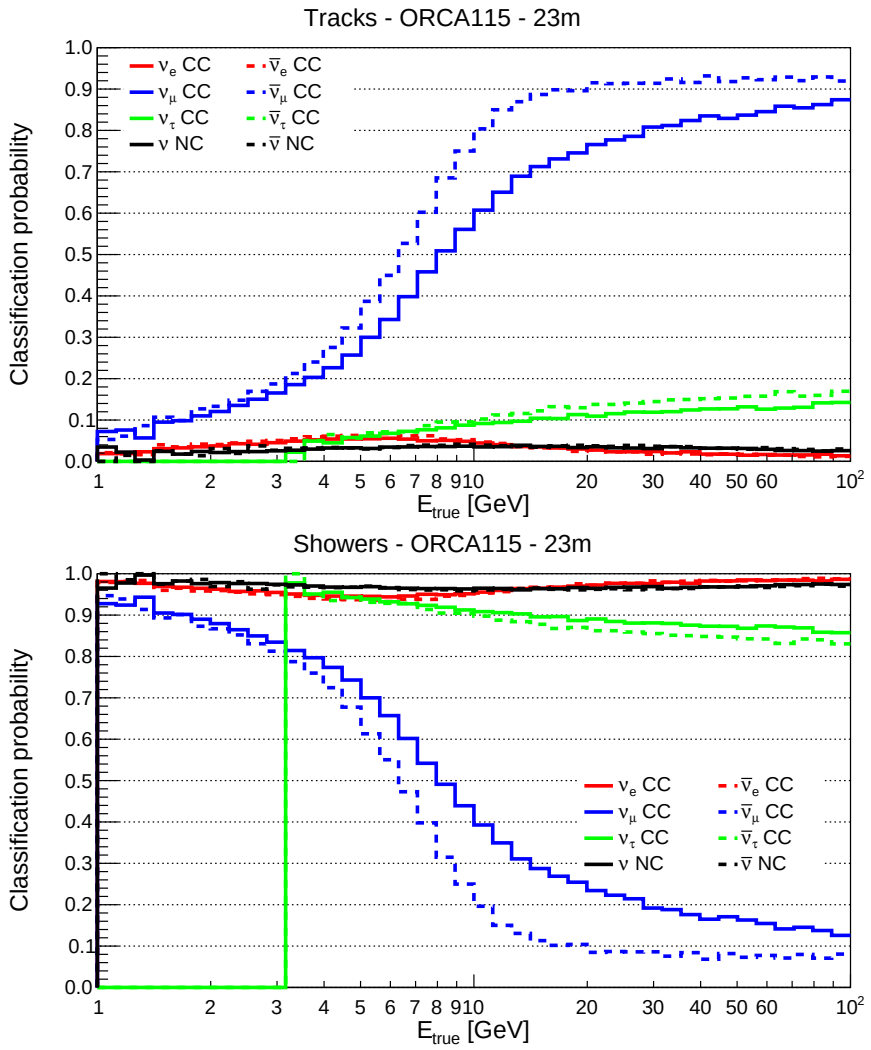

Figure 3.29: The RDF-based event selection probability for detected events to be classified as a track $f^{\mathcal{X}}_{tracks}$ (top) or shower $f^{\mathcal{X}}_{shower}$ (bottom) for each of the different interaction types $\mathcal{X}$ at ORCA for 23 m horizontal spacing between DUs.

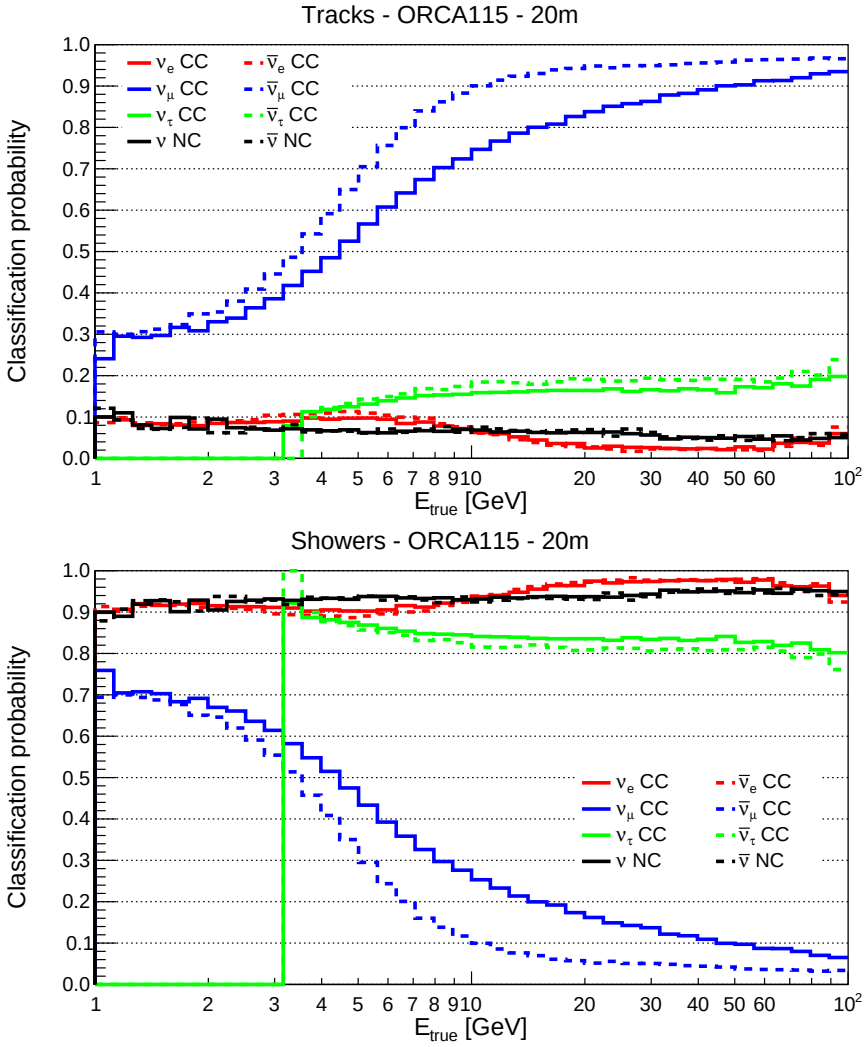

Figure 3.30: The RDF-based event selection probability for detected events to be classified as a track $f^{\mathcal{X}}_{tracks}$ (top) or shower $f^{\mathcal{X}}_{shower}$ (bottom) for each of the different interaction types $\mathcal{X}$ at ORCA for 20 m horizontal spacing between DUs.

For E_ν ~20 GeV the classifier reaches a plateau with 90% of $\overline{\nu}_\mu$ CC and 80% ν_μ CC events correctly classified and 5% of ν_e CC and 5% of ν-NC mis-classified events as tracks for 23 m horizontal spacing detector geometry. In the case of a 20 m spacing, the classifier reaches a plateau with 95% of $\overline{\nu}_\mu$ CC and 85% ν_μ CC events correctly classified and 5% of ν_e CC and 8% of ν-NC mis-classified events as tracks.

An improvement of the classifier for 20 m results from a denser instrumentation and additional hit-features (based on the likelihood ratios of the time and position of the hits expected from ν_e and ν_μ CC events with respect to the reconstructed position and direction from the shower reconstruction algorithm) that has been fed to train the classifier. The difference in the classification performance for $\overline{\nu}_\mu$ CC and ν_μ CC is due to the differences in the inelasticity of the Bjorken-y distributions (Eq. 2.9). The fraction of ν_τ CC events classified as tracks is relatively higher due to the 17% branching ratio of muonic τ decays.

3.4.4 Event spectra

The eight distributions indexed by interaction type $\mathcal{X} \in \{(\nu_e, \overline{\nu}_e, \nu_\mu, \overline{\nu}_\mu, \nu_\tau, \overline{\nu}_\tau$ - CC) and (ν, $\overline{\nu}$ - NC)} are merged and split into two distributions corresponding to the two event topologies: tracks and showers. The final event spectra observed at the detector are shown in Fig. 3.31. Now the oscillation pattern is not well visible. The event spectra are segregated by cutting on in the `track_score`[9] at 0.6. The contamination from mis-reconstructed atmospheric muons is estimated from MC simulated atmospheric muons with a livetime of $\sim$ 14 days. However the absolute number of events that passes the selection cuts is very small and accounts for 2% of the total sample. A total number of $\sim$ 63,000 (55,000) up-going neutrino events per year (corresponding to a rate of $\sim$ 2 mHz) is expected at ORCA for 23 m (20 m) horizontal spacing detector geometry.

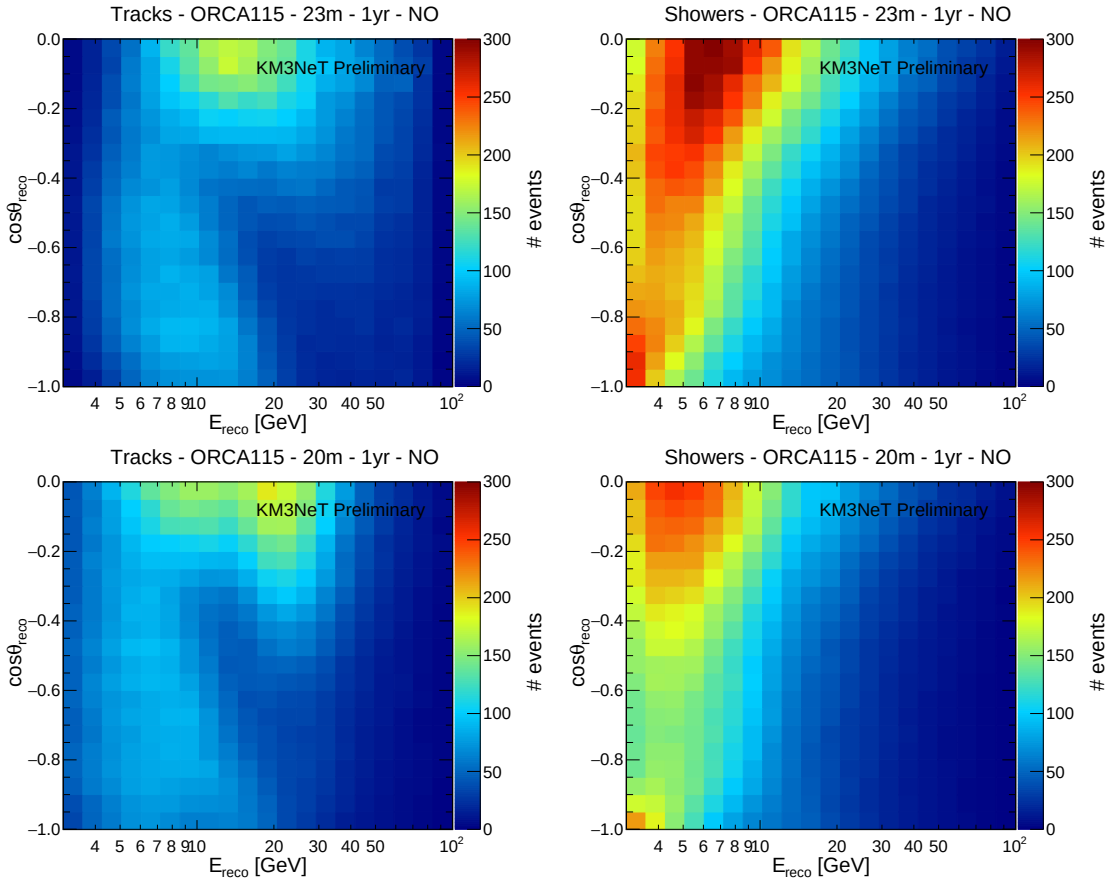

Figure 3.31: The expected event rates for up-going neutrinos at ORCA per year for 23 m (top panels) and 20 m (bottom panels) horizontal spacing as a function of the reconstructed energy and zenith angle for track-like (left) and shower-like (right) event topologies. Normal Ordering is assumed.

[9] A value of `track_score` = 1 corresponds to perfect track, while 0 corresponds to perfect shower.

4 Search for NSIs with ANTARES and ORCA

"Neutrinos, they are very small.
They have no charge and no mass
And do not interact at all.
\# \# \# \# \# \# \# \# \# \# \# \# \# \# \# \# \# \# \# \#
At night, they enter at Nepal
And pierce the lover and his lass
From underneath the bed; you call
It wonderful; I call it crass."

— JOHN UPDIKE

Contents

As explained in Chapter 1, the presence of Non-Standard Interactions (NSIs) of neutrinos with matter can produce a significant departure of the event spectra from the predictions with standard three-flavour neutrino oscillations. In this chapter, we search for such departures using the data provided by the ANTARES detector and estimate how sensitive the ORCA detector will be to such effects using simulated events.

In the case of ANTARES, a measurement of the parameters that describe the NSI can be obtained and in the absence of a statistical significant deviation from the standard oscillation pattern, limits on these parameters can be established. For ORCA, we can provide sensitivities to these parameters, i.e. estimates of the values for which the detector would be able to observe a deviation at a given confidence level.

Since NSIs would show up as sub-dominant effects above the main contribution of the atmospheric neutrino oscillations, it is natural that the selection of events for the

standard oscillation analysis is used also for the NSI search. Indeed, a common event selection allows us to reproduce the results of the standard oscillation analysis and cross-check and compare to our results for NSIs. Therefore, the event selection criteria and the data–taking period used in this PhD thesis follows that of the latest analysis of atmospheric neutrino oscillations with ANTARES, published in [60] and explained in greater detail in [186]. We have first reproduced the analysis explained in these references and then used it as a starting point to perform the NSI analysis as presented in Sec. 4.2.

Likewise, for ORCA, final event templates are simulated for a predicted exposure of 3 years of runtime comprising 115 DUs with 23 m and 20 m horizontal spacing between DUs. The expected event numbers are weighted according to various possible NSI signal hypotheses (in the light of agreement of pseudo-data with standard three-flavour oscillations) in order to quantify how large such sub-dominant effects coming from NSIs can still be viable at ORCA. The method used to compute the sensitivity of ORCA to NSIs is reported in Sec. 4.3.

In both cases, the analysis methodology follows an Asimov dataset approach [187] to quantify the median significance of the experiments towards the NSI signal hypothesis. Finally, after performing a binned likelihood maximisation, the limits in the NSI $\mu - \tau$ sector with ANTARES have been constructed (Sec. 4.2) and discovery potential of ORCA towards various NSI model parameters has been reported (Sec. 4.3).

4.1 Non-Standard Interactions

The study presented in this section employs a three-flavour neutrino scheme in presence of NSIs (see Sec. 1.3.1 for details) to calculate bounds on NSIs in the $\mu - \tau$ sector. In experiments like ANTARES, where the atmospheric neutrino flux is dominated by ν_μ events in the GeV energy range, NSIs in the $\mu - \tau$ sector can be discerned by probing the deficit of ν_μ events, since these events primarily transform into ν_τ governed by a large mixing angle θ_{23} and by the NSI coupling parameter $\epsilon_{\mu\tau}$ [188].

The effective Hamiltonian governing the propagation of neutrino flavour states in matter in the presence of NSIs in the $\mu - \tau$ sector reads [76]

$$H_{ij} = \frac{1}{2E_\nu} U_{ik} \begin{bmatrix} 0 & 0 & 0 \\ 0 & \Delta m^2_{21} & 0 \\ 0 & 0 & \Delta m^2_{31} \end{bmatrix} U^\dagger_{kj} + V_{CC} \frac{n_d(x)}{n_e(x)} \begin{bmatrix} \delta_{de} & 0 & 0 \\ 0 & 0 & \epsilon_{\mu\tau} \\ 0 & \epsilon^*_{\mu\tau} & \epsilon_{\tau\tau} - \epsilon_{\mu\mu} \end{bmatrix}, \tag{4.1}$$

where E_ν is the neutrino energy and U_{ik} is the PMNS matrix [81]. $n_d(x)$ and $n_e(x)$ are the d-quark and electron number densities along the neutrino path, respectively, and the $\epsilon_{\alpha\beta}$ with $\alpha \in \{\mu, \tau\}$ represent the strength of NSI coupling in the $\mu - \tau$ sector. All NSIa that couple to ν_e ($\epsilon_{e\alpha}$) are set to zero to switch off the electron neutrino NSIs. The remaining non-zero parameters ($\epsilon_{\mu\mu}, \epsilon_{\mu\tau}$ and $\epsilon_{\tau\tau}$) introduce matter-dependent distortions to standard $\nu_\mu \leftrightarrow \nu_\tau$ oscillations and can be exploited to set limits on the NSI parameters in the $\mu - \tau$ sector.

Under the one mass scale dominance (OMSD) approximation, the *asymmetry* in the muon disappearance channel to first order in $\epsilon_{\mu\mu}, \epsilon_{\mu\tau}$ and $\epsilon_{\tau\tau}$ is defined as [189, 190, 191]

$$\begin{aligned}\Delta P_{\mu\mu} &\equiv P^{\text{NSI}}_{\mu\mu} - P^{\text{Std.}}_{\mu\mu} \\ &\simeq -|\epsilon_{\mu\tau}| A[\sin^3(2\theta_{23})\Delta\sin(\Delta) + 4\sin(2\theta_{23})cos^2(2\theta_{23})\sin^2(\frac{\Delta}{2})] \\ &+ |\epsilon_{\mu\mu} - \epsilon_{\tau\tau}| A \sin^2(2\theta_{23})cos(2\theta_{23})[\frac{\Delta}{2}\sin(\Delta) - 2\sin^2(\frac{\Delta}{2})],\end{aligned} \tag{4.2}$$

where $\Delta \equiv \Delta m^2_{31} L/2E_\nu$, $A \equiv \sqrt{2} G_F N_e L/\Delta$.

A convenient approximation for the series expansion of otherwise complicated three-flavour oscillation probabilities is the *two-flavour hybrid model* including matter NSIs with two parameters $\epsilon_{\mu\tau} \equiv \epsilon$ and $\epsilon' \equiv \epsilon_{\tau\tau} - \epsilon_{\mu\mu}$. In such a model, NSI effects in the $\nu_\mu - \nu_\tau$ coexist with the standard two-flavour (θ_{12}, θ_{13} and $\Delta m^2_{21} = 0$) $\nu_\mu \leftrightarrow \nu_\tau$ oscillations.

The signatures of *asymmetry* in the muon disappearance channel, predicted in presence of $\nu_\mu \to \nu_\tau$ NSI, parameterised by $\epsilon_{\mu\tau} = 0.033$ and $\epsilon_{\tau\tau} = 0.147$ for up-going neutrinos[1], is shown in Fig. 1. The asymmetry is maximal for a wide region of core-crossing neutrinos with energies of ~ 25 GeV.

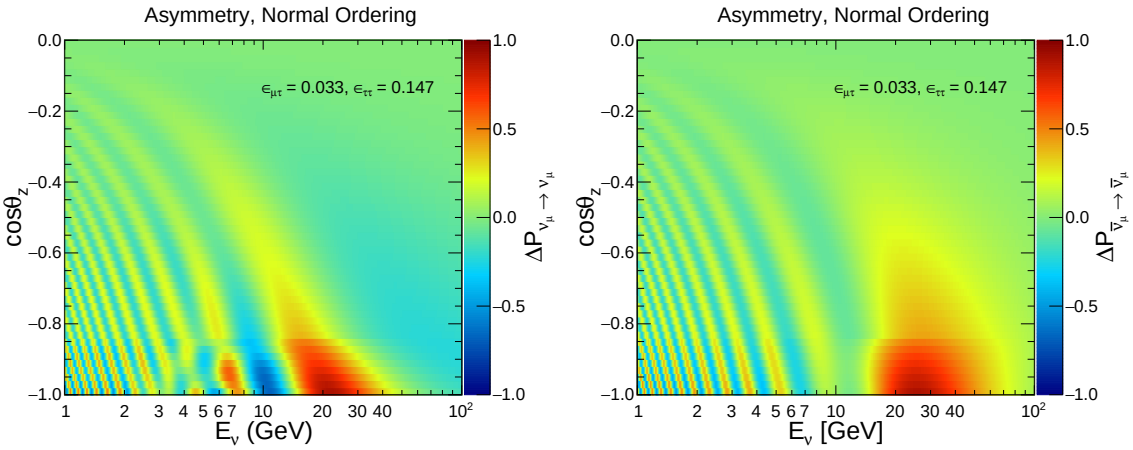

Figure 4.1: Asymmetry in ν_μ (left) and $\bar{\nu}_\mu$ (right) survival probabilities as a function of the neutrino energy and cosine of the zenith angle. The NSI hypothesis has been parameterised as $\epsilon_{\mu\tau} = 0.033$ and $\epsilon_{\tau\tau} = 0.147$. NO is assumed.

Similarly, a model in which the NSI effects in the $\nu_e - \nu_\tau$ coexist with the standard two-flavour (θ_{12}, θ_{13}, and $\Delta m^2_{21} = 0$) $\nu_\mu \leftrightarrow \nu_\tau$ neutrino oscillations is labelled as the *three-flavour hybrid model*. All NSIs that couple to ν_μ ($\epsilon_{\mu\alpha}$) are set to zero. All three flavours are present in this case. An overall $\nu_\mu \to \nu_e$ transition occurs via standard $\nu_\mu \to \nu_\tau$ oscillations driven by large θ_{23} working in concurrence with the $\epsilon_{e\tau}$ induced $\nu_\tau \to \nu_e$ conversion:

$$\nu_\mu \xrightarrow{\theta_{23}} \nu_\tau \xrightarrow{\epsilon_{e\tau}} \nu_e \tag{4.3}$$

[1]This choice of values of NSI parameters is motivated by the experimental bounds set by Super-K [192] at 90% C.L.

The effective Hamiltonian governing the propagation of neutrino flavour states in matter in the presence of NSIs in the $e-\tau$ sector reads [76]

$$H_{ij} = \frac{1}{2E_\nu} U_{ik} \begin{bmatrix} 0 & 0 & 0 \\ 0 & \Delta m^2_{21} & 0 \\ 0 & 0 & \Delta m^2_{31} \end{bmatrix} U^\dagger_{kj} + V_{CC} \frac{n_d(x)}{n_e(x)} \begin{bmatrix} \delta_{de} + \epsilon_{ee} & 0 & \epsilon_{e\tau} \\ 0 & 0 & 0 \\ \epsilon^*_{e\tau} & 0 & \epsilon_{\tau\tau} \end{bmatrix}. \tag{4.4}$$

The signatures of asymmetry in the muon disappearance channel, predicted in presence of $\nu_e \to \nu_\tau$ NSI, parameterised by $\epsilon_{e\tau} = 0.1$ and $\epsilon_{\tau\tau} = 0.147$ for up-going neutrinos, is shown in Fig. 4.2. Although, the electron NSIs do not appear in leading order terms in the expressions of muon survival probabilities, it can still be discerned as sub-leading effects in the muon disappearance channel.

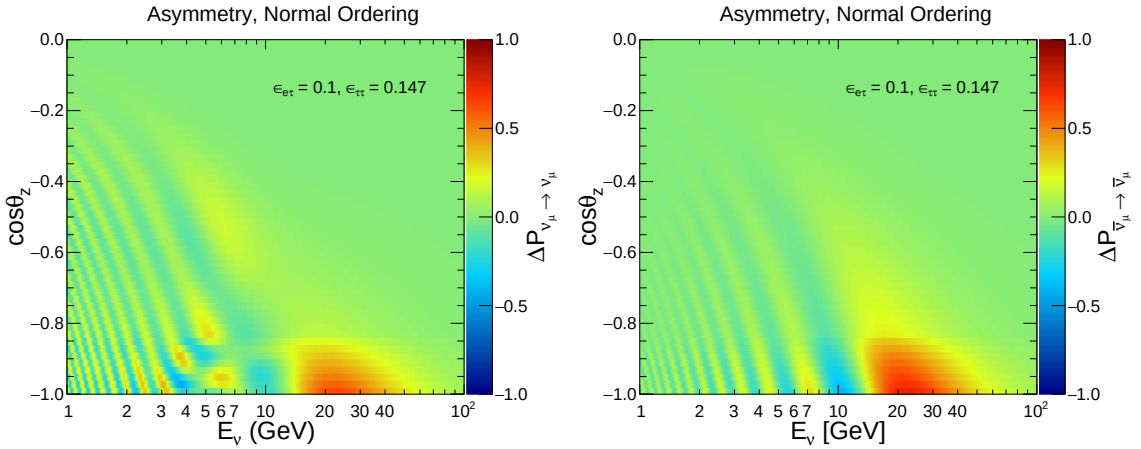

Figure 4.2: Asymmetry in ν_e (left) and $\bar{\nu}_e$ (right) survival probabilities as a function of neutrino energy and cosine of the zenith angle. The NSI hypothesis has been parameterised as $\epsilon_{e\tau} = 0.1$ and $\epsilon_{\tau\tau} = 0.147$. NO is assumed.

In our case, for the calculation of oscillation probabilities, the neutrino evolution equation in the full three-flavour neutrino scheme in presence of NSIs is solved numerically with the OscProb [52] package taking into account the PREM density profile [53].

4.2 Search for NSIs with ANTARES

When searching for NSIs, the first step is to select the event sample on which our analysis will be performed. This selection is optimised to select charged current interactions of muon neutrinos, which yield a muon crossing the detector and produces a *track-like* event. The muon disappearance channel is selected since it is sensitive to the NSI sector which we would try to constrain. The background will be dominated by poorly reconstructed atmospheric muons, ν_e CC interactions that produce electromagnetic showers and neutral-current (NC) interactions of all flavours that produce hadronic showers. In addition, oscillations of ν_μ to ν_τ will produce ν_τ CC events with or without muons in the final state that can be a potential source of background for this study.

In this section, the event selection procedure followed to obtain the oscillation parameters, including the possible existence of a sterile neutrino, is described [60]. We first show the results when the method is applied to simulated data, and summarise the results obtained when applied to the oscillation analysis.

4.2.1 Event selection

A total livetime of 2830 days corresponding to a data acquisition from 2007 to 2016 (both years included) has been used. The event selection criteria employed here has been optimised by performing a MC-only sensitivity study [186] to select track-like events coming from ν_μ and $\overline{\nu}_\mu$ CC interactions.

Method $\mathcal{A}$ criteria

- **Direction cut**: Events reconstructed with $\cos\theta_z > 0.15$ ($\cos\theta_z = 0$ correspond to horizontal-going events) are discarded in order to avoid misreconstructed atmospheric muons closer than 9° from the horizon. For events passing the selection criteria of both methods (Sec. 3.2), an additional constraint is imposed, which requires the difference between reconstructed zenith angle values to lie within an uniform circle of radius 0.15: $|\cos\theta_\mathcal{A} - \cos\theta_\mathcal{B}| < 0.15$ ($\theta_\mathcal{B}$ refer to the reconstructed zenith direction with method $\mathcal{B}$ (Sec. 3.2.1)). However, some of the down-going atmospheric muon background events are still reconstructed as up-going, which requires further quality cuts.
- **Quality cut**: The quality parameter $\lambda_\mathcal{A}$ (Fig. 3.3) tends to have larger values for atmospheric muons. A cut on $\lambda_\mathcal{A} = 0.8$ for SL events and $\lambda_\mathcal{A} = 1.3$ for ML events has been chosen to discard events with quality parameter larger than the cut value.
- **Multiplicity cut**: Algorithm $\mathcal{A}$ reconstructs SL and ML events if hits in at least 4 and 5 storeys are found, respectively. However, hits at a minimum number of 5 storeys is required for both SL and ML events to pass the selection criterion.
- **Containment cut**: A containment condition is applicable to ML events, such that events with interaction vertex reconstructed far away from the instrumented volume are discarded. A containment cut, which requires the reconstructed track vertex to lie within a cube of sides 340 m around the detector center, has been applied for ML events.

Method $\mathcal{B}$ criteria

- **Direction cut**: In order to curtail the contamination of down-going atmospheric muon background, only events reconstructed as up-going ($\cos\theta_z > 0.0$) are considered.
- **Quality cut**: A quality cut is decided by "goodness of the track fit", a quantity equivalent to χ^2 per number of degrees of freedom ($N_{d.o.f.}$). The quality parameter $\lambda_\mathcal{B}$ (Fig. 3.5) tends to have smaller values for atmospheric muons. A cut on $\lambda_\mathcal{B} > -5$ and $\beta_\mathcal{B} < 1$ has been chosen to discard events with quality parameter smaller and larger than the cut value, respectively.

Events reconstructed by method $\mathcal{A}$ and passing the selection criteria are kept. Events failing to surpass the selection cuts of method $\mathcal{A}$ are reconstructed by method $\mathcal{B}$. These events are also included in the final sample if the corresponding quality cuts of method $\mathcal{B}$ are achieved.

MC composition

The MC expectation from different channels, oscillations excluded, for the final sample, that pass the selection criteria of cuts are listed in Table 4.1. The muon neutrino

purity (relative abundance) is 94% and is always the largest over the entire phase space covered by the observables, as shown in Fig. 4.3. Additional sources of background, at sub-percent level, are made of events from both ν_e CC and NC interactions of all flavours at sub-percent level.

The atmospheric muon background has been obtained from the normalised (and smeared) PDF of simulated events passing the event selection criteria. These up-going mis-reconstructed MC muon PDF is then weighted according to the best-fit expectation value obtained from the fit of standard oscillations [60]. The muon background contamination is the largest and about 5%.

When applied to data, the event selection criteria leads to a total of 7710 events: 1950 from SL (method $\mathcal{A}$), 3682 from ML (method $\mathcal{A}$) and 2078 from method $\mathcal{B}$.

Component	**Events**	**%**
$\nu_\mu + \bar{\nu}_\mu$ CC	7591.2	94.4
$\nu_e + \bar{\nu}_e$ CC	15.8	0.2
NC	23.5	0.3
Atm. μ (normalised)	414.0	5.1
Total (MC no osc.)	8044.48	100

Table 4.1: Expected composition and number of data events of the final sample surpassing the selection criteria and corresponding to a livetime of 2830 days of ANTARES.

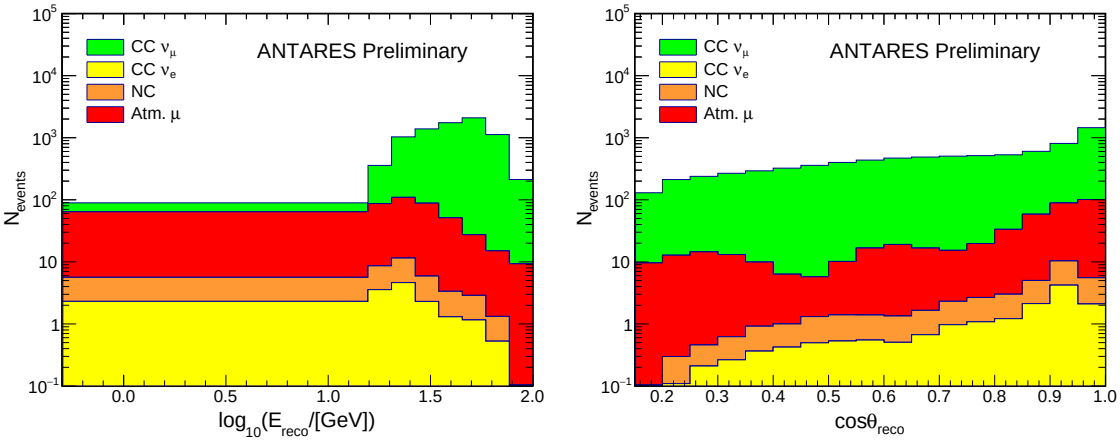

Figure 4.3: The unoscillated MC event distribution, binned in logarithm of reconstructed muon energy (left), and the reconstructed zenith angle (right), of the muon track. The colour code depicts the composition of MC after the final event selection.

The correlated true–reconstructed energy distributions are shown in Fig. 4.4. Although the true energies of the neutrino events span few TeV, the reconstructed muon energies of the fully and partially contained events extend till 100 GeV.

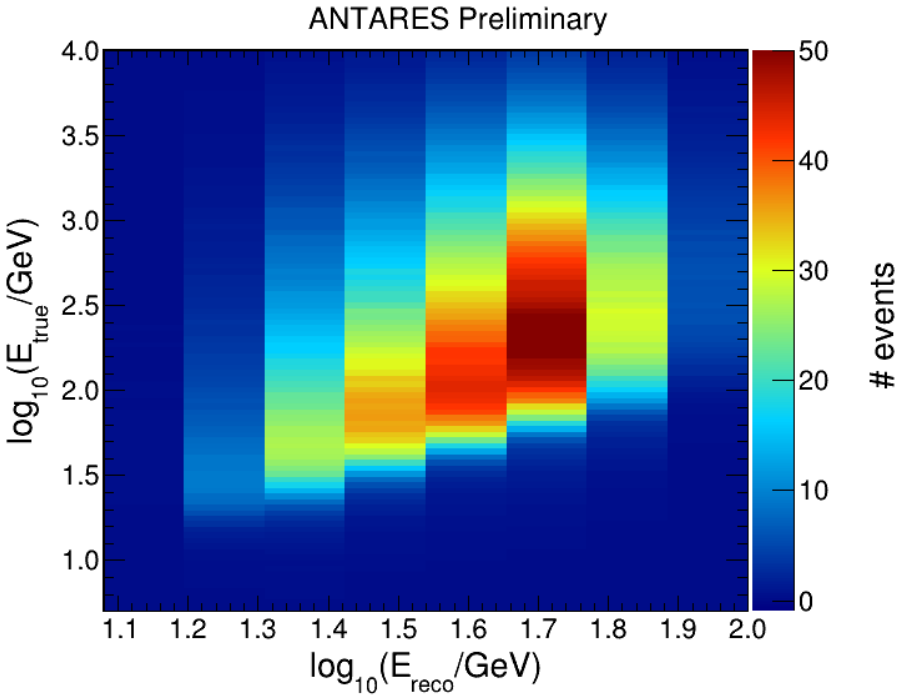

Figure 4.4: The unoscillated energy distribution of the final MC sample in the $E_{true} - E_{reco}$ phase space, summed over zenith bins with $\cos\theta_z \in [0.15, 1.0]$.

Results of standard oscillation analysis

The low-energy threshold of ANTARES ($\sim$ 20 GeV) sits above the energy range sensitive to neutrino mass ordering. However, it is still close to the first oscillation minimum in the muon disappearance channel, thereby making it sensitive to oscillations irrespective of the mass ordering. In 2019, ANTARES published the result [60] of fitting 7710 events, obtaining three-neutrino oscillation parameters to a precision comparable with that from dedicated neutrino oscillation experiments [193, 194, 195, 62]. The non-oscillation hypothesis was disfavoured at 4.6σ. Fig. 4.5 shows the 90% C.L. contours constructed in the $\sin^2\theta_{23} - \Delta m^2_{32}$ plane obtained from the analysis assuming a standard three-flavour neutrino oscillation hypothesis. The best-fit Δm^2_{32} is found at $2 \times 10^{-3}\text{eV}^2$ and θ_{23} compatible with maximal mixing. The data was found to have a mild preference for an energy shifted first oscillation minimum. This feature of data in fact motivates the consideration of fitting the non-standard oscillation hypotheses to search for new physics with the ANTARES data.

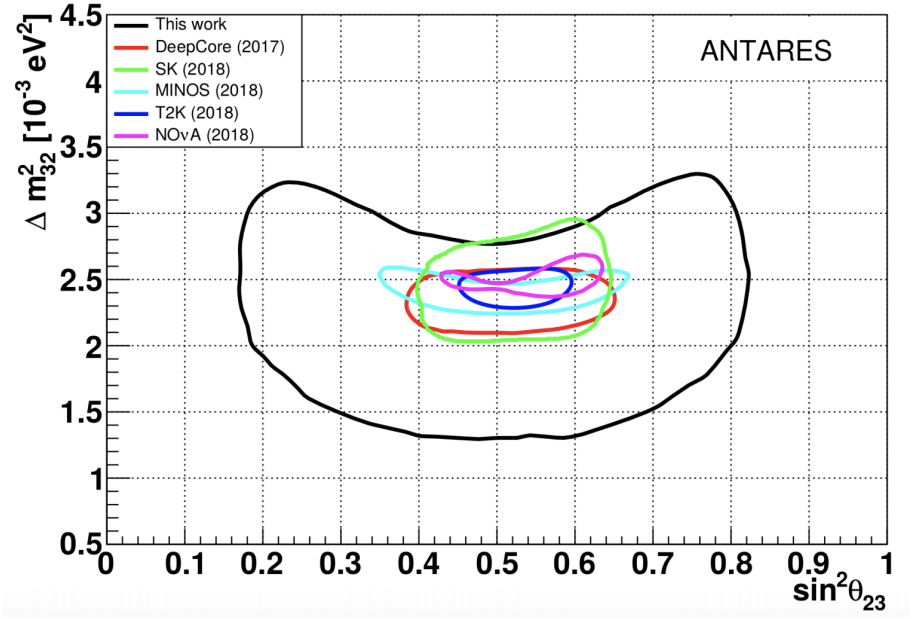

Figure 4.5: Constraints on $\sin^2\theta_{23} - \Delta m^2_{32}$ plane at 90% C.L. from the analysis of standard oscillation fit with ANTARES data. In the plot, the black line refers to the results published in [60]. From [60].

Comparison with sterile neutrino search

Under the assumption of 3+1 PMNS mixing matrix and to cross-check the validity of NSI search, the measurement of atmospheric neutrino oscillations in the presence of a sterile neutrino, has been carried out following the analysis in [60]. A non-zero best-fit value of θ_{34} has been found at 25.9°, while θ_{24} is found compatible with zero. Left panel of Fig. 4.6 shows the 99% C.L. allowed region in the sterile phase space of $|U_{\mu 4}|^2 (= \sin^2\theta_{24})$ and $|U_{\tau 4}|^2 (= \sin^2\theta_{34} \cdot \cos^2\theta_{24})$ obtained with the event selection described in this thesis. The 99% C.L. contour are in agreement with the allowed region reported in [60], as shown in the right panel of Fig. 4.6 with solid black curve.

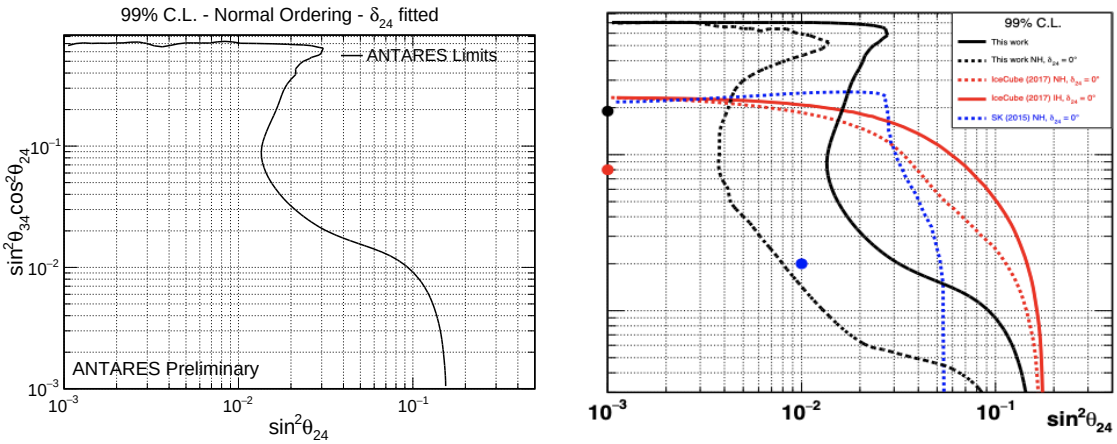

Figure 4.6: Left: Constraints on the 3+1 sterile neutrino model obtained based on the event selection perfromed in this thesis. Right: 99% C.L limits from the publication [60]. In the right plot, the black line refers to the results published in [60]. Both results are consistent.

4.2.2 Analysis

The analysis procedure to probe the presence of non-standard interactions consists on comparing the data with the MC template oscillated with some NSI model hypothesis. The parameters in the model are varied and the set of parameters that results most compatible with the data is obtained after a likelihood maximisation.

Statistical method

The method employed in this pursuit of search for NSI signals is the binned likelihood approach in presence of nuisance parameters [196].

In our analysis, the likelihood used in the fit is defined as

$$\mathcal{L}(\mu, n) = \prod_{i \in \{bins\}} \frac{\mu_i^{n_i} e^{-\mu_i}}{n_i!} \prod_{j \in \{syst\}} \frac{1}{\sqrt{2\pi\sigma_j^2}} e^{-\frac{(s_j - \hat{s}_j)^2}{2\sigma_j^2}}. \tag{4.5}$$

The Poisson term defines the probability for the expected number of entries μ_i from a certain simulation prediction for observable[2] in bin i to reproduce the observed number of events in that data bin n_i. The number of predicted events μ_i in the i^{th} bin is a function of the set of oscillation parameters, $\bar{o}$ (see Tab. 4.2), as well as on the set of parameters related to systematic uncertainties, $\bar{s}$. The nuisance parameters s_j enter within the Gaussian term labelled with the subscript j. The hypothesis is allowed to change based on the change in s_j, thereby penalizing their deviation about their mean value $\hat{s}_j$ in units of their uncertainty σ_j.

However since we are comparing hypotheses, the absolute value of the log-likelihood is irrelevant, what matters is the relative difference. The expression in Eq. 4.5 is simplified by taking a logarithm and dropping the constant terms:

$$\ln \mathcal{L}(\mu, n) = -\sum_i \mu_i(\bar{o}, \bar{s}) + \sum_i n_i \ln \mu_i(\bar{o}, \bar{s}) - \sum_j \frac{(s_j - \hat{s}_j)^2}{2\sigma_j^2}. \tag{4.6}$$

In the case of a Poissonian distribution, the number of events μ_i diverges from the Gaussian approximation because of the small number of entries. However, an alternative to the Gaussian-motivated Neyman's [197] or Pearson's [198] χ^2 has been proposed in [199], suggesting the use of the following logarithm of likelihood ratio (LLR):

$$-2LLR(\mu, n) = -2 \cdot \ln \prod_i \frac{\mathcal{L}(\mu_i, n_i)}{\mathcal{L}(n_i, n_i)} = -2 \cdot \ln \prod_i \frac{\mu_i^{n_i} e^{-\mu_i}}{n_i!} \cdot \frac{n_i!}{n_i^{n_i} e^{-n_i}} \tag{4.7}$$

$$= 2 \cdot \sum_i \left[\mu_i(\bar{o}, \bar{s}) - n_i + n_i \ln \left(\frac{n_i}{\mu_i(\bar{o}, \bar{s})} \right) \right] \tag{4.8}$$

Eq. 4.8 gives the same values of $(\bar{o}, \bar{s})$ at the minimum as Eq. 4.6, since only a constant term has been added to the log-likelihood function in Eq. 4.6 (if we avoid the Gaussian penalty term for now). It provides a goodness-of-fit information and motivates the choice of Eq. 4.8 as the test statistic according to the Wilks' theorem [200], since it asymptotically obeys a χ^2 distribution.

[2] E_ν and $\cos\theta_z$ in our case.

In the event of n_i being large enough to be approximated by a Gaussian with standard deviation $\sqrt{n_i}$, the LLR reads

$$-2LLR(\mu) = \sum_i \frac{(n_i - \mu_i(\bar{o},\bar{s}))^2}{n_i} + n_i(\ln 2\pi + 2ln\sigma_j) \tag{4.9}$$

$$= \chi^2(\mu) + const. \tag{4.10}$$

Eq. 4.10 defines the so-called Neymans's χ^2 variable; when n_i is replaced by μ_i, it is called Pearson's χ^2. Maximising LLR is equivalent to minimising χ^2 (off by a sign inversion).

However, the test statistic (TS), that we will consider assuming Poisson statistics including the Gaussian penalty terms for nuisance parameters, is

$$-2LLR(\mu) = 2 \cdot \sum_{i\in\{bins\}} \left[\mu_i(\bar{o},\bar{s}) - n_i + n_i \ln\left(\frac{n_i}{\mu_i(\bar{o},\bar{s})}\right)\right] + \sum_{j\in\{syst\}} \frac{(s_j - \hat{s}_j)^2}{\sigma_j^2}. \tag{4.11}$$

Binning scheme

The resulting MC and data events are split into 136 bins in reconstructed muon energy and cosine of the zenith angle. The reconstructed energy is split into 8 bins: the low energy part of the spectrum has a wide logarithmic bin between $10^{-0.3}$ and $10^{1.2}$ GeV, while the rest has 7 logarithmic bins between $10^{1.2}$ and 10^2 GeV. The reconstructed cosine of zenith angle, $\cos\theta_z$, is split into 17 bins between 0.15 and 1.0, the latter referring to vertically up-going events.

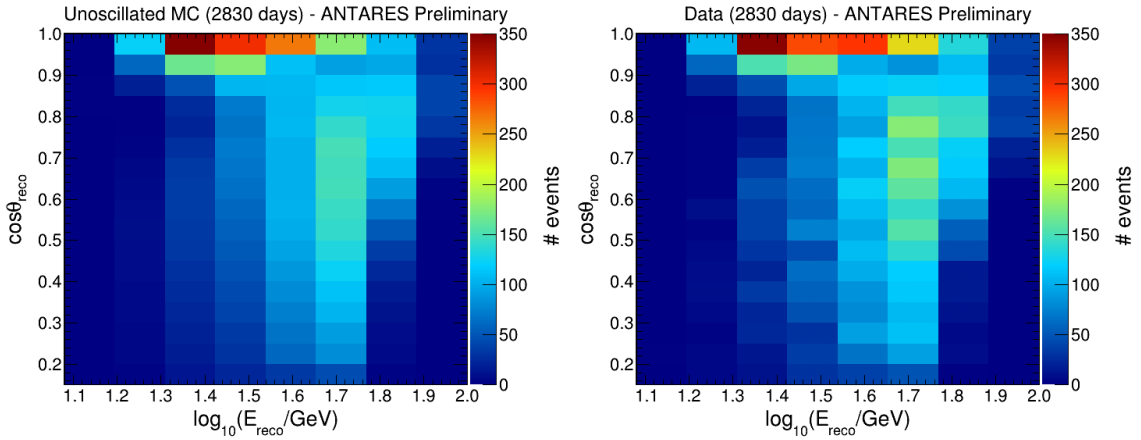

Figure 4.7: The un-oscillated MC event distribution (left) and selected data (right), binned in logarithm of reconstructed muon energy, $\log_{10}(E_{reco}/\text{GeV})$, and the reconstructed cosine of the zenith, $\cos\theta_{reco}$, of the muon track. ($\cos\theta_{reco} = 1$ corresponds to vertically up-going neutrinos.)

Statistical Significance

Fig. 4.8 shows the signed-$\sqrt{\chi^2}$ maps: the total number of events expected with and without NSI, for reconstructed events. The absolute value of $\sqrt{\chi^2}$ is stored, so that each bin content represents the contribution to the total $\sqrt{\chi^2}$ from each event class. The sign information is retained to represent the excesses and deficits. The total statistical $\sqrt{\chi^2}$ for each bin is computed from:

$$\sqrt{\chi^2_{E,\theta_z}(\epsilon_{\alpha\beta})} = \frac{N^{\text{test}}_{E,\theta_z}(\epsilon_{\alpha\beta}) - N^{\text{true}}_{E,\theta_z}(\epsilon_{\alpha\beta}=0)}{\sqrt{N^{\text{true}}_{E,\theta_z}(\epsilon_{\alpha\beta}=0)}}. \tag{4.12}$$

$N^{\text{true}}_{E,\theta_z}$ is the expected number of events in the corresponding $(\log_{10}(E_{reco}), \cos\theta_{reco})$ bin weighted under standard oscillation hypothesis with parameters adopted from NuFit 4.1 [90]; while, $N^{\text{test}}_{E,\theta_z}$ is the number of expected events in the same $(\log_{10}(E_{reco}), \cos\theta_{reco})$ bin but with non-zero test values of NSI parameters, as quoted on the plots.

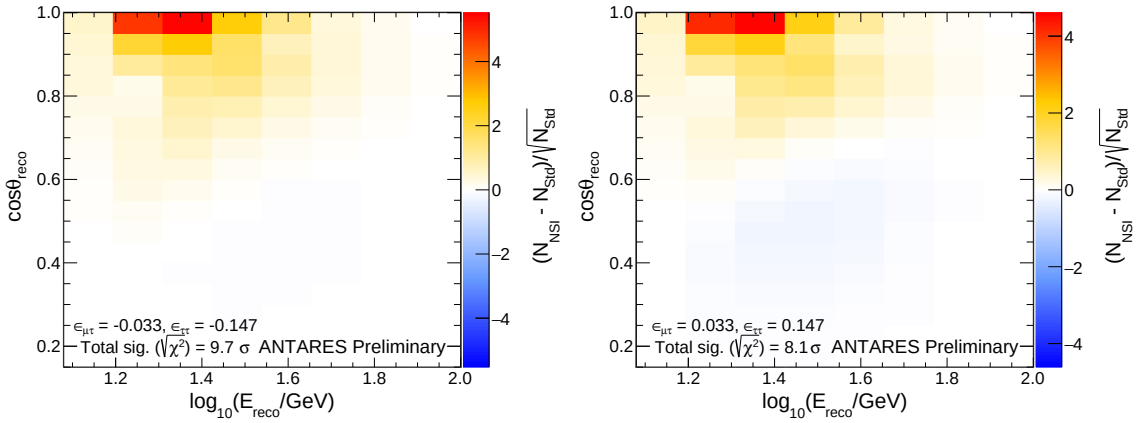

Figure 4.8: Expected pulls of predicted event numbers as a function of the reconstructed neutrino energy ($\log_{10}(E_{reco})$) and direction ($\cos\theta_{reco}$). Both panels correspond to different NSI hypothesis parameterised by $\epsilon_{\alpha\beta}$s as quoted on the plots. Normal Ordering is assumed. The color code indicates the values of signed-$\sqrt{\chi^2}$, as defined in Eq. 4.12. The total significance quoted is the sum of the absolute values of the $\sqrt{\chi^2}$ from each bin. Mind the difference in the colour scales.

Fig. 4.8 demonstrates that the effect of NSIs is manifested for up-going events since larger amount of matter is traversed. This is also the zenith region where MSW resonances manifest themselves such that interference with them is possible.

4.2.3 Systematics

Systematic uncertainties (s_i) included as nuisance parameters affecting the shape and normalisation of the expected event distribution are listed in Table 4.2. Their central values, $\hat{s}_j$, and priors, σ_{s_j}, are motivated in this section.

Nuisance parameters	Treatment	Central value	Prior
Oscillation parameters ($\bar{o}$)			
$\theta_{12}(^\circ)$	fixed	33.82	-
$\Delta m^2_{21}(\times 10^{-5}\text{eV}^2)$	fixed	7.39	-
$\Delta m^2_{31}(\times 10^{-3}\text{eV}^2)$	fitted	2.494	-
$\theta_{23}(^\circ)$	fitted	47.2	-
$\theta_{13}(^\circ)$	fitted	8.54	0.28
$\delta_{CP}(^\circ)$	fitted	234	-
Systematic uncertainties ($\bar{s}$)			
Atmo. μ	fixed	441.0	-
N_ν	fitted	1	-
$\Delta\gamma$	fitted	0	0.05
$\Delta\nu/\bar{\nu}$ (σ)	fitted	0	1.0
$\Delta M_A(\sigma)$	fitted	0	1

Table 4.2: List of nuisance parameters along with their central values and priors (if any). The parameter values refer to the ANTARES NSI analysis.

Minimisation

The ROOT MINUIT package [201] has been used to minimise Eq. 4.13. The program performs a scan of the multi-dimensional log-likelihood landscape in the gradient-descent approach, and returns a set of parameter values that yields the minimum value of TS (or maximum LLR). Different values of parameters are injected as starting points on the parameter space to ensure that the minimiser finds the true global mimima.

The NSI parameters are extracted from the global minimum obtained by the likelihood maximisation of the two-dimensional histograms in the plane of $\log_{10}(\text{E}_{reco}/\text{GeV})$ and $\cos\theta_{reco}$ (shown in Fig. 4.7) weighted under a certain oscillation hypothesis with parameters adopted from NuFit 4.1 [90]. The fit is done following an Asimov dataset[3] [187] approach, by minimising the Poissonian log-likelihood ratio function:

$$-2LLR = 2 \cdot \sum_{i\in\{bins\}} \left[N_i^{\text{test}}(\bar{o},\bar{s}) - N_i^{\text{data}}(\bar{o},\bar{s}) + N_i^{\text{data}} \cdot \ln \frac{N_i^{\text{data}}(\bar{o},\bar{s})}{N_i^{\text{test}}(\bar{o},\bar{s})} \right] + \sum_{j\in\{syst\}} \frac{(s_j - \hat{s}_j)^2}{\sigma^2_{\hat{s}_j}}, \tag{4.13}$$

where the first sum runs over the histogram bins, $N_i^{\text{data}}(\bar{o},\bar{s})$ is the number of data events in the i^{th} bin and $N_i^{\text{test}}(\bar{o},\bar{s})$ is the number of expected MC events in the i^{th} bin. The second sum runs over penalty terms of the number of nuisance parameters, j, taken into account, $\hat{s}_j$ and $\sigma^2_{\hat{s}_j}$ being the assumed prior and Gaussian standard deviation of the parameter j, respectively.

Oscillation parameters

The solar mass splitting Δm^2_{21} is fixed to 7.5×10^{-5} eV^2 and the mixing angle θ_{12} to 33.48°. The reactor angle θ_{13} is treated as a systematic uncertainty and is assigned a Gaussian prior with a central value of 8.54° and an uncertainty of $\pm 0.28°$. Although no impact was found on the final results, δ_{CP} has been fitted without prior. No prior constraints are

[3] An Asimov dataset is a single instance of "representative dataset" obtained by replacing all random observables with their expected values.

used on the atmospheric oscillation parameters Δm^2_{31} and θ_{23} which vary freely in the fit. A normal neutrino mass ordering is assumed. The fit is done is both octants ($\sin^2\theta_{23} <$ 0.5 and > 0.5) and the value yielding the maximum likelihood is accepted. All the above values are taken from [90].

Flux parameters

Our nominal flux model is based on the calculation of Honda et al. [103]. A global neutrino normalisation factor, N_ν, is accounted without constraints and treated as a free parameter. The spectral index γ, applied as a function of E_ν^γ, accounts for a change in the neutrino spectrum due to uncertainties in the primary cosmic ray spectrum. $\Delta\gamma$ is the change in spectral index γ; its central value is $\Delta\gamma = 0$. The spectral index is fitted with a 5%-width Gaussian prior. Uncertainties on the neutrino-antineutrino flux ratio, $\nu/\bar{\nu}$, and on the flux asymmetry between up-going and horizontal flux, ν_{up}/ν_{hor}, come from calculations done in [104]. A unique nuisance parameter based on parameterised uncertainties on the flux ratios by the IceCube Collaboration [62], is considered in the fit.

Cross-section parameter

Uncertainties on the neutrino interaction models can be parameterised using axial masses from quasi-elastic (QE) and resonant (RES) scattering cross-sections. Dedicated studies have been performed by the ANTARES Collaboration with gSeaGen [202], which uses GENIE [174] to model neutrino interaction cross-sections. For the CC resonant production, its value is M_A^{CCRES} = 1.12 GeV with an uncertainty of $\pm$20%. Expected event numbers are computed in the final fit by varying this parameter by $\pm1\sigma$.

Detector and sea water parameters

Detector and sea water related systematics in ANTARES has been studied in [167, 203]. Two different MC productions have been made with modified OM photon efficiency [204] and water absorption lengths[4] varied at $\pm$10% from their nominal values. The effect has been accounted while estimating the event weights as a function of true energy. The effect of the modified OM photon efficiency and water absorption lengths are found compatible with the functional form of $f(E) \sim A \cdot E^B$ (Fig. 4.9) and hence are absorbed within the global normalisation factor N_ν ($\equiv$ A), which is left unconstrained, and by the uncertainty on the spectral index $\Delta\gamma$ ($\equiv$ B), which is fitted with a prior.

[4]For a photon wavelength of $\sim$ 470 nm, an absorption length $\lambda_a \approx$ 60 m is measured in sea water [121, 122].

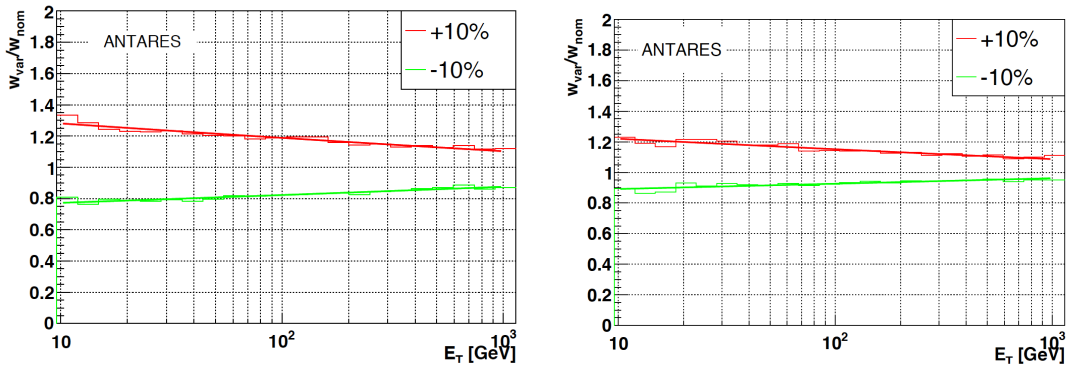

Figure 4.9: Expected event weight corrections for a $+10\%$ (red) and -10% variation from the nominal value of OM photon detection efficiency and water absorption length as a function of true neutrino energy, computed for $\nu_\mu + \overline{\nu}_\mu$ CC events. From [186].

Atmospheric muon background

The value and the uncertainty of the atmospheric muon background contamination has been obtained with a data-driven technique [205], by fitting the muon data distribution extrapolated to the signal-like region, as shown in Fig. 4.10.

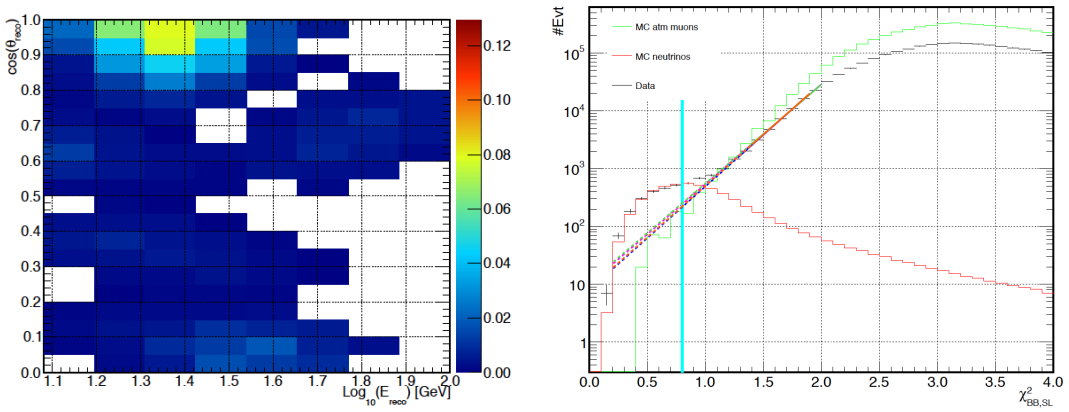

Figure 4.10: Left: normalised muon background PDF used in this analysis. Right: distribution of $\chi^2_{BB,SL}$ values ($\equiv \lambda_\mathcal{B}$) variable of *BBFit* for data (black) compared to MC sample comprising atmospheric neutrinos (red) and muons (green). The fit is shown along with its extrapolation to the signal-like region. The vertical line at $\chi^2_{BB,SL} = 0.8$ indicates the value of the applied cut on this parameter. From [186].

The fitted mean value of the atmospheric muon background and its standard deviation have been injected as the starting point and corresponding prior, respectively, in the fit of ANTARES data with the standard oscillation hypothesis [60]. The muon background PDF in this work has been normalised to 414.0, the best-fit value obtained from the fit with the standard oscillation hypothesis. Fixing the muon background at $\pm 1\sigma$ variations from the best-fit value yields compatible results (as will be shown in Fig. 4.17).

4.2.4 Results

The complete list of fitted parameters obtained from the minimisation of the log-likelihood function for the NSI hypothesis is shown in Table 4.3.

The best-fit value for $\epsilon_{\tau\tau}$ has been found at a non-zero value of 3.5×10^{-2}, which is in compliment with $U^2_{\tau 4}$ for the sterile search with ANTARES [60]. $\epsilon_{\tau\tau}$ finds a value distant from origin (corresponding to standard oscillations), to mimic the mild preference of ANTARES data for an energy-shifted first oscillation minimum [60]. The best-fit value for $\epsilon_{\mu\tau}$ has been found at 1.3×10^{-3}, which is consistent with results reported by other analyses [93]. The non-NSI hypothesis has been examined by performing the minimisation by setting null values for NSI parameters and is found to be slightly disfavoured with a significance of $\sim 2.3\sigma$ ($-2\Delta LLR = 5.5$), which corresponds to a 2-parameter p-value of 9.3%.

A strong pull is found for Δm^2_{31} due to a strong anti-correlation with $\epsilon_{\mu\tau}$. The best-fit Δm^2_{31} is found at a higher value of $3.1 \times 10^{-3}\text{eV}^2$. The mixing angle θ_{23} is found to be compatible with maximal mixing within its error at 52.2°. The reactor angle θ_{23} finds a best-fit value at 8.41°. The effect of δ_{CP} was found flat on all parts of the likelihood landscape. The best-fit δ_{CP} is found at 0.01°.

The global normalisation factor for neutrinos, N_ν, is found to be 15% lower than unity, which falls within the atmospheric neutrino flux uncertainties. This is compensated by a non-negligible pull on $\nu/\bar{\nu}$, which finds a minimum at 1.2. No significant deviation from the mean value is obtained for the spectral index correction $\Delta\gamma$.

Parameter	**best-fit**
NSIs	
$\epsilon_{\mu\tau}$	-1.3 $\times 10^{-3}$
$\epsilon_{\tau\tau}$	3.5 $\times 10^{-2}$
Oscillation	
$\Delta m^2_{31}(\text{eV}^2)$	3.1 $\times 10^{-3}$
$\theta_{23}(^\circ)$	52.25
$\theta_{13}(^\circ)$	8.41
$\delta_{CP}(^\circ)$	0.01
Flux	
N_ν	0.85
$\Delta\gamma$	-0.01
$\nu/\bar{\nu}$	1.2
Cross-section	
$\Delta M_A(\sigma)$	0.1

Table 4.3: Best-fit point (*bfp*) values obtained from the minimisation for all parameters considered in the analysis. NO is assumed.

The distribution of MC events as a function of the ratio of the reconstructed energy and the cosine of the reconstructed zenith is shown in Fig. 4.11. The red dashed line assumes MC with no oscillations, whereas the black points refer to data. All the $\text{E}_{\text{reco}}/\cos\theta_{\text{reco}}$ bins nicely match the simulation. This is reflected by the goodness-of-fit parameter $\chi^2/d.o.f. = 164.31/126$, where $d.o.f.$ is the number of bins ($\sum i = 8 \times 17$) minus the number of nuisance parameters (= 10) varied in the fit.

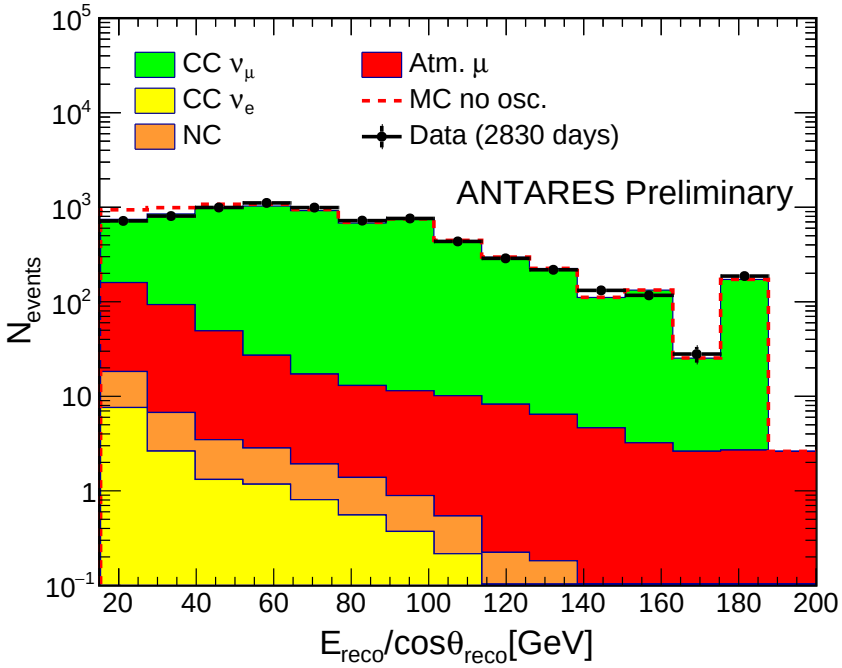

Figure 4.11: $E_{reco}/\cos\theta_{reco}$ distribution for data (black points), MC without oscillations (red dashed line) and MC assuming best-fit values of this analysis (stacked).

The oscillation effects are more prominent in linear scale, as shown in Fig. 4.13 and Fig. 4.12. In Fig. 4.12, the MC distributions are compared to the data bin-by-bin. The data and MC at the best-fit point are in good agreement after the fit.

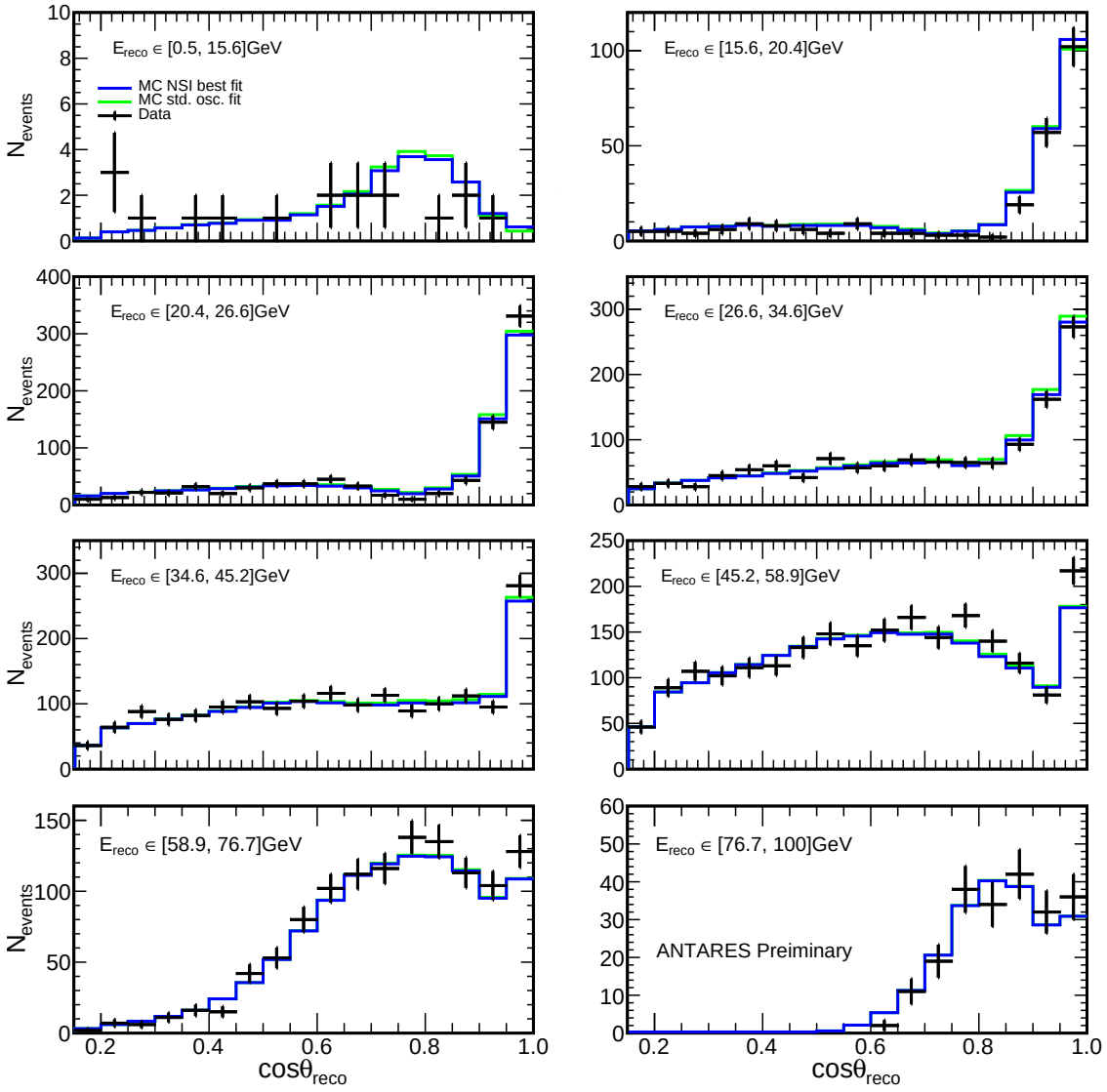

Figure 4.12: Data (black points) and MC (solid lines) comparisons of this analysis, as a function of the reconstructed zenith angle, $\cos\theta_{reco}$, for the eight different energy, E_{reco} bins. The blue colour corresponds to the MC at the best-fit from this work and the green to the MC assuming standard oscillations.

The ratio of data and MC assuming best-fit oscillation from this work with MC assuming the standard oscillation hypothesis is plotted in Fig. 4.13. The mild preference of data towards the NSI hypothesis is visible at the first few bins. The MC no oscillation hypothesis is discarded at $\sim 4.6\sigma$.

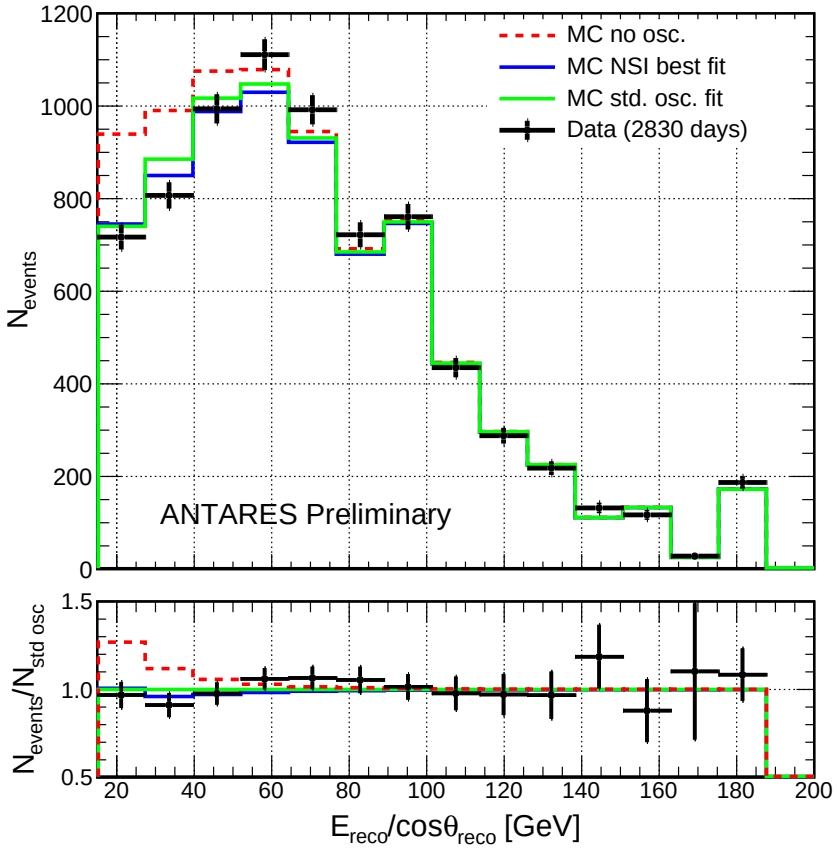

Figure 4.13: $E_{reco}/\cos\theta_{reco}$ distribution for data (black points), MC without oscillations (red dashed line) and MC assuming standard oscillations fit (green) and MC assuming best-fit values of this analysis (blue). Top plot shows the number of events whereas the bottom plot gives the event ratio with respect to MC standard oscillations fit (green).

Exclusion regions

After finding the log-likelihood ratio value LLR_{min} at the global minimum represented by $(\bar{o}_{min}, \bar{s}_{min})$ by fitting N (= 10, in our case) number of total fitted parameters, we can construct confidence limits in a reduced parameter space of $\epsilon_{\mu\tau}$ and $\epsilon_{\tau\tau}$. This is done by calculating LLR values around the global minimum with respect to LLR_{min}:

$$-2\Delta LLR = -2LLR(\epsilon_{\mu\tau}, \epsilon_{\tau\tau}) - \Big(-2LLR_{min}(\bar{o}_{min}, \bar{s}_{min}) \Big), \tag{4.14}$$

where $LLR(\epsilon_{\mu\tau}, \epsilon_{\tau\tau})$ is the value of LLR in the $N-2$ phase space. This is obtained by fitting all N parameters, except the two in which the confidence region is to be built.

Thus, using Eq. 4.13, a value of LLR is computed over a 2-dimensional grid of parameter phase space defined by $\epsilon_{\mu\tau}$ and $\epsilon_{\tau\tau}$, where $\epsilon_{\mu\tau}$ ranges from -1.2×10^{-3} to 1.2×10^{-3} and $\epsilon_{\tau\tau}$ ranges from -1.5×10^{-2} to 1.5×10^{-2}. The fit is performed on a 151×101 grid over this space by maximising the likelihood over the $N - 2 = 8$ fit parameters listed in Table 4.2.

Exclusion contours are drawn in the form of confidence level intervals for two *d.o.f.* assuming Wilks' theorem [200]. The median significance of the test statistic is computed

in this way without the need of producing ensembles of toy-MC. However, in the absence of asymptotic approximations, based on Wilk's theorem, there are other methods as proposed by Feldman and Cousins [206]. However, they are computationally expensive and require comparison of test statistic distributions of pseudo-experiments for each point in the parameter space. In this work, we restrict ourselves to the choice of Wilks' theorem, which allows to approximate asymptotically $-2LLR$ as χ^2.

The resulting sensitivity and exclusion limit contours at 90% C.L., derived from this analysis in the $\epsilon_{\mu\tau} - \epsilon_{\tau\tau}$ plane, are shown in Fig. 4.14 and Fig. 4.15. Fig. 4.14 corresponds to a MC-only sensitivity analysis with the toy-MC weighted according to the standard oscillation hypothesis (point (0,0) in the NSI phase space). Fig. 4.15 shows the 90% C.L. upper limit obtained with data. The red cross depicts the best-fit point in the $\epsilon_{\mu\tau} - \epsilon_{\tau\tau}$ phase space. The $(\bar{o}_{min}, \bar{s}_{min})$ parameters that do not appear on the plot are marginalised over.

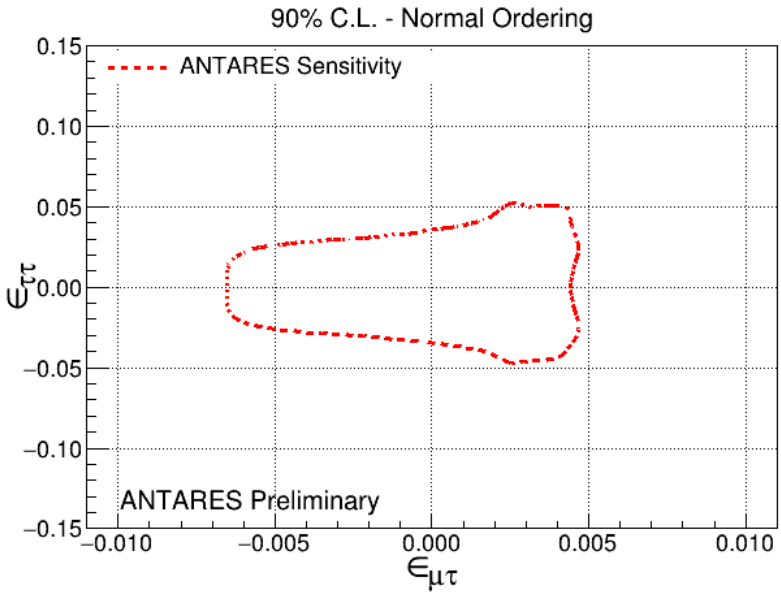

Figure 4.14: MC-only sensitivity at 90% C.L. after 10 years of ANTARES livetime obtained in this work is shown.

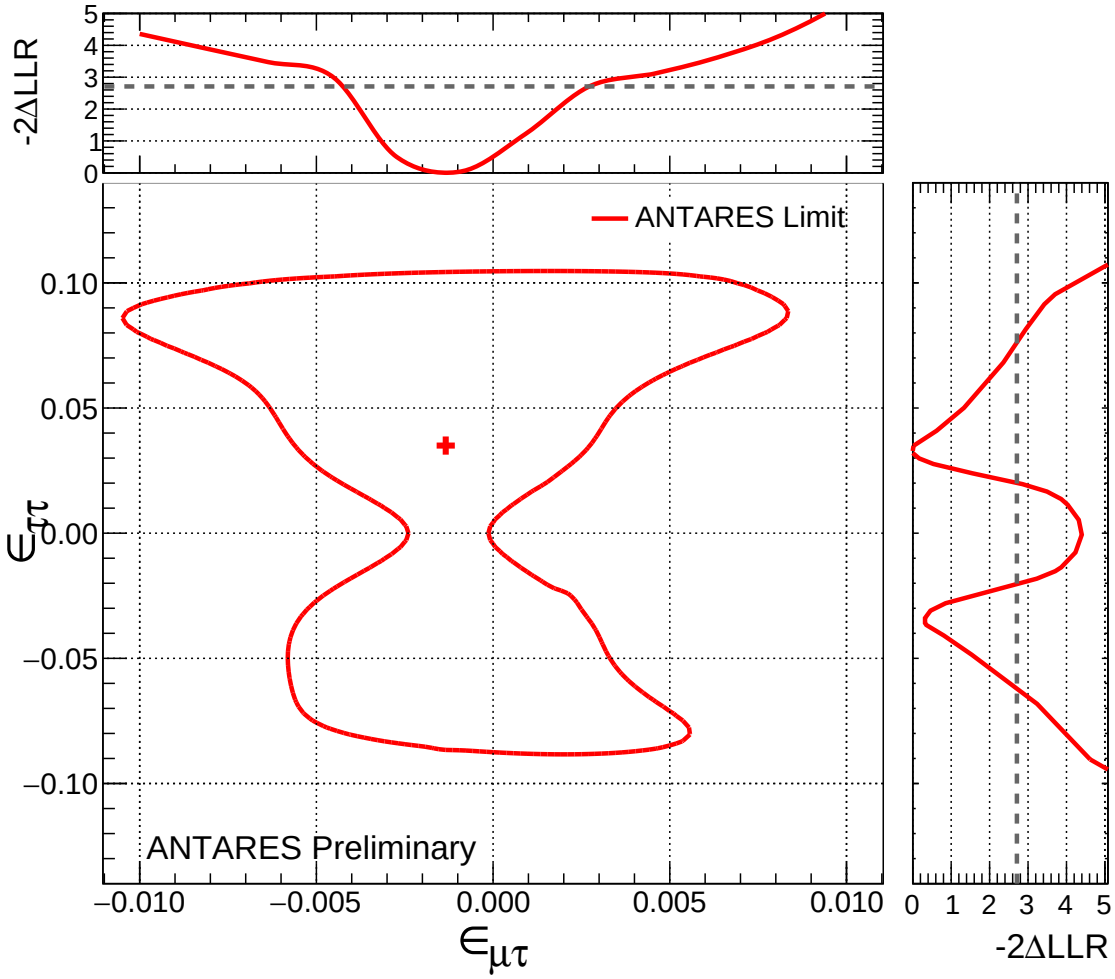

Figure 4.15: 90% C.L. upper limits allowed after 10 years of ANTARES livetime obtained in this work are shown. The cross depicts the best-fit point obtained. The top and right lateral plots show the 1D projections on $\epsilon_{\mu\tau}$ and $\epsilon_{\tau\tau}$ axes respectively.

Finally, limits on the NSI matrix elements are obtained by profiling over the other variable:

$$\begin{aligned} -4.2 \times 10^{-3} < \epsilon_{\mu\tau} < 2.7 \times 10^{-3} \quad & (\text{at } 90\% \text{ C.L}), \\ -6.1 \times 10^{-2} < \epsilon_{\tau\tau} < -2.1 \times 10^{-2} \quad \text{and} \quad 2.1 \times 10^{-2} < \epsilon_{\tau\tau} < 7.3 \times 10^{-2} \quad & (\text{at } 90\% \text{ C.L}). \end{aligned} \tag{4.15}$$

Comparisons with other experiments

Fig. 4.16 shows the exclusion regions in the first quadrant of log-scaled $\epsilon_{\mu\tau} - \epsilon_{\tau\tau}$ phase space. In this case, a coarser grid of 60×50 points over the parameter phase space defined by $\epsilon_{\mu\tau}$ and $\epsilon_{\tau\tau}$, where both $\epsilon_{\mu\tau}$ and $\epsilon_{\tau\tau}$ range from 10^{-3} to 1, is chosen. Finally, 90% C.L. and 99% C.L. contours are drawn w.r.t. to the best-fit point lying in the second quadrant (Tab. 4.3). Note that the Super-K constraints have been drawn assuming a *two-flavour hybrid model* approximation (Sec. 4.1).

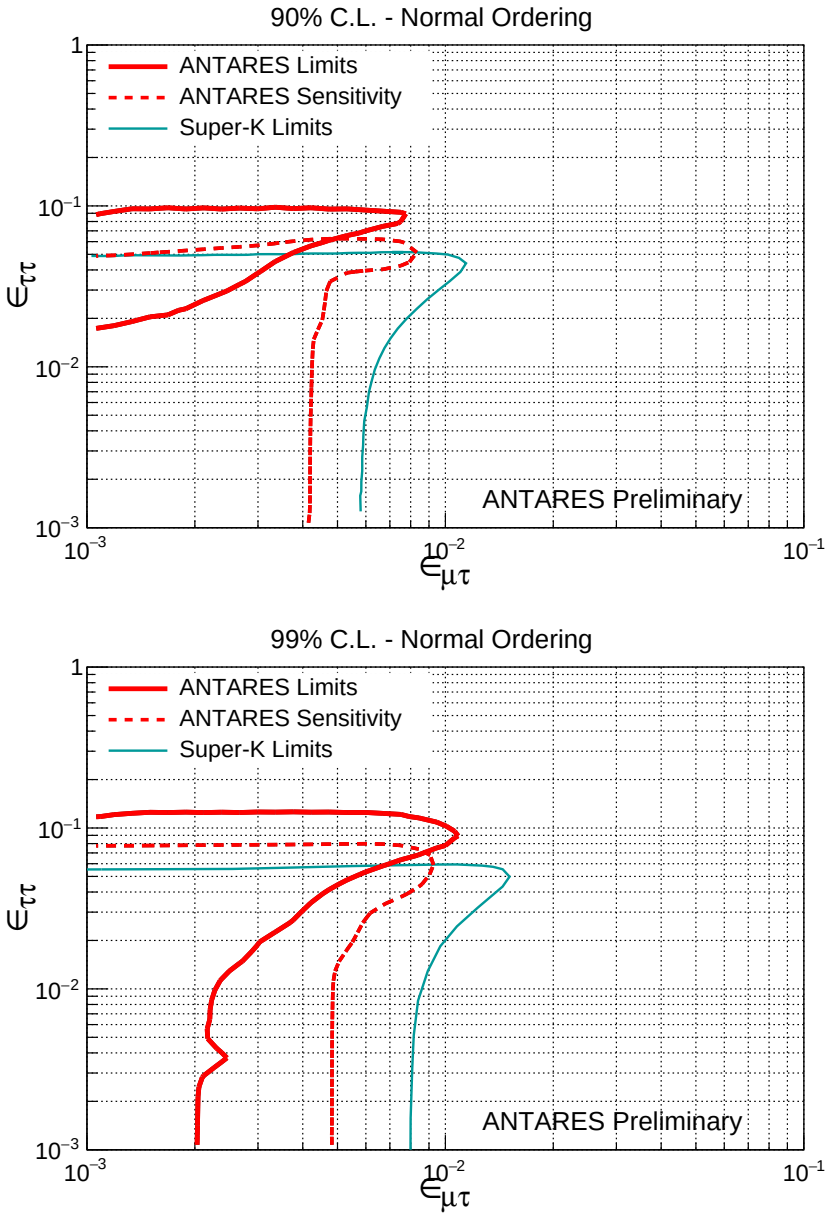

Figure 4.16: 90% (top) and 99% (bottom) C.L. upper limits in the $\epsilon_{\mu\tau} - \epsilon_{\tau\tau}$ phase space allowed after 10 years of ANTARES livetime obtained in this work, together with MC-only sensitivities (dashed) and limits (assuming a *two-flavour hybrid model* approximation) from Super-K [192] are shown.

Contours for 90% C.L. have been re-evaluated by setting the atmospheric muon background at $\pm 1\sigma$ errors from the nominal value of 414^{+48}_{-24}, obtained from the best

fit with standard oscillations [60]. The muon background was found to be negatively correlated with $\epsilon_{\mu\tau}$. Nevertheless, as shown in Fig. 4.17 the effect on the final results is rather small.

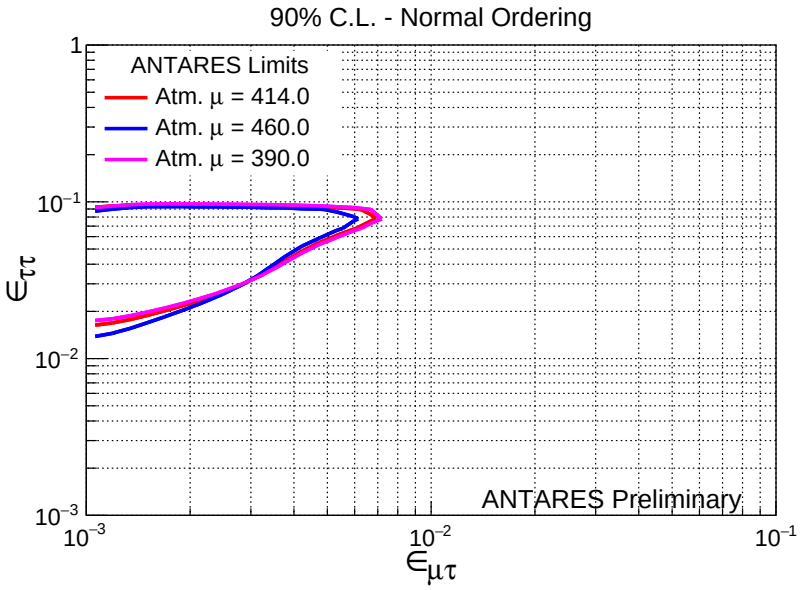

Figure 4.17: Comparison of 90% C.L. upper limits for different muon background estimations.

We also considered an effective Hamiltonian in the presence of NSIs in the $e-\tau$ sector to compare with Super-K. A similar analysis has been pursued thereafter, resulting in limits in the $\epsilon_{e\tau} - \epsilon_{\tau\tau}$ phase space. Best-fit points obtained on fitting this NSI model hypothesis are listed in Tab. 4.4. 90% C.L. contour for $\epsilon_{ee} = 0$ (fixed) is drawn as shown in Fig. 4.18. Note that the Super-K constraints have been drawn assuming a *three-flavour hybrid model* approximation (Sec. 4.1).

Parameter	**best-fit**
NSIs	
$\epsilon_{e\tau}$	-6.8×10^{-2}
$\epsilon_{\tau\tau}$	-1.9×10^{-2}
ϵ_{ee}	0 (fixed)
Oscillations	
$\Delta m^2_{31}(\mathrm{eV}^2)$	3.0×10^{-3}
$\theta_{23}(^\circ)$	38.52
$\theta_{13}(^\circ)$	8.41
$\delta_{CP}(^\circ)$	0.01
Flux	
N_ν	0.84
$\Delta\gamma$	-0.01
$\nu/\bar{\nu}$	1.06
Cross-section	
$\Delta M_A(\sigma)$	0.1

Table 4.4: Best-fit point (*bfp*) values obtained from the minimisation for all parameters considered in this analysis. NO is assumed.

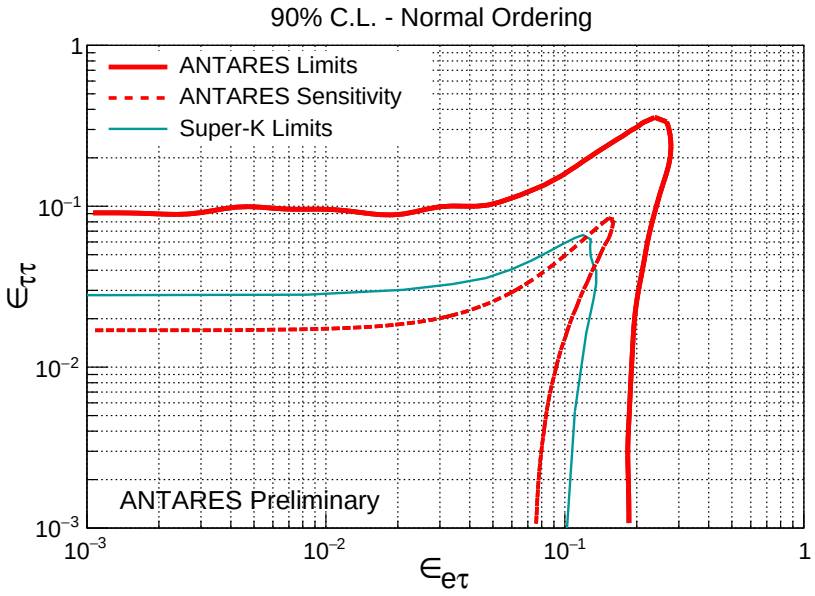

Figure 4.18: 90% C.L. upper limit in the $\epsilon_{e\tau} - \epsilon_{\tau\tau}$ phase space allowed after 10 years of ANTARES livetime obtained in this work, together with MC-only sensitivities (dashed) and limits (assuming a *three-flavour hybrid model* approximation) from Super-K [192] are shown.

For comparison with IceCube Deepcore [93], limits on NSI $\epsilon_{\mu\tau}$ with $\epsilon_{\tau\tau}$ being kept fixed or fitted, have been computed and drawn in Fig. 4.19. The case when $\epsilon_{\tau\tau}$ is fitted, the best-fit points *bfp* coincides with the previous analyses presented in Table 4.3. The *bfp*, when $\epsilon_{\tau\tau}$ is fixed at zero, is presented in Table 4.5. A $\chi^2/d.o.f. = 169.24/127$ is obtained in this case with nine free parameters in the fit.

Parameter	**best-fit**
NSIs	
$\epsilon_{\mu\tau}$	-1.2×10^{-3}
$\epsilon_{\tau\tau}$	0 (fixed)
Oscillations	
$\Delta m^2_{31}(\mathrm{eV}^2)$	2.0×10^{-3}
$\theta_{23}(^\circ)$	45.83
$\theta_{13}(^\circ)$	8.41
$\delta_{CP}(^\circ)$	360
Flux	
N_ν	0.8
$\Delta\gamma$	-0.01
$\nu/\bar{\nu}$	1.2
Cross-section	
$\Delta M_A(\sigma)$	0.1

Table 4.5: Best-fit point (*bfp*) values obtained from the minimisation for all parameters when $\epsilon_{\tau\tau}$ is fixed to zero. NO is assumed.

A limit on the NSI parameter $\epsilon_{\mu\tau}$ ($\forall\, \epsilon_{\tau\tau} = 0$) is obtained:

$$\boxed{-3.8 \times 10^{-3} < \epsilon_{\mu\tau} < 1.6 \times 10^{-3} \quad (\text{at } 90\% \text{ C.L}),} \tag{4.16}$$

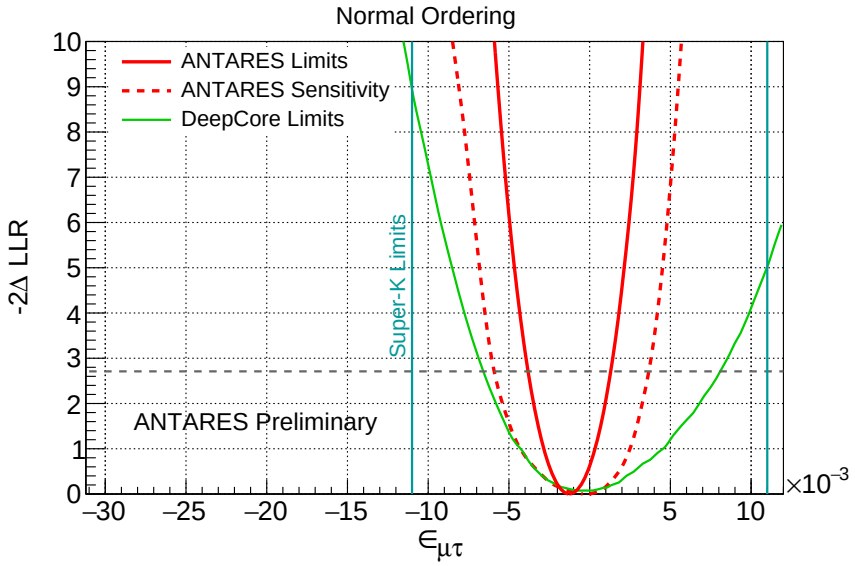

Figure 4.19: Limits on $\epsilon_{\mu\tau}$ after 10 years of ANTARES livetime obtained in this work when $\epsilon_{\tau\tau}$ is fixed at zero. Sensitivity projections from ANTARES (red dashed) as well as limits from IceCube DeepCore [93] (green) and Super-K [192] (cyan) are drawn for comparisons.

While, the IceCube Deepcore analysis restricts high energy events with a fiducial volume cut, which is essentially equivalent to a cut on reconstructed energy at 56 GeV, the ANTARES true energies of events considered in this analysis span till 10 TeV. These partially contained high energy neutrino events bring enhanced sensitivity to non-standard effects in ANTARES. However, to be in line with IceCube Deepcore, it has been verified that the limit degrades (marginally) when a cut on true/reco energy is imposed as shown in Fig. 4.20.

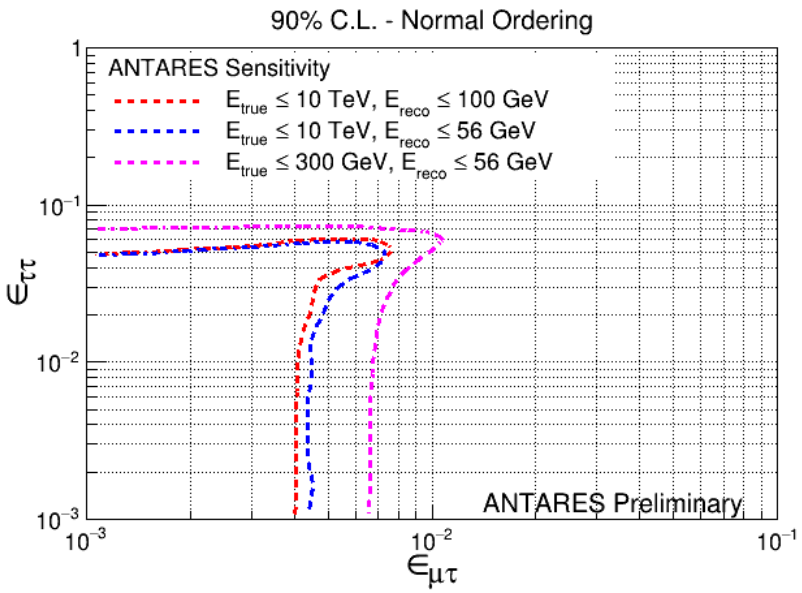

Figure 4.20: Comparison of 90% C.L. limits for cuts on true and reconstructed energies. The cut on true energy has the largest impact, since partially-contained high energy events bring enhanced sensitivity to NSI effects.

In conclusion, a first ANTARES analysis constraining the NSI sector has been presented. In this analysis, ANTARES data has been used to set world-wide competitive limits in the NSI parameter space, using the same dataset used in the analysis of standard oscillations [60]. The limits for NSI obtained with ten years of atmospheric muon disappearance data collected by ANTARES are more stringent than allowed by current experimental limits, and thereby constitutes the world's best limits in the $\mu - \tau$ sector.

4.3 Sensitivity to NSIs at ORCA

This section details the method employed to estimate of the sensitivity of KM3NeT-ORCA towards different NSI sectors. The strategy for event selection, statistical methods for calculating the sensitivity and the list of systematics included in this study are discussed in detail.

4.3.1 Event selection

The analyses concerning ORCA have been pursued adopting two different strategies for event selection and two possible detector geometries, on what the horizontal spacing between DUs is concerned. We shall refer to them as **ORCA115–20m** and **ORCA115–23m** MC throughout this thesis:

- **23 m – 2 PID bins**: assuming 23 m horizontal spacing between DUs and with two event classes (tracks and showers) with the following selection criteria:
  - *muon cut*: a relatively aggressive cut on `atmospheric_muon_score` < 0.05 for the neutrino to atmospheric muon background is used to reach a few percent muon contamination in the final sample;
  - *noise cut*: a cut on `pure_noise_score` < 0.1 is imposed to reject pure-noise events;
  - *zenith cut*: only up-going events with $\cos\theta_{reco} < 0$ are considered;
  - *shower cut*: passes shower selection (trigger and reconstructed by the shower algorithm) && (`track_score` ≤ 0.6);
  - *track cut*: passes track selection (triggered and reconstructed by the track algorithm) && (`track_score` > 0.6).

The resulting event distributions passing the selection cuts for tracks and showers are shown in Fig. 4.21.

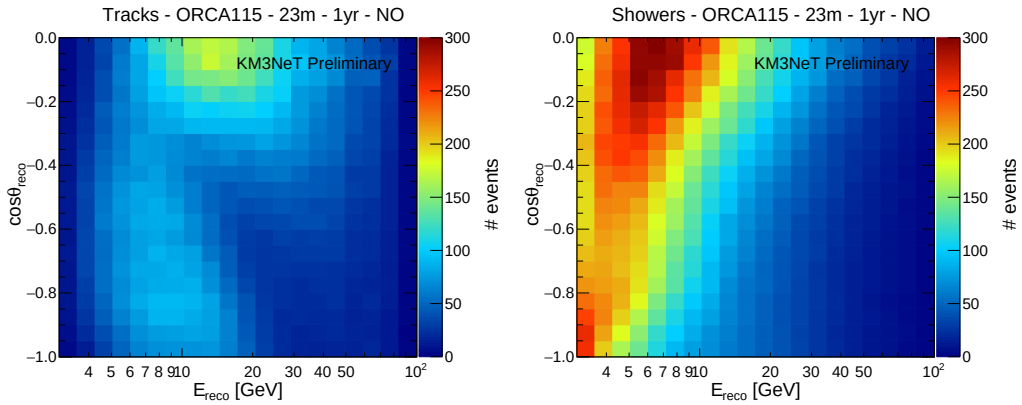

Figure 4.21: The expected event rates at ORCA with 23 m horizontal spacing per year as a function of reconstructed energy and zenith angle for each event topology. NO is assumed.

- **20 m – 3 PID bins**: assuming 20 m horizontal spacing between DUs and with three event classes (tracks, middles and showers) with the following selection criteria:
  - *muon cut*: `atmospheric_muon_score` < 0.05;
  - *noise cut*: `pure_noise_score` < 0.1;

- *zenith cut*: only up-going events with $\cos\theta_{reco} < 0$ are considered;
- *shower cut*: passes shower selection && (`track_score` ≤ 0.3);
- *middle cut*: passes shower selection && ($0.3 <$ `track_score` < 0.7). An extra event class translates into having an extra binning in Bjorken-y distribution (or PID), which adds up an extra component at the χ^2 level.;
- *track cut*: passes track selection && (`track_score` ≥ 0.7).

The resulting event distributions passing the selection cuts for each topology are shown in Fig. 4.22.

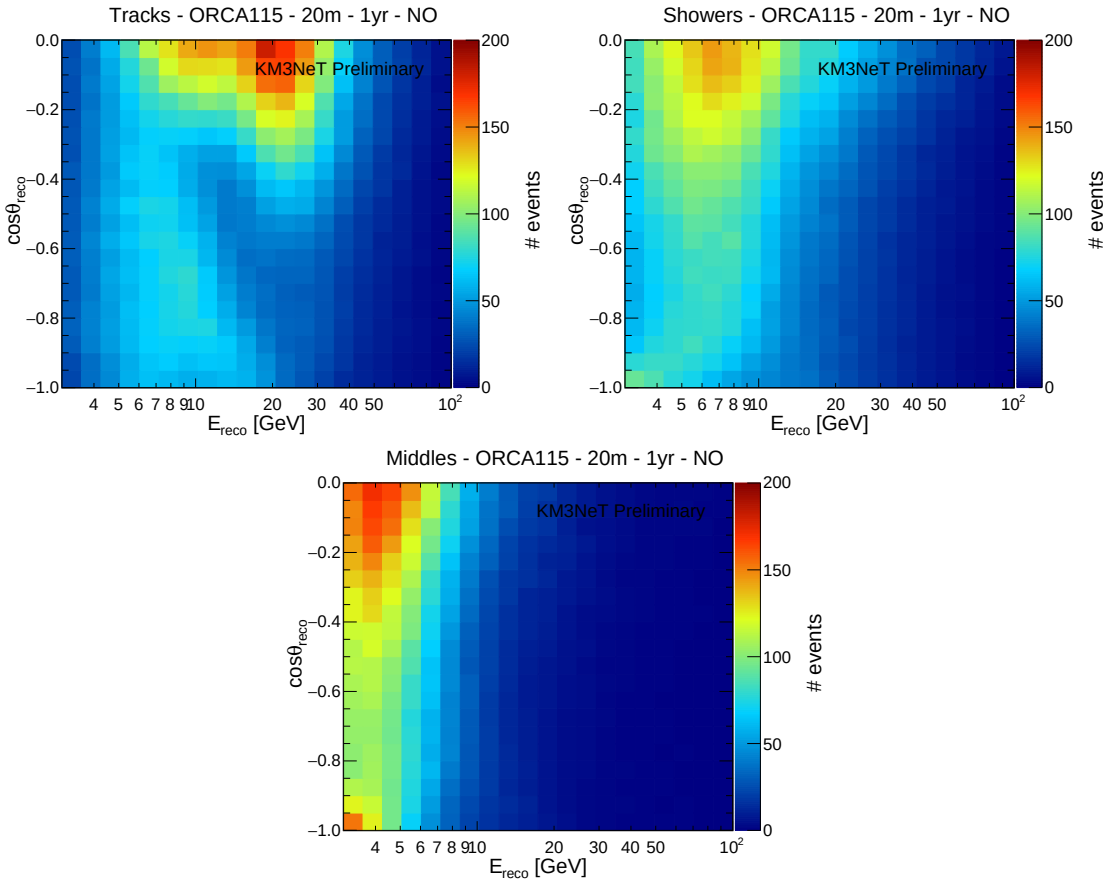

Figure 4.22: The expected event rates at ORCA with 20 m horizontal spacing per year as a function of reconstructed energy and zenith angle for each event topology. NO is assumed.

The MC expectation for one year of ORCA exposure comprising 115 DUs from the eight different interaction channels, oscillations included (weighted under standard oscillation hypothesis with parameters adopted from NuFit 4.1 [90]), for the final samples that pass the selection criteria of cuts are listed in Table 4.6.

Component	Tracks (23m/20m)	Middles (23m/20m)	Showers (23m/20m)
ν_μ CC	12508/12000	-/4423	9149/2295
$\overline{\nu}_\mu$ CC	6760/6679	-/1997	3489/501
ν_e CC	807/511	-/3998	14268/8351
$\overline{\nu}_e$ CC	333/208	-/1539	5328/3117
ν_τ CC	313/280	-/516	2476/1364
$\overline{\nu}_\tau$ CC	156/140	-/231	1038/573
ν NC	208/143	-/1197	5007/2981
$\overline{\nu}$ NC	60/40	-/348	1401/824
Total	21145/20001	-/14249	42156/20006

Table 4.6: Expected composition of the final oscillated MC sample of atmospheric neutrinos surpassing the selection criteria and corresponding to a livetime of one year of full ORCA with 115 DUs for 23 m and 20 m detector geometries. The "middle" selection is only applied to the 20 m geometry. NO is assumed.

In the track selection, a 93.3% purity of $\nu_\mu + \overline{\nu}_\mu$ is achieved for a 20 m detector geometry compared to 91.1% in case of a 23 m geometry. In the shower selection, $\nu_e + \overline{\nu}_e$ events comprise 57% (46.4%) of the total events for a 20 m (23 m) detector geometry. A higher purity is achieved in the case of a 20 m geometry due to the hard PID cuts. The events which are not classified as "good" tracks (`track_score` ≥ 0.7) or "good" showers (`track_score` ≤ 0.3) fall into the intermediate middle class.

4.3.2 Statistical significance

Fig. 4.23 – Fig. 4.26 show the signed-χ^2 maps for reconstructed events in the three event classes for 3 years of full ORCA (115 DUs) runtime with 20 m horizontal spacing. 20 logarithmic bins were chosen in the reconstructed neutrino energy $(E_\nu) \in [3, 100]$ GeV, while 20 linear bins in cosine of the reconstructed zenith angle $(\theta_z) \in [-1, 0]$. The absolute value of χ^2 is stored, so that each bin content represents the contribution to the total χ^2 from each event class. The sign information is retained to represent the excesses and deficits. The statistical signed-χ^2 for each bin is computed as:

$$\chi^2_{E,\theta_z}(\epsilon_{\alpha\beta}) = \frac{\left(N^{\text{test}}_{E,\theta_z}(\epsilon_{\alpha\beta}) - N^{\text{true}}_{E,\theta_z}(\epsilon_{\alpha\beta}=0)\right) \times \left|N^{\text{test}}_{E,\theta_z}(\epsilon_{\alpha\beta}) - N^{\text{true}}_{E,\theta_z}(\epsilon_{\alpha\beta}=0)\right|}{N^{\text{true}}_{E,\theta_z}(\epsilon_{\alpha\beta}=0)}. \tag{4.17}$$

$N^{\text{true}}_{E,\theta_z}$ is the expected number of track/middle/shower events in the corresponding (E, θ_z) bin weighted under standard oscillation hypothesis with parameters adopted from NuFit 4.1 [90], while $N^{\text{test}}_{E,\theta_z}$ is the number of expected events in the same (E, θ_z) bin but with non-zero test values of NSI parameters, $\epsilon_{\alpha\beta}$.

The ***"total sensitivity"***, $\chi^2_{tot}(\epsilon_{\alpha\beta})$, at any given NSI point represented by $\epsilon_{\alpha\beta}$, refers to the sum of the absolute values of the statistical χ^2 from every (E, θ_z) bins for that particular NSI hypothesis. In case of Poissonian distribution of events, χ^2 is replaced by the log-likehood ratio, $-2LLR$ (Eq. 4.8)[5]. $\chi^2_{tot}(\epsilon_{\alpha\beta})$ is calculated in the following way:

$$\chi^2_{tot}(\epsilon_{\alpha\beta}) = \sum_{E,\theta_z} \chi^2_{E,\theta_z}(\epsilon_{\alpha\beta})\Big|_{\text{tracks}} + \sum_{E,\theta_z} \chi^2_{E,\theta_z}(\epsilon_{\alpha\beta})\Big|_{\text{middles}} + \sum_{E,\theta_z} \chi^2_{E,\theta_z}(\epsilon_{\alpha\beta})\Big|_{\text{showers}}. \tag{4.18}$$

[5]We use $-2LLR$ as our test statistic for further calculations.

The square-root of the absolute value of total sensitivity is termed as the ***"significance"***, $\sigma_{tot}(\epsilon_{\alpha\beta})$. The significance gives an estimate of how well an experiment can measure $\epsilon_{\alpha\beta}$ from a given experimental dataset.

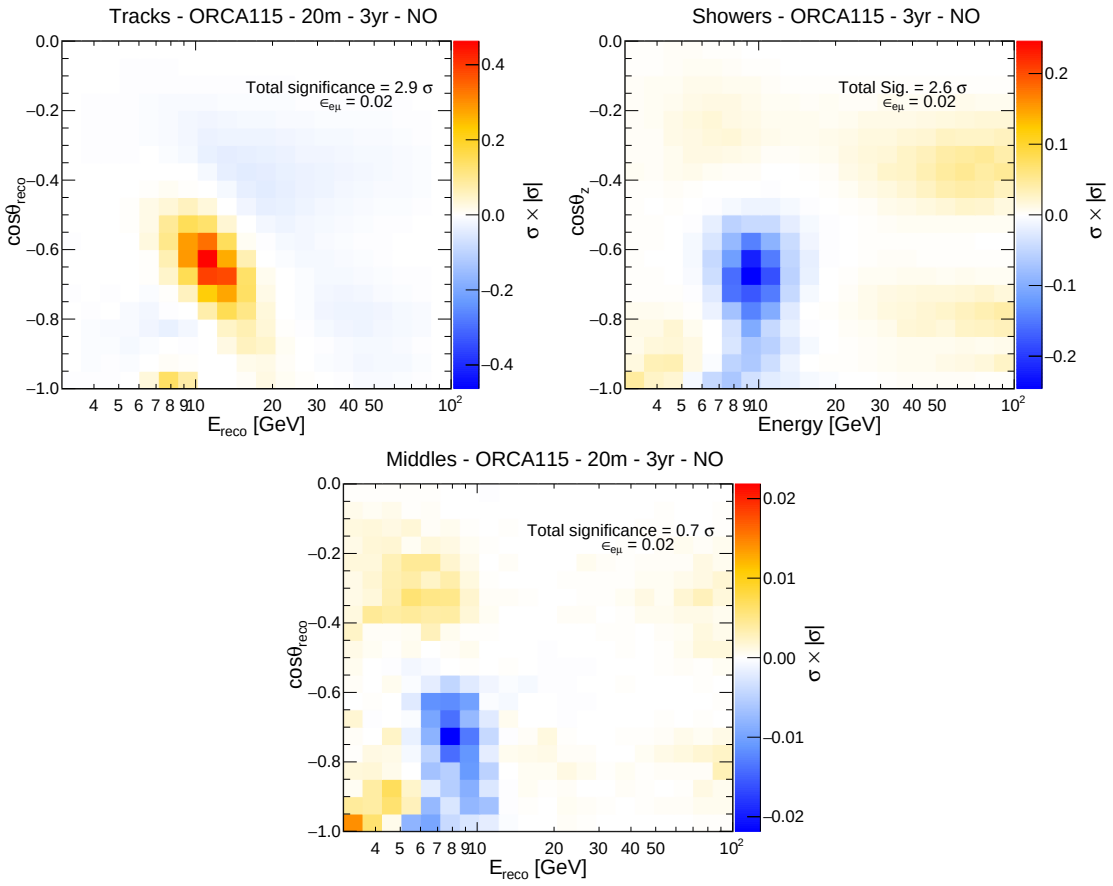

Figure 4.23: Statistical signed-χ^2 maps for 3 years of exposure of ORCA-115 lines corresponding to 20 m horizontal spacing between DUs as a function of reconstructed neutrino energy (E_{reco}) and zenith direction ($\cos\theta_{reco}$) for track (left column), middle (middle), and shower (right) event topologies. The NSI hypothesis parameterised by $\epsilon_{e\mu} = 0.02$. NO is assumed. The plots for IO assumption are not shown for brevity. The color code indicates the values of signed-χ^2, as defined in Eq. 4.17. The total sensitivity quoted is the square-root of the sum of the absolute values of the χ^2 from each bin. Mind the difference in the colour scales.

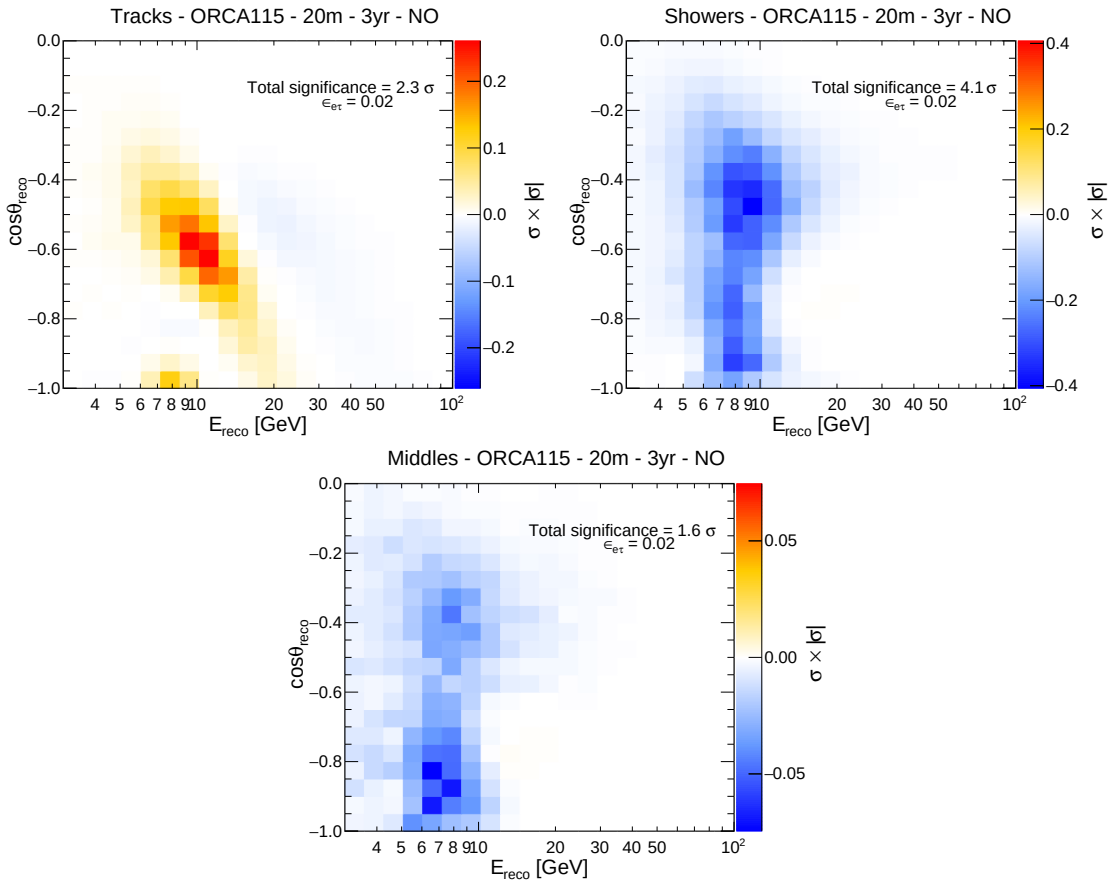

Figure 4.24: Statistical signed-χ^2 maps for 3 years of exposure of ORCA-115 lines corresponding to 20 m horizontal spacing between DUs as a function of reconstructed neutrino energy (E_{reco}) and zenith direction ($\cos\theta_{reco}$) for track (left column), middle (middle), and shower (right) event topologies. The NSI hypothesis parameterised by $\epsilon_{e\tau} = 0.02$. NO is assumed. See caption of Fig. 4.23 for more info.

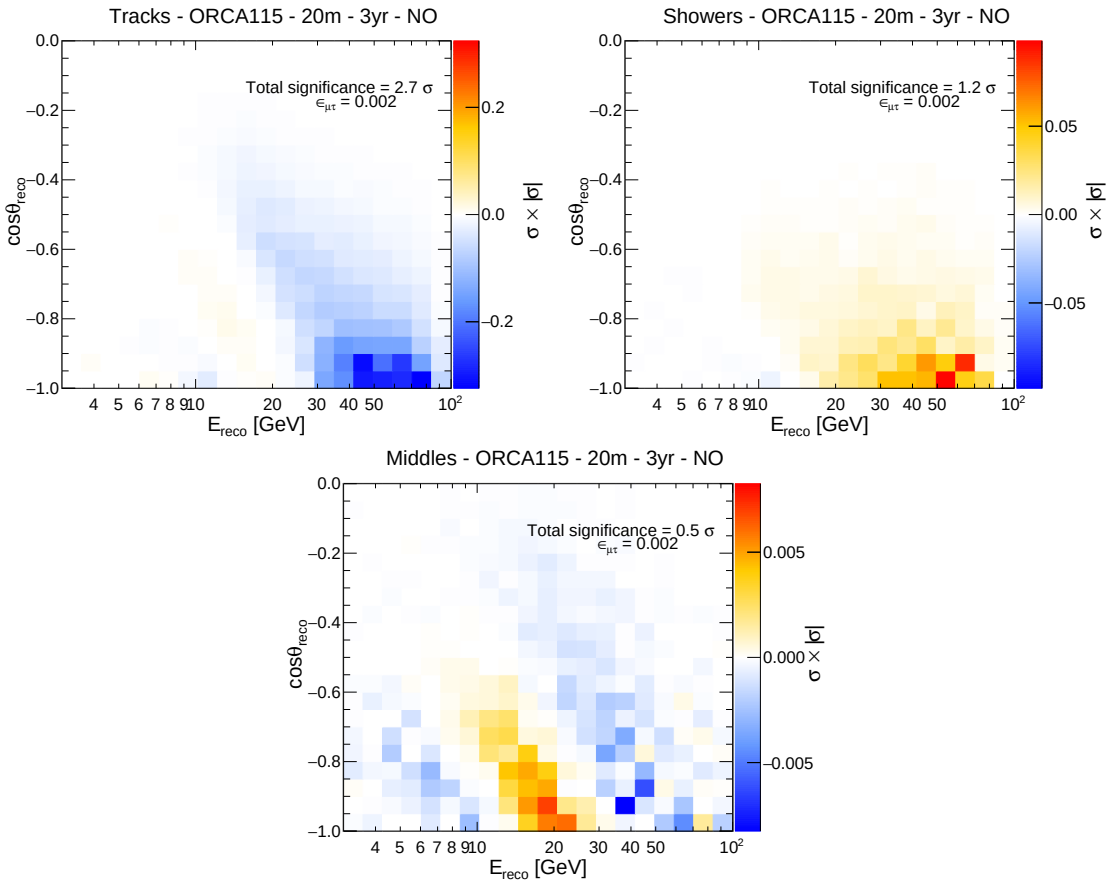

Figure 4.25: Statistical signed-χ^2 maps for 3 years of exposure of ORCA-115 lines corresponding to 20 m horizontal spacing between DUs as a function of reconstructed neutrino energy (E_{reco}) and zenith direction ($\cos\theta_{reco}$) for track (left column), middle (middle), and shower (right) event topologies. The NSI hypothesis parameterised by $\epsilon_{\mu\tau}$ = 0.002 . NO is assumed. See caption of Fig. 4.23 for more info.

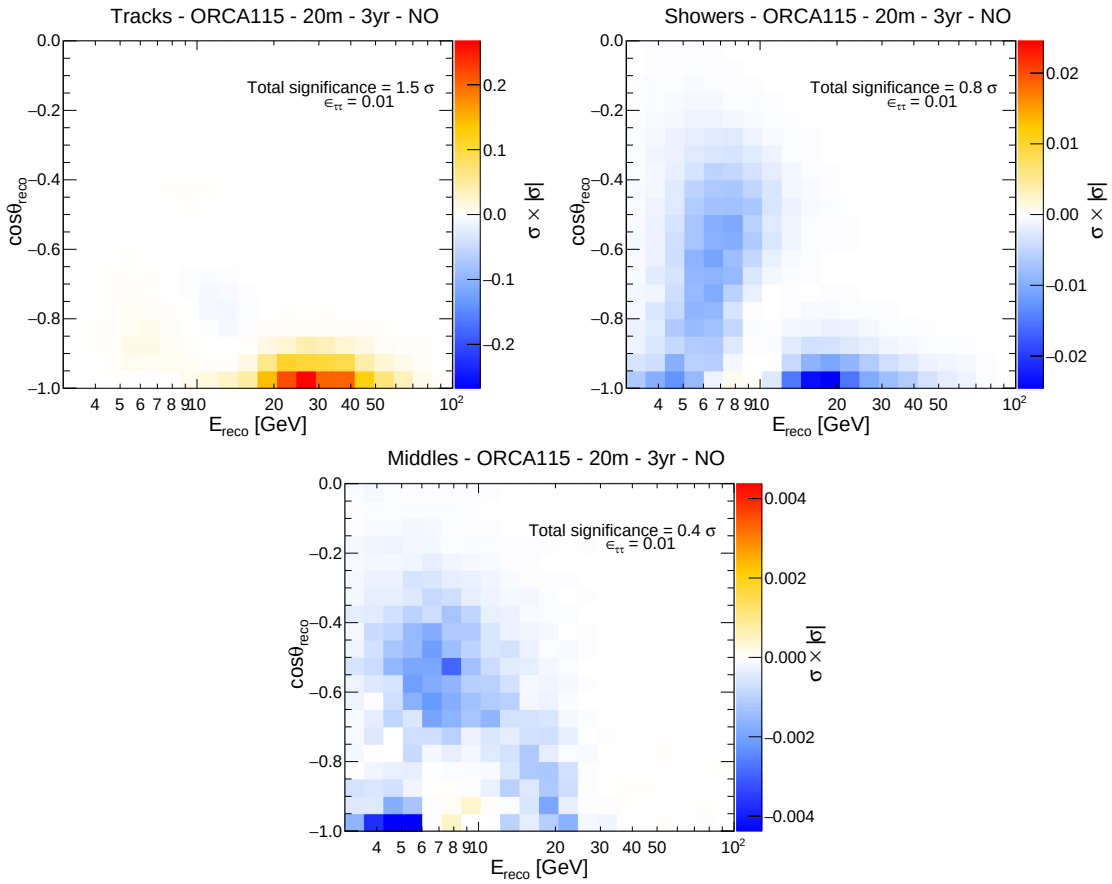

Figure 4.26: Statistical signed-χ^2 maps for 3 years of exposure of ORCA-115 lines corresponding to 20 m horizontal spacing between DUs as a function of reconstructed neutrino energy (E_{reco}) and zenith direction ($\cos\theta_{reco}$) for track (left column), middle (middle), and shower (right) event topologies. The NSI hypothesis parameterised by $\epsilon_{\tau\tau} = 0.01$. NO is assumed. See caption of Fig. 4.23 for more info.

Thus the individual contributions from track, middle and shower event classes are added in quadrature to compute the ***"total significance"***, σ_{tot}:

$$\begin{aligned}\sigma_{tot} &= \sqrt{-2\ln\mathcal{L}_{stat}} \\ &= \sqrt{(-2\ln\mathcal{L})\Big|_{\text{tracks}} + (-2\ln\mathcal{L})\Big|_{\text{middles}} + (-2\ln\mathcal{L})\Big|_{\text{showers}}}\end{aligned} \tag{4.19}$$

The contribution from three event classes to the total statistical significance for different assumed NSI model hypotheses are shown in Fig. 4.27 to Fig. 4.30. Sensitivity curves corresponding to IO assumption are also drawn.

NSI $\epsilon_{e\mu}$

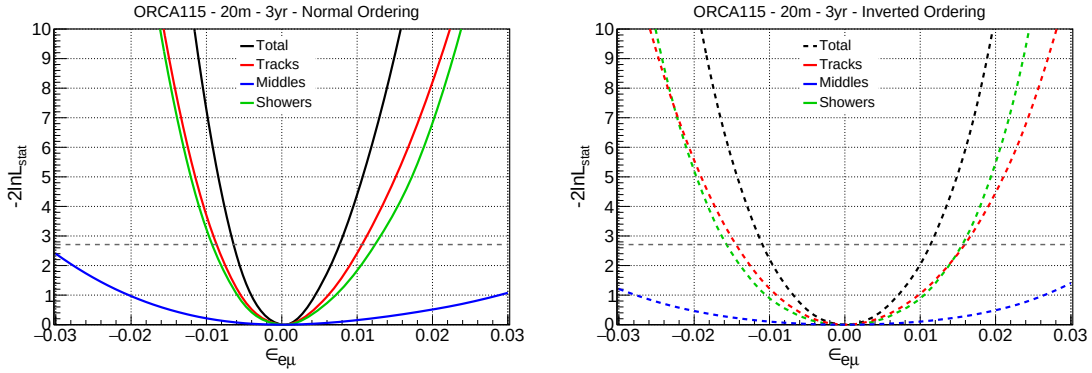

(a) 20 m geometry with 3 event classes: tracks (red), middles (blue) and showers (green).

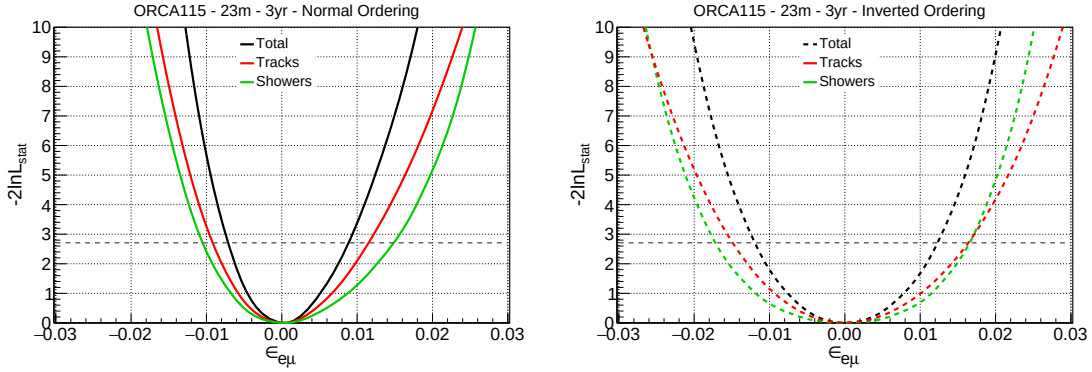

(b) 23 m geometry with 2 event classes: tracks (red) and showers (green).

Figure 4.27: Contribution from tracks (red), middles (blue) and showers (red) to the total statistical significance as a function different test values of $\epsilon_{e\mu}$. For 20 m (top panels) and 23 m geometries (bottom) assuming NO (left) and IO (right). The dashed horizontal line corresponds to 90% C.L. limit.

NSI $\epsilon_{e\mu}$ receives contribution from both the track (primarily muon appearance channel) and shower (primarily electron disappearance) classes as shown in Fig. 4.27.

NSI $\epsilon_{e\tau}$

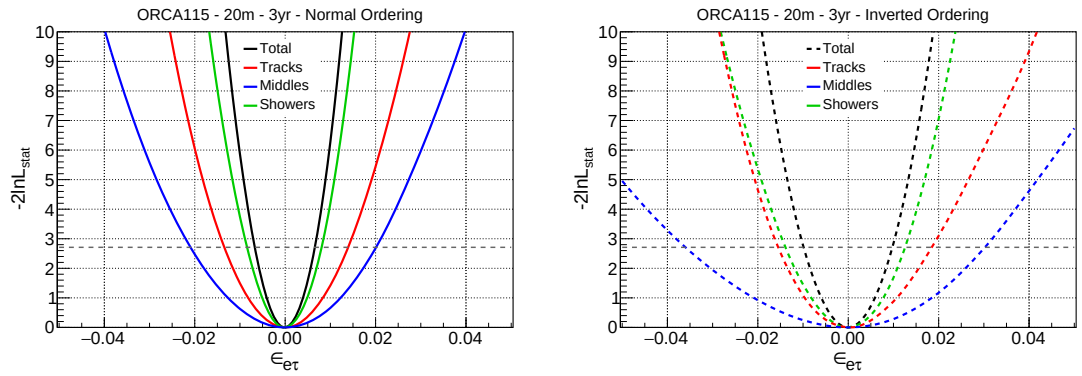

(a) 20 m geometry with 3 event classes: tracks (red), middles (blue) and showers (green).

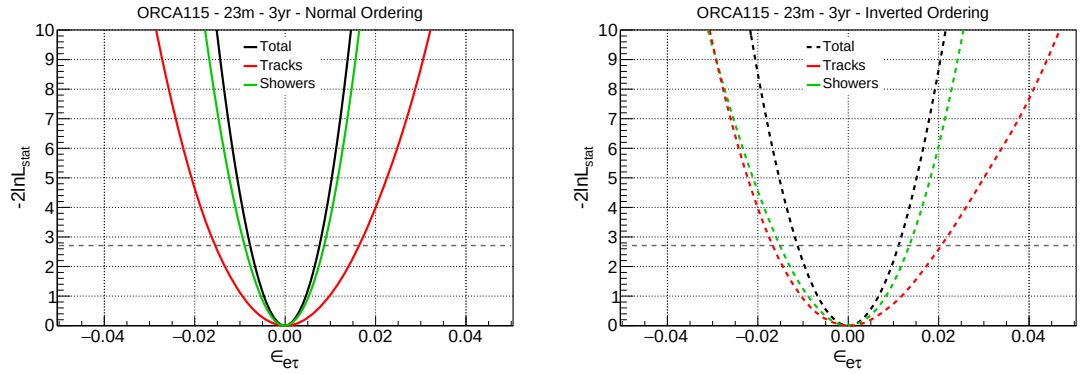

(b) 23 m geometry with 2 event classes: tracks (red) and showers (green).

Figure 4.28: Contribution from tracks (red), middles (blue) and showers (red) to the total statistical significance as a function different test values of $\epsilon_{e\tau}$. See caption of Fig. 4.27 for more info.

NSI $\epsilon_{e\tau}$ modify the ν_e oscillation probabilities and hence get the largest contributions from the shower class (Fig. 4.28). The contribution from the middle class is most pronounced for NSI $\epsilon_{e\tau}$.

NSI $\epsilon_{\mu\tau}$

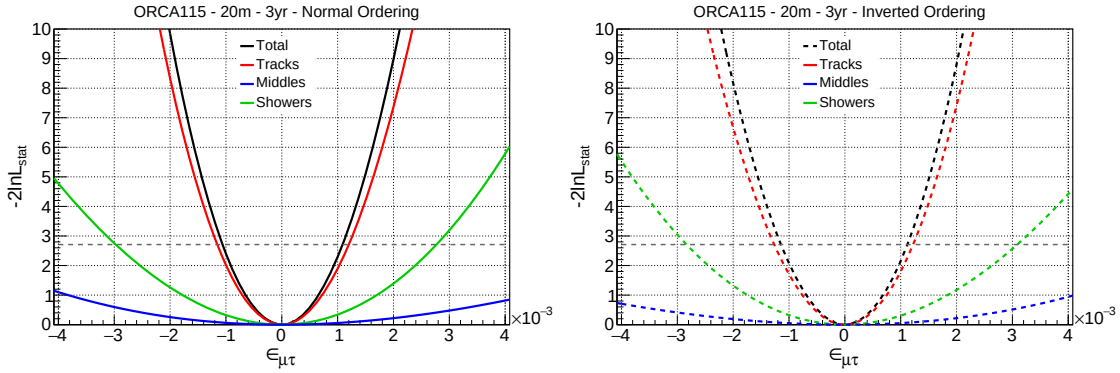

(a) 20 m geometry with 3 event classes: tracks (red), middles (blue) and showers (green).

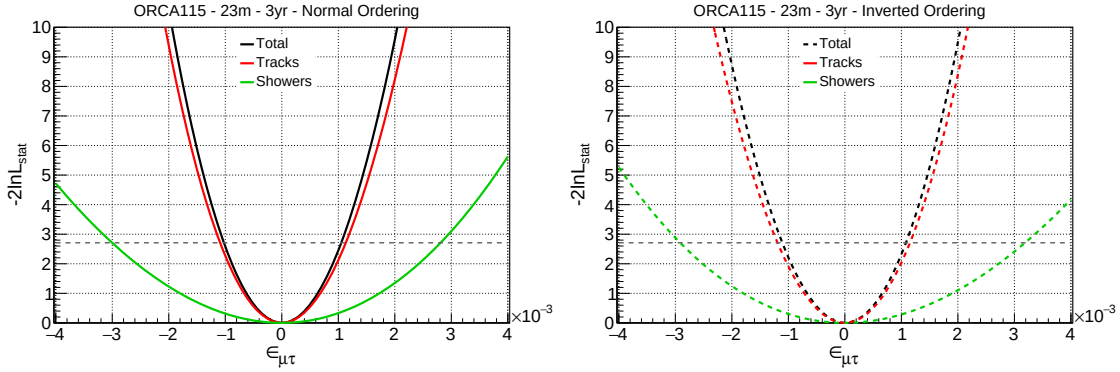

(b) 23 m geometry with 2 event classes: tracks (red) and showers (green).

Figure 4.29: Contribution from tracks (red), middles (blue) and showers (red) to the total statistical significance as a function different test values of $\epsilon_{\mu\tau}$. See caption of Fig. 4.27 for more info.

NSI $\epsilon_{\tau\tau}$

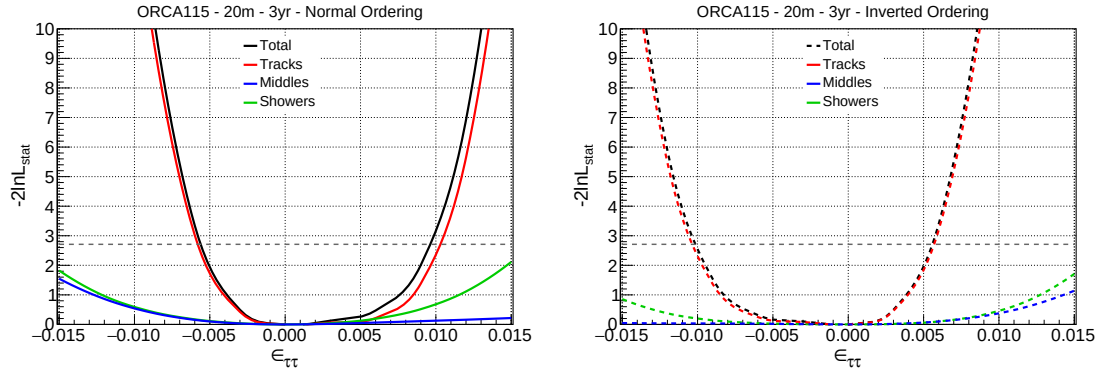

(a) 20 m geometry with 3 event classes: tracks (red), middles (blue) and showers (green).

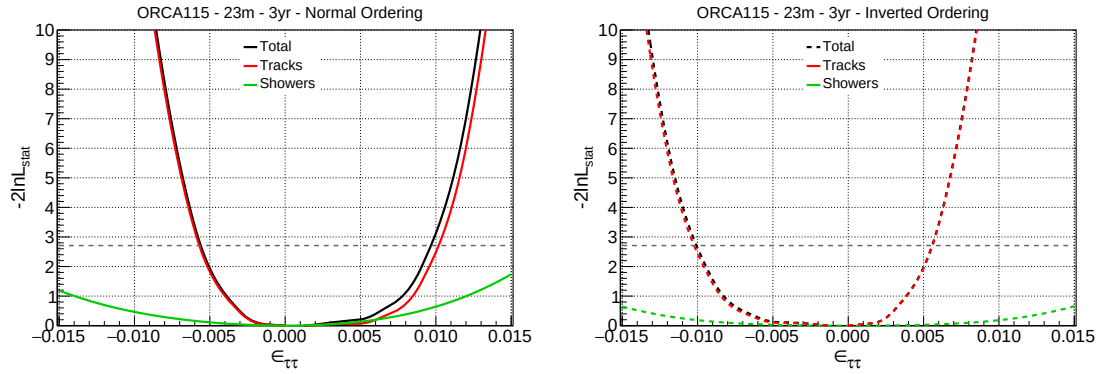

(b) 23 m geometry with 2 event classes: tracks (red) and showers (green).

Figure 4.30: Contribution from tracks (red), middles (blue) and showers (red) to the total statistical significance as a function different test values of $\epsilon_{\mu\tau}$. See caption of Fig. 4.27 for more info.

NSI $\epsilon_{\mu\tau}$ and $\epsilon_{\tau\tau}$ distort the ν_μ oscillation probabilities and get the largest contributions from the track class (Fig. 4.29 and Fig. 4.30).

4.3.3 Systematics

This section discusses the uncertainties associated with the systematics and their impact on the event distribution corresponding to different NSI hypotheses. Tab. 4.7 summarises the exhaustive list of systematic parameters considered in the fit, along with their statistical treatment (fixed or fitted), nominal values and external constraints, if used. They can be grouped in four categories:

Nuisance parameters	Treatment	Nominal values	Priors
Oscillation			
$\theta_{12}(^\circ)$	fixed	33.82	-
$\theta_{13}(^\circ)$	fitted	8.60	0.13
$\theta_{23}(^\circ)$	fitted	48.6	free
$\delta_{CP}(^\circ)$	fitted	221	free
$\Delta m^2_{21}(\times 10^{-5}\text{eV}^2)$	fixed	7.39	-
$\Delta m^2_{31}(\times 10^{-3}\text{eV}^2)$	fitted	2.528	free
Flux			
Track norm.	fitted	1	free
Shower norm.	fitted	1	free
Middle norm.	fitted	1	free
ν_μ/ν_e skew	fitted	0	5%
$\nu_\mu/\overline{\nu}_\mu$ skew	fitted	0	5%
$\nu_e/\overline{\nu}_e$ skew	fitted	0	5%
Energy slope ($\Delta\gamma$)	fitted	0	5%
Zenith slope	fitted	0	2%
Cross-section			
NC scale	fitted	1	5%
Detector			
Energy scale	fitted	1	10%

Table 4.7: The list of systematics studied in the NSI ORCA analysis, along with their statistical treatment, injected nominal and prior values (if any).

- **Oscillation parameters**: The solar parameters (θ_{12}, Δm^2_{21}) are kept fixed at their nominal values (adopted from NuFit v4.1 [90]), since ORCA being an atmospheric oscillation experiment is not very sensitive to them. The mixing angle θ_{13} has a large effect on oscillation probabilities. Hence existing experimental constraints are used to exploit the full potential of ORCA for estimating the sensitivity to the NSI parameters. It is reflected by a prior of 0.13°. No priors are used on the atmospheric oscillation parameters (θ_{23}, Δm^2_{31}) and δ_{CP} since they are also supposed to be measured by ORCA. Due to the degeneracy between the octant of θ_{23} and the sign of Δm^2_{31} ($+/-$ correspond to NO/IO), a starting value of θ_{23} in both octants ($\theta_{23} < 45^\circ \in$ lower octant or $\theta_{23} > 45^\circ \in$ higher octant) is chosen and the minimum value of $-2 \ln \mathcal{L}$ is stored. The effect of these uncertainties on oscillation parameters on the final event distributions are shown in Fig. 4.31 to Fig. 4.34.

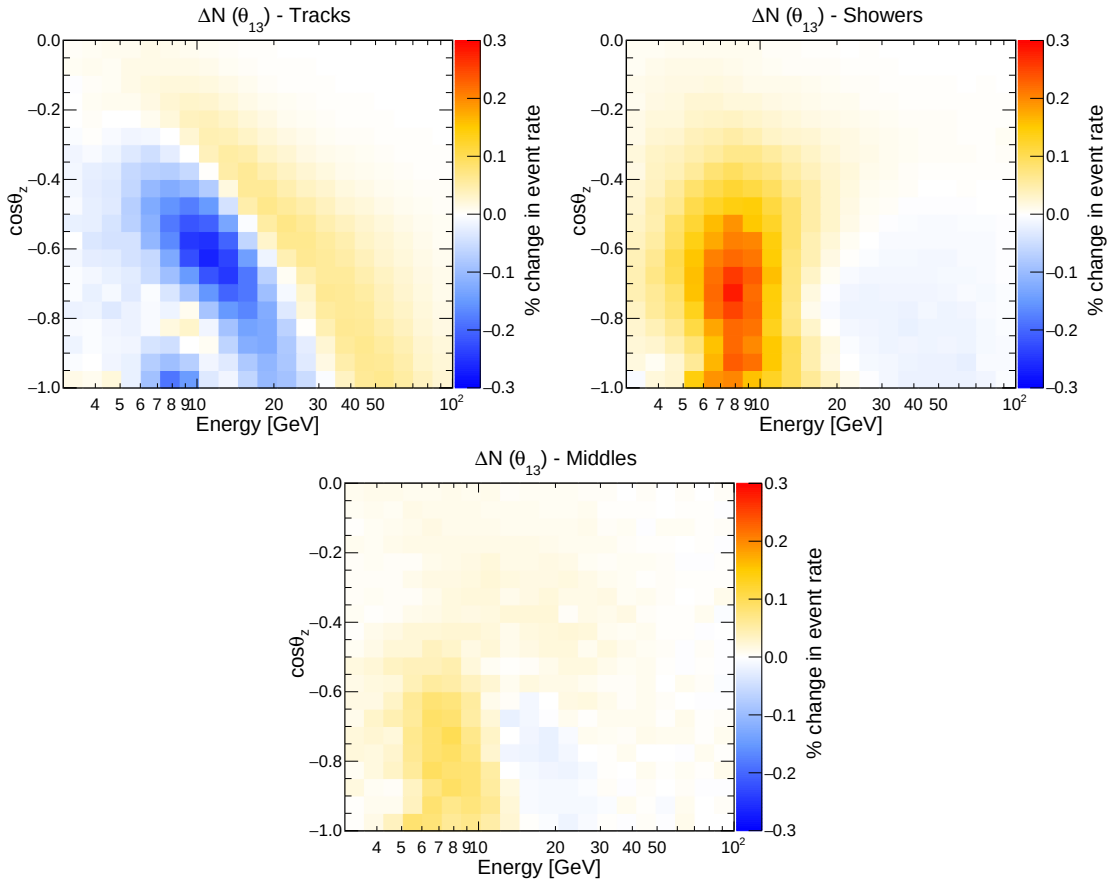

Figure 4.31: Percentage modification of event numbers for tracks (left), middles (middle) and shower (right) classes when θ_{13} is set at $+1\sigma$ away from its nominal value listed in Tab. 4.7. $X-$ and $Y-$axis represent reconstructed energy and cosine of the reconstructed zenith direction, respectively. Modification of event numbers for a test point of θ_{13} at -1σ away from its nominal value is not shown for brevity.

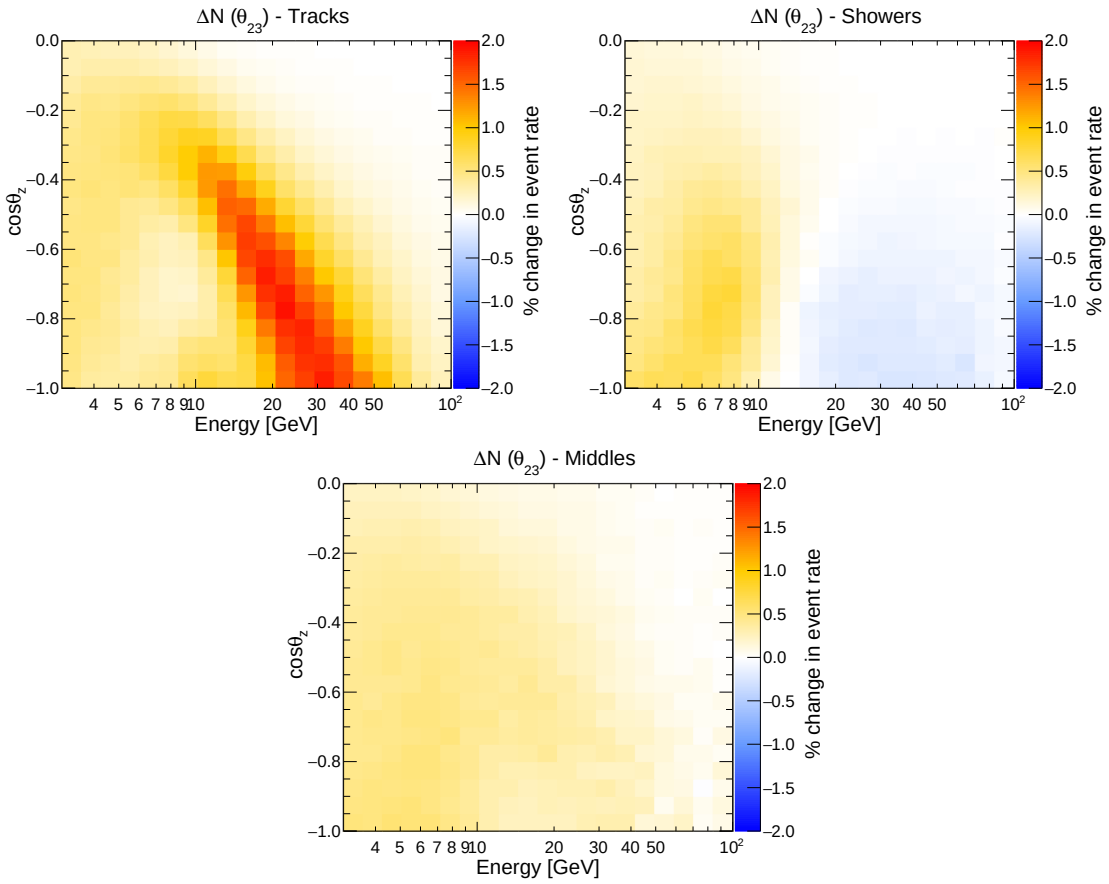

Figure 4.32: Percentage modification of event numbers for tracks (left), middles (middle) and shower (right) classes when θ_{23} is set at $+1\sigma$ away from its nominal value listed in Tab. 4.7. Read caption of Fig. 4.31 for more info.

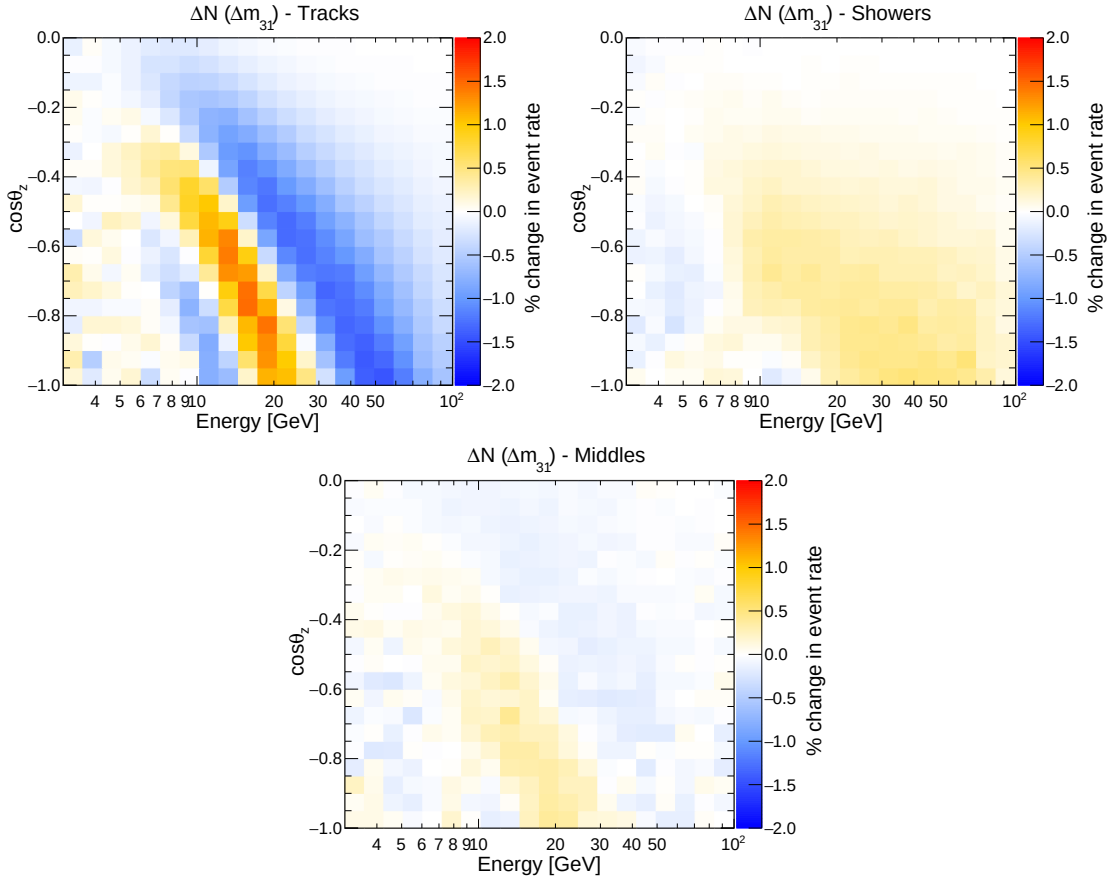

Figure 4.33: Percentage modification of event numbers for tracks (left), middles (middle) and shower (right) classes when Δm^2_{31} is set at $+1\sigma$ away from its nominal value listed in Tab. 4.7. Read caption of Fig. 4.31 for more info.

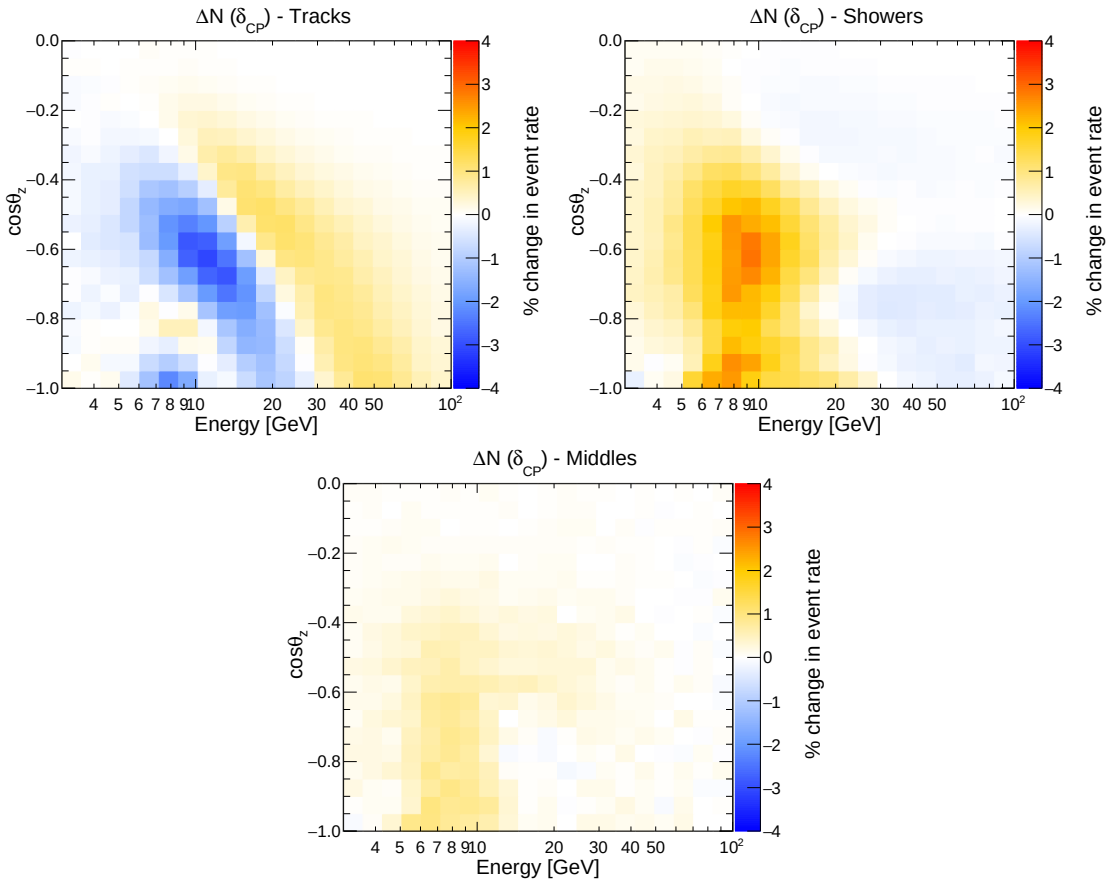

Figure 4.34: Percentage modification of event numbers for tracks (left), middles (middle) and shower (right) classes when δ_{CP} is set at $+1\sigma$ away from its nominal value listed in Tab. 4.7. Read caption of Fig. 4.31 for more info.

- **Flux systematics**: Systematic parameters compared to atmospheric neutrino flux uncertainties are considered. The total number of events in each event class has an associated normalisation factor: "Track norm.", "Middle norm." and "Shower norm.", which is fitted without any constraint. This also takes into account the uncertainty on the effective mass and on the interaction cross-sections of neutrinos. The effective change in the event numbers in any $[E, \cos\theta_z]$ bin is directly proportional to the normalisation factor.

  The ratio between the total number of ν_μ and ν_e ("ν_μ/ν_e skew"), ν_μ and $\overline{\nu}_\mu$ ("$\nu_\mu/\overline{\nu}_\mu$ skew") and ν_e and $\overline{\nu}_e$ ("$\nu_e/\overline{\nu}_e$ skew") events are allowed to vary with a standard deviation of 5% of the parameter nominal value. The prior value (5%), which is independent of energy and zenith angle, is more conservative than the current estimated flux uncertainties [207]. The effect of these uncertainties on the final event distributions are shown in Fig. 4.35 to Fig. 4.37.

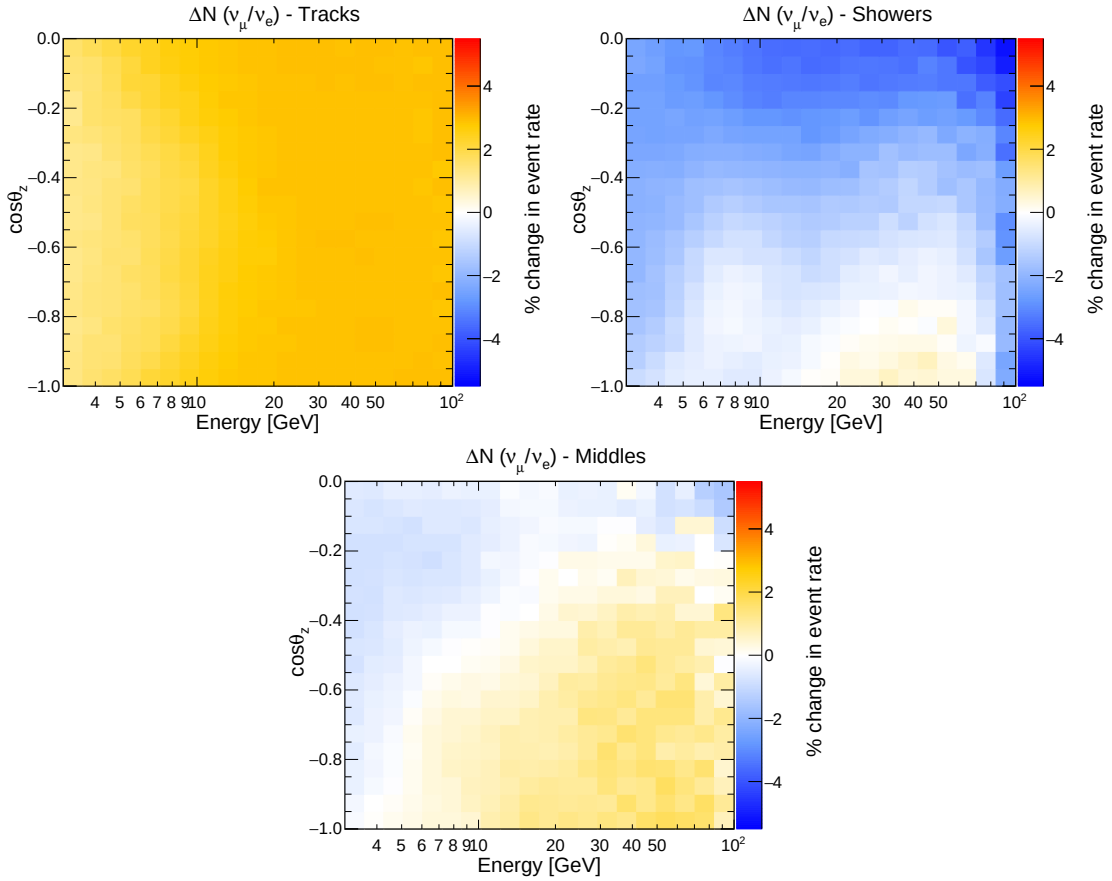

Figure 4.35: Percentage modification of event numbers for tracks (left), middles (middle) and shower (right) classes when ν_μ/ν_e is set at $+5\%$ away from its nominal value listed in Tab. 4.7. Read caption of Fig. 4.31 for more info.

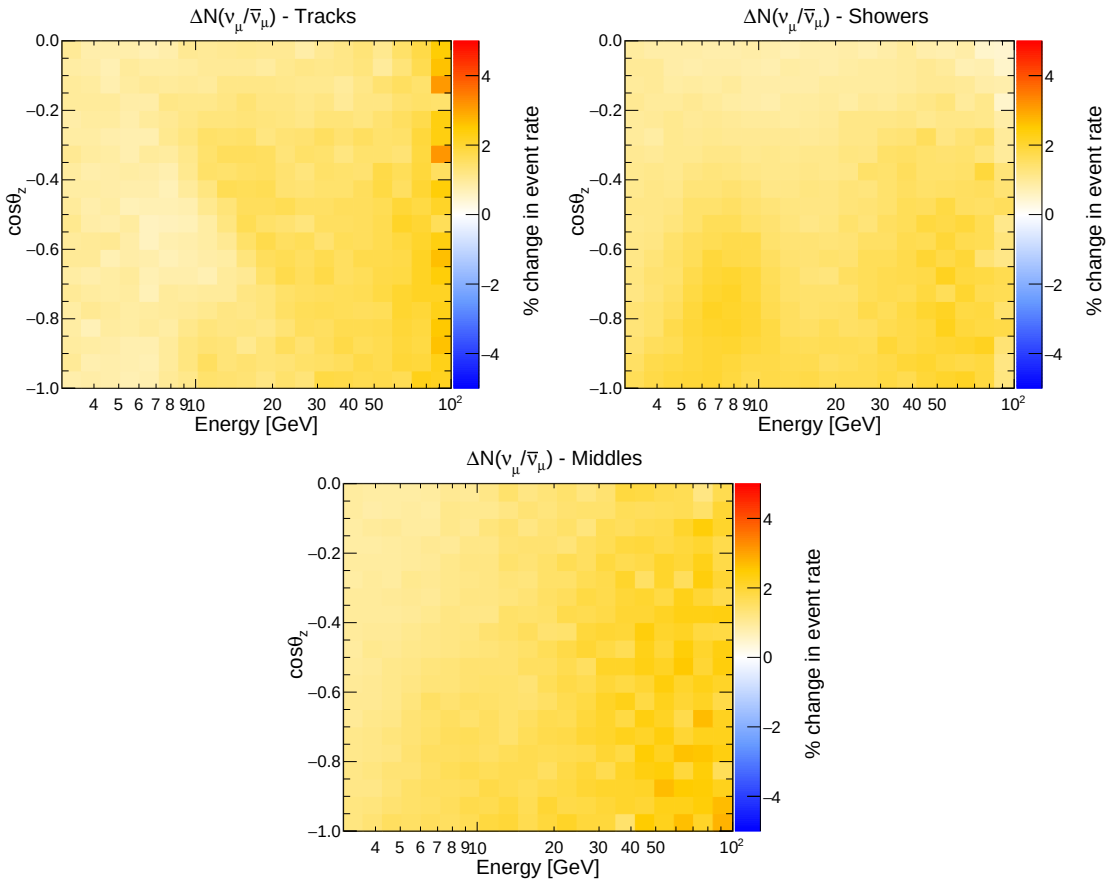

Figure 4.36: Percentage modification of event numbers for tracks (left), middles (middle) and shower (right) classes when $\nu_\mu/\overline{\nu}_\mu$ is set at $+5\%$ away from its nominal value listed in Tab. 4.7. Read caption of Fig. 4.31 for more info.

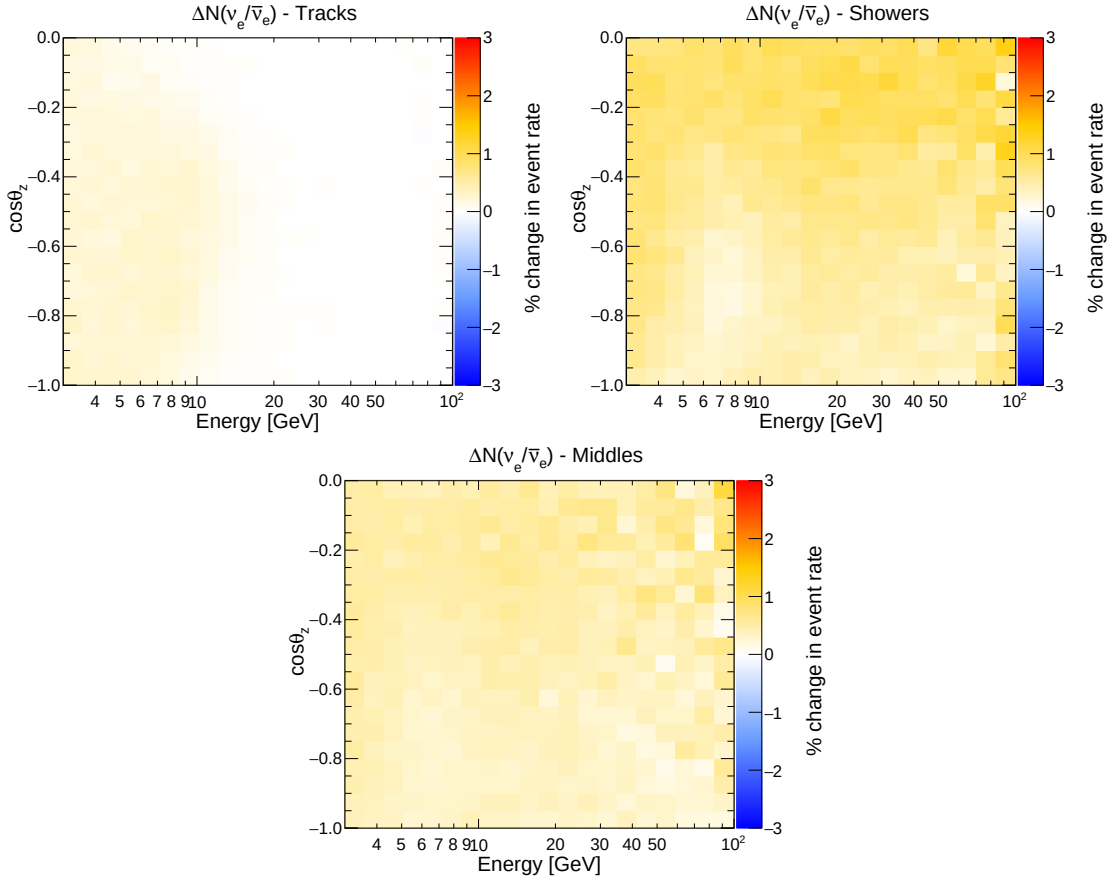

Figure 4.37: Percentage modification of event numbers for tracks (left), middles (middle) and shower (right) classes when $\nu_e/\overline{\nu}_e$ is set at $+5\%$ away from its nominal value listed in Tab. 4.7. Read caption of Fig. 4.31 for more info.

The "energy slope" error $\Delta\gamma$, applied as a function of E_ν^γ, accounts for a change in the neutrino spectrum due to uncertainties in the primary cosmic ray spectrum. The energy slope error is allowed to vary within $\pm 5\%$ around its central value of $\Delta\gamma = 0$. Similarly, the uncertainty on the ratio of up-going to horizontal-going neutrinos, named "zenith slope", is allowed to vary with a standard deviation of 2% of its nominal value. The effect of these uncertainties on the final event distribution is shown in Fig. 4.38 and Fig. 4.39.

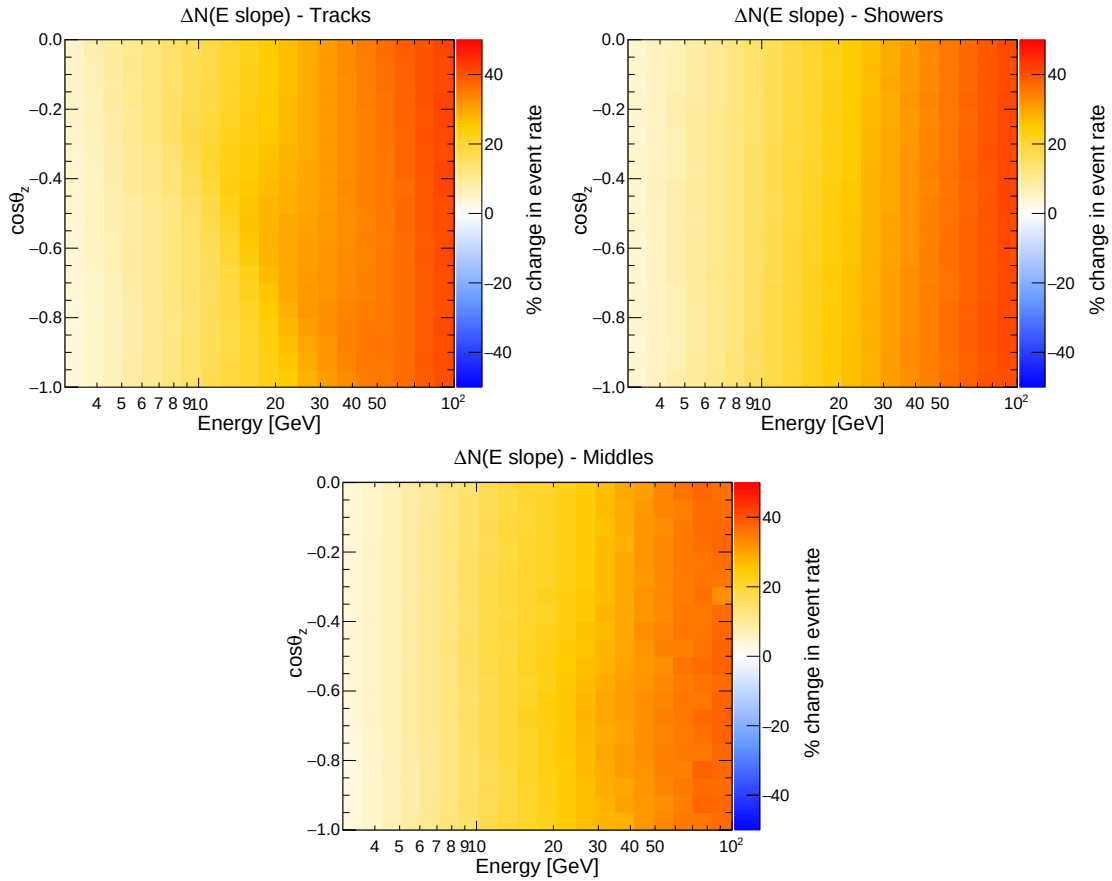

Figure 4.38: Percentage modification of event numbers for tracks (left), middles (middle) and shower (right) classes when energy slope ($\Delta\gamma$) is set at $+10\%$ away from its nominal value listed in Tab. 4.7. Read caption of Fig. 4.31 for more info.

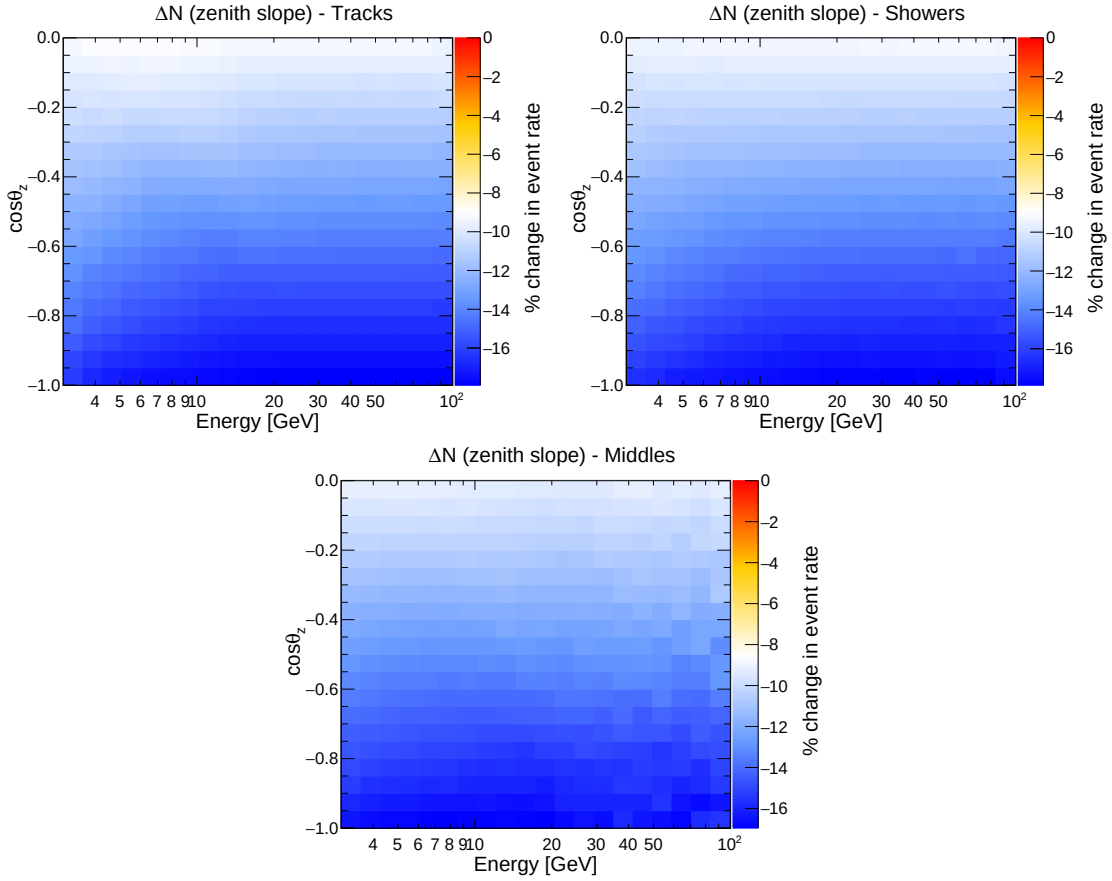

Figure 4.39: Percentage modification of event numbers for tracks (left), middles (middle) and shower (right) classes when zenith slope (ν_{up}/ν_{hor}) is set at $+10\%$ away from its nominal value listed in Tab. 4.7. Read caption of Fig. 4.31 for more info.

- **Cross-section systematics**: While lepton universality means the cross section ratios between flavours are well known, the same is not necessarily the case for the ratio between CC and NC events. Therefore, the neutral current event normalisation is also fitted with a prior of 5%. Uncertainties on the absolute CC and NC cross-sections are not considered in this study. However they would be somewhat absorbed within the flux normalisations. The effect of NC scale normalisation on the final event distribution is shown in Fig. 4.40.

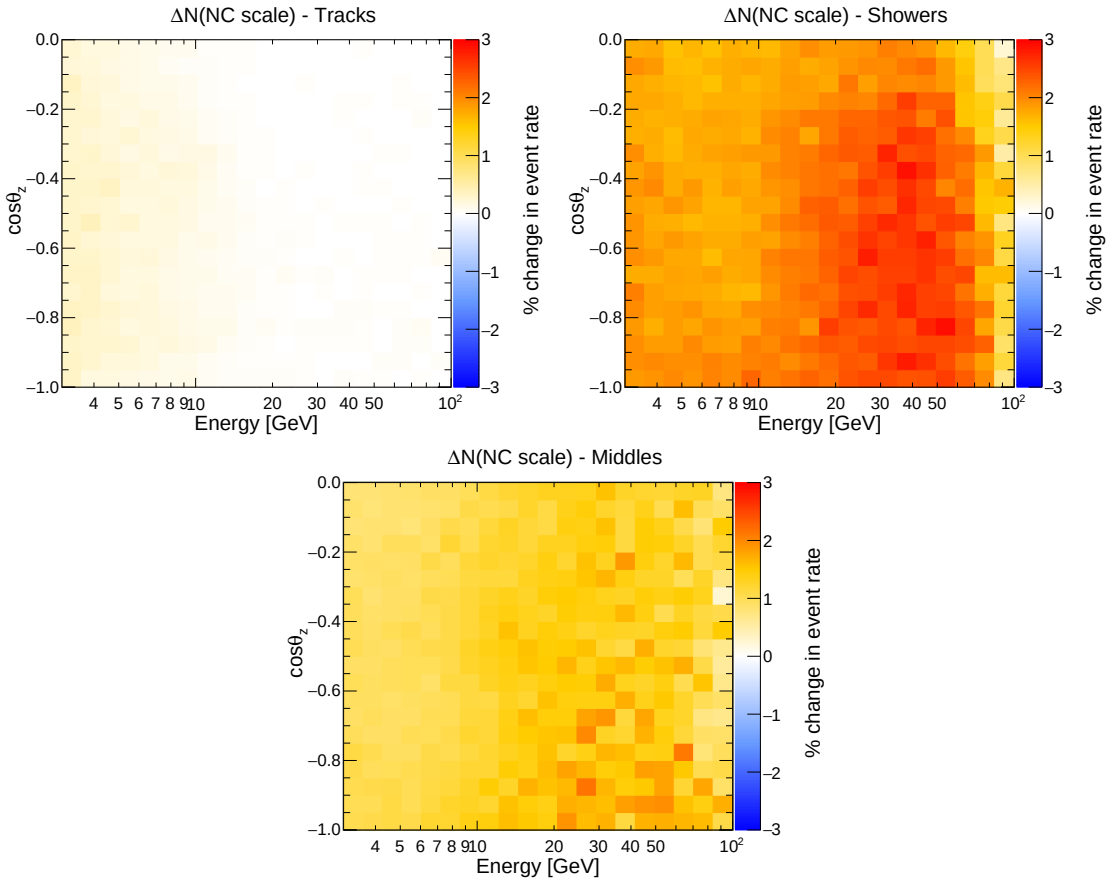

Figure 4.40: Percentage modification of event numbers for tracks (left), middles (middle) and shower (right) classes when NC scale factor is set at $+1\sigma$ away from its nominal value listed in Tab. 4.7. Read caption of Fig. 4.31 for more info.

- **Detector systematics**: Among the systematic parameters incorporated into this analysis, the track, middle and shower normalisations and energy scale can be considered detector effects. The energy scale depends on the PMT efficiencies and water properties [179]. If events are systematically brighter or less bright than expected, this will cause a shift to the normalisation of the effective mass. This is accounted in the energy scale which is fitted with a 10% Gaussian width across its nominal value.

Analysis

Systematics are included in our simulation using the "pull" method described in [208, 209]. The final fit is done following an Asimov dataset [187] approach, by minimising the Poissonian log-likelihood ratio function:

$$-2\ln\mathcal{L} = 2\cdot\sum_{i\in\{bins\}}\left[N_i^{\text{test}}(\bar{o},\bar{s}) - N_i^{\text{true}}(\bar{o},\bar{s}) + N_i^{\text{true}}\cdot\ln\frac{N_i^{\text{true}}(\bar{o},\bar{s})}{N_i^{\text{test}}(\bar{o},\bar{s})}\right] + \sum_{j\in\{syst\}}\frac{(s_j-\hat{s}_j)^2}{\sigma_{s_j}^2}. \tag{4.20}$$

The number of predicted events N_i in the i^{th} bin is a function of the set of oscillation and NSI parameters, $\bar{o}$, as well as on the the set of parameters related to systematic uncertainties, $\bar{s}$. $N_i^{\text{true}}(\bar{o},\bar{s})$ is the expected number of track/middles/shower events in the i^{th} bin weighted under a certain standard oscillation hypothesis with parameters adopted from NuFit 4.1 [90]; while, $N_i^{\text{test}}(\bar{o},\bar{s})$ is the number of expected events in the i^{th} bin with non-zero test values of NSI parameters. The first sum runs over the histogram bins $E_{reco}, \cos\theta_{reco}$. The second sum runs over penalty terms of the number of nuisance parameters, j, listed in Tab. 4.7, $\hat{s}_j$ and $\sigma_{s_j}^2$ being the assumed prior and Gaussian standard deviation of the parameter j, respectively.

The effect of systematics on the sensitivity to NSI parameters ($\epsilon_{e\mu}$, $\epsilon_{e\tau}$, $\epsilon_{\mu\tau}$ and $\epsilon_{\tau\tau}$), when fitted uniquely or cumulatively are shown in Fig. 4.41 to Fig. 4.56 for two possible detector geometries corresponding to 20 m and 23 m horizontal spacing between DUs and for NO and IO truth assumptions. The systematic with the most drastic effect on the sensitivity to a particular NSI parameter corresponds to the curve that lies farthest from the statistical-only (black) curve in all the figures.

NSI $\epsilon_{e\mu}$ - Normal Ordering

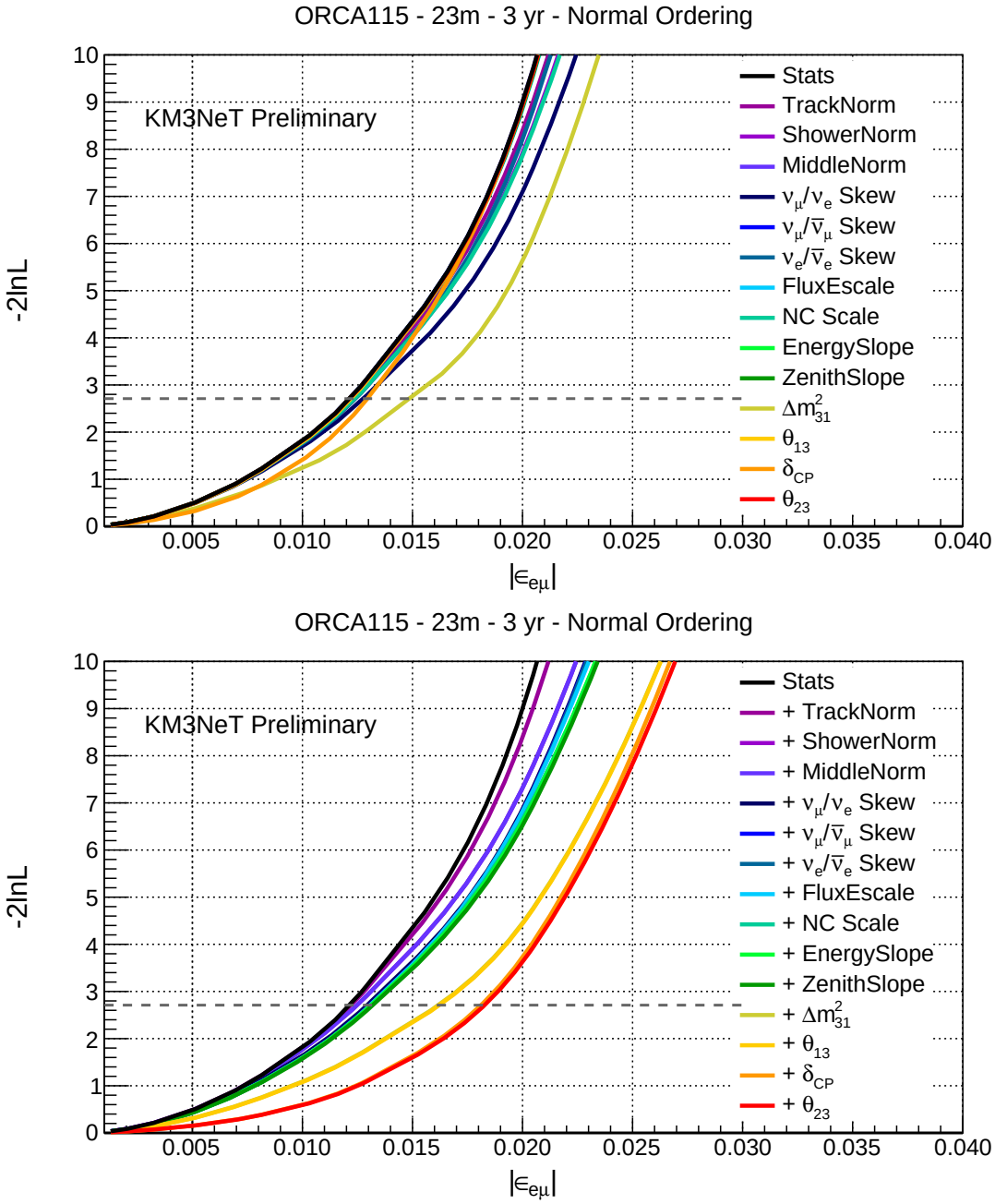

Figure 4.41: Effect of systematics (listed in Tab. 4.7), when fitted uniquely (top) and incrementally (bottom), on the sensitivity to $\epsilon_{e\mu}$ at ORCA with 23 m horizontal spacing for NO assumption and 3 years of runtime. The black curve on both panels corresponds to the statistical-only sensitivity. The effect of systematics represented by colour coded curves at a particular NSI point can be gauged by looking at the relative separation from the stat-only curve. **Top**: each colour coded curve refers to the effect of that particular systematic which is uniquely fitted while the rest are kept fixed at their nominal values. **Bottom**: each colour coded curve corresponds to the effect of that particular systematic plus (+) the ones appearing on top of it being fitted simultaneously. The systematics are added cumulatively in the sequence as they appear in the legends from violet to red. The final sensitivity can be read from the widest (red) curve, which refers to the case of inclusion of all the systematic uncertainties accounted in this study throughout this thesis. Negative NSI points are not scanned for brevity.

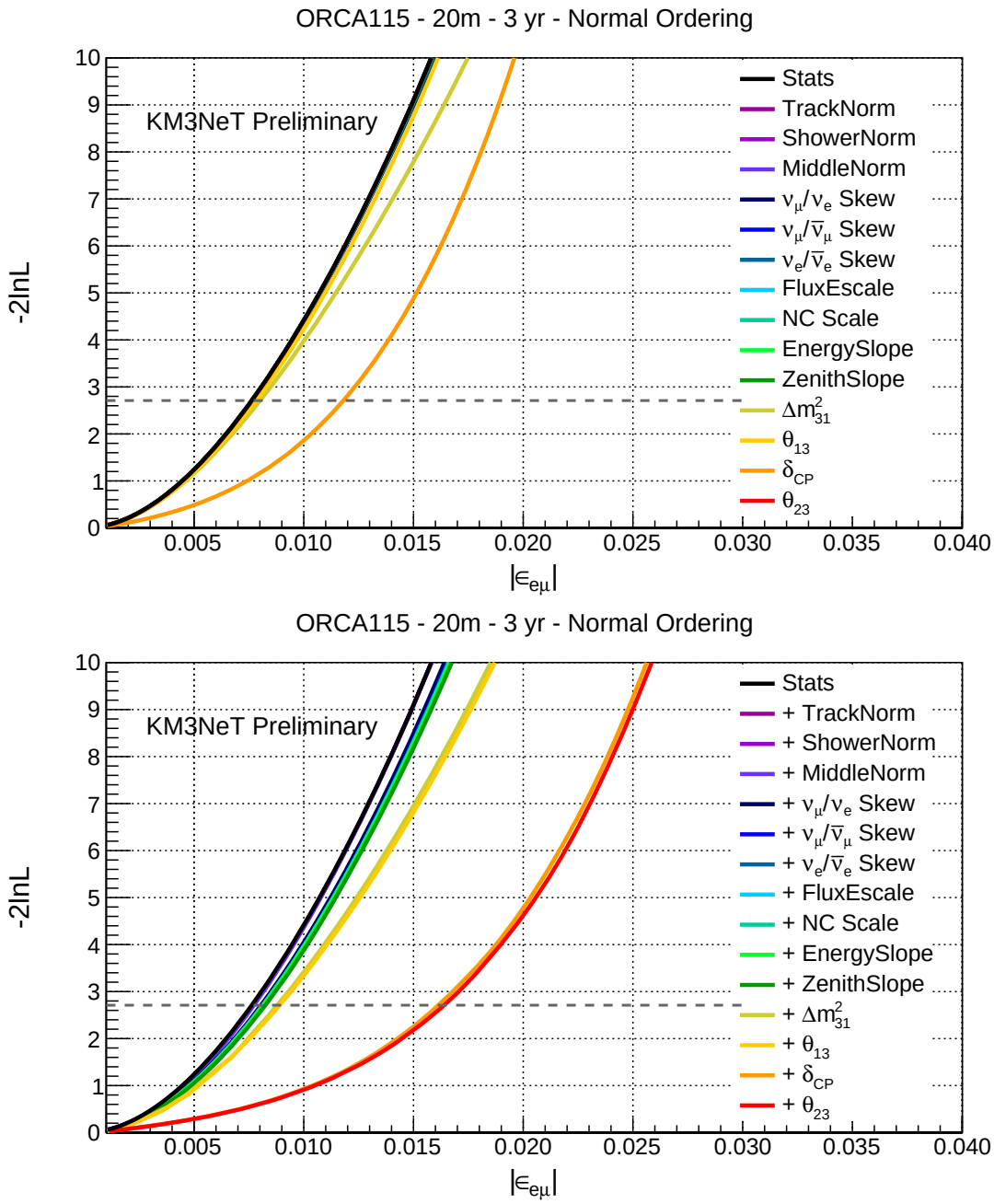

Figure 4.42: Effect of systematics (Tab. 4.7) when fitted uniquely (top) and incrementally (bottom) on the sensitivity to $\epsilon_{e\mu}$ at ORCA with 20 m horizontal spacing for NO assumption. See caption of Fig. 4.41 for more info.

θ_{13} and δ_{CP} are found to exhibit strong pulls in the cumulative fits of NSI $\epsilon_{e\mu}$ assuming normal ordering (NO), as seen in the lower panels of Fig. 4.41 and Fig. 4.42. The effect of the uncertainty on θ_{23} (which is fitted with a starting value in both octants) is rather negligible. The ordering is assumed to be known (NO) and kept fixed in the fit.

NSI $\epsilon_{e\mu}$ - Inverted Ordering

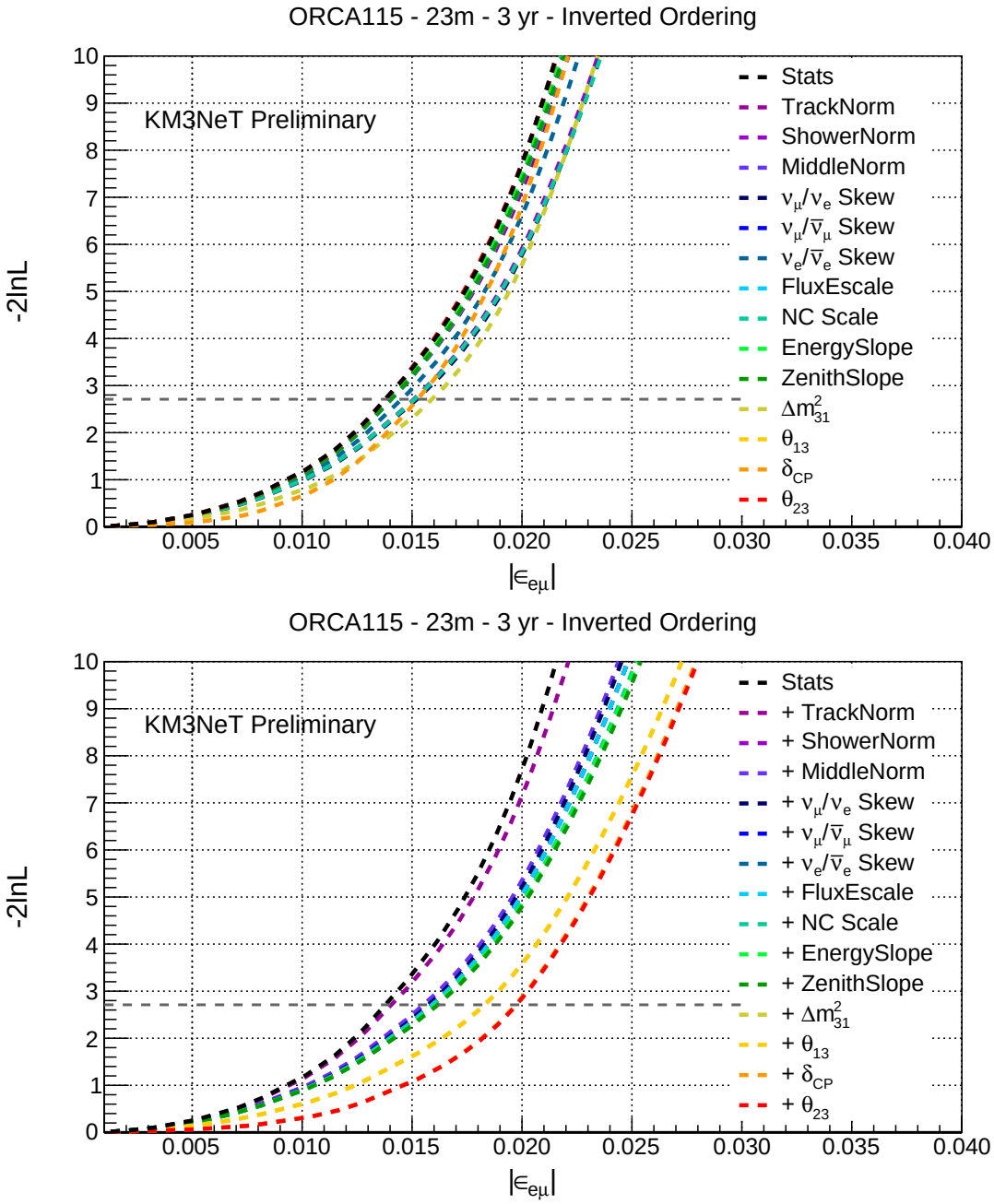

Figure 4.43: Effect of systematics (Tab. 4.7), when fitted uniquely (top) and incrementally (bottom), on the sensitivity to $\epsilon_{e\mu}$ at ORCA with 23 m horizontal spacing for IO assumption. See caption of Fig. 4.41 for more info.

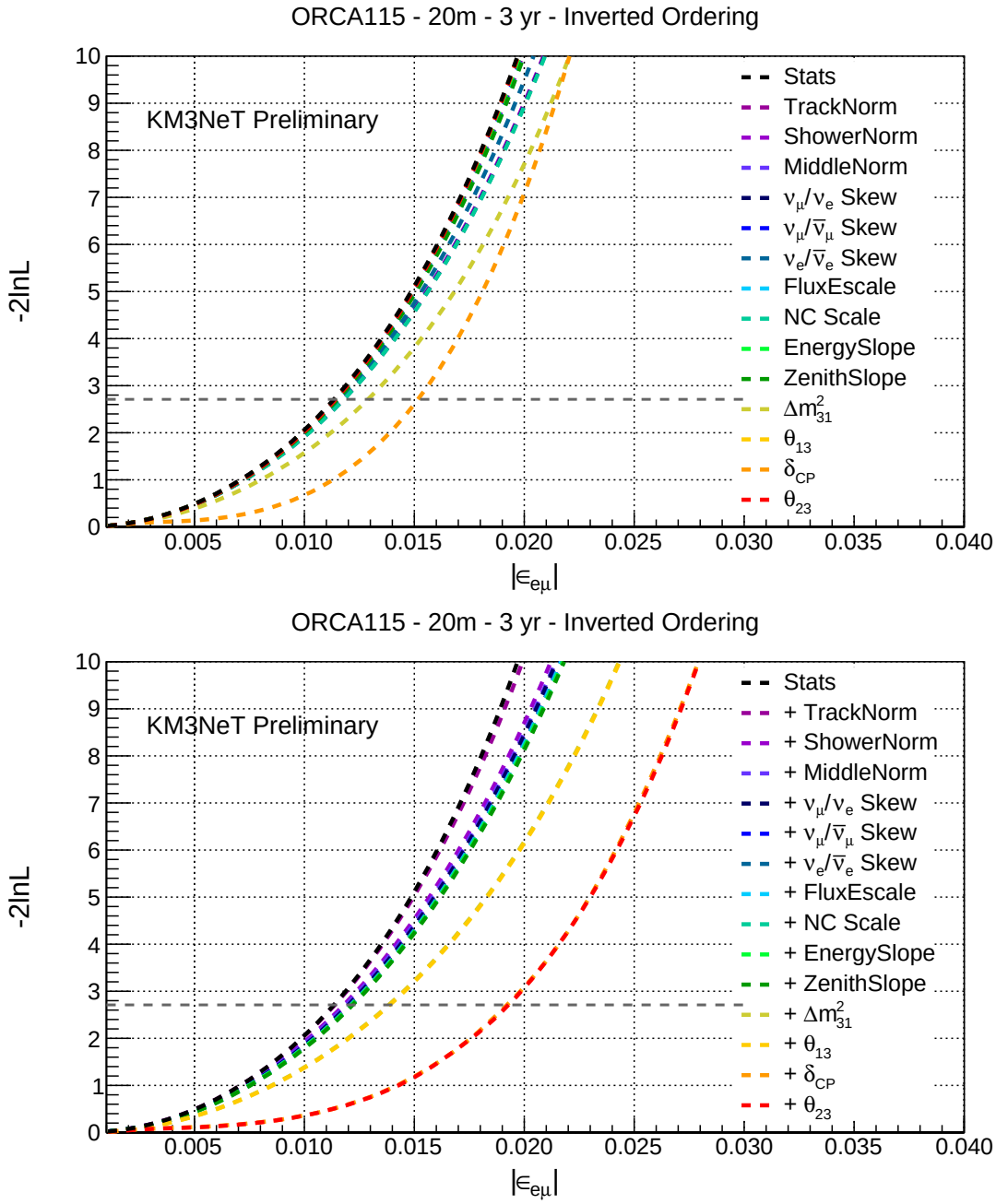

Figure 4.44: Effect of systematics (Tab. 4.7), when fitted uniquely (top) and incrementally (bottom), on the sensitivity to $\epsilon_{e\mu}$ at ORCA with 20 m horizontal spacing for IO assumption. See caption of Fig. 4.41 for more info.

θ_{13} and δ_{CP} are found to exhibit strong pulls in the cumulative fits of NSI $\epsilon_{e\mu}$ assuming inverted ordering (IO), as seen in the lower panels of Fig. 4.43 and Fig. 4.44. The effect of the uncertainty on θ_{23} (which is fitted with a starting value in both octants) is rather negligible. The ordering is assumed to be known (IO) and kept fixed in the fit.

NSI $\epsilon_{e\tau}$ - Normal Ordering

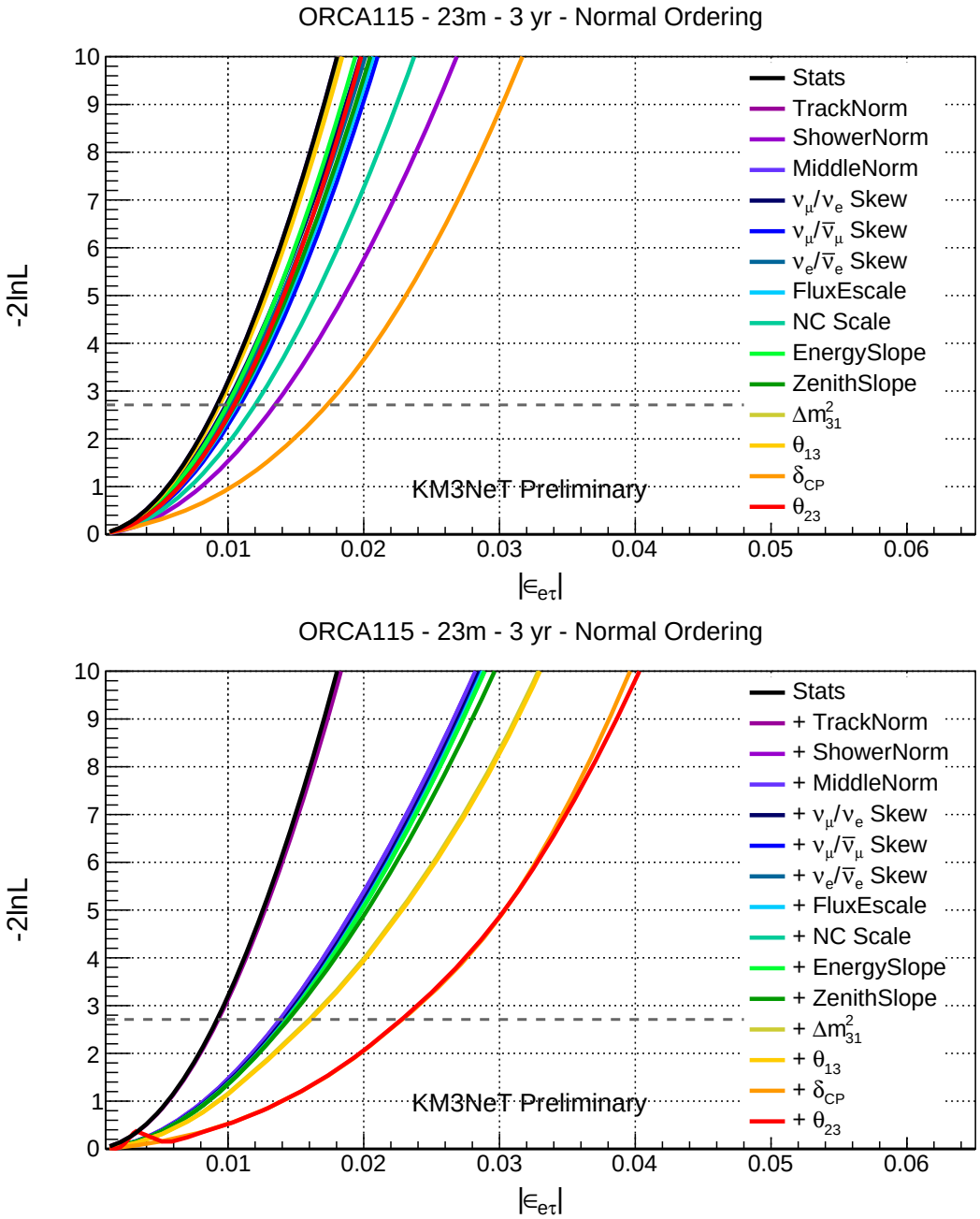

Figure 4.45: Effect of systematics (Tab. 4.7) when fitted uniquely (top) and incrementally (bottom) on the sensitivity to $\epsilon_{e\tau}$ at ORCA with 23 m horizontal spacing for NO assumption. See caption of Fig. 4.41 for more info.

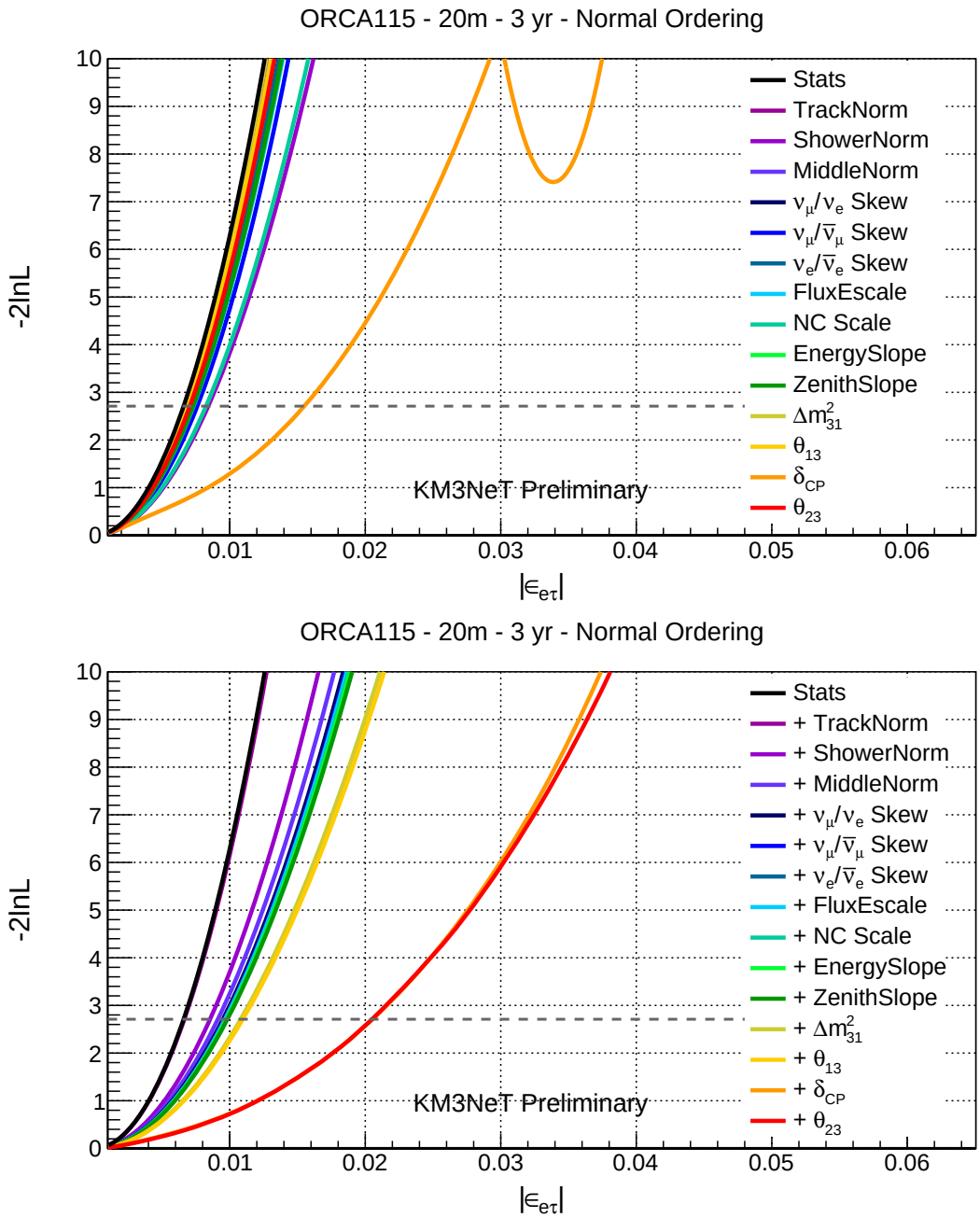

Figure 4.46: Effect of systematics (Tab. 4.7) when fitted uniquely (top) and incrementally (bottom) on the sensitivity to $\epsilon_{e\tau}$ at ORCA with 20 m horizontal spacing for NO assumption. See caption of Fig. 4.41 for more info.

Since sensitivity on $\epsilon_{e\tau}$ is mostly driven by the shower channel, a non-trivial pull is exhibited by the shower normalisation. Besides this, δ_{CP} is found to employ a strong pull in the cumulative fits of NSI $\epsilon_{e\tau}$ assuming normal ordering, as seen in the lower panels of Fig. 4.45 and Fig. 4.46. The effect of the uncertainty on θ_{23} (which is fitted with a starting value in both octants) is rather negligible. The ordering is assumed to be known (NO) and kept fixed in the fit.

NSI $\epsilon_{e\tau}$ - Inverted Ordering

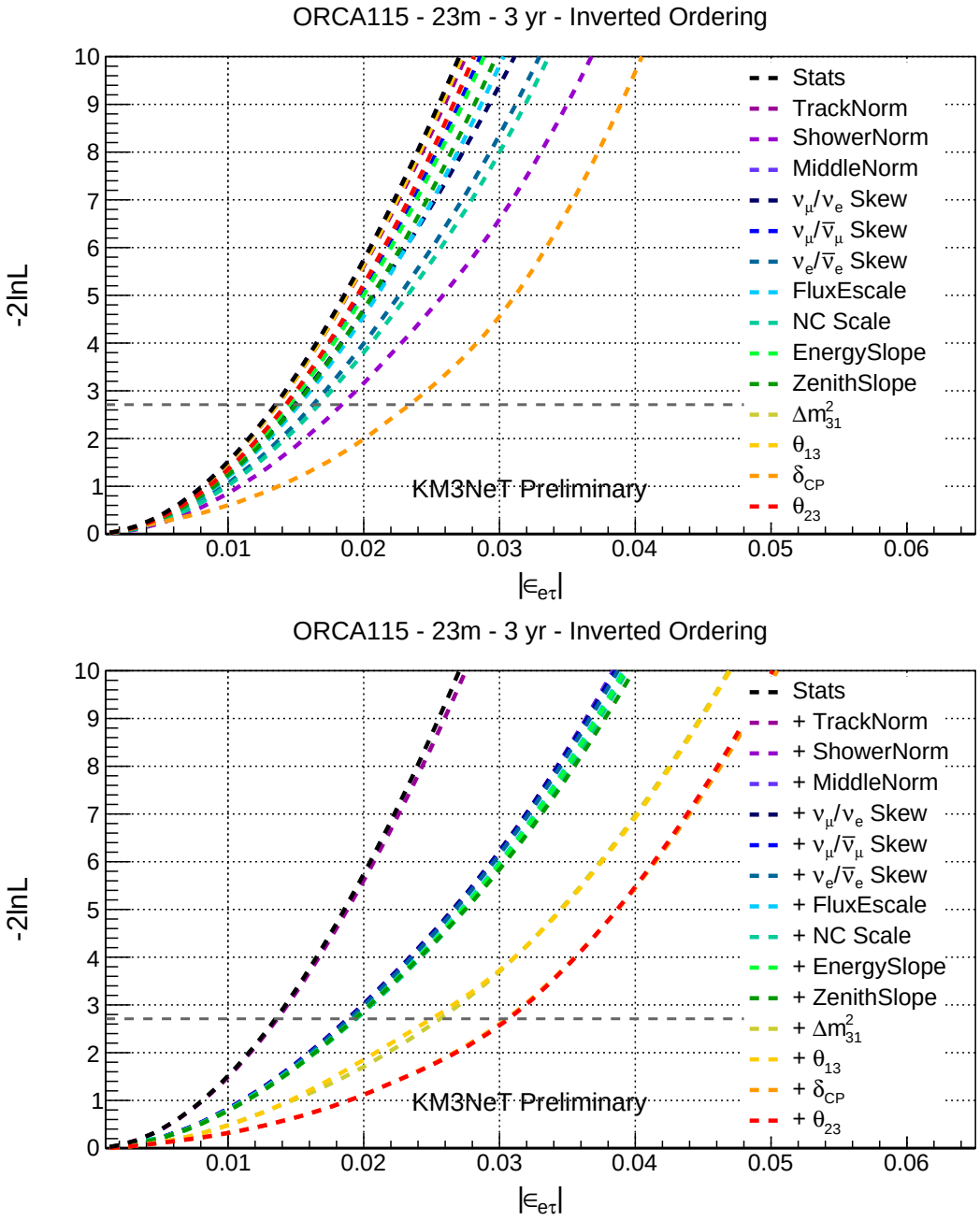

Figure 4.47: Effect of systematics (Tab. 4.7) when fitted uniquely (top) and incrementally (bottom) on the sensitivity to $\epsilon_{e\tau}$ at ORCA with 23 m horizontal spacing for IO assumption. See caption of Fig. 4.41 for more info.

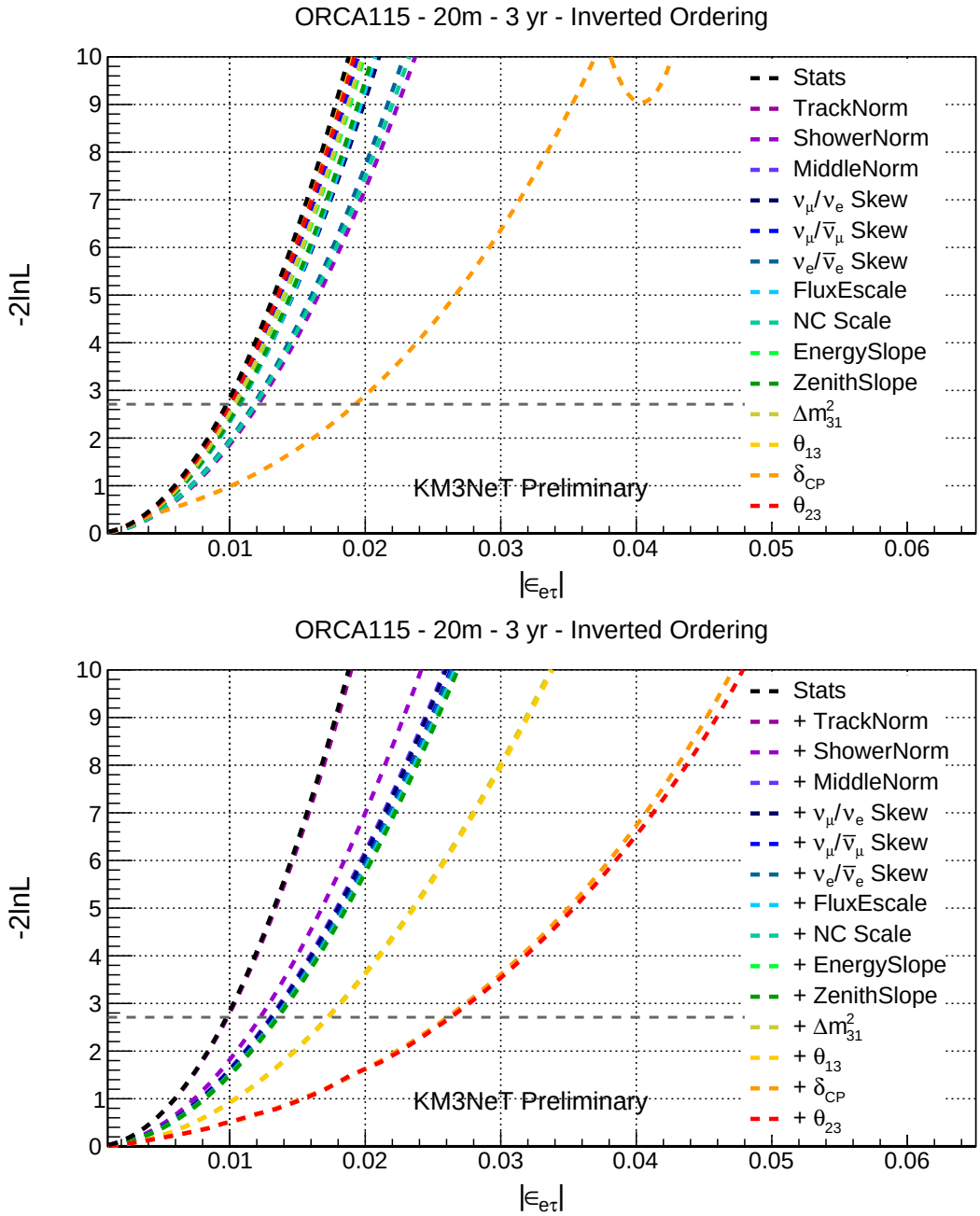

Figure 4.48: Effect of systematics (Tab. 4.7) when fitted uniquely (top) and incrementally (bottom) on the sensitivity to $\epsilon_{e\tau}$ at ORCA with 20 m horizontal spacing for IO assumption. See caption of Fig. 4.41 for more info.

Similar to the NO case, a non-trivial pull is exhibited by the shower normalisation, since sensitivity on $\epsilon_{e\tau}$ is mostly driven by the shower channel. δ_{CP} is found to employ a strong pull in the cumulative fits of NSI $\epsilon_{e\tau}$ assuming inverted ordering, as seen in the lower panels of Fig. 4.47 and Fig. 4.48. The effect of the uncertainty on θ_{23} (which is fitted with a starting value in both octants) is rather negligible. The ordering is assumed to be known (IO) and kept fixed in the fit.

NSI $\epsilon_{\mu\tau}$ - Normal Ordering

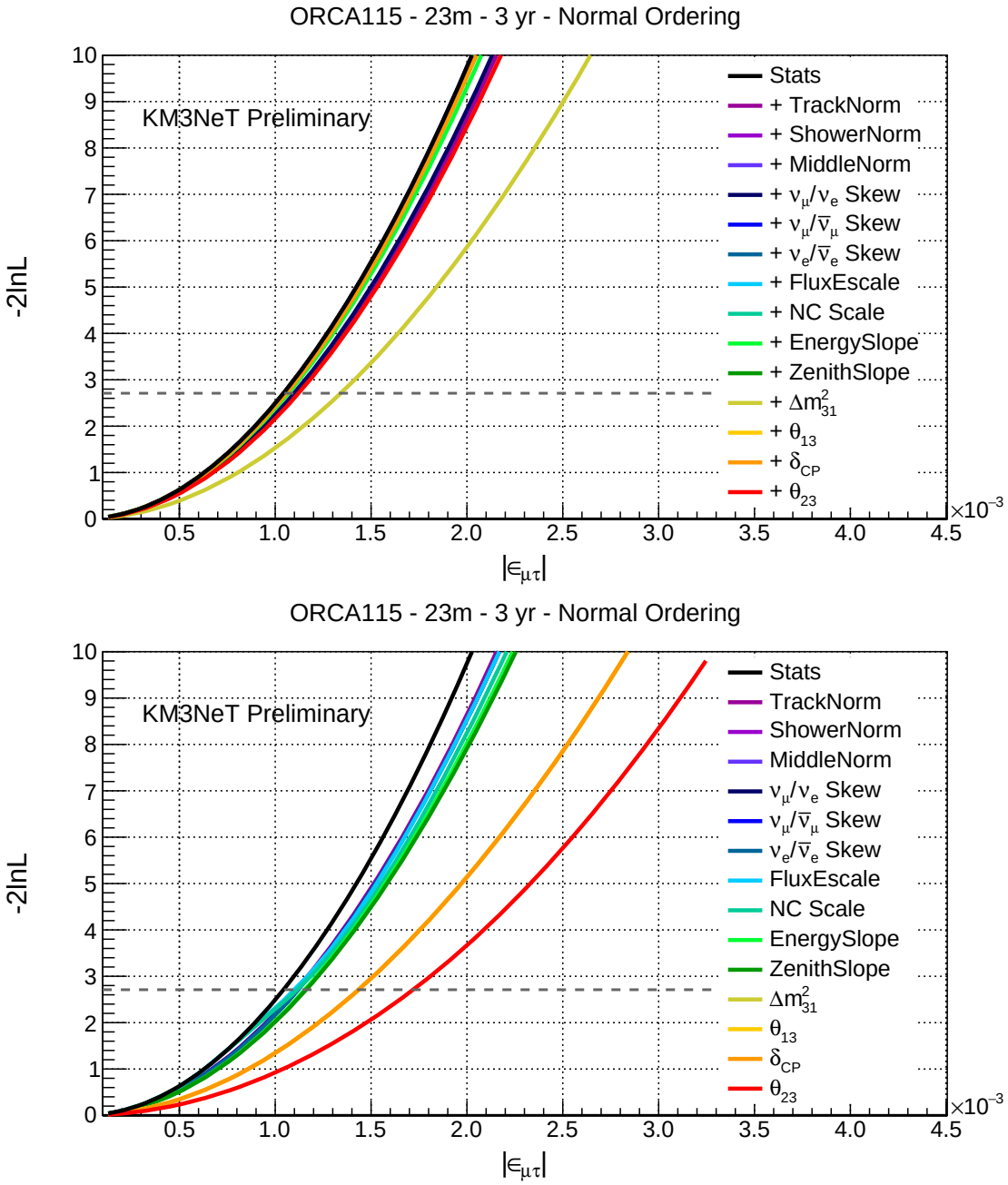

Figure 4.49: Effect of systematics (Tab. 4.7) when fitted uniquely (top) and incrementally (bottom) on the sensitivity to $\epsilon_{\mu\tau}$ at ORCA with 23 m horizontal spacing for NO assumption. See caption of Fig. 4.41 for more info.

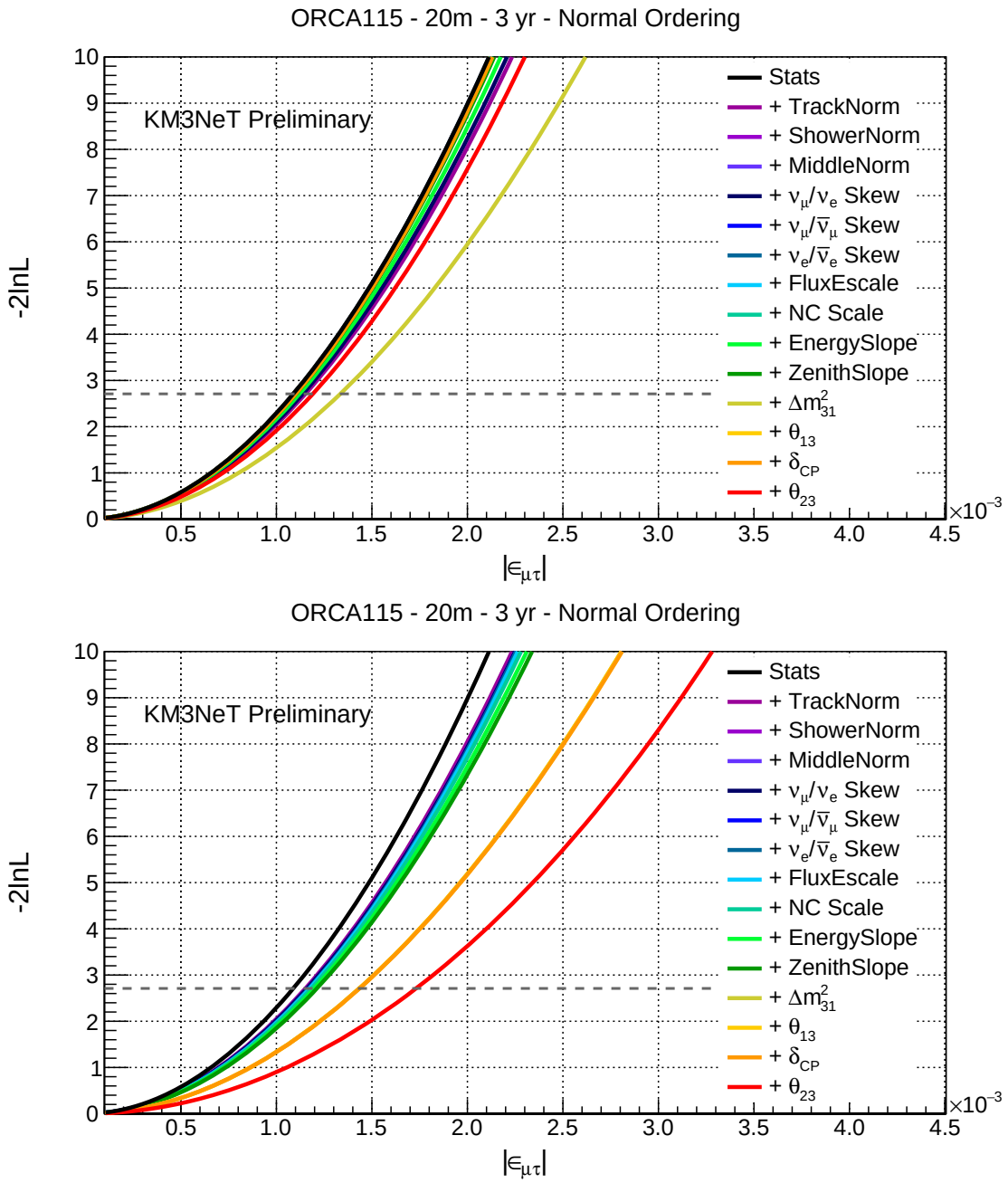

Figure 4.50: Effect of systematics (Tab. 4.7) when fitted uniquely (top) and incrementally (bottom) on the sensitivity to $\epsilon_{\mu\tau}$ at ORCA with 20 m horizontal spacing for NO assumption. See caption of Fig. 4.41 for more info.

Since sensitivity on $\epsilon_{\mu\tau}$ is mostly driven by the track channel, a non-trivial pull is exhibited by the track normalisation. Besides this, δ_{CP} and θ_{23} are found to employ strong pulls in the cumulative fits of NSI $\epsilon_{\mu\tau}$ assuming normal ordering, as seen in the lower panels of Fig. 4.49 and Fig. 4.50. The ordering is assumed to be known (NO) and kept fixed in the fit.

NSI $\epsilon_{\mu\tau}$ - Inverted Ordering

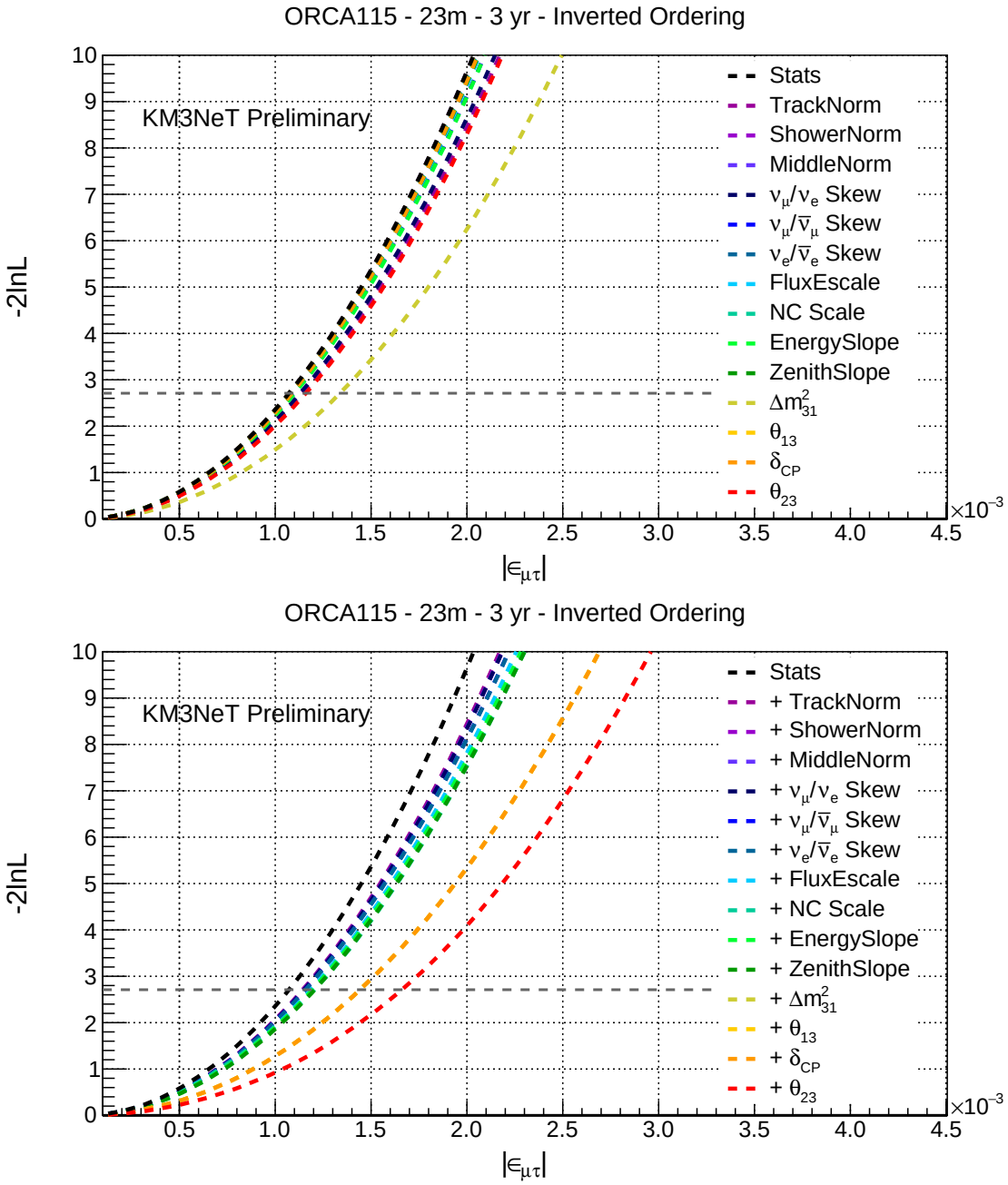

Figure 4.51: Effect of systematics (Tab. 4.7) when fitted uniquely (top) and incrementally (bottom) on the sensitivity to $\epsilon_{\mu\tau}$ at ORCA with 23 m horizontal spacing for IO assumption. See caption of Fig. 4.41 for more info.

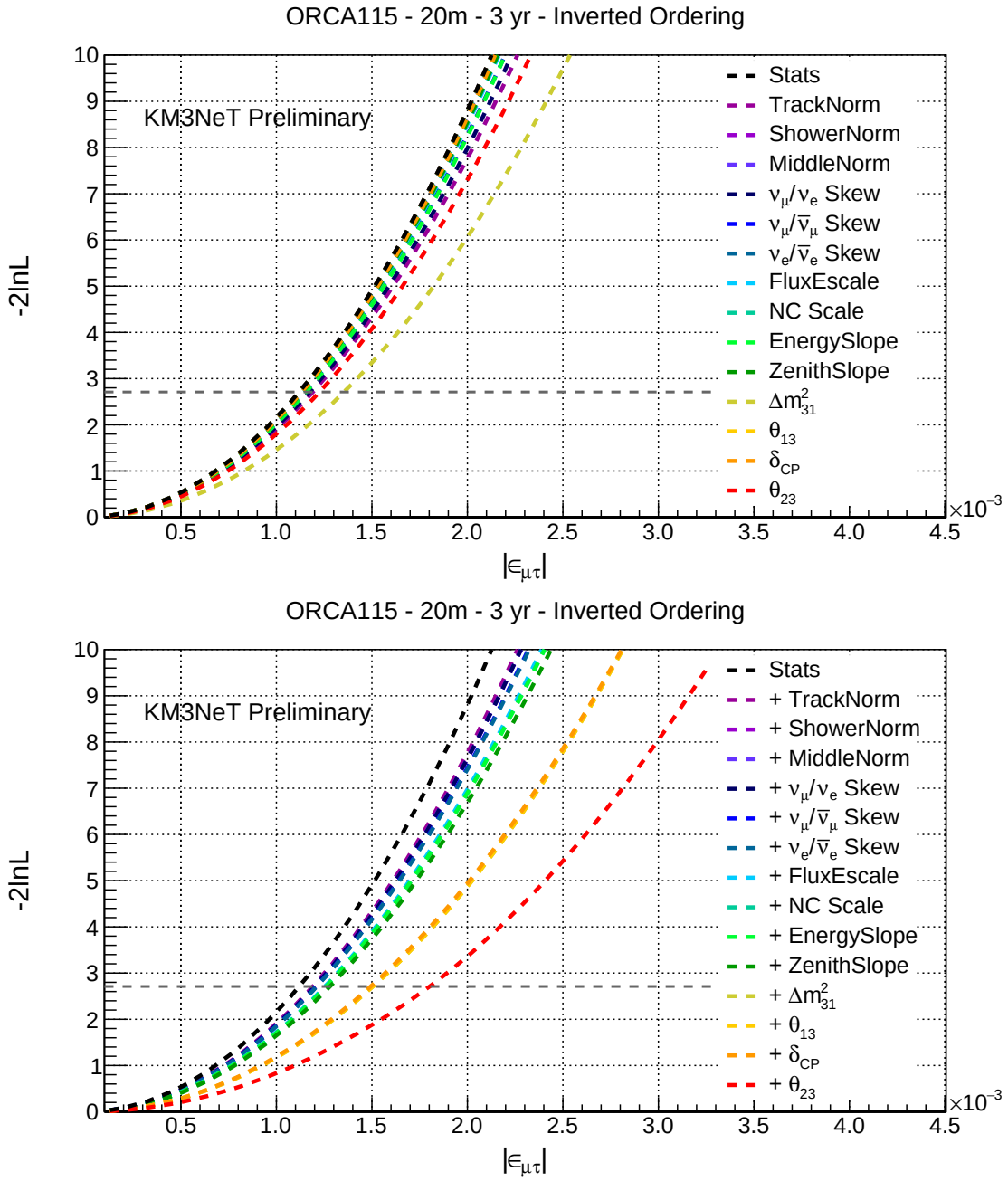

Figure 4.52: Effect of systematics (Tab. 4.7) when fitted uniquely (top) and incrementally (bottom) on the sensitivity to $\epsilon_{\mu\tau}$ at ORCA with 20 m horizontal spacing for IO assumption. See caption of Fig. 4.41 for more info.

Similar to NO case, a non-trivial pull is exhibited by the track normalisation, since sensitivity on $\epsilon_{\mu\tau}$ is mostly driven by the track channel. Besides this, δ_{CP} and θ_{23} are found to employ strong pulls in the cumulative fits of NSI $\epsilon_{\mu\tau}$ assuming inverted ordering, as seen in the lower panels of Fig. 4.51 and Fig. 4.52. The ordering is assumed to be known (IO) and kept fixed in the fit.

NSI $\epsilon_{\tau\tau}$ - Normal ordering

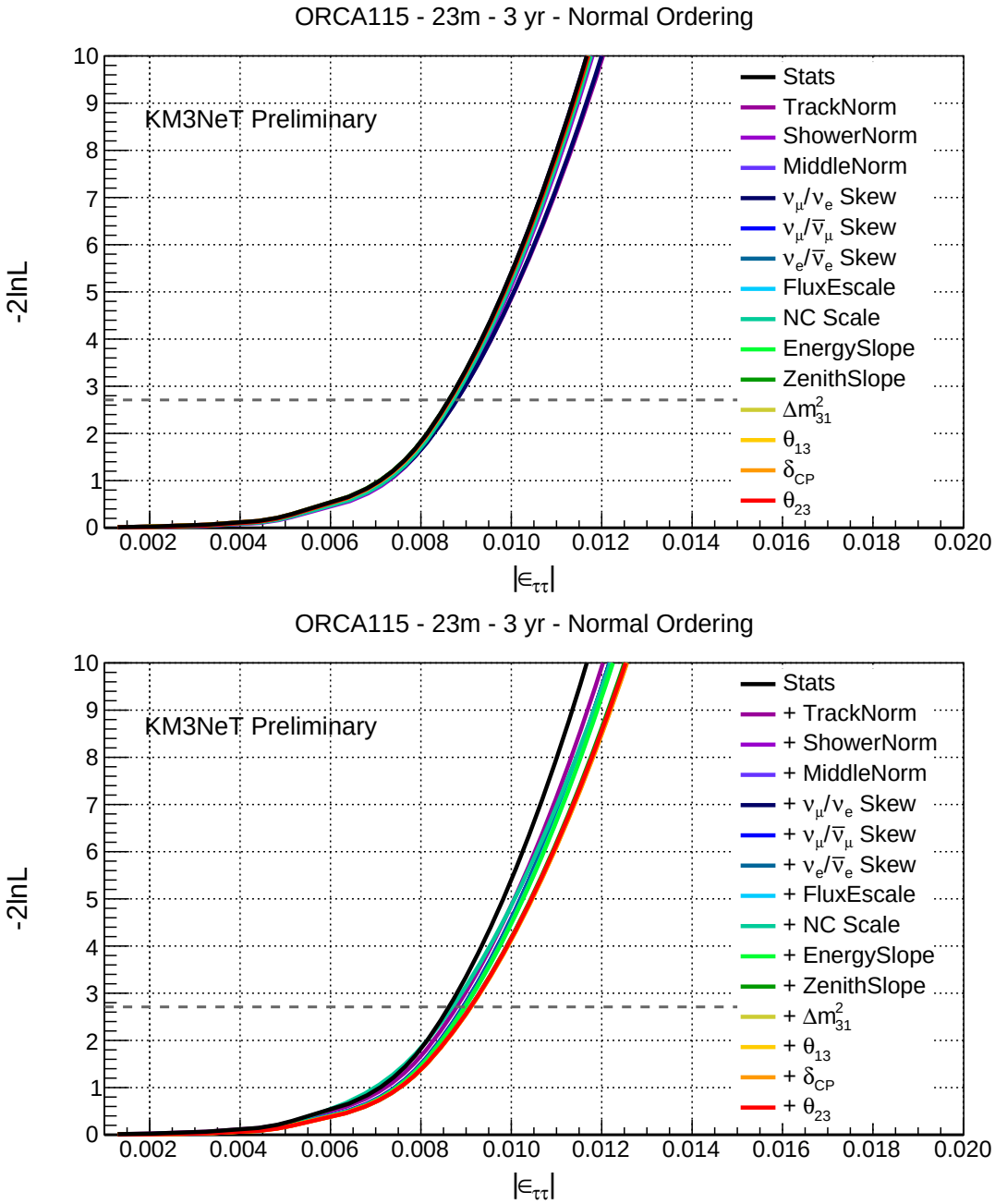

Figure 4.53: Effect of systematics (Tab. 4.7) when fitted uniquely (top) and incrementally (bottom) on the sensitivity to $\epsilon_{\tau\tau}$ at ORCA with 23 m horizontal spacing for NO assumption. See caption of Fig. 4.41 for more info.

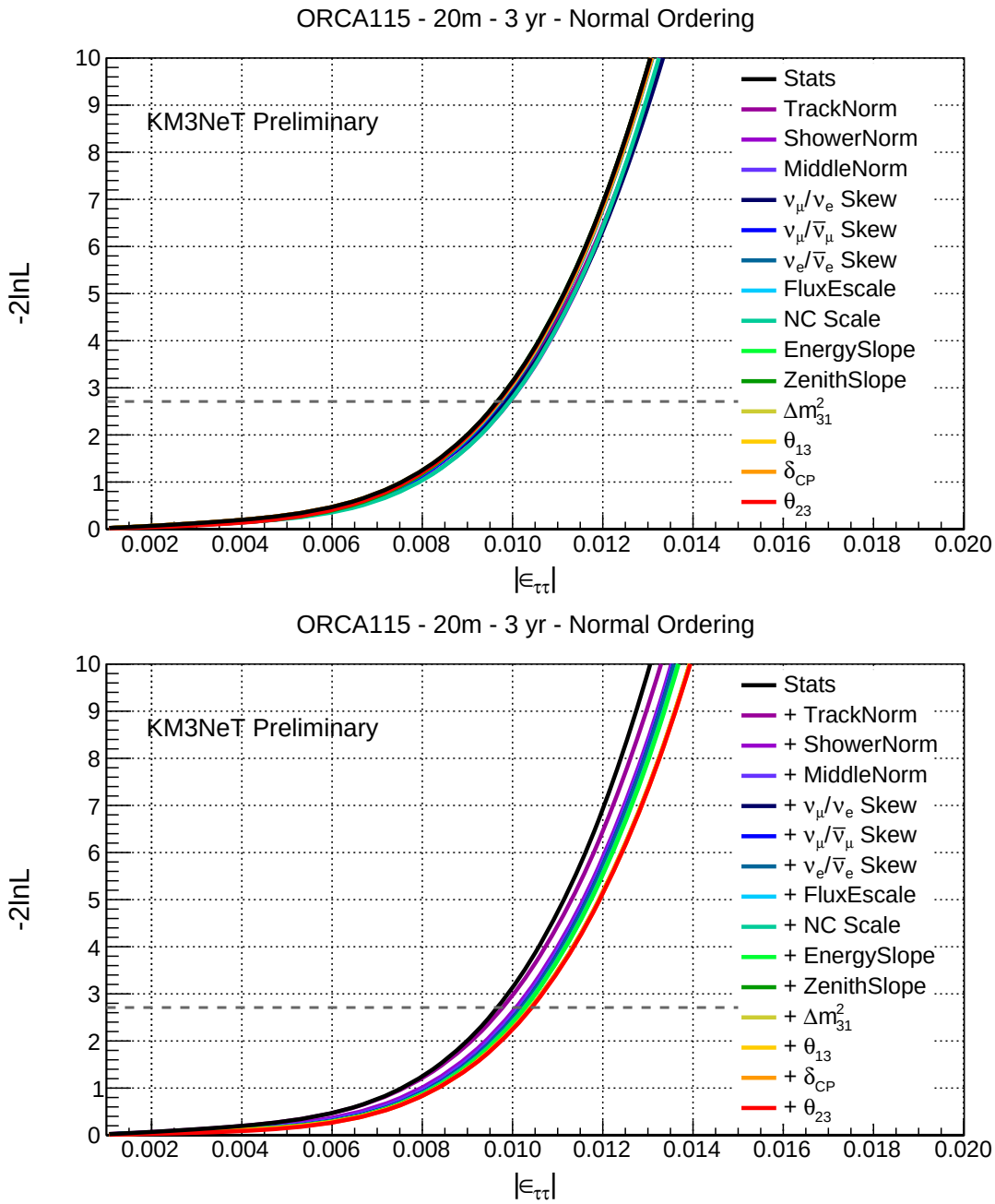

Figure 4.54: Effect of systematics (Tab. 4.7) when fitted uniquely (top) and incrementally (bottom) on the sensitivity to $\epsilon_{\tau\tau}$ at ORCA with 20 m horizontal spacing for NO assumption. See caption of Fig. 4.41 for more info.

Since sensitivity on $\epsilon_{\tau\tau}$ is mostly driven by the track channel, a non-trivial pull is exhibited by the track normalisation. Only θ_{23} is found to employ a non-negligible pull in the cumulative fits of NSI $\epsilon_{\tau\tau}$ assuming normal ordering, as seen in the lower panels of Fig. 4.53 and Fig. 4.54. The ordering is assumed to be known (NO) and kept fixed in the fit.

NSI $\epsilon_{\tau\tau}$ - Inverted ordering

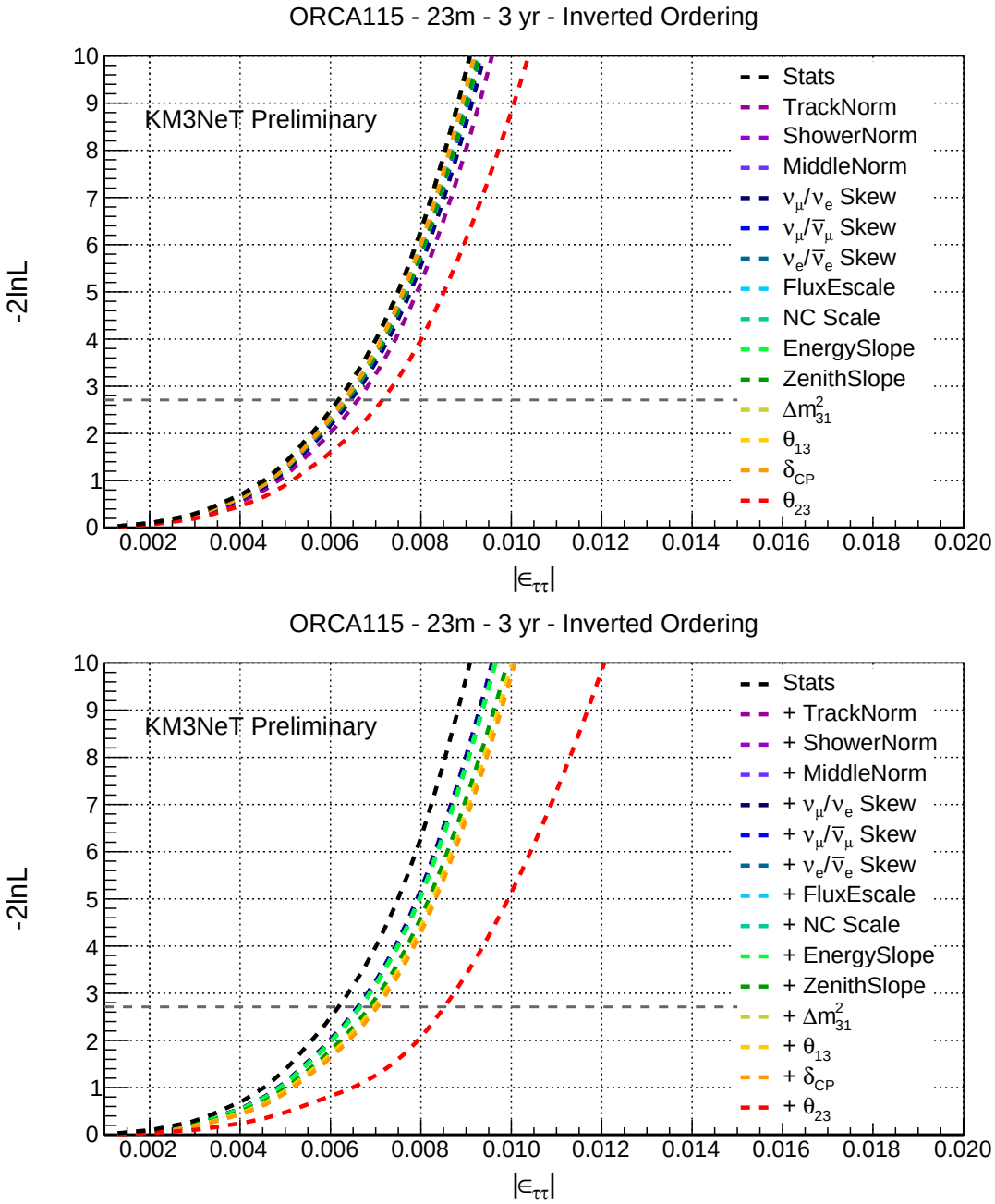

Figure 4.55: Effect of systematics (Tab. 4.7) when fitted uniquely (top) and incrementally (bottom) on the sensitivity to $\epsilon_{\tau\tau}$ at ORCA with 23 m horizontal spacing for IO assumption. See caption of Fig. 4.41 for more info.

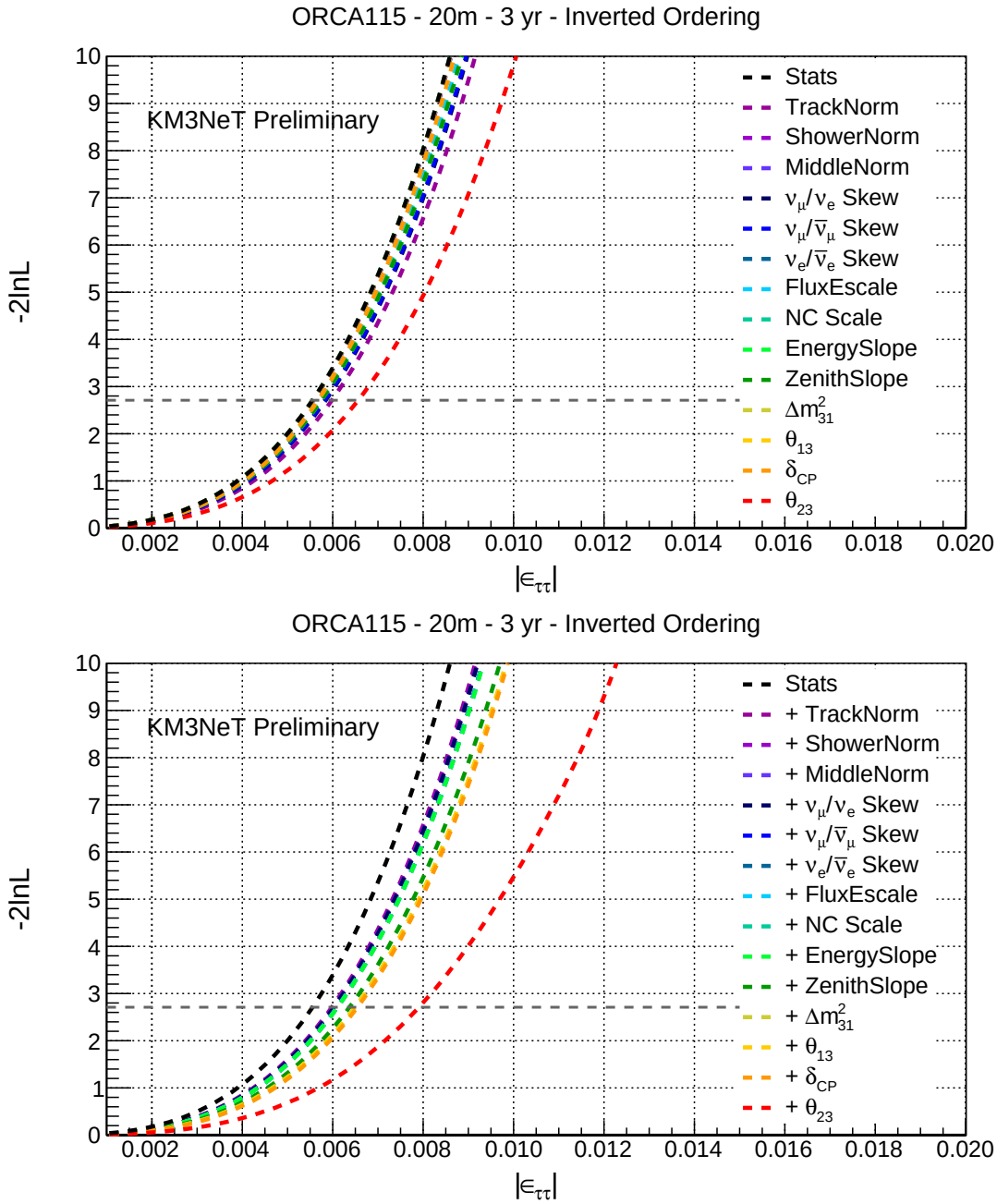

Figure 4.56: Effect of systematics (Tab. 4.7) when fitted uniquely (top) and incrementally (bottom) on the sensitivity to $\epsilon_{\tau\tau}$ at ORCA with 20 m horizontal spacing for IO assumption. See caption of Fig. 4.41 for more info.

Similar to the NO case, a non-trivial pull is exhibited by the track normalisation, since sensitivity on $\epsilon_{\tau\tau}$ is mostly driven by the track channel. Only θ_{23} is found to employ a non-negligible pull in the cumulative fits of NSI $\epsilon_{\tau\tau}$ assuming normal ordering, as seen in the lower panels of Fig. 4.55 and Fig. 4.56 The ordering is assumed to be known (IO) and kept fixed in the fit.

4.3.4 Results

The final sensitivities after inclusion of all the systematics listed in Tab. 4.7 can be grouped in two categories:

- **One-NSI sensitivities**: one-dimensional sensitivities when only one NSI parameter is allowed to be non-zero, while the rest are kept fixed at zero.
- **Correlated NSI sensitivities**: two-dimensional sensitivities when two NSI parameters are allowed to be non-zero, while the rest are kept fixed at zero.

One-NSI sensitivities

ORCA one-dimensional sensitivities to $\epsilon_{e\mu}$, $\epsilon_{e\tau}$, $\epsilon_{\mu\tau}$ and $\epsilon_{\tau\tau}$ are shown in Fig. 4.57 to Fig. 4.60. The sensitivities are calculated after fitting over the nuisance parameters and marginalising over the oscillation parameters as listed in Tab. 4.7. Marginal improvements have been observed for the 20 m geometry with 3 PID classes for the electron NSIs: $\epsilon_{e\mu}$ and $\epsilon_{e\tau}$. A higher instrumentation density with better resolution in the shower channel leads to this marginal improvement. Final limits are read from curves referring to the 20 m geometry in coherence with the benchmark set by the KM3NeT Collaboration.

NSI $\epsilon_{e\mu}$

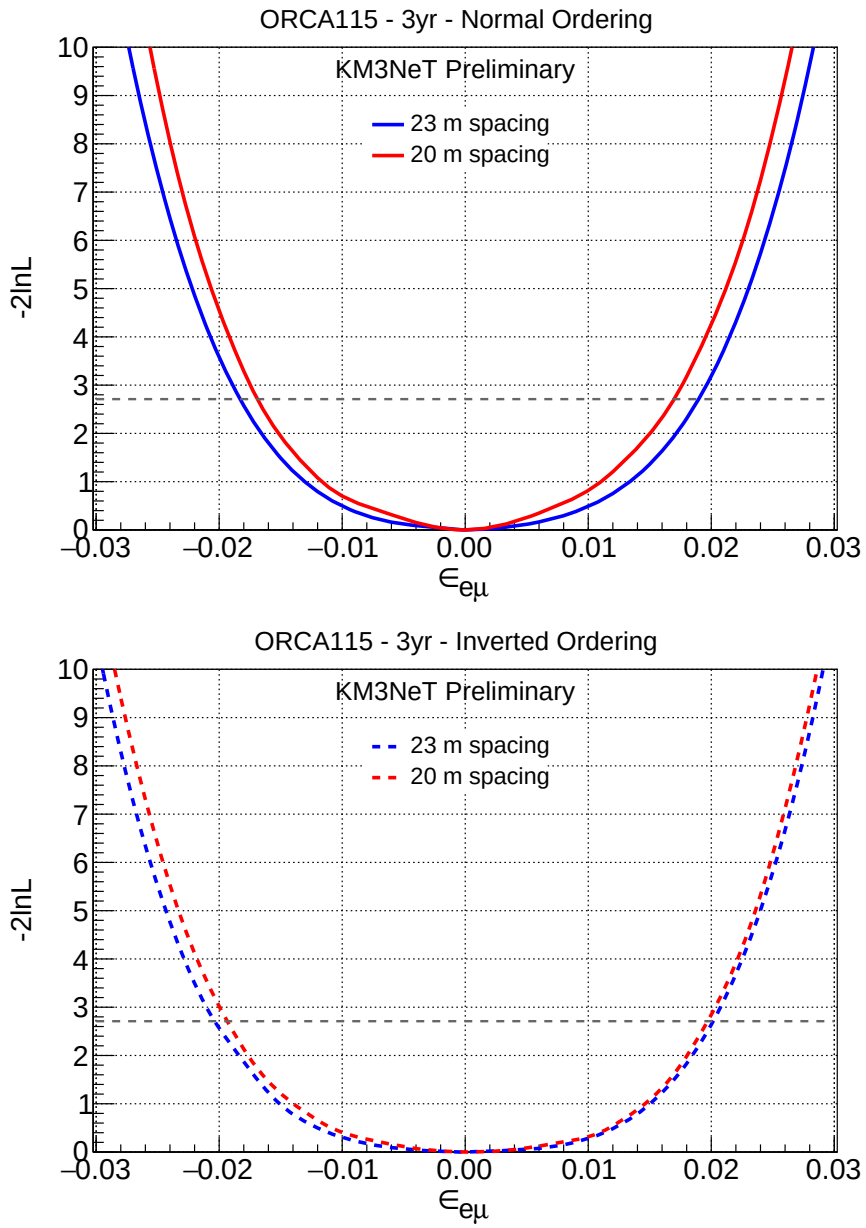

Figure 4.57: Projected sensitivity to $\epsilon_{e\mu}$, for three years of running of full ORCA detector comprising 115 string, with either 23 m (blue) or 20 m (red) horizontal DU spacing. Normal (Inverted) ordering is assumed in the top (bottom) plot. All NSI parameters except $\epsilon_{e\mu}$ are kept fixed at zero. The dashed horizontal line correspond to the 90% C.L. limit.

NSI $\epsilon_{e\tau}$

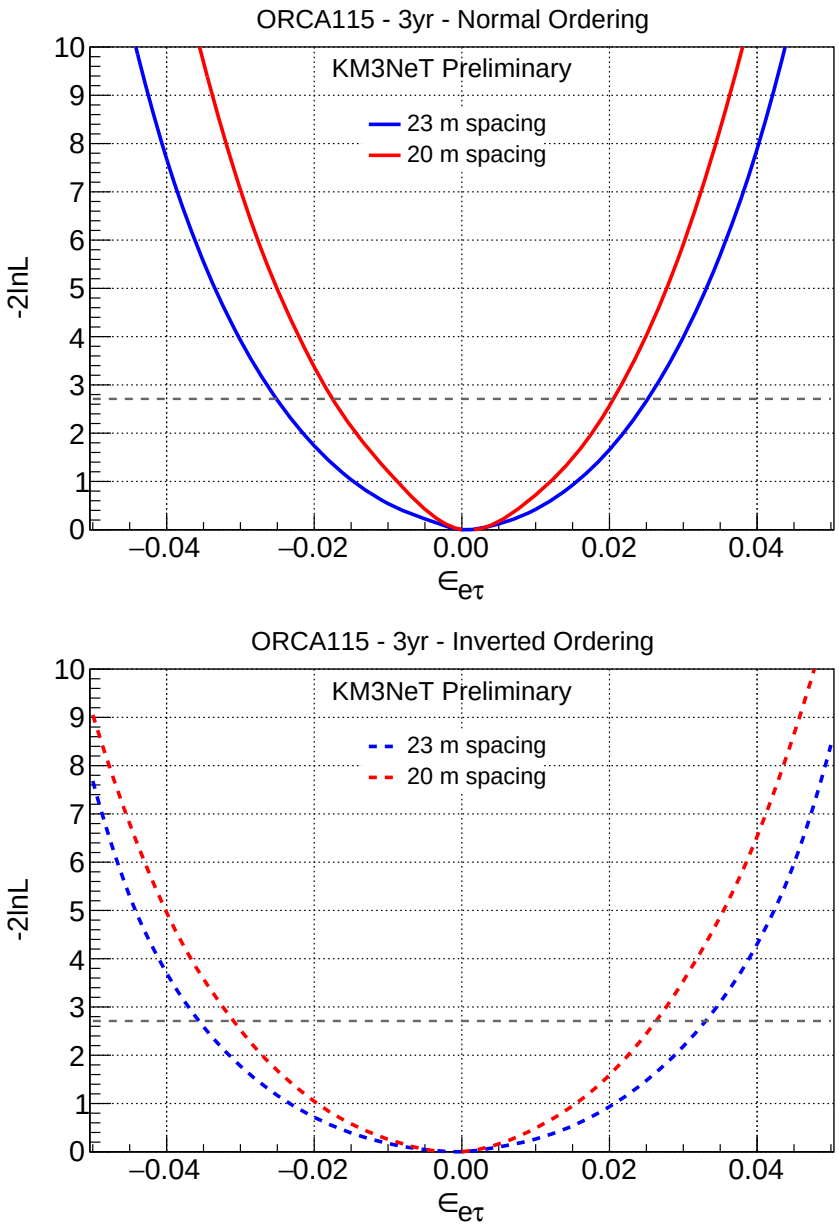

Figure 4.58: Projected sensitivity to $\epsilon_{e\tau}$. See caption of Fig. 4.57 for more info.

NSI $\epsilon_{\mu\tau}$

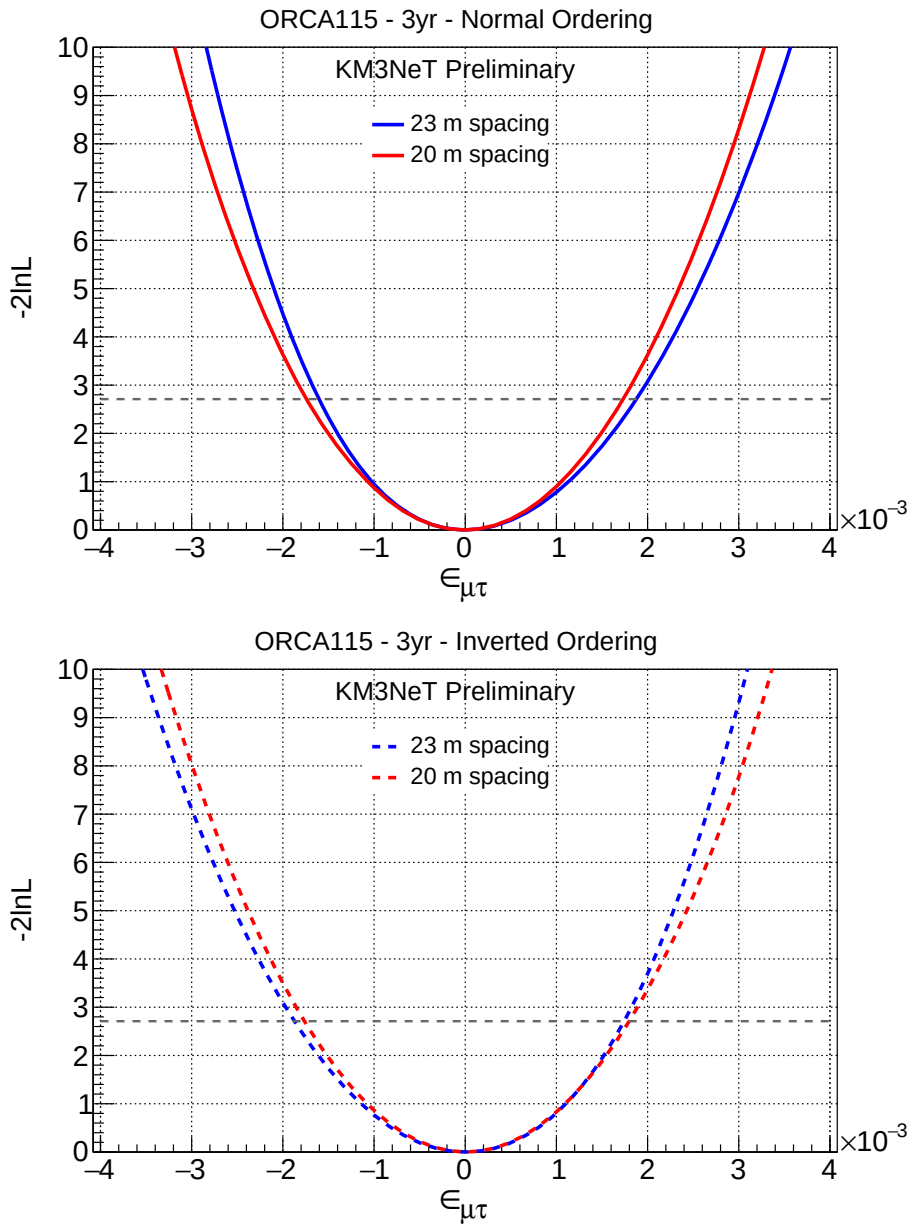

Figure 4.59: Projected sensitivity to $\epsilon_{\mu\tau}$. See caption of Fig. 4.57 for more info.

NSI $\epsilon_{\tau\tau}$

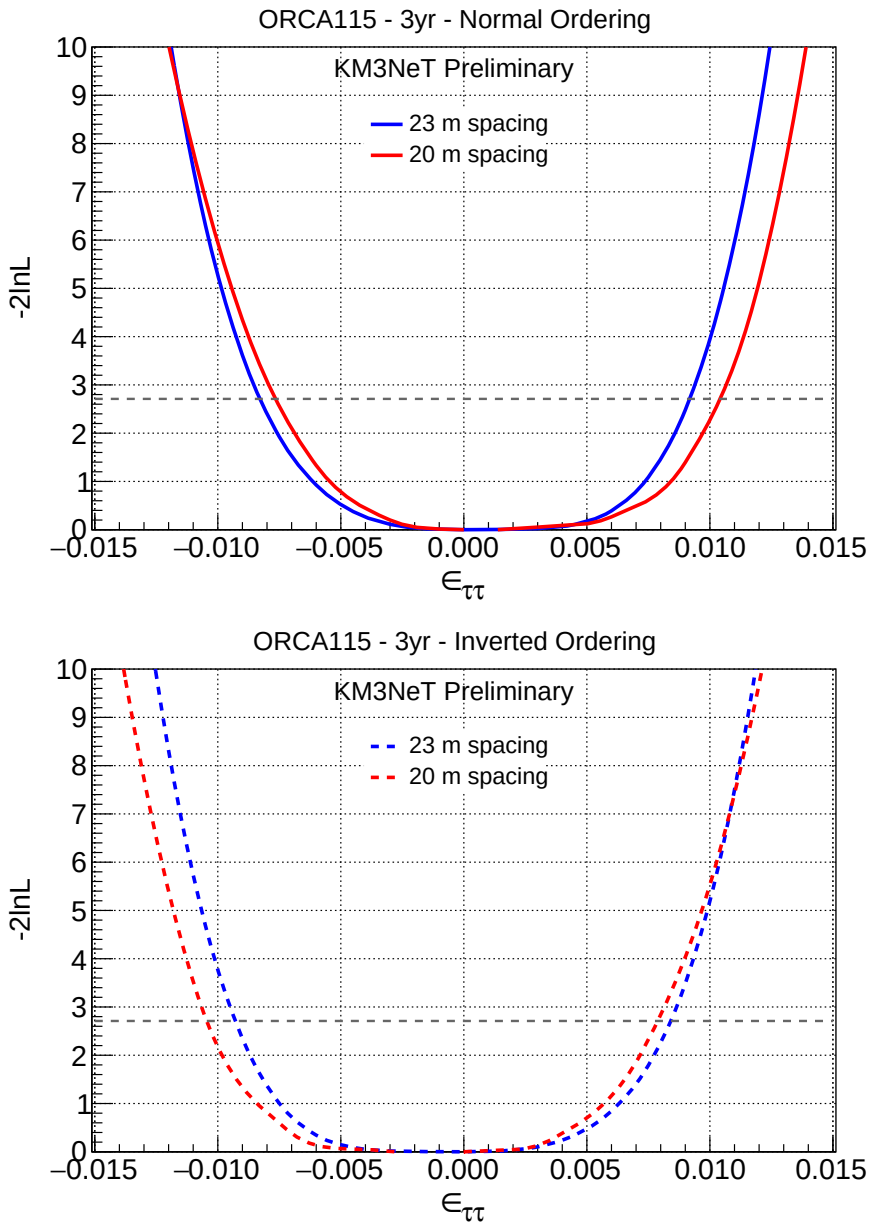

Figure 4.60: Projected sensitivity to $\epsilon_{\tau\tau}$. See caption of Fig. 4.57 for more info.

Correlated-NSI sensitivities

The 90% C.L. interval regions in the NSI parameter space allowed after 3 years of running of ORCA are shown in Fig. 4.61 to Fig. 4.66 for NO and IO assumptions, respectively. Each panel depicts the sensitivities for two considered detector geometries corresponding to 23 m and 20 m horizontal spacing between DUs. The sensitivity contours are drawn around the orgin (0, 0), where the pseduo-data is simulated keeping all NSI parameters fixed at zero. The contours are drawn after profiling over the nuisance parameters and marginalisation over the oscillation parameters listed in Tab. 4.7. The allowed region corresponds to the area contained within the contours at a given C.L.

NSI $\epsilon_{e\mu} - \epsilon_{e\tau}$

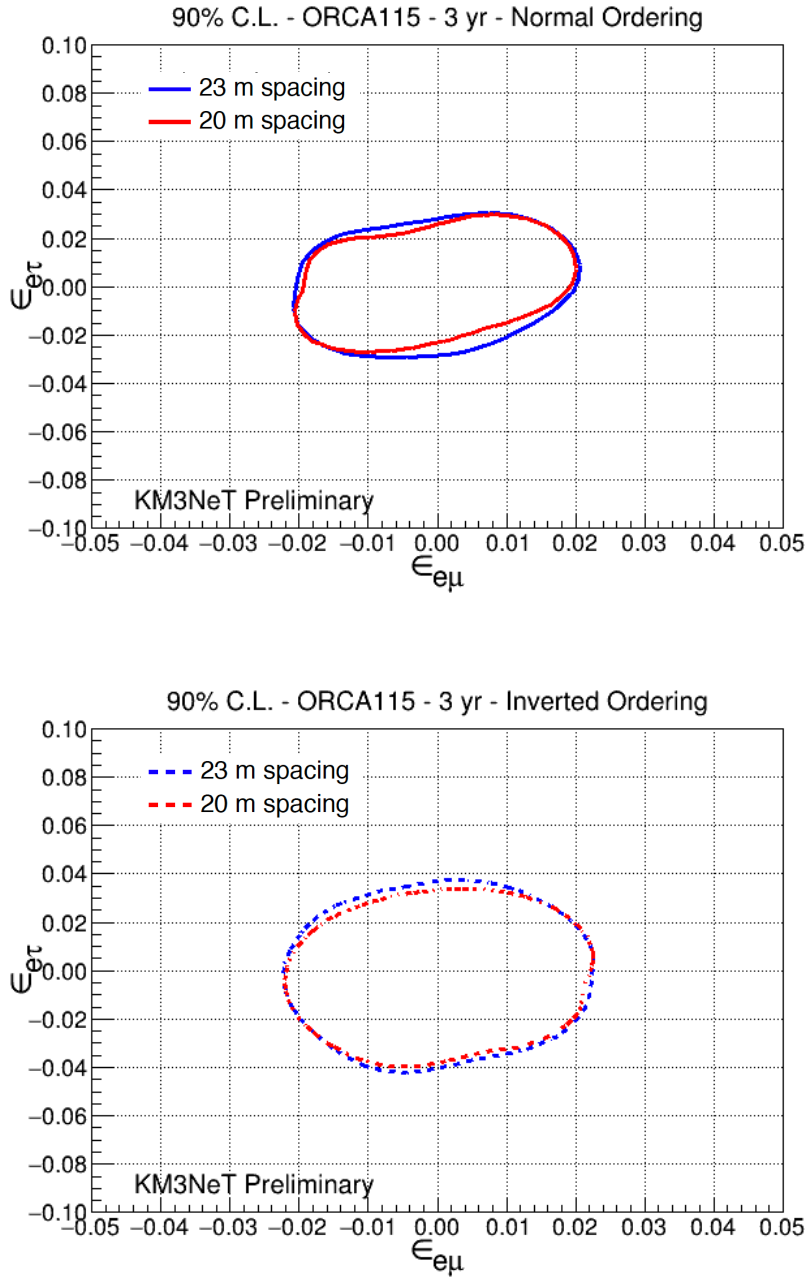

Figure 4.61: 90% C.L. regions in the correlated $\epsilon_{e\mu} - \epsilon_{e\tau}$ NSI phase space, allowed after three years of running of full ORCA detector comprising 115 strings, with either 23 m (blue) or 20 m (red) horizontal spacing. Normal (Inverted) ordering is assumed in the top (bottom) plot. The NSI parameters not appearing on the plots are kept fixed at zero. Pseudo-data is simulated at the standard oscillation point, represented by $(\epsilon_{e\mu}, \epsilon_{e\tau}) = (0, 0)$, which corresponds to the assumed best-fit point (*bfp*).

NSI $\epsilon_{e\mu} - \epsilon_{\mu\tau}$

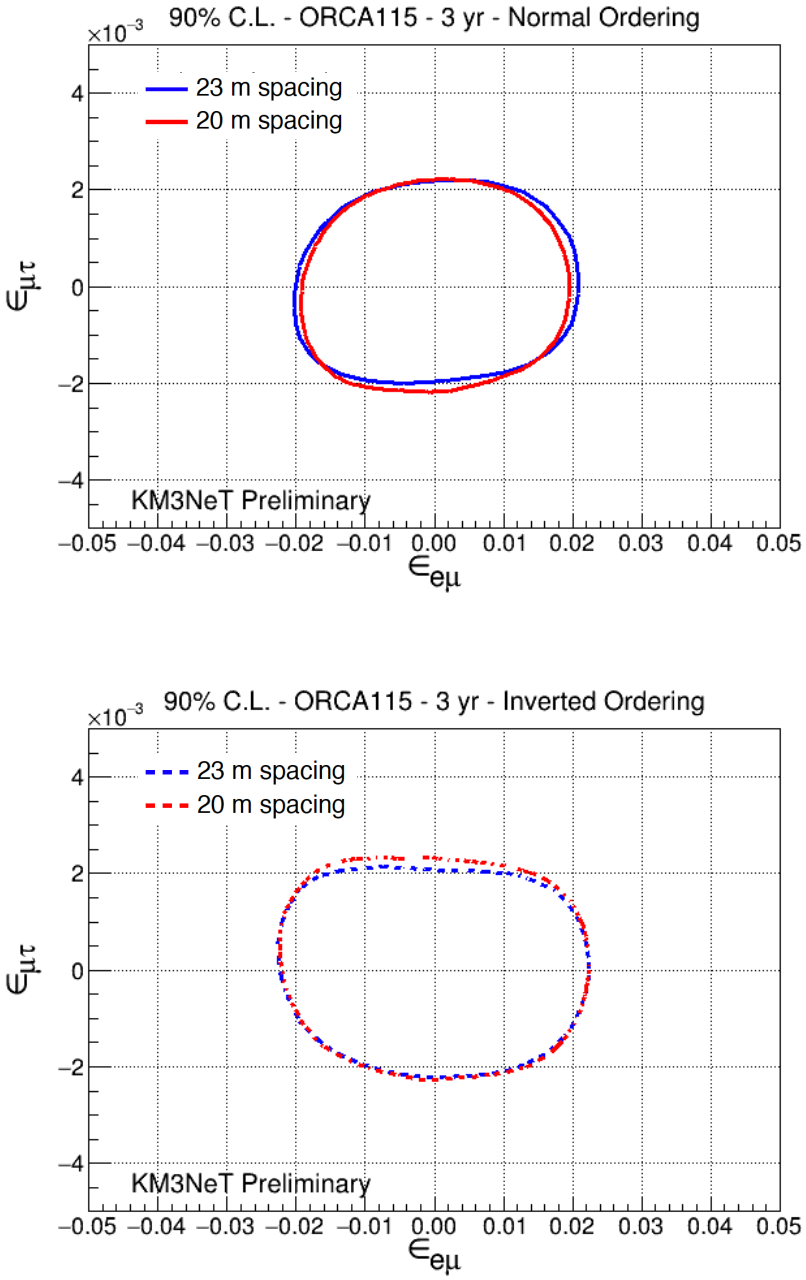

Figure 4.62: 90% C.L. regions in the correlated $\epsilon_{e\mu} - \epsilon_{\mu\tau}$ NSI phase space, allowed after three years of running of full ORCA detector comprising 115 strings, with either 23 m (blue) or 20 m (red) horizontal spacing. Normal (Inverted) ordering is assumed in the top (bottom) plot. See caption of Fig. 4.61 for more info.

NSI $\epsilon_{e\mu} - \epsilon_{\tau\tau}$

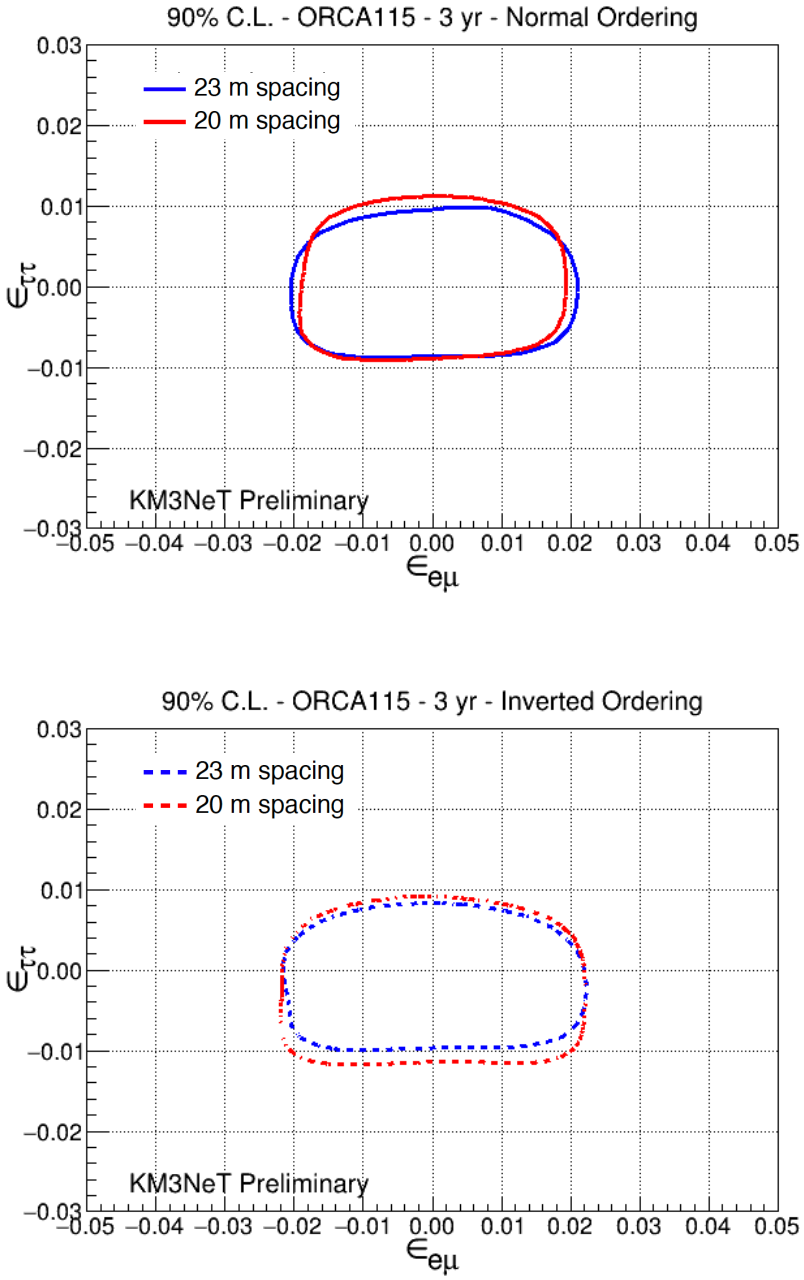

Figure 4.63: 90% C.L. regions in the correlated $\epsilon_{e\mu} - \epsilon_{\tau\tau}$ NSI phase space, allowed after three years of running of full ORCA detector comprising 115 strings, with either 23 m (blue) or 20 m (red) horizontal spacing. Normal (Inverted) ordering is assumed in the top (bottom) plot. See caption of Fig. 4.61 for more info.

NSI $\epsilon_{e\tau} - \epsilon_{\mu\tau}$

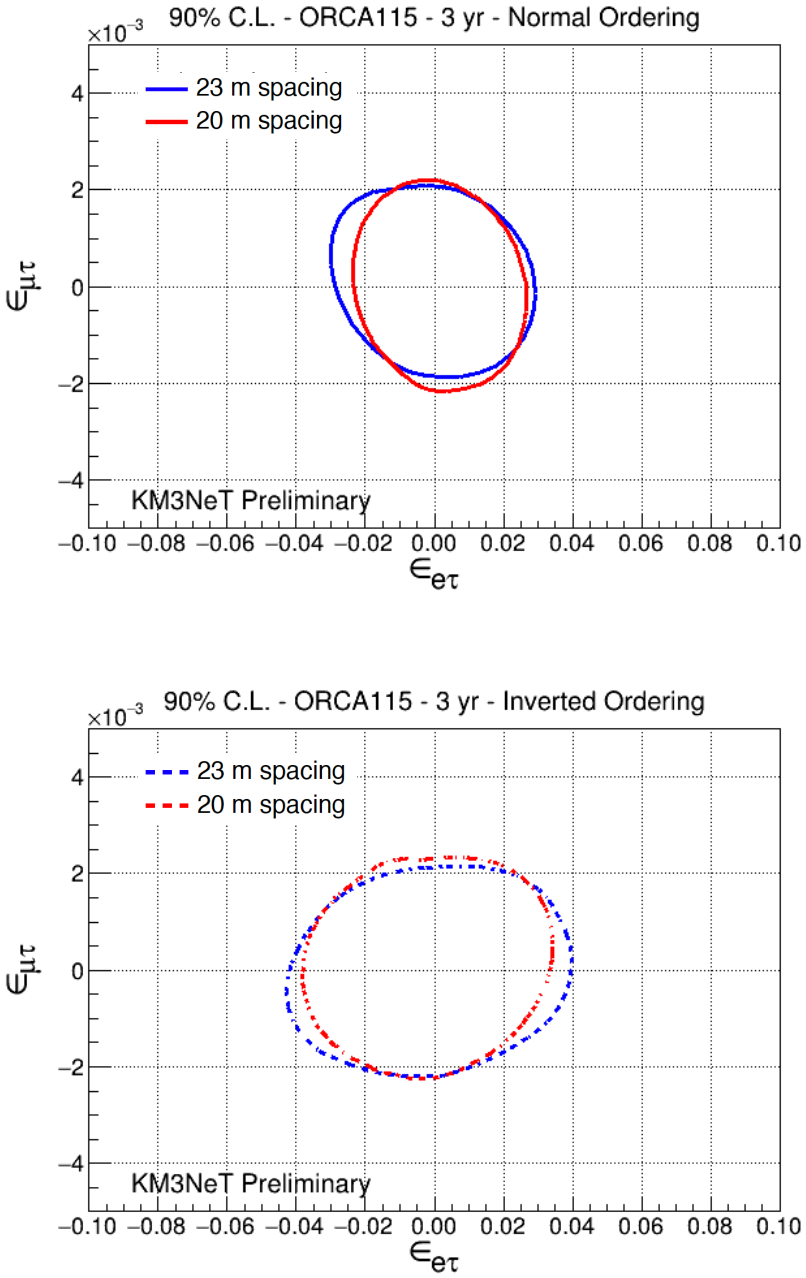

Figure 4.64: 90% C.L. regions in the correlated $\epsilon_{e\tau} - \epsilon_{\mu\tau}$ NSI phase space, allowed after three years of running of full ORCA detector comprising 115 strings, with either 23 m (blue) or 20 m (red) horizontal spacing. Normal (Inverted) ordering is assumed in the top (bottom) plot. See caption of Fig. 4.61 for more info.

NSI $\epsilon_{e\tau} - \epsilon_{\tau\tau}$

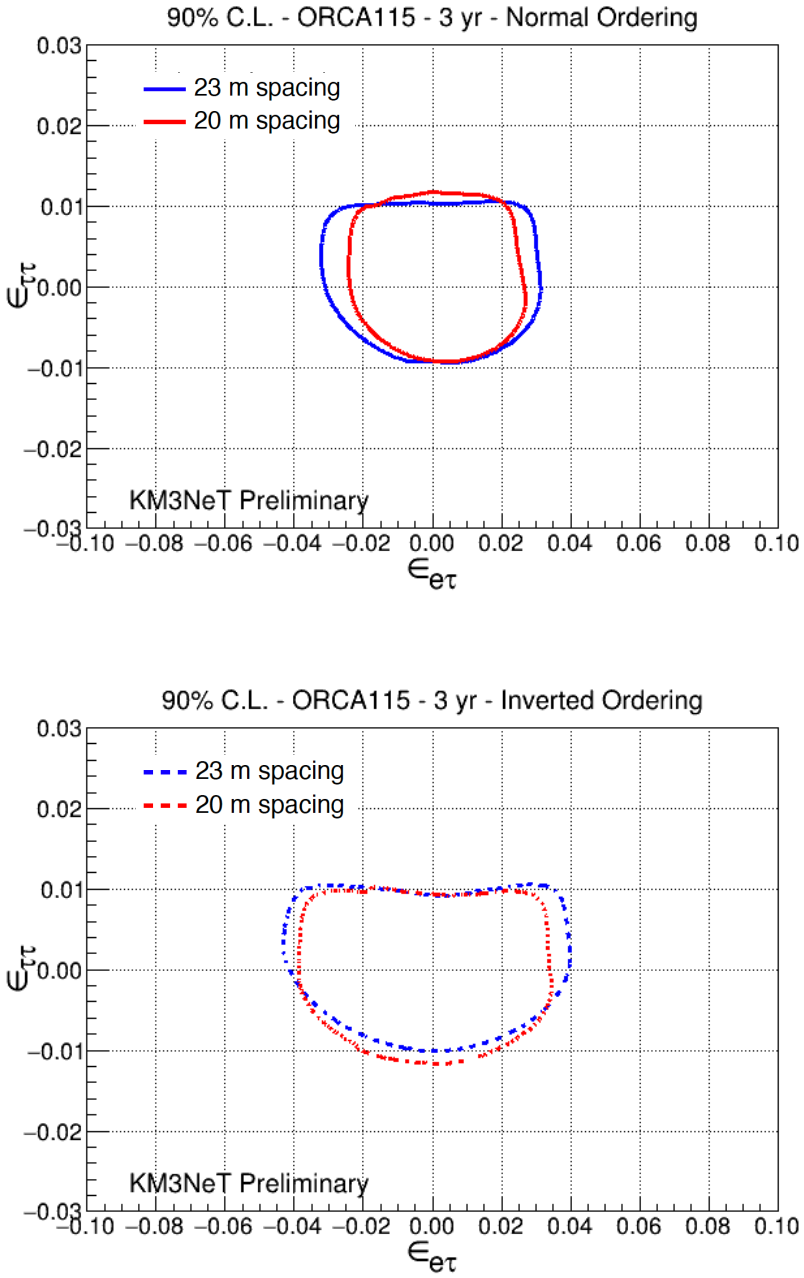

Figure 4.65: 90% C.L. regions in the correlated $\epsilon_{e\tau} - \epsilon_{\tau\tau}$ NSI phase space, allowed after three years of running of full ORCA detector comprising 115 strings, with either 23 m (blue) or 20 m (red) horizontal spacing. Normal (Inverted) ordering is assumed in the top (bottom) plot. See caption of Fig. 4.61 for more info.

NSI $\epsilon_{\mu\tau} - \epsilon_{\tau\tau}$

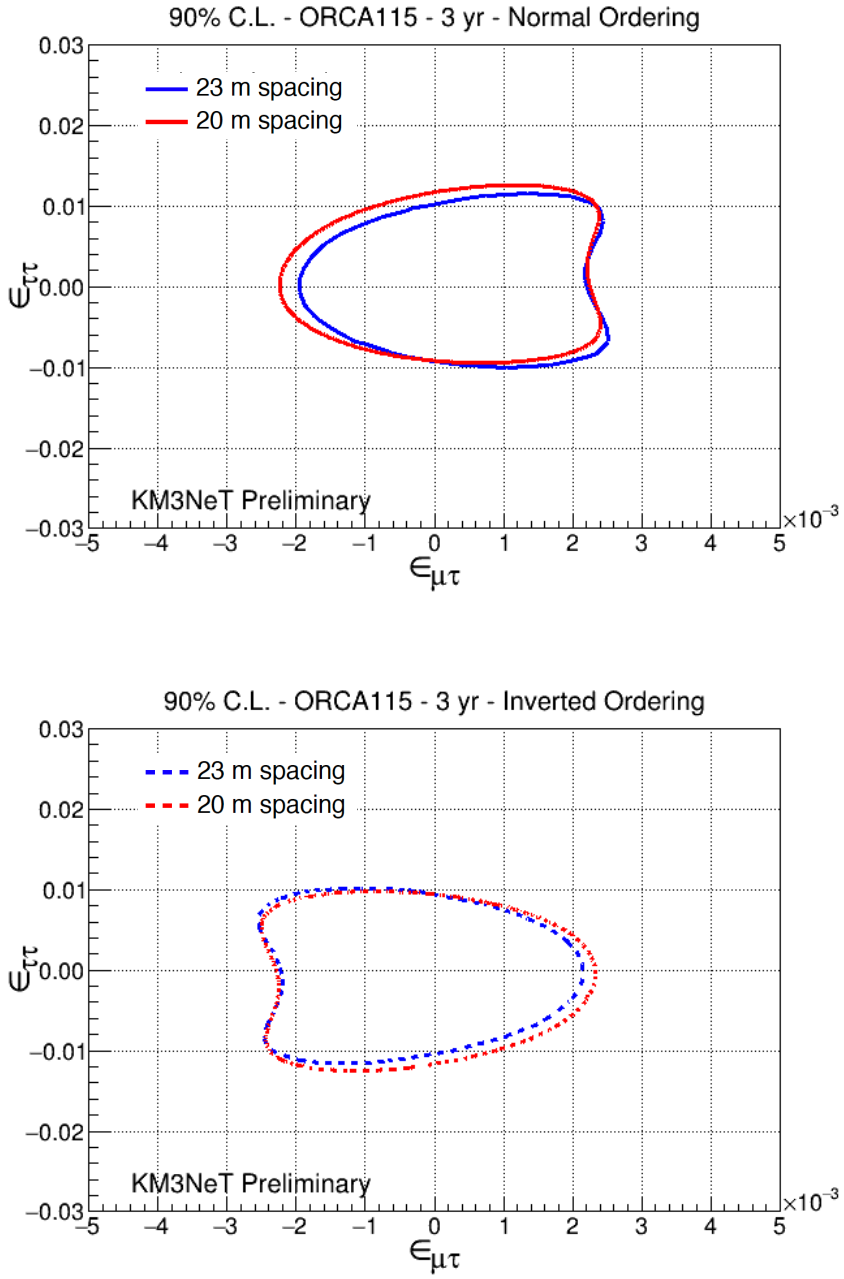

Figure 4.66: 90% C.L. regions in the correlated $\epsilon_{\mu\tau} - \epsilon_{\tau\tau}$ NSI phase space, allowed after three years of running of full ORCA detector comprising 115 strings, with either 23 m (blue) or 20 m (red) horizontal spacing. Normal (Inverted) ordering is assumed in the top (bottom) plot. See caption of Fig. 4.61 for more info.

Finally, expected bounds on NSIs obtained from this work are reported in Tab. 4.8. The projected limits correspond to the ORCA configuration of 115 strings spaced 20 m apart horizontally and for a livetime of 3 years.

NSI Couplings	Assumed True NMO	Bounds (90% C.L.)
$\epsilon_{e\mu}$	NO	$(-1.7 \times 10^{-2}, 1.7 \times 10^{-2})$
	IO	$(-2.0 \times 10^{-2}, 2.0 \times 10^{-2})$
$\epsilon_{e\tau}$	NO	$(-1.8 \times 10^{-2}, 2.1 \times 10^{-2})$
	IO	$(-3.1 \times 10^{-2}, 2.7 \times 10^{-2})$
$\epsilon_{\mu\tau}$	NO	$(-1.7 \times 10^{-3}, 1.7 \times 10^{-3})$
	IO	$(-1.7 \times 10^{-3}, 1.7 \times 10^{-3})$
$\epsilon_{\tau\tau}$	NO	$(-0.8 \times 10^{-2}, 1.1 \times 10^{-2})$
	IO	$(-1.1 \times 10^{-2}, 0.8 \times 10^{-2})$

Table 4.8: Bounds on NSI couplings of neutrinos with d-quarks at 90% C.L. for a runtime of 3 years of full ORCA comprising 115 DUs with 20 m horizontal DU spacing. Only one NSI parameter is considered at a time.

Comparisons with other experiments

Fig. 4.67 shows the exclusion regions in the first quadrant for comparison of ORCA sensitivites obtained from this work with limits from Super-K [192]. Note that the Super-K constraints have been drawn assuming a *two-flavour hybrid model* approximation (Sec. 4.1).

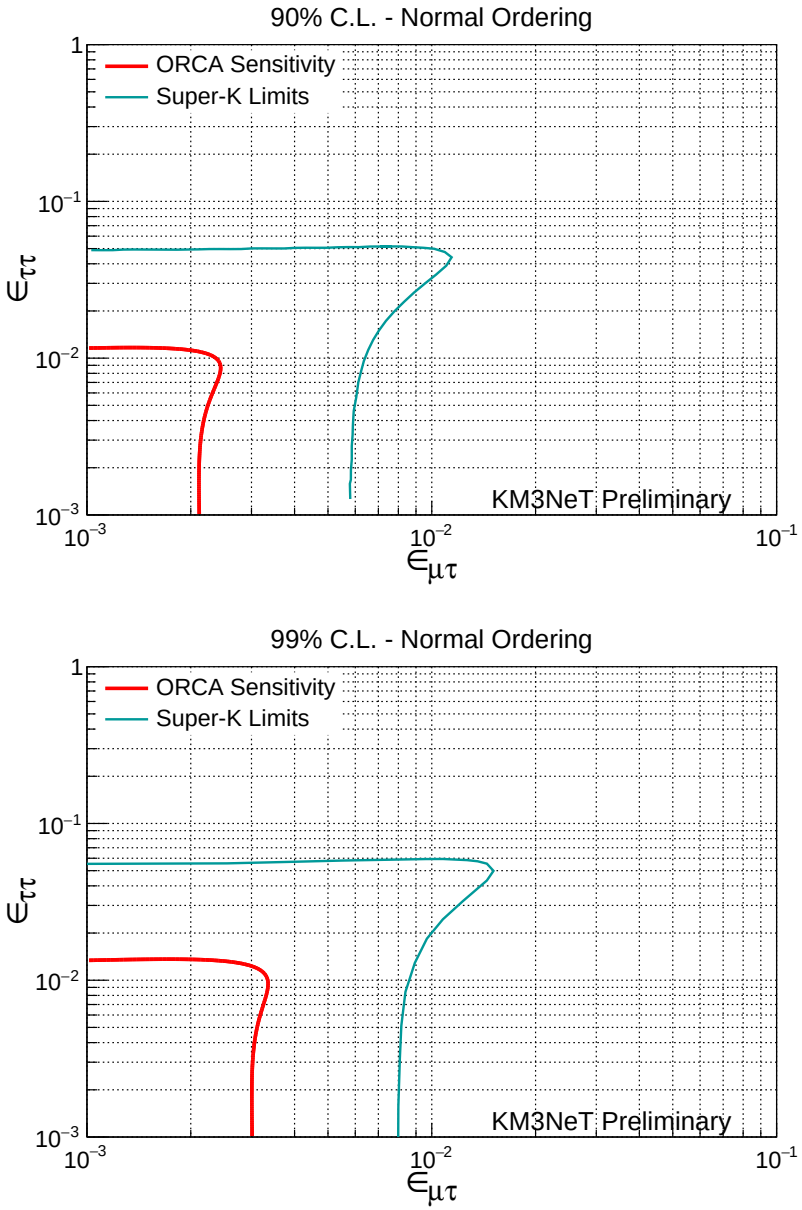

Figure 4.67: 90% (top) and 99% (bottom) C.L. intervals in the $\epsilon_{\mu\tau} - \epsilon_{\tau\tau}$ phase space allowed after 3 years of ORCA livetime obtained in this work is shown together with limits (assuming a *two-flavour hybrid model* approximation) from Super-K [192].

We also considered an effective Hamiltonian in the presence of NSIs in the $e - \tau$ sector to compare with Super-K. A similar analysis has been pursued thereafter, resulting in limits in the $\epsilon_{e\tau} - \epsilon_{\tau\tau}$ phase space. The 90% C.L. contour for $\epsilon_{ee} = 0$ (fixed) is shown in Fig. 4.68. Note that the Super-K constraint has been drawn assuming a *three-flavour hybrid model* approximation (Sec. 4.1).

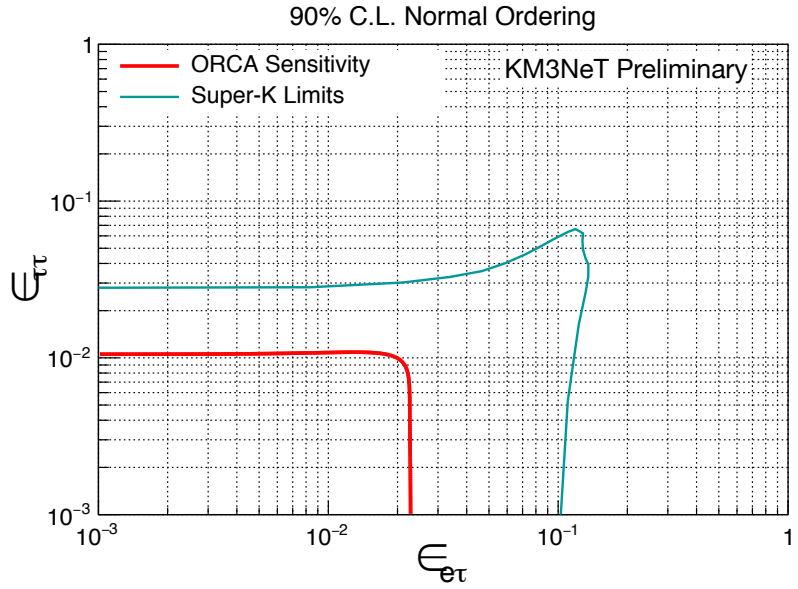

Figure 4.68: 90% C.L. region in the $\epsilon_{e\tau} - \epsilon_{\tau\tau}$ plane assuming $\epsilon_{ee} = 0$ allowed after 3 years of ORCA livetime obtained in this work is shown along with limits (assuming a *three-flavour hybrid model* approximation) from Super-K [192].

For comparison with IceCube Deepcore [93], sensitivities on NSI $\epsilon_{\mu\tau}$ have been drawn in Fig. 4.69. The ORCA sensitivity curve has been superimposed on contours from IceCube [93] and Super-K [192] assuming a *two-flavour hybrid model* approximation (Sec. 4.1) for comparison.

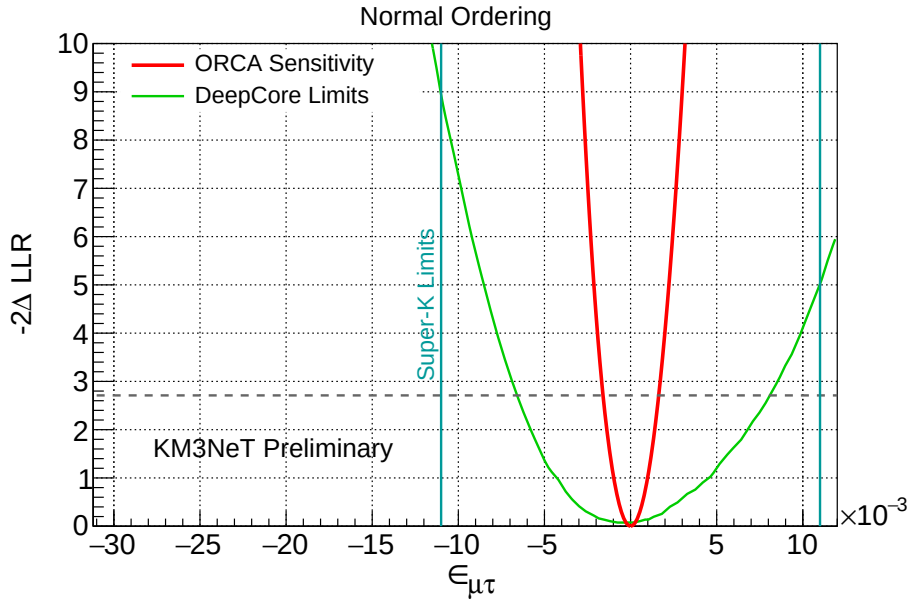

Figure 4.69: Sensitivity to $\epsilon_{\mu\tau}$ after 3 years of ORCA livetime obtained in this work when $\epsilon_{\tau\tau}$ is fixed at zero. Limits from IceCube DeepCore [93] (green) and Super-K [192] (cyan) are drawn for comparison.

In conclusion, an analysis to estimate the discovery potential of KM3NeT-ORCA for different NSI sectors has been presented. It has been demonstrated that ORCA has an excellent potential to put tighter constraints on various NSI parameter spaces by one order of magnitude better than what is allowed by current experimental limits. Finally, expected bounds on NSI parameters have been reported.

5 Neutrino Mass Ordering and NSI at ORCA

"I turned my attention for a while to gamma ray astronomy and soon began the first in a continuous series of experiments at the Savannah River site to study the properties of the neutrino."

— FREDERICK REINES

Contents

In Chapter 4, we have explored the discovery reach of ANTARES and KM3NeT-ORCA neutrino experiments for the search for NSI of neutrinos. Thereafter, limits in the NSI $\mu - \tau$ sector with ANTARES are constructed and sensitivity of ORCA towards various NSI model parameters are reported. Infusing non-standard interactions of neutrinos with matter fermions is one of the minimal extensions of the Standard Model (SM), which leads to a rich phenomenology. This Chapter demonstrates the phenomenological implications of NSIs on the neutrino mass ordering measurement with KM3NeT-ORCA.

Analyses estimating the sensitivity for neutrino mass ordering (NMO) at ORCA have been covered in great detail in previous works within the KM3NeT Collaboration. These studies [120, 180, 182, 210] entail a detailed estimation of the ORCA sensitivity to the NMO measurement, corresponding to a detector geometry of 23 m horizontal spacing between DUs. In order to estimate the NMO sensitivity with ORCA in a NSI test hypothesis, the study of NMO in the standard oscillation framework has been pursued earlier for completeness and reference. The study laid out in this Chapter, not only presents an updated study of the NMO sensitivity based on a denser instrumentation of ORCA with 20 m horizontal spacing between DUs, but also estimates the impact of sub-dominant effects in neutrino oscillations coming from NSIs on the NMO sensitivity at ORCA.

After a short introduction in Sec. 5.1 on the NMO problem, Sec. 5.2 reports the sensitivity study for NMO in the standard paradigm of three-flavour neutrino oscillations. Sec. 5.3 investigates the interplay between the mass ordering and NSIs and estimates the degenerate effects on the final sensitivity of NMO at ORCA in the presence of NSIs.

5.1 The Neutrino Mass Ordering

As seen in Sec. 1.2.2, for three neutrino states, ν_1, ν_2, ν_3 with masses m_1, m_2, m_3, there are two unique mass-squared differences Δm^2_{21} and Δm^2_{31} ($\Delta m^2_{21} + \Delta m^2_{32} + \Delta m^2_{13} = 0$). The sign of Δm^2_{31} is one of the three current unknowns in the recipe of standard three-flavour neutrino oscillations, the octant of the atmospheric mixing angle θ_{23} (See Chapter 6) and the CP violating phase δ_{CP} between neutrinos and antineutinos being the other two. Depending on the sign of the mass-squared splitting Δm^2_{31}, the relative mass spectrum of neutrinos can have two possible scenarios: Normal Ordering (NO) with $m_3 > m_2 > m_1$ or Inverted Ordering (IO) with $m_2 > m_1 > m_3$. The two scenarios are represented in Figure 1.1.

Oscillations in vacuum cannot tell us about the sign of Δm^2_{31}. The sensitivity towards the sign of $|\Delta m^2_{31}|$ stems from the differential matter-induced modifications of neutrino oscillation probabilities for neutrino and antineutrino channels. However there is a serious degeneracy between the helicity states and the mass ordering. The degeneracy is exact if we assume no CP violation ($\delta_{CP} = 0$), and partial if we assume that there is non-zero CP violation in the neutrino sector. To be sensitive to helicity states ($-1 \implies$ "left-handed"[1] neutrinos and $+1 \implies$ "right-handed" antineutrinos), one requires a detector which can discriminate between neutrinos and antineutino events on an event-by-event basis. This is achieved in atmospheric neutrino experiments like the magnetised Iron Calorimeter at INO [211], which is sensitive to the charge of the outgoing lepton from the neutrino interaction, or in long-baseline experiments like NOνA [212], T2K [213], DUNE [214], where the initial helicity (and flavour) state is known a priori. However, for iso-scalar charge-blind detectors like ANTARES [130], KM3NeT [66], IceCube or Super-K, an event-by-event separation of particles and antiparticles is not possible. However, Nature comes to our rescue in this case. The atmospheric neutrino flux is almost twice the corresponding antineutino flux (Fig. 3.7 and Fig. 3.8). Moreover, interaction cross-sections (Fig. 2.4) of neutrinos and antineutrinos are also different. Since the distortions in oscillations due to matter effects are different, the expected event counts are different for either orderings (NO or IO). This gives a handle to disentangle the two orderings by looking for a statistical excess or deficit of $(\nu + \overline{\nu})$ events in the ***"asymmetry distribution"*** $(N^{\mathrm{IO}}_{E_\nu,\cos\theta_z} - N^{\mathrm{NO}}_{E_\nu,\cos\theta_z})$ of event predictions with either ordering assumptions. In case of real data, the best-fit to data decides the true ordering.

5.2 NMO in the Standard Oscillation Framework

The basic idea to determine the NMO is to identify if matter induced resonance occurs for neutrinos (NO) or antineutinos (IO). Before going into how it is usually achieved at helicity blind detectors like ORCA, let us explore first the partial degeneracy between the helicity and the NMO at the probability level.

[1] For (Dirac) neutrinos the intrinsic spin is opposite to the linear momentum which is referred to as "left-handed", whereas the antineutrinos are always "right-handed". "Right-handed" neutrinos and "left-handed" antineutrinos do not exist within the SM.

Figure 5.1 (and Fig. 5.2) depicts oscillograms for electron (and muon) neutrinos (helicity state = -1) and antineutrinos (helicity state = $+1$) for normal ($\Delta m^2_{31} > 0$) and inverted ordering ($\Delta m^2_{31} < 0$) hypotheses. Matter effects are prominent for neutrinos in case of NO and for antineutrinos in case of IO. As shown in the figures, the behaviour of neutrinos in NO is identical to antineutrinos in IO, as expected.

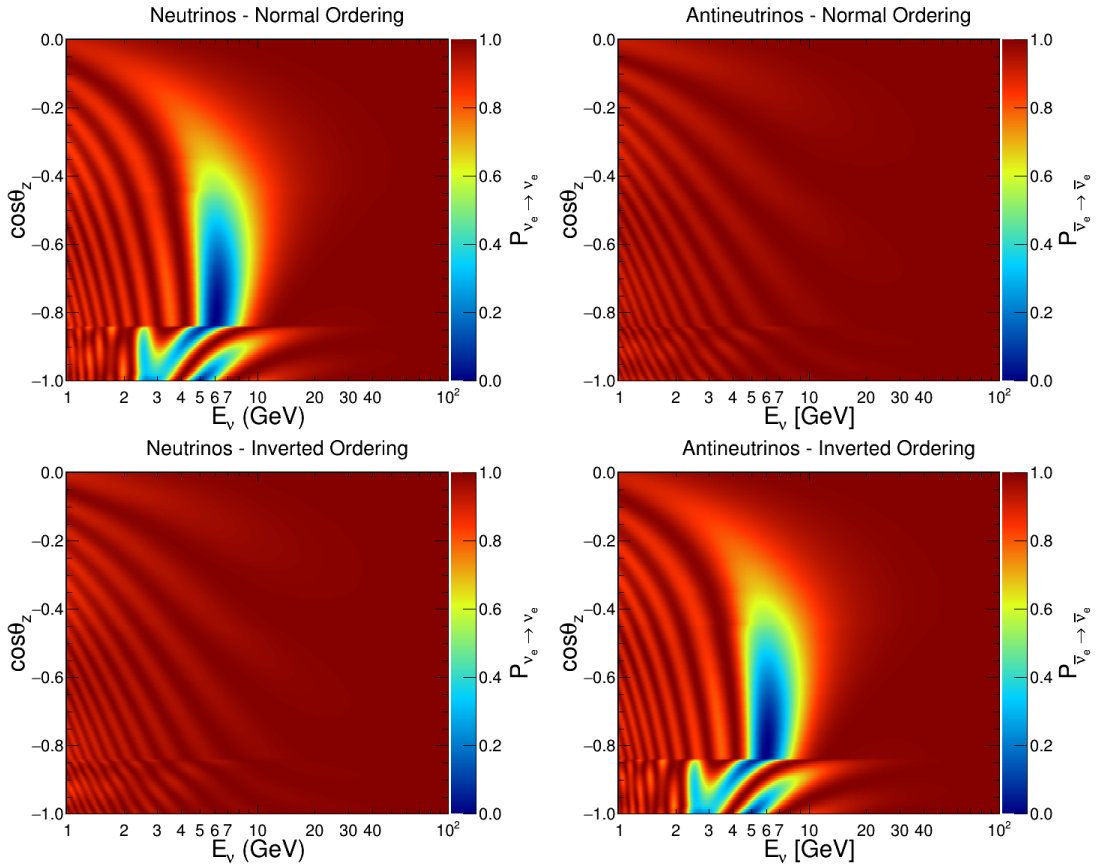

Figure 5.1: $P_{\nu_e \to \nu_e}$ for NO (top panels) and IO (bottom). Neutrinos on the left and antineutrinos on the right. Behaviour of neutrinos in NO (IO) is identical to antineutrinos in IO (NO).

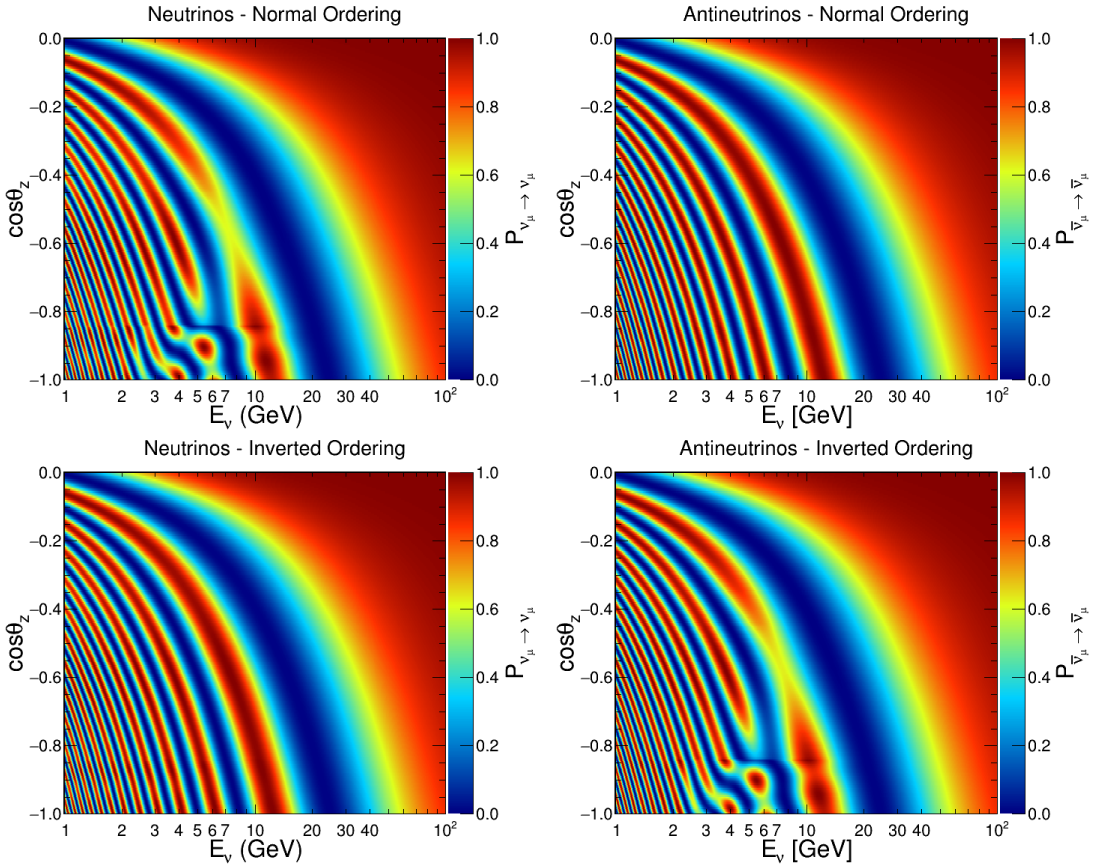

Figure 5.2: $P_{\nu_\mu \to \nu_\mu}$ for NO (top panels) and IO (bottom). Neutrinos on the left and antineutrinos on the right. Behaviour of neutrinos in NO (IO) is identical to antineutrinos in IO (NO).

Thus, the oscillation probabilities for ν in NO are nearly degenerate with $\overline{\nu}$ in IO. However, due to the difference in the atmospheric neutrino flux and interaction cross-sections, a net asymmetry in the $\nu + \overline{\nu}$ events between NO and IO for a particular neutrino flavour can be observed. This asymmetry $\mathcal{A}$ can be defined as

$$\mathcal{A} = \frac{N_{WO} - N_{TO}}{N_{TO}}, \tag{5.1}$$

where N_{TO} is the number of expected interacting events in a (E, θ_z) bin for an assumed true mass ordering (TO = NO or IO) and N_{WO} is the number of expected interacting events for the wrong mass ordering (WO = IO or NO, respectively). Fig. 5.3 shows the asymmetry for muon and electron CC events (no smearing due to detector resolutions have been applied). If resolution effects are incorporated, the asymmetry is further blurred and partially washed out.

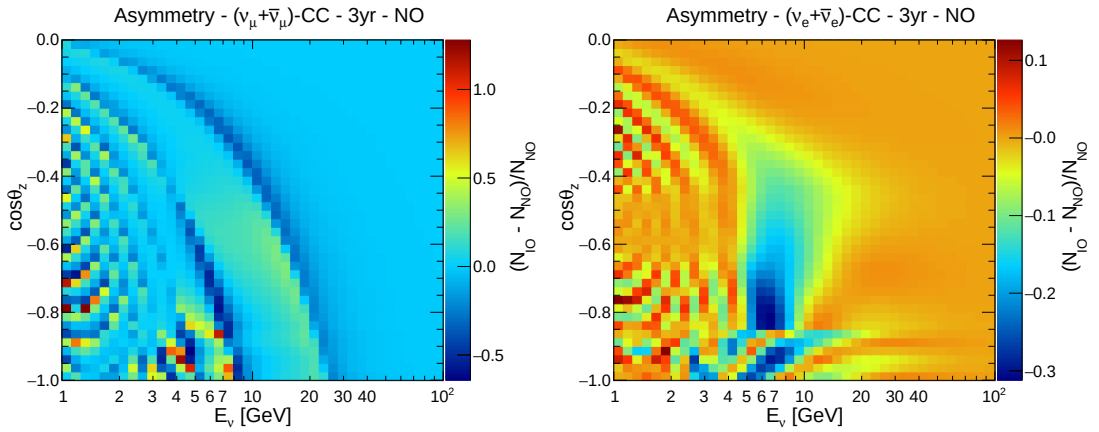

Figure 5.3: Asymmetry (Eq. 5.1) between the number of $\nu + \bar{\nu}$ events expected in case of NO and IO as a function of true neutrino energy and cosine of zenith angle for muon- (left) and electron-CC (right) events. The colour code indicates the value of $\mathcal{A}$ in each bin. True NO is assumed. The results are computed for a 115 lines ORCA detector with 20 m spacing between DUs for 3 years of runtime. Mind the scales on individual plots.

A higher asymmetry is observed in the muon channel than in the electron channel at the interaction level. However, the detector cannot separate (ν_e, $\bar{\nu}_e$, ν_μ, $\bar{\nu}_\mu$, ν_τ, $\bar{\nu}_\tau$ - CC) and (ν, $\bar{\nu}$ - NC) events but distinguish them as two event classes: track and showers (a third class "middles" is also used for ambiguous cases (Sec. 4.3.1)). The asymmetry from each class after incorporating the detector effects is discussed in the next subsection.

5.2.1 Event selection and statistical significance

The event selection strategy is kept at par with what has been pursued for the NSI analysis with ORCA (Sec. 4.3.1) corresponding to a detector geometry of 20 m horizontal spacing between DUs. The number of expected events from different channels entering into the final MC sample can be found in Tab. 4.6.

The test statistic in this case is defined as

$$\chi^2_{E,\theta_z} = \frac{\left(N^{\mathrm{WO}}_{E,\theta_z} - N^{\mathrm{TO}}_{E,\theta_z}\right) \times \left|N^{\mathrm{WO}}_{E,\theta_z} - N^{\mathrm{TO}}_{E,\theta_z}\right|}{N^{\mathrm{TO}}_{E,\theta_z}}. \tag{5.2}$$

$N^{\mathrm{TO}}_{E,\theta_z}$ is the expected number of track/middle/shower events in the corresponding (E, θ_z) bin weighted under an assumed true mass ordering (TO) hypothesis (NO or IO); while, $N^{\mathrm{WO}}_{E,\theta_z}$ is the number of expected events in the same (E, θ_z) bin for the wrong mass ordering (WO) hypothesis (IO or NO, respectively).

Fig. 5.4 shows the signed-χ^2 maps for reconstructed events in the three event classes for 3 years of full ORCA (115 DUs) runtime with 20 m horizontal spacing. 20 logarithmic bins were chosen in reconstructed neutrino energy $(E) \in [3, 100]$ GeV; while 20 linear bins in cosine of the reconstructed zenith angle $(\theta_z) \in [-1, 0]$. The absolute value of χ^2 is stored, so that each bin content represents the contribution to the total χ^2 from the respective event class. The colour codes represent the excesses and deficits.

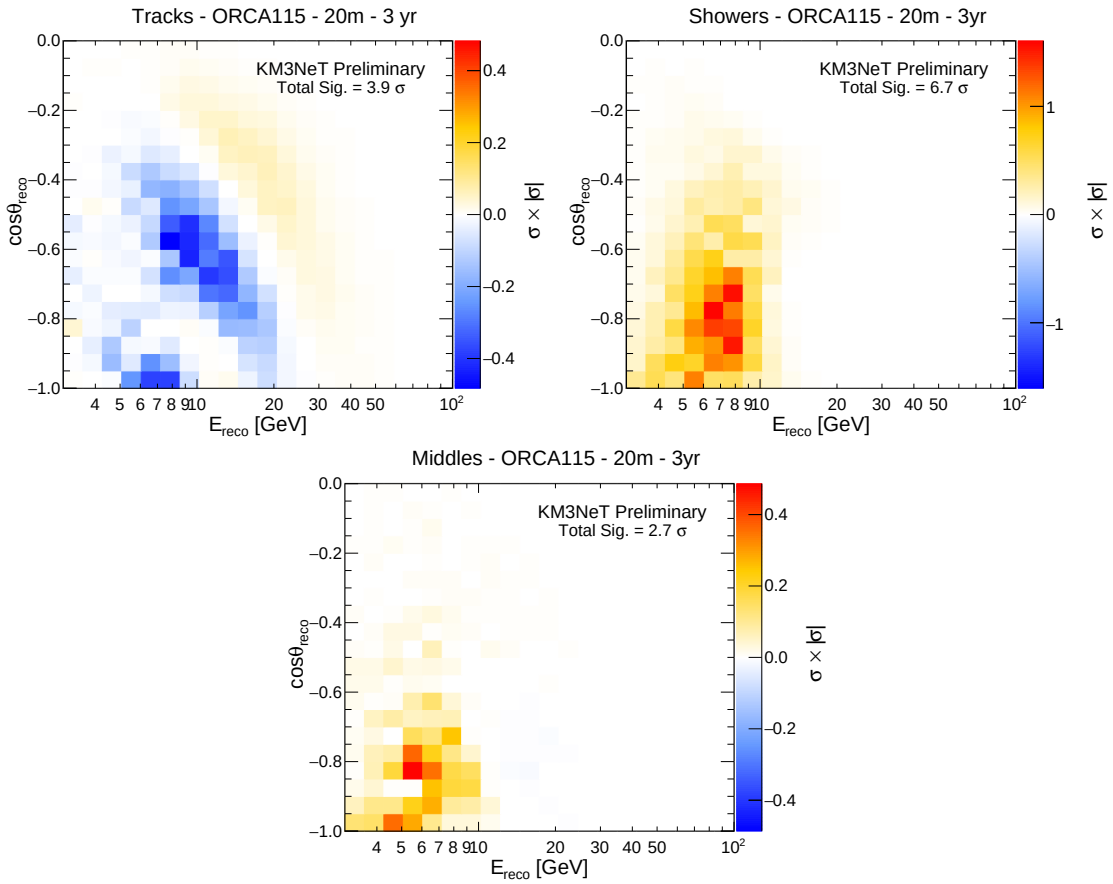

Figure 5.4: Statistical χ^2 maps for 3 years of exposure of ORCA corresponding to 20 m horizontal spacing between DUs as a function of reconstructed neutrino energy (E_{reco}) and zenith direction ($\cos\theta_{reco}$) for track (left column), middle (middle), and shower (right) event topologies. The color code indicates the values of signed-χ^2, as defined in Eq. 5.2. The total sensitivity quoted is the square-root of the sum of the absolute values of the χ^2s from each bin. Mind the difference in the colour scales on individual plots.

The individual contributions from track, middle and shower event classes are added in quadrature to compute the total significance, σ_{tot}(Eq. 4.19).

A higher (statistical-only) sensitivity ($\sim 6.7\sigma$) is observed in the shower class (mostly $\nu_e + \overline{\nu}_e$ CC events). This happens due to an interesting feature of oscillation probabilities and atmospheric neutrino fluxes. The transitions between ν_μ and ν_e are almost symmetrical, i.e. $P_{\nu_\mu \to \nu_e} \approx P_{\nu_e \to \nu_\mu}$, as seen in Fig. 1.4 and Fig. 1.6. Now, since $\nu_\mu\,(\overline{\nu}_\mu)$ flux is almost 4 times larger than the $\nu_e\,(\overline{\nu}_e)$ flux, the resulting $\nu_e\,(\overline{\nu}_e)$ flux reaching the detector is significantly higher compared to the unoscillated flux in case of NO (IO). Furthermore, the difference in $\nu_e/\overline{\nu}_e$ cross-sections (Fig. 2.4) and the initial $\nu_\mu/\overline{\nu}_\mu$ flux difference (Fig. 3.8) lead to a significant different number of $\nu_e\,(\overline{\nu}_e)$ events for NO and IO in a large $(E_{reco}, \theta_{reco})$ region of interest. The difference in event numbers are robust compared to the detector resolutions leading to a higher asymmetry effect in the shower channel.

5.2.2 Systematics

A similar set of systematics as accounted in the NSI analysis (Sec. 4.3.3) has been considered for the NMO sensitivity analysis. Tab. 4.7 summarises the exhaustive list of systematic parameters considered in the fit along with their statistical treatment, nominal values and external constraints, if any.

The final fit is done following an Asimov dataset [187] approach, by minimising the Poissonian log-likelihood ratio function:

$$-2\ln\mathcal{L} = 2\cdot\sum_{i\in\{bins\}}\left[N_i^{\mathrm{WO}}(\bar{o},\bar{s}) - N_i^{\mathrm{TO}}(\bar{o},\bar{s}) + N_i^{\mathrm{TO}}\cdot\ln\frac{N_i^{\mathrm{TO}}(\bar{o},\bar{s})}{N_i^{\mathrm{WO}}(\bar{o},\bar{s})}\right] + \sum_{j\in\{syst\}}\frac{(s_j-\hat{s}_j)^2}{\sigma_{s_j}^2}, \tag{5.3}$$

where the first sum runs over the histogram bins. $N_i^{\mathrm{TO}}(\bar{o},\bar{s})$ is the expected number of track/middles/shower events in the i^{th} bin weighted under an assumed true mass ordering (NO or IO); while, $N_i^{\mathrm{WO}}(\bar{o},\bar{s})$ is the number of expected events in the i^{th} bin for the wrong mass ordering (IO or NO, respectively) hypothesis. Both $N_i^{\mathrm{TO}}(\bar{o},\bar{s})$ and $N_i^{\mathrm{WO}}(\bar{o},\bar{s})$ are a function of the set of oscillation parameters, $\bar{o}$, as well as on the set of nuisance parameters, $\bar{s}$. The second sum runs over penalty terms of the number of nuisance parameters, j, listed in Tab. 4.7, $\hat{s}_j$ and $\sigma_{s_j}^2$ being the assumed prior and Gaussian standard deviation of the parameter j, respectively.

The effect of systematics on the sensitivity to neutrino mass ordering at ORCA, when fitted uniquely and/or cumulatively, are shown in Fig. 5.5 and Fig. 5.6 for NO and IO true orderings, respectively.

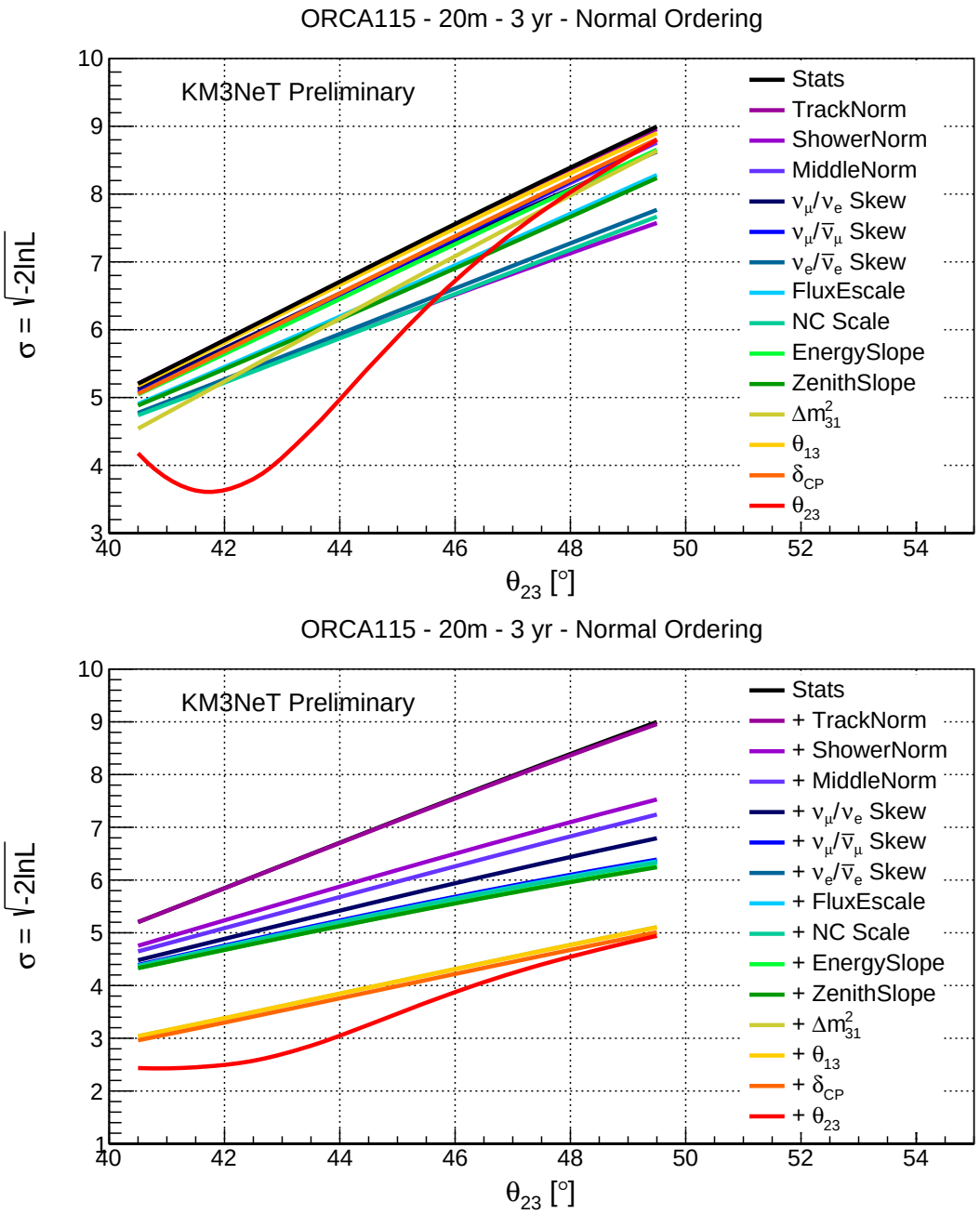

Figure 5.5: Effect of systematics (see Tab. 4.7), when fitted uniquely (top) and incrementally (bottom), on the projected NMO sensitivity at ORCA with 20 m horizontal spacing for true NO assumption. The black curve on both panels corresponds to the statistical-only sensitivity. The effect of systematics represented by colour coded curves for a particular value of θ_{23} can be gauged by looking at the relative separation from the stat-only curve. **Top**: each colour coded curve refers to the effect of that particular systematic which is uniquely fitted while the rest being kept fixed at their nominal values. **Bottom**: each colour coded curve corresponds to the effect of that particular systematic plus (+) the ones appearing on top of it being fitted simultaneously. Systematics are added cumulatively in the sequence as they appear in the legends from violet to red. The final sensitivity can be read from the widest (red) curve, which refers to the case of inclusion of all the systematic uncertainties accounted in this study.

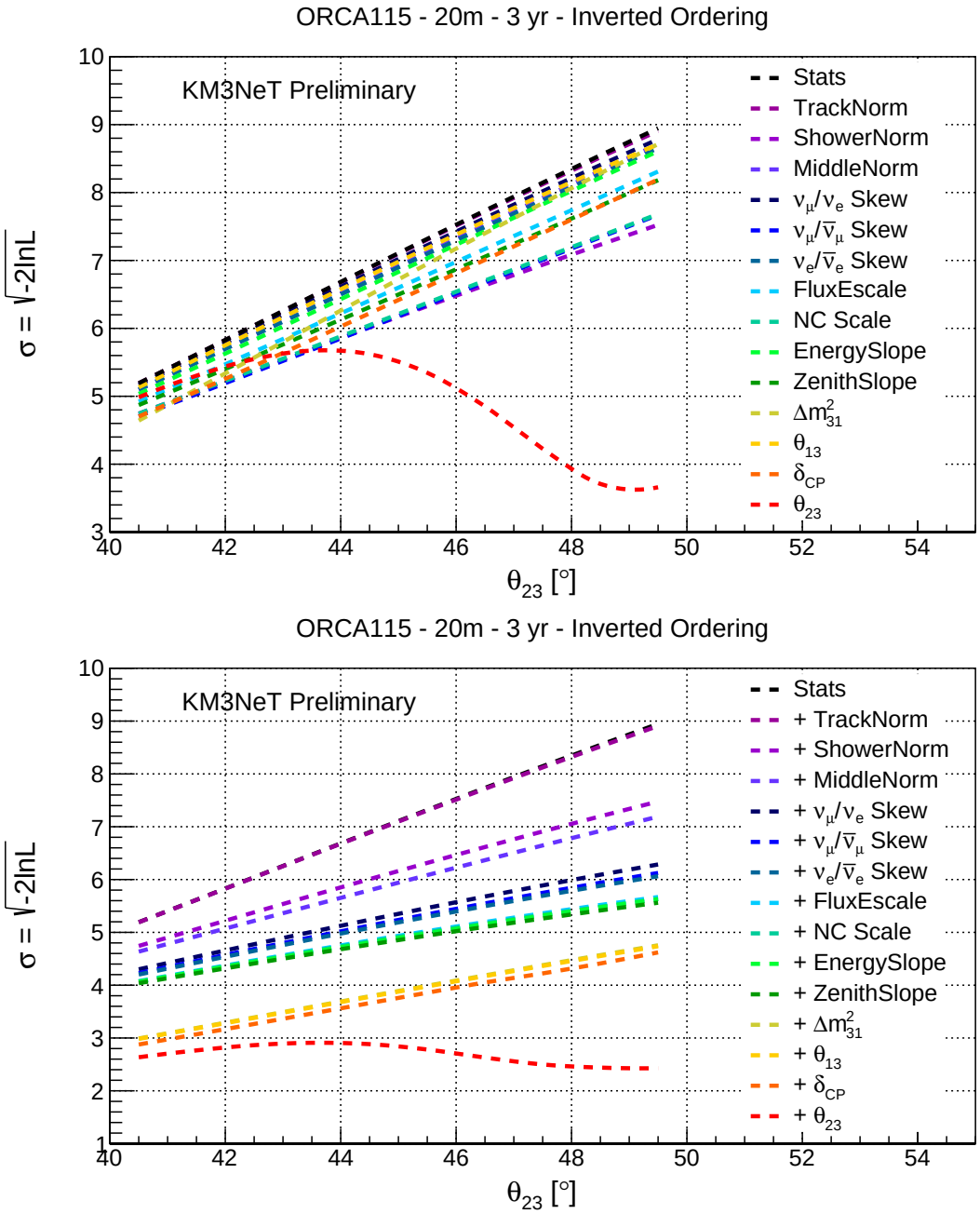

Figure 5.6: Effect of systematics, when fitted uniquely (top) and incrementally (bottom), on the projected NMO sensitivity at ORCA with 20 m horizontal spacing for true IO assumption. Read the caption of Fig. 5.5 for more info..

A starting value of θ_{23} in both octants ($\theta_{23} < 45^\circ \in$ lower octant and $\theta_{23} > 45^\circ \in$ higher octant) is given to the fitter and the minimum yield for $-2\ln\mathcal{L}$ is adopted. The drastic effect of marginalising over θ_{23} around $\sim 42^\circ(48^\circ)$ for NO (IO) happens due to the degeneracy between the octant of θ_{23} and the sign of $|\Delta m^2_{31}|$. For true NO, values of $\theta_{23} \in$ lower octant (LO) are in partial degeneracy with values of $\theta_{23} \in$ higher octant (HO) in the IO hypothesis. So the fitter finds the global minimum in the wrong (higher) octant for true NO. The situation is exactly reversed for true IO assumption.

Precise measurement of θ_{23} or deciphering its true octant is imperative for disentangling the mass ordering in a relatively quicker time frame. Vice versa, it can also be said

that knowledge of the true mass ordering will help in ruling out the wrong octant in a smaller time scale compared to the case when the NMO is unknown. We will study the later case in Chapter 6 in more detail. Besides this fact, the shower normalisation factor ("ShowerNorm") is seen to exhibit a "strong-pull" on the wrong-ordering fits.

5.2.3 Results

The final predicted mass ordering resolution achieved at ORCA is plotted as a function of true values of θ_{23} for both NO and IO assumptions including the effect of all other oscillation and systematic parameters. Sensitivity curves for sparse detector geometry of 23 m horizontal spacing are also estimated and drawn for comparison.

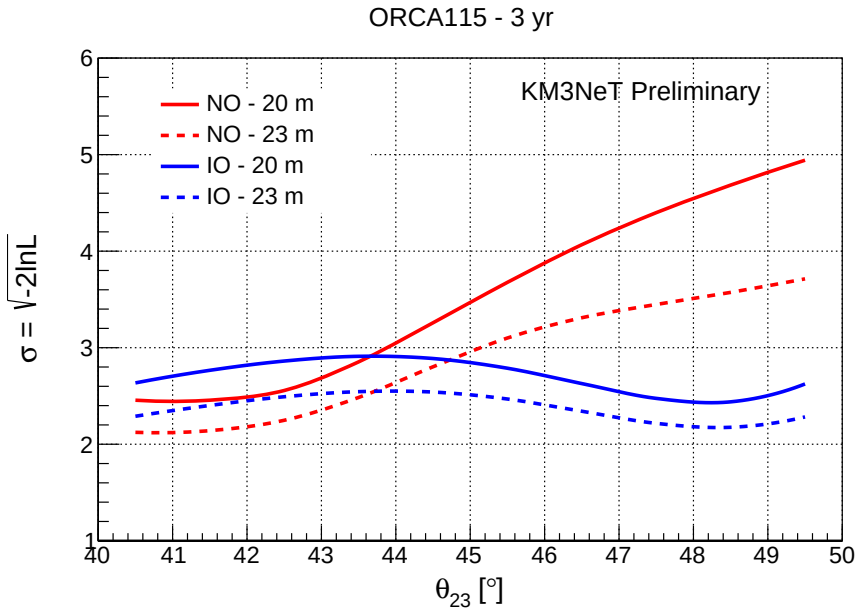

Figure 5.7: Projected sensitivity to the NMO after 3 years of ORCA runtime, as a function of true θ_{23}, for NO (red) and IO (blue) assumptions, with a global best-fit δ_{CP} of 221° (228°) for NO (IO). Solid (dashed) lines refer to 20 m (23 m) horizontal spacing between DUs.

A higher sensitivity with a denser detector geometry of 20 m horizontal spacing is achieved due to the improved resolutions and additional "hit-features" used for training the PID classifier, leading to a purer event sample and finally three event classes which adds up their contribution at the χ^2 level.

After 3 years of data taking, the NMO can be determined at the level of $\sim [2.5-5]\sigma$ ($[2.5-3]\sigma$) depending on the true value of θ_{23}, given the true ordering is NO (IO). The sensitivity is maximum for NO at true $\theta_{23} \in$ HO since, in the NO hypothesis, MSW resonance [26] happens in the neutrino channels, for which the initial atmospheric flux and the cross-sections are higher which further undergo large oscillation effects driven by high values of θ_{23}.

5.3 NMO in presence of NSIs

The conventional model of three-flavour neutrino oscillations provides a successful interpretation of the data taken by various experiments. This is true since the statistical fits to experimental data are usually done in the context of no NSI. One of the goals of

the present and future generation neutrino experiments is to firmly establish the correct framework to understand neutrino interactions. This motivates the phenomenological study of neutrino oscillations in the context of various exotic scenarios like the presence of NSIs [215, 216, 217]. In this work, we study the NMO sensitivity of ORCA in an assumed hypothesis of three-flavour neutrino oscillations in presence of NSI of neutrinos with d-quarks.

5.3.1 Ordering - NSI degeneracy

First, let us explore the partial degeneracy between the mass ordering and the sign of the NSI parameter $\epsilon_{\mu\tau}$. The muon disappearance probability, in presence of $\nu_\mu \rightarrow \nu_\tau$ NSIs, parameterised by non-zero $\epsilon_{\mu\tau}$, reads (Eq. 1.51)

$$P_{\nu_\mu \rightarrow \nu_\mu} = 1 - sin^2 2\tilde{\theta} sin^2 \left[\frac{\Delta m^2 L}{4E} \epsilon_{\mu\tau} \right]. \tag{5.4}$$

From Eq. 5.4, it is clear that a sign change in $\epsilon_{\mu\tau}$ ($\epsilon_{\mu\tau} \rightarrow -\epsilon_{\mu\tau}$) is equivalent to flipping the ordering ($\Delta m^2 \rightarrow -\Delta m^2$). Fig. 5.8 demonstrates the sign dependence of $\epsilon_{\mu\tau}$ in the muon disappearance channel. In the [30, 100] GeV range, we can see a parametric enhancement in the oscillation signature for $\epsilon_{\mu\tau} = -0.033$ in NO (top-left) which is congruent with $\epsilon_{\mu\tau} = 0.33$ in IO (botom-right). Similarly, a parametric suppression is also seen for $\epsilon_{\mu\tau} = -0.033$ in IO (top-right), which is in congruence with $\epsilon_{\mu\tau} = 0.33$ in NO (bottom-left).

This boils down to the problem that experimentally obtained $N_\nu^{NO}(\epsilon_{\mu\tau} = 0)$ and $N_\nu^{IO}(\epsilon_{\mu\tau} \neq 0)$ or $N_\nu^{IO}(\epsilon_{\mu\tau} = 0)$ spectra and $N_\nu^{NO}(\epsilon_{\mu\tau} \neq 0)$ spectra might look very similar. Moreover, this degeneracy can have serious implications on the task of fitting theoretical models to experimental data. We will account for these degenerate effects coming from NSIs while estimating the mass ordering sensitivity at ORCA in the next section.

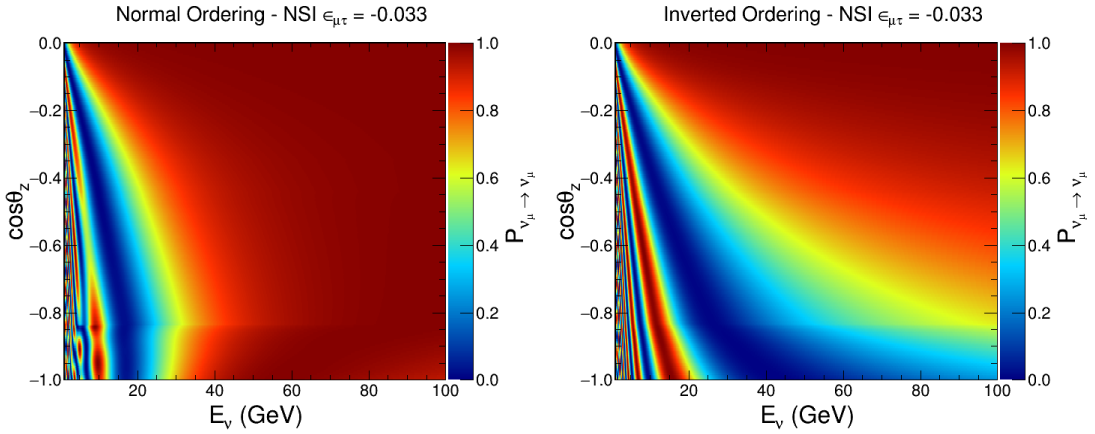

(a) $\epsilon_{\mu\tau} = -0.33$

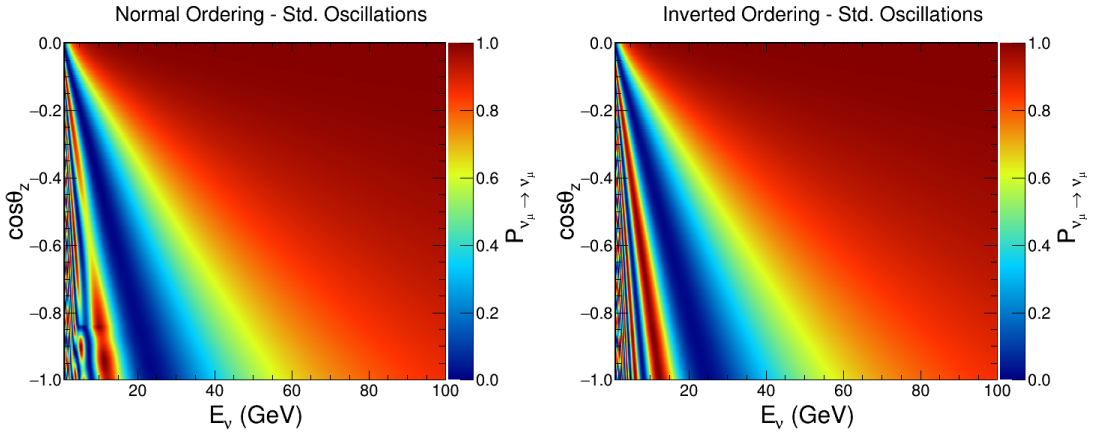

(b) $\epsilon_{\mu\tau} = 0$

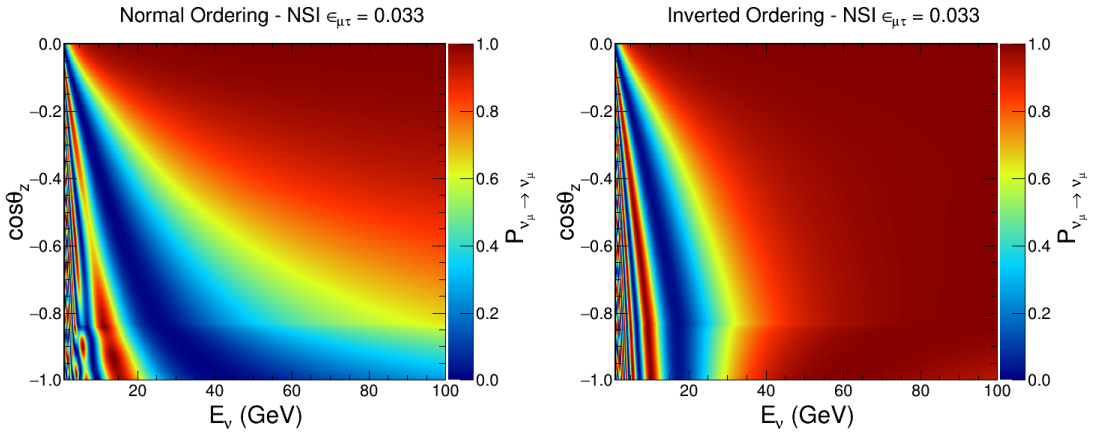

(c) $\epsilon_{\mu\tau} = 0.33$

Figure 5.8: $P_{\nu_\mu \to \nu_\mu}$ for (a) NSI $\epsilon_{\mu\tau} = -0.033$ (top panels) (b) NSI $\epsilon_{\mu\tau} = 0$ (middle) and (c) NSI $\epsilon_{\mu\tau} = 0.033$ (bottom). NO on the left and IO on the right. Negative NSI $\epsilon_{\mu\tau}$ in NO (top-left) is similar to positive NSI $\epsilon_{\mu\tau}$ in IO (bottom-right plot). Similarly, negative NSI $\epsilon_{\mu\tau}$ in IO (top-right) is similar to positive NSI $\epsilon_{\mu\tau}$ in NO (bottom-left). The case is exactly reversed for antineutrinos.

5.3.2 Systematics

In presence of sub-dominant new physics effects such as NSI, the resolution of neutrino mass ordering can be severely affected. If we assume $\epsilon_{\alpha\beta} = 0$, then a certain level of experimental precision is required to resolve the NO oscillation spectrum from an IO

oscillation spectrum. But, if $\epsilon_{\alpha\beta} \neq 0$ is assumed, much better experimental precision is needed to distinguish between both ordering spectra. The degree of precision can be quantified by doing a log-likelihood analysis with a modified test statistic:

$$-2\ln\mathcal{L} = 2 \cdot \sum_{i\in\{bins\}} \left[N_i^{\mathrm{WO}}(\bar{o},\bar{s},\bar{\epsilon}_{\alpha\beta}) - N_i^{\mathrm{TO}}(\bar{o},\bar{s},\bar{\epsilon}_{\alpha\beta}=0) + N_i^{\mathrm{TO}} \cdot \ln \frac{N_i^{\mathrm{TO}}(\bar{o},\bar{s},\bar{\epsilon}_{\alpha\beta}=0)}{N_i^{\mathrm{WO}}(\bar{o},\bar{s},\bar{\epsilon}_{\alpha\beta})} \right] + \sum_{j\in\{syst\}} \frac{(s_j-\hat{s}_j)^2}{\sigma_{s_j}^2}. \tag{5.5}$$

$N_i^{\mathrm{TO}}(\bar{o},\bar{s},\bar{\epsilon}_{\alpha\beta}=0)$ is the expected number of track/middles/shower events in the i^{th} bin weighted under standard oscillations ($\epsilon_{\alpha\beta}=0$) with an assumed true mass ordering, $N_i^{\mathrm{WO}}(\bar{o},\bar{s},\bar{\epsilon}_{\alpha\beta})$ is the number of expected events in the i^{th} bin for the wrong mass ordering (IO or NO, respectively) hypothesis weighted under a certain NSI hypothesis ($\epsilon_{\alpha\beta}\neq 0$). The second sum runs over penalty terms of the number of nuisance parameters, j, which now also include the NSI parameters. They are allowed to vary without any constraints/priors during the fitting procedure.

The effect of treating NSI parameters (over which we have obtained constraints in the previous chapters) as systematic uncertainties while fitting over in the alternate mass ordering hypothesis is shown in Fig. 5.9.

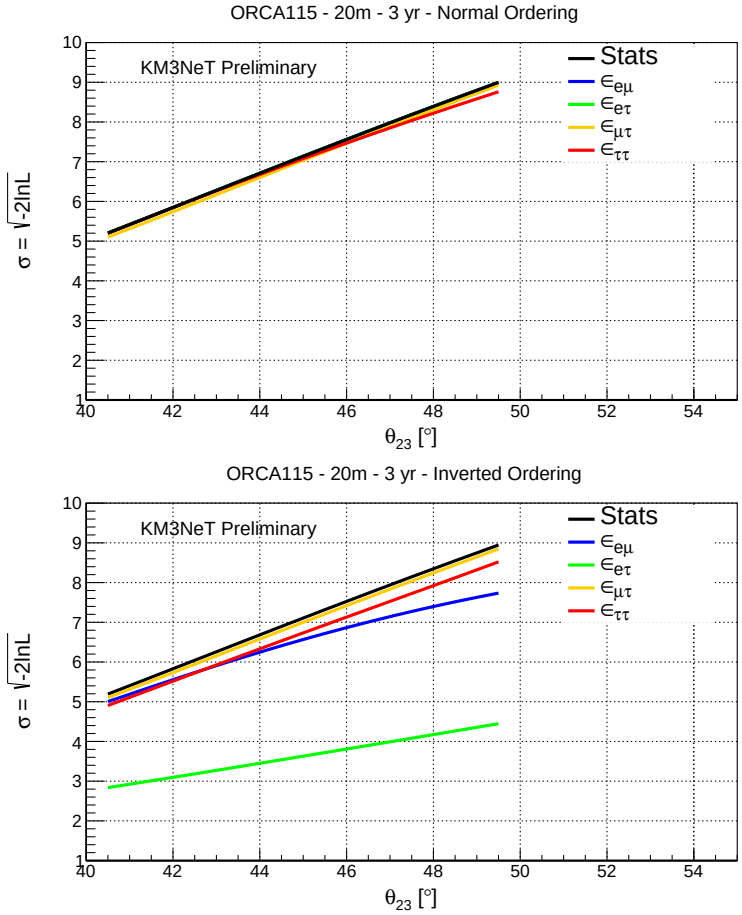

Figure 5.9: Effect of NSI parameters, when fitted uniquely on the projected NMO sensitivity at ORCA with 20 m horizontal spacing for true NO (top) and IO (bottom) assumptions.

5.3.3 Results

The impact of NSI on the expected mass ordering resolution at ORCA for an exposure of 3 years is shown in Fig. 5.10. While the effect of fitting an NSI model is seen to be marginal in the case of true NO for possible values of θ_{23}, in case of true IO, depending on true value of θ_{23}, there can be $\sim 1\sigma$ dilution in the sensitivity at ORCA. This is caused by the pulls exerted by the NSI parameters in the true IO fits (see Fig. 5.11).

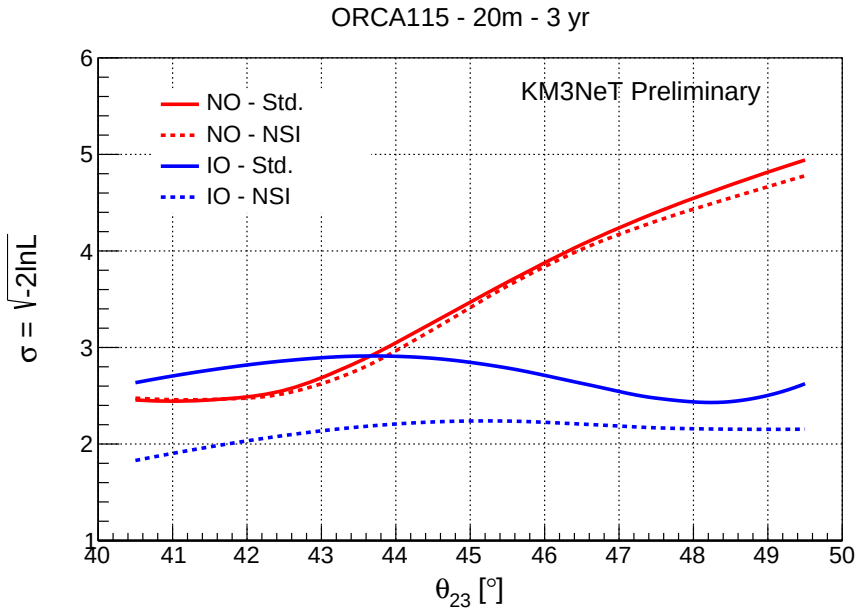

Figure 5.10: Projected sensitivity to the NMO after 3 years of ORCA runtime, as a function of true θ_{23}, for NO (red) and IO (blue) assumptions, with a global best-fit δ_{CP} of 221° (228°) for NO (IO) assumptions. Dashed (solid) lines refer to the case when the NSI parameters are simultaneously fitted (fixed at 0).

The resulting best-fit values of NSI parameters in the wrong ordering fits remain within the allowed range of the projected ORCA sensitivities (listed in Tab. 4.8), which are by far tighter than the current experimental limits and bounds from cosmology [76]. The best-fit values of NSI $\epsilon_{\alpha\beta}$ are shown in Fig. 5.11. While only NSI $\epsilon_{\tau\tau}$ is seen to exhibit a negligible pull in the true NO fit, in the case of true IO fit, all the NSI parameters exert non-negligible pulls on the final sensitivity, as seen in Fig. 5.10. Their best-fit values are compatible with current experimental limits.

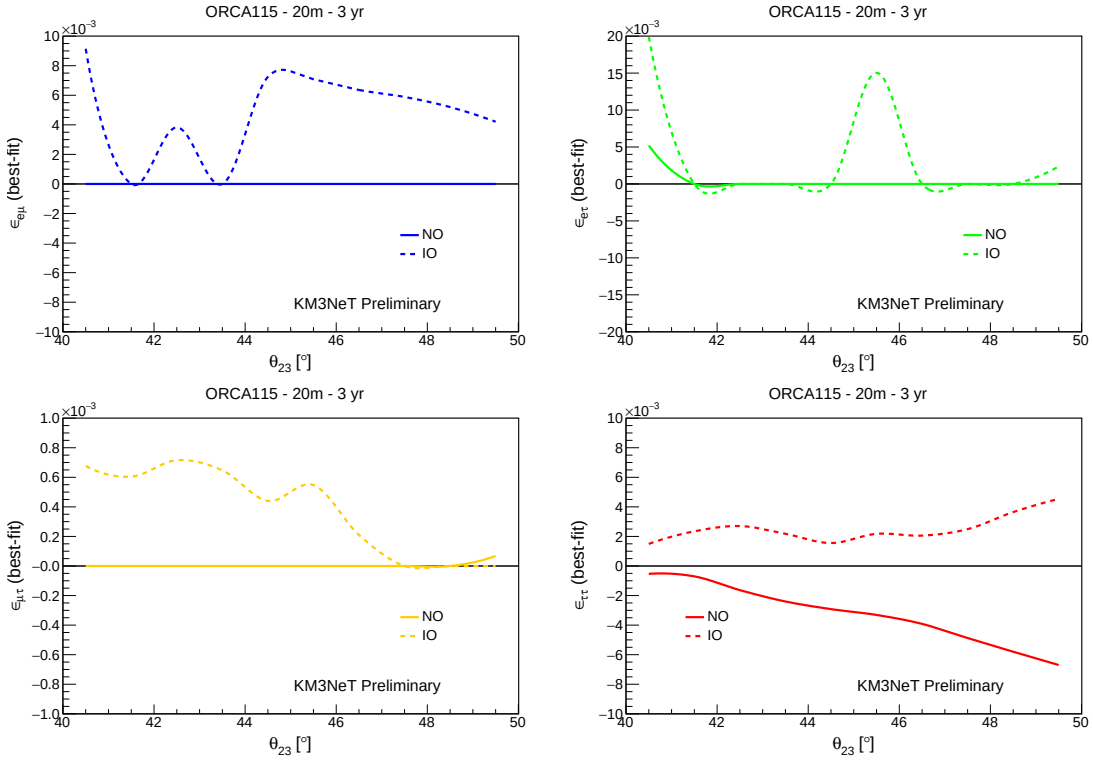

Figure 5.11: The best-fit values of NSI parameters for true NO (solid) and IO (dashed) fits, when they are all simultaneously fitted, as a function of true θ_{23}. Strong pulls are exhibited in the true IO fits. Mind the difference on Y-axis scales.

In conclusion, this work takes into account the uncertainty of fitting models to experimentally observed oscillation spectra and emphasizes the importance of testing different frameworks for better understanding and high precision measurements of the oscillation parameters. It also estimates how much the presence of NSIs can impair the sensitivity of ORCA to the measurement of neutrino mass ordering. Synergistic measurements from different experiments can resolve these ambiguities and point out to the correct framework realised in Nature.

6 Octant Sensitivity at ORCA

"Neutrinos are a billion times more abundant than the elementary particles of which we're made. So clearly, if you want to understand the universe, you have to understand the neutrinos."

— BORIS KAYSER

Contents

In Chapter 5, we have estimated the potential of ORCA to identify the true neutrino mass ordering (NMO) and explored the degenerate effects between the ordering and the octant of θ_{23} on the NMO sensitivity at ORCA. In this Chapter, we will quantify the resolving power of ORCA to disentangle the two octants of θ_{23} and explore the effects of this degeneracy on the octant sensitivity.

Sec. 6.1 poses the ambiguity in the determination of the true octant of θ_{23} and possible ways to resolve it in the light of three-flavour neutrino oscillations in matter driven by a non-zero θ_{13}. Sec. 6.2 and Sec. 6.3 present the event selection strategy and list of systematics, respectively, employed in this study. Finally, based on an Asimov dataset approach [187], sensitivities to the octant of θ_{23} are reported in Sec. 6.4.

6.1 The Octant Problem

The "general" definition of the octant problem refers to the present uncertainty in the measurement of θ_{23} [90]. However, the octant degeneracy implies the indistinguishability between θ_{23} and $\pi/2 - \theta_{23}$. This is exact in case of vacuum oscillations, since the oscillation probabilities are functions of $\sin^2 2\theta_{23}$. Depending on the true value of θ_{23}, we can have three solutions:

- Maximal mixing: $\theta_{23} = 45°$. This is called maximal mixing since $\sin^2 2\theta_{23}$ appears as an amplitude term in the oscillation probabilities and a value of 45° correspond to maximum oscillation effects driven by $\sin^2 2\theta_{23} = 1$.
- Lower Octant[1] (LO): $\theta_{23} \in [0°, 45°)$.
- Higher Octant[2] (HO): $\theta_{23} \in (45°, 90°]$.

The source of this ambiguity in the determination of the value of θ_{23} can be classified into two categories:

- **Intrinsic degeneracy:** This happens when oscillation probabilities are function of $\sin^2 2\theta_{23}$ and hence it is impossible to distinguish between θ_{23} and $\pi/2 - \theta_{23}$. This is inherent and cannot be lifted if θ_{23} corresponds to maximal mixing 45°. Mathematically,
$$P(\theta_{23}^{true}) = P(\pi/2 - \theta_{23}^{true}). \tag{6.1}$$
- **Parameter degeneracy:** This refers to the degeneracy of θ_{23} with other oscillation parameters, which leads to the confusion of the true octant in this case. This happens when oscillation probabilities are function of $\sin\theta_{23}$ or $\cos\theta_{23}$: $P(\theta_{23}^{true}) \neq P(\pi/2 - \theta_{23}^{true})$. However, for different values of the parameters θ_{13} and δ_{CP} and the uncertainty of the knowledge of the true mass ordering, the oscillation probability functions become identical for values of θ_{23} in opposite octants for different choices of values of these parameters. Mathematically,
$$P(\theta_{23}^{true}, \Delta m^2_{32}, \theta_{13}, \delta_{CP}) = P(\pi/2 - \theta_{23}^{true}, -\Delta m^{2\prime}_{32}, \theta'_{13}, \delta'_{CP}). \tag{6.2}$$
More generically, it can be expressed as
$$P(\theta_{23}^{true}, \Delta m^2_{32}, \theta_{13}, \delta_{CP}) = P(\theta_{23}^{wrong}, -\Delta m^{2\prime}_{32}, \theta'_{13}, \delta'_{CP}). \tag{6.3}$$
Although θ_{13} is known with great precision from current experiments, δ_{CP} covers a wide range of allowed values [90]. Apart from this, the neutrino mass ordering is still unidentified, which is one of the biggest sources of uncertainty in the determination of the octant of θ_{23}. These degeneracies are studied closely in the next section.

6.1.1 Parameter degeneracies

A continuous degeneracy in the $\theta_{23} - \theta_{13} - \delta_{CP}$ plane has been studied in [218]. However, for our study, we present the estimation of octant sensitivity in the light of well-constrained non-zero θ_{13} [219]. This drastically reduces the uncertainty on the measurement of θ_{23}. A precise measurement of θ_{13} is imperative for resolving the octant degeneracy [220, 221]. We classify eight degenerate solutions corresponding to different combinations of hierarchy[3] – octant – δ_{CP}. The harmonic δ_{CP} plane can be divided into two parts, "Lower-Half-Plane" (LHP) (with $\delta_{CP} \in [0°, 180°]$) and "Upper-Half-Plane" (UHP) (with $\delta_{CP} \in [180°, 360°]$).

Let us look at occurrence of different degenerate combinations one by one. We restrict our arguments to the electron appearance channels $P_{\nu_\mu \to \nu_e}$ (and/or $P_{\bar{\nu}_\mu \to \bar{\nu}_e}$), since this "golden channel" is sensitive to all three parameters (δ_{CP}, θ_{23} and sign of Δm^2_{32}) and is also one of the dominant channels in both atmospheric and long-baseline experiments.

[1] Also known as First Octant (FO) in literature.
[2] Also known as Second Octant (SO).
[3] The term "hierarchy" is used here instead of "ordering" to avoid confusion with the initials of octant.

1. Wrong hierarchy (WH) – Wrong octant (WO) – Wrong δ_{CP}: This corresponds to isoprobability curves such that P(NH, LO, LHP) = P(IH, HO, UHP).
2. Wrong hierarchy (WH) – Wrong octant (WO) – Right δ_{CP}: P(NH, LO, LHP) = P(IH, HO, LHP).
3. Wrong hierarchy (WH) – Right octant (RO) – Wrong δ_{CP}: P(NH, LO, LHP) = P(IH, LO, UHP).
4. Wrong hierarchy (WH) – Right octant (RO) – Right δ_{CP}: This does not exist at the probability level.
5. Right hierarchy (RH) – Wrong octant (WO) – Wrong δ_{CP}: P(NH, LO, LHP) = P(NH, HO, UHP).
6. Right hierarchy (RH) – Wrong octant (WO) – Right δ_{CP}: This does not exist at the probability level.
7. Right hierarchy (RH) – Right octant (RO) – Wrong δ_{CP}: P(NH, LO, LHP) = P(NH, LO, UHP).
8. Right hierarchy (RH) – Right octant (RO) – Right δ_{CP}: The correct solution.

The eight combinations are schematically represented in Fig. 6.1 (for neutrinos) and in Fig. 6.2 (for antineutrinos). In each figure, the right (left) annular rings represent the parameter space for NO (IO). The outer (inner) ring corresponds to the choice of octant HO (LO). In each ring, the angular direction denotes the value of δ_{CP}, which is divided into two half planes: LHP and UHP. Thus, the complete parameter space in each figure is divided into eight regions, corresponding to the two choices of ordering, octant and half-plane of δ_{CP}. The ordering – octant degeneracy is depcited in yellow while the ordering – δ_{CP} degeneracy is shaded with red stripes. The parts of the rings that are marked in green are free of parameter degeneracies.

Note that, moving from neutrinos in Fig. 6.1 to antineutrinos in Fig. 6.2 is equivalent to flipping the mass ordering (rings switched sideways) followed by a CP phase change by π (rings rotated upside-down). The ordering – octant degeneracy is discrete, while the octant – δ_{CP} is continuous.

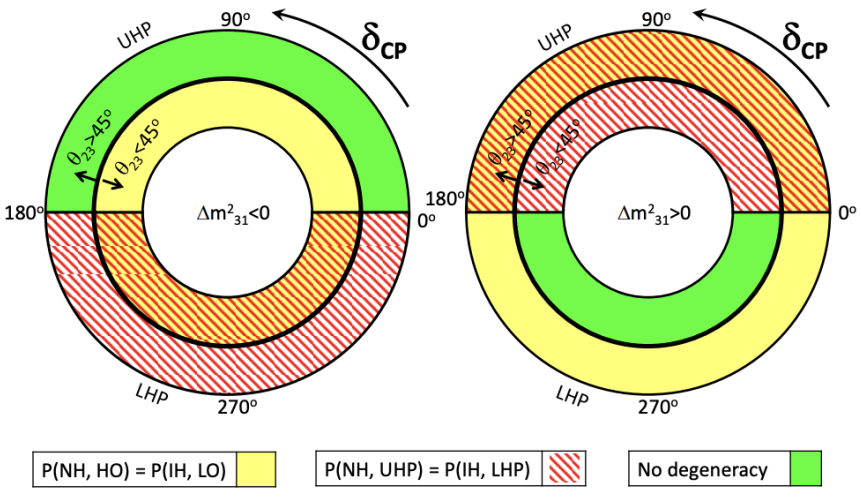

Figure 6.1: Schematic representation of parameter degeneracies in three-flavour *neutrino* oscillations. From [222].

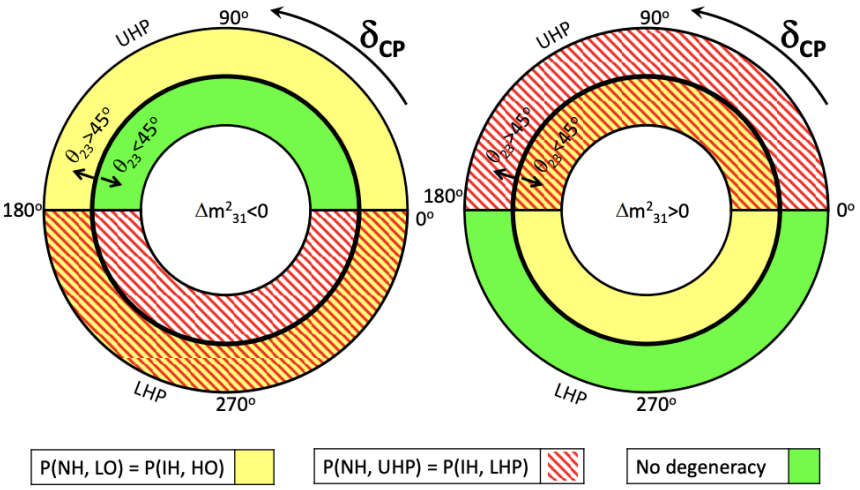

Figure 6.2: Schematic representation of parameter degeneracies in three-flavour *antineutrino* oscillations. From [222].

Some of these degenerate cases can be alleviated at long-baseline experiments by looking at the neutrino and antineutino data separately. But in our case, this is not possible since neither ORCA is sensitive to the helicity states, nor it can differentiate between appearance and disappearance channels. However, we can still measure the true θ_{23} by looking for statistical excess or deficit of $(\nu + \overline{\nu})$ event distributions relative to the combination of hierarchy – octant – δ_{CP} that fits the data most accurately. This will lead to the rejection of hypotheses that correspond to some of these eight combinations.

6.1.2 Lifting the degeneracy

In the light of atmospheric experiments like ORCA, the relevant oscillation channels to which the octant of θ_{23} is mostly sensitive to are the muon disappearance and electron appearance channels. The probability expressions in the OMSD approximations [219] read

$$\begin{aligned} P^m_{\nu_\mu \to \nu_\mu} = 1 &- \cos^2\theta^m_{13}\sin^2 2\theta_{23}\sin^2\left(\frac{[\Delta m^2_{31} + A_{CC} + (\Delta m^2_{31})^m]L}{E}\right) \\ &- \sin^2\theta^m_{13}\sin^2 2\theta_{23}\sin^2\left(\frac{[\Delta m^2_{31} + A_{CC} + (\Delta m^2_{31})^m]L}{E}\right) \\ &- \sin^4\theta_{23}\sin^2 2\theta^m_{13}\sin^2\left(\frac{(\Delta m^2_{32})^m L}{E}\right) \end{aligned} \tag{6.4}$$

and

$$P^m_{\nu_\mu \to \nu_e} = \sin^2\theta_{23}\sin^2 2\theta^m_{13}\sin^2\left(\frac{\Delta m^{2m}_{32} L}{E}\right), \tag{6.5}$$

where,

$$\sin^2 2\theta^m_{13} = \frac{\sin^2(2\theta_{13})}{(\cos 2\theta_{13} - A_{CC}/\Delta m^2_{31})^2 + \sin^2 2\theta_{13}} \tag{6.6}$$

$$(\Delta m^2_{31})^m = \Delta m^2_{31}[(\cos 2\theta_{13} - A_{CC}/\Delta m^2_{31})^2 + \sin^2 2\theta_{13}]. \tag{6.7}$$

$P^m_{\nu_\mu \to \nu_\mu}$ has leading terms proportional to $\sin^2 2\theta_{23}$, which give rise to the intrinsic octant degeneracy. However, θ^m_{13} in matter gets amplified to maximal values near resonance and the combination $\sin^4\theta^m_{23}\sin^2 2\theta_{13}$ no longer remains invariant over opposite octants of θ_{23}.

The value of $\sin^2 2\theta_{13}$ becomes close to unity in both octants, irrespective of the value of θ_{13} in vacuum.

The signatures of the asymmetry in the muon neutrino disappearance channel, predicted for a true value of $\theta_{23}^{true} = 48.6^\circ$ in HO and corresponding degenerate test value of $\theta_{23}^{test} = (90 - 48.6)^\circ$ in LO, are shown in Fig. 6.3. The asymmetry is maximal for a wide region of core-crossing neutrinos with energies $\in$ [20, 30] GeV.

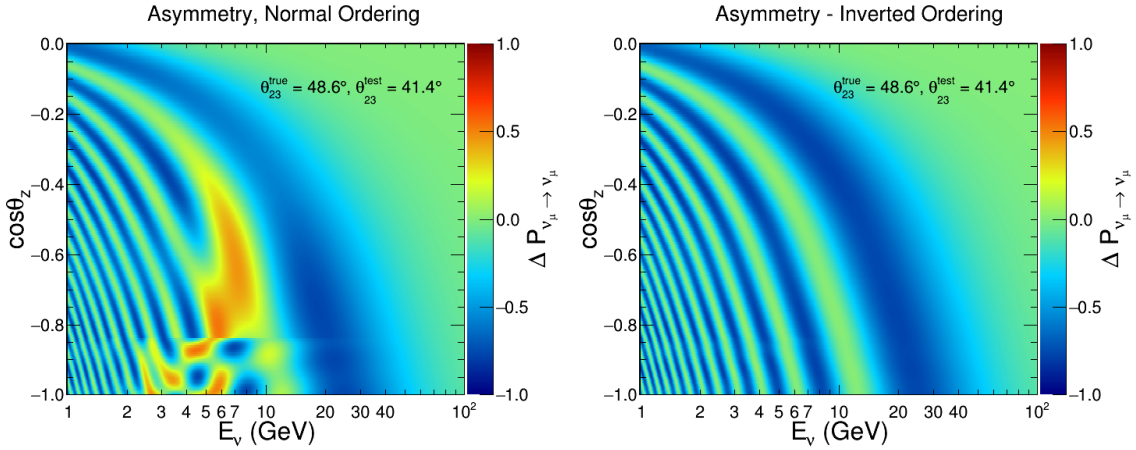

Figure 6.3: Asymmetry in $P^m_{\nu_\mu \to \nu_\mu}$ channel as a function of neutrino energy and cosine of the zenith angle for NO (left) and IO (right) assumptions. The true value of θ_{23} is set at 48.6° (adopted from [90]) in HO and the test value at $\theta_{23}^{test} = 41.4^\circ$. The behaviour for antineutrinos is equivalent to mass ordering being flipped (given $\delta_{CP} = 0$).

$P^m_{\nu_\mu \to \nu_e}$ has the leading term proportional to $\sin^2 \theta_{23}$, which is sensitive to the octant. The strong octant-sensitive behaviour of the term $\sin^2 \theta_{23} \sin^2 2\theta^m_{13}$ near resonance can alleviate the degeneracy. However, this channel is affected by the large uncertainty in δ_{CP} since, in this case, sub-leading corrections appear while estimating the oscillation probabilities numerically.

The signatures of asymmetry in the electron neutrino appearance channel, predicted for a true value of $\theta_{23}^{true} = 48.6^\circ$ in HO and corresponding degenerate test value of $\theta_{23}^{test} = (90 - 48.6)^\circ$ in LO, are shown in Fig. 6.4. The asymmetry is maximal for a wide region of mantle-crossing neutrinos with energies $\in$ [4, 10] GeV. Since matter effects happen for antineutinos in IO, the asymmetry in the electron neutrino appearance channel for IO is negligible.

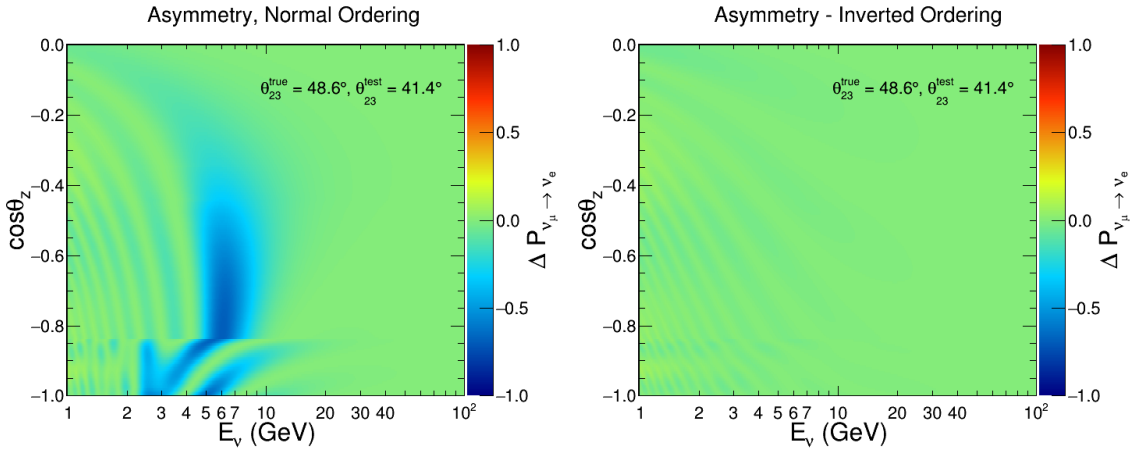

Figure 6.4: Asymmetry in $P^{m}_{\nu_\mu \to \nu_e}$ channel as a function of neutrino energy and cosine of the zenith angle for NO (left) and IO (right) assumptions. The true value of θ_{23} is set at 48.6° (adopted from [90]) in HO and the test value at $\theta_{23}^{test} = 41.4°$. The behaviour for antineutrinos is equivalent to mass ordering being flipped (given $\delta_{CP} = 0$).

6.2 Event selection and statistical significance

The strategy for event selection is kept at par with what has been employed in the NSI and NMO analyses with ORCA (Sec. 4.3.1) corresponding to a detector geometry of 20 m horizontal spacing. The number of expected events from different channels entering into the final MC sample can be found in Tab. 4.6.

The test statistic in this case to disentangle the octants of θ_{23} is defined as

$$\chi^2_{E,\theta_z} = \frac{\left(N^{\mathrm{WO}}_{E,\theta_z} - N^{\mathrm{TO}}_{E,\theta_z}\right) \times \left|N^{\mathrm{WO}}_{E,\theta_z} - N^{\mathrm{TO}}_{E,\theta_z}\right|}{N^{\mathrm{TO}}_{E,\theta_z}}. \tag{6.8}$$

$N^{\mathrm{TO}}_{E,\theta_z}$ is the expected number of track/middle/shower events in the corresponding (E, θ_z) bin weighted with a true value of θ_{23} under an assumed octant hypothesis (LO or HO), while $N^{\mathrm{WO}}_{E,\theta_z}$ is the number of expected events in the same (E, θ_z) bin in the wrong octant (HO or LO, respectively). We set the values of true and test values such that, $\theta_{23}^{test} = \pi/2 - \theta_{23}^{true}$.

Fig. 6.5 and Fig. 6.6 show the signed-χ^2 maps for reconstructed events in the three event classes for 3 years of full ORCA (115 DUs) runtime with 20 m horizontal spacing. 20 logarithmic bins were chosen in reconstructed neutrino energy $(E_\nu) \in [3, 100]$ GeV, while 20 linear bins in cosine of the reconstructed zenith angle $(\theta_z) \in [-1, 0]$. The absolute value of χ^2 is stored, so that each bin content represents the contribution to the total χ^2 from respective event class. The colour codes represent the excesses and deficits.

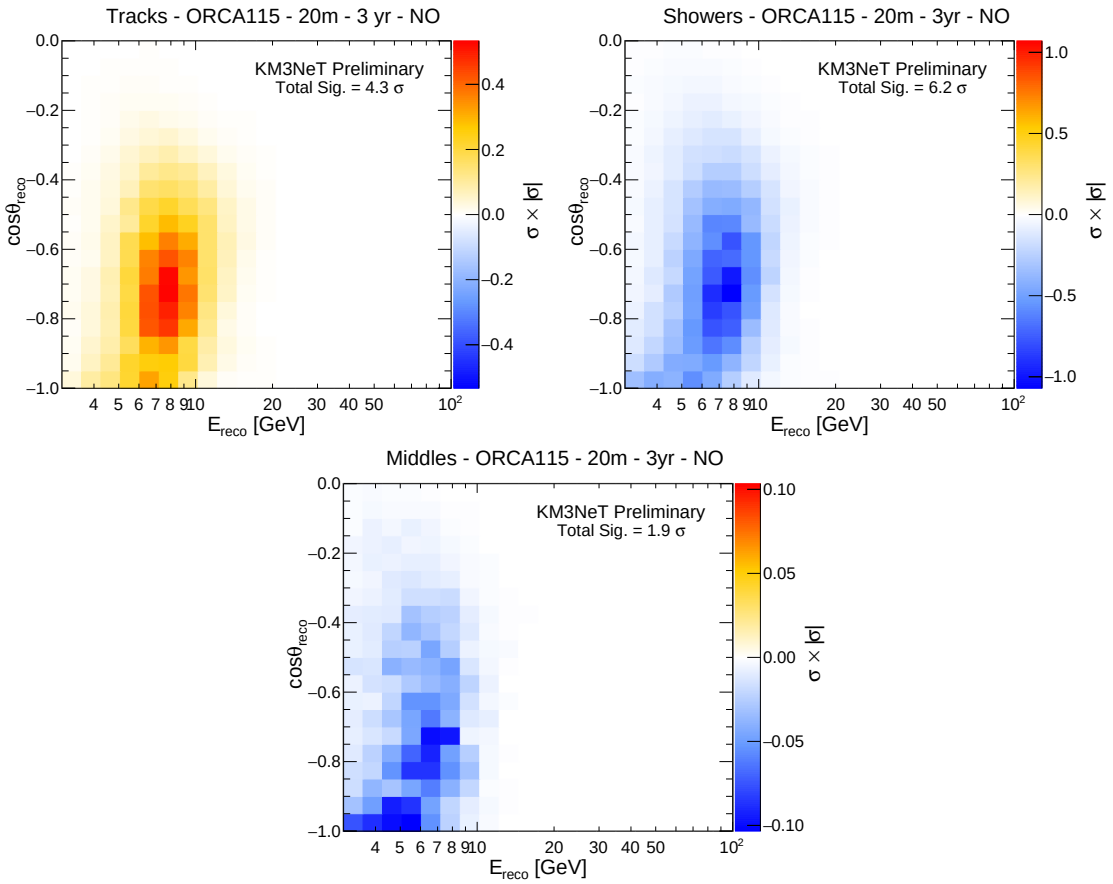

Figure 6.5: Statistical χ^2 maps for 3 years of exposure of ORCA corresponding to 20 m horizontal spacing between DUs as a function of reconstructed neutrino energy (E_{reco}) and zenith direction ($\cos\theta_{reco}$) for track (left column), middle (middle), and shower (right) event topologies. The true θ_{23} is kept in HO ($= 48.6°$) [90], while the test point is fixed at $\theta_{23} = 41.4°$ in the wrong octant. Normal Ordering (NO) is assumed. The color code indicates the values of signed-χ^2, as defined in Eq. 6.8. The total sensitivity quoted is the square-root of the sum of the absolute values of the χ^2 from each bin. Mind the difference in the colour scales on individual plots.

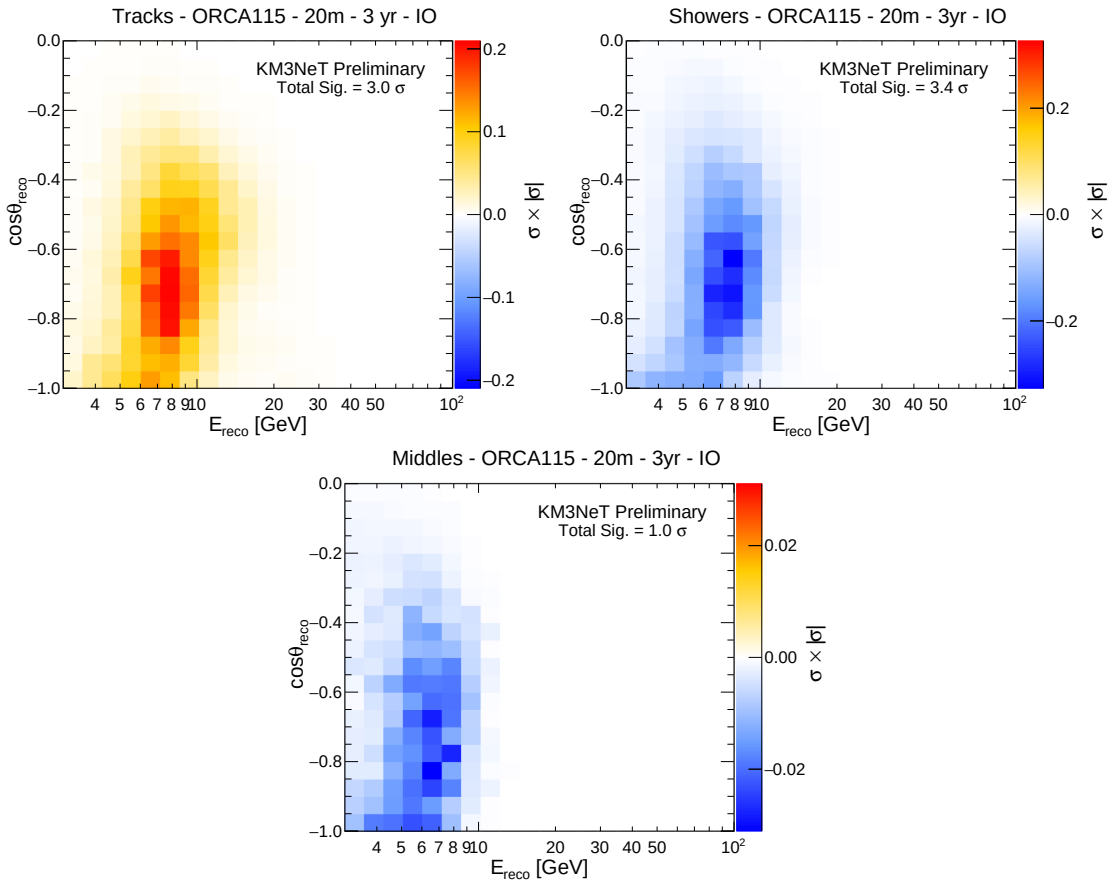

Figure 6.6: Statistical χ^2 maps for 3 years of exposure of ORCA corresponding to true Inverted Ordering (IO). See also caption of Fig. 6.5.

A higher (statistical-only) sensitivity is observed in the shower class for both orderings. The statistical-only sensitivities are higher for true NO, since in the true NO hypothesis (top panels), matter effects [26] happen in the neutrino channels, for which the initial atmospheric (neutrino) flux and (neutrino) cross-section are larger than for antineutrinos. The individual contributions from track, middle and shower event classes are added in quadrature to compute the total significance, σ_{tot} Eq. 4.19.

6.3 Systematics

A similar set of systematics as accounted in the NSI and NMO analysis (Sec. 4.3.3) has been considered for the octant sensitivity analysis. Tab. 4.7 summarises the exhaustive list of systematic parameters considered in the fit along with their statistical treatment, nominal values and external constraints, if any.

The final fit is done following an Asimov dataset [187] approach, by minimising the Poissonian log-likelihood ratio function

$$-2\ln\mathcal{L} = 2\cdot\sum_{i\in\{bins\}}\left[N_i^{\mathrm{WO}}(\bar{o},\bar{s}) - N_i^{\mathrm{TO}}(\bar{o},\bar{s}) + N_i^{\mathrm{TO}}\cdot\ln\frac{N_i^{\mathrm{TO}}(\bar{o},\bar{s})}{N_i^{\mathrm{WO}}(\bar{o},\bar{s})}\right] + \sum_{j\in\{syst\}}\frac{(s_j-\hat{s}_j)^2}{\sigma_{s_j}^2}, \tag{6.9}$$

where the first sum runs over the histogram bins. $N_i^{\mathrm{TO}}(\bar{o},\bar{s})$ is the expected number of track/middles/shower events in the i^{th} bin weighted under an assumed true octant (LO

or HO), while $N_i^{\mathrm{WO}}(\bar{o}, \bar{s})$ is the number of expected events in the i^{th} bin for the wrong octant (HO or LO, respectively) hypothesis. Both $N_i^{\mathrm{TO}}(\bar{o}, \bar{s})$ and $N_i^{\mathrm{WO}}(\bar{o}, \bar{s})$ are a function of the set of oscillation parameters, $\bar{o}$, as well as on the set of nuisance parameters, $\bar{s}$. The second sum runs over penalty terms of the number of nuisance parameters, j, listed in Tab. 4.7, $\hat{s_j}$ and $\sigma_{s_j}^2$ being the assumed prior and Gaussian standard deviation of the parameter j, respectively.

The effect of systematics on the resolution of the octant at ORCA, when fitted uniquely or cumulatively, is shown in Fig. 6.7 and Fig. 6.8 for NO and IO true orderings, respectively.

Note that, for each curve, except the widest (red) curve that corresponds to the case of marginalising over θ_{23} in the wrong octant, the test values of θ_{23}^{test} have been fixed at $\pi/2 - \theta_{23}^{true}$. This is rather an arbitrary choice of θ_{23}^{test}, motivated by the fact θ_{23}^{test} is partially degenerate with $\pi/2 - \theta_{23}^{true}$ (as we have seen at the probability level discussions in Sec. 6.1). Thus, the effect of θ_{23} appears to be the most drastic among all other systematic parameters considered in the fit. Apart from θ_{23}, the shower normalisation factor ("Shower Norm") is seen to exhibit a strong pull in the wrong-octant fits.

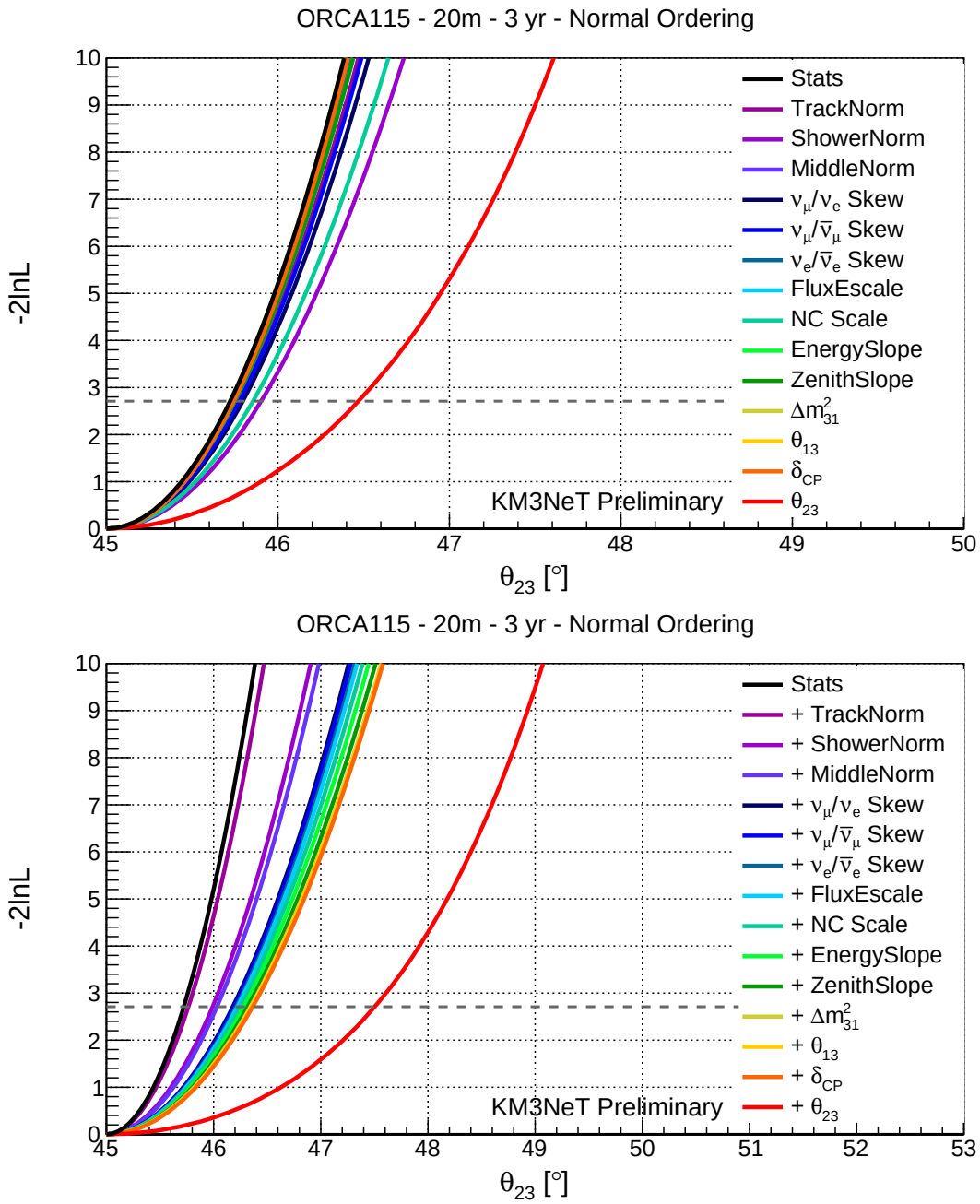

Figure 6.7: Effect of systematics (Tab. 4.7), when fitted uniquely (top) and incrementally (bottom), on the octant resolution at ORCA with 20 m horizontal spacing for true NO assumption. The black curve on both panels corresponds to the statistical-only sensitivity. The effect of systematics represented by colour coded curves for a particular value of θ_{23} can be gauged by looking at the relative separation from the stat-only curve. **Top**: each colour coded curve refers to the effect of that particular systematic which is uniquely fitted while the rest being kept fixed at their nominal values. **Bottom**: each colour coded curve corresponds to the effect of that particular systematic plus (+) the ones appearing on top of it being fitted simultaneously. Systematics are added cumulatively in the sequence as they appear in the legends from violet to red. The final sensitivity can be read from the widest (red) curve which refers to the case of inclusion of all the systematic uncertainties accounted in this study.

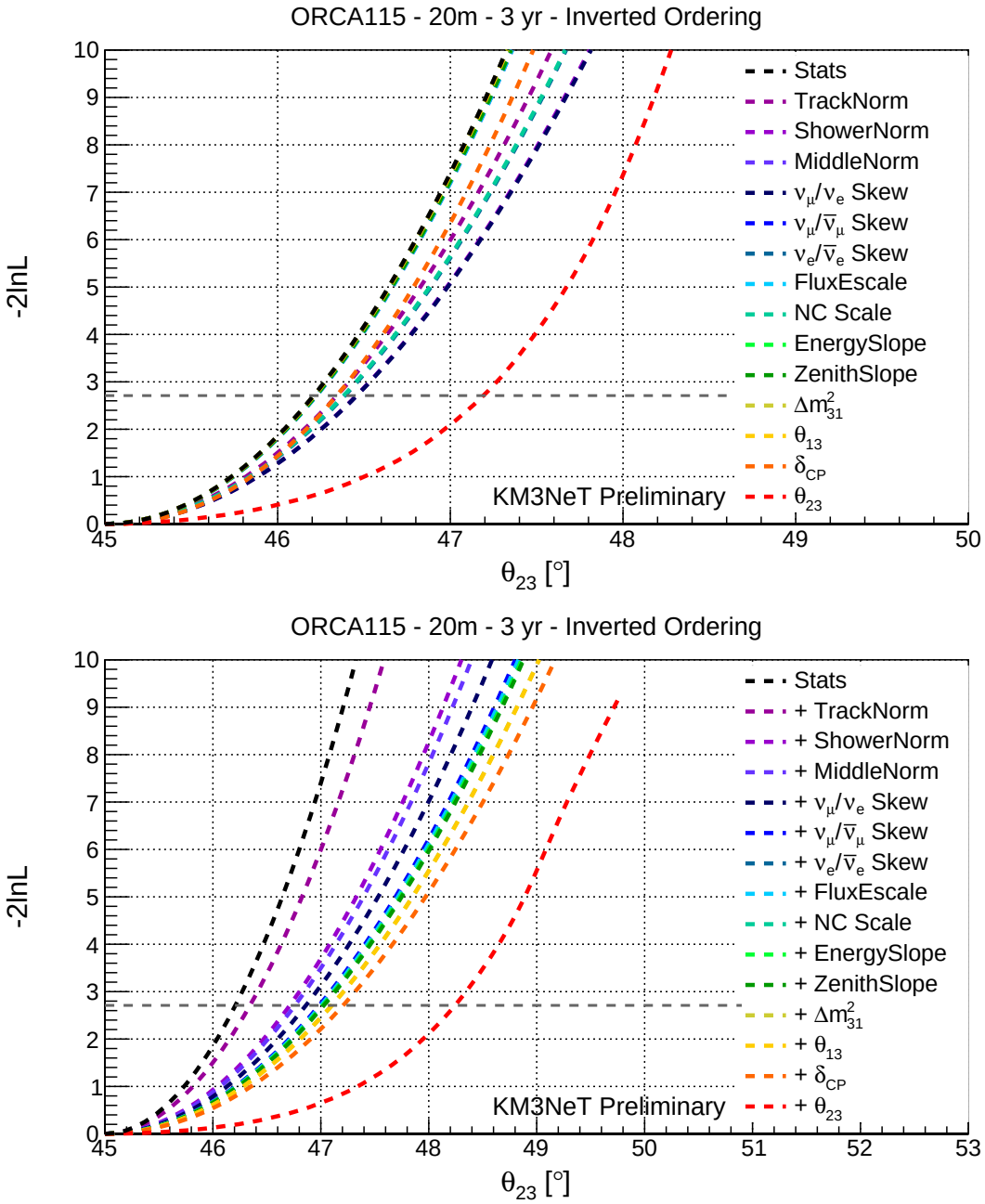

Figure 6.8: Effect of systematics, when fitted uniquely (top) and incrementally (bottom), on the octant resolution at ORCA with 20 m horizontal spacing for true IO assumption. Read the caption of Fig. 6.7 for more info..

6.4 Results

Results of the sensitivity to the octant resolution of θ_{23} at ORCA are presented in different physics planes in the following sub-sections.

6.4.1 Sensitivity vs δ_{CP}

The final octant sensitivity achieved at ORCA is plotted in Fig. 6.9 as a function of true values of δ_{CP} including the effect of all other oscillation and systematic parameters. For each true value of δ_{CP}, sensitivities corresponding to four possible combinations of

ordering – octant are drawn. Note that for each case, the true ordering is kept fixed in the test hypothesis which is fitted. Hence, the Wrong Ordering – Wrong Octant combinations are not taken into account for brevity. This translates into the optimistic assumption of the NMO being correctly identified beforehand ORCA is set to resolve the octant.

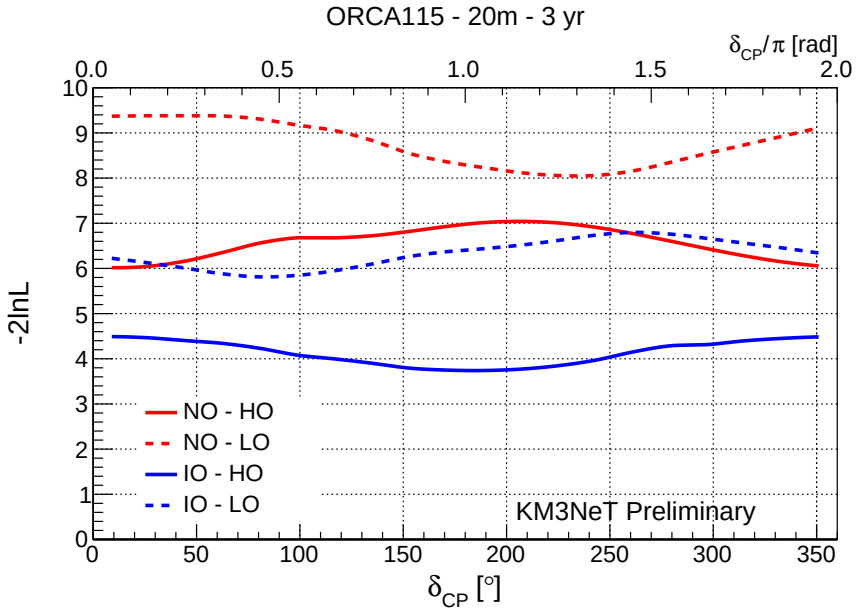

Figure 6.9: Resolving power of ORCA in disentangling the octant of θ_{23} as a function of true δ_{CP} for various possible combinations of the true ordering and the octant. Normal (Inverted) ordering is assumed for the red (blue) curves. True θ_{23} is assumed at 48.6° in the higher octant (solid curves) or at 42.4° in the lower octant (dashed).

If we compare the true HO cases (solid lines), the sensitivities are higher in NO than IO due to higher statistics of neutrinos encountering matter effects in true NO hypothesis. On the other hand, if we compare true HO and true LO cases (solid and dashed) for a specific mass ordering (NO or IO), sensitivities are higher for true LO than true HO. This is because $\chi^2 \sim (N^{\mathrm{LO/HO}} - N^{\mathrm{HO/LO}})^2 / N^{\mathrm{HO/LO}}$ for true HO/LO. The numerator is the same in both cases whereas the denominator is larger for a true HO resulting in a lower sensitivity. Note that, to a first order approximation, the octant sensitivity is mostly flat in the δ_{CP} plane. This is expected since atmospheric experiments are not so sensitive to δ_{CP}, stemming from the fact that they observe events from disappearance (sensitive to δ_{CP}) as well as appearance channels simultaneously.

6.4.2 Sensitivity vs θ_{23}

Since atmospheric experiments are not so sensitive to δ_{CP}, it is more appropriate to plot the sensitivities as a function of true values of θ_{23}. In Fig. 6.10, the octant sensitivity is plotted as a function of true values of θ_{23} for both NO and IO assumptions for a predicted exposure of 3 years of ORCA. Due to the existence of the ordering-octant degeneracy, two additional curves are obtained by minimizing over not only the regular set of systematic parameters, but also over the ordering itself. This translates into the case when the true mass ordering is not identified.

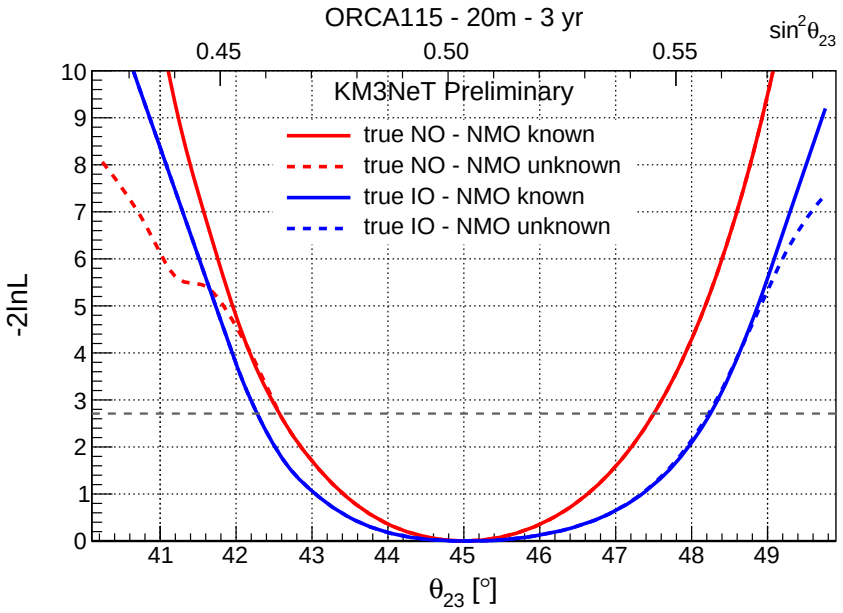

Figure 6.10: ORCA sensitivity to the octant of θ_{23} after three years of runtime for the true neutrino mass ordering. The solid curves refer to the test ordering being kept fixed at the truth, while for the dashed curves it is treated as a free parameter in the fit. The dashed horizontal line indicate the 90% C.L. sensitivity.

If the ordering is normal and correctly identified, ORCA will allow the octant to be determined at more than 90% C.L. if $\theta_{23} < 42.5^\circ$ and $\theta_{23} > 47.5^\circ$. However, if the ordering is inverted, it will resolve the octant at more than 90% C.L. if $\theta_{23} < 42.2^\circ$ and $\theta_{23} > 48.2^\circ$. Sensitivities are, in general, higher in NO.

The "shoulders" at $\theta_{23} \sim 42^\circ$ (true NO) and $\theta_{23} \sim 49^\circ$ (true IO) correspond to the regions where the uncertainty in the true knowledge of the NMO degrades the octant sensitivity. If the true ordering is NO, testing for a wrong octant solution within the IO has a significant effect on the octant sensitivity for $\theta_{23} < 42^\circ$. For true IO, testing for a wrong octant solution within the NO has rather mild effect on the octant sensitivity for $\theta_{23} > 49^\circ$.

6.4.3 Sensitivity vs runtime

In addition to a fixed exposure of 3 years, we have also investigated how many years it would require for ORCA to make a $1/2/3\sigma$ C.L. measurement of the octant, again depending on the true NMO and true θ_{23}. The results are shown in Fig. 6.11 and Fig. 6.12. Curves referring to minimization over the ordering are also included.

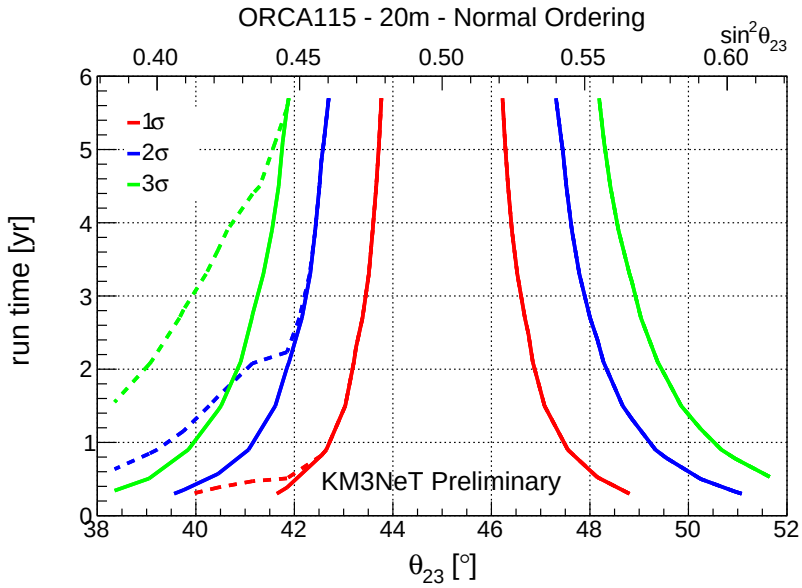

Figure 6.11: Expected runtime in years required for ORCA to exclude the wrong octant of θ_{23} at $1/2/3\sigma$ C.L. as a function of true θ_{23} for NO assumption. The solid curves refer to the test ordering being kept fixed at the truth, while for the dashed curves it is treated as a free parameter in the fit.

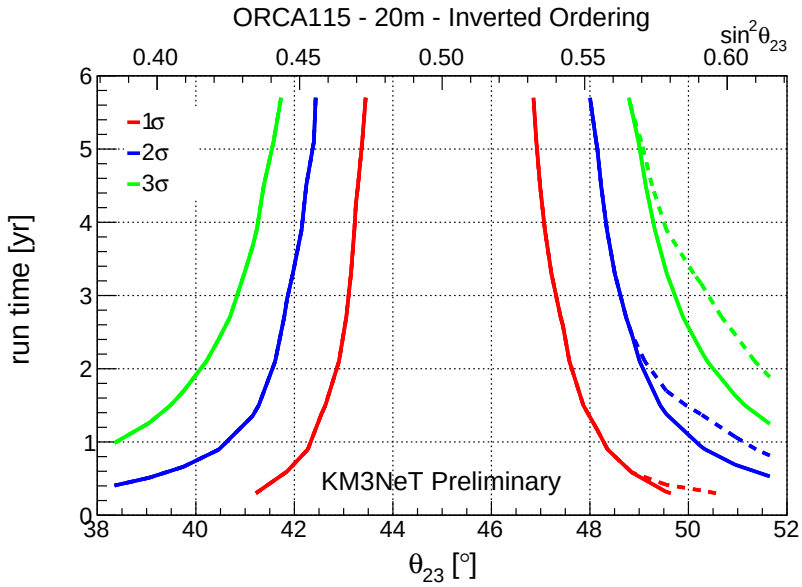

Figure 6.12: Expected runtime in years required for ORCA to exclude the wrong octant of θ_{23} at $1/2/3\sigma$ C.L. as a function of true θ_{23} for IO assumption. The solid curves refer to the test ordering being kept fixed at the truth, while for the dashed curves it is treated as a free parameter in the fit.

The very flat behavior of the value of $-2\ln\mathcal{L}$ when θ_{23} is near the maximal mixing value observed in Fig. 6.10 finds its counterpart here in the very steep rise in runtime as maximal mixing is approached from both sides. The "shoulder" in the true NO case for $\theta_{23} < 42^\circ$ and $\theta_{23} > 49^\circ$ for IO again correspond to the regions where misidentification of the NMO degrades the octant sensitivity and leads to an increase in the runtime required

to determine it. ORCA is projected to make a 1σ C.L. determination of the octant of θ_{23} within less than a year if the NO is true and either $\theta_{23} < 42.5^\circ$ or $\theta_{23} > 47.6^\circ$, or if the IO is true and either $\theta_{23} < 42.2^\circ$ or $\theta_{23} > 48.0^\circ$. A five-year measurement at the 1σ C.L. is achieved for NO and $\theta_{23} < 42.2^\circ$ or $\theta_{23} > 46.2^\circ$, or for IO and $\theta_{23} < 42.4^\circ$ or $\theta_{23} > 47.0^\circ$.

Summary

> "Light thinks it travels faster than anything but it is wrong. No matter how fast light travels, it finds the darkness has always got there first, and is waiting for it."
>
> — TERRY PRATCHETT,
> *The Reaper Man.*

During the past decades, a plethora of evidences, accumulated from solar [29], atmospheric [223], accelerator [224] and reactor [36, 38, 39] experiments, testify for the transmutation of neutrino flavours while they propagate through macroscopic distances. This phenomenon, called *neutrino oscillation*, is simply explained by the non-degenerate neutrino mass and lepton flavour eigenstates. The discovery of the neutrino oscillations itself caps the study of new physics beyond the Standard Model (SM). Although the paradigm of the SM plus neutrino mass, mixing and oscillations has been verified by a gamut of experiments, there are a few experimental signals that cannot be accommodated within this model, which motivates the study of new physics Beyond the Standard Model. The study of non-standard interactions (NSIs) of neutrinos with matter fermions is envisaged from this phenomenological point of view, since their existence provides a probe to the nature of new physics beyond the Standard Model.

The presence of such additional interactions of neutrinos are expected to produce a significant modification in the spectra of events predicted with the standard three-flavour neutrino oscillations. The ANTARES neutrino telescope and its successor low energy sub-array, KM3NeT-ORCA (ORCA in what follows), have the potential to measure atmospheric neutrino oscillations with enhanced precision to sub-dominant effects arising from new physics beyond the SM like NSIs.

Objectives

The thesis ventured out in the development of a strategy to identify the signal from non-standard neutrino interactions at ANTARES and ORCA neutrino telescopes. The signal is affected by uncertainties on the atmospheric neutrino flux models and the neutrino-nucleon cross-sections in sea water, as well as by the detector performances, like thresholds and resolutions. The effect of these individual systematic uncertainties on the final signal strength has been quantified and the physics reach of ANTARES and ORCA explored.

The major objectives of the thesis can be grouped as follows:

- Search for NSIs with 10 years of ANTARES: The atmospheric muon-neutrino disappearance data collected by ANTARES in the period 2007–2016 has been analysed and bounds on the NSI phase space in the $\mu - \tau$ sector has been constructed.
- Sensitivity to NSIs at ORCA: Future sensitivities at ORCA towards the discovery of NSIs with three years of run-time has been evaluated.
- Effect of NSIs on neutrino mass ordering (NMO) at ORCA: Apart from the standard 8 fold octant–ordering–CP-phase degeneracy, the presence of NSI causes additional degeneracies, which might affect the determination of neutrino mass ordering at ORCA. The impact of various NSI parameters on the ORCA sensitivity to the NMO has been explored.
- Sensitivity to the octant of θ_{23} at ORCA: Non-zero θ_{13} drives large matter effects in atmospheric neutrino oscillations and can be used to study deviations of θ_{23} from maximal mixing and deciphering its octant. The projected sensitivity of ORCA to the θ_{23} octant has been estimated for an exposure of three years.

Theory: Neutrino Oscillations and Non-Standard Interactions

Neutrinos $\{\nu_\alpha\}$ (α representing the flavour family) are produced in charged current (CC) and neutral current (NC) weak interaction processes. Each (neutrino) flavour eigenstate ν_α is a quantum superposition of multiple mass eigenstates $\{\nu_i\}$ with masses m_i. Oscillations are generated due to interference between different massive neutrinos $\{\nu_i\}$, which are produced and detected coherently as $\{\nu_\alpha\}$ with small mass differences. This implies that when a neutrino of a certain flavour (say ν_α) is produced in a weak interaction process and propagates through space (or medium), each of the mass eigenstates $\{\nu_i\}$ travel with different speed leading to a phase lag between them. After a certain distance, the composition of the mass eigenstates is different from the initial state. The final composition of mass eigenstates might constitute a neutrino of completely different flavour $\{\nu_\beta : \beta \neq \alpha\}$. This process of transmutation of flavour from a ν_α into a ν_β is called *neutrino oscillation*. It is basically analogous to the quantum mechanics of mixed states, which itself is equivalent to the classical theory of coupled oscillators. Let us discuss the theory of neutrino oscillations in a quantitative way in the following.

In the standard theory of neutrino oscillations[4] with n number of light neutrino generations[5], a neutrino flavour eigenstate can be expressed as a linear superposition of n mass eigenstates (or the other way round):

$$|\nu_\alpha\rangle = \sum_{i=1}^{n} U^*_{\alpha i} |\nu_i\rangle, \quad (or\, |\nu_i\rangle = \sum_{\alpha} U_{\alpha i} |\nu_\alpha\rangle,) \tag{10}$$

where $U_{\alpha i}$ is the mixing matrix, which relates the mass basis $\{\nu_i\}$ (eigenstates of the Hamiltonian) to the flavour basis $\{\nu_\alpha\}$ (eigenstates of the gauge group). $U_{\alpha i}$ satisfies the following conditions:

$$U^\dagger U = \mathbb{I}_{n\times n}, \quad \sum_i U_{\alpha i} U^*_{\beta i} = \delta_{\alpha\beta}, \quad \sum_\alpha U_{\alpha i} U^*_{\alpha j} = \delta_{ij}. \tag{11}$$

[4] For a concrete derivation, see [47].

[5] Precision measurement of the decay width of Z at LEP [48] indicate that there are three generation of neutrinos, (accompanying their charged lepton partners) which take part in weak interactions.

The Latin indices $i, j = 1, 2, 3...$ correspond to the mass eigenstates, while the Greek indices $\alpha, \beta = e, \mu, \tau....$ correspond to the flavour eigenstates.

The amplitude of $|\nu_\alpha\rangle \to |\nu_\beta\rangle$ transition as a function of time is given by

$$A_{\nu_\alpha \to \nu_\beta}(t) = \langle \nu_\alpha | \nu_\beta \rangle_t = \sum_i U^*_{\alpha i} U_{\beta i} e^{-iE_i t}. \tag{12}$$

The transition probability then reads

$$P_{\nu_\alpha \to \nu_\beta}(t) = |A_{|\nu_\alpha\rangle \to |\nu_\beta\rangle}(t)|^2 = \sum_{i,j} U^*_{\alpha i} U_{\beta i} U_{\alpha j} U^*_{\beta j} e^{-(E_i - E_j)t}. \tag{13}$$

For ultra relativistic neutrinos ($E_i \simeq P_i + \frac{m_i^2}{2E}$ in the limit $m_i^2 \ll P_i$), assuming same momentum for all massive neutrino components ($P_i = P \ \forall i$) and using light-ray approximation ($t \simeq L\,(c = 1)$), the transition probability can be approximated by [47, 49]

$$\begin{aligned} P_{\nu_\alpha \to \nu_\beta}(L) = \delta_{\alpha\beta} &- 4 \sum_{i>j} \mathbb{R}e[U^*_{\alpha i} U_{\beta i} U_{\alpha j} U^*_{\beta j}] \sin^2 \phi_{ij} \\ &\pm 2 \sum_{i>j} \mathbb{I}m[U^*_{\alpha i} U_{\beta i} U_{\alpha j} U^*_{\beta j}] \sin 2\phi_{ij}, \end{aligned} \tag{14}$$

where

$$\phi_{ij} = \Delta m^2_{ij} \frac{L}{4E_\nu} \simeq 1.267 \Delta m^2_{ij} \frac{L}{E_\nu} \frac{[\text{eV}^2][\text{km}]}{[\text{GeV}]}. \tag{15}$$

The coefficients of the massive neutrino components of flavour antineutrinos are simply related to the corresponding coefficients of massive neutrino components of flavour neutrinos by complex conjugation $U_{\alpha i} \to U^*_{\alpha i}$. Hence, the antineutrino oscillation probabilities differ from the corresponding neutrino oscillation probabilities only in the sign of the terms depending on the imaginary parts of the quartic products of the mixing matrix elements. The imaginary part in Eq. 27 depends on whether neutrinos ($+$) or antineutrinos ($-$) are considered.

The oscillation process is determined by the Pontecorvo-Maki-Nakawaga-Sakata mixing matrix (PMNS) [14, 13] and the difference of squared masses. In the conventional three-flavour scheme with Dirac neutrinos, the relevant parameters are three mixing angles, θ_{12}, θ_{13}, θ_{23}, two mass-squared differences, Δm^2_{21}, Δm^2_{31}, and one CP phase, δ_{CP}. Our present knowledge of these parameters can be summarised as follows: $\theta_{12} \approx 31$–36°, $\theta_{13} \approx 8$–9°, $\theta_{23} \approx 41$–51°, $\Delta m^2_{12} \approx 7$–$8 \times 10^{-5}$ eV^2, $|\,\Delta m^2_{23}\,|$ ($\approx |\,\Delta m^2_{13}\,|$) ≈ 2.4–2.6×10^{-3} eV^2 and $\delta_{CP} \approx 200 - 350^\circ$. We ignore if θ_{23} is in the first or second octant, the sign of Δm^2_{23} (the mass ordering) and we lack an accurate determination of δ_{CP} (see review 14 in [225] for conventional definitions and further details).

When neutrinos propagate in matter, their evolution is further affected by interactions with the medium due to the coherent forward elastic scattering of neutrinos with matter. The overall effect can be described by effective potentials associated to the charged (CC) and neutral (NC) currents. In the case of neutrinos travelling through Earth, the only relevant potential is the one stemming from the electron neutrino components interacting with electrons in matter, that turns out to be [24]: $V_{CC} = \sqrt{2}\, G_F\, n_e$, where G_F is the Fermi

coupling constant and n_e is the electron number density across the neutrino path. The relevant Hamiltonian is:

$$H^{3\nu} = \frac{1}{2E_\nu} U M^2 U^\dagger + V_{CC}\,\mathrm{diag}(1,0,0), \tag{16}$$

where U, the PMNS mixing matrix, performs the rotation of the relevant mass matrix $M^2 = \mathrm{diag}(0, \Delta m^2_{21}, \Delta m^2_{31})$ in the neutrino flavour space.

The existence of NSI can be described as a new potential that will translate into an additional term in the Hamiltonian:

$$H^{NSI} = V_{CC}\,\frac{n_f}{n_e}\,\epsilon, \tag{17}$$

where n_f and n_e are the fermion and electron number density along the neutrino path and neutrinos are assumed to interact with down quarks which are roughly three times as abundant as electrons, $n_f = n_d \approx 3\, n_e$ and the matrix ϵ ($\epsilon_{\alpha\beta}$, α, β = e, μ, τ) gives the strength of the NSI. The diagonal terms of this matrix, if different from each other, can give rise to the violation of leptonic universality, while the off-diagonal terms can induce flavour changing neutral currents, which are highly suppressed in the SM. Hermiticity, unitarity constraints and the tracelessnes of the ϵ matrix reduce its components to six effective parameters [226]. Furthermore, in an experiment like ANTARES in which the atmospheric neutrino flux is highly dominated by ν_μ transforming mainly to ν_τ, the main contribution to NSI would come from the matrix elements with $\alpha, \beta = \mu$ or τ. Moreover, it is customarily assumed that $\epsilon_{\mu\mu} \approx \epsilon_{\tau\tau}$. Therefore, in our analysis we will investigate the two real parameters $\epsilon_{\tau\tau}$ and $\epsilon_{\mu\tau}$.

The dominant atmospheric neutrino oscillation $\nu_\mu \to \nu_\tau$ gives rise to the disappearance of ν_μ's, whose magnitude depends on their energy and path length. Since a neutrino telescope as ANTARES mainly detects ν_μ CC interactions that yield track-like events, the influence of neutrino oscillations can be studied measuring the deficit of these events as a function of their energy and arrival direction. In the range from ∼10 GeV to above ∼100 GeV, the detector is able to provide an estimate of the neutrino energy measuring the muon range [60]. Furthermore, given the actual values of θ_{23} and Δm^2_{23}, the effect of the $\nu_\mu \to \nu_\tau$ oscillation is important in that energy range: a minimum of the survival probability takes place at ∼25 GeV and the ν_μ deficit is noticeable up to 100 GeV [60].

NSI are expected to have sub-dominant effects and therefore they would be observed as deviations from the distributions of the the energy and arrival direction expected for standard oscillations. As an example of the expected effect, we show in in Fig. 1 the variation of the oscillation pattern due to NSI. The difference of the survival probabilities for the NSI and the standard oscillations cases is shown as a function of cos θ_z and E_ν. The left plot shows the difference for neutrinos and the right plot for antineutrinos. Normal ordering is assumed in both cases. Although the NSI effects are anti-symmetric for neutrinos and anti-neutrinos, they are not exactly opposite, thereby leading to small but appreciable effects at a charge-blind isoscalar detector as ANTARES. The plots have been produced for a value of $\epsilon_{\mu\tau}$ of 0.01, to which most of the current neutrinos telescopes are sensitive. The effect of NSI is more prominent for vertical events (cos $\theta_z \approx 1$) and since NSI shift the minima of the oscillation, they also produce more impact at the corresponding energies, although the effect of NSI on the survival probability extends to higher energies.

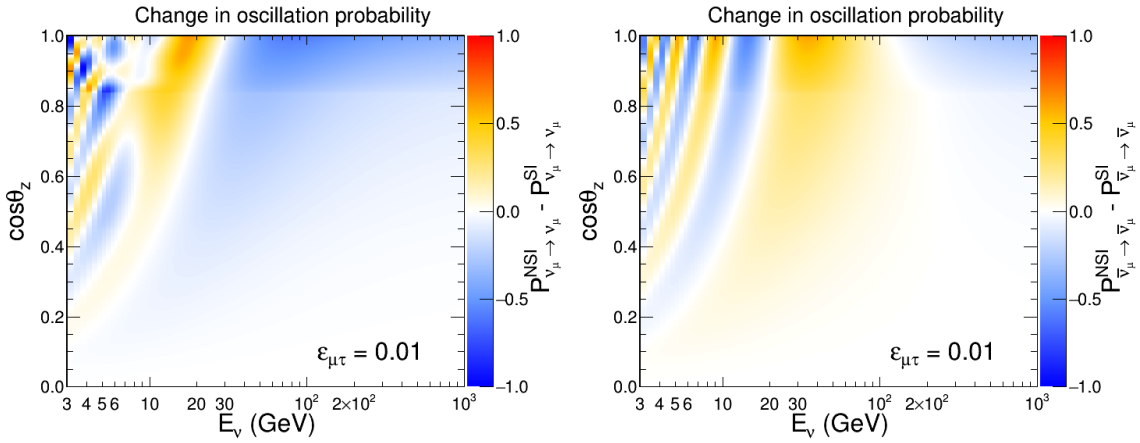

Figure 1: NSI induced modifications in ν_μ (left) and $\bar{\nu}_\mu$ (right) disappearance probabilities as a function of the neutrino energy and cosine of the zenith angle. The NSI test point has been set at $\epsilon_{\mu\tau} = 0.01$. Normal ordering is assumed.

Instrument: Neutrino Telescopes

The term neutrino telescope refers to an array of optical devices arranged in a definite geometry within a large volume of natural (and transparent) medium with the objective of detecting Cherenkov radiation from neutrino interactions [126]. The directional sensitivity is the reason to call them telescopes.

ANTARES

ANTARES (acronym for Astronomy with a Neutrino Telescope and Abyss environmental RESearch) [130] is an under-water neutrino telescope located 40 km offshore from Toulon, France at (42° 48′ N, 6° 10′ E), anchored about 2475 m below the surface of the Mediterranean Sea. The first line was deployed in March 2006 and the detector was completed in May 2008.

Fig. 2 shows a schematic view of the ANTARES detector. ANTARES consists of 12 vertical detection lines, instrumented in an octagonal configuration with a (horizontal) separation of 60–75 m. The lines are anchored to the sea floor by means of a titanium structure (Bottom String Socket) acting as a dead weight and buoy on its top to stay vertical (optical modules have also their own buoyancy). Each line holds 25 storeys (apart from line 12 with 20 storeys) starting 100 m above the sea floor with a (vertical) separation of 14.5 m amounting to a total height of 450 m. The instrumented volume of ANTARES is ~ 0.01 km^3.

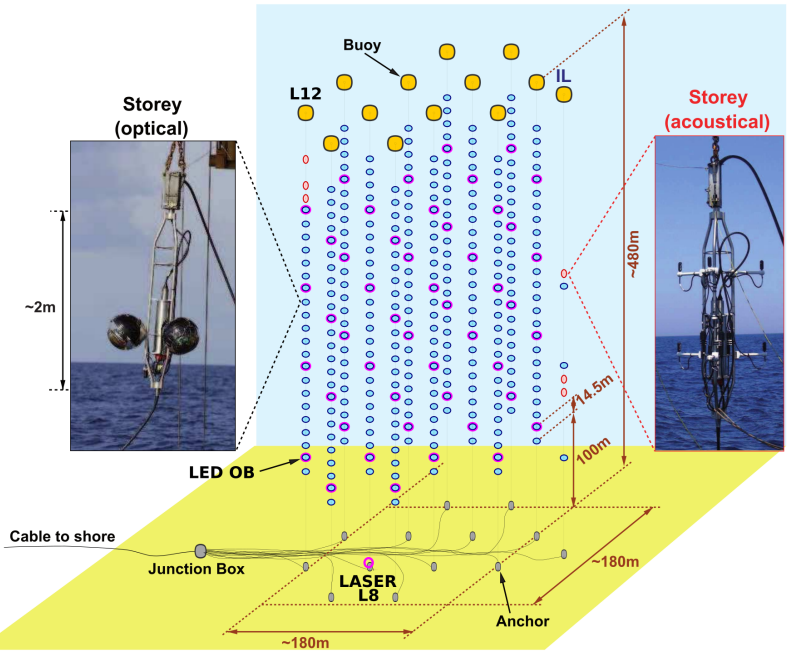

Figure 2: Schematic diagram of the ANTARES detector. Photos of two storeys holding optical and acoustic equipment are shown. From [130].

KM3NeT

KM3NeT (acronym for KiloMetre cube Neutrino Telescope) [66] is a next generation deep-sea Cherenkov neutrino observatory, currently under construction in the Mediterranean Sea. Based on the granularity of the optical modules (to target different neutrino energy regimes), KM3NeT will house two detector sub-arrays:

- **ORCA** (Oscillation Research with Cosmics in the Abyss): densely instrumented sub-array of $\sim 5 \times 10^{-3}$ km^3 volume, located offshore of Toulon, France at (42°41′ N, 6°02′ E), designed primarily for studying neutrino properties and low-energy astrophysics;
- **ARCA** (Astroparticle Research with Cosmics in the Abyss): sparsely instrumented sub-array of ~ 1 km^3 volume, located offshore of Sicily, Italy at (36°16′ N, 16°06′ E), designed primarily for detection of high-energy cosmic neutrinos and neutrino astronomy.

The term "ORCA" ("ARCA") will be used henceforth to designate the KM3NeT-ORCA (-ARCA) detector.

The three-dimensional array built in a particular layout is called a “building block” (BB). KM3NeT will consist of two BBs for ARCA and one BB for ORCA to reach the desired instrumented volumes. Fig. 3 shows a schematic view of one BB of the KM3NeT detector. Each building block will consist of a three-dimensional array of $\sim$ 64,000 PMTs distributed among 115 detection strings (also known as "DUs"[6]) with 18 spherical Digital Optical Modules (DOMs) per line. Starting about 40 m (80 m) from the sea floor, the DUs of ORCA (ARCA) are 200 m (700 m) high, horizontally separated by about 20 m (95 m), with 18 DOMs spaced 9 m (36 m) apart in the vertical direction.

[6]The terms "DU", "string" and "line" have been used interchangeably in this thesis.

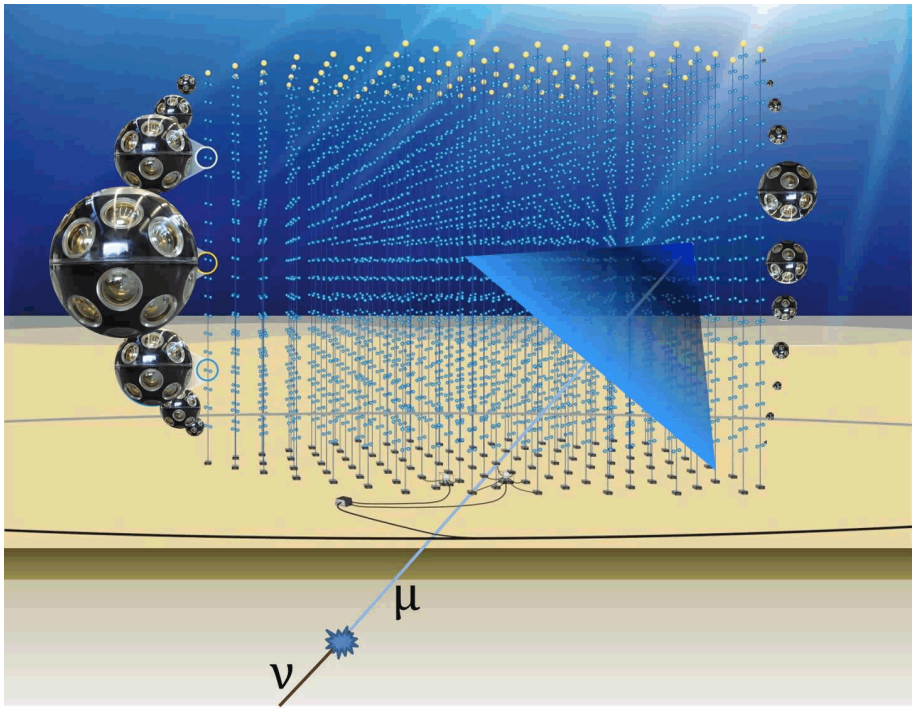

Figure 3: Conceptual view of the KM3NeT detector. The blue line represents an up-going neutrino undergoing ν_μ–CC interaction close to the fiducial volume leading to track-like event and creating a Cherenkov cone along its path. From KM3NeT internal documentation.

Methodology

An event-by-event separation of the NSI signal at the detectors is too challenging. What is possible is to look for a statistical excess or deficit of neutrino plus antineutrino events at the detectors predicted with a certain NSI test hypothesis. The first step is to compute the number of events corresponding to a specific oscillation hypothesis with or without NSI. The total number of charged current muon neutrino events expected at the detector for a certain runtime t is given by:

$$\begin{aligned}\frac{d^2N_\mu^{CC}}{dE\,d\cos\theta} = &\left(\frac{d^2\phi_{\nu_\mu}}{dE\,d\cos\theta}P_{\mu\mu} + \frac{d^2\phi_{\nu_e}}{dE\,d\cos\theta}P_{e\mu}\right) \times \sigma_{\nu_\mu}^{CC} A_{\nu_\mu}^{CC} \times t \\ &+ \left(\frac{d^2\phi_{\bar{\nu}_\mu}}{dE\,d\cos\theta}P_{\bar{\mu}\bar{\mu}} + \frac{d^2\phi_{\bar{\nu}_e}}{dE\,d\cos\theta}P_{\bar{e}\bar{\mu}}\right) \times \sigma_{\bar{\nu}_\mu}^{CC} A_{\bar{\nu}_\mu}^{CC} \times t.\end{aligned} \tag{18}$$

N_μ is the number of detected muon events within the range of energy dE and cosine of zenith angle $d\cos\theta$; ϕ_{ν_x} ($\phi_{\bar{\nu}_x}$) is the atmospheric flux of neutrinos (antineutrinos) of flavour x at the detector site; $P_{\alpha\beta}$ is the probability of oscillation of a neutrino flavour ν_α to a neutrino flavour ν_β; $\sigma_{\nu_\mu}^{CC}$ is the charged current cross-section of muon neutrino with nucleons in sea water; $A_{\nu_\mu}^{CC}$ ($A_{\bar{\nu}_\mu}^{CC}$) is the energy and zenith angle dependent effective area of the detector corresponding to muon neutrinos (antineutrinos) undergoing CC interaction within the detector.

However, the detector cannot separate (ν_e, $\overline{\nu}_e$, ν_μ, $\overline{\nu}_\mu$, ν_τ, $\overline{\nu}_\tau$ - CC) and (ν, $\overline{\nu}$ - NC) events. Depending on the Cherenkov signatures of the outgoing lepton from the ν_e and ν_μ CC and NC interactions, two distinct event topologies are observed at the detector: track-like

and shower-like events. ν_μ CC and ν_τ CC interactions with muonic τ decays mostly account for the track-like topology, since the outgoing muon appears as a track within the detector. The shower-like topology corresponds to events from ν_e CC, ν_τ CC interactions with non-muonic τ decays and NC interactions of all flavours. The eight distributions indexed by interaction type $\mathcal{X} \in \{(\nu_e, \overline{\nu}_e, \nu_\mu, \overline{\nu}_\mu, \nu_\tau, \overline{\nu}_\tau$ - CC) and (ν, $\overline{\nu}$ - NC)$\}$ are merged and split into two distributions corresponding to the two event topologies: tracks and showers.

The method to estimate the sensitivity to a test parameter in a model hypothesis is based on a binned likelihood approach [196]. In the case of a Poissonian distribution of event numbers, the test statistic after inclusion of Gaussian penalty terms reads

$$-2LLR(\lambda, n) = 2 \cdot \sum_{i \in \{bins\}} \left[\lambda_i(\bar{o}, \bar{s}) - n_i + n_i \ln \left(\frac{n_i}{\lambda_i(\bar{o}, \bar{s})} \right) \right] + \sum_{j \in \{syst\}} \frac{(s_j - \hat{s}_j)^2}{2\sigma_j^2}. \quad (19)$$

The number of predicted events λ_i in the i^{th} bin is a function of the set of oscillation parameters, $\bar{o}$, as well as on the the set of parameters related to systematic uncertainties, $\bar{s}$. The second term runs over penalty terms of the number, j, of nuisance parameters, $\hat{s_j}$ and σ_j^2 being the assumed prior and Gaussian standard deviation of the parameter j, respectively.

The individual contributions from track and shower classes are summed to compute the total significance, σ_{tot}:

$$\begin{aligned} \sigma_{tot} &= \sqrt{-2LLR(\lambda, n)} \\ &= \sqrt{(-2LLR)\Big|_{\text{tracks}} + (-2LLR)\Big|_{\text{showers}}} \end{aligned} \quad (20)$$

The value of σ_{tot} indicates the level of agreement or disagreement between a model prediction $\lambda(\bar{o}, \bar{s})$ and the dataset n and quantifies the *sensitivity* of the detector to that particular model hypothesis given a certain runtime.

Systematics

Tab. 1 summarises the exhaustive list of systematic parameters considered in the fit, along with their statistical treatment (fixed or fitted), nominal values and external constraints, if used. They can be grouped in four categories:

Nuisance parameters	Treatment	Nominal values	Priors
Oscillation			
$\theta_{12}(^\circ)$	fixed	33.82	-
$\theta_{13}(^\circ)$	fitted	8.60	0.13
$\theta_{23}(^\circ)$	fitted	48.6	free
$\delta_{CP}(^\circ)$	fitted	221	free
$\Delta m^2_{21}(\times 10^{-5}\text{eV}^2)$	fixed	7.39	-
$\Delta m^2_{31}(\times 10^{-3}\text{eV}^2)$	fitted	2.528	free
Flux			
Track norm.	fitted	1	free
Shower norm.	fitted	1	free
Middle norm.	fitted	1	free
ν_μ/ν_e skew	fitted	0	5%
$\nu_\mu/\overline{\nu}_\mu$ skew	fitted	0	5%
$\nu_e/\overline{\nu}_e$ skew	fitted	0	5%
Energy slope ($\Delta\gamma$)	fitted	0	5%
Zenith slope	fitted	0	2%
Cross-section			
NC scale	fitted	1	5%
Detector			
Energy scale	fitted	1	10%

Table 1: The list of systematics studied in the NSI ORCA analysis, along with their statistical treatment, injected nominal and prior values (if any).

- **Oscillation parameters**: The solar parameters (θ_{12}, Δm^2_{21}) are kept fixed at their nominal values (adopted from NuFit v4.1 [90]), since ORCA being an atmospheric oscillation experiment is not very sensitive to them. The mixing angle θ_{13} has a large effect on oscillation probabilities. Hence existing experimental constraints are used to exploit the full potential of ORCA for estimating the sensitivity to the NSI parameters. It is reflected by a prior of 0.13°. No priors are used on the atmospheric oscillation parameters (θ_{23}, Δm^2_{31}) and δ_{CP} since they are also supposed to be measured by ORCA. Due to the degeneracy between the octant of θ_{23} and the sign of Δm^2_{31} ($+/-$ correspond to NO/IO), a starting value of θ_{23} in both octants ($\theta_{23} < 45^\circ \in$ lower octant or $\theta_{23} > 45^\circ \in$ higher octant) is chosen and the minimum value of $-2 \ln \mathcal{L}$ is stored. The effect of these uncertainties on oscillation parameters on the final event distributions are shown in Fig. 4.31 to Fig. 4.34.

- **Flux systematics**: Systematic parameters compared to atmospheric neutrino flux uncertainties are considered. The total number of events in each event class has an associated normalisation factor: "Track norm.", "Middle norm." and "Shower norm.", which is fitted without any constraint. This also takes into account the uncertainty on the effective mass and on the interaction cross-sections of neutrinos. The effective change in the event numbers in any $[E, \cos\theta_z]$ bin is directly proportional to the normalisation factor.

  The ratio between the total number of ν_μ and ν_e ("ν_μ/ν_e skew"), ν_μ and $\overline{\nu}_\mu$ ("$\nu_\mu/\overline{\nu}_\mu$ skew") and ν_e and $\overline{\nu}_e$ ("$\nu_e/\overline{\nu}_e$ skew") events are allowed to vary with a standard deviation of 5% of the parameter nominal value. The prior value (5%), which is independent of energy and zenith angle, is more conservative than the current estimated flux uncertainties [207]. The effect of these uncertainties on the final event distributions are shown in Fig. 4.35 to Fig. 4.37.

  The "energy slope" error $\Delta\gamma$, applied as a function of E_ν^γ, accounts for a change in the neutrino spectrum due to uncertainties in the primary cosmic ray spectrum. The energy slope error is allowed to vary within ±5% around its central value of $\Delta\gamma = 0$. Similarly, the uncertainty on the ratio of up-going to horizontal-going neutrinos, named "zenith slope", is allowed to vary with a standard deviation of 2% of its nominal value. The effect of these uncertainties on the final event distribution is shown in Fig. 4.38 and Fig. 4.39.

- **Cross-section systematics**: While lepton universality means the cross section ratios between flavours are well known, the same is not necessarily the case for the ratio between CC and NC events. Therefore, the neutral current event normalisation is also fitted with a prior of 5%. Uncertainties on the absolute CC and NC cross-sections are not considered in this study. However they would be somewhat absorbed within the flux normalisations. The effect of NC scale normalisation on the final event distribution is shown in Fig. 4.40.

- **Detector systematics**: Among the systematic parameters incorporated into this analysis, the track, middle and shower normalisations and energy scale can be considered detector effects. The energy scale depends on the PMT efficiencies and water properties [179]. If events are systematically brighter or less bright than expected, this will cause a shift to the normalisation of the effective mass. This is accounted in the energy scale which is fitted with a 10% Gaussian width across its nominal value.

Results

The results of the four physics analyses have been summarised in subsequent subsections below for both mass orderings: Normal Ordering (NO) and Inverted Ordering (IO). The results of the search for NSIs with ANTARES and the performance estimation of ORCA has been grouped together for brevity. This is followed by the estimation of the neutrino mass ordering resolution at ORCA in presence of NSIs. The last one corresponds to the resolution of the octant of θ_{23} at ORCA.

Search for NSIs with ANTARES and KM3NeT-ORCA

A first ANTARES analysis looking for NSIs in the atmospheric neutrino oscillation data has been presented. No significant excess/deficit was observed and the data was found consistent with standard oscillation hypothesis at $> 2.2\sigma$. This resulted in limits in the NSI $\mu - \tau$ sector.

For KM3NeT-ORCA, final event templates are simulated for a predicted exposure of 3 years of running. The expected event numbers are weighted according to various possible NSI signal hypotheses in order to explore the detection potential of ORCA towards NSIs. The ANTARES limits and ORCA sensitivities are shown in Fig. 4 to Fig. 6 along with comparisons from other experiments.

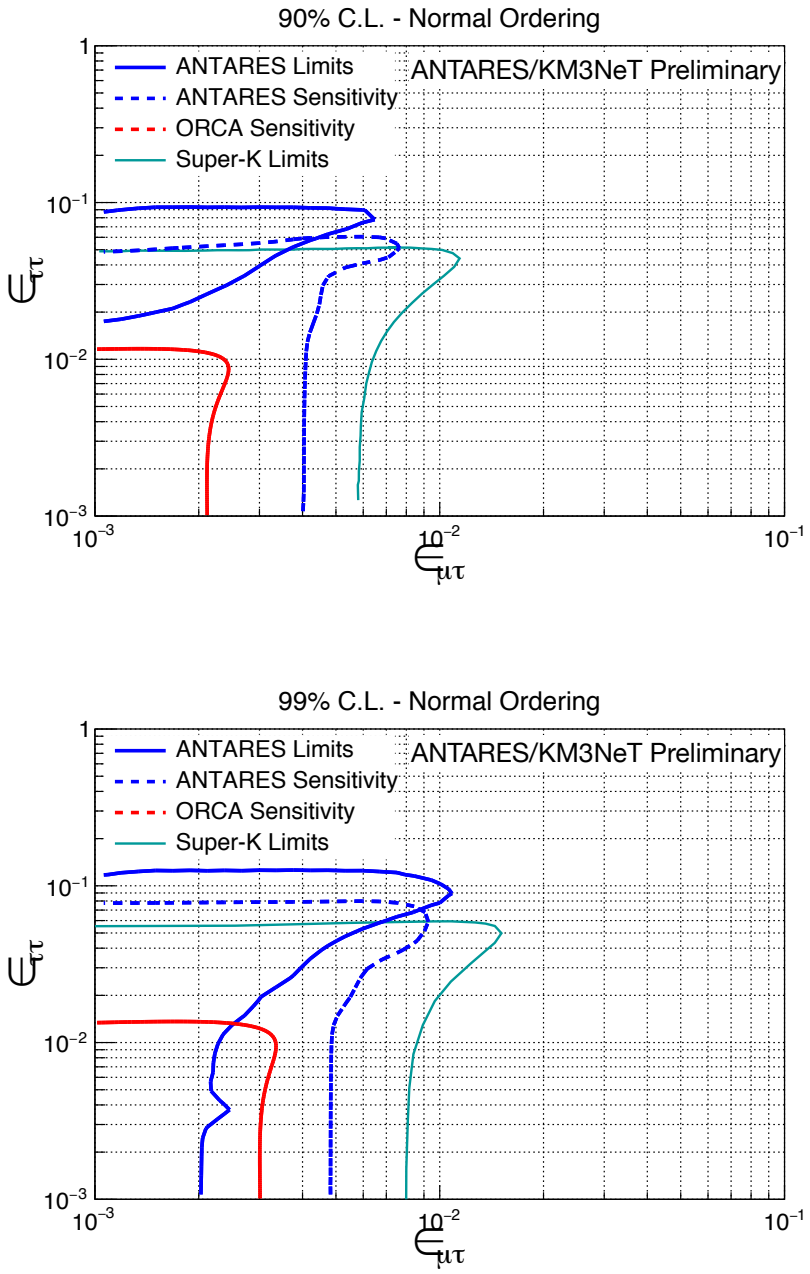

Figure 4: 90% (top) and 99% (bottom) C.L. limits (blue solid curve) in the $\epsilon_{\mu\tau} - \epsilon_{\tau\tau}$ phase space set after 10 years of ANTARES running obtained in this work, shown along with MC-only sensitivities with ANTARES (blue dashed) and ORCA (red) and limits from Super-K [192].

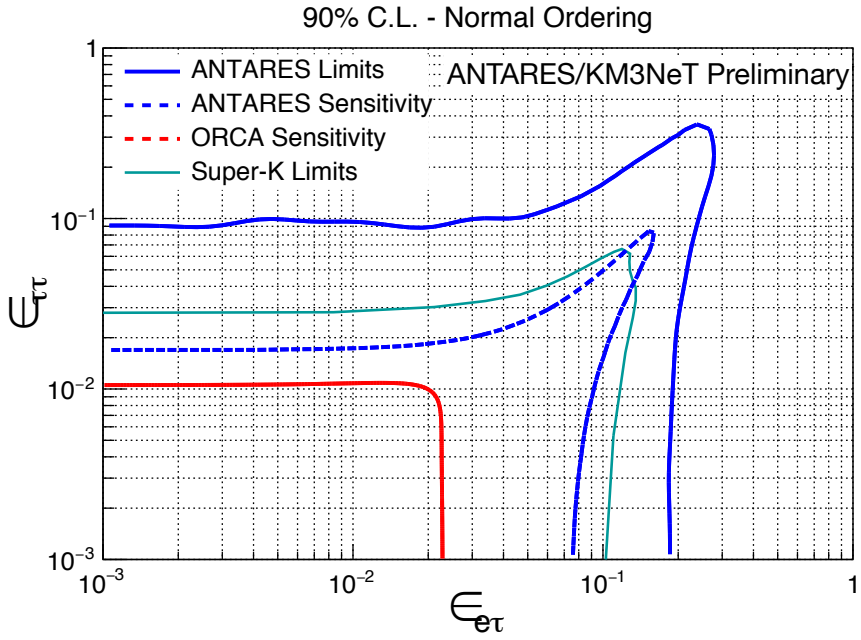

Figure 5: 90% C.L. limits (blue solid curve) in the $\epsilon_{e\tau} - \epsilon_{\tau\tau}$ phase space set after 10 years of ANTARES running obtained in this work, shown along with MC-only sensitivities with ANTARES (blue dashed) and ORCA (red) and limits from Super-K [192].

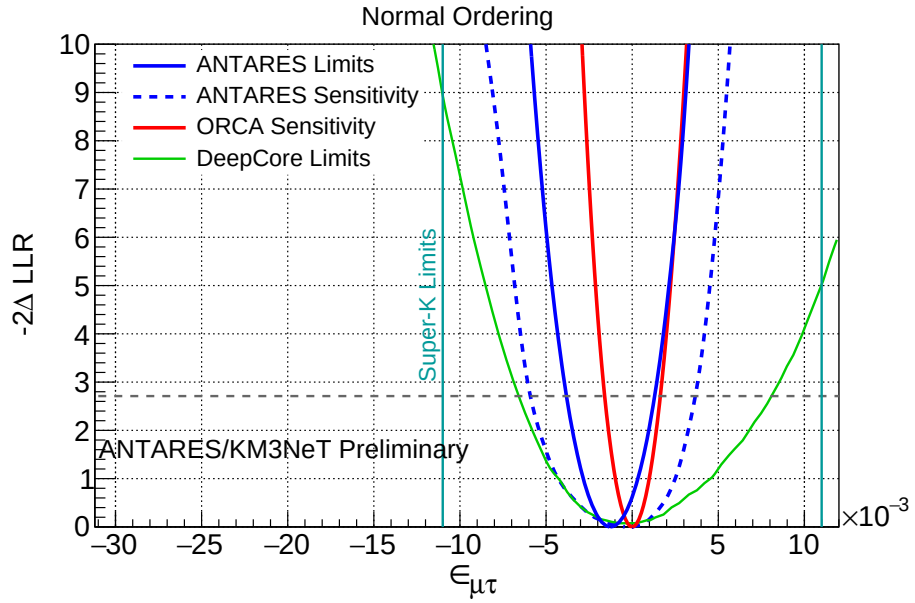

Figure 6: Limits on $\epsilon_{\mu\tau}$ phase space (blue solid curve) set after 10 years of ANTARES running obtained in this work, shown along with MC-only sensitivities with ANTARES (blue dashed) and ORCA (red) and limits from Super-K [192].

The limits for NSI obtained with 10 years of atmospheric muon disappearance data collected by ANTARES is more stringent than allowed by current experimental limits, thereby constitutes the world's-best limits in the $\mu - \tau$ sector. ORCA demonstrates

an excellent potential to put tighter constraints on various NSI parameter spaces by one order of magnitude better than what is allowed by current experimental limits. Finally, expected bounds on NSIs with ORCA are collected in Tab. 2 and the limits from ANTARES in the $\mu - \tau$ sector are defined in Eq. 21 and Eq. 22.

NSI Couplings	**Assumed True NMO**	**Bounds (90% C.L.)**
$\epsilon_{e\mu}$	NO	$(-1.7 \times 10^{-2}, 1.7 \times 10^{-2})$
	IO	$(-2.0 \times 10^{-2}, 2.0 \times 10^{-2})$
$\epsilon_{e\tau}$	NO	$(-1.8 \times 10^{-2}, 2.1 \times 10^{-2})$
	IO	$(-3.1 \times 10^{-2}, 2.7 \times 10^{-2})$
$\epsilon_{\mu\tau}$	NO	$(-1.7 \times 10^{-3}, 1.7 \times 10^{-3})$
	IO	$(-1.7 \times 10^{-3}, 1.7 \times 10^{-3})$
$\epsilon_{\tau\tau}$	NO	$(-0.8 \times 10^{-2}, 1.1 \times 10^{-2})$
	IO	$(-1.1 \times 10^{-2}, 0.8 \times 10^{-2})$

Table 2: Bounds on NSI of neutrinos with d-quarks at 90% C.L. for a runtime of 3 years of full ORCA comprising 115 DUs with 20 m horizontal DU spacing. Only one NSI parameter is considered at a time.

$$\begin{aligned} -4.2 \times 10^{-3} < \epsilon_{\mu\tau} < 2.7 \times 10^{-3} \quad & (\text{at } 90\% \text{ C.L}), \\ -6.1 \times 10^{-2} < \epsilon_{\tau\tau} < -2.1 \times 10^{-2} \quad \text{and} \quad 2.1 \times 10^{-2} < \epsilon_{\tau\tau} < 7.3 \times 10^{-2} \quad & (\text{at } 90\% \text{ C.L}). \end{aligned} \tag{21}$$

$$-3.8 \times 10^{-3} < \epsilon_{\mu\tau} < 1.6 \times 10^{-3} \quad \forall\, \epsilon_{\tau\tau} = 0 \quad (\text{at } 90\% \text{ C.L}), \tag{22}$$

Impact of NSIs on the NMO sensitivity at KM3NeT-ORCA

The sensitivity of ORCA towards the neutrino mass ordering (NMO) in the light of an assumed NSI hypothesis is presented in Fig. 7. This incorporates the uncertainty of fitting models to experimentally observed oscillation spectra and emphasizes the importance of testing different frameworks high precision measurements of oscillation parameters. In case of true IO, the NMO resolution at ORCA can be significantly impaired in presence of sub-dominant effects in neutrino oscillations coming from NSIs depending on the true value of θ_{23}. The effect is negligible if the true mass ordering in normal. Hence, the presence of NSIs can affect the physics potential of ORCA in measuring the standard oscillation parameters.

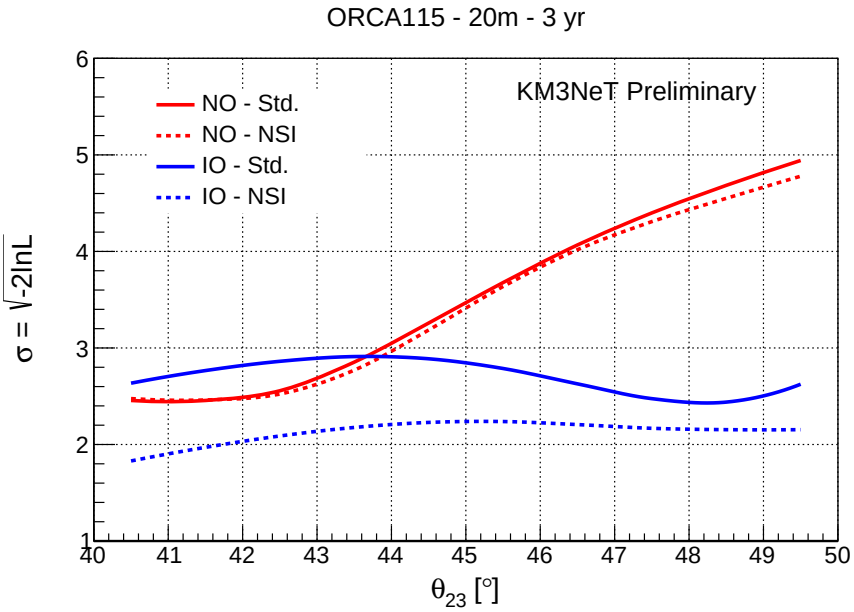

Figure 7: Projected sensitivity to the NMO after 3 years of ORCA run time, as a function of true θ_{23}, for NO (red) and IO (blue) assumptions, with a global best-fit δ_{CP} of 221° (228°) for NO (IO) assumptions. Dashed (solid) lines refer to the case when the NSI parameters are simultaneously fitted (fixed at 0).

Sensitivity to the octant of θ_{23} at KM3NeT-ORCA

We have investigated how many years it would require for ORCA to make a $1/2/3\sigma$ C.L. measurement of the octant, depending on the true NMO and true θ_{23}. The results are shown in Fig. 8 and Fig. 9. Sensitivity curves referring to minimization over the ordering are also included.

The "shoulders" at $\theta_{23} \sim 42°$ (true NO) and $\theta_{23} \sim 49°$ (true IO) correspond to the regions where the uncertainty in the true knowledge of the NMO degrades the octant sensitivity and leads to an increase in the exposure time required to determine it. If the true ordering is NO, testing for a wrong octant solution within the IO has a significant effect on the octant sensitivity for $\theta_{23} < 42°$. For true IO, testing for a wrong octant solution within the NO has rather mild effect on the octant sensitivity for $\theta_{23} > 49°$.

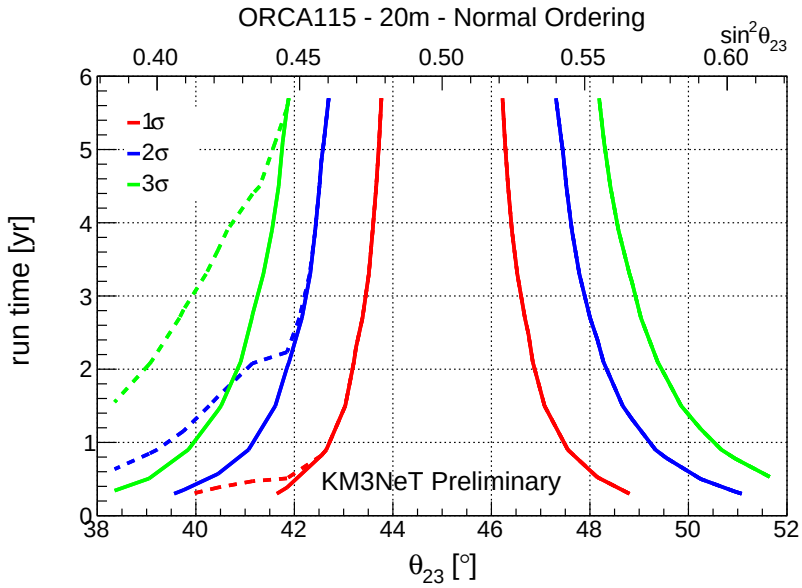

Figure 8: Exposure time in years required for ORCA to exclude the wrong octant of θ_{23} at $1/2/3\sigma$ C.L., as a function of true θ_{23} for true NO assumption. The solid curves refer to the test ordering being kept fixed at the truth, while for the dashed curves it is treated as a free parameter in the fit.

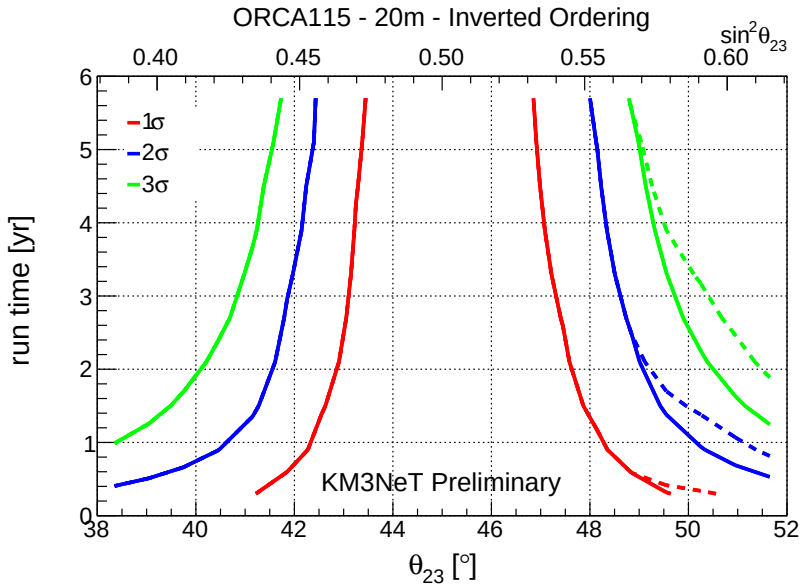

Figure 9: Exposure time in years required for ORCA to exclude the wrong octant of θ_{23} at $1/2/3\sigma$ C.L., as a function of true θ_{23} for true IO assumption. The solid curves refer to the test ordering being kept fixed at the truth, while for the dashed curves it is treated as a free parameter in the fit.

ORCA is projected to make a 1σ C.L. determination of the octant of θ_{23} within less than a year if the NO is true and either $\theta_{23} < 42.5^\circ$ or $\theta_{23} > 47.6^\circ$, or if the IO is true and either $\theta_{23} < 42.2^\circ$ or $\theta_{23} > 48.0^\circ$. A five-year measurement at the 1σ C.L. is achieved for NO and $\theta_{23} < 42.2^\circ$ or $\theta_{23} > 46.2^\circ$, or for IO and $\theta_{23} < 42.4^\circ$ or $\theta_{23} > 47.0^\circ$.

Conclusions

Atmospheric neutrinos and antineutrinos of muon and electron flavours represent a rich source of information on neutrino oscillations stemming from its energy and zenith angle dependent multi-layer matter effects. In the light of high statistics atmospheric neutrino experiments, ANTARES and KM3NeT can make strong contributions in understanding of neutrinos as well in the precise measurement of neutrino oscillation parameters.

Studies explored in the scope of this thesis indicate that ORCA is going to be the first atmospheric experiment to measure the neutrino mass ordering with a significance of 3σ. However, before ascribing any measurement to the oscillation parameters in the standard vanilla three-flavour neutrino paradigm, it is crucial to study the correlations and degeneracies that might arise due to extra parameters from new physics scenarios like NSIs. ORCA is expected to constrain many of such exotic physics cases that might contribute to the signal in the extraction of standard oscillation parameters. Moreover, ORCA is envisaged to precisely determine the value of θ_{23} with just few months of data taking.

Apart from this, the possibility of sending a neutrino beam from Protvino, Russia to ORCA (project nicknamed P2O) to measure CP violation in the neutrino sector is underway [70]. P2O will provide unparalleled sensitivity to matter effects in Earth, thereby allowing a measurement of CP violation at $>2\sigma$ level within 15 years at a modest beam power of 90 kW ($\approx 0.8 \times 10^{20}$ protons on target). The prospect of a ten times denser ORCA configuration, a so-called Super-ORCA [227], is also under consideration. Super-ORCA can probe the neutrino mass ordering (NMO) at $>2\sigma$ level within 5 years. In this exciting era of neutrino physics, ANTARES and KM3NeT can make significant contributions in addressing many unresolved issues in particle physics by studying neutrinos at the abyss of the Mediterranean sea.

Resumen

> "La luz piensa que viaja más rápido que cualquier cosa, pero se equivoca. No importa cuán rápido viaje la luz, siempre encuentra que la oscuridad ha llegado allí antes y le está esperando"
>
> — TERRY PRATCHETT,
> *El Segador.*

Durante las últimas décadas, una plétora de evidencias, acumuladas en experimentos solares [29], atmosféricos [223], de aceleradores [224] y de reactores [36, 38, 39], ha demostrado la transformación del sabor de los neutrinos cuando se propagan a través de distancias macroscópicas. Este fenómeno, llamado "oscilaciones de neutrinos", es explicado de manera simple por estados propios de sabor y de masa no degenerados. El descubrimiento de las oscilaciones de neutrinos por sí mismo supone el estudio de nueva física más allá del Modelo Estándar (MS). Aunque el paradigma del MS con neutrinos masivos, mezcla y oscilaciones se ha comprobado por multitud de experimentos, hay algunas señales experimentales que no han podido ser acomodadas por este modelo, lo que motiva el estudio de nueva física más allá del Modelo Estándar. El estudio de interacciones no estándar de neutrinos (INE o NSIs por sus siglas en inglés) con los fermiones de la materia proporciona una sonda para estudiar la naturaleza de nueva física.

Se espera que la presencia de interacciones adicionales de neutrinos produzca una modificación significativa en los espectros de sucesos predichos por las oscilaciones estándar de tres sabores de neutrinos. El telescopio de neutrinos ANTARES y la configuración de bajas energías de su sucesor, KM3NeT-ORCA, tienen el potencial de medir oscilaciones de neutrinos atmosféricos con buena precisión para efectos subdominantes provenientes de nueva física como las INE.

Objetivos

Esta tesis tiene por objetivo el desarrollo de una estrategia para identificar la señal de interacciones no estándar de neutrinos (INE) en los observatorios ANTARES y ORCA. La señal está afectada por incertidumbres en los modelos de flujos de neutrinos atmosféricos y en las secciones eficaces neutrino-nucleón en el agua, así como en las características del detector como su umbral y sus resoluciones. Se ha cuantificado el efecto de estas incertidumbres sistemáticas en la intensidad de la señal y se ha explorado el alcance de física de ANTARES y ORCA.

Los objetivos principales de la tesis se han agrupado de la siguiente manera:

- Búsqueda de INE con diez años de datos de ANTARES: Los datos de desaparición de neutrinos muónicos atmosféricos tomados por ANTARES en el periodo 2007-2016 se han analizado y se han puesto límites en el espacio de fase de las INE en el sector $\mu - \tau$.
- Sensitividad a INE en ORCA: Se ha evaluado la futura sensitividad de ORCA para el descubrimiento de INE en tres años de funcionamiento.
- El efecto de las INE en el ordenamiento de las masas de los neutrinos (OMN) en ORCA: Además de las degeneraciones óctuples estándar en octante-ordenamiento y fase CP, la presencia de INE causa degeneraciones adicionales, que pueden afectar la determinación del ordenamiento de masas con ORCA. Se ha explorado el impacto de varios parámetros de INE en la sensitividad de ORCA.
- Sensitividad de ORCA al octante de θ_{23}: El valor no nulo de θ_{13} lleva a grandes efectos de materia en las oscilaciones de neutrinos atmosféricos y puede ser usado para estudiar la desviación de θ_{23} respecto al ángulo máximo de mezcla y aclarar su octante. Se ha estimado la sensitividad de ORCA para el octante θ_{23} para una exposición de tres años.

Teoría: Oscilaciones de neutrinos e interacciones no estándar

Los neutrino, $\{\nu_\alpha\}$ (donde α representa la familia de sabor) son producidos en procesos de interacción débil de corrientes cargadas (CC) y corrientes neutras (NC). Cada estado propio de sabor $\{\nu_\alpha\}$ es una superposición cuántica de varios estados propios de masa m_i. Las oscilaciones se generan debido a la interferencia entre distintos neutrinos masivos que son producidos y detectados coherentemente como $\{\nu_\alpha\}$ con pequeñas diferencias de masa. Esto implica que cuando un neutrino de un cierto sabor (por ejemplo $\{\nu_\alpha\}$ es producido en un proceso de interacción débil y se propaga a través del espacio (o un medio), cada estado propio de masa viaja con una velocidad diferente, dando lugar a un retraso de fases entre ellos. Después de cierta distancia, la composición de los estados de masa puede hacer que se detecte como un estado de sabor diferente. Este proceso de transmutación de un sabor $\{\nu_\alpha\}$ en $\{\nu_\beta\}$ se conoce como *oscilaciones de neutrinos*. Es análogo a los estados cuánticos de mezcla, que son a su vez equivalentes a los osciladores acoplados en mecánica clásica. Podemos discutir la teoría de las oscilaciones de neutrinos en un modo cuantitativo de la siguiente manera. En la teoría estándar de oscilaciones de neutrinos con n generaciones de neutrino ligeros, un estado propio de sabor puede ser expresado como una superposición lineal de estados de masa (o viceversa):

$$|\nu_\alpha\rangle = \sum_{i=1}^{n} U^*_{\alpha i}|\nu_i\rangle, \quad (or\ |\nu_i\rangle = \sum_{\alpha} U_{\alpha i}|\nu_\alpha\rangle,) \tag{23}$$

donde $U_{\alpha i}$ es la matriz de mezcla, que relaciona la base de sabor (los estados propios del hamiltoniano) con la base de sabor (los estados propios de grupo gauge). $U_{\alpha i}$ satisface las siguientes condiciones:

$$U^\dagger U = \mathbb{I}_{n\times n}, \quad \sum_i U_{\alpha i}U^*_{\beta i} = \delta_{\alpha\beta}, \quad \sum_\alpha U_{\alpha i}U^*_{\alpha j} = \delta_{ij}. \tag{24}$$

Los índices latinos $i, j = 1, 2, 3$...corresponden a los estados propios de masa mientras que los índices griegos $\alpha, \beta = e, \mu, \tau$.... corresponden a los autoestados de sabor.

La amplitud de la transición $|\nu_\alpha\rangle \to |\nu_\beta\rangle$ en función del tiempo es

$$A_{\nu_\alpha \to \nu_\beta}(t) = \langle \nu_\alpha | \nu_\beta \rangle_t = \sum_i U^*_{\alpha i} U_{\beta i} e^{-iE_i t}. \tag{25}$$

La probabilidad de transición queda como

$$P_{\nu_\alpha \to \nu_\beta}(t) = |A_{|\nu_\alpha\rangle \to |\nu_\beta\rangle}(t)|^2 = \sum_{i,j} U^*_{\alpha i} U_{\beta i} U_{\alpha j} U^*_{\beta j} e^{-(E_i - E_j)t}. \tag{26}$$

Para neutrinos ultra-relativistas, ($E_i \simeq P_i + \frac{m_i^2}{2E}$ en la limita $m_i^2 \ll P_i$), asumiendo el mismo momento para tods las componentes de neutrinos masivos, ($P_i = P \ \forall i$) y usando la aproximación de rayo de luz ($t \simeq L$ ($c = 1$)), la transición se puede aproximar como [47, 49]:

$$\begin{aligned} P_{\nu_\alpha \to \nu_\beta}(L) = \delta_{\alpha\beta} &- 4 \sum_{i>j} \mathbb{R}e[U^*_{\alpha i} U_{\beta i} U_{\alpha j} U^*_{\beta j}] \sin^2 \phi_{ij} \\ &\pm 2 \sum_{i>j} \mathbb{I}m[U^*_{\alpha i} U_{\beta i} U_{\alpha j} U^*_{\beta j}] \sin 2\phi_{ij}, \end{aligned} \tag{27}$$

donde

$$\phi_{ij} = \Delta m^2_{ij} \frac{L}{4E_\nu} \simeq 1.267 \Delta m^2_{ij} \frac{L}{E_\nu} \frac{[\text{eV}^2][\text{km}]}{[\text{GeV}]}. \tag{28}$$

Los coeficientes de las componentes de sabor de los antineutrinos neutrinos están relacionados con los coeficientes correspondientes de los neutrinos como el complejo-conjugado $U_{\alpha i} \to U^*_{\alpha i}$. Por lo tanto, las probabilidades de oscilación correspondientes difieren solamente en el signo de los términos dependientes de las partes imaginarias en los productos cuárticos de los elementos de la matriz de mezcla. La parte imaginaria en la ecuación 5 depende de si los neutrinos ($+$) o antineutrinos ($-$) son considerados.

El proceso de oscilación está determinado por la matriz de mezcla Pontecorvo-Maki-Nakawaga-Sakata. (PMNS) [14, 13] y las diferencias de los cuadrados de las masas. En esquema de tres sabores con neutrinos de Dirac, los parámetros relevantes son los tres ángulos de mezcla, θ_{12}, θ_{13}, θ_{23}, dos diferencias de masas al cuadrado, Δm^2_{21}, Δm^2_{31}, y una fase CP, δ_{CP}. Nuestro actual conocimiento de estos parámetros se puede resumir como: $\theta_{12} \approx 31$–36°, $\theta_{13} \approx 8$–9°, $\theta_{23} \approx 41$–51°, $\Delta m^2_{12} \approx 7$–$8 \times 10^{-5}$ eV^2, $|\ \Delta m^2_{23}\ | (\approx |\ \Delta m^2_{13}\ |) \approx 2.4$–$2.6 \times 10^{-3}$ eV^2 y $\delta_{CP} \approx 200 - 350^\circ$.. Ignoramos si θ_{23} está en el primer o segundo octante, el signo de Δm^2_{23} (el ordenamiento de masas) y tampoco tenemos una determinación precisa de δ_{CP} (ver revisión 14 in [225] para las definiciones convencionales y para más detalles).

Cuando los neutrinos se propagan en la materia, su evolución está además afectada por las interacciones con el medio debido a la dispersión forward coherente de los neutrinos con la materia. El efecto global se puede describir mediante potenciales efectivos asociados a las corrientes cargadas (CC) y neutras (NC). En el caso de neutrinos viajando a través de la Tierra, el único potencial relevante es el que viene de las componentes de neutrino electrónico interaccionando con electrones de la materia, que

resulta ser [24]:$V_{CC} = \sqrt{2}\, G_F\, n_e$, donde G_F es la constante de Fermi yn_e es la densidad número de electrones a lo largo del camino del neutrino. El hamiltoniano relevantes es:

$$H^{3\nu} = \frac{1}{2E_\nu} U M^2 U^\dagger + V_{CC}\,\mathrm{diag}(1,0,0), \tag{29}$$

donde U, la matriz de mezcla PMNS, realiza la rotación de la matriz de masa $M^2 = \mathrm{diag}(0, \Delta m^2_{21}, \Delta m^2_{31})$ en el espacio de sabor.

La existencia de INEs puede ser descrita como un nuevo potencial que se traducirá en un nuevo término en el hamiltoniano.

$$H^{INE} = V_{CC}\, \frac{n_f}{n_e}\, \epsilon, \tag{30}$$

donde n_f y n_e son la densidad número de fermiones a lo largo del camino del neutrino y se asume que los neutrinos interaccionan con los quarks down, que son aproximadamente tres veces más abundantes que los electrones, $n_f = n_d \approx 3\, n_e$ y que la matriz ϵ ($\epsilon_{\alpha\,\beta}$, α, β = e, μ, τ) da la fuerza de la INE. Los términos diagonales de esta matriz, si son diferentes entre ellos, pueden dar lugar a la violación de la universalidad leptónica, mientras que los elementos fuera de la diagonal pueden inducir corrientes de neutras que cambien el sabor, algo fuertemente suprimido en el Modelo Estándar. Condiciones de hermicidad y unitariedad y la falta de traza de la matriz ϵ reducen sus componentes a seis parámetros efectivos [226]. Además, en un experimento como ANTARES en el que el flujo de neutrinos atmosféricos está fuertemente dominado por ν_μ transformándose principalmente en ν_τ, la principal contribución a INE vendría por los elementos de matriz con $\alpha, \beta = \mu$ or τ. Además, es usual asumir $\epsilon_{\mu\mu} \approx \epsilon_{\tau\tau}$. Por lo tanto, en nuestro análisis investigaremos los dos parámetros reales $\epsilon_{\tau\tau}$ and $\epsilon_{\mu\tau}$.

La oscilación dominante atmosférica $\nu_\mu \to \nu_\tau$ da lugr a la desaparición de ν_μ's, cuya magnitud depende de su energía y camino. Dado que un telescopio de neutrinos como ANTARES detecta principalmente interacciones ν_μ CC que dan lugar a eventos de traza, la influencia de las oscilaciones de neutrinos se puede estudiar midiendo el déficit de esos sucesos como función de su energía y dirección de llegada. En el intervalo de ∼10 GeV hasta más de ∼100 GeV, el detector es capaz de proporcionar una estimación de la energía del muon a partir de la medida del rango del muon [60]. Además, dados los valores actuales de θ_{23} y Δm^2_{23}, el efecto de la probabilidad de oscilación $\nu_\mu \to \nu_\tau$ es importante en ese intervalo de energía: un mínimo de la probabilidad de supervivencia ocurre a unos 25 GeV y el déficit de ν_μ es apreciable hasta 100 GeV [60].

Se espera que las INEs tengan un efecto sub-dominante y por tanto serían observdas como desviaciones de las distribuciones de energía y direcciones de llegada respecto a las oscilaciones estándar. Como ejemplo de los efectos esperados, mostramos en la Fig. 10 la variación del patrón de oscilación debido a INE. La diferencia entre la probabilidad de supervivencia para INE se muestran en función de cos θ_z y E_ν. El plot de la izquierda muestra la diferencia para neutrinos y el plot de la derecha, para antineutrinos. Se asume ordenamiento normal en ambos casos. Aunque los efectos de INEs son anti-simétricos para neutrinos y anti-neutrinos, no son exactamente opuestos, lo que da lugar a diferencias pequeñas pero apreciables en detectores insensibles a la carga isoscalar como ANTARES. Los plots han sido generados para un valor de $\epsilon_{\mu\tau}$ de 0.01, para el que la mayoría de los telescopios de neutrinos actuales son sensibles. El efecto de INEs es más prominente para sucesos verticales (cos $\theta_z \approx 1$) y dado que

las INEs desplazan el mínimo de oscilación, también producen mayor impacto a las correspondientes energías, aunque el efecto de INEs en la probabilidad de supervivencia se extiende a energías más altas.

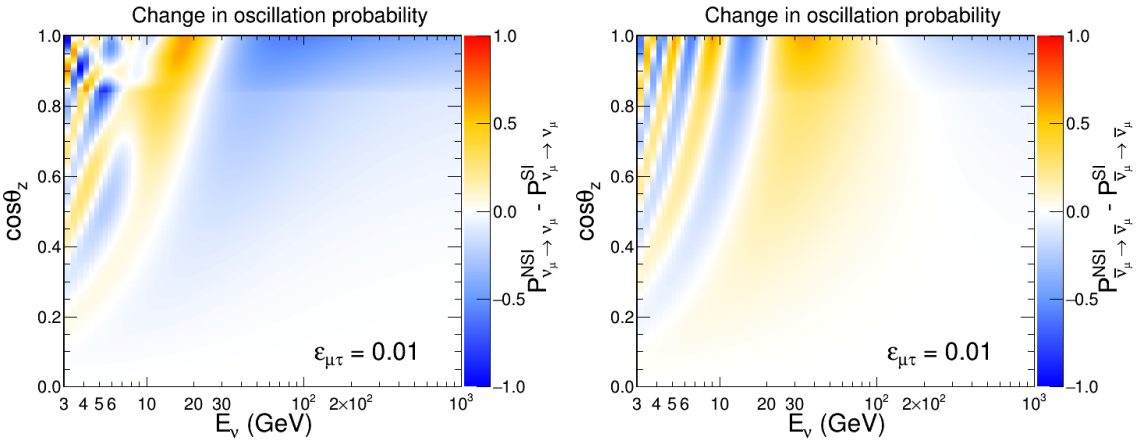

Figure 10: INE inducen modificaciones en las probabilidades de desaparición de ν_μ (izquierda) y $\bar{\nu}_\mu$ (derecha) en función de la energía del neutrino y el coseno del ángulo cenital. El punto de prueba INE se ha establecido en $\epsilon_{\mu\tau} = 0.01$. Se asume un orden normal.

Instrumento: Telescopios de neutrinos

El término telescopio de neutrinos se refiere a una red de dispositivos ópticos distribuidos en un gran volumen de un medio transparente y natural con el objetivo de detectar la luz Cherenkov de las interacciones de neutrinos [126]. La sensitividad a la dirección es la razón de que se llamen telescopios.

ANTARES

ANTARES (acrónimo de Astronomy with a Neutrino Telescope and Abyss environmentalRESearch) [130] es un telescopio de neutrinos submarine localizado a 40 km de la costa de Tolón (Francia) a (42° 48′ N, 6° 10′ E), situado a 2475 m bajo la superficie del mar Mediterráneo. La primera línea se instaló en marzo de 2006 y el detector fue completado en mayo de 2008. La Fig. 11 muestra un esquema del detector ANTARES. ANTARES consiste en 12 líneas de detección verticales instrumentadas en una configuración octagonal con una separación horizontal de 60–75 m. Las líneas están ancladas al lecho marino mediante una estructura de titanio (Bottom String Socket) que actúa de peso muerto y una boya en su parte superior para que la línea permanezca vertical (los módulos ópticos también tienen su propia flotabilidad). Cada línea tiene 25 pisos (salvo la línea 12 con 20 pisos) empezando a 100 sobre el fondo marino con una separación vertical de 14.5 metros, lo que da una altura total de 450 m. El volumen total instrumentado en ANTARES es ~ 0.01 km^3.

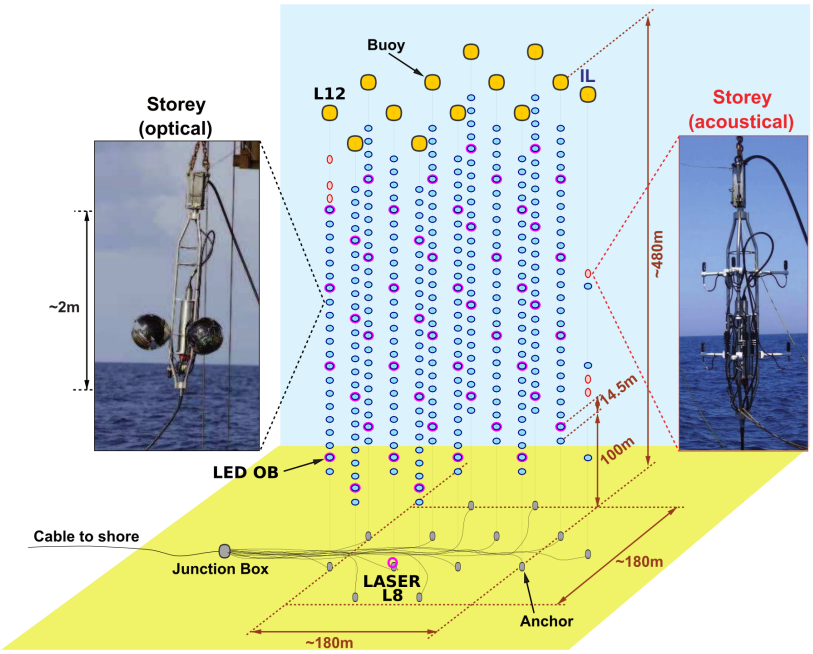

Figure 11: Diagrama esquemático del detector ANTARES. Se muestran fotos de dos pisos con equipamiento óptico y acústico. De [130].

KM3NeT

KM3NeT (acrónimo de KiloMetre cube Neutrino Telescope) [66] es un telescopio de neutrinos de nueva generación actualmente en construcción en el mar Mediterráneo. Según la granularidad de los módulos ópticos (para estudiar distintos intervalos de energía de los neutrinos), KM3NeT albergará dos sub-detectores:

- **ORCA** (Oscillation Research with Cosmics in the Abyss): detector densamente instrumentado de of un volume $\sim 5 \times 10^{-3}$ km^3, situado frente a la costa de Tolón (Francia) en (42°41′ N, 6°02′ E), diseñado para estudiar las propiedades de los neutrinos y astrofísica de bajas energías.
- **ARCA** (Astroparticle Research with Cosmics in the Abyss): detector instrumentado con baja densidad, con un volumen de ~ 1 km^3, localizado frente a la costa de Sicilia (Italia) a (36°16′ N, 16°06′ E), diseñado para la detección de neutrinos de alta energía y astronomía de neutrinos.

Los términos ORCA y ARCA se usarán en lo que sigue para designar a los detectores KM3NeT-ORCA y KM3NeT-ARCA respectivamente. La red tridimensional de cada configuración particular se denomina "Building Block" (BB). KM3NeT consistirá en dos BBs para ARCA y un BB para ORCA para alcanzar los volúmenes instrumentados deseados. La Fig. 12 muestra una vista esquemática de uno de los BBs del detector KM3NeT. Cada builiding block consistirá en una red tridimensional de 64,000 PMTs distribuidos en 115 líneas de detección (también llamadas DUs) con 18 módulos digitales (DOMs) por línea. Empezando a unos 40 m (80 m) del fondo marino, las DUs de ORCA (ARCA) tienen una altura de 200 m (700 m) y están separados horizontalmente por unos 20 m (95 m), con 18 DOMs separados 9 m (36 m) verticalmente.

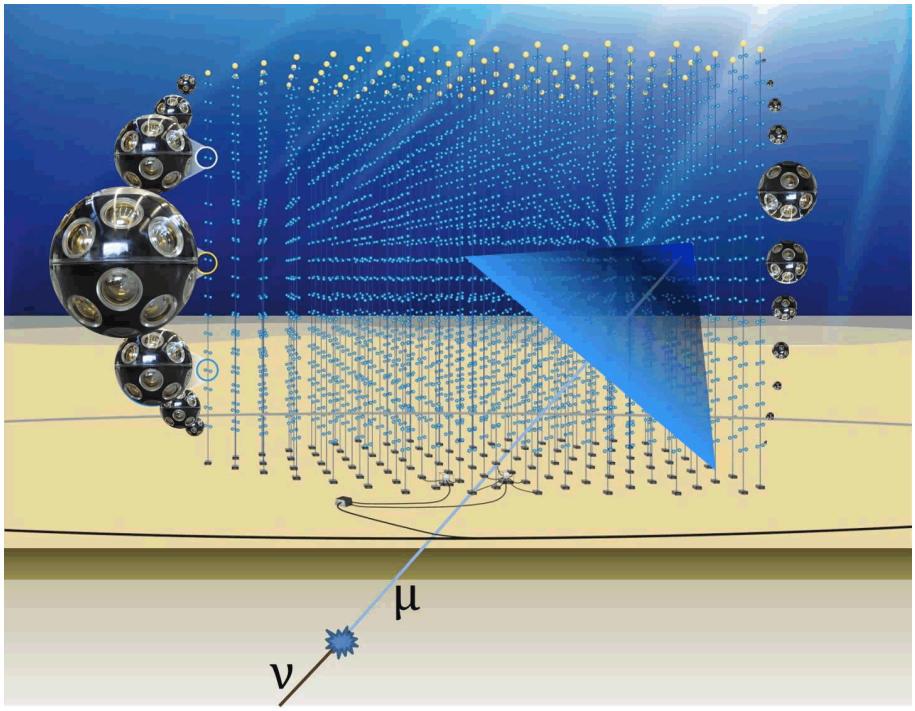

Figure 12: Vista conceptual del detector KM3NeT. La línea azul representa un neutrino ascendente que experimenta una interacción ν_μ - CC cerca del volumen fiducial que conduce a un evento similar a una pista y crea un cono de Cherenkov a lo largo de su trayectoria. De la documentación interna de KM3NeT.

Metodología

Una separación suceso a suceso de la señal de INE en los detectores es demasiado complicada. Lo que es posible en cambio es buscar un exceso o déficit estadístico en los sucesos de neutrinos y antineutrinos predichos por una determinada hipótesis test de INE. El primer paso es calcular el número de sucesos correspondiente a una determinada hipótesis de oscilación con o sin INE. El número total de sucesos de corriente cargada con neutrinos muónicos esperado en el detector para un periodo t es:

$$\begin{aligned}\frac{d^2N_\mu^{CC}}{dE\,d\cos\theta} = &\left(\frac{d^2\phi_{\nu_\mu}}{dE\,d\cos\theta}P_{\mu\mu} + \frac{d^2\phi_{\nu_e}}{dE\,d\cos\theta}P_{e\mu}\right)\times\sigma_{\nu_\mu}^{CC}A_{\nu_\mu}^{CC}\times t \\ &+\left(\frac{d^2\phi_{\bar\nu_\mu}}{dE\,d\cos\theta}P_{\bar\mu\bar\mu} + \frac{d^2\phi_{\bar\nu_e}}{dE\,d\cos\theta}P_{\bar e\bar\mu}\right)\times\sigma_{\bar\nu_\mu}^{CC}A_{\bar\nu_\mu}^{CC}\times t.\end{aligned} \tag{31}$$

N_μ es el número de sucesos muónicos en el intervalo de energía dE y de coseno de ángulo zenital $d\cos\theta$; ϕ_{ν_x} ($\phi_{\bar\nu_x}$) es el flujo de neutrinos (antineutrinos) de sabor x en la localización del detector; $P_{\alpha\beta}$ es la probabilidad de oscilación de un neutrino de sabor ν_α a neutrino de sabor ν_β, $\sigma_{\nu_\mu}^{CC}$ es la sección eficaz de corriente cargada del neutrino con nucleones del agua del mar; $A_{\nu_\mu}^{CC}$ ($A_{\bar\nu_\mu}^{CC}$) es área efectiva del detector, dependiente de la energía y del ángulo, correspondiente a neutrinos (antineutrinos) que ha sufrido una interacción CC en el detector.

Sin embargo, el detector no puede separar sucesos (ν_e, $\bar\nu_e$, ν_μ, $\bar\nu_\mu$, ν_τ, $\bar\nu_\tau$ - CC) y (ν, $\bar\nu$ - NC). Dependiendo de las señales Cherenkov de los leptones salientes de las interacciones CC de ν_e y ν_μ, se observan dos topologías distintas en el detector: sucesos tipo traza y

tipo cascada. Las interacciones CC ν_μ, CC y ν_τ con desintegración muónica del τ dan cuenta de la mayoría de los muones que aparecen como traza en el detector. La topología tipo cascada corresponde a sucesos de interacciones CC ν_e, CC ν_τ con desintegración del tau no muónica y las interacciones de corriente cargada de cualquier sabor. Las ocho distribuciones indexadas por tipo $\mathcal{X} \in \{(\nu_e, \overline{\nu}_e, \nu_\mu, \overline{\nu}_\mu, \nu_\tau, \overline{\nu}_\tau$ - CC) and (ν, $\overline{\nu}$ - NC)$\}$ se han mezclado en dos distribuciones correspondientes a las dos topologías: trazas y cascadas.

El método para estimar la sensitividad a un parámetro test en una hipótesis del modelo está basado en una estrategia de verosimilitud con bines [196]. En el caso de distribución poissoniana en el número de sucesos el test estadístico tras incluir los términos de penalización gaussianos es

$$-2LLR(\lambda, n) = 2 \sum_{i \in \{bins\}} \left[\lambda_i(\bar{o}, \bar{s}) - n_i + n_i \ln \left(\frac{n_i}{\lambda_i(\bar{o}, \bar{s})} \right) \right] + \sum_{j \in \{syst\}} \frac{(s_j - \hat{s}_j)^2}{2\sigma_j^2}. \quad (32)$$

El número de sucesos predicho λ_i en el bin i-ésimo es una función de un conjunto de parámetros, $\bar{o}$, así como del conjunto de parámetros relacionado con las incertidumbres sistemáticas $\bar{s}$. El segundo término corre sobre los términos de penalización j de los parámetros de ruido, siendo $\hat{s_j}$ y σ_j^2 los priors y la desviación estándar gaussiana del parámetro j, respectivamente.

Las contribuciones individuales de las clases de traza y cascada se suman para calcular la significancia total, σ_{tot}:

$$\begin{aligned} \sigma_{tot} &= \sqrt{-2LLR(\lambda, n)} \\ &= \sqrt{(-2LLR)\Big|_{\text{tracks}} + (-2LLR)\Big|_{\text{showers}}} \end{aligned} \quad (33)$$

El valor de σ_{tot} indica el nivel de acuerdo o desacuerdo entre la predicción $\lambda(\bar{o}, \bar{s})$ de un modelo y el conjunto n de datos y cuantifica la *sensitividad* del detector a una hipótesis de modelo particular dado un tiempo de funcionamiento.

Incertidumbres sistemáticas

La Tab. 3 muestra una lista exhaustiva de los parámetros de incertidumbres sistemáticas considerados en el ajuste junto con su tratamiento (ajustados o fijos), valores nominales y restricciones externas, si se usan. Pueden ser agrupados en cuatro categorías:

Parámetros molestos	Tratamiento	Valor nominal	Priors
Oscilación			
$\theta_{12}(^\circ)$	fijos	33.82	-
$\theta_{13}(^\circ)$	ajustados	8.60	0.13
$\theta_{23}(^\circ)$	ajustados	48.6	libre
$\delta_{CP}(^\circ)$	ajustados	221	libre
$\Delta m^2_{21}(\times 10^{-5}\text{eV}^2)$	fijos	7.39	-
$\Delta m^2_{31}(\times 10^{-3}\text{eV}^2)$	ajustados	2.528	libre
Flujo			
Normalización de la traza	ajustados	1	libre
Normalización de las cascadas	ajustados	1	libre
Normalización de los intermedios	ajustados	1	libre
ν_μ/ν_e skew	ajustados	0	5%
$\nu_\mu/\overline{\nu}_\mu$ skew	ajustados	0	5%
$\nu_e/\overline{\nu}_e$ skew	ajustados	0	5%
Pendiente de la energía ($\Delta\gamma$)	ajustados	0	5%
Pendiente de zénit	ajustados	0	2%
Secciones eficaces			
Escala de NC	ajustados	1	5%
Detector			
Escala de energías	ajustados	1	10%

Table 3: El listado de sistemáticas estudiadas en el análisis INE ORCA, junto con su tratamiento estadístico, valores nominales y previos inyectados (si los hubiere).

- **Parámetros de oscilación**: los parámetros solares (θ_{12}, Δm^2_{21}) se mantienen fijos a su valor nominal (adoptado de NuFit v4.1 [90]), ya que ORCA, al ser un experimento de oscilaciones atmosféricas, no es muy sensible a ellos. El ángulo de mezcla θ_{13} tiene un efecto grande en las probabilidades de oscilación. Por tanto, los límites experimentales actuales se han usado para aprovechar plenamente el potencial de ORCA para estimar la sensitividad de los parámetros de INEs. Esto se refleja en un prior de 0.13°. No se han usado priores para los parámetros de oscilación atmosféricos ((θ_{23}, Δm^2_{31}) y δ_{CP}, ya que se supone que se medirán por ORCA. Debido a la degeneración entre el octante de θ_{23} y el signo de Δm^2_{31} ($+/-$ corresponde a NO/IO), se usa un valor inicial de θ_{23} en ambos octantes ($\theta_{23} < 45^\circ \in$ primer octante o $\theta_{23} > 45^\circ \in$ segundo octante) y se toma el valor mínimo de $-2\ln\mathcal{L}$. El efecto de estas incertidumbres en los parámetros de oscilación se muestra en las Fig. 4.31 hasta Fig. 4.34.
- **Incertidumbres en el flujo**: Se han considerado los efectos sistemáticos de los parámetros del flujo atmosférico. El número total de sucesos de cada clase tiene un número asociado de factor de normalización: "Normalización de la traza", "Normalización de las cascadas", "Normalización de los intermedios", que son ajustados sin ninguna restricción. También se tienen en cuenta las incertidumbres en la masa efectiva del detector y de las secciones eficaces de interacción de los neutrinos. Se permite variar hasta un 5% respecto al valor nominal el cociente entre el número total de ν_μ y de ν_e ("ν_μ/ν_e skew"), ν_μ y $\overline{\nu}_\mu$ ("$\nu_\mu/\overline{\nu}_\mu$ skew") y ν_e y $\overline{\nu}_e$ ("$\nu_e/\overline{\nu}_e$ skew"). El margen del 5%, que es independiente del ángulo zenital y la energía, es más conservador que las actuales incertidumbres estimadas para el flujo de atmosfércos [207]. El efecto de estas incertidumbres en la distribuciones finales

se muestra en las Fig. 4.35 hasta Fig. 4.37.

El error en la "pendiente de la energía", $\Delta\gamma$, aplicado en función de E_ν^γ, tiene en cuenta el cambio en el espectro de la energía debido a incertidumbres en el espectro primario de rayos cósmicos. Se permite variar la pendiente de la energía hasta un 5% alrededor del valor central $\Delta\gamma = 0$. Análogamente, se permite variar hasta un 2% el cociente de neutrinos ascendentes respecto a descendentes, llamado "pendiente de zénit". El efecto de estas incertidumbres en las distribuciones finales de sucesos se muestra en las Fig. 4.38 y Fig. 4.39.

- **Incertidumbres en las secciones eficaces**: Mientras que la universalidad de leptones implica que los cocientes entre distintos sabores son bien conocidos, lo mismo no ocurre necesariamente para los cocientes entre sucesos CC y NN. Por tanto, también se ajusta la normalización de las corrientes neutras dentro de un 5%. Las incertidumbres en las secciones eficaces de CC y NC absolutas no se consideran en este estudio. Sin embargo, son absorbidas en la normalización del flujo. El efecto de la normalización de la escala de NC sobre la distribución de sucesos se muestra en la Fig. 4.40.
- **Incertidumbres del detector**: Entre las incertidumbres incorporadas a este análisis, las normalizaciones de trazas, intermedios y cascadas y en la escala de energías pueden ser consideradas efectos del detector. La escala de energía depende de las eficiencias de los PMTs y las propiedades del agua [23]. Si los sucesos son sistemáticamente más brillantes o menos de lo esperado, esto causará un desplazamiento en la normalización de la masa efectiva. Esto se tiene en cuenta en la escala de energía, que se ajusta dentro de una incertidumbre de 10% alrededor de su valor nominal.

Resultados

Los resultados de los cuatro análisis de física se resumen en las siguientes subsecciones para ambos ordenamientos de masa: ordenamiento normal (ON) y ordenamiento inverso (OI). Los resultados de la búsqueda de INE con ANTARES y la estimación de la capacidad de ORCA se han agrupado en aras de la brevedad. A esto sigue la estimación de la resolución de ORCA para la determinación del ordenamiento de masas en presencia de INE. Por último, se muestra la resolución de ORCA para el octante de θ_{23}.

Búsqueda de INE con ANTARES y KM3NeT-ORCA

Se presenta a continuación el análisis de ANTARES en busca de INE en los datos de oscilación de neutrinos atmosféricos. No se ha observado un exceso o déficit significativo y los datos son consistentes con la hipótesis de oscilaciones estándar a $> 2.2\sigma$. Esto resulta en límites en el sector $\mu - \tau$ de las INE.

Para KM3NeT-ORCA, se han simulado distribuciones de sucesos para un periodo de exposición de tres años. El número esperado de sucesos se ha pesado de acuerdo a varias hipótesis de señal de INE para explorar el potencial de ORCA para INE. Los límites de ANTARES y la sensitividad de ORCA se muestran en las Fig. 13 – Fig. 15 con comparaciones con otros experimentos.

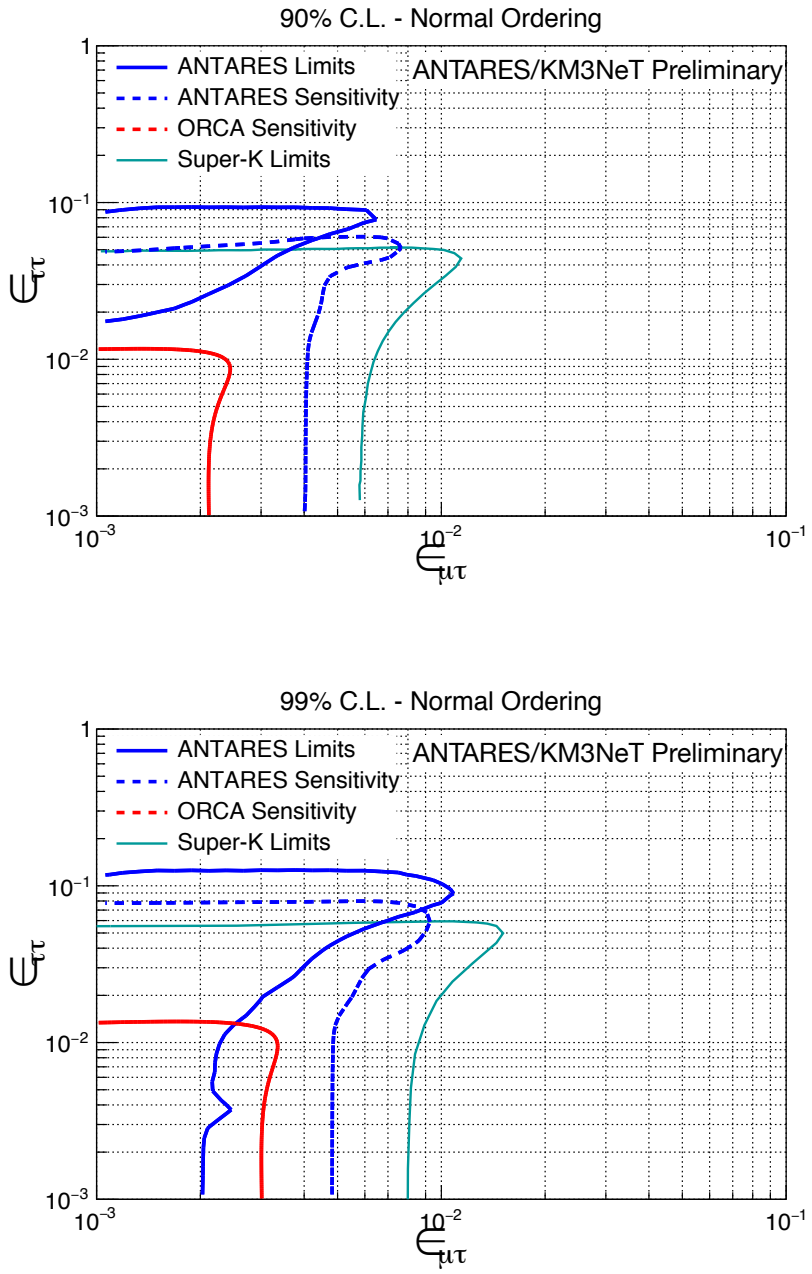

Figure 13: Límites (izquierda: 90% C.L., derecha: 99% C.L.) en el espacio de fase $\epsilon_{\mu\tau} - \epsilon_{\tau\tau}$ tras diez años de funcionamiento de ANTARES, comparado con la sensitividad del detector y los límites de Super-K [192].

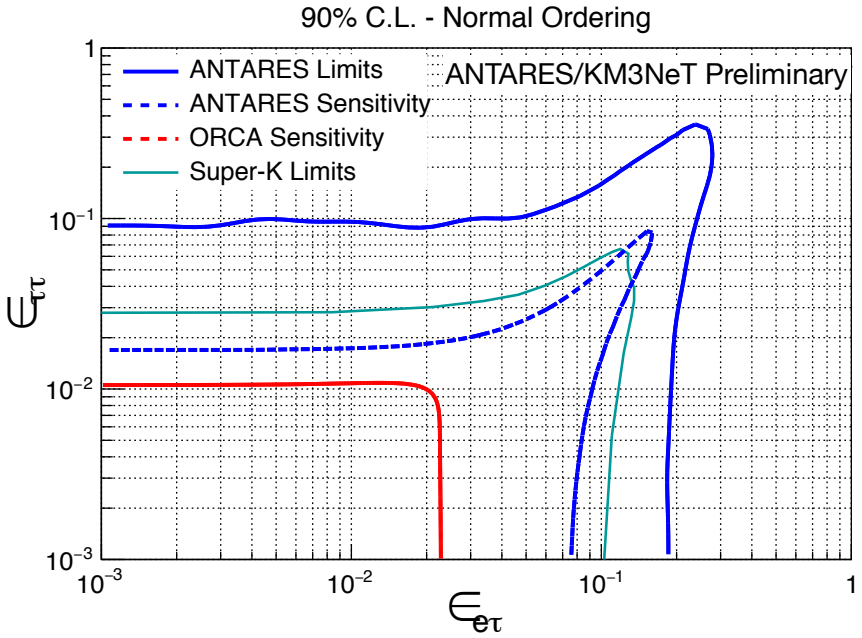

Figure 14: Límites (90% C.L.) en el espacio de fase $\epsilon_{e\tau} - \epsilon_{\tau\tau}$ obtenidos tras diez años de funcionamiento de ANTARES, junto con la sensitividad del detector y los límites obtenidos por Super-K [192].

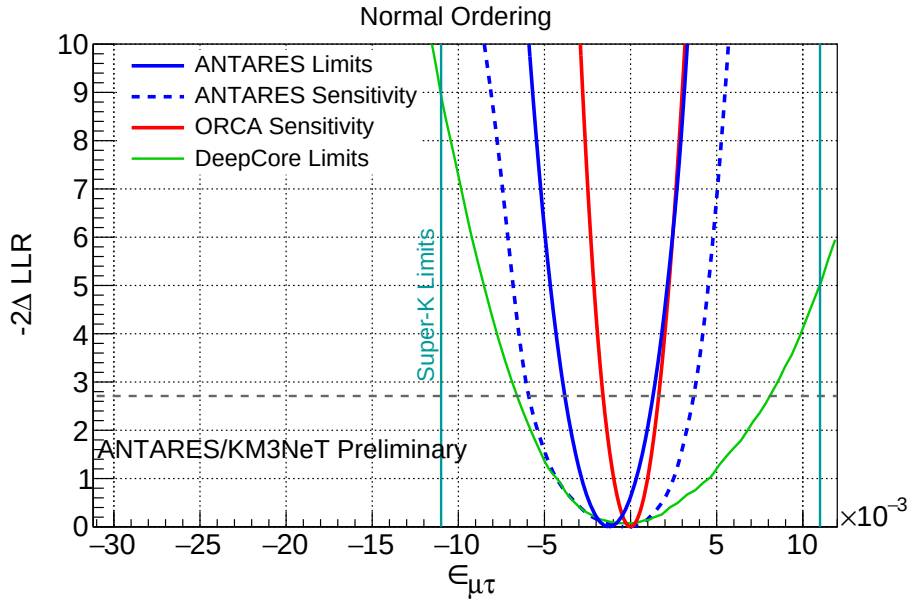

Figure 15: Límite en el espacio de fase $\epsilon_{\mu\tau}$ obtenidos tras diez años de funcionamiento de ANTARES, junto con la sensitividad del detector y los límites de Super-K [192].

Los límites para INE obtenidos tras diez años de datos de desaparición de muones atmosféricos tomados por ANTARES son más restrictivos que los obtenidos por otros experimentos, de manera que son los mejores límites existentes hasta la fecha en el sector $\mu - \tau$. ORCA muestra un excelente potencial para poner límites más restrictivos

en un orden de magnitud en varios espacios de parámetros de INE. Finalmente, las sensitividades para INE esperados para ORCA y los límites obtenidos por ANTARES en el sector mu-tau se muestran en la Tab. 4 y en las Eq. 34 y Eq. 35, respectivamente.

INE Couplings	**Assumed True NMO**	**Bounds (90% C.L.)**
$\epsilon_{e\mu}$	NO	$(-1.7 \times 10^{-2}, 1.7 \times 10^{-2})$
	IO	$(-2.0 \times 10^{-2}, 2.0 \times 10^{-2})$
$\epsilon_{e\tau}$	NO	$(-1.8 \times 10^{-2}, 2.1 \times 10^{-2})$
	IO	$(-3.1 \times 10^{-2}, 2.7 \times 10^{-2})$
$\epsilon_{\mu\tau}$	NO	$(-1.7 \times 10^{-3}, 1.7 \times 10^{-3})$
	IO	$(-1.7 \times 10^{-3}, 1.7 \times 10^{-3})$
$\epsilon_{\tau\tau}$	NO	$(-0.8 \times 10^{-2}, 1.1 \times 10^{-2})$
	IO	$(-1.1 \times 10^{-2}, 0.8 \times 10^{-2})$

Table 4: Sensitividades (90% C.L.) para INE de neutrinos con quarks d para tres años de datos de ORCA con 115 líneas espaciadas 20 m horizontalmente. Solo un parámetro de INE se considera cada vez.

$$\begin{aligned} -4.2 \times 10^{-3} < \epsilon_{\mu\tau} < 2.7 \times 10^{-3} \quad & (\text{at } 90\% \text{ C.L}), \\ -6.1 \times 10^{-2} < \epsilon_{\tau\tau} < -2.1 \times 10^{-2} \quad \text{and} \quad 2.1 \times 10^{-2} < \epsilon_{\tau\tau} < 7.3 \times 10^{-2} \quad & (\text{at } 90\% \text{ C.L}). \end{aligned} \tag{34}$$

$$-3.8 \times 10^{-3} < \epsilon_{\mu\tau} < 1.6 \times 10^{-3} \quad \forall\, \epsilon_{\tau\tau} = 0 \quad (\text{at } 90\% \text{ C.L}), \tag{35}$$

Impacto de las INE en la sensitividad de KM3NeT-ORCA

La sensitividad de ORCA para el ordenamiento de masas de los neutrinos para la hipótesis de INE se presenta en la Fig. 16. Esta incorpora la incertidumbre de los modelos de ajuste a los espectros experimentalmente observados y enfatiza la importancia de probar diferentes marcos con medidas de alta precisión de los parámetros de oscilación. En el caso de OI verdadero, la resolución de ORCA para el ordenamiento de las masas se puede ver perjudicada de manera significativa en presencia de efectos subdominantes provenientes de INE, dependiendo del valor verdadero de θ_{23}. El efecto es despreciable si el ordenamiento de masas es normal. Por tanto, la presencia de INE puede afectar al potencial de ORCA para medir los parámetros de oscilaciones estándar.

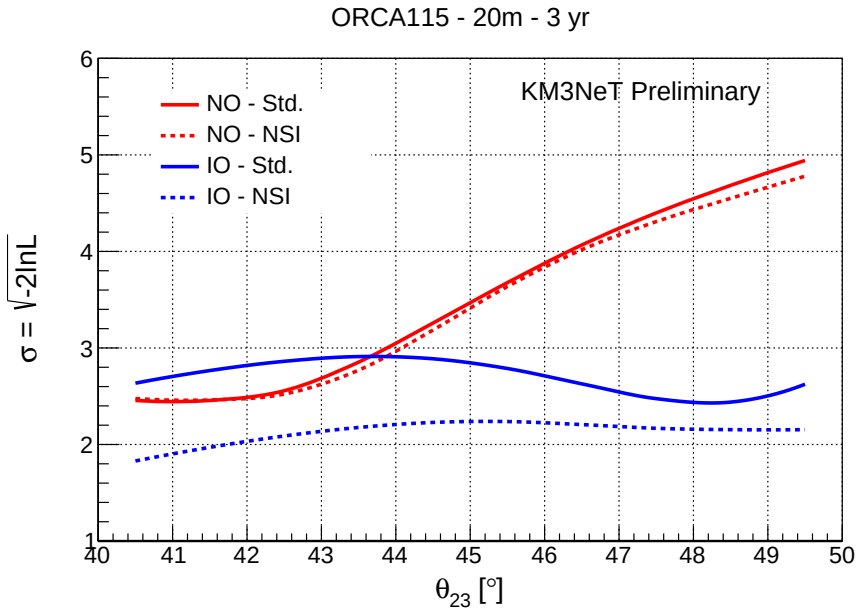

Figure 16: Sensitividad prevista para el ordenamiento de masas tras tres años de funcionamiento de ORCA en función del valor verdadero de θ_{23}para ON (rojo) y OI (azul), con un mejor ajuste global δ_{CP} de 221° (228°) para la hipótesis ON (OI). Las líneas discontinuas (continuas) corresponden al caso en el que los parámetros de INE se ajustan simultáneamente (fijados en 0).

Sensitividad de KM3NeT-ORCA al octante de θ_{23}

Hemos investigado cuántos años requeriría ORCA para hacer una medida a $1/2/3\sigma$ del octante de θ_{23}, dependiendo de los verdaderos valores del ordenamiento de masas y de θ_{23}. Los resultados se muestran en las Fig. 17 y Fig. 18. Las curvas de sensitividad correspondientes a la minimización sobre el ordenamiento también se incluyen.

Los "hombros" en $\theta_{23} \sim 42°$ (ON) y $\theta_{23} \sim 49°$ (OI) corresponden a regiones donde la incertidumbre en el conocimiento del ordenamiento degrada la sensitividad del octante y lleva a un incremento del tiempo de exposición necesario para determinarlo. Si el ordenamiento verdadero es ON, probar una solución falsa del octante en la hipótesis OI tiene un efecto significativo en la sensitividad el octante para $\theta_{23} < 42°$. Cuando el ordenamiento verdadero es OI, la solución falsa del octante para ON tiene un efecto pequeño sobre la sensitividad para $\theta_{23} > 49°$.

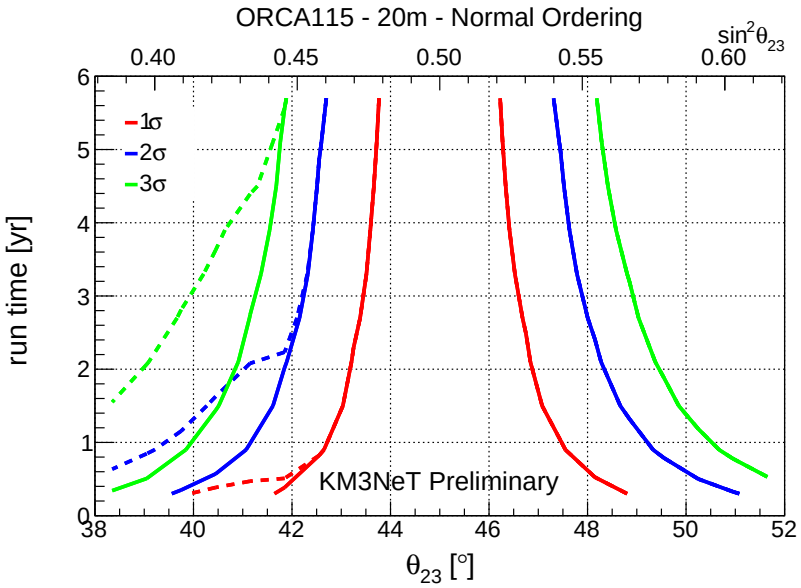

Figure 17: Tiempo de exposición (en años) requerido para que ORCA pueda excluir el octante falso de θ_{23} a $1/2/3\sigma$, en función del valor verdadero de θ_{23} asumiendo ordenamiento ON. La curva continua se refiere al caso donde el ordenamiento se ha fijado al valor verdadero, mientras que la curva discontinua corresponde al caso en el que el ordenamiento se trata como un parámetro libre en el ajuste.

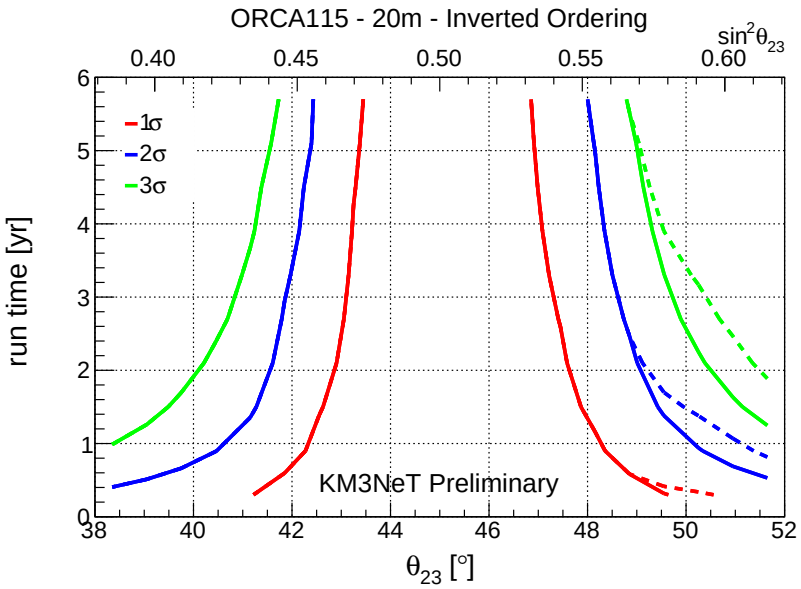

Figure 18: Tiempo de exposición (en años) requerido para que ORCA pueda excluir el octante falso de θ_{23} a $1/2/3\sigma$, en función del valor verdadero de θ_{23} asumiendo ordenamiento OI. La curva continua se refiere al caso donde el ordenamiento se ha fijado al valor verdadero, mientras que la curva discontinua corresponde al caso en el que el ordenamiento se trata como un parámetro libre en el ajuste.

Se prevé que ORCA pueda hacer una determinación a 1σ el octante de θ_{23} en menos de un año si el ordenamiento de masas es normal y si $\theta_{23} < 42.5°$ o $\theta_{23} > 47.6°$, o si el ordenamiento es inverso y $\theta_{23} < 42.2°$ o $\theta_{23} > 48.0°$. Con cinco años de datos se puede

hacer una medida a 1σ para ON y $\theta_{23} < 42.2°$ o $\theta_{23} > 46.2°$, o para OI y $\theta_{23} < 42.4°$ o $\theta_{23} > 47°$.

Conclusiones

Los neutrinos y antineutrinos atmosféricos de sabor muónico y electrónico representan una rica fuente de información sobre las oscilaciones de neutrinos gracias a la dependencia de sus flujos con el ángulo y la energía y los efectos de materia. Gracias a la alta estadística de neutrinos atmosféricos, ANTARES y KM3NeT pueden hacer fuertes contribuciones a la comprensión de los neutrinos la medida precisa de sus parámetros de oscilación.

Los estudios llevados a cabo en esta tesis indican que ORCA será el primer detector de neutrinos atmosféricos capaz de medir el ordenamiento de masas con una precisión de 3σ. Sin embargo, antes de atribuir cualquier medida a las oscilaciones estándar en el paradigma básico tres sabores de neutrinos, es crucial estudiar posibles correlaciones y degeneraciones que podrían aparecer debidas a nuevos parámetros de nuevos escenarios físicos como las interacciones no estándar de neutrinos. Se espera que ORCA pueda restringir muchos de esos casos de física exóticos que podrían contribuir a la señal en la extracción de los parámetros de oscilaciones estándar. Además, se prevé que ORCA pueda medir con precisión el valor de θ_{23} tras solo unos meses de toma de datos.

Además, se ha propuesto el proyecto P2O con el objetivo de mandar un haz de neutrinos desde Protvino (Rusia) a ORCA para medir la violación de CP en el sector de neutrinos [70]. P2O proporcionará excelente sensitividad a los efectos de materia en la Tierra, permitiendo una medida de la violación de CP a $>2\sigma$ en 15 años con un haz de potencia modesta (90 kW $\approx 0.8 \times 10^{20}$ protones en el destino). La posibilidad de una versión de ORCA diez veces más densa, llamada Super-ORCA [227], también está en consideración. Super-ORCA puede probar la hipótesis de ordenamiento (NMO) a $>2\sigma$ en cinco años. En esta excitante era de física de neutrinos, ANTARES y KM3NeT pueden hacer contribuciones significativas a muchas cuestiones no resueltas en física de partículas estudiando neutrinos en el fondo del mar Mediterráneo.

List of Abbreviations

ANTARES	**A**stronomy with a **N**eutrino **T**elescope and **A**byss environmental **RES**earch
ARCA	**A**stroparticle **R**esearch with **C**osmics in the **A**byss.
ARS	**A**nalogue **R**ing **S**ampler
AVC	**A**nalog to **V**oltage **C**onverter
BSM	**B**eyond the **S**tandard **M**odel
CC	**C**harged **C**urrent
CLB	**C**entral **L**ogic **B**oard
DAQ	**D**ata **A**c**Q**uisition system
DIS	**D**eep **I**nelastic **Sc**attering
DOM	**D**igital **O**ptical **M**odule
DU	**D**etection **U**nit
HO	**H**igher **O**ctant
IO	**I**nverted **O**rdering
KM3NeT	**K**ilo**M**etre Cube **Ne**utrino **T**elescope.
LCM	**L**ocal **C**ontrol **M**odule
LLR	**L**og **L**ikelihood **R**atio
LO	**L**ower **O**ctant
MC	**M**onte **C**arlo
MEOC	**M**ain **E**lectro**O**ptical **C**able
NC	**N**eutral **C**urrent
NMO	**N**eutrino **M**ass **O**rdering
NO	**N**ormal **O**rdering
NSI	**N**on **S**tandard **I**nteractions
ORCA	**O**scillation **R**esearch with **C**osmics in the **A**byss.
p.e.	**p**hoto **e**lectron
P2O	**P**rotvino to **O**rca
PID	**P**article **ID**entification
PMT	**P**hoto **M**ultiplier **T**ube
PREM	**P**reliminary **R**eference **E**arth **M**odel
QE	**Q**uasi **E**lastic
RES	**RES**onant pion production
SCM	**S**tring **C**ontrol **M**odule
SM	**S**tandard **M**odel
TCS	**T**iltmeter **C**ompass **S**ystem
ToT	**T**ime **o**ver **T**hreshold
TS	**T**est **S**tatistic
TTS	**T**ransit **T**ime **S**pread
TVC	**T**ime to **V**oltage **C**onverter
w.e.	**w**ater **e**quivalent

List of Figures

List of Tables

Bibliography

[1] W. Pauli. “Dear radioactive ladies and gentlemen”. In: *Phys. Today* 31N9 (1978), p. 27.
(Cited on p: ix.).

[2] C. N. Yang and R. L. Mills. “Conservation of Isotopic Spin and Isotopic Gauge Invariance”. In: *Phys. Rev.* 96 (1954). Ed. by Jong-Ping Hsu and D. Fine, p. 191.
(Cited on p: 3.).
DOI: 10.1103/PhysRev.96.191.

[3] S. Weinberg. “A Model of Leptons”. In: *Phys. Rev. Lett.* 19 (1967).
(Cited on p: 4.).
DOI: 10.1103/PhysRevLett.19.1264.

[4] S. L. Glashow. “Partial Symmetries of Weak Interactions”. In: *Nucl. Phys.* 22 (1961), p. 579.
(Cited on p: 4.).
DOI: 10.1016/0029-5582(61)90469-2.

[5] A. Salam and J. C. Ward. “Electromagnetic and weak interactions”. In: *Phys. Lett.* 13 (1964), p. 168.
(Cited on p: 4.).
DOI: 10.1016/0031-9163(64)90711-5.

[6] F. Englert and R. Brout. “Broken Symmetry and the Mass of Gauge Vector Mesons”. In: *Phys. Rev. Lett.* 13 (1964).
(Cited on p: 4.).
DOI: 10.1103/PhysRevLett.13.321.

[7] P. W. Higgs. “Broken Symmetries and the Masses of Gauge Bosons”. In: *Phys. Rev. Lett.* 13 (1964), p. 508.
(Cited on p: 4.).
DOI: 10.1103/PhysRevLett.13.508.

[8] M. Gell-Mann. “The interpretation of the new particles as displaced charge multiplets”. In: *Nuovo Cim.* 4.S2 (1956), p. 848.
(Cited on p: 4.).
DOI: 10.1007/BF02748000.

[9] K. Nishijima. “Charge Independence Theory of V Particles*”. In: *Prog. of Theo. Phys.* 13.3 (Mar. 1955), p. 285.
(Cited on p: 4.).
DOI: 10.1143/PTP.13.285.

[10] B. Pontecorvo. "Inverse beta processes and nonconservation of lepton charge". In: *Sov. Phys. JETP* 7 (1958), p. 172.
(Cited on p: 5.).

[11] M. Gell-Mann and A. Pais. "Behavior of Neutral Particles under Charge Conjugation". In: *Phys. Rev.* (1955).
(Cited on p: 5.).
DOI: 10.1103/PhysRev.97.1387.

[12] G. Danby et al. "Observation of High-Energy Neutrino Reactions and the Existence of Two Kinds of Neutrinos". In: *Phys. Rev. Lett.* 9 (1962), p. 36.
(Cited on p: 5.).
DOI: 10.1103/PhysRevLett.9.36.

[13] Z. Maki, M. Nakagawa, and S. Sakata. "Remarks on the unified model of elementary particles". In: *Prog. Theor. Phys.* 28 (1962), p. 870.
(Cited on pp: 5, 219, 237.).
DOI: 10.1143/PTP.28.870.

[14] B. Pontecorvo. "Neutrino Experiments and the Problem of Conservation of Leptonic Charge". In: *Sov. Phys. JETP* 26 (1968), pp. 984–988.
(Cited on pp: 5, 219, 237.).

[15] R. Davis. "A review of the Homestake solar neutrino experiment". In: *Prog. Part. Nucl. Phys.* 32 (1994), pp. 13–32.
(Cited on p: 5.).
DOI: 10.1016/0146-6410(94)90004-3.

[16] John N. Bahcall and R. Davis. "Solar Neutrinos - a Scientific Puzzle". In: *Science* 191 (1976), pp. 264–267.
(Cited on p: 5.).
DOI: 10.1126/science.191.4224.264.

[17] T.A. Kirsten. "GALLEX solar neutrino results and status of GNO". In: *Nucl. Phys. B Proc. Suppl.* 77 (1999). Ed. by Y. Suzuki and Y. Totsuka, pp. 26–34.
(Cited on p: 5.).
DOI: 10.1016/S0920-5632(99)00389-8.

[18] O.L. Anosov et al. "Results from the Russian-American gallium experiment (SAGE)". In: *International Symposium on Neutrino Astrophysics*. June 1992, pp. 39–46.
(Cited on p: 5.).

[19] J.N. Aburashitov et al. "First results from SAGE II". In: *AIP Conf. Proc.* 338 (1995). Ed. by S.J. Seestrom, pp. 866–873.
(Cited on p: 5.).
DOI: 10.1063/1.48459.

[20] Y. Fukuda et al. "Solar neutrino data covering solar cycle 22". In: *Phys. Rev. Lett.* 77 (1996), pp. 1683–1686.
(Cited on p: 5.).
DOI: 10.1103/PhysRevLett.77.1683.

[21] Y. Fukuda et al. "Measurements of the solar neutrino flux from Super-Kamiokande's first 300 days". In: *Phys. Rev. Lett.* 81 (1998). [Erratum:

Phys.Rev.Lett. 81, 4279 (1998)], pp. 1158–1162.
(Cited on p: 5.).
DOI: 10.1103/PhysRevLett.81.1158.
arXiv: hep-ex/9805021.

[22] S. M. Bilenky and B. Pontecorvo. "Lepton Mixing and Neutrino Oscillations". In: *Phys. Rept.* 41 (1978), p. 225.
(Cited on p: 5.).
DOI: 10.1016/0370-1573(78)90095-9.

[23] S. M. Bilenky and S. T. Petcov. "Massive neutrinos and neutrino oscillations". In: *Rev. Mod. Phys.* (1987).
(Cited on p: 5.).
DOI: 10.1103/RevModPhys.59.671.

[24] L. Wolfenstein. "Neutrino Oscillations in Matter". In: *Phys. Rev. D* 17 (1978), pp. 2369–2374.
(Cited on pp: 5, 13, 22, 219, 238.).
DOI: 10.1103/PhysRevD.17.2369.

[25] S.P. Mikheyev and A.Yu. Smirnov. "Resonance Amplification of Oscillations in Matter and Spectroscopy of Solar Neutrinos". In: *Sov. J. Nucl. Phys.* 42 (1985), pp. 913–917.
(Cited on p: 5.).

[26] S. Mikheev and A. Y. Smirnov. "Resonance Oscillations of Neutrinos in Matter". In: *Sov. Phys. Usp.* 30 (1987), p. 759.
(Cited on pp: 5, 12, 194, 208.).
DOI: 10.1070/PU1987v030n09ABEH002961.

[27] H.H. Chen. "Direct Approach to Resolve the Solar Neutrino Problem". In: *Phys. Rev. Lett.* 55 (1985), pp. 1534–1536.
(Cited on p: 5.).
DOI: 10.1103/PhysRevLett.55.1534.

[28] Q.R. Ahmad et al. "Measurement of the rate of $\nu_e + d \rightarrow p + p + e^-$ interactions produced by ^8B solar neutrinos at the Sudbury Neutrino Observatory". In: *Phys. Rev. Lett.* 87 (2001), p. 071301.
(Cited on p: 5.).
DOI: 10.1103/PhysRevLett.87.071301.
arXiv: nucl-ex/0106015.

[29] Q. R. Ahmad et al. "Direct evidence for neutrino flavor transformation from neutral current interactions in the Sudbury Neutrino Observatory". In: *Phys. Rev. Lett.* 89 (2002).
(Cited on pp: 5, 9, 217, 235.).
DOI: 10.1103/PhysRevLett.89.011301.
arXiv: nucl-ex/0204008 [nucl-ex].

[30] Y. Fukuda et al. "Evidence for Oscillation of Atmospheric Neutrinos". In: *Phys. Rev. Lett.* 81.8 (1998).
(Cited on p: 5.).
DOI: 10.1103/physrevlett.81.1562.

[31] S. Hatakeyama et al. "Measurement of the flux and zenith angle distribution of upward through going muons in Kamiokande II + III". In: *Phys. Rev. Lett.* 81 (1998), pp. 2016–2019.
(Cited on p: 5.).
DOI: 10.1103/PhysRevLett.81.2016.
arXiv: hep-ex/9806038.

[32] R. Clark et al. "Atmospheric muon-neutrino fraction above 1-GeV". In: *Phys. Rev. Lett.* 79 (1997), pp. 345–348.
(Cited on p: 5.).
DOI: 10.1103/PhysRevLett.79.345.

[33] M.H. Ahn et al. "Measurement of Neutrino Oscillation by the K2K Experiment". In: *Phys. Rev. D* 74 (2006), p. 072003.
(Cited on p: 6.).
DOI: 10.1103/PhysRevD.74.072003.
arXiv: hep-ex/0606032.

[34] P. Adamson et al. "Measurement of Neutrino and Antineutrino Oscillations Using Beam and Atmospheric Data in MINOS". In: *Phys. Rev. Lett.* 110.25 (2013), p. 251801.
(Cited on p: 6.).
DOI: 10.1103/PhysRevLett.110.251801.
arXiv: 1304.6335 [hep-ex].

[35] K. Abe et al. "Measurement of Neutrino Oscillation Parameters from Muon Neutrino Disappearance with an Off-axis Beam". In: *Phys. Rev. Lett.* 111.21 (2013), p. 211803.
(Cited on p: 6.).
DOI: 10.1103/PhysRevLett.111.211803.
arXiv: 1308.0465 [hep-ex].

[36] K. Eguchi et al. "First results from KamLAND: Evidence for reactor anti-neutrino disappearance". In: *Phys. Rev. Lett.* 90 (2003), p. 021802.
(Cited on pp: 6, 18, 217, 235.).
DOI: 10.1103/PhysRevLett.90.021802.
arXiv: hep-ex/0212021.

[37] A. Gando et al. "Reactor On-Off Antineutrino Measurement with KamLAND". In: *Phys. Rev. D* 88.3 (2013), p. 033001.
(Cited on p: 6.).
DOI: 10.1103/PhysRevD.88.033001.
arXiv: 1303.4667 [hep-ex].

[38] Y. Abe et al. "Indication of Reactor $\bar{\nu}_e$ Disappearance in the Double Chooz Experiment". In: *Phys. Rev. Lett.* 108 (2012), p. 131801.
(Cited on pp: 6, 217, 235.).
DOI: 10.1103/PhysRevLett.108.131801.
arXiv: 1112.6353 [hep-ex].

[39] F. P. An et al. "Observation of electron-antineutrino disappearance at Daya Bay". In: *Phys. Rev. Lett.* 108 (2012), p. 171803.
(Cited on pp: 6, 217, 235.).
DOI: 10.1103/PhysRevLett.108.171803.
arXiv: 1203.1669 [hep-ex].

[40] J.K. Ahn et al. "Observation of Reactor Electron Antineutrino Disappearance in the RENO Experiment". In: *Phys. Rev. Lett.* 108 (2012), p. 191802.
(Cited on p: 6.).
DOI: 10.1103/PhysRevLett.108.191802.
arXiv: 1204.0626 [hep-ex].

[41] P.A. Zyla et al. "Review of Particle Physics". In: *PTEP* 2020.8 (2020), p. 083C01.
(Cited on p: 6.).
DOI: 10.1093/ptep/ptaa104.

[42] M. Lindner, T. Ohlsson, and G. Seidl. "Seesaw mechanisms for Dirac and Majorana neutrino masses". In: *Phys. Rev. D* 65.5 (2002).
(Cited on p: 6.).
DOI: 10.1103/physrevd.65.053014.

[43] S. M. Boucenna, S. Morisi, and J. W. F. Valle. "The Low-Scale Approach to Neutrino Masses". In: *Advances in High Energy Physics* 2014 (2014), p. 1.
(Cited on pp: 6, 20.).
DOI: 10.1155/2014/831598.

[44] E. Ma. *Neutrino Mass: Mechanisms and Models*. 2009.
(Cited on p: 6.).
arXiv: 0905.0221 [hep-ph].

[45] S. F King and C. Luhn. "Neutrino mass and mixing with discrete symmetry". In: *Rep. on Prog. in Phys.* 76.5 (2013).
(Cited on p: 6.).
DOI: 10.1088/0034-4885/76/5/056201.

[46] R. N. Mohapatra and J. W. F. Valle. "Neutrino Mass and Baryon number Nonconservation in Superstring Models". In: *Phys. Rev. D* 34 (1986).
(Cited on p: 6.).
DOI: 10.1103/PhysRevD.34.1642.

[47] C. Giunti and C. W. Kim. *Fundamentals of Neutrino Physics and Astrophysics*. Apr. 2007.
(Cited on pp: 7, 218, 219, 237.).

[48] S. Schael et al. "Precision electroweak measurements on the Z resonance". In: *Phys. Rept.* 427 (2006), p. 257.
(Cited on pp: 7, 218.).
DOI: 10.1016/j.physrep.2005.12.006.
arXiv: hep-ex/0509008.

[49] K. Zuber. *Neutrino physics*. Mar. 2004.
(Cited on pp: 7, 219, 237.).

[50] E. K. Akhmedov et al. "Series expansions for three cfflavor neutrino oscillation probabilities in matter". In: *JHEP* 2004.04 (2004).
(Cited on pp: 10, 12.).
DOI: 10.1088/1126-6708/2004/04/078.

[51] B. T. Cleveland et al. "Measurement of the solar electron neutrino flux with the Homestake chlorine detector". In: *Astrophys. J.* 496 (1998), p. 505.
(Cited on p: 12.).
DOI: 10.1086/305343.

[52] J. Coelho. "OscProb: The Oscillation Probability Calculator". In: *https://github.com/joaoabcoelho/OscProb/*. ().
(Cited on pp: 12, 78, 108.).

[53] A. M. Dziewonski and D. L. Anderson. "Preliminary reference Earth model." In: *Physics of the Earth and Planetary Interiors* 25 (1981), p. 297.
(Cited on pp: 12, 13, 78, 108.).
DOI: http://dx.doi.org/10.1016/0031-9201(81)90046-7.

[54] T. Araki et al. "Measurement of Neutrino Oscillation with KamLAND: Evidence of Spectral Distortion". In: *Phys. Rev. Lett.* 94.8 (2005).
(Cited on p: 18.).
DOI: 10.1103/physrevlett.94.081801.

[55] K. Abe et al. "Solar neutrino results in Super Kamiokande III". In: *Phys. Rev. D* 83.5 (2011).
(Cited on p: 18.).
DOI: 10.1103/physrevd.83.052010.

[56] A. M. Gago et al. "Global analysis of the post SNO solar neutrino data for standard and nonstandard oscillation mechanisms". In: *Phys. Rev. D* 65.7 (2002).
(Cited on p: 18.).
DOI: 10.1103/physrevd.65.073012.

[57] F. P. An et al. "Observation of Electron-Antineutrino Disappearance at Daya Bay". In: *Phys. Rev. Lett.* 108.17 (2012).
(Cited on p: 18.).
DOI: 10.1103/physrevlett.108.171803.

[58] J. K. Ahn et al. "Observation of Reactor Electron Antineutrinos Disappearance in the RENO Experiment". In: *Phys. Rev. Lett.* 108.19 (2012).
(Cited on p: 18.).
DOI: 10.1103/physrevlett.108.191802.

[59] Y. Abe et al. "Improved measurements of the neutrino mixing angle θ_{13} with the Double Chooz detector". In: *JHEP* 2014.10 (2014).
(Cited on p: 18.).
DOI: 10.1007/jhep10(2014)086.

[60] A. Albert et al. "Measuring the atmospheric neutrino oscillation parameters and constraining the 3+1 neutrino model with ten years of ANTARES data". In: *JHEP* 06 (2019), p. 113.
(Cited on pp: 18, 49, 106, 108, 110–112, 118, 119, 126, 129, 220, 238.).
DOI: 10.1007/JHEP06(2019)113.
arXiv: 1812.08650 [hep-ex].

[61] Y. Ashie et al. "Measurement of atmospheric neutrino oscillation parameters by Super-Kamiokande I". In: *Phys. Rev. D* 71.11 (2005).
(Cited on p: 18.).
DOI: 10.1103/physrevd.71.112005.

[62] M. G. Aartsen et al. "Measurement of Atmospheric Neutrino Oscillations at 6-56 GeV with IceCube DeepCore". In: *Phys. Rev. Lett.* 120.7 (2018).
(Cited on pp: 18, 111, 117.).
DOI: 10.1103/physrevlett.120.071801.

[63] P. Adamson et al. "Combined Analysis of $\nu_\mu \to \nu_\mu$ Disappearance and $\nu_\mu \to \nu_e$ Appearance in MINOS Using Accelerator and Atmospheric Neutrinos". In: *Phys. Rev. Lett.* 112.19 (2014).
(Cited on p: 18.).
DOI: 10.1103/physrevlett.112.191801.

[64] K. Abe et al. "Measurement of neutrino and antineutrino oscillations by the T2K experiment including a new additional sample of ν_e interactions at the far detector". In: *Phys. Rev. D* 96.9 (2017).
(Cited on p: 18.).
DOI: 10.1103/physrevd.96.092006.

[65] P. Adamson et al. "First Measurement of Electron Neutrino Appearance in NOvA". In: *Phys. Rev. Lett.* 116.15 (2016).
(Cited on p: 18.).
DOI: 10.1103/physrevlett.116.151806.

[66] S. Adrian-Martinez et al. "Letter of intent for KM3NeT 2.0". In: *J. Phys.* G43.8 (2016).
(Cited on pp: 18, 46, 49, 53, 92, 186, 222, 240.).
DOI: 10.1088/0954-3899/43/8/084001.
arXiv: 1601.07459 [astro-ph.IM].

[67] The IceCube-PINGU Collaboration. *Letter of Intent: The Precision IceCube Next Generation Upgrade (PINGU)*. 2014.
(Cited on p: 18.).
arXiv: 1401.2046 [physics.ins-det].

[68] K. Abe et al. *Letter of Intent: The Hyper-Kamiokande Experiment Detector Design and Physics Potential*. 2011.
(Cited on p: 18.).
arXiv: 1109.3262 [hep-ex].

[69] K. Abe et al. *Constraint on the Matter-Antimatter Symmetry-Violating Phase in Neutrino Oscillations*. 2019.
(Cited on p: 18.).
arXiv: 1910.03887 [hep-ex].

[70] A. V. Akindinov et al. "Letter of interest for a neutrino beam from Protvino to KM3NeT/ORCA". In: *The European Physical Journal C* 79.9 (2019).
(Cited on pp: 18, 233, 250.).
DOI: 10.1140/epjc/s10052-019-7259-5.

[71] DUNE Collaboration et al. *Long-Baseline Neutrino Facility (LBNF) and Deep Underground Neutrino Experiment (DUNE) CDR vol2: The Physics Program for DUNE*

at LBNF. 2015.
(Cited on p: 18.).
arXiv: 1512.06148 [physics.ins-det].

[72] K. Abe et al. "Physics potential of a long-baseline neutrino oscillation experiment using a JPARC neutrino beam and Hyper Kamiokande". In: *Prog. of Theo. and Exp. Phys.* 2015.5 (2015).
(Cited on p: 18.).
DOI: 10.1093/ptep/ptv061.

[73] I. Esteban et al. "The fate of hints: updated global analysis of three-flavor neutrino oscillations". In: *Journal of High Energy Physics* 2020.9 (2020).
(Cited on p: 19.).
DOI: 10.1007/jhep09(2020)178.

[74] J. Heeck et al. "Non-Standard neutrino interactions and neutral gauge bosons". In: *SciPost Physics* 6.3 (2019).
(Cited on p: 20.).
DOI: 10.21468/scipostphys.6.3.038.

[75] O. G. Miranda and H. Nunokawa. "Non standard neutrino interactions: current status and future prospects". In: *New J. Phys.* 17.9 (2015).
(Cited on pp: 20, 22, 24.).
DOI: 10.1088/1367-2630/17/9/095002.
arXiv: 1505.06254 [hep-ph].

[76] T. Ohlsson. "Status of non-standard neutrino interactions". In: *Rept. Prog. Phys.* (2013).
(Cited on pp: 20, 24, 106, 108, 198.).
DOI: 10.1088/0034-4885/76/4/044201.
arXiv: 1209.2710 [hep-ph].

[77] D. V. Forero et al. "Lepton flavor violation and non-unitary lepton mixing in low-scale type-I seesaw". In: *JHEP* 2011.9 (2011).
(Cited on p: 20.).
DOI: 10.1007/jhep09(2011)142.

[78] K.S. Babu et al. "Non-Standard Interactions in Radiative Neutrino Mass Models". In: *JHEP* 03 (2020), p. 006.
(Cited on p: 20.).
DOI: 10.1007/JHEP03(2020)006.
arXiv: 1907.09498 [hep-ph].

[79] R. Barbier et al. "R-Parity-violating supersymmetry". In: *Physics Reports* 420.1-6 (2005), p. 1.
(Cited on p: 20.).
DOI: 10.1016/j.physrep.2005.08.006.

[80] Y. Farzan and M. Tortola. "Neutrino oscillations and Non-Standard Interactions". In: *Front.in Phys.* 6 (2018), p. 10.
(Cited on p: 22.).
DOI: 10.3389/fphy.2018.00010.
arXiv: 1710.09360 [hep-ph].

[81] Z. Maki, M. Nakagawa, and S. Sakata. "Remarks on the Unified Model of Elementary Particles". In: *Prog. of Theo. Phys.* 28.5 (Nov. 1962), p. 870.
(Cited on pp: 22, 106.).
DOI: 10.1143/PTP.28.870.

[82] J. W. F. Valle. "Resonant Oscillations of Massless Neutrinos in Matter". In: *Phys. Lett. B* 199 (1987), p. 432.
(Cited on p: 22.).
DOI: 10.1016/0370-2693(87)90947-6.

[83] M. M. Guzzo, A. Masiero, and S. T. Petcov. "On the MSW effect with massless neutrinos and no mixing in the vacuum". In: *Phys. Lett. B* 260 (1991), p. 154.
(Cited on p: 22.).
DOI: 10.1016/0370-2693(91)90984-X.

[84] M. C. Gonzalez-Garcia et al. "NewCPviolation in neutrino oscillations". In: *Phys. Rev. D* 64.9 (2001).
(Cited on p: 22.).
DOI: 10.1103/physrevd.64.096006.

[85] E. K. Akhmedov. "Neutrino physics," in: *in Proceedings, Summer School in Particle Physics: Trieste, Italy, p. 103.* (1999).
(Cited on p: 22.).

[86] J. Liao, D. Marfatia, and K. Whisnant. "Degeneracies in long-baseline neutrino experiments from nonstandard interactions". In: *Phys. Rev. D* 93 (2016).
(Cited on p: 22.).
DOI: 10.1103/PhysRevD.93.093016.

[87] D. Meloni, T. Ohlsson, and H. Zhang. "Exact and approximate formulas for neutrino mixing and oscillations with non-standard interactions". In: *JHEP* 2009.04 (2009), p. 033.
(Cited on p: 23.).
DOI: 10.1088/1126-6708/2009/04/033.

[88] M. Blennow and T. Ohlsson. "Approximative two-flavor framework for neutrino oscillations with nonstandard interactions". In: *Phys. Rev. D* 78.9 (2008).
(Cited on p: 23.).
DOI: 10.1103/physrevd.78.093002.

[89] M. C. Gonzalez-Garcia et al. "Atmospheric Neutrino Observations and Flavor Changing Interactions". In: *Phys. Rev. Lett.* 82.16 (1999).
(Cited on p: 24.).
DOI: 10.1103/physrevlett.82.3202.

[90] I. Esteban et al. "Global analysis of three-flavour neutrino oscillations: synergies and tensions in the determination of θ_{23}, δ_{CP}, and the mass ordering". In: *Journal of High Energy Physics* 2019.1 (2019).
(Cited on pp: 25, 26, 115–117, 131, 132, 142, 152, 201, 202, 205–207, 226, 243.).
DOI: 10.1007/jhep01(2019)106.

[91] S. K. Agarwalla et al. "Constraints on flavor-diagonal non-standard neutrino interactions from Borexino Phase-II". In: *JHEP* 2 (2020).
(Cited on p: 33.).
DOI: 10.1007/jhep02(2020)038.

[92] G. Mitsuka et al. "Study of nonstandard neutrino interactions with atmospheric neutrino data in Super-Kamiokande I and II". In: *Phys. Rev. D* (2011).
(Cited on pp: 33, 34.).
DOI: 10.1103/physrevd.84.113008.

[93] M. G. Aartsen et al. "Search for Nonstandard Neutrino Interactions with IceCube DeepCore". In: *Phys. Rev.* (2018).
(Cited on pp: 33, 34, 119, 127, 128, 182.).
DOI: 10.1103/PhysRevD.97.072009.

[94] P. Adamson et al. "Search for flavor-changing non-standard neutrino interactions by MINOS". In: *Phys. Rev. D* (2013).
(Cited on pp: 33, 34.).
DOI: 10.1103/physrevd.88.072011.

[95] F. J. Escrihuela et al. "Global constraints on muon-neutrino nonstandard interactions". In: *Phys. Rev. D* 83.9 (2011).
(Cited on p: 33.).
DOI: 10.1103/physrevd.83.093002.

[96] F.J. Escrihuela et al. "Constraining nonstandard neutrino-quark interactions with solar, reactor and accelerator data". In: *Phys. Rev. D* 80 (2009). [Erratum: Phys.Rev.D 80, 129908 (2009)].
(Cited on p: 33.).
DOI: 10.1103/PhysRevD.80.129908.
arXiv: 0907.2630 [hep-ph].

[97] I. Esteban et al. "Updated constraints on non-standard interactions from global analysis of oscillation data". In: *JHEP* (2018).
(Cited on p: 33.).
DOI: 10.1007/jhep08(2018)180.

[98] M. C. Gonzalez-Garcia and M. Maltoni. "Determination of matter potential from global analysis of neutrino oscillation data". In: *JHEP* 2013.9 (2013).
(Cited on p: 34.).
DOI: 10.1007/jhep09(2013)152.

[99] A. Esmaili and A. Y. Smirnov. "Probing non-standard interaction of neutrinos with IceCube and DeepCore". In: *JHEP* (2013).
(Cited on p: 34.).
DOI: 10.1007/jhep06(2013)026.

[100] J. Salvado et al. "Non-standard interactions with high-energy atmospheric neutrinos at IceCube". In: *Journal of High Energy Physics* 2017.1 (2017).
(Cited on p: 34.).
DOI: 10.1007/jhep01(2017)141.

[101] M. Tanabashi et al. "Review of Particle Physics". In: *Phys. Rev. D* 98.3 (2018), p. 030001.
(Cited on p: 36.).
DOI: 10.1103/PhysRevD.98.030001.

[102] J. P. Yañez and A. Kouchner. "Measurement of atmospheric neutrino oscillations with very large volume neutrino telescopes". In: *Adv. High Energy Phys.* 2015

(2015), p. 271968.
(Cited on p: 36.).
DOI: 10.1155/2015/271968.
arXiv: 1509.08404 [hep-ex].

[103] M. Honda et al. "Atmospheric neutrino flux calculation using the NRLMSISE-00 atmospheric model". In: *Phys. Rev. D* 92.2 (2015).
(Cited on pp: 37, 67, 75, 77, 78, 81, 117.).
DOI: 10.1103/PhysRevD.92.023004.
arXiv: 1502.03916 [astro-ph.HE].

[104] G. D. Barr et al. "Uncertainties in atmospheric neutrino fluxes". In: *Phys. Rev. D* 74.9 (2006).
(Cited on pp: 37, 117.).
DOI: 10.1103/physrevd.74.094009.

[105] A. Trovato. "Development of reconstruction algorithms for large volume neutrino telescopes and their application to the KM3NeT detector". PhD thesis. Catania U., SSC, 2014.
(Cited on p: 37.).

[106] F. Halzen and Alan D. Martin. *QUARKS AND LEPTONS: AN INTRODUCTORY COURSE IN MODERN PARTICLE PHYSICS*. Jan. 1984. ISBN: 978-0-471-88741-6.
(Cited on pp: 38, 39.).

[107] K. McFarland. *Neutrino Interactions*. 2008.
(Cited on pp: 38, 39.).
arXiv: 0804.3899 [hep-ex].

[108] Kevin McFarland. *Neutrino Interactions*. 2008.
(Cited on p: 38.).
arXiv: 0804.3899 [hep-ex].

[109] J. A. Formaggio and G. P. Zeller. "From eV to EeV: Neutrino cross sections across energy scales". In: *Reviews of Modern Physics* 84.3 (2012), p. 13071.
(Cited on p: 38.).
DOI: 10.1103/revmodphys.84.1307.

[110] D. Casper. "The nuance neutrino physics simulation, and the future". In: *Nuclear Physics B - Proceedings Supplements* 112.1-3 (2002), p. 161.
(Cited on p: 40.).
DOI: 10.1016/s0920-5632(02)01756-5.

[111] *Fundamental Physics at the Intensity Frontier*. May 2012.
(Cited on pp: 40, 41.).
DOI: 10.2172/1042577.
arXiv: 1205.2671 [hep-ex].

[112] S. Kretzer and M. H. Reno. "Tau neutrino deep inelastic charged current interactions". In: *Physical Review D* 66.11 (2002).
(Cited on p: 40.).
DOI: 10.1103/physrevd.66.113007.

[113] P. Cerenkov. "Visible radiation produced by electrons moving in a medium with velocities exceeding that of light". In: *Phys. Rev.* 52 (1937), pp. 378–379.
(Cited on p: 41.).
DOI: 10.1103/PhysRev.52.378.

[114] T. Gluesenkamp. "On the Detection of Subrelativistic Magnetic Monopoles with the IceCube Neutrino Observatory". PhD thesis. 2010.
(Cited on p: 42.).

[115] W. Lohmann et al. "Energy Loss of Muons in the Energy Range 1-GeV to 10000-GeV". In: (1985).
(Cited on p: 43.).

[116] K. Mitsui. "Muon energy-loss distribution and its applications to muon energy determination". In: *Physical Review D* 45.9 (1992), pp. 3051–3060.
(Cited on p: 43.).
DOI: 10.1103/PhysRevD.45.3051.

[117] K. A. Olive. "Review of Particle Physics". In: *Chin. Phys. C* 40.10 (2016).
(Cited on pp: 43, 73.).
DOI: 10.1088/1674-1137/40/10/100001.

[118] C. H Wiebusch. "The Detection of Faint Light in Deep Underwater Neutrino Telescopes." PhD thesis. 1995.
(Cited on p: 43.).

[119] J. Brunner. "Cherenkov light from HE elctromagnetic and hadronic showers". In: *ANTARES internal note, ANTARES-Soft/2012-015* (2012).
(Cited on p: 43.).

[120] J. Hofestadt. "Measuring Neutrino Mass Hierarchy with the Future KM3NeT-ORCA Detector." PhD thesis. ECAP, University of Erlangen Nurenberg, 2017.
(Cited on pp: 43, 97, 98, 185.).

[121] G Riccobene et al. "Deep seawater inherent optical properties in the Southern Ionian Sea". In: *Astroparticle Physics* 27.1 (2007), p. 1.
(Cited on pp: 44, 117.).
DOI: 10.1016/j.astropartphys.2006.08.006.

[122] J.A. Aguilar et al. "Transmission of light in deep sea water at the site of the Antares neutrino telescope". In: *Astropart. Phys.* 23.1 (2005), p. 131.
(Cited on pp: 44, 69, 117.).
DOI: 10.1016/j.astropartphys.2004.11.006.

[123] C. W. james. "Ice and water optical properties". In: *ANTARES internal note, ANTARES-Soft/2012-015* (2012).
(Cited on p: 44.).

[124] Christian Tamburini et al. "Deep-Sea Bioluminescence Blooms after Dense Water Formation at the Ocean Surface". In: *PLOS ONE* 8.7 (July 2013), p. 1.
(Cited on p: 45.).
DOI: 10.1371/journal.pone.0067523.

[125] T. Chiarusi and M. Spurio. "High-energy astrophysics with neutrino telescopes". In: *The European Physical Journal C* 65.3-4 (2010), 649–701. ISSN: 1434-6052.
(Cited on p: 46.).
DOI: 10.1140/epjc/s10052-009-1230-9.
URL: http://dx.doi.org/10.1140/epjc/s10052-009-1230-9.

[126] M.A. Markov. "On high energy neutrino physics". In: *10th International Conference on High Energy Physics*. 1960, pp. 578–581.
(Cited on pp: 46, 221, 239.).

[127] A. Roberts. "The birth of high-energy neutrino astronomy: A personal history of the DUMAND project". In: *Rev. Mod. Phys.* 64 (1 1992), p. 259.
(Cited on p: 46.).
DOI: 10.1103/RevModPhys.64.259.

[128] I.A. Belolaptikov et al. "The Baikal underwater neutrino telescope: Design, performance and first results". In: *Astropart. Phys.* 7 (1997), pp. 263–282.
(Cited on p: 46.).
DOI: 10.1016/S0927-6505(97)00022-4.

[129] E. Andres et al. "The AMANDA neutrino telescope: Principle of operation and first results". In: *Astropart. Phys.* 13 (2000), pp. 1–20.
(Cited on p: 46.).
DOI: 10.1016/S0927-6505(99)00092-4.
arXiv: astro-ph/9906203.

[130] J. A. Aguilar et al. "ANTARES: the first undersea neutrino telescope". In: *Nucl. Inst. and Methods in Physics Research, A 656 (2011) pp. 11-38* (2011).
(Cited on pp: 46–48, 186, 221, 222, 239, 240.).
arXiv: 1104.1607v1.

[131] M.G. Aartsen et al. "The IceCube Neutrino Observatory: Instrumentation and Online Systems". In: *JINST* 12.03 (2017), P03012.
(Cited on p: 46.).
DOI: 10.1088/1748-0221/12/03/P03012.
arXiv: 1612.05093 [astro-ph.IM].

[132] A.D. Avrorin et al. "Baikal-GVD: Results, status and plans". In: *EPJ Web Conf.* 116 (2016). Ed. by A. Capone et al., p. 11005.
(Cited on p: 46.).
DOI: 10.1051/epjconf/201611611005.

[133] *Photomultiplier tube, R12199*.
(Cited on p: 47.).
URL: https://www.hamamatsu.com/eu/en/product/type/R12199/index.html.

[134] J. A. Aguilar et al. "The data acquisition system for the ANTARES Neutrino Telescope". In: *Nucl. Instrum. Meth. A* 570 (2007), p. 107.
(Cited on pp: 48, 70.).
DOI: 10.1016/j.nima.2006.09.098.
arXiv: astro-ph/0610029.

[135] M. de Jong. "The ANTARES trigger software." In: *ANTARES internal note, ANTARES-Soft/2005-005* (2005).
(Cited on pp: 48, 49.).

[136] A. Albert et al. "ANTARES and IceCube Combined Search for Neutrino Point-like and Extended Sources in the Southern Sky". In: *Astrophys. J.* 892 (2020), p. 92.
(Cited on p: 49.).
DOI: 10.3847/1538-4357/ab7afb.
arXiv: 2001.04412 [astro-ph.HE].

[137] H.A. Ayala Solares et al. "A Search for Cosmic Neutrino and Gamma-Ray Emitting Transients in 7.3 Years of ANTARES and Fermi LAT Data". In: *Astrophys. J.* 886 (2019), p. 98.
(Cited on p: 49.).
DOI: 10.3847/1538-4357/ab4a74.
arXiv: 1904.06420 [astro-ph.HE].

[138] A. Albert et al. "All-flavor Search for a Diffuse Flux of Cosmic Neutrinos with Nine Years of ANTARES Data". In: *The Astrophysical Journal* (2018), p. L7.
(Cited on p: 49.).
DOI: 10.3847/2041-8213/aaa4f6.
URL: http://dx.doi.org/10.3847/2041-8213/aaa4f6.

[139] A. Albert et al. "Search for high-energy neutrinos from bright GRBs with ANTARES". In: *Mon. Not. Roy. Astron. Soc.* 469 (2017), p. 906.
(Cited on p: 49.).
DOI: 10.1093/mnras/stx902.
arXiv: 1612.08589 [astro-ph.HE].

[140] A. Albert et al. "Search for dark matter towards the Galactic Centre with 11 years of ANTARES data". In: *Phys. Lett. B* 805 (2020).
(Cited on p: 49.).
DOI: 10.1016/j.physletb.2020.135439.
arXiv: 1912.05296 [astro-ph.HE].

[141] S. Aiello et al. "Characterisation of the Hamamatsu photomultipliers for the KM3NeT Neutrino Telescope". In: *JINST* 13.05 (2018), P05035.
(Cited on p: 51.).
DOI: 10.1088/1748-0221/13/05/P05035.

[142] Annarita Margiotta. "The KM3NeT deep-sea neutrino telescope". In: *Nuclear Instruments and Methods in Physics Research Section A: Accelerators, Spectrometers, Detectors and Associated Equipment* (2014).
(Cited on pp: 52, 53.).
DOI: 10.1016/j.nima.2014.05.090.
URL: http://dx.doi.org/10.1016/j.nima.2014.05.090.

[143] C. Pellegrino and T. Chiarusi. "The Trigger and Data Acquisition System for the KM3NeT neutrino telescope". In: *EPJ Web Conf.* 116 (2016). Ed. by A. Capone et al., p. 05005.
(Cited on pp: 53, 86, 92.).
DOI: 10.1051/epjconf/201611605005.

[144] M. de Jong. "The TriggerEfficiency program". In: *ANTARES internal note, ANTARES-Soft/2009-001* (2009).
(Cited on pp: 53, 69.).

[145] S. Viola et al. "Acoustic positioning system for KM3NeT". In: *PoS* ICRC2015 (2016), p. 1169.
(Cited on p: 54.).
DOI: 10.22323/1.236.1169.

[146] S. Adrian-Martinez et al. "The Positioning System of the ANTARES Neutrino Telescope". In: *JINST* 7 (2012), T08002.
(Cited on p: 54.).
DOI: 10.1088/1748-0221/7/08/T08002.
arXiv: 1202.3894 [astro-ph.IM].

[147] J.A. Aguilar et al. "A fast algorithm for muon track reconstruction and its application to the ANTARES neutrino telescope". In: *Astropart. Phys.* 34.9 (2011), p. 652.
(Cited on pp: 54, 55, 73.).
DOI: 10.1016/j.astropartphys.2011.01.003.

[148] I. Di Palma. "KM3NeT Time Calibration". In: *EPJ Web Conf.* 207 (2019). Ed. by C. Spiering, p. 07001.
(Cited on pp: 54, 55.).
DOI: 10.1051/epjconf/201920707001.

[149] J. P. G. Gonzalez. "Time calibration and search for cosmic sources of high enrgy neutrino with the ANTARES neutrino telescope". In: *Ph.D. Thesis, IFIC, University of Valencia* (2013).
(Cited on p: 55.).

[150] A. S. Losa. "Search for high energy cosmic muon neutrinos from variable gamma-ray sources and time calibration of the optical modules of the ANTARES telescope". In: *Ph.D. Thesis, IFIC, University of Valencia* (2015).
(Cited on p: 55.).

[151] C. Tonnis. "Indirect search for dark matter in the Sun and the Galactic Centre with the ANTARES neutrino telescope". In: *Ph.D. Thesis, IFIC, University of Valencia* (2017).
(Cited on p: 55.).

[152] J. B. Marti. "Search for cosmic sources in neutrino telescopes and time calibration in the ANTARES neutrino telescope". In: *Ph.D. Thesis, IFIC, University of Valencia* (2018).
(Cited on p: 55.).

[153] G. Illuminati. "Searches for cosmic neutrino sources with ANTARES, KM3NeT and IceCube and time calibration of ANTARES". In: *Ph.D. Thesis, IFIC, University of Valencia* (2017).
(Cited on p: 55.).

[154] K. Melis. "In-Situ Calibration of KM3NeT". In: vol. 301. 2017, p. 1059.
(Cited on pp: 55–57.).
DOI: 10.22323/1.301.1059.

[155] K. Melis, A. Heijboer, and M. de Jong. "KM3NeT/ARCA Event Reconstruction Algorithms". In: *PoS* ICRC2017 (2018), p. 950.
(Cited on pp: 55, 92, 97.).
DOI: 10.22323/1.301.0950.

[156] Khan Chowdhury N. R. et al. "Time calibration with atmospheric muons at KM3NeT-ORCA". In: *https://indico.cern.ch/event/697740/contributions/2996315/attachments/1645015/2628787/2018-05-07_Granada.pdf* ().
(Cited on pp: 55, 63.).

[157] L. A. Fusco and A. Margiotta. "The Run-by-Run Monte Carlo simulation for the ANTARES experiment". In: *EPJ Web Conf.* 116 (2016).
(Cited on p: 66.).
DOI: 10.1051/epjconf/201611602002.

[158] D. Bailey. "Monte Carlo tools and analysis methods for understanding the ANTARES experiment and predicting its sensitivity to dark matter". PhD thesis. Oxford University, 2002.
(Cited on pp: 67, 68.).

[159] J. Pumplin et al. "New Generation of Parton Distributions with Uncertainties from Global QCD Analysis". In: *JHEP* 2002.07 (2002), p. 12.
(Cited on p: 67.).
DOI: 10.1088/1126-6708/2002/07/012.

[160] J. Brunner. "Updated tag list for the new antares event format." In: *ANTARES internal note, ANTARES-Soft/1993-003* (1999).
(Cited on p: 69.).

[161] D. Heck et al. "CORSIKA: A Monte Carlo code to simulate extensive air showers". In: *FZKA-6019* (Feb. 1998).
(Cited on p: 69.).

[162] S. Agostinelli et al. "GEANT4: A Simulation toolkit". In: *Nucl. Instrum. Meth. A* 506 (2003), p. 250.
(Cited on p: 69.).
DOI: 10.1016/S0168-9002(03)01368-8.

[163] S. Navas and L. Thompson. "Km3 user guide and reference manual". In: *KM3NeT internal note, KM3NeT-SIM/2015-001* (2015).
(Cited on pp: 69, 86.).

[164] G. Carminati et al. "Atmospheric MUons from PArametric formulas: A Fast GEnerator for neutrino telescopes (MUPAGE)". In: *Comput. Phys. Commun.* 179 (2008), p. 915.
(Cited on pp: 69, 86.).
DOI: 10.1016/j.cpc.2008.07.014.
arXiv: 0802.0562 [physics.ins-det].

[165] P. Antonioli et al. "A three-dimensional code for muon propagation through the rock: MUSIC". In: *Astropart. Phys.* 7.4 (1997), p. 357.
(Cited on p: 69.).
DOI: 10.1016/s0927-6505(97)00035-2.

[166] B. Bakker. "Trigger studies for the Antares and KM3NeT neutrino telescopes". In: *Master's Thesis, University of Amsterdam* (2011).
(Cited on p: 69.).

[167] P. Amram et al. "The ANTARES optical module". In: *Nucl. Instrum. Meth.* A484 (2002), p. 369.
(Cited on pp: 70, 117.).
DOI: 10.1016/S0168-9002(01)02026-5.
arXiv: astro-ph/0112172 [astro-ph].

[168] J.A. Aguilar et al. "A fast algorithm for muon track reconstruction and its application to the ANTARES neutrino telescope". In: *Astropart. Phys.* 34 (2011), p. 652.
(Cited on pp: 70, 71.).
DOI: 10.1016/j.astropartphys.2011.01.003.
arXiv: 1105.4116 [astro-ph.IM].

[169] S. Adrián-Martínez et al. "Searches for point-like and extended neutrino sources close to the galactic center using the ANTARES neutrino telescope". In: *The Astrophys. J* 786.1 (2014).
(Cited on p: 71.).
DOI: 10.1088/2041-8205/786/1/l5.

[170] A. J. Heijboer. "Track Reconstruction and Point Source Searches with ANTARES". In: *PhD thesis, NIKHEF, Amsterdam* (2004).
(Cited on pp: 71–73, 97.).
URL: http://www.nikhef.nl/pub/services/newbiblio/theses.php..

[171] E. Visser. "Neutrinos from the Milky Way". In: *Ph.D. Thesis, Universiteit Leiden* (2015).
(Cited on p: 71.).

[172] The ANTARES Collaboration. *Cont. 33st Int. Cos. Ray Conf.* 2013.
(Cited on p: 74.).
arXiv: 1312.4308 [astro-ph.HE].

[173] S. Aiello et al. "gSeaGen: The KM3NeT GENIE-based code for neutrino telescopes". In: *Computer Physics Communications* 256 (2020), p. 107477.
(Cited on pp: 81, 86.).
DOI: 10.1016/j.cpc.2020.107477.

[174] C. Andreopoulos et al. "The GENIE neutrino Monte Carlo generator". In: *Nuclear Instruments and Methods in Physics Research Section A: Accelerators, Spectrometers, Detectors and Associated Equipment* 614.1 (2010), 87–104.
(Cited on pp: 81, 117.).
DOI: 10.1016/j.nima.2009.12.009.

[175] M. Ageron et al. "Dependence of atmospheric muon flux on seawater depth measured with the first KM3NeT detection units". In: *The European Physical Journal C* 80.2 (2020).
(Cited on p: 86.).
DOI: 10.1140/epjc/s10052-020-7629-z.

[176] A. Albert et al. "An algorithm for the reconstruction of high-energy neutrino-induced particle showers and its application to the ANTARES neutrino telescope". In: *The European Physical Journal C* 77.6 (2017).
(Cited on p: 97.).
DOI: 10.1140/epjc/s10052-017-4979-2.

[177] F. Folger. "Search for diffuse cosmic neutrino flux using shower events in the ANTARES Neutrino Telescope." PhD thesis. ECAP, University of Erlangen Nurenberg, 2014.
(Cited on p: 97.).

[178] F. Folger. "The Dusj shower reconstrcution project". In: *ANTARES internal note, ANTARES-PHYS-2013-003* (2013).
(Cited on p: 97.).

[179] S. Adrián-Martínez et al. "Intrinsic limits on resolutions in muon- and electron-neutrino charged-current events in the KM3NeT/ORCA detector". In: *Journal of High Energy Physics* 2017.5 (2017).
(Cited on pp: 97, 98, 151, 226.).
DOI: 10.1007/jhep05(2017)008.

[180] L. Quinn. "Determining the Neutrino Mass Hierarchy with KM3NeT-ORCA". In: *Ph.D. Thesis, CPPM, Aix-Marseille University* (2018).
(Cited on pp: 97–99, 185.).

[181] S. Bourret. *C++ framework for neutrino oscillation analyses*. https://git.km3net.de/sbourret/Swim.
(Cited on p: 99.).

[182] S. Bourret. "Neutrino Oscillations and Earth Tomography with KMK3NeT-ORCA". In: *Ph.D. Thesis, Université Sorbonne Paris Cité* (2018).
(Cited on pp: 99, 185.).

[183] L. Breiman. "Random Forests". In: *Machine Learning* 45.1 (2001), pp. 5–32.
(Cited on p: 101.).
DOI: 10.1023/A:1010933404324.

[184] S. Hallmann. "Sensitivity to atmospheric tau-neutrino appearance and all-flavour search for neutrinos from the Fermi Bubbles with the deep-sea telescopes KM3NeT/ORCA and ANTARES". PhD thesis. FAU Erlangen-Nuremberg, 2020.
(Cited on p: 101.).

[185] R. Brun and F. Rademakers. "ROOT: An object oriented data analysis framework". In: *Nucl. Instrum. Meth. A* 389 (1997). Ed. by M. Werlen and D. Perret-Gallix, p. 81.
(Cited on p: 101.).
DOI: 10.1016/S0168-9002(97)00048-X.

[186] I. Salvadori. "Study of atmospheric neutrino oscillations with the ANTARES neutrino telescope". In: *Ph.D. Thesis, CPPM, Aix-Marseille University* (2018).
(Cited on pp: 106, 109, 118.).

[187] G. Cowan et al. "Asymptotic formulae for likelihood–based tests of new physics". In: *The European Physical Journal C* 71.2 (2011).
(Cited on pp: 106, 116, 152, 191, 201, 208.).
DOI: 10.1140/epjc/s10052-011-1554-0.

[188] M. C. Gonzalez-Garcia and M. Maltoni. "Determination of matter potential from global analysis of neutrino oscillation data". In: *Journal of High Energy Physics* 2013.9 (2013).
(Cited on p: 106.).
DOI: 10.1007/jhep09(2013)152.

[189] T. Kikuchi, H. Minakata, and S. Uchinami. "Perturbation theory of neutrino oscillation with nonstandard neutrino interactions". In: *Journal of High Energy Physics* 2009.03 (2009), p. 114.
(Cited on p: 107.).
DOI: 10.1088/1126-6708/2009/03/114.

[190] N. Cipriano Ribeiro et al. "Probing non-standard neutrino interactions with neutrino factories". In: *Journal of High Energy Physics* 2007.12 (2007), p. 002.
(Cited on p: 107.).
DOI: 10.1088/1126-6708/2007/12/002.

[191] J. Kopp et al. "Nonstandard neutrino interactions in reactor and superbeam experiments". In: *Physical Review D* 77.1 (2008).
(Cited on p: 107.).
DOI: 10.1103/physrevd.77.013007.

[192] G. Mitsuka et al. "Study of Non-Standard Neutrino Interactions with Atmospheric Neutrino Data in Super-Kamiokande I and II". In: *Phys. Rev.* D84 (2011).
(Cited on pp: 107, 125, 127, 128, 181, 182, 228, 229, 245, 246.).
DOI: 10.1103/PhysRevD.84.113008.
arXiv: 1109.1889 [hep-ex].

[193] A. Habig. "MINOS neutrino oscillation results". In: *Mod. Phys. Lett.* A25 (2010).
(Cited on p: 111.).
DOI: 10.1142/S0217732310033232.
arXiv: 1004.2647 [hep-ex].

[194] M. A. Acero et al. "First Measurement of Neutrino Oscillation Parameters using Neutrinos and Antineutrinos by NOvA". In: *Phys. Rev. Lett.* 123.15 (2019).
(Cited on p: 111.).
DOI: 10.1103/PhysRevLett.123.151803.
arXiv: 1906.04907 [hep-ex].

[195] Y. Ashie et al. "A Measurement of atmospheric neutrino oscillation parameters by SUPER-KAMIOKANDE I". In: *Phys. Rev.* D71 (2005).
(Cited on p: 111.).
DOI: 10.1103/PhysRevD.71.112005.
arXiv: hep-ex/0501064 [hep-ex].

[196] N. Reid and D. A. S. Fraser. *Likelihood inference in the presence of nuisance parameters*. 2003.
(Cited on pp: 113, 224, 242.).
arXiv: physics/0312079 [physics.data-an].

[197] J. Neyman. "Outline of a Theory of Statistical Estimation Based on the Classical Theory of Probability". In: *Phil. Trans. Roy. Soc. Lond. A* 236.767 (1937), p. 333.
(Cited on p: 113.).
DOI: 10.1098/rsta.1937.0005.

[198] C. J. Clopper and E. S. Pearson. "The use of confidence or fiducial limits illustrated in the case of the Binomial". In: *Biometrika* 26.4 (Dec. 1934), p. 404.
(Cited on p: 113.).
DOI: 10.1093/biomet/26.4.404.

[199] S. Baker and R. D. Cousins. "Clarification of the Use of Chi Square and Likelihood Functions in Fits to Histograms". In: *Nucl. Instrum. Meth.* 221 (1984), p. 437.
(Cited on p: 113.).
DOI: 10.1016/0167-5087(84)90016-4.

[200] S. S. Wilks. "The Large-Sample Distribution of the Likelihood Ratio for Testing Composite Hypotheses". In: *Annals Math. Statist.* 9.1 (1938), p. 60.
(Cited on pp: 113, 122.).
DOI: 10.1214/aoms/1177732360.

[201] F. James and M. Roos. "Minuit: A System for Function Minimization and Analysis of the Parameter Errors and Correlations". In: *Comput. Phys. Commun.* 10 (1975), p. 343.
(Cited on p: 116.).
DOI: 10.1016/0010-4655(75)90039-9.

[202] C. Distefano. "gSeaGen: a GENIE-based code for neutrino telescopes". In: *EPJ Web Conf.* 116 (2016).
(Cited on p: 117.).
DOI: 10.1051/epjconf/201611608001.
arXiv: 1602.00501 [astro-ph.IM].

[203] J. A. Aguilar et al. "Transmission of light in deep sea water at the site of the ANTARES Neutrino Telescope". In: *Astropart. Phys.* 23 (2005), p. 131.
(Cited on p: 117.).
DOI: 10.1016/j.astropartphys.2004.11.006.
arXiv: astro-ph/0412126.

[204] A. Albert et al. "Long-term monitoring of the ANTARES optical module efficiencies using ^{40}K decays in sea water". In: *Eur. Phys. J. C* 78.8 (2018), p. 669.
(Cited on p: 117.).
DOI: 10.1140/epjc/s10052-018-6132-2.
arXiv: 1805.08675 [astro-ph.IM].

[205] M. G. Aartsen et al. "Determining neutrino oscillation parameters from atmospheric muon neutrino disappearance with three years of IceCube DeepCore data". In: *Phys. Rev.* D91.7 (2015).
(Cited on p: 118.).
DOI: 10.1103/PhysRevD.91.072004.
arXiv: 1410.7227 [hep-ex].

[206] G. J. Feldman and R. D. Cousins. "Unified approach to the classical statistical analysis of small signals". In: *Phys. Rev. D* 57 (7 1998).
(Cited on p: 123.).
DOI: 10.1103/PhysRevD.57.3873.

[207] G. D. Barr et al. "Uncertainties in atmospheric neutrino fluxes". In: *Phys. Rev. D* 74 (2006).
(Cited on pp: 146, 226, 243.).
DOI: 10.1103/PhysRevD.74.094009.

[208] R. Gandhi et al. "Mass Hierarchy Determination via future Atmospheric Neutrino Detectors". In: *Phys. Rev.* D76 (2007).
(Cited on p: 152.).
DOI: 10.1103/PhysRevD.76.073012.
arXiv: 0707.1723 [hep-ph].

[209] A. Ghosh, T. Thakore, and S. Choubey. "Determining the Neutrino Mass Hierarchy with INO, T2K, NOvA and Reactor Experiments". In: *JHEP* 04 (2013), p. 9.
(Cited on p: 152.).
DOI: 10.1007/JHEP04(2013)009.
arXiv: 1212.1305 [hep-ph].

[210] M. H. G. Jongen. "Neutrino Physics in the Mediterranean sea." PhD thesis. Nikhef, University of Amsterdam, 2018.
(Cited on p: 185.).

[211] A. Kumar et al. "Invited review: Physics potential of the ICAL detector at the India-based Neutrino Observatory (INO)". In: *Pramana* 88.5 (2017).
(Cited on p: 186.).
DOI: 10.1007/s12043-017-1373-4.

[212] M. A. Acero et al. "First measurement of neutrino oscillation parameters using neutrinos and antineutrinos by NOvA". In: *Phys. Rev. Lett.* 123 (2019).
(Cited on p: 186.).
DOI: 10.1103/PhysRevLett.123.151803.

[213] D. Karlen. "Latest Results from the T2K Neutrino Experiment". In: *Universe* 5.1 (2019), p. 21.
(Cited on p: 186.).
DOI: 10.3390/universe5010021.

[214] DUNE Collaboration et al. *Long-baseline neutrino oscillation physics potential of the DUNE experiment*. 2020.
(Cited on p: 186.).
arXiv: 2006.16043 [hep-ex].

[215] I. Mocioiu and W. Wright. "Non-standard neutrino interactions in the mu–tau sector". In: *Nucl. Phys.* (2015).
(Cited on p: 195.).
DOI: 10.1016/j.nuclphysb.2015.02.016.
arXiv: 1410.6193 [hep-ph].

[216] M. Masud and P. Mehta. "Nonstandard interactions and resolving the ordering of neutrino masses at DUNE and other long baseline experiments". In: *Phys. Rev. D* 94.5 (2016), p. 053007.
(Cited on p: 195.).
DOI: 10.1103/PhysRevD.94.053007.
arXiv: 1606.05662 [hep-ph].

[217] K. N. Deepthi et al. "Can nonstandard interactions jeopardize the hierarchy sensitivity of DUNE?" In: *Phys. Rev. D* 96.7 (2017), p. 075023.
(Cited on p: 195.).
DOI: 10.1103/PhysRevD.96.075023.
arXiv: 1612.00784 [hep-ph].

[218] P. Coloma, H. Minakata, and S. J. Parke. "Interplay between appearance and disappearance channels for precision measurements of θ_{23} and δ_{CP}". In: *Physical Review D* 90.9 (2014). ISSN: 1550-2368.
(Cited on p: 202.).
DOI: 10.1103/physrevd.90.093003.

[219] A. Chatterjee et al. "Octant sensitivity for large θ_{23} in atmospheric and long-baseline neutrino experiments". In: *Journal of High Energy Physics* 2013.6 (2013). ISSN: 1029-8479.
(Cited on pp: 202, 204.).
DOI: 10.1007/jhep06(2013)010.

[220] H. Minakata et al. "Reactor measurement of theta(13) and its complementarity to long baseline experiments". In: *Phys. Rev. D* 68 (2003). [Erratum: Phys.Rev.D 70, 059901 (2004)], p. 033017.
(Cited on p: 202.).
DOI: 10.1103/PhysRevD.70.059901.
arXiv: hep-ph/0211111.

[221] K. Hiraide et al. "Resolving θ_{23} degeneracy by accelerator and reactor neutrino oscillation experiments". In: *Physical Review D* 73.9 (2006). ISSN: 1550-2368.
(Cited on p: 202.).
DOI: 10.1103/physrevd.73.093008.

[222] S. K. Raut. *Synergies and complementarities between proposed future neutrino projects*. 2017.
(Cited on pp: 203, 204.).
arXiv: 1712.02096 [hep-ph].

[223] Y. Fukuda et al. "Evidence for oscillation of atmospheric neutrinos". In: *Phys. Rev. Lett.* 81 (1998), pp. 1562–1567.
(Cited on pp: 217, 235.).
DOI: 10.1103/PhysRevLett.81.1562.
arXiv: hep-ex/9807003.

[224] K. Abe et al. "Indication of Electron Neutrino Appearance from an Accelerator-produced Off-axis Muon Neutrino Beam". In: *Phys. Rev. Lett.* 107 (2011).
(Cited on pp: 217, 235.).
DOI: 10.1103/PhysRevLett.107.041801.
arXiv: 1106.2822 [hep-ex].

[225] P. A. Zyla et al. "Review of Particle Physics". In: *PTEP* 2020.8 (2020), p. 083C01.
(Cited on pp: 219, 237.).
DOI: 10.1093/ptep/ptaa104.

[226] Jiajun Liao, Danny Marfatia, and Kerry Whisnant. "Degeneracies in long-baseline neutrino experiments from nonstandard interactions". In: *Phys. Rev. D* 93.9 (2016), p. 093016.
(Cited on pp: 220, 238.).
DOI: 10.1103/PhysRevD.93.093016.
arXiv: 1601.00927 [hep-ph].

[227] J. Hofestädt, M. Bruchner, and T. Eberl. *Super-ORCA: Measuring the leptonic CP-phase with Atmospheric Neutrinos and Beam Neutrinos*. 2019.
(Cited on pp: 233, 250.).
arXiv: 1907.12983 [hep-ex].

Publications

Journals:

- **Search for Neutrino Non-Standard Interactions with 10 years of ANTARES data.**
  In Collaboration review.
- **Sensitivity towards Neutrino Non-Standard Interactions with KM3NeT-ORCA.**
  In preparation.

Proceedings:

- **Neutrino Oscillations and Non-Standard Interactions with KM3NeT-ORCA.**
  2004.05004
- **Sensitivity to Non-Standard Interactions (NSIs) with KM3NeT-ORCA.**
  PoS(ICRC2019)931

Internal Notes:

- **Sensitivity to Non-Standard Interactions (NSIs) and it's implications on the Neutrino Mass Ordering (NMO) measurement at KM3NeT-ORCA.**
  ORCA-PHYS/2019-001

Acknowledgements

First and foremost, I am grateful to my supervisors, **Pr. Juande Zornoza** and **Pr. Sergio Navas**, for imbibing me in this group and offering me the opportunity to work within the ANTARES and KM3NeT Collaborations. I thank them for their extreme patience, relentless guidance and immense support throughout my doctorate. I also want to thank them for spending countless hours on reviewing this document. ¡Muchísimas Gracias!

I'm also grateful to the members of my doctoral committee: **Pr. Nuria Rius**, **Pr. Jose Illana**, **Pr. Mariam Tortola**, **Pr. João Coelho**, **Pr. Dmitry Zabarov** and **Pr. Mathieu Terrin** for spending their invaluable time on reviewing and assessing my dissertation.

This thesis would have been significantly less aesthetically pleasing without the inputs and comments from **Pr. Juanjo Hernández**. He has been an incredible reviewer and an outstanding support. Thanks to **Pr. Juan Zuniga** for always helping me with the formalities of the Doctoral School of University of Valencia.

This work would not have been possible without the help of my long-time office colleague and friend, **Dr. Tarak Thakore**. Thank you so much for all the helpful discussions, recommendations and for sharing your in-depth knowledge on the field. Working with you has been a pleasure!

I have been fortunate to count on the knowledge and expertise of **Pr. Juergen Brunner**, the working group leader of ORCA oscillations. Thanks for letting me present in the oscillation sessions for numerous times over the past 3 years. I'd also like to thank **Pr. Miguel Ardid** and **Pr. Yahya Tayalati** for letting me present in the ANTARES exotics sessions. I'd like to acknowledge **Pr. Dorothea Samtleben**, **Pr. Thomas Eberl**, **Pr. Carla Distefano** and **Pr. Piotr Mijakowski** for reviewing my contributions on multiple occasions.

I'd like to thank **Pr. Marco Agniholfi** for accepting me at INFN, Genoa for a research stay. Especially, thanks to **Dr. Alba Domi** for making sure I was not feeling alone and taking me around Genoa. I'd like to thank **Pr. Srubabati Goswami** for accepting me at PRL, Ahmedabad for another research stay and being very cooperative with logistical constraints.

I take this opportunity to express my gratitude to **Pr. Rudrajyoti Palit** for offering me to work in his group in the INGA experiment at TIFR, Mumbai. He has given me the freedom to explore my research interests and pursue my passion.

None of this would have happened, were it not for **Pr. Jim Libby**, who offered me to work in his group during my Master's project. My first venture into the field of neutrino oscillations happened under his guidance in the INO experiment. I'd also like to thank **Dr. Rajan Rebin**, who mentored me during my formative years at IIT, Madras.

I'd like to thank my colleagues in ANTARES/KM3NeT Collaborations: **Dr. Alba Domi**, **Dr. Mukharbek Organokov**, **Dr. Salvadore Palacios**, **Nhan Chau**, **Dr. Agustin Sanchez**, **Dr. Steffen Hallman**, **Dr. Jannik Hofestaedt** for the interesting discussions. Special thanks to **Dr. Simon Bourret**, **Dr. Joao Coelho** and **Dr. Ilenia Salvdori** whose software development laid the ground work for this thesis. Heartfelt thanks to **Dr. Ankur Sharma**

for swapping PhD-war-stories and always being there for me, be it academic or non-academic concerns.

The ANTARES/KM3NeT group at IFIC is like a close-knit family. Thanks to **Dr. Moritz Lotze**, **Dr. Javier Marti**, **Dr. Giullia Illuminati**, **Dr. Marta Colomer**, **Dr. Rebecca Gozzini**, **Dr. Paco Salesa**, **Victor Carratero**, **Sergio Alves**, **Jerzy Manzack**, **Camiel Peterse**, **Juan Palacios** for making the office hours joyful.

I am thankful to the entire **ANTARES and KM3NeT Collaborations**. Ours is a relatively small collaboration, where everyone is very approachable and everybody knows each other by their first name. Thank you everybody for treating me no different.

I acknowledge the technical support of **Ifremer**, **AIM** and **Foselev Marine** for the sea operations and the **CC-IN2P3** for the computing facilities.

My life at Valencia was more enjoyable for the friends I made here. Thanks to **Dr. Mehran Zahiri**, **Dr. Anantha Kumar**, **Dr. Arka Santra**, **Dr. Sanjoy Mandal**, **Dr. Rafi Alam**, **Dr. Mouli Chakroborty**, **Dr. Rusa Mandal**, **Dr. Rahul Srivastava** for the potlucks and dinner outings. Special thanks to **Dr. Masud Mehedi** for letting me stay at his place on my arrival to Spain and for the insightful discussions on neutrino phenomenology.

Gratitude is also due to the **Administrative, Informatic, Electronic, Mechanical and Maintenance** members of the **Parque Científico** in general, and of **IFIC** in particular, for creating an international ambience conducive to research. **Ms. Elena Pastor** and **Mrs. Maria Jose** deserves special mention for helping me with the paperworks.

I gratefully acknowledge the financial support of the **Programa Estatal de Promoción del Talento y su Empleabilidad en I+D+i** (ref. FPA2015-65150-C3-1-P) throughout my doctoral tenure.

A life in Spain would have been incomplete without having to play football. I appreciate the efforts of the **Football group**, the **Beach Volley group** and the **Swimming club** as a whole in organising the games, that formed the most of my social life in Valencia. I really looked forward to the match days every week.

I am fortunate to have wonderful friends, who have accompanied me on my journey through my doctoral years. I'd like to thank **Suvasis Swain**, **Farhan Babra**, **Sazedur Laskar**, **Anustup Chakroborty**, **Uttiya Sarkar**, **Subhajit Ghosh**, **Sabir Ali**, **Joydeep Datta**, **Nishat Fiza**, **Pallabi Bhuyan**, **Chayan Majumdar**, **Supriya Senapati** for the close times we have shared. All soon to-be-doctors! I'd like to acknowledge **Dr. Shamik Bhattacharjee** for helping me pick-up Python and credit the Machine Learning course together.

Thanks to the **people in Valencia** in general for hosting me and making my stay eventful and memorable. I will cherish the memories forever. ***Nunca perderé la oportunidad de pasar por aquí!***

Thank you to **Dr. Farhat Fatima** for all her love and patience. Let's try to live in the same country from now on.

My beloved **mother** and twin **brother** have been a constant support of my desire to pursue research and have tolerated my absence since many years. I will be forever indebted to the sacrifices they made to put me at this position.

Finally, I thank **everyone** whose names I happen to miss.

ANTARES has received funding from the following agencies:
Centre National de la Recherche Scientifique (CNRS), Commissariat à l'énergie atomique et aux énergies alternatives (CEA), Commission Européenne (FEDER fund and Marie Curie Program), Institut Universitaire de France (IUF), LabEx UnivEarthS (ANR-10-LABX-0023 and ANR-18-IDEX-0001), Région Ile-de-France (DIM-ACAV), Région Alsace (contrat CPER), Région Provence-Alpes-Côte d'Azur, Département du Var and Ville de La Seyne-sur-Mer, France; Bundesministerium fur Bildung und Forschung (BMBF), Germany; Istituto Nazionale di Fisica Nucleare (INFN), Italy; Nederlandse organisatie voor Wetenschappelijk Onderzoek (NWO), the Netherlands; Council of the President of the Russian Federation for young scientists and leading scientific schools supporting grants, Russia; Executive Unit for Financing Higher Education, Research, Development and Innovation (UEFISCDI), Romania; Ministerio de Ciencia, Innovación, Investigación y Universidades (MCIU): Programa Estatal de Generación de Conocimiento (refs. PGC2018-096663-B-C41, -A-C42, -B-C43, -B-C44) (MCIU/FEDER), Severo Ochoa Centre of Excellence and MultiDark Consolider (MCIU), Junta de Andalucìa (ref. SOMM17/6104/UGR and A-FQM-053-UGR18), Generalitat Valenciana: Grisolìa (ref. GRISOLIA/2018/119), Spain; Ministry of Higher Education, Scientific Research and Professional Training, Morocco.

KM3NeT is funded by the following agencies:
Agence Nationale de la Recherche (contract ANR-15-CE31-0020), Centre National de la Recherche Scientifique (CNRS), Commission Europèenne (FEDER fund and Marie Curie Program), Institut Universitaire de France (IUF), IdEx program and UnivEarthS Labex program at Sorbonne Paris Citè (ANR-10- LABX-0023 and ANR-11-IDEX-0005-02), Paris Ile-de-France Region, France; Shota Rustaveli National Science Foundation of Georgia (SRNSFG, FR-18- 1268), Georgia; Deutsche Forschungsgemeinschaft (DFG), Germany; The General Secretariat of Research and Technology (GSRT), Greece; Istituto Nazionale di Fisica Nucleare (INFN), Ministero dell'Istruzione, dell'Università e della Ricerca (MIUR), PRIN 2017 program (Grant NAT-NET 2017W4HA7S) Italy; Ministry of Higher Education, Scientific Research and Professional Training, Morocco; Nederlandse organisatie voor Wetenschappelijk Onderzoek (NWO), the Netherlands; The National Science Centre, Poland (2015/18/E/ST2/00758); National Authority for Scientific Research (ANCS), Romania; Ministerio de Ciencia, Innovación, Investigación y Universidades (MCIU): Programa Estatal de Generación de Conocimiento (refs. PGC2018-096663-B-C41, -AC42, -B-C43, -B-C44) (MCIU/FEDER), Severo Ochoa Centre of Excellence and MultiDark Consolider (MCIU), Junta de Andalucía (ref. SOMM17/6104/UGR), Generalitat Valenciana: Grisolía (ref. GRISOLIA/2018/119) and GenT (ref. CIDEGENT/2018/034) programs, La Caixa Foundation (ref. LCF/BQ/IN17/11620019), EU: MSC program (ref. 713673), Spain.